SAND2000-1369
Unlimited Release
Printed June 2000

Proceedings of 1999 US/Japan Workshop (99FT-05) On High Heat Flux Components and Plasma Surface Interactions For Next Fusion Devices

Santa Fe, NM
November 1 – 4, 1999

Edited by

Richard Nygren and Diana Stavros
Fusion Technology Department, 6428
Sandia National Laboratories
P. O. Box 5800
Albuquerque, New Mexico 87185-1129

Abstract

The 1999 US-Japan Workshop on High Heat Flux Components and Plasma Surface Interactions in Next Step Fusion devices was held at the St. Francis Hotel in Santa Fe, New Mexico, on November 1-4, 1999. There were 42 presentations as well as discussion on technical issues and planning for future collaborations. The participants included 22 researchers from Japan and the United States as well as seven researchers from Europe and Russia.

There have been important changes in the programs in both the US and Japan in the areas of plasma surface interactions and plasma facing components. The US has moved away from a strong focus on the ITER Project and has introduced new programs on use of liquid surfaces for plasma facing components, and operation of NSTX has begun. In Japan, the Large Helical Device began operation. This is the first large world-class confinement device operating in a magnetic configuration different than a tokamak. In selecting the presentations for this workshop, the organizers sought a balance between research in laboratory facilities or confinement devices related to plasma surface interactions and experimental research in the development of plasma facing components. In discussions about the workshop itself, the participants affirmed their preference for a setting where "work-in-progress" could be informally presented and discussed.

DISCLAIMER

Table of Contents

Plasma Edge Studies – 1

Helical Divertor Installation and Its Impact on LHD Plasmas

Presented by N. Noda
National Institute for Fusion Science

Contents

LHD (Large Helical Device) Project

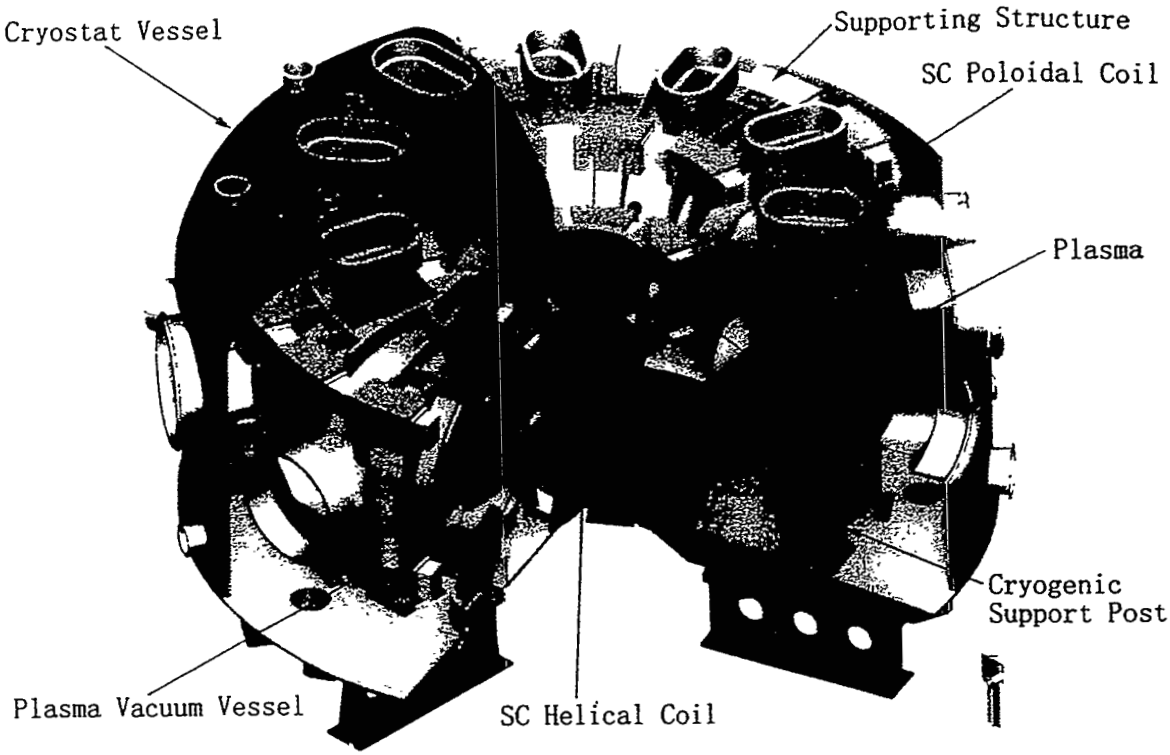

Specifications of LHD device

	Target Phase I (II)	Operation 1st-3^{rd}cycle exp.
Major radius	3.9 m	
Plasma radius	0.5-0.65m	
Plasma volume	20-30m^3	
l/m, ι(0)/ι(a)	2/10, <0.5/1	
B_0/B_{max}	3/6.6T (4/9.2T)	2.75T
LHe temp.	4.4K (1.8K)	
Magnetic energy	0.9GJ (1.6GJ)	
Plasma duration	10s – CW	0.5-35s
Heating power		
ECRH	10MW	0.9MW (84GHz,168GHz)
NBI	180keV/15MW (20MW)	150keV/4.2MW
ICRF	3MW(12MW)	1.0MW

Features & Requirements for LHD Divertor

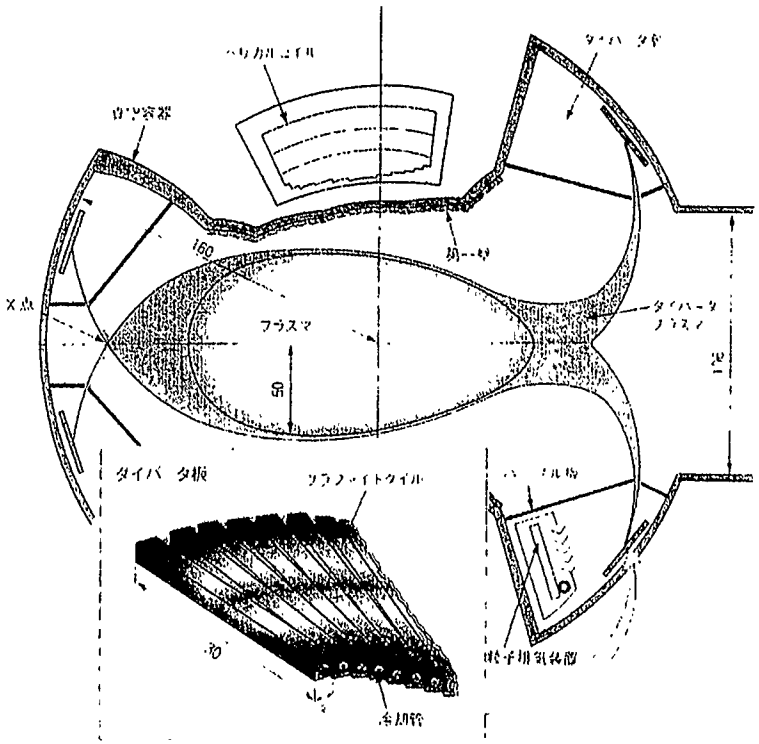

- Double null, 4 legs
- Helically running,
  3-dimensional
- Direction of mag. field lines at striking point is poloidal
  → Discrete bar array

- Heat load to divertor targets
  20 MW /10s pulse 5 MW/m^2
  3MW/steady state 0.75 MW/m^2
- Heat load to vacuum vessel
  20 MW /10s pulse 0.1 MW/m^2
  3MW/steady state 0.015 MW/m^2

N. Noda

Divertor Element →

graphite armor + copper heat sink
bolted to stainless steel cooling pipe
typical size 250 x 100 x 12

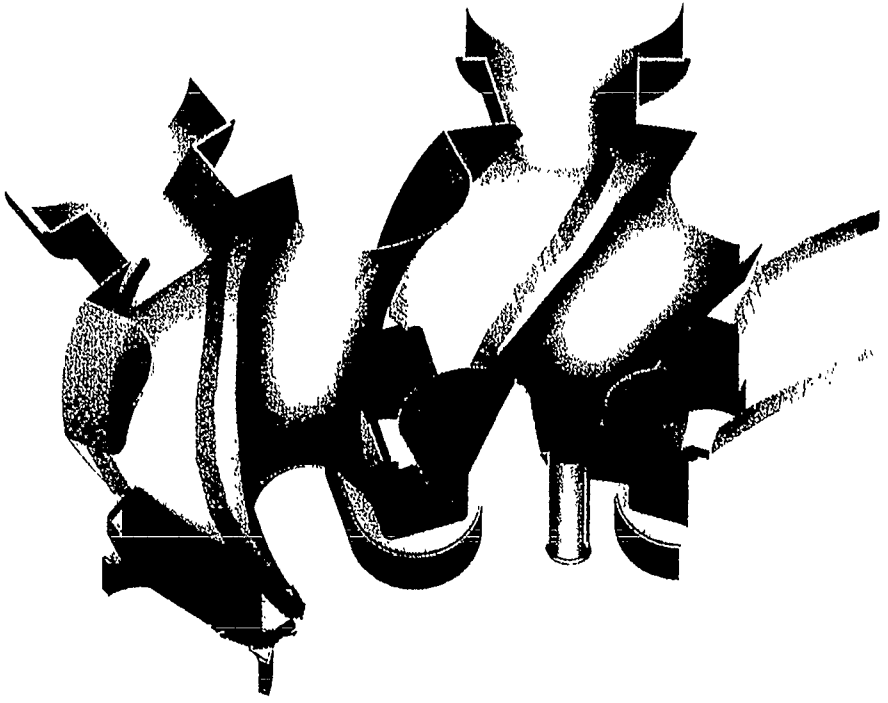

1 unit
poloidal angle 180°

40 units in total
number of C tiles
--- around 1700

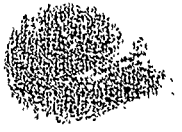

NIF

N. Nada

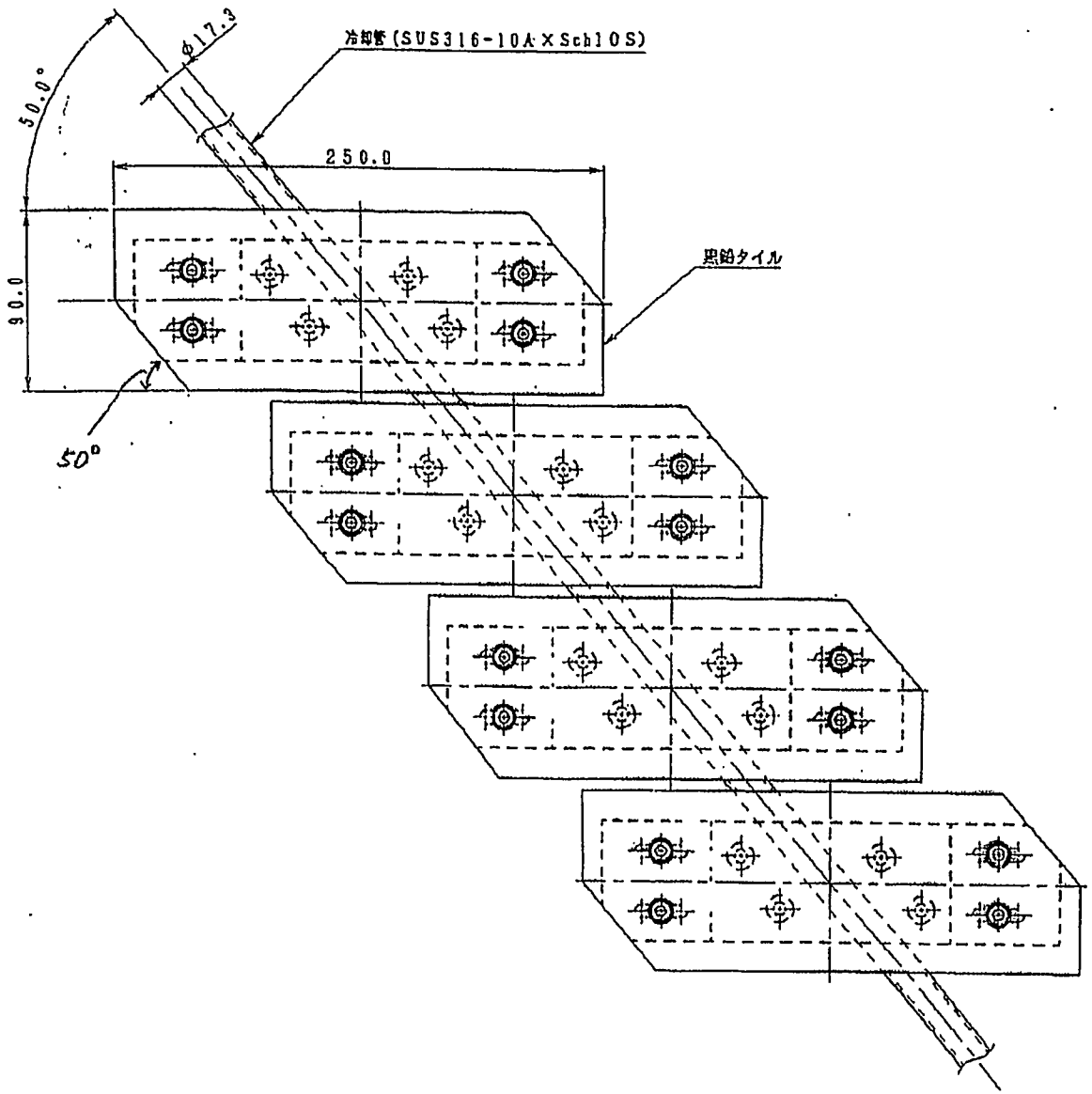
冷却管(SUS316-10A×Sch10S)
φ17.3
50.0°
250.0
90.0
黒鉛タイル
50°

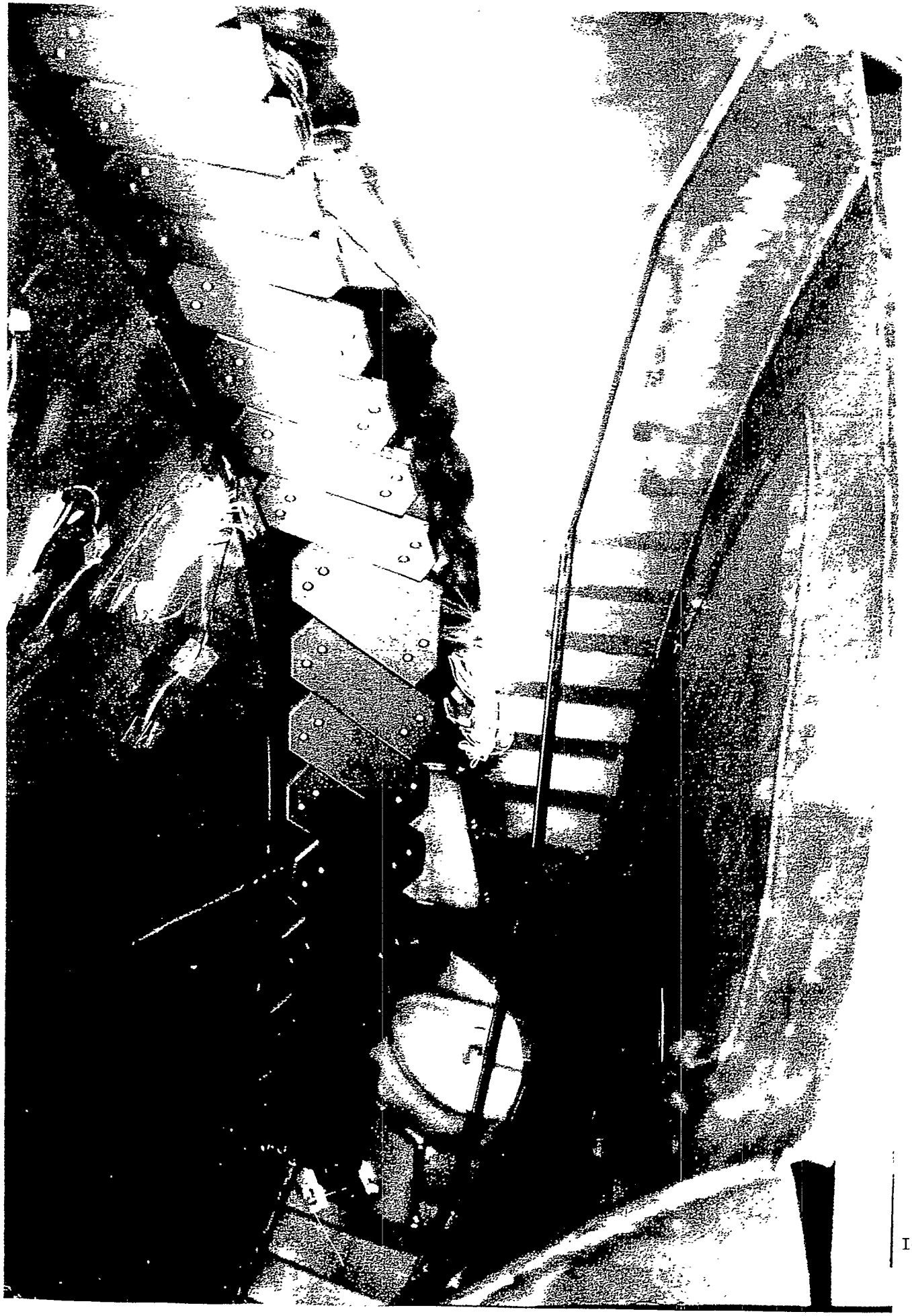

Outside of the torus,

Horizontal + tangential port holes cooling pipe is going around the tangential port and the target plates are inside the port hole

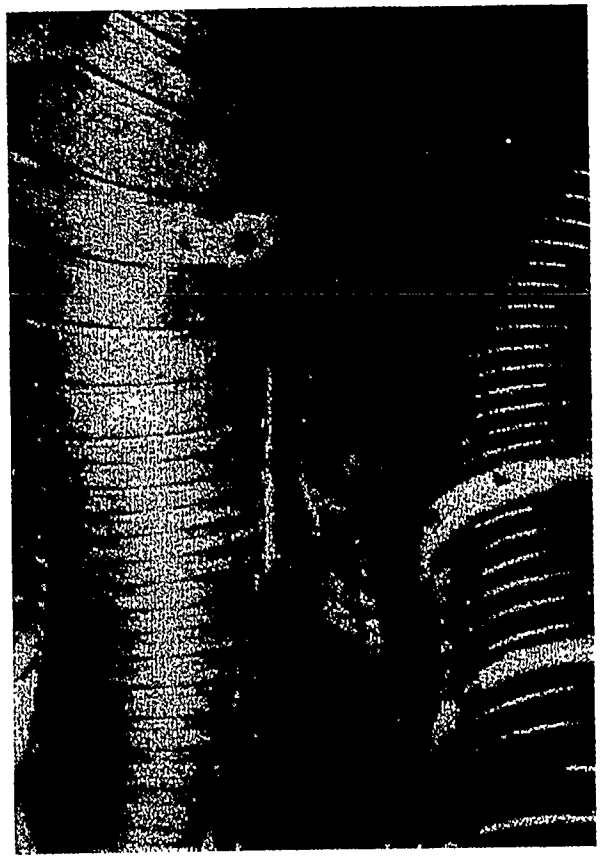

↑

Inside of torus

without port hole

N. Noda

Heat Removal Capability improved up to 2 MW/m^2

1. C armor + Cu heat sink + SS tube (present)
2. Cu heat sink from OF-Cu to DS-Cu

3 – 6 , heat sink unified with graphite armor

3 → 5 optimization of carbon sheet

6 : copper cooling tube

Results of heat load test by electron beam

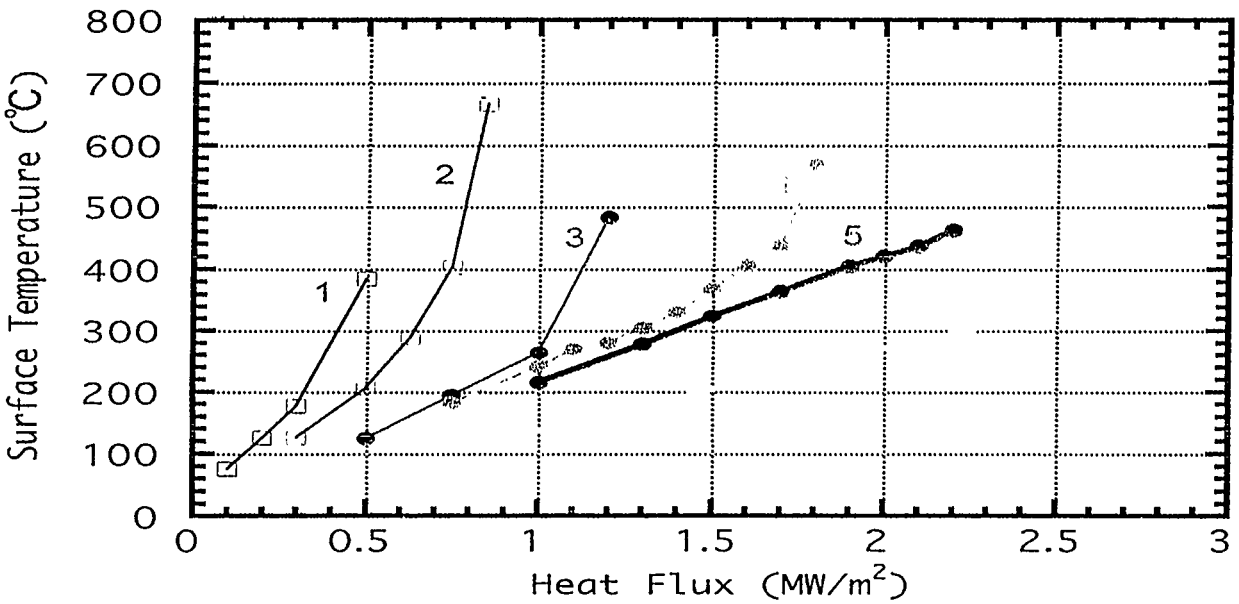

Divertor Element
(armor bolted to heat sink)

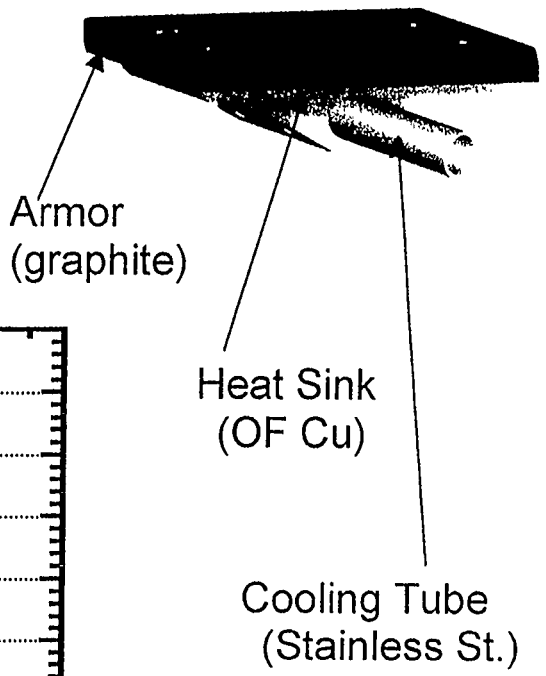

N. Noda

Impurities

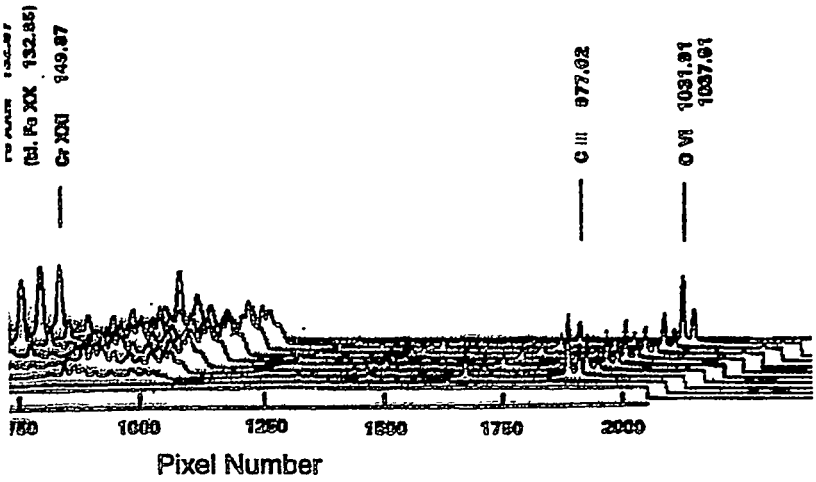

- Befor
tile in
#6616
$B_t = 2$
and F

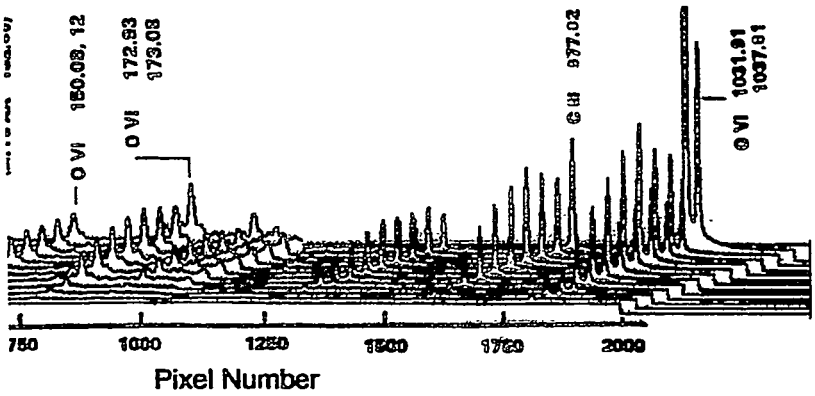

- After
tile in
#8355
$B_t = 2$
and F

orbed from the stainless-steel wall are reduced ex
use the iron emission line for the spectroscopic r
ature.

$P_{rad}(r)$ is reduced in central region

W/O C divertor

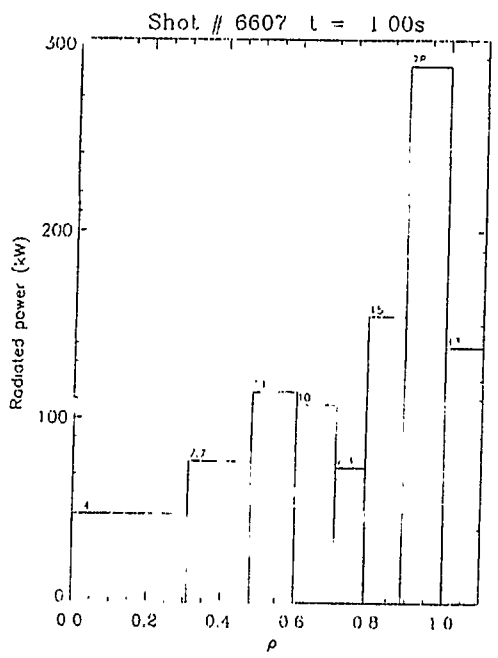

With C divertor

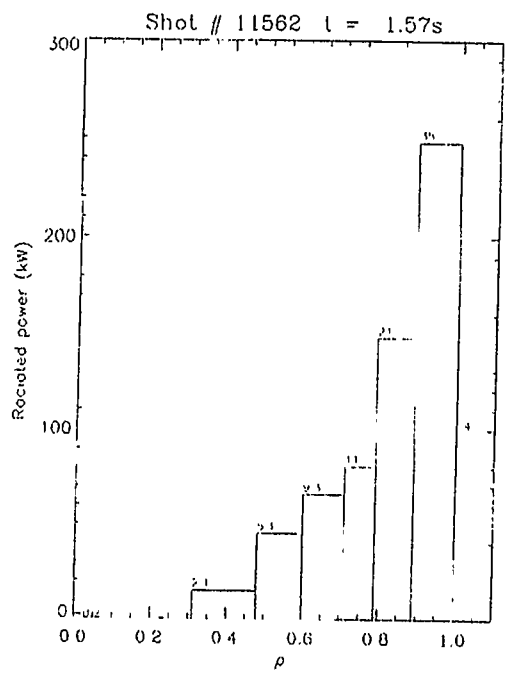

$n_e = 3.3E19/m^3$

$P_{in} = 3.4$ MW

B= 2.5 T
for #6607

B= 2.75 T
for #11562

$R_{axis} = 3.6$ m

After V. J. Peterson

N. Noda

Soft X-ray is reduced in central region with C divertor

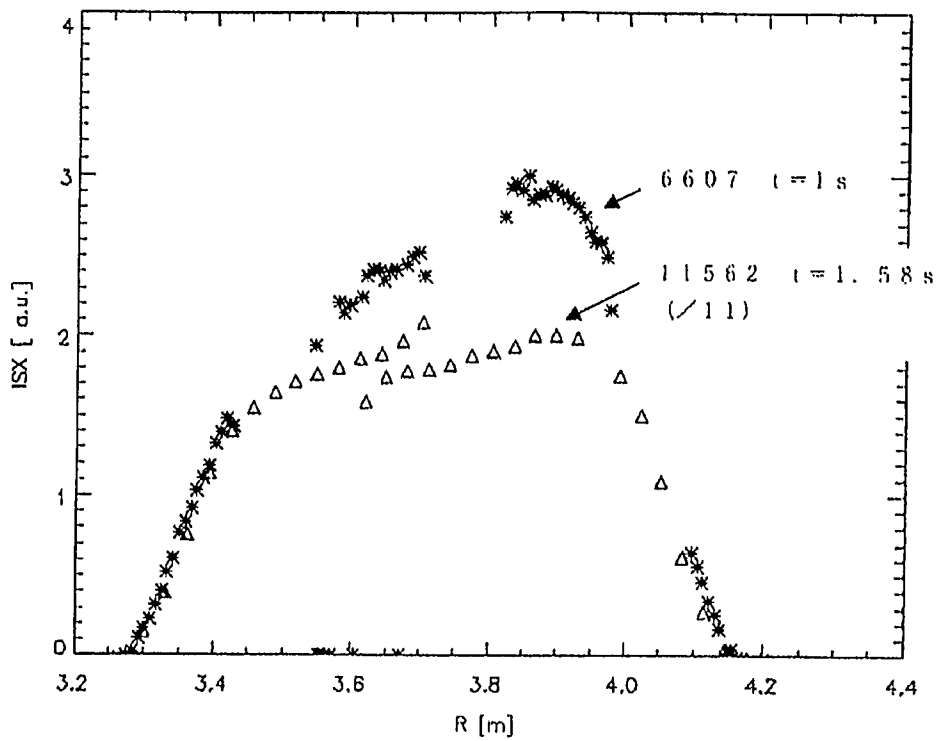

N. Noda

Heating devices

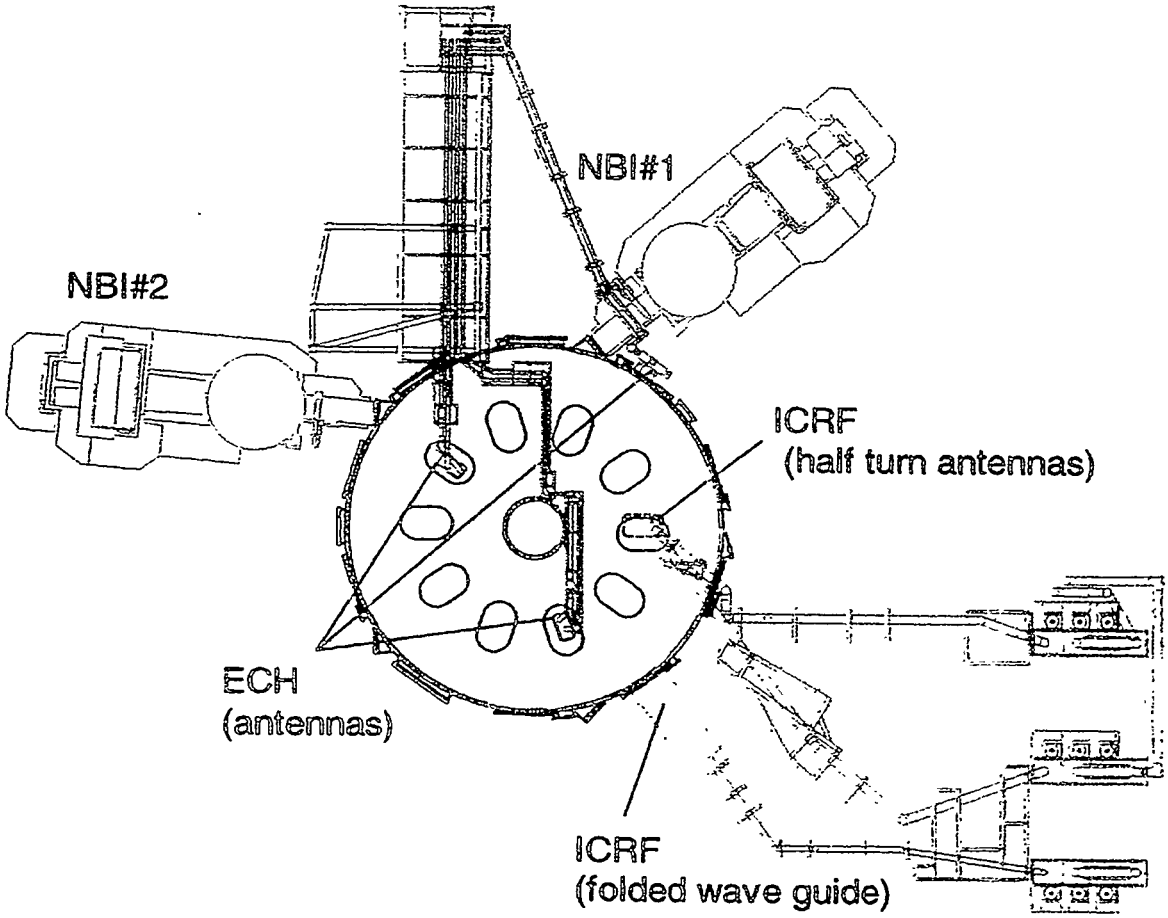

ECH (82.6, 84 and 168 GHz)

- Two upper and one outer ports are used for injection, and two transmission lines are installed in each port.

NBI (two 180 keV, 7.5 MW beams for 10 s, and also one 100 keV, 0.5 MW beam for 90s)

- Two negative ion based NBI are aligned for tangential injection in opposite directions (co- and counter-injection).

ICRF (25-100 MHz)

- Two kinds of wave launchers are prepared; one pair of loop antennas and a folded wave guide.

Highest temperature NBI plasma

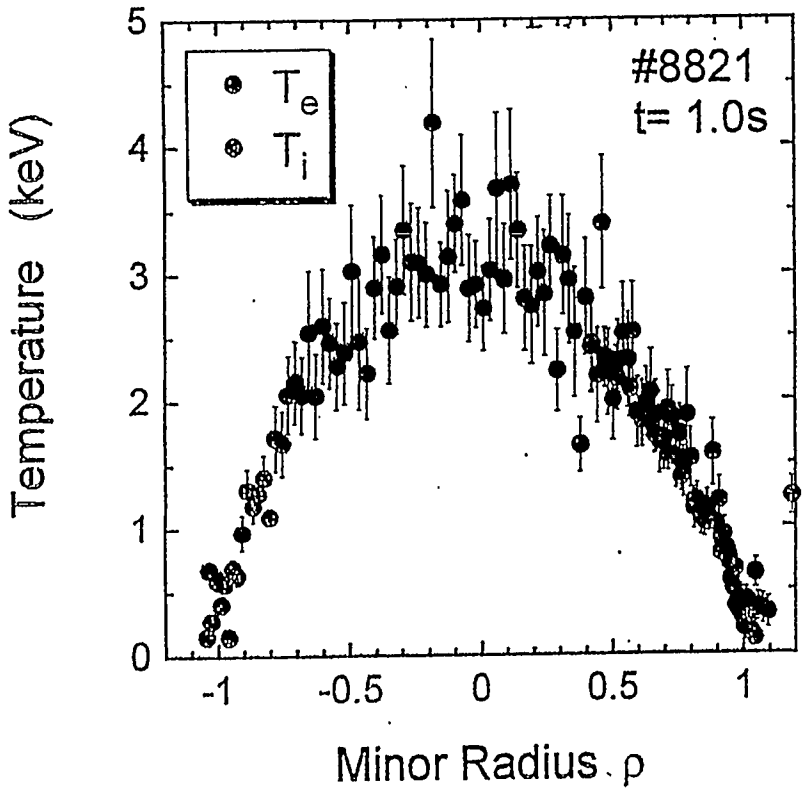

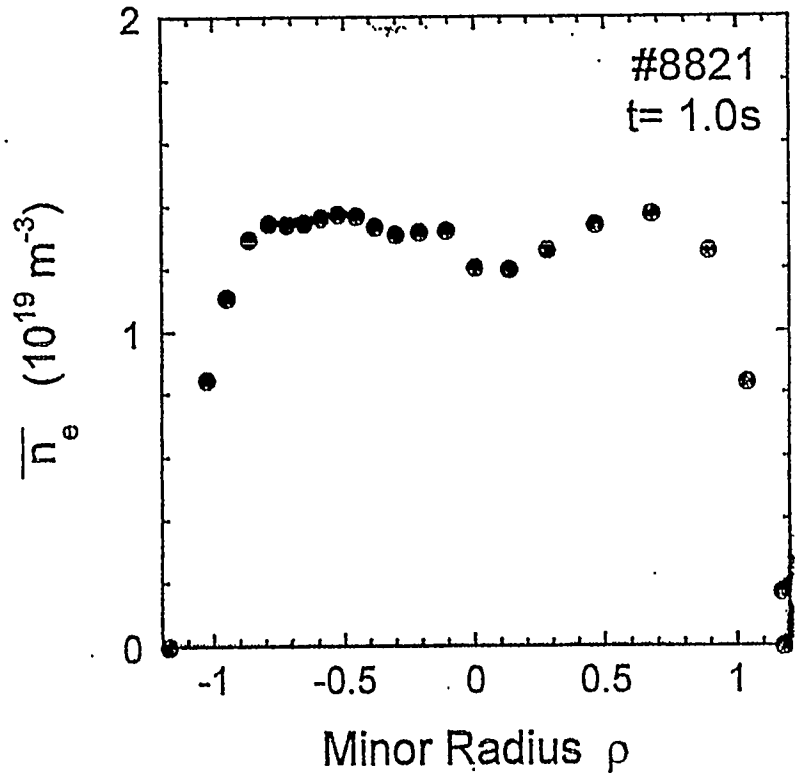

- B_t = 2.75 T, R_{ax} = 3.6 m and P_{abs} = 2.6 MW
  $T_e(0)$ = 3.3 keV and $T_i(0.4)$ = 2.4 keV
- High edge temperatures
- Ne puffing is required for *Ti* profile measurement by the charge exchange recombination spectroscopy.

Pellet injection experiment

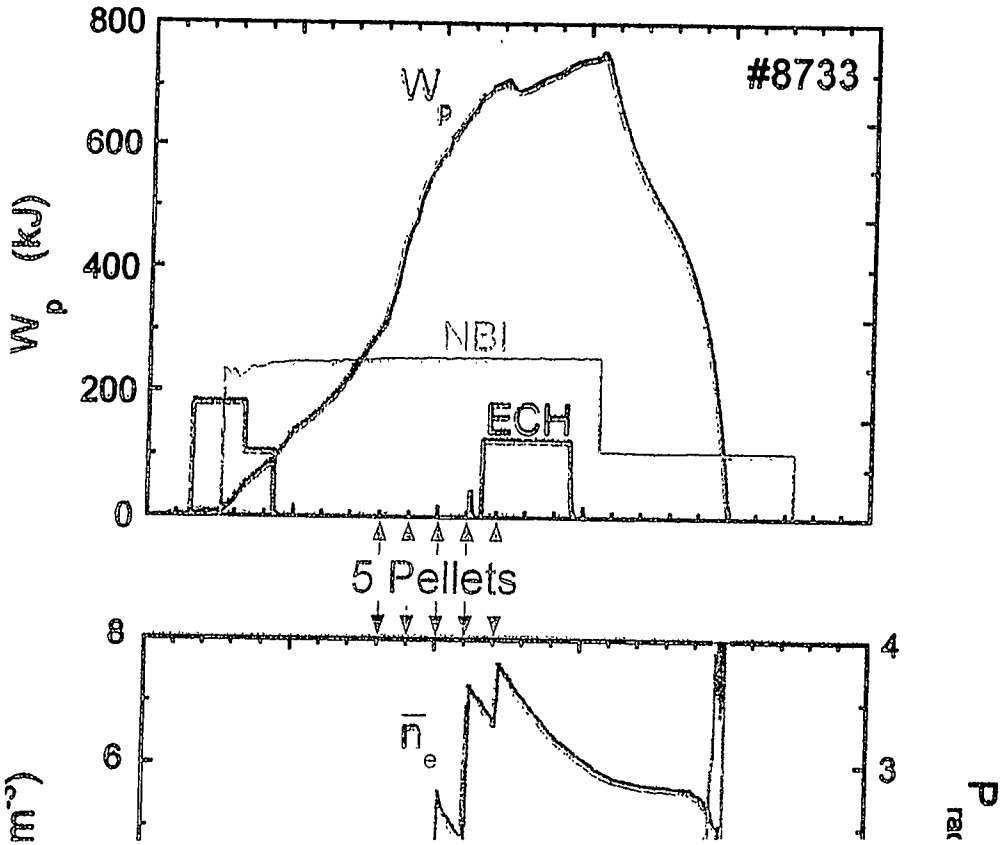

- **Experimental Conditions**
  - B_t = 2.75 T
  - R_{ax} = 3.6 m
  - $T_e(0)$ of target plasma = 2.5keV
- Successful sequence of pellets
  - Density n_e increases up to 7.7×10^{19} m^{-3}.
  - Stored energy Wp is raised up to 750 kJ.

Highest temperature ECH plasma

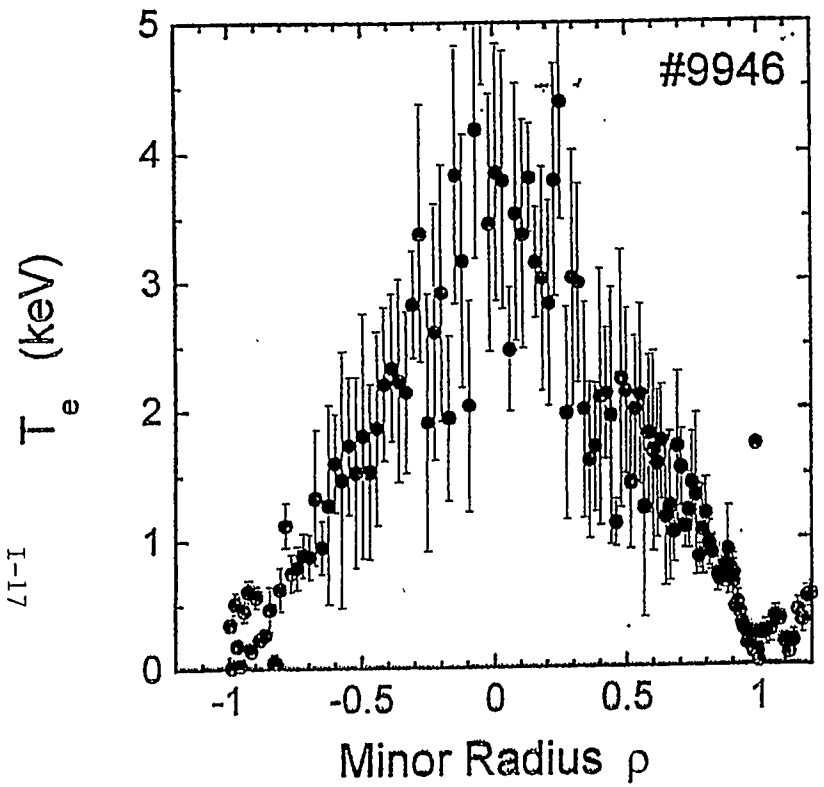

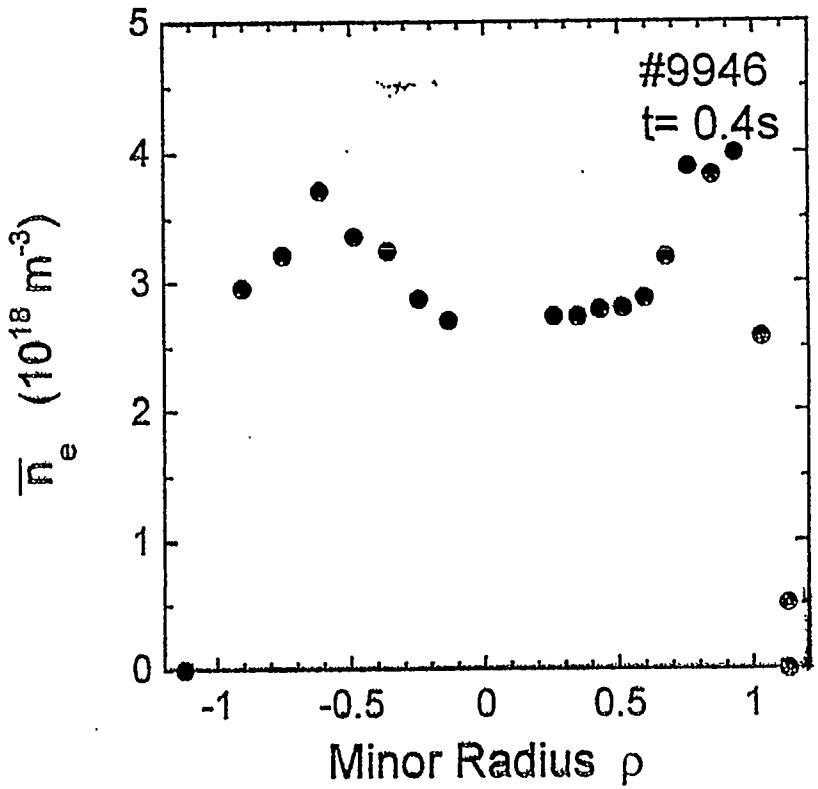

- B_t = 2.75 T and R_{ax} = 3.6 m.
- ECH beams from the upper ports do not cross the resonance zones. There are the resonance zones at ρ = -0.2 ~ -0.3 for the ECH beams from the outer port.
- Total Input power = 0.88 MW; one 84 + two 82.6 GHz (0.25 s) = 0.48 MW and three 168 GHz (0.2 s) = 0.4 MW
- *Te* is an averaged value from 0.32 s to 0.42 s. *Wp* = 70 kJ and $n_e = (3 - 5)\times10^{18}$ m^{-3}.

ICRF heating

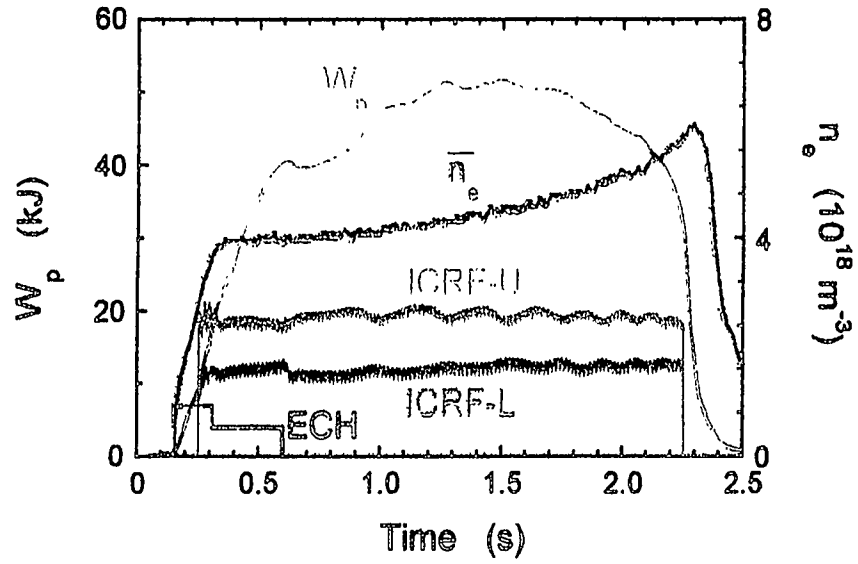

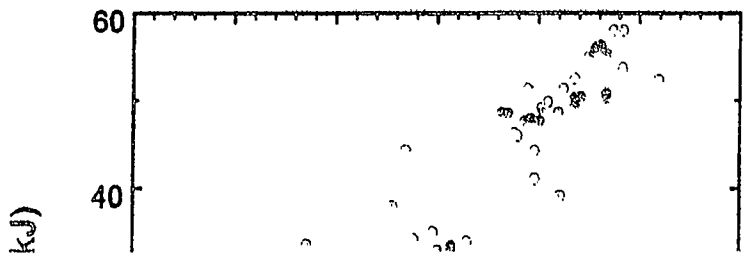

ICRF conditions

One pair of half turn antennas for fast wave heating

Frequency = 38.47 MHz

Distance from the LCFS = 3 cı

Coupling resistance = 5 Ohm

(0.8 Ohm in vacuum

Input power= 500 kW

Experimental Conditions

B_t = 2.75 T and R_{ax} = 3.6 m

H/(He+H) = 50%

ECH target plasma

n_e = (3-4)x10^{18} m^{-3}

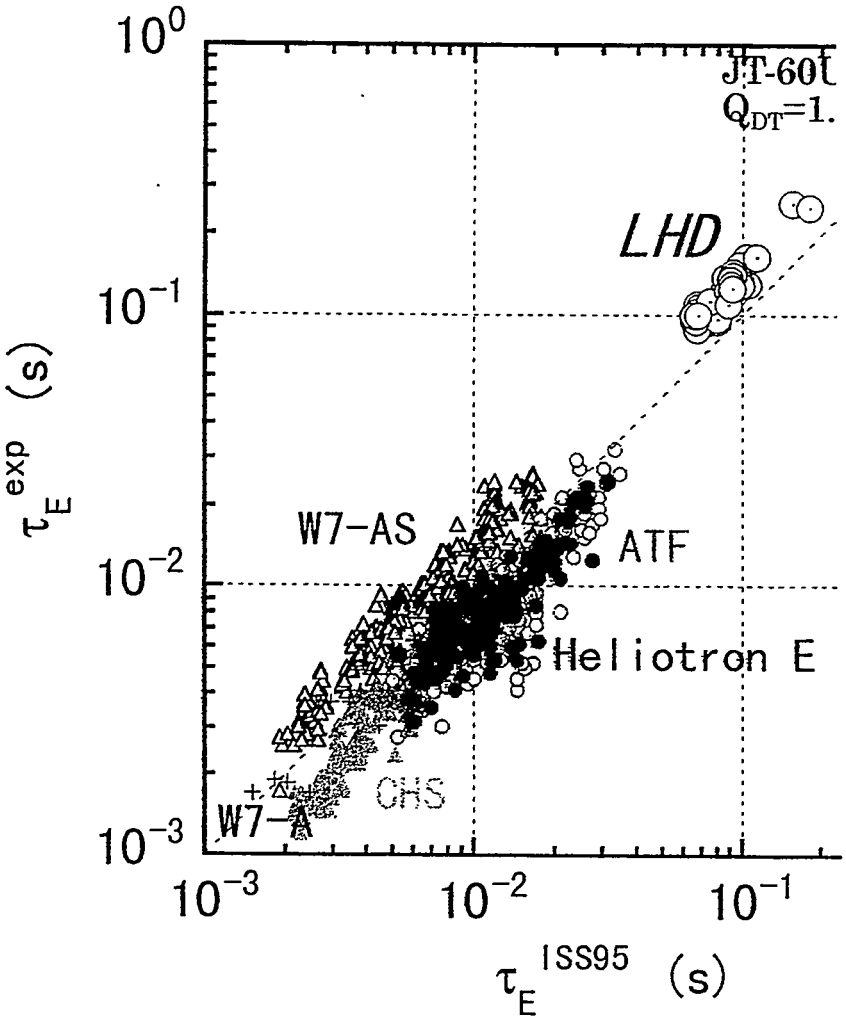

International Stellarator Scal
Based on International Collab
on Stellarator Database

$$\tau_E^{ISS95} = 0.08a^{2.21} R^{0.65} P^{-0.59} \bar{n}_e^{0.51} E$$

◎ **LHD has achieved the targe**

◎ **Experiments of helical devi**
extended to a large tokamaks

Summary

1. Full helicai divertor has been successfully installed
2. Divertor consists of graphite armors, OFC heat-sinks and SS cooling tubes.
3. Total length of the divertor is aound 180 m
4. One unit corresponds to half turn in poloidal direction.
5. The divertor has 40 units and total number of the tiles is close to 1700.
6. Clear reduction has been observed in iron impurity radiations, central bolometric and soft X-ray signals.
7. The following parameters have been achieved with high power, short pulse operation

   $T_e(0) \sim 4$ keV (ECH), 3.5 keV (NBI)
   n_e-bar ~ 8E19/m^3
   Stored Energy ~ 800 kJ (not simultaneously)
   $n\tau T \sim 2$ E19 keVs/m^3

N. Noda

Long Pulse Discharges in LHD

Presented by N. Noda

National Institute for Fusion Science

Contents

- Aims
- Vacuum Vessel & Divertor Cooling
- Long Pulse Discharges with NB
  Development of stable discharges
  "Breathing" Oscillation
- Possibilities in ICRF and ECH
- Summary & Future Plan

Long Pulse Operation in LHD

- ✧Long-pulse steady-state is one of major milestones of present fusion research.
- ✧It is one of main programs of the LHD project.
- ✧3MW, > 60 min. is near-term target in LHD.
- ✧Aims are to investigate physics and technological issues for steady-state operations, such as heat and particle removal, net erosion of divertor plates, real time control of field etc.

NIFS

N. Noda

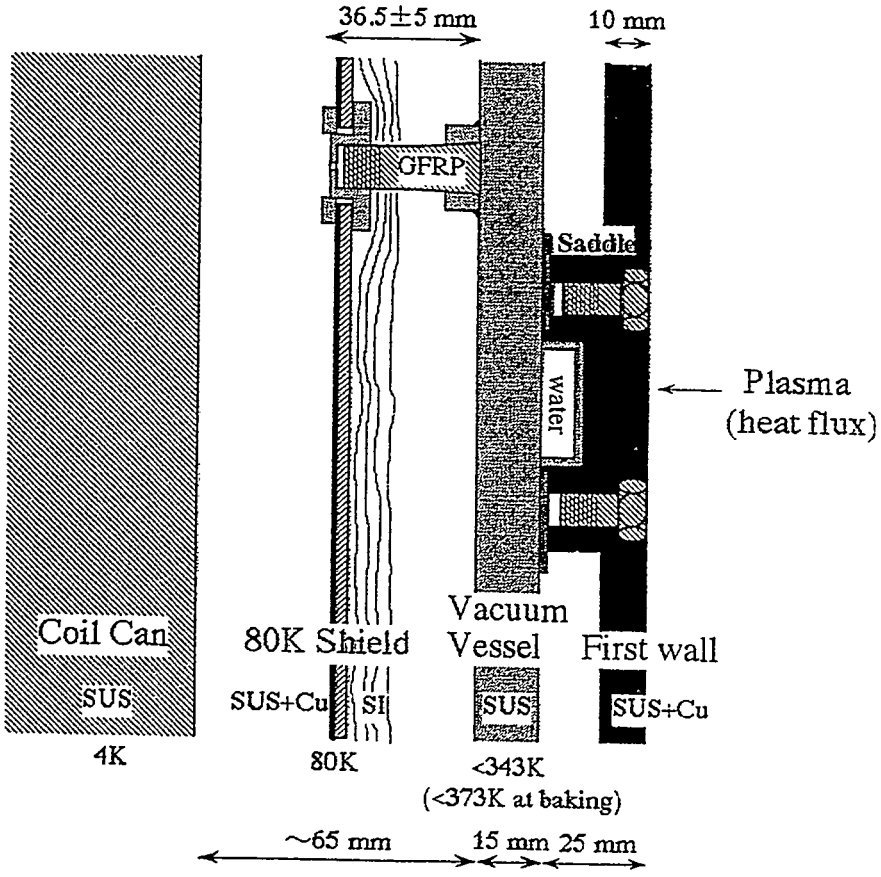
36.5±5 mm
10 mm
GFRP
Saddle
water
Plasma
(heat flux)
Coil Can
SUS
4K
80K Shield
SUS+Cu
SI
80K
Vacuum
Vessel
SUS
<343K
(<373K at baking)
First wall
SUS+Cu
~65 mm
15 mm
25 mm

Progress in Long Pulse Discharge by NBI

- Operational regime of steady state plasma was limited to low density region (< 0.5 x 10^{19} m^{-3}) by "breathing" oscillation.

- After installation of carbon divertor, no "breathing" oscillation was observed and it was possible to operate with high plasma density.

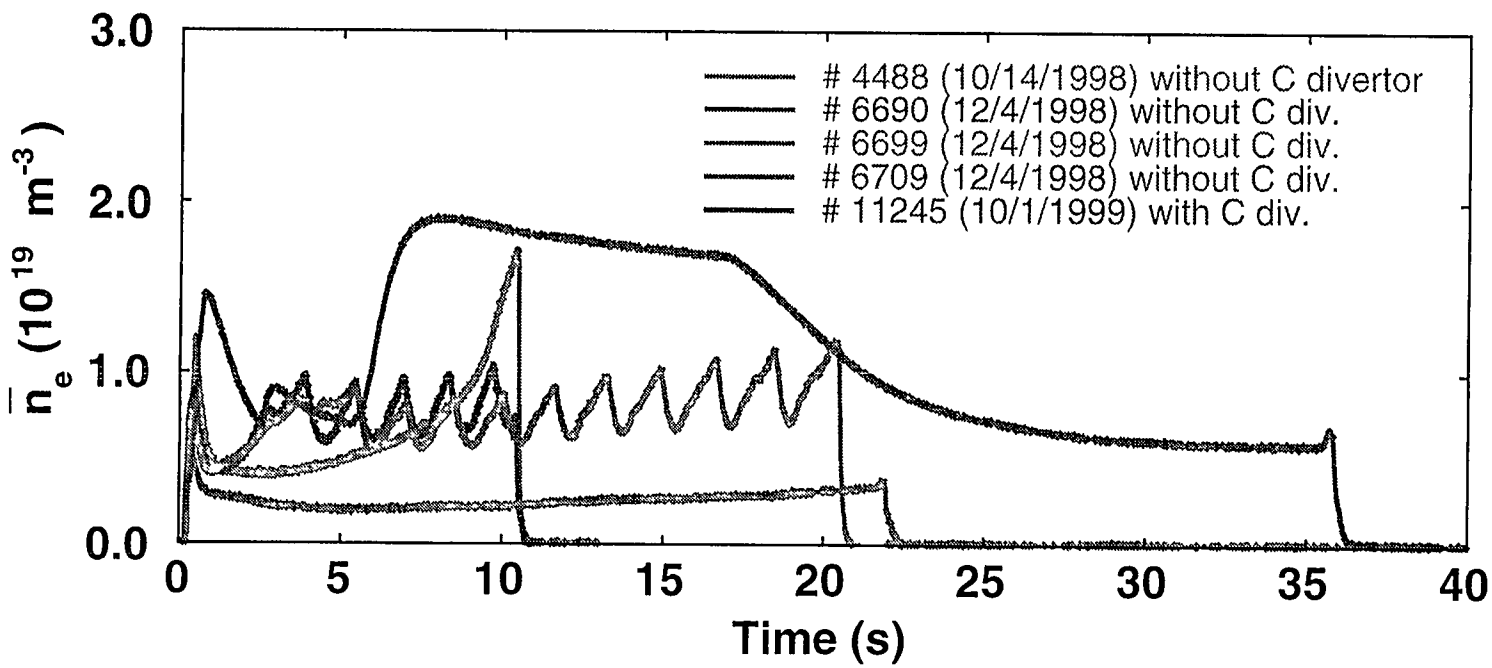

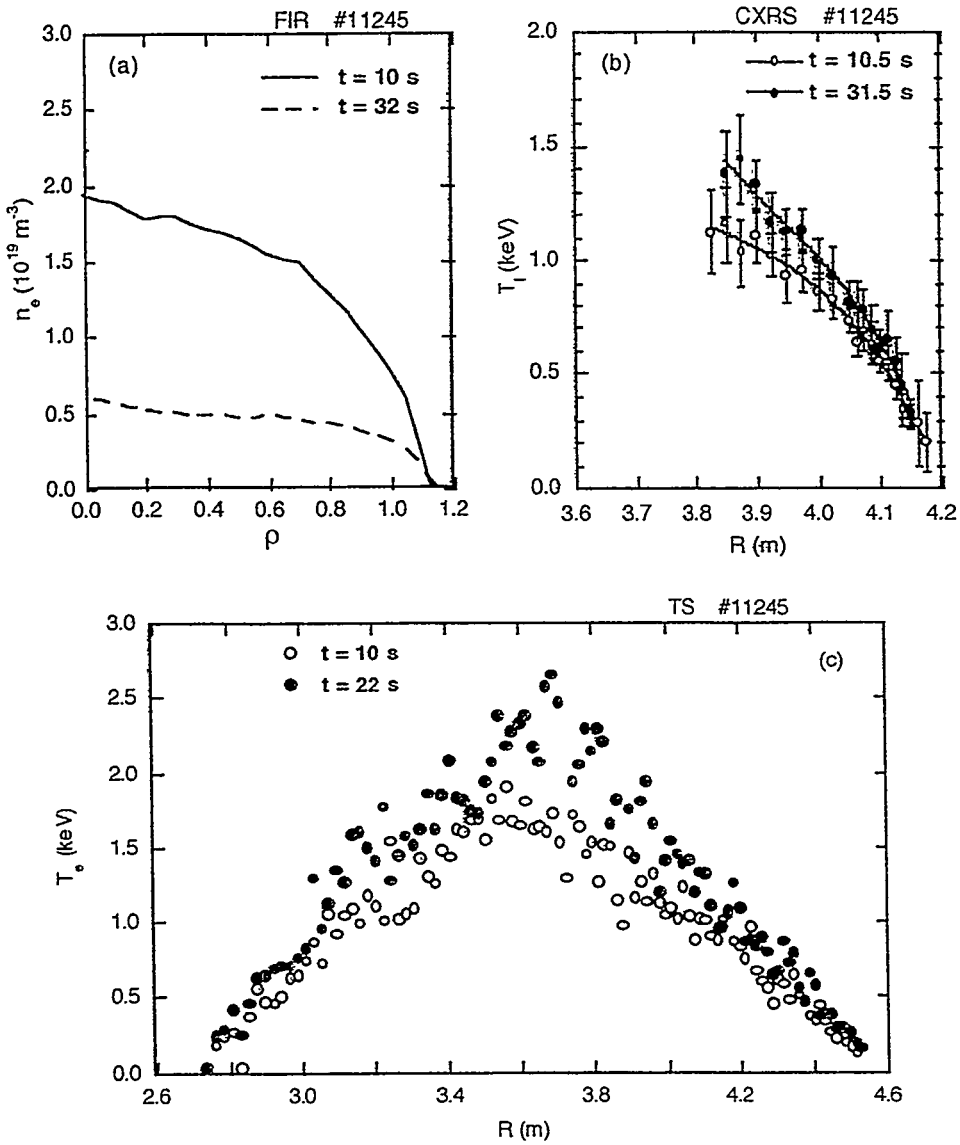

Fig. 4 Radial profiles of (a) n_e, (b) T_i, (c) T_e in the long pulse discharge in Fig. 3.

35 s Long Pulse NBI Discharge

- Carbon divertor plates are installed into the plasma chamber.
- Neutral beam injection with 0.7 MW lasts for 35 s.
- Injection time is limited by the capability of power generator (MG).
- High density plasma is maintained by the feedback control of He gas puffing (t= 7~17 s).
- "Breathing" oscillation is not observed even in high density region.

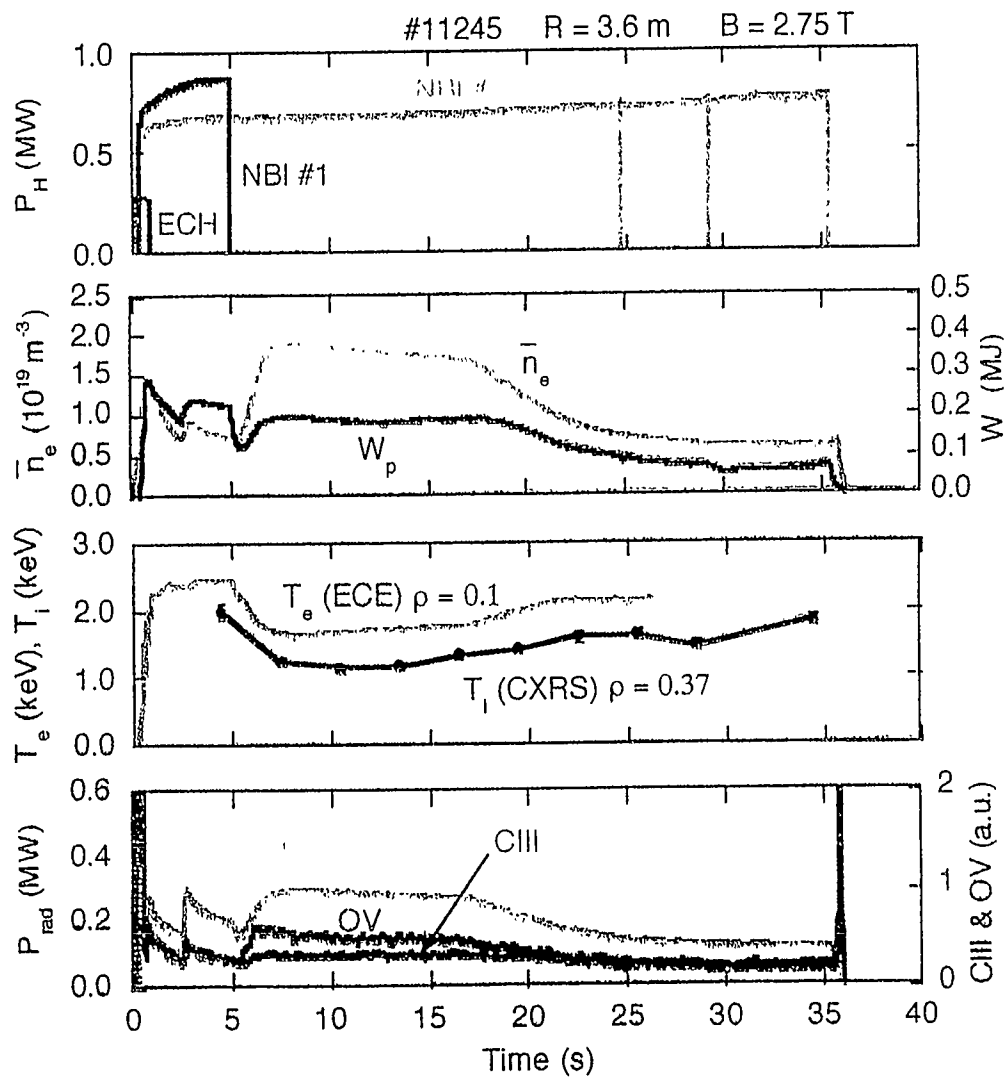

LHD長時間放電と振動現象

- NBI 21 秒放電
  密度を上げると遅い振動
  (“Breathing”)

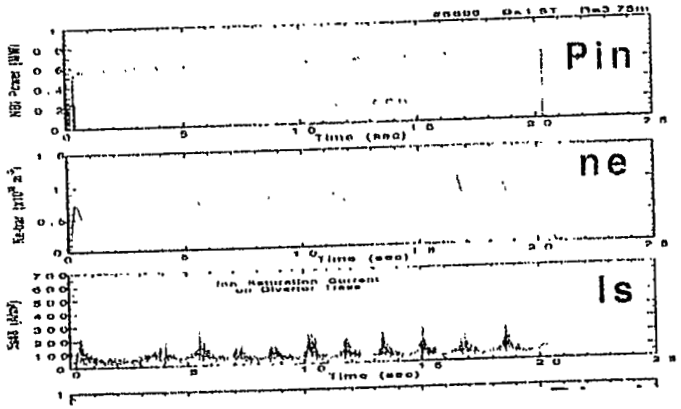

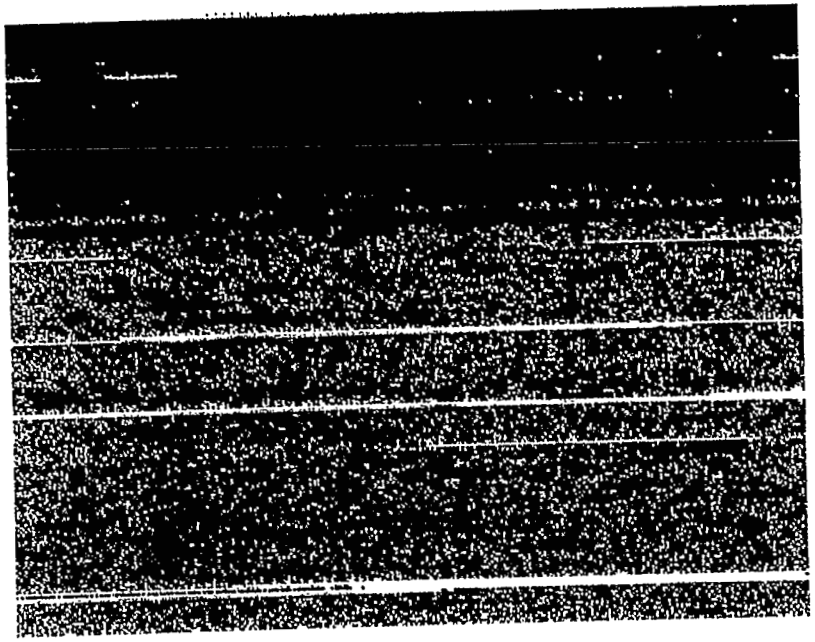

Density profile becomes flat/hollow in a decreasing phase, and peaked in an increasing phase.

NIFS

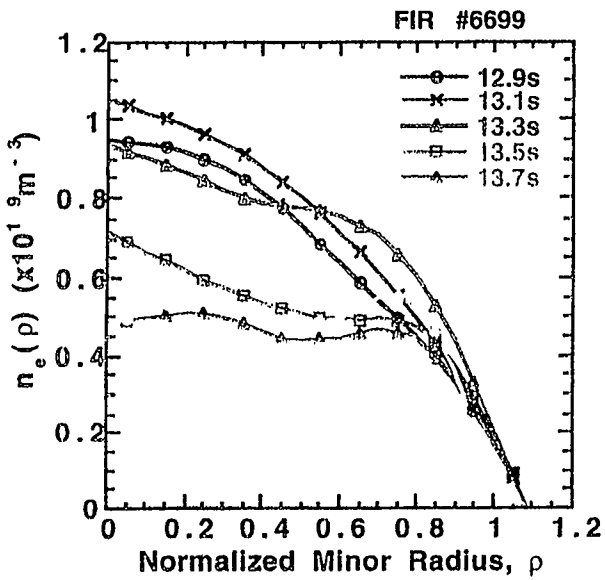

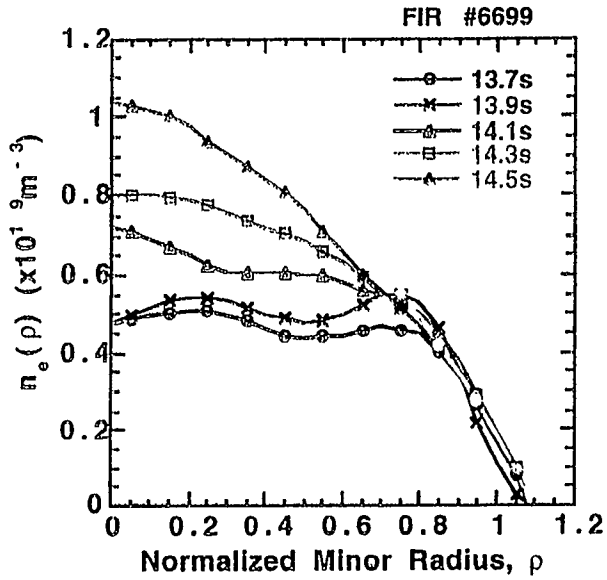

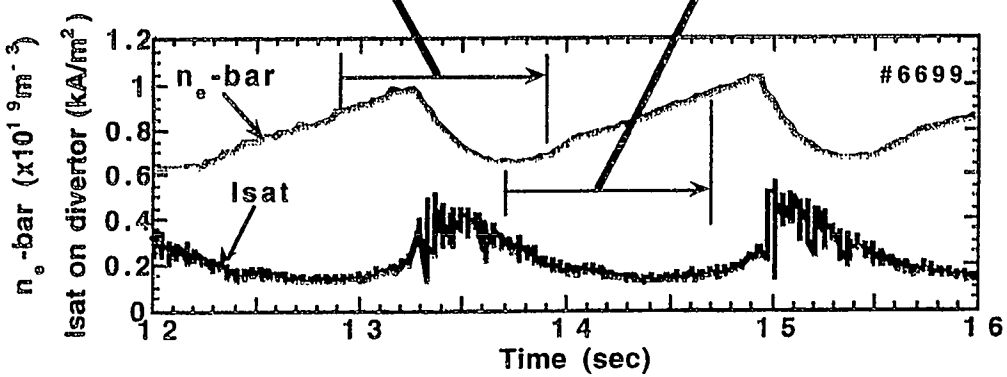

- In a density decreasing phase, the profile is flattened rapidly and the diverter flux is increased, indicating an increase in an outward flux.
- In a density increasing phase, the profile gradually becomes centrally peaked and the diverter flux is decreased.

Model for 'Breathing' Plasma due to Iron Transport

NIFS

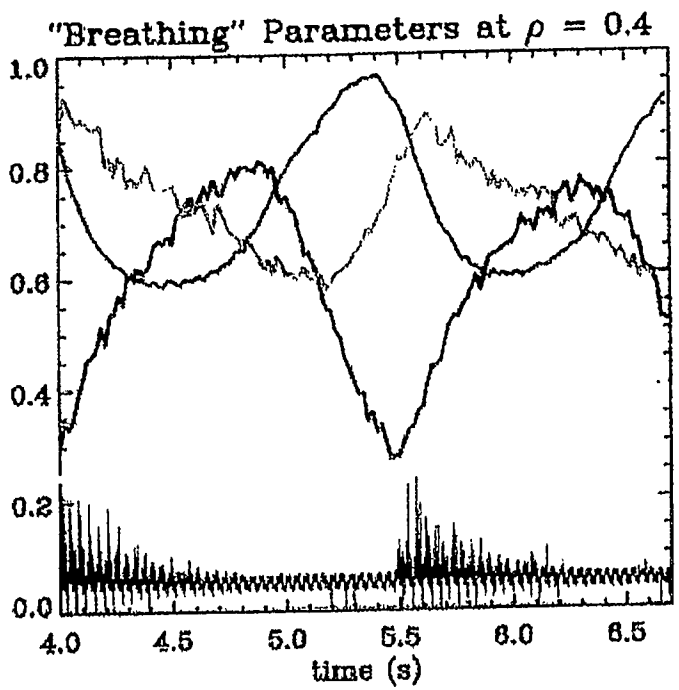

T_e (keV) from Thomson Scattering
n_e ($10^{19}/m^3$) from FIR Interferometer
S_{rad} (A.U.) from Bolometer array
—— I_{sat} at divertor plate
—— n_{Fe} ($10^{17}/m^3$) Iron density calculated from T_e, n_e, S_{rad} assuming average-ion, coronal-equilibrium radiation model

During Attached Phase (indicated by presence of I_{sat})

- T_e is high causing iron to be sputterd off SS divertor plate
- Iron density in core increases and radiation is low but increasing
- Increasing radiation cools plasma
- Density decreases due to particle loss to divertor
- Plasma shrinks and cools to point where iron sputtering stops
- Plasma becomes detached from divertor

During Detached Phase (indicated by lack of Isat)

- Iron Density decreases (due to outward transport?)
- As iron density decreases radiation decreases
- As radiation decreases plasma is heated and T_e increases
- Plasma expands and density increases due to lack of loss channel to divertor
- Plasma expands to and attaches to divertor plate
- T_e reaches temperature where iron sputtering starts

Summary

- ✧ Vacuum vessel, divertor tiles, and many of in-vessel components are actively cooled by water, which meets 3MW steady state operation.
- ✧ The following operations have been achieved:

  NBI: 35 sec., 0.8 MW, T_e~2keV, n_e ~$0.6 \times 10^{19}/m^3$

  Longer than τ_E, τ_p, L/R, but still shorter than $\tau_{recycling}$

  ECH: 120 sec. 50 kW, $n_e < 1 \times 10^{18}/m^3$

  ICRF: 5 sec. with ICRF alone
- ✧ "Breathing" oscillation mechanism is discussed in relation to impurity radiation. Iron impurity is probably playing a key role.

  Density increase during the shrinking phase can be explained as A result of longer penetration in recycled neutrals.

NIFS

N. Noda

Future Plan

✧NBI: extended to 60 sec. with 1 MW
(30 min. is the target for the time being)

✧ICRF, ECH: a few minutes with few hundreds kW
aiming real-time swing of the magnetic field

✧Problems for several issues will be investigated.
For instance, closed divertor & active pumping

NIFS

N. Noda

Experimental Set-up (2)

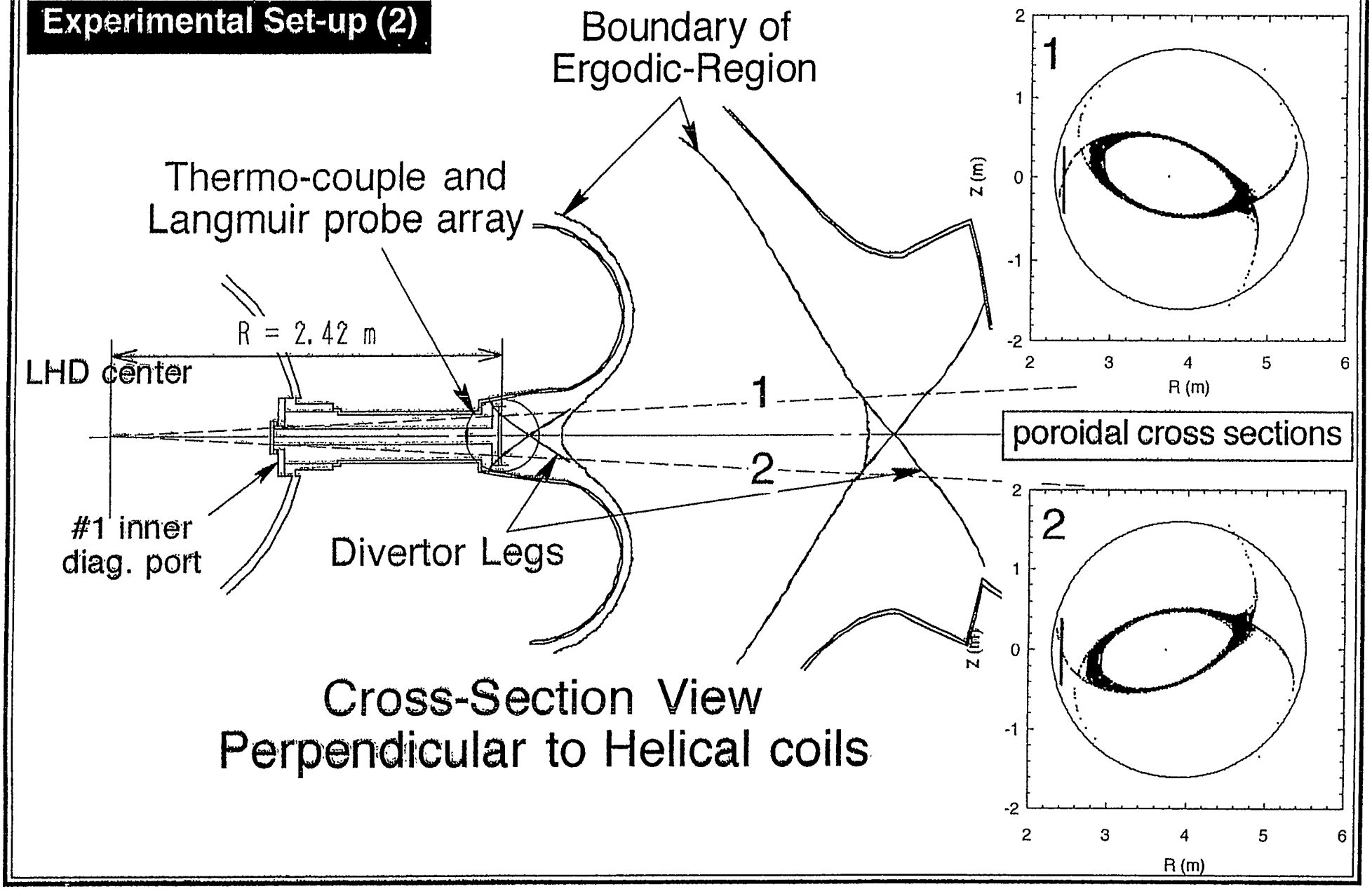

Experimental Set-up (1)

- 30 ch. Langmuir probe array which is set on a carbon tile is installed in the LHD from #1 inner diagnostics port.
- Probe tips are on the plane which is perpendicular to the helical coils.
- Spatial Resolution: 5 mm ~ 15mm
- Probe tips: Dome type (R 1 mm)
- The angle between the magnetic field line and the carbon tile surface is about 30 degree.

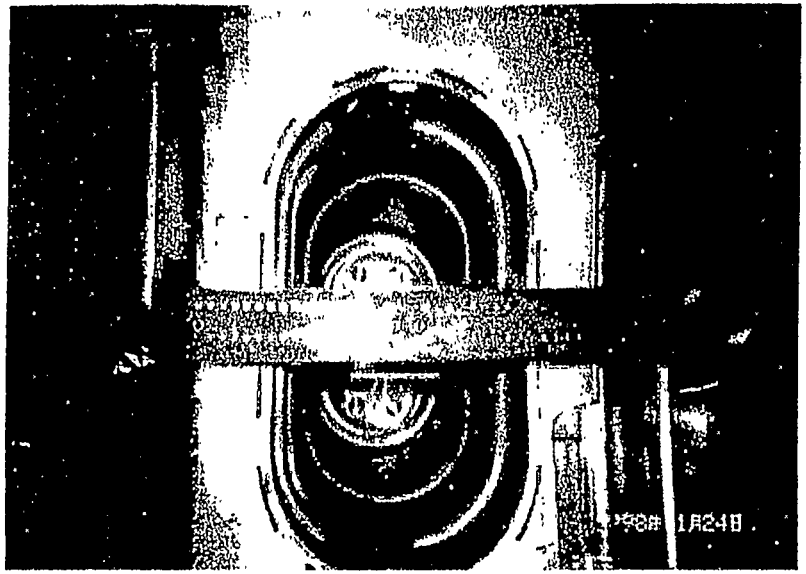

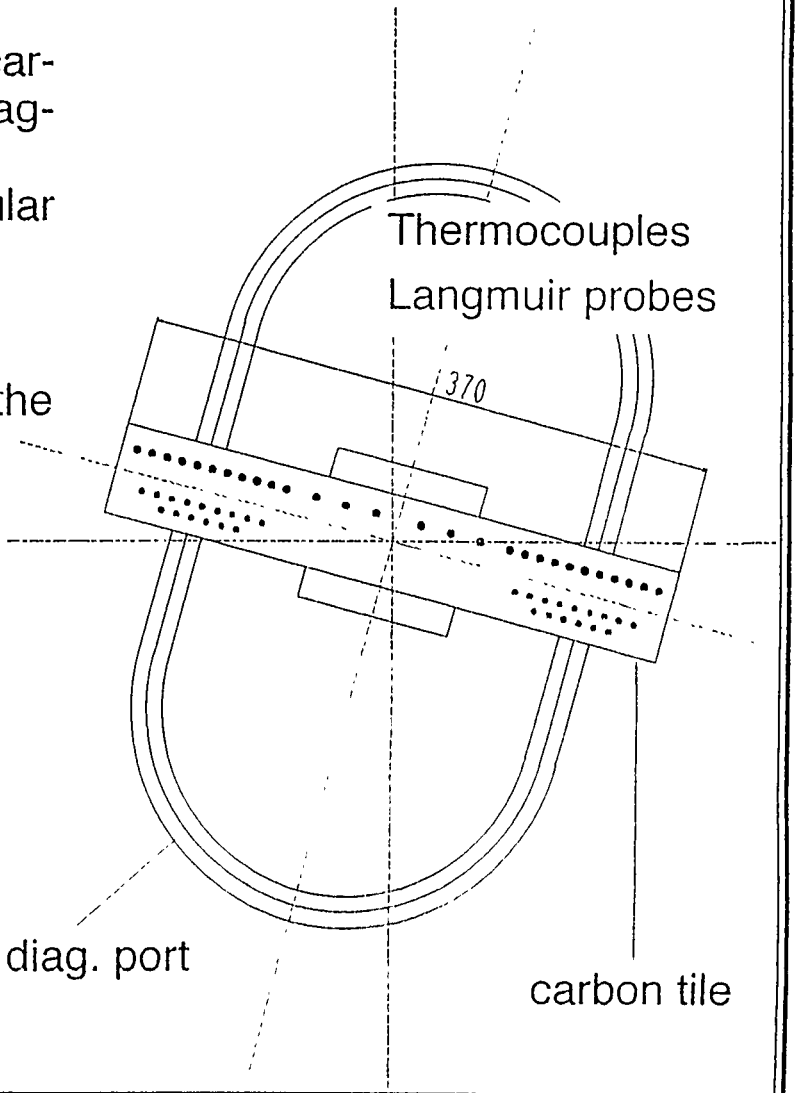

Particle Flux Profiles on the Divertor Plate

NIFS

- Measured particle flux (Γ_{div}) profiles are shown (●) for 3 discharges with different magnetic axes.
- Connection length profiles of the magnetic field line connecting to the divertor plate are also indicated.
- Connection lengths at the peaks of Γ_{div} are longer than 1000 m.
  → Much longer than those in tokamaks divertor.
- The peaks positions of Γ_{div} agree with the long magnetic fields' position.
- The width of the Γ_{div} profile is independent of the plasma parameter.
  it is considered to be restricted by magnetic sturcture.
  This result is agree with the previous calculation [1] qualitatively.

[1] N. Ohyabu, et al., Nucl. Fusion 34(1994) P.384.

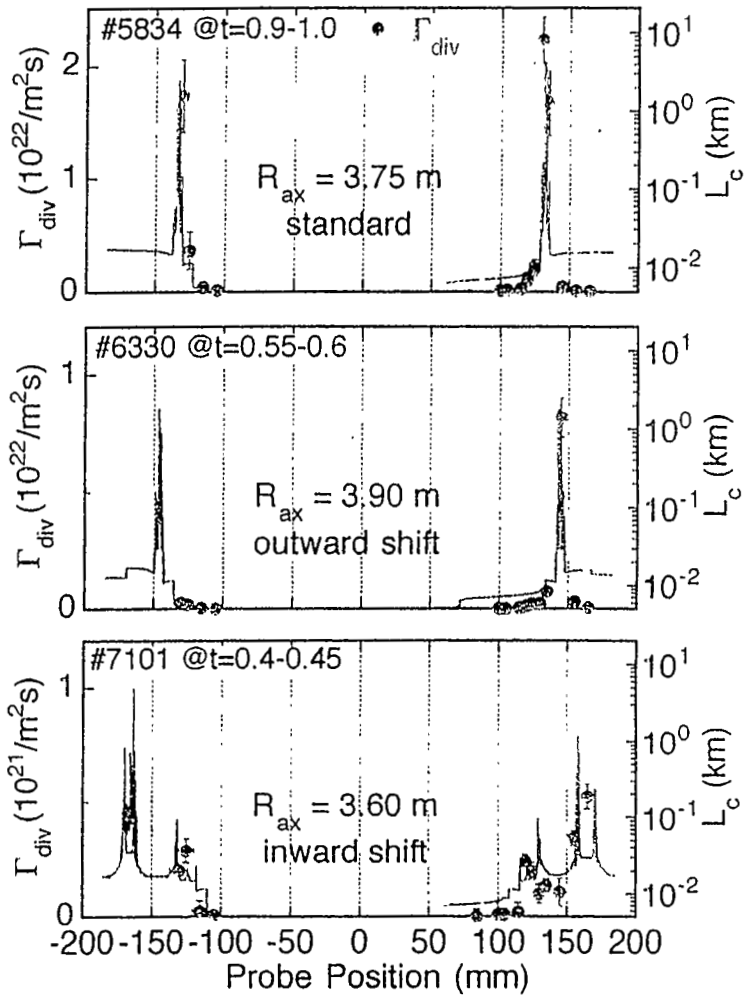

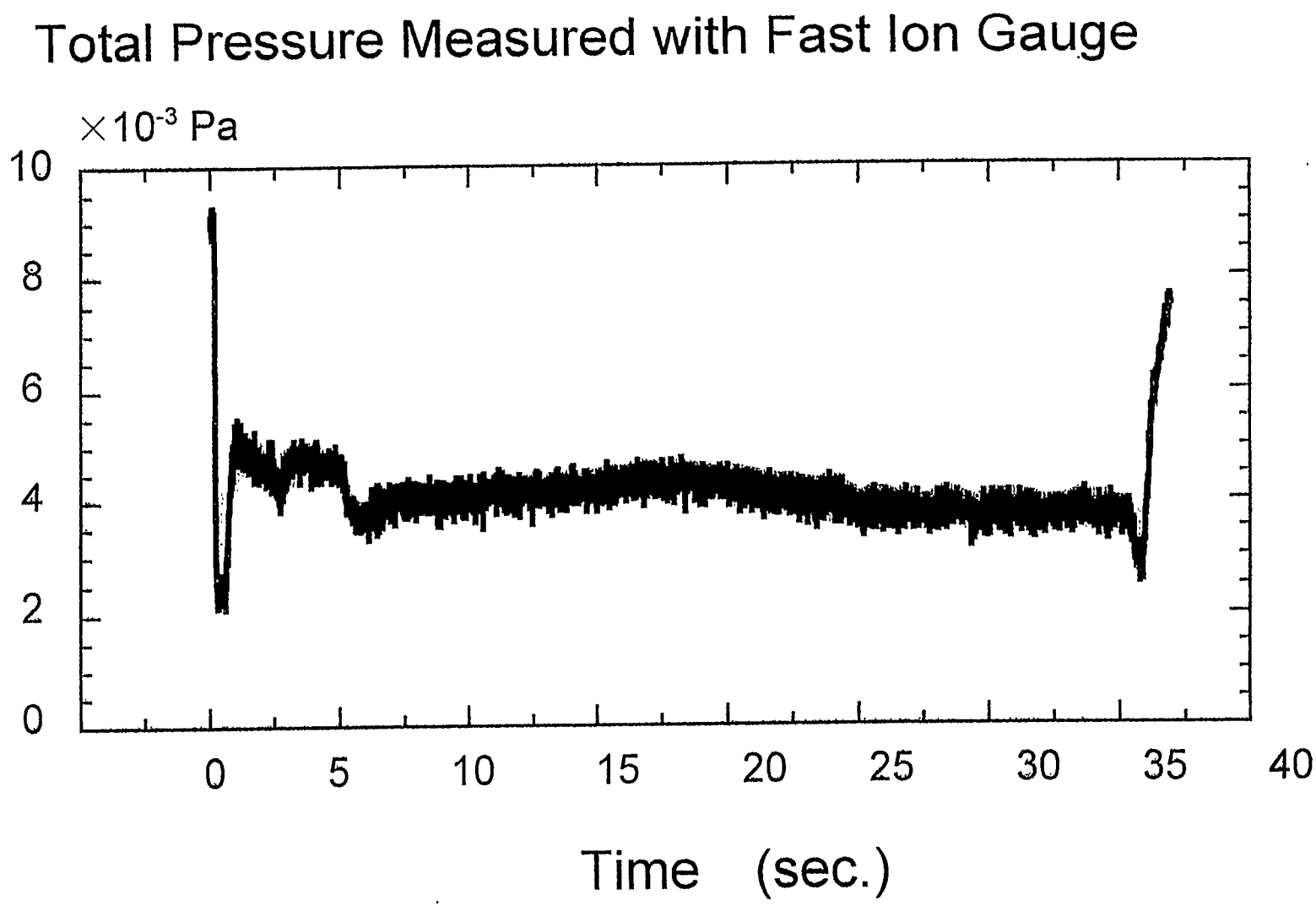
Total Pressure Measured with Fast Ion Gauge
×10-3 Pa
10
8
6
4
2
0
0
5
10
15
20
25
30
35
40
Time (sec.)

Structure of Helical Divertor Plasmas in LHD

H.Suzuki
National Institute for Fusion Science

Topics

1.Poincare Plot of magnetic line of the LHD

2.Simple View

3.Structure of the magnetic line of helical device

4.Structure of the magnetic line at the edge and the divertor legs

5.Calculated prediction and experimental measurements

6.Conclusion

1.Poincare Plot of the Magnetic line of the LHD

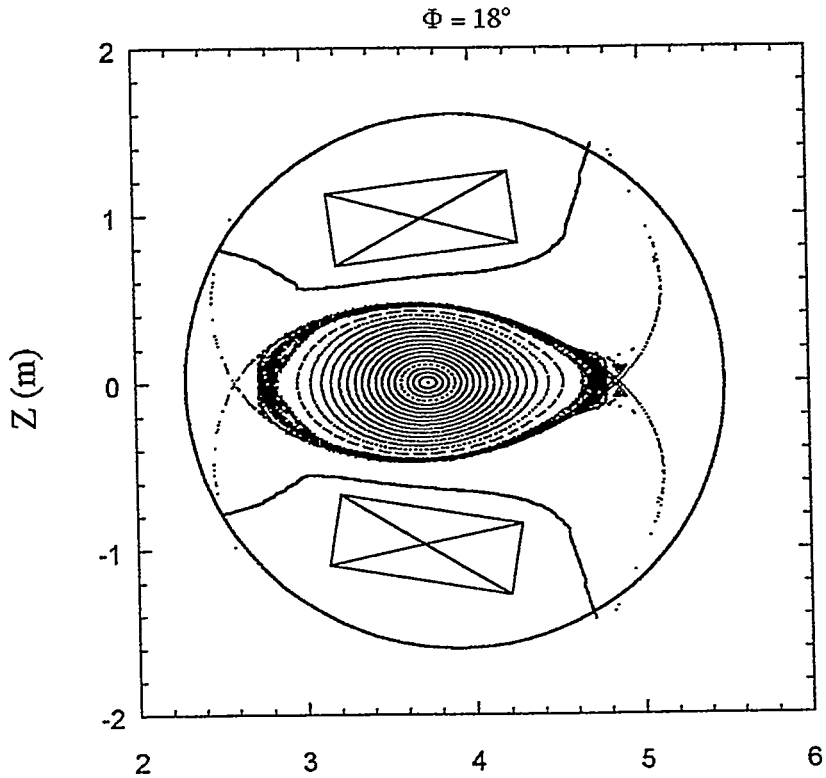

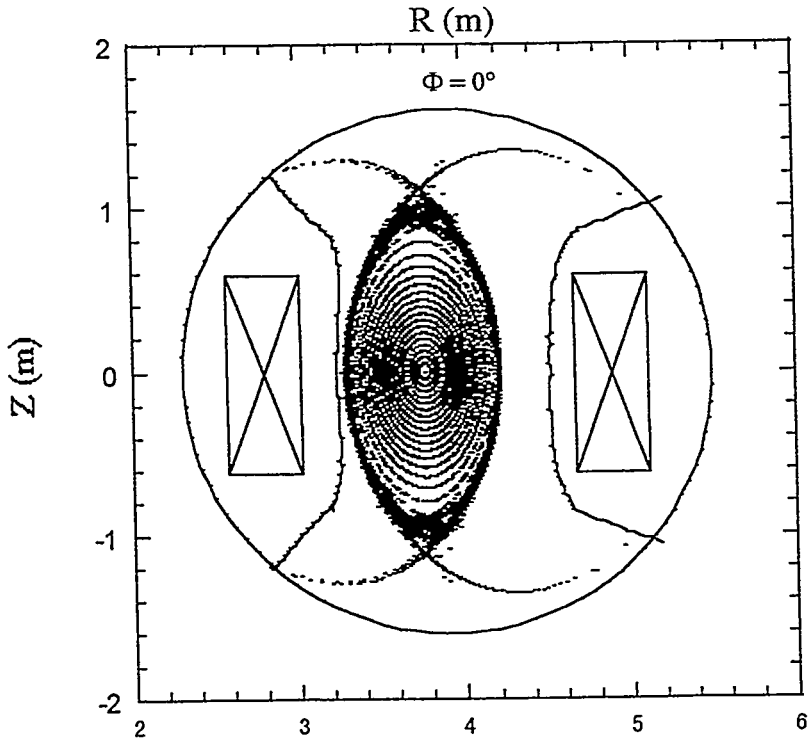

2.Simple View

Direction of Magnetic field

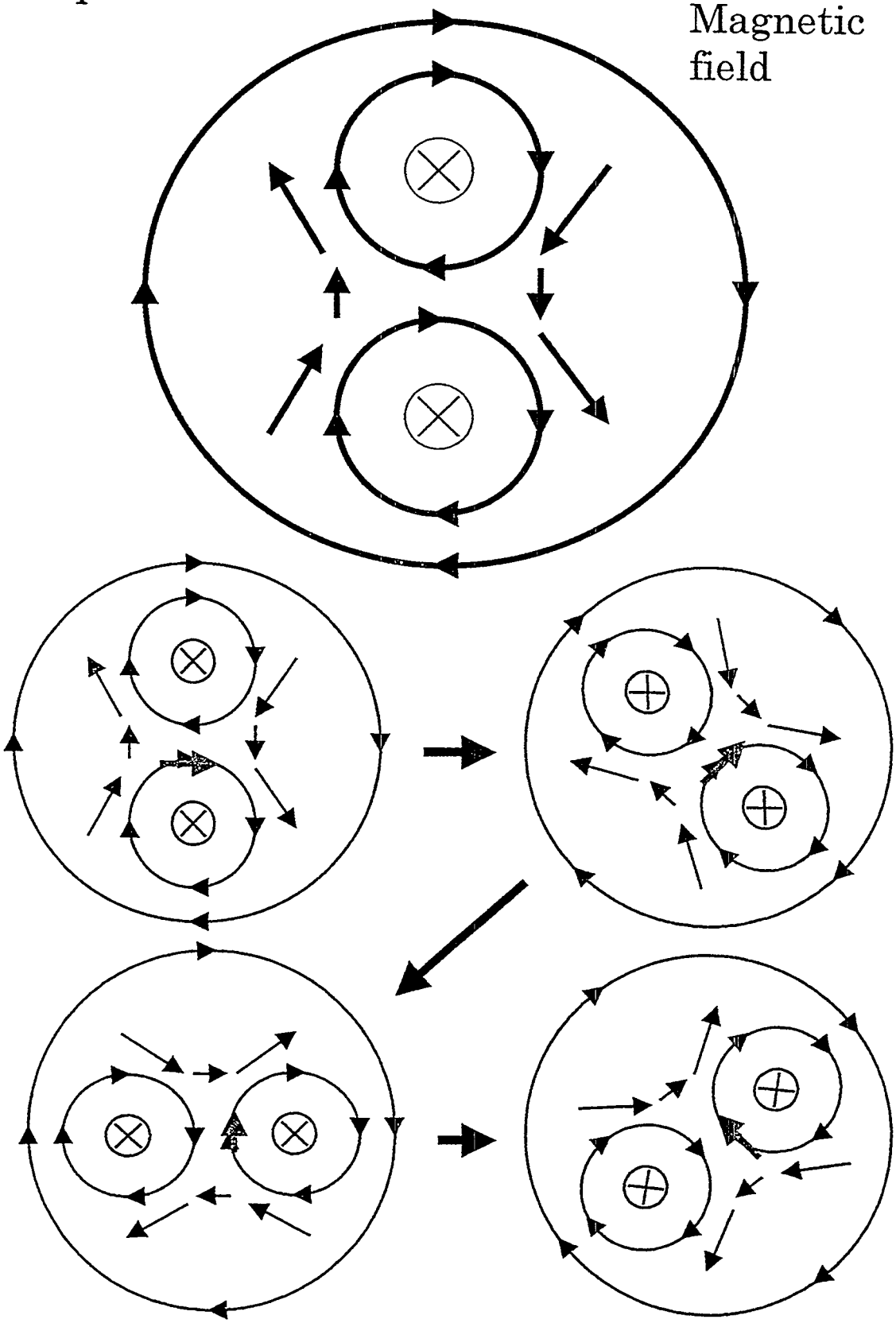

3.Structure of the magnetic line of helical device

3-1. Lagrangian of a charged particle in a magnetic field

$$L = \frac{1}{2}m\left(\dot{r}^2 + \left(r\dot{\varphi}\right)^2 + \dot{z}^2\right) + e\left(\dot{r}A_r + r\dot{\varphi}A_\varphi + \dot{z}A_z\right)$$

3-2. toroidal symmetry and Lagrangian invariant. (tokamak case)

$$L(r,\varphi+\Delta\varphi,z) - L(r,\varphi,z)$$
$$= \frac{\partial L}{\partial \varphi}\Delta\varphi + \frac{\partial L}{\partial \dot{\varphi}}\Delta\dot{\varphi} = 0$$

$$\frac{d}{dt}\left(mr^2\dot{\varphi} + erA_\varphi\right) = 0$$
$$P_\varphi = mr^2\dot{\varphi} + erA_\varphi = const.$$

3-3. Hamiltonian of a charged particle in a magnetic field

$$H = P_r \dot{r} + P_\varphi \dot{\varphi} + P_z \dot{z} - L$$
$$= \frac{1}{2} m \left(\dot{r}^2 + (r\dot{\varphi})^2 + \dot{z}^2 \right)$$
$$= \frac{1}{2}\left(P_r - eA_r\right)^2 + \frac{1}{2}\left(P_z - eA_z\right)^2 + \frac{1}{2}\left(P_\varphi - erA_\varphi\right)^2$$

magnetic surface function

$$\Psi = rA_\varphi$$

$$P_0 = P_\varphi = const.$$

$$H = \frac{1}{2}\left(P_r - eA_r\right)^2 + \frac{1}{2}\left(P_z - eA_z\right)^2 + \frac{1}{2}\left(P_0 - e\Psi\right)^2$$

To do the same, a magnetic surface function of a linear helical device can be obtained.

3-4. helical symmetry and Lagrangian invariant. (linear helical device case)

$$L(r,\varphi+\Delta\varphi,z+\Delta z)-L(r,\varphi,z)=\Delta L=0$$
$$\Delta\varphi=\alpha\Delta z$$

$$\Delta L=\frac{\partial L}{\partial\varphi}\Delta\varphi+\frac{\partial L}{\partial\dot{\varphi}}\Delta\dot{\varphi}+\frac{\partial L}{\partial z}\Delta z+\frac{\partial L}{\partial\dot{z}}\Delta\dot{z}$$

$$\frac{d}{dt}\left(\alpha mr^2\dot{\varphi}+\alpha erA_\varphi+m\dot{z}+eA_z\right)=0$$

$$P_0=\alpha mr^2\dot{\varphi}+\alpha erA_\varphi+m\dot{z}+eA_z$$
$$=\alpha mr^2\dot{\varphi}+m\dot{z}+e\left(\alpha rA_\varphi+A_z\right)=const.$$

Magnetic surface function of linear helical device

$$\Psi=\left(\alpha rA_\varphi+A_z\right)$$

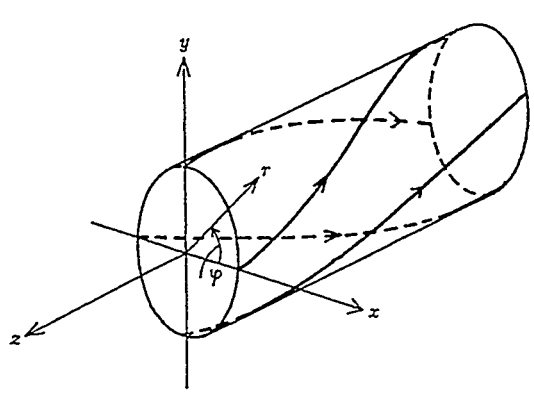

3-5. Magnetic potential ϕ

No electric current, stable condition

rot H = curl H =0 $\longrightarrow$ H=grad ϕ

Poisson equation

$$\nabla^2\phi = \frac{1}{r}\frac{\partial}{\partial r}\left(r\frac{\partial\phi}{\partial r}\right) + \frac{1}{r^2}\frac{\partial^2\phi}{\partial\theta^2} + \frac{\partial^2\phi}{\partial z^2}$$

$$\phi = R(r)\Theta(\theta)Z(z)$$

Linear helical symmetry

$$\phi(r,\theta,z) = \phi(r, \theta+\Delta\theta, z+\Delta z) = \phi(r, \theta+\alpha\Delta z, z+\Delta z)$$

$$\frac{\partial\phi}{\partial\theta}\Delta\theta + \frac{\partial\phi}{\partial z}\Delta z = \left(\alpha\frac{\partial\phi}{\partial\theta} + \frac{\partial\phi}{\partial z}\right)\Delta z = 0$$

$$\alpha\frac{\partial\phi}{\partial\theta} + \frac{\partial\phi}{\partial z} = \alpha RZ\frac{\partial\Theta}{\partial\theta} + R\Theta\frac{\partial Z}{\partial z} = 0$$

$$\alpha\frac{1}{\Theta}\frac{\partial\Theta}{\partial\theta} + \frac{1}{Z}\frac{\partial Z}{\partial z} = 0$$

Each part should be a constant.

$$\frac{1}{\Theta}\frac{\partial\Theta}{\partial\theta} = il$$
$$\frac{1}{\alpha}\frac{1}{Z}\frac{\partial Z}{\partial z} = -il$$

$$\Theta = e^{il\theta}$$

$$Z = e^{-il\alpha z}$$

Poisson equation becomes,

$$\frac{1}{R}\frac{1}{r}\frac{\partial}{\partial r}\left(r\frac{\partial R}{\partial r}\right) - l^2\frac{1}{r^2} - (l\alpha)^2 = 0$$

$$\rho = l\alpha r$$

$$\frac{\partial^2}{\partial\rho^2}R + \frac{1}{\rho}\frac{\partial}{\partial\rho}R - \left(1 + \frac{l^2}{\rho^2}\right)R = 0$$

Bessel function I

$$R(\rho) = I_l(\rho) = I_l(l\alpha r)$$

Magnetic potential

$$\phi = I_l(l\alpha r)e^{il(\theta - \alpha z)} = I_l(l\alpha r)\sin(l(\theta - \alpha z))$$

General representation

$$\phi = B_0 z + \frac{1}{\alpha} \sum_{l=1}^{\infty} b_l I_l(l\alpha r) \sin(l(\theta - \alpha z))$$

Magnetic field

$$B_r = \sum_{l=1}^{\infty} l b_l I_l'(l\alpha r) \sin(l(\theta - \alpha z))$$

$$B_\theta = \sum_{l=1}^{\infty} \frac{1}{\alpha r} l b_l I_l(l\alpha r) \cos(l(\theta - \alpha z))$$

$$B_z = B_0 - \sum_{l=1}^{\infty} l b_l I_l(l\alpha r) \cos(l(\theta - \alpha z))$$

Vector potential

$$A_r = -\frac{1}{\alpha 2 r} \sum_{l=1}^{\infty} b_l I_l(l\alpha r) \sin(l(\theta - \alpha z))$$

$$A_\theta = \frac{B_0}{2} r - \frac{1}{\alpha} \sum_{l=1}^{\infty} b_l I_l'(l\alpha r) \cos(l(\theta - \alpha z))$$

$$A_z = 0$$

Magnetic surface

$$\psi = A_z + \alpha r A_\theta$$

$$= \frac{B_0}{2} r^2 - r \sum_{l=1}^{\infty} b_l I_l'(l\alpha r) \cos(l(\theta - \alpha z))$$

$$= const.$$

$$\psi = A_z + \alpha r A_\theta$$
$$= \frac{B_0}{2} r^2 - r \sum_{l=1}^{\infty} b_l I_l'(l\alpha r) \cos(l(\theta - \alpha z))$$
$$= const.$$

(l is corresponded with a number of coils.)

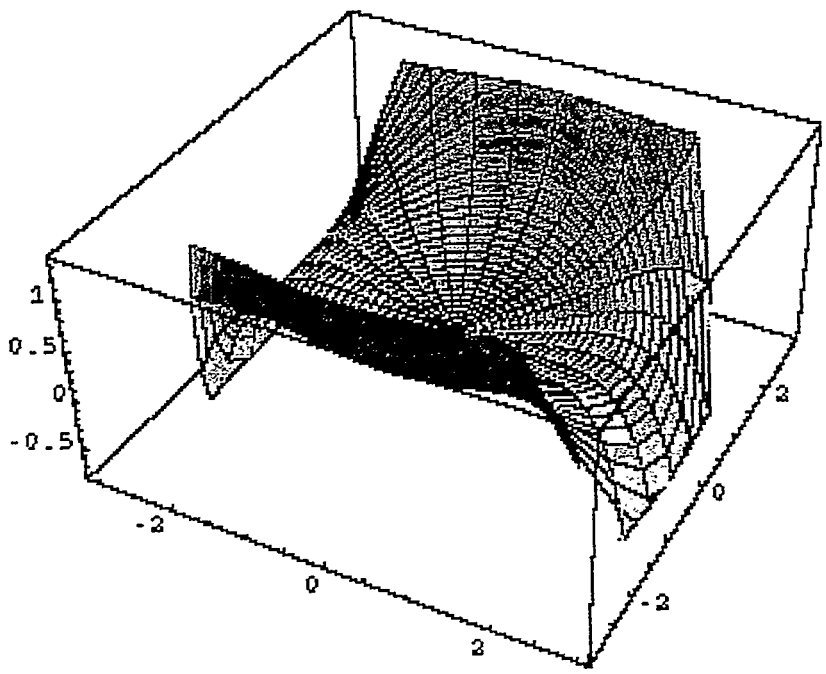

Magnetic Surface Function l=2,z=0

Equilibrium point (center) O-point

Equilibrium point (saddle) X-point

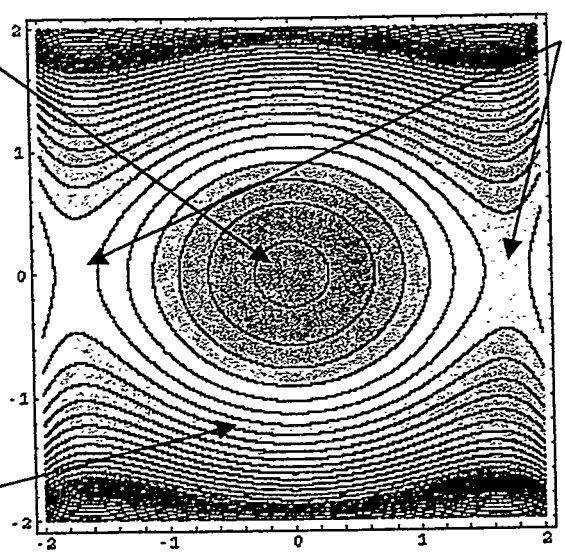

Separatrix

Contour plot

3-6. Magnetic surface of circular helical device

No symmetry!

No analytic magnetic surface function!

Consider:

Magnetic surface of linear helical device
+
perturbation

1) The X-point and the separatrix still remain?

No.
Separatrix breaks and ergodic (chaotic) structure appears.

2) The toruses around the O-point still remain?

YES.
KAM torus theory shows an existence of stable torus orbit.

4.Structure of the magnetic line at the edge and the divertor legs

4-1. two kinds of chaotic structure

1) Overlapping of magnetic islands.

Rational surface is unstable.
If the rational surface resonates with a perturbation field (error field),
the rational surface splits and make magnetic islands.

If a width of the islands is greater than a distance between two resonated rational surfaces, the islands overlap, and magnetic lines make a chaotic structure.

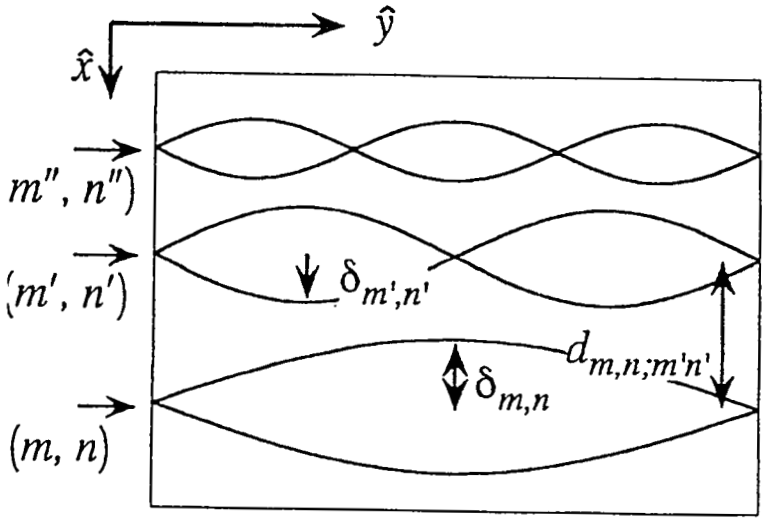

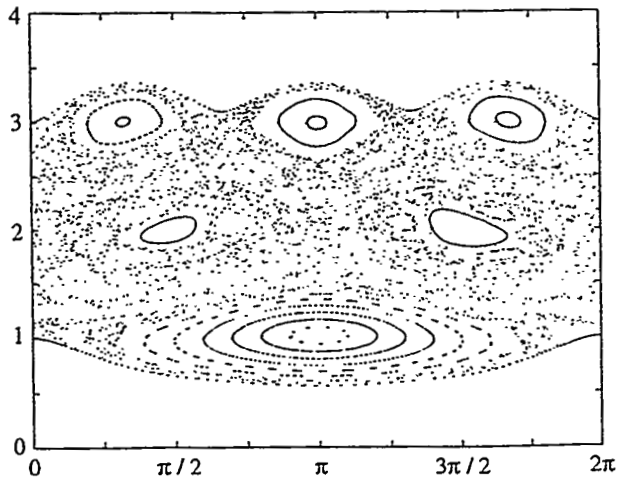

2) Deformation of torus and separatrix
(Whisker structure)

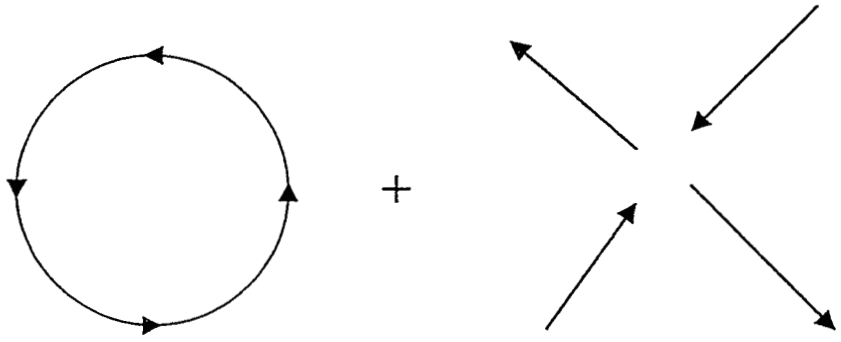

Torus Perturbation

Torus is pulled, folded up, and pushed.

So called baker mapping.

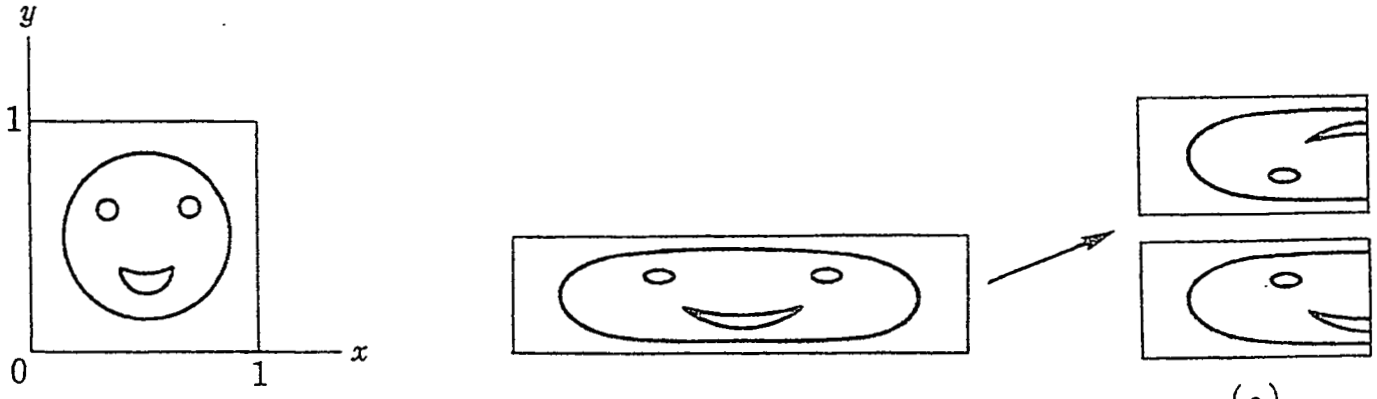

(a) (b) (c)

Moving of points

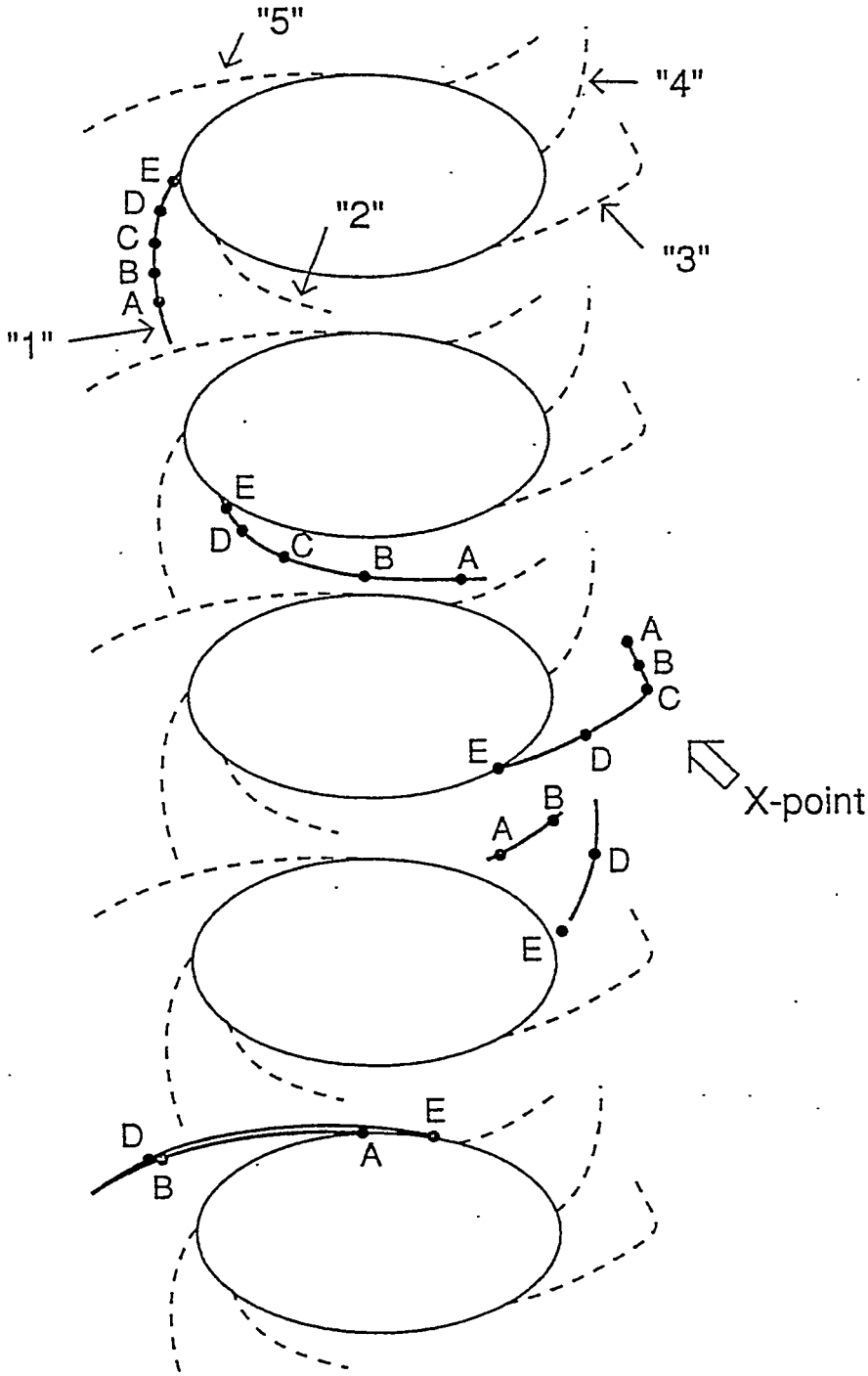

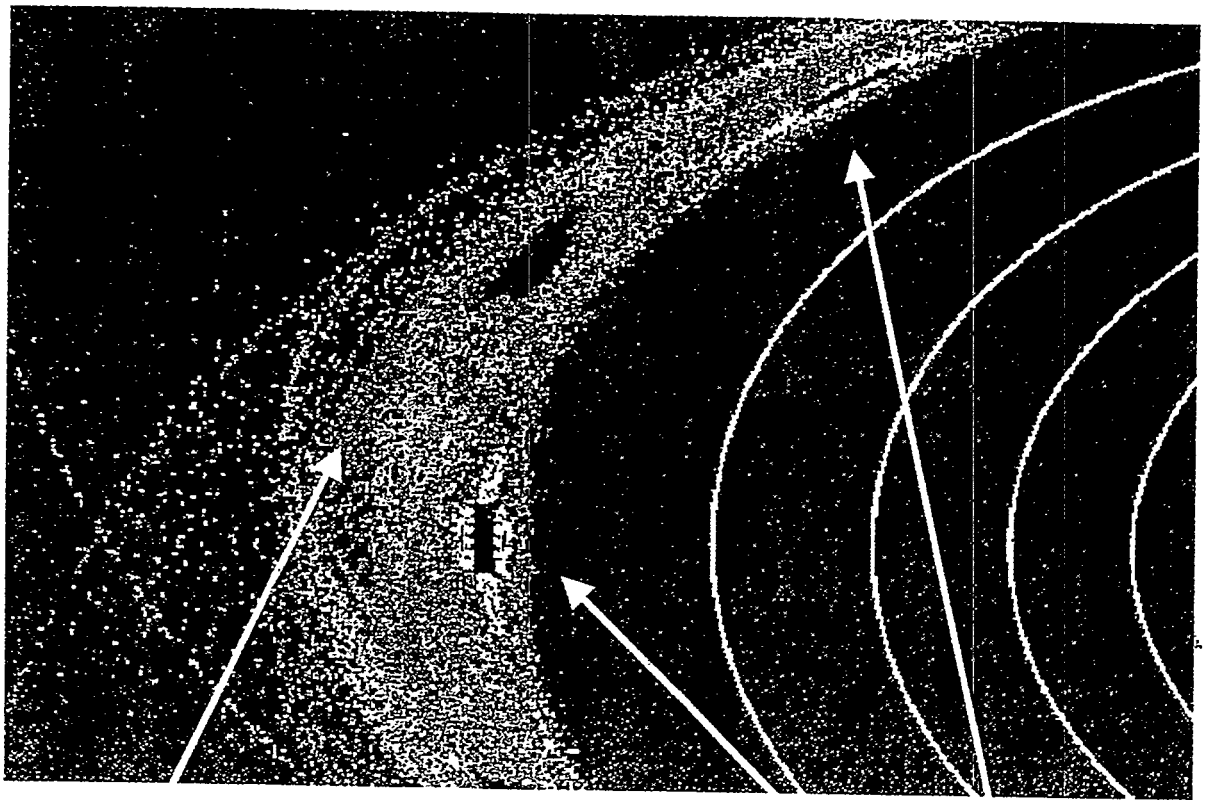

Whisker region

Natural
magnetic island

Experimental Setup ~ Langmuir Probe Array ~

NIFS

- 30 ch. Langmuir probe array which is set on a carbon tile is installed in the LHD from #1 inner diagnostics port.
- Probe tips are on the plane which is perpendicular to the helical coils.
- Spatial Resolution: 5 mm ~ 15mm
- Probe tips: Dome type (R 1 mm)
- The angle between the magnetic field line and the carbon tile surface is about 30 degree.

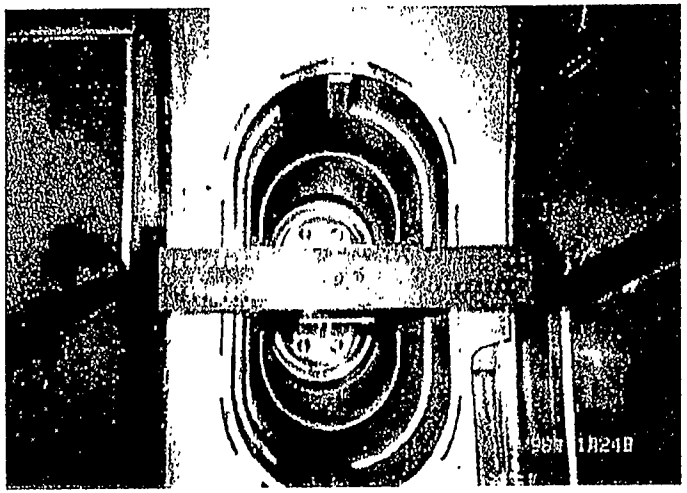

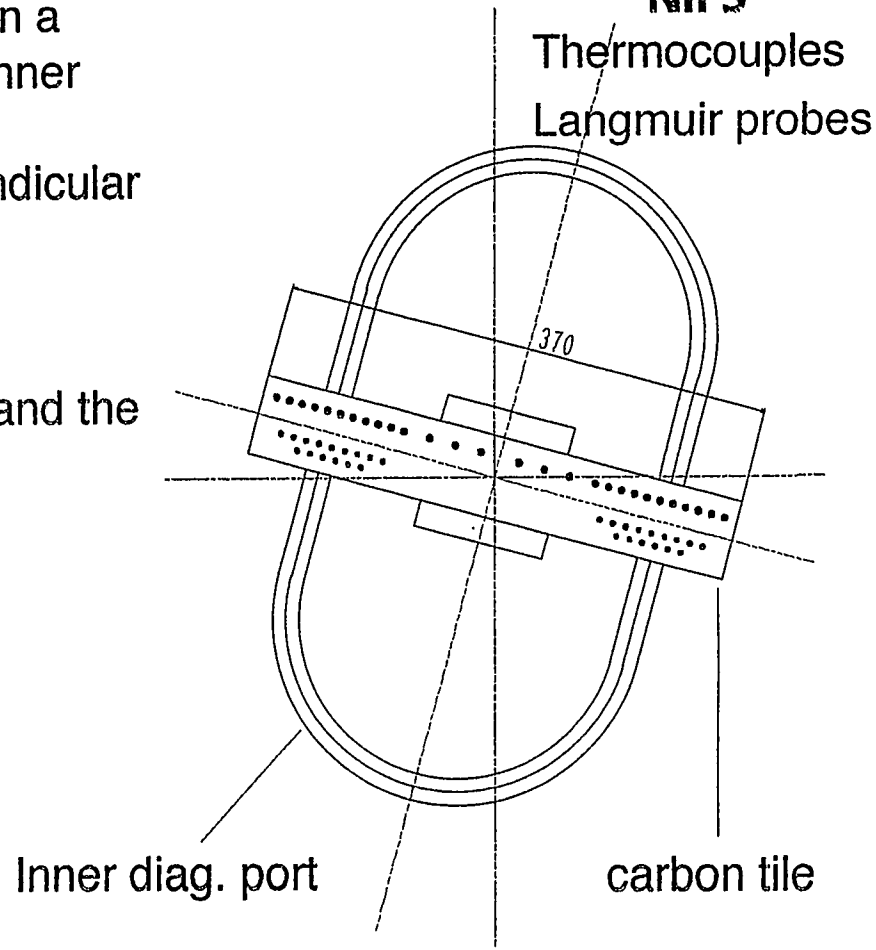

Particle Flux Profiles on the Divertor Plate

NIFS

- Measured particle flux (Γ_{div}) profiles are shown (●) for 3 discharges with different magnetic axes.
- Connection length profiles of the magnetic field line connecting to the divertor plate are also indicated.
- Connection lengths at the peaks of Γ_{div} are longer than 1000 m.
  → Much longer than those in tokamaks divertor.
- The peaks positions of Γ_{div} agree with the long magnetic fields' position.
- The width of the Γ_{div} profile is independent of the plasma parameter.

it is considered to be restricted by magnetic sturcture.
This result is agree with the previous calculation [1] qualitatively.

[1] N. Ohyabu, et al., Nucl. Fusion 34(1994) P.384.

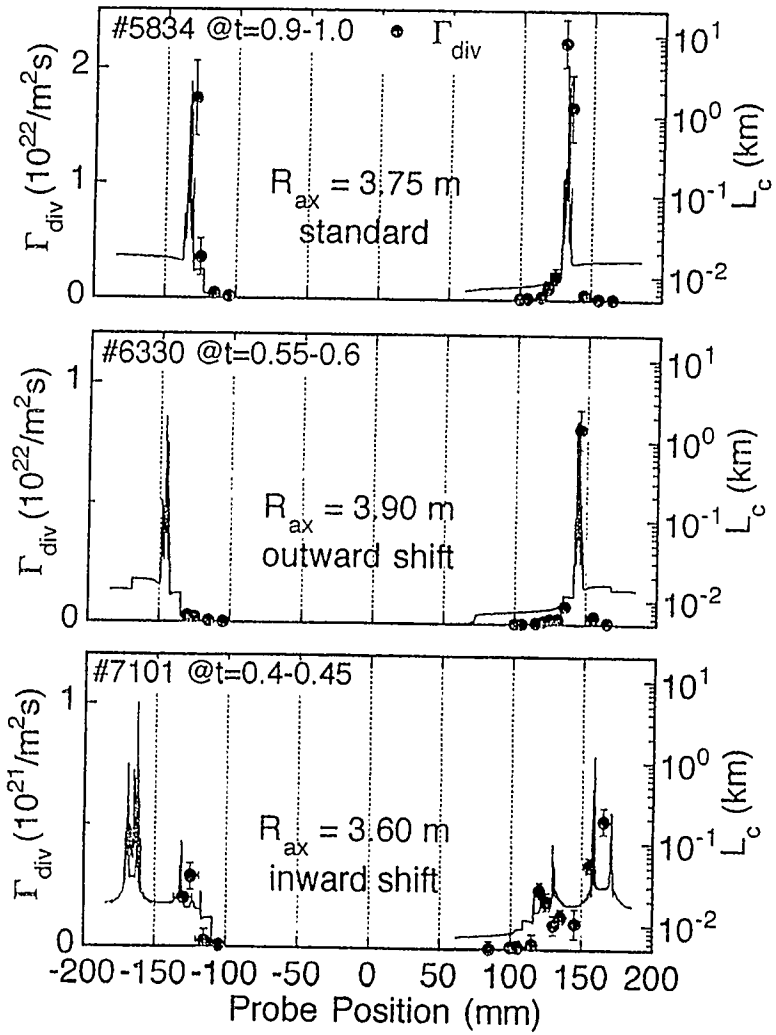

Schematic view of divertor leg

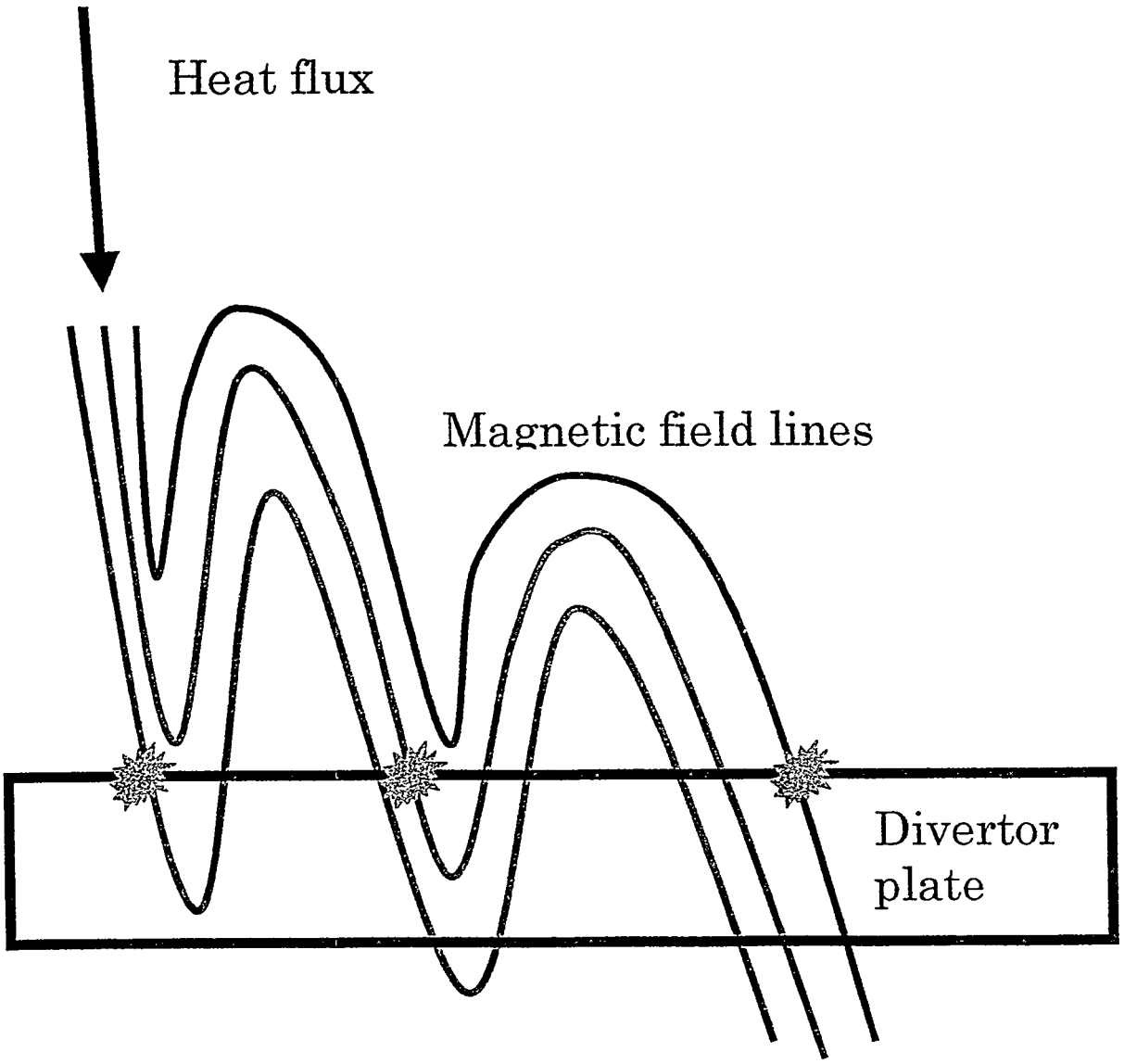

Because of special structure of magnetic field lines, hit points of plasma on divertor plate are discrete.

Asymmetry of heat flux

θ: direction of divertor plate
r: distance between center and cross point

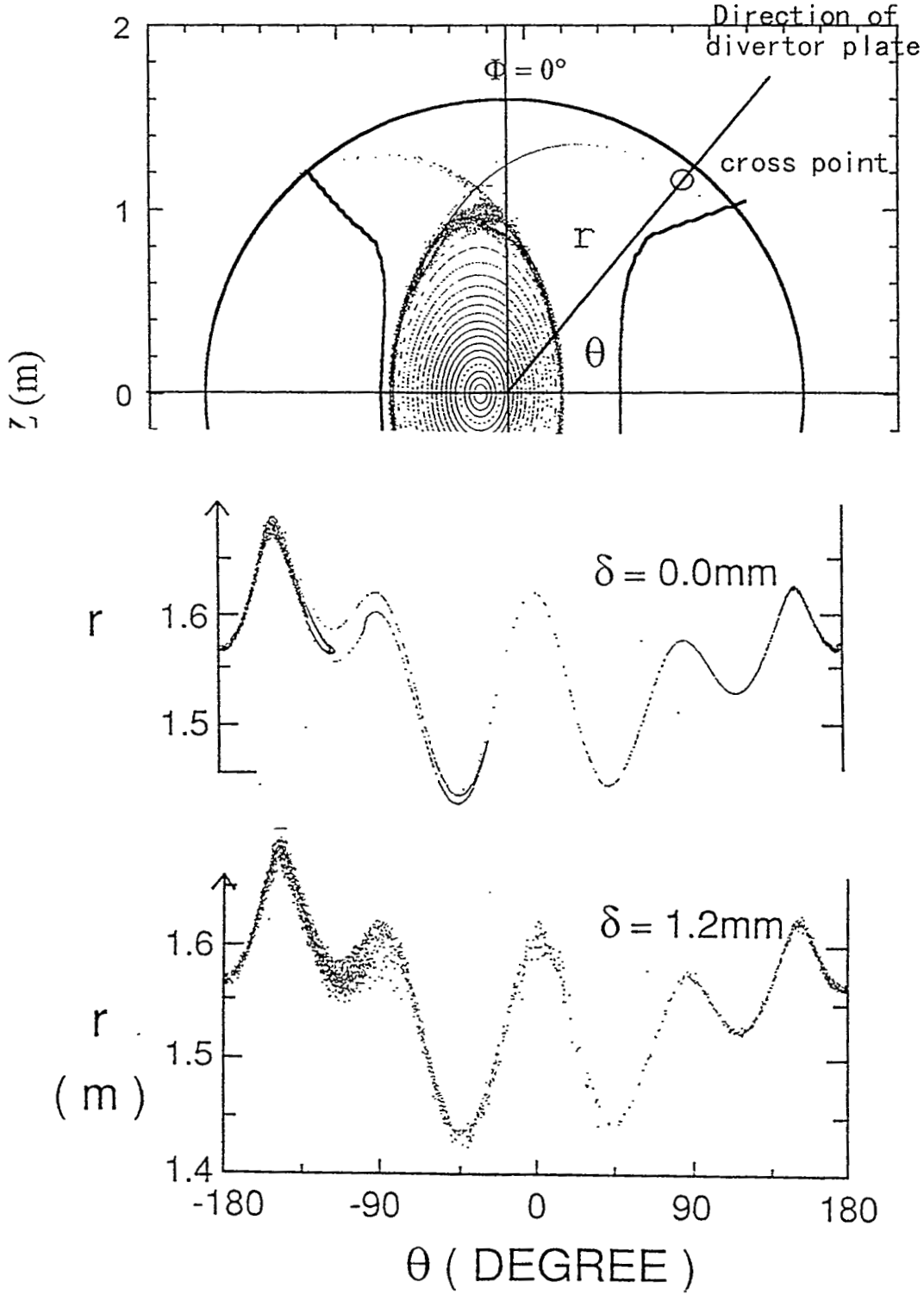

6. Conclusion

1) LHD has four divertor legs.

2) LHD has magnetic surface.

3) Structure of magnetic field at the edge of LHD plasma is chaotic.

4) Divertor legs have also complicated structure.

5) Because of the structure of magnetic field line, hit point on the divertor plate is discrete. And this structure has been observed experimentally at inside of the torus.

6) According to a Monte Carlo simulation, asymmetry of heat flux is predicted.

Negative transferred arc cleaning: a method for roughening and removing surface contamination from beryllium and other metallic surfaces

R.G. Castro[a], K.J. Hollis[a], C. J. Maggiore[a], R.P. Doerner[b], A.Ayala[a], and B.D. Bartram[a]

[a]Los Alamos National Laboratory, Materials Science and Technology Division, Los Alamos, New Mexico 87545, USA
[b] University of California - San Diego, Fusion Energy Research, , La Jolla, CA 92093, USA

TA cleaning has been investigated for preparing the surface of beryllium plasma facing components (PFC's) inside of the International Thermonuclear Experimental Reactor (ITER) prior to depositing beryllium by plasma spraying. Plasma spraying of beryllium was evaluated during the ITER Engineering Design Activity (EDA) for *in-situ* repair and initial fabrication of the beryllium first wall armor. Results have shown that surface roughening of beryllium, during the TA cleaning process, can result in bond strengths greater than 100 MPa between beryllium surfaces and plasma sprayed beryllium. In addition, the TA cleaning process was shown to be an effective method for removing contaminate layers of carbon and tungsten from the surface of beryllium. Investigations have been performed to characterize the different arc-types that occur during the TA cleaning process (Type I, I and III arcs) and the effectiveness of the TA cleaning process for potentially removing co-deposited layers of carbon and deuterium from the surface of beryllium, stainless steel and tungsten.

1. INTRODUCTION

Negative transferred-arc (TA) cleaning has been used throughout the thermal spray community as a method for cleaning and roughening surfaces prior to the deposition of materials during vacuum plasma spraying (VPS). TA cleaning results when a potential difference (voltage) is applied between the front of a DC plasma torch (anode) and a metallic surface to be cleaned (cathode). A cathodic condition is created at the surface of the workpiece that results in the transfer of electrons from the workpiece to the front of the plasma torch during an electric arc discharge. This electron transfer can result in the removal of the oxide surface layer and surface contaminates from metallic materials. One possible application for TA cleaning is the removal of co-deposited layers of carbon and tritium from first wall surfaces inside of a magnetic fusion energy device. Tritium co-deposition is raising significant concern because of operation and safety implications associated with large tritium inventory build-up on the first wall structure of a magnetic fusion energy device [1]. Tritium co-deposition with carbon has been verified in laboratory studies conducted by Hsu and Causey [2-3] and by examination of first wall samples removed from many present-day fusion devices. Due primarily to the safety hazard in some potential accident scenarios (releaseable T-inventory), it is essential to incorporate methods and procedures to detect and efficiently remove tritium from co-deposited layers.

One cleaning method that is being highly considered is the introduction of oxygen into the confinement vessel while heating the first wall. Oxidation of the co-deposited layer can remove both the carbon and hydrogen by eroding the hydrogenated graphite layer producing $(D/T)_2O$ and CO/O_2 which than can be removed by the tritium clean-up system. A major drawback to this approach is that in order to get an acceptable removal rate of the co-deposited carbon layer (> 2 x 10^{-9} m/hr for carbon) the wall temperature of the reactor will need to be heated to 350°C. In addition, this process loads the wall with O_2 that will need to be removed before tokamak operations re-commence.

The use of TA cleaning for removal of co-deposited carbon/tritium layers can provide the following advantages: 1) a non-line-of-sight

process which provides accessibility in shadowed regions, gaps, and recessed areas, 2) non intrusive method requiring short operational shut down times if used in conjunction with plasma spraying for *in-situ* repair, 3) gaseous/vapor residue may be processed by the existing tritium fuel clean-up system, 4) minimal wall conditioning after cleaning and 5) TA cleaning locally heats the surface for removal of contaminates and does not require bulk heating of the first wall.

To better understand the mechanisms of TA cleaning, investigations on the arc characteristics and cleaning efficiency were performed on beryllium, stainless steel and tungsten.

2. EXPERIMENTAL

The TA experiments were carried out in an inert environment plasma spray chamber. In order to purge the air from the system, the chamber was pumped down to 60 Pa and backfilled twice with argon before conducting experiments. The plasma torch used was a commercially available Praxair SG-100 using a 40kW Plasmadyne DC power supply. The torch gas used was argon and the flow rate was 40 standard liters per minute for all experiments. The TA power supply used was a 250 amp constant current DC supply built by Miller Electric, Inc. For all TA cleaning experiments the plasma torch arc was started with the torch away from the substrate. The torch was then moved close to the substrate and the TA power supply engaged manually. For the stainless steel and tungsten samples TA cleaning experiments were captured by a Canon (Canon, Tokyo, Japan) XL-1 digital video camera that was placed in front of a window port in the chamber. Voltage signals from the TA power supply were recorded with a Tektronix (Tektronix, Beaverton, OR) TDS 420A digital oscilloscope and P5200 high voltage differential probe. The TA power supply current was measured with the same oscilloscope using a Tektronix 503S current probe system with a high DC current probe.

The effect of TA cleaning of beryllium surfaces prior to plasma spraying was investigated by cleaning eight beryllium samples (25.4 mm wide x 12.7 mm long x 3.2 mm thick) which had been sputtered coated with 10 to 100 monolayers of tungsten and carbon. This combination of materials was chosen to simulate a contaminated surface similar to what might be expected in the ITER reactor if carbon, tungsten and beryllium are used as plasma facing materials. The sputtered coatings were produced from both tungsten and carbon anodes using 100 eV of Ar and D_2 at a 1:2 ratio, and a current of 100 mA for 30 minutes. The beryllium samples were located 76.2 mm from the sputter targets. Rutherford Backscattering Spectrometry (RBS) using 1.6 MeV He ions was used to characterize the surface of the beryllium before and after TA cleaning. The surface analysis included detection of carbon, tungsten, oxygen, argon and copper.

To investigate the TA removal efficiency of deuterium containing carbon films from stainless steel and tungsten, the PISCES-A device at the University of California, San Diego [4] was used to deposit carbon coatings on stainless and tungsten samples by installing an impurity gas puffing system (CD_4) in the target interaction region of the device. The fraction of impurity gas present was monitored prior to the plasma initiation by use of a quadrupole residual gas analyzer (RGA). Several identical samples were exposed to deuterium plasmas containing varying amounts of impurity fractions (from 0.1% carbon, up to 10% carbon). The temperature of the samples was monitored using thermocouples and an IR pyrometer. All samples were exposed to the deuterium containing plasma for 30 minutes. The radial profile of the plasma was measured using a fast reciprocating Langmuir probe. The ion flux across the face of the sample was measured to be constant within a few percent throughout the duration of the exposure.

The surface compositions of the stainless steel and tungsten samples before and after TA cleaning were measured at the Ion Beam Materials Laboratory using resonant backscattering of alpha particles and elastic recoil detection of the hydrogen isotopes [5]. An incident beam of 5.6 MeV alpha particles was focussed on a 2 x 2 mm^2 spot on the sample and the backscattered yield was measured with a Si solid state detector at a scattering angle of 167 degrees. The samples were tilted at 75 degrees from beam normal and the recoiling hydrogen isotopes were detected at a forward scattering angle of 30 degrees. A combination of Al and mylar absorber foils were used to stop the forward scattered alpha particles but allow transmission of the recoiling hydrogen and deuterium to the detector.

3. RESULTS AND DISCUSSION

3.1. Cathodic Arcing Characteristics on Beryllium, Stainless Steel, and Tungsten

The initiation of an arc at a cathode is though to take place by a combination of thermionic and field-enhanced emission of electrons as described by Juttner *et al.* [6]. Of interest when TA cleaning and roughening a metal surface is the erosion craters that result from the cathodic arc attachments. Figure 1 summarizes the mechanisms that occur during arc attachment and crater formation. A surface explosion, followed by melting and acceleration of molten metal initially forms the crater. After the crater formation, the discharge center is displaced to the rim and the cycle then repeats itself at another localized arc spot. The arcing/crater formation is categorized into one of three spot modes of operation, Types I, II and III. Table 1 gives the spot types and characteristic behavior associated with each.

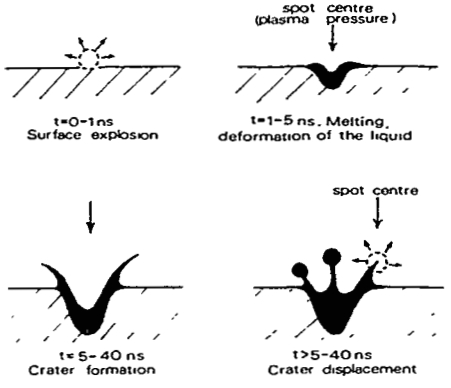

Figure 1. Mechanism for development of erosion craters on clean surfaces in vacuum [7].

Type I spots occur on oxidized or contaminated surfaces. The arc moves relatively quickly from place to place and leaves small, distinct craters while eroding a relative small amount of material per coulomb of electrons conducted. Type I cathode arc spots on stainless steel after TA removal of a carbon surface film are shown in Figure 2a. The arc attachments are discontinuous with a crater radius of less than 1 μm. Type II arc spots are also present in this figure. Type II spots appear on initially clean surfaces or surfaces that have been cleaned by Type I arcs.

Table 1. Cathode spot types and their characteristics[7].

Characteristic	Type I	Type II	Type III
occurrence conditions	oxidized surfaces	clean surfaces	small electrodes, ambient gas, hot cathodes
velocity (m/s)	10-1000	1-150	<1
spot current (A)	<10	5-50	5-50
lifetime (μs)	<0.01	<0.1	>10
crater appearance	discontinuous	overlapping	overlapping
crater radius (μm)	≤1	3-10	>10
erosion rate (μg/C)	<10	10-100	>100

Type II arcs have slower motion and leave connected craters of intermediate size (3-10μm) while eroding material much faster than Type I arcs. Figure 2b shows an example of Type II arc spots on beryllium after TA cleaning. Crater sizes are approximately 2-10 μm.

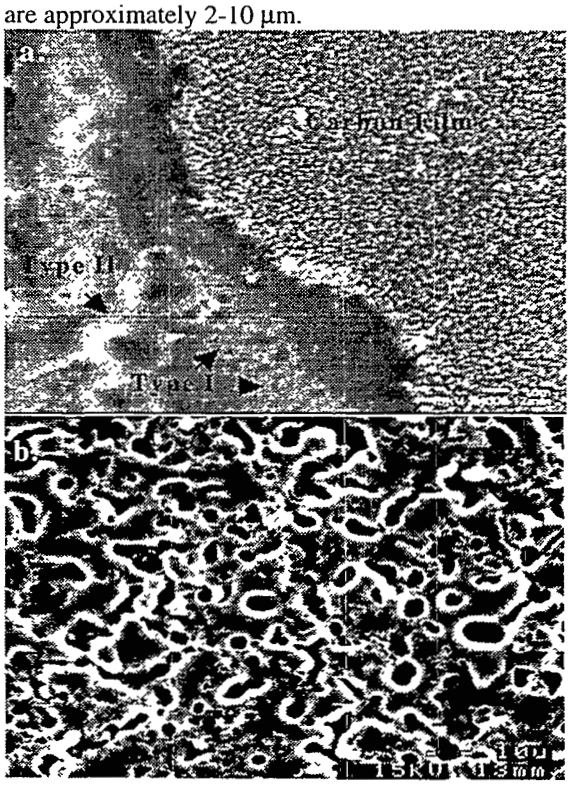

Figure 2. a) Type I and Type II cathode arc spots on stainless steel after TA removal of a carbon film,

b) Type II cathode arc spots on beryllium after TA cleaning.

Type III arc spots occur under conditions where the arc is fixed in place by special conditions such as special surface geometries, certain gas pressures, and/or elevated cathode temperatures. These spots move relatively slowly while leaving connected craters of large size (>10μm) and eroding relatively large amounts of material. Type III arc spots on beryllium, stainless steel and tungsten after TA cleaning are shown in Figure 3.

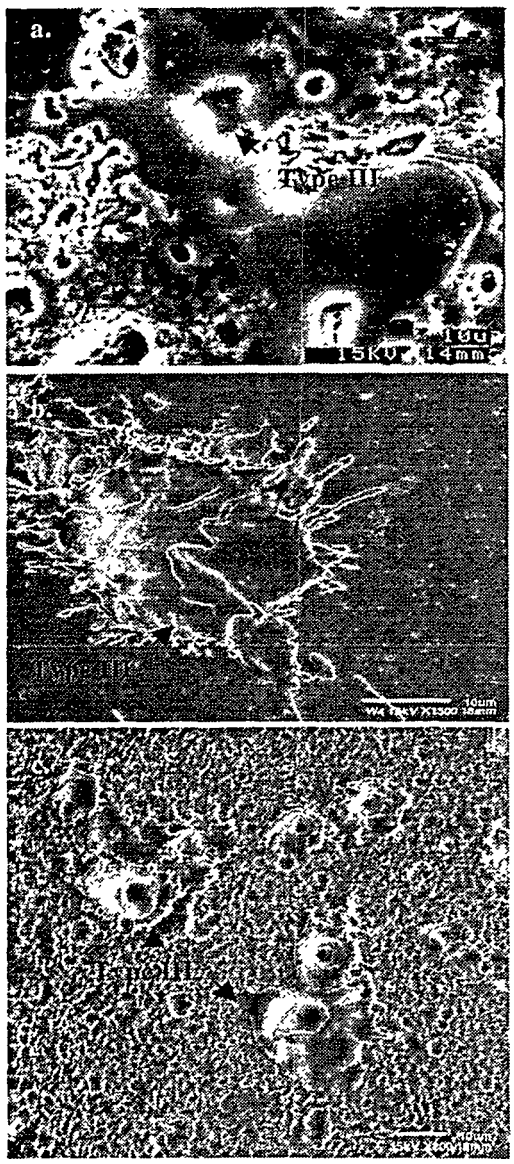

Figure 3. Type III arc spots on a) beryllium, b) tungsten and c) stainless steel after TA cleaning.

A Type III arc attachment is typically desired to maximize the roughness and improve the mechanical interlocking between a plasma spray coating and the TA cleaned surface. Evidence of the mechanical interlocking that occurs between a plasma sprayed beryllium coating on a TA cleaned beryllium surface is shown in Figure 4.

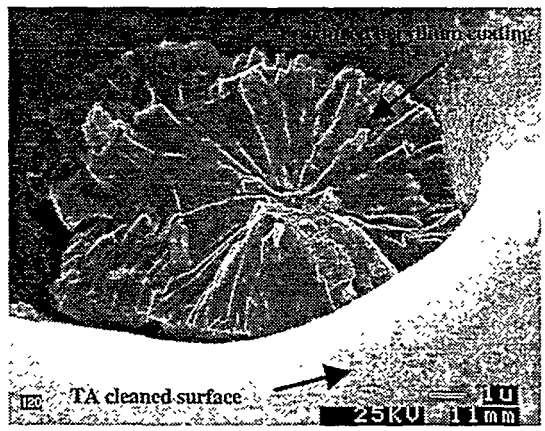

Figure 4. Fracture surface of a beryllium coating entrapped in a surface pore of a TA cleaned beryllium surface.

Surface craters present on the beryllium surface after TA cleaning act as sites where impacting molten beryllium particles can become entrapped during plasma spraying. This results in an interlocking between the coating and the beryllium surface. Bond strengths between plasma sprayed beryllium coatings and beryllium surfaces, which have been roughened by TA cleaning, have been reported to be as high as 250 MPa [8].

Other differences between Type I and II cathode arc spots include the amplitude of arc voltage and arc voltage fluctuations. The arc voltage is typically 20-30% lower for Type I spots and the fluctuation in arc voltage is higher for Type II spots. The lower arc voltage from the Type I spots is due to the presence of the impurity material that acts as a better electron emitter than the base metal. The better electron emission may result from a lower electron work function or the ability to develop a high local electric field due to space charge buildup on the impurity. The higher voltage fluctuation for Type II spots is due to the higher spot current. The

fluctuations are due to the extinguishing and restriking of individual arcs. Since the spot current is larger for type II spots than for Type I spots, there will be more Type I arcs than Type II arcs for a given total arc current. Since there are fewer arcs for Type II spots, the extinguishing and restriking of a single arc causes a larger voltage fluctuation than a single arc extinguishing and restriking for a Type I arc.

The voltage between the plasma torch face (anode) and surface to be cleaned (cathode) has been measured during TA cleaning runs. Figure 5 shows a typical voltage trace recorded during a TA cleaning run for copper. While the TA power supply was engaged with no arc between the torch face and sample, the voltage signal showed a sinusoidal fluctuation between 0 and 85 V with a frequency of 120 Hz (regions I and V in Fig. 5). When the arc attached to the substrate, the current signal increased and the voltage decreased in amplitude. Synchronization of the voltage data to video images allowed the determination of the voltage signal as a function of the observed arc behavior. This allowed, for instance, for the determination of the voltage for cleaning of the thin film contaminants (region II in Fig. 5) and a separate voltage for the arc attached to the base copper substrate (region IV in Fig. 5). Region III in Fig. 5 is the transition from the cleaning arc (Type I) to the metal arc (Type II).

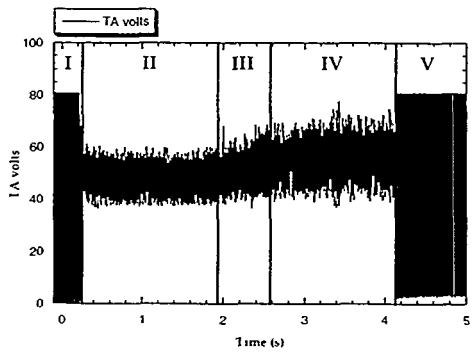

Figure 5 TA voltage during a copper cleaning run [9].

3.2. TA Cleaning Experiments

Beryllium

Results of the RBS analysis (reported in density free units) of the sputtered coated beryllium samples before TA cleaning are given in Table 2. The values reported for the tungsten and carbon correspond to a thickness of 1.0 to 3.5 nm for tungsten, and a thickness of 4.0 to 15.0 nm for carbon at "normal" densities. The detection of argon on the beryllium surface is a result of the argon sputtering process that may also account for the near surface detection of copper. As would be expected oxygen is present as a result of the native oxide that readily forms on the surface of beryllium. Results of the sputtered coated beryllium samples after TA cleaning are given in Table 3.

Table 2. 1.6 MeV He RBS at centerpoint of Be samples prior to TA cleaning (10^{15} atoms/cm^2).

I.D.	C	O	Ar	Cu	W
1	43.49	73.56	0 89	1.28	13.45
2	114.10	149 20	3 35	1.28	15 97
3	50.41	76.00	2 38	0 63	19 12
4	152.10	116.30	1 72	7.72	21 59
5	37.58	79.08	1.84	0 06	17 78
6	96.16	75.05	1.86	0 08	12 73
7	68.55	98.63	1.39	3 45	10 54
8	116.80	83 73	2 02	5 74	6.73

Table 3. 1.6 MeV He RBS at centerpoints of Be samples following TA cleaning (10^{15} atoms/cm^2).

I.D.	C	O	Ar	Cu	W
1	n.d	85.00	n.d	u d	1.10
2	n.d	65.00	n d	u d	0.68
3	n.d	55.00	n d	u d	3 00
4	n.d	93.00	n.d	u.d.	0.41
5	n.d	61 00	n.d.	u.d.	7 00
6	n d.	43 00	n.d.	u d	9 60
7	n.d	83.00	n.d	u d	0 71
8	n.d	120 00	n d	u d	1 30

n.d. = not detectable
u.d = present but undetermined quantity

RBS analysis showed that both the carbon and argon present on the surface of all eight beryllium samples were no longer detectable (minimum detection limit < 10^{13} atoms/cm^2) For most of the beryllium samples, the surface tungsten was also reduced by an order of magnitude. An increase in the amount of copper on the surface of the beryllium was detected which extended beyond the range of the RBS analysis (>4.2 x 10^{18} atoms/cm^2). The elevated

levels of copper may result from the TA cleaning process which utilizes the copper face of the plasma torch as the anode when cleaning the beryllium surface. Oxygen was still present on all the beryllium samples as a result of air exposure to the samples prior to the RBS analysis.

Table 4. PISCES-A exposure conditions for stainless steel and tungsten.

Sample	Time (s)	Temp (C)	Bias (V)	Carbon %	D+ fluence (cm-2)
Tungsten	1800	325	-150	10	2.20E+20
Stainless Steel	1800	525	-150	5	2.90E+21

Stainless Steel and Tungsten

The exposure conditions for stainless steel and tungsten samples (25.4 mm diameter x 3.175 mm thick) in the PISCES-A device is given in Table 4. The surface analysis of the stainless steel and tungsten samples before and after TA cleaning can be summarized as follows:

- The tungsten sample had a starting deuterium areal density of 53.1 x 10^{16} atoms/cm^2 and an ending value below the backscattering detection limit (~ 1 x 10^{14} atoms/cm^2) after cleaning. This represents a cleaning efficiency of > 1/5310 or 99.98%. The tungsten sample had a 1000 angstrom layer of carbon intermixed with tungsten before TA cleaning and no detectable carbon after cleaning. Surface analysis results for tungsten are shown in Figure 6 before and after TA cleaning.
- The stainless steel sample had a starting deuterium areal density of 7.4 x 10^{16} atoms/cm^2 before cleaning. The amount of deuterium after cleaning was below the backscattering detection limit (~ 1 x 10^{14} atoms/cm^2). A 3000 angstrom surface layer which contained 67% carbon was detected on the stainless steel before TA cleaning. The carbon level was substantially reduced to 27% after cleaning. Surface analysis results for stainless steel are shown in Figures 7 before and after TA cleaning.

The mechanism for removal of deuterium by TA cleaning is most likely a combination of thermal desorption and material removal. Large power densities (~1.5 x 10^9 W/cm^2) can result at the cathode spots as a result of current densities on the order of 10^8 A/cm^2 [7]. Power densities of this order can cause melting and erosion of the surface in addition to producing localized thermal gradients, which promotes the diffusion of deuterium from the sample surface.

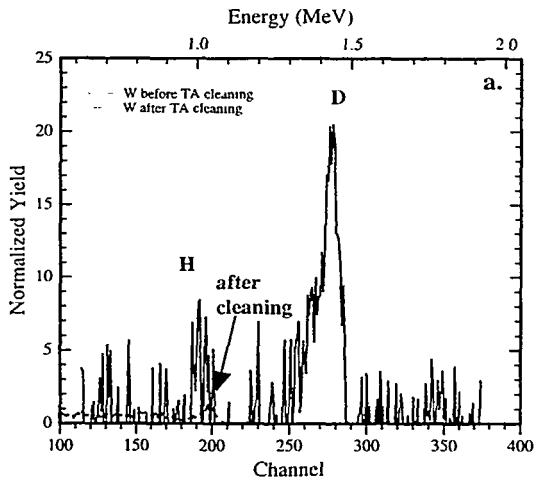

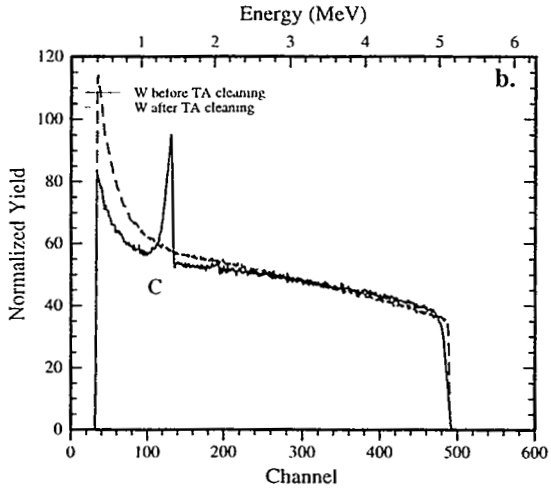

Figure 6 Surface analysis of tungsten before and after TA cleaning a) hydrogen and deuterium and b) carbon.

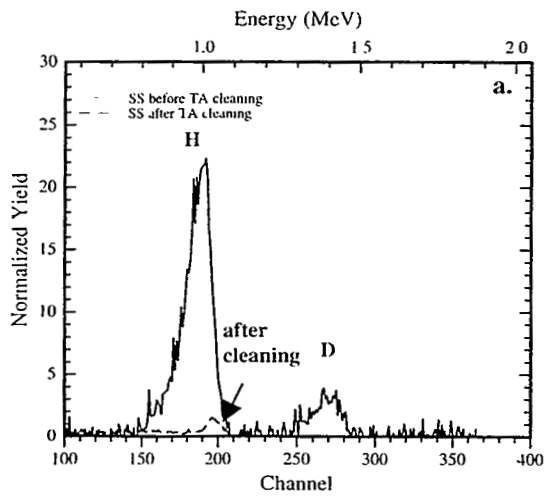

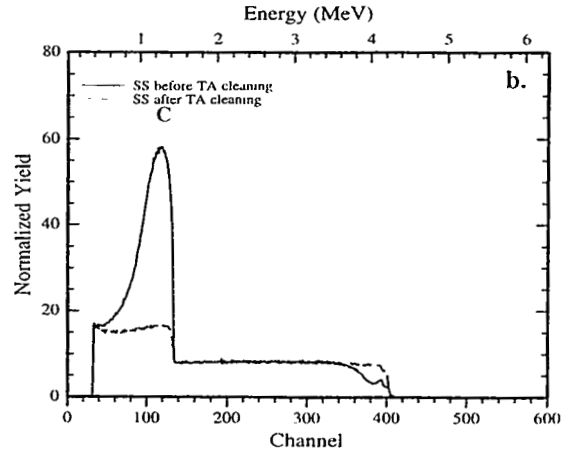

Figure 7. Surface analysis of stainless steel before and after TA cleaning. a) hydrogen and deuterium and b) carbon

4. CONCLUSION

Results of TA cleaning for roughening and removing surface contamination from beryllium, tungsten and stainless steel can be summarized as follows:

- During TA cleaning arc attachments on the surface of beryllium, tungsten and stainless leaves surface craters that were formed by the displacement of melted material. The arc attachments/craters can be classified as either Type I, II or III cathode spot types as defined by Juttner *et al* [7].
- Type III arc attachments leave large (>10μm) connected craters which is desirable to maximize the mechanical interlocking and bond strength between a plasma sprayed coating and the underlying material.
- TA cleaning was shown to be an effective method for removing carbon and hydrogen isotopes from the surface of beryllium, tungsten and stainless steel.

ACKNOWLEGMENTS

The authors would like to thank Keith Elliott for his contributions on the TA cleaning of beryllium. This research was funded through the Technology

Partnership Program Office at Los Alamos National Laboratory and the DOE Office of Fusion Energy.

REFERENCES

1. G. Federici, R. Causey, P.L. Andrew and C.H. Wu, Fusion Engineering and Design 28 (1995) 136-148.
2. W. Hsu and R.A. Causey, J. Vac. Sci. Technol. A, Vol. 5 No.4 (1987) 2768-2772.
3. R.A. Causey, W.L. Chrisman, W.L. Hsu, R. Andrel and B. Wishard, J. Vac. Sci Technol. A, Vol. 7, No. 3 (1989) 1078-1082.
4. D. M. Goebel, J. Bohdansky, R. W. Conn et , Nucl. Fusion 28 (1988) 1041.
5. Handbook of Modern Ion Beam Analysis, Eds. Joseph R. Tesmer and Michael Nastasi, Materials Research Society, Pittsburgh, PA (1995).
6. B. Juttner, V. Puchkarev, E. Hantzsche, I. Beilis, "Cathode Spots", *Handbook of Vacuum Arc Science and Technology*, R. Boxman, P. Martin, D. Sanders, Eds., Noyes Publications, 1995, p 73.
7. A.E. Guile and B. Juttner, IEEE Transactions on Plasma Science, Vol. PS-8, No. 3, Sept 1980, pp. 259-269
8. R.G. Castro, A.H. Bartlett, K.J. Hollis and R.D. Fields, Fusion Eng. and Design 37 (1997) 243-252.
9. K.J. Hollis, R.G. Castro, and B.D. Bartram, Proceedings United Thermal Spray Conf., March 17-19, Dusseldorf, Germany, pp. 202-207.

Structure of Helical Divertor Plasmas in LHD

H.Suzuki
National Institute for Fusion Science

Topics

1.Poincare Plot of magnetic line of the LHD

2.Simple View

3.Structure of the magnetic line of helical device

4.Structure of the magnetic line at the edge and the divertor legs

5.Calculated prediction and experimental measurements

6.Conclusion

1.Poincare Plot of the Magnetic line of the LHD

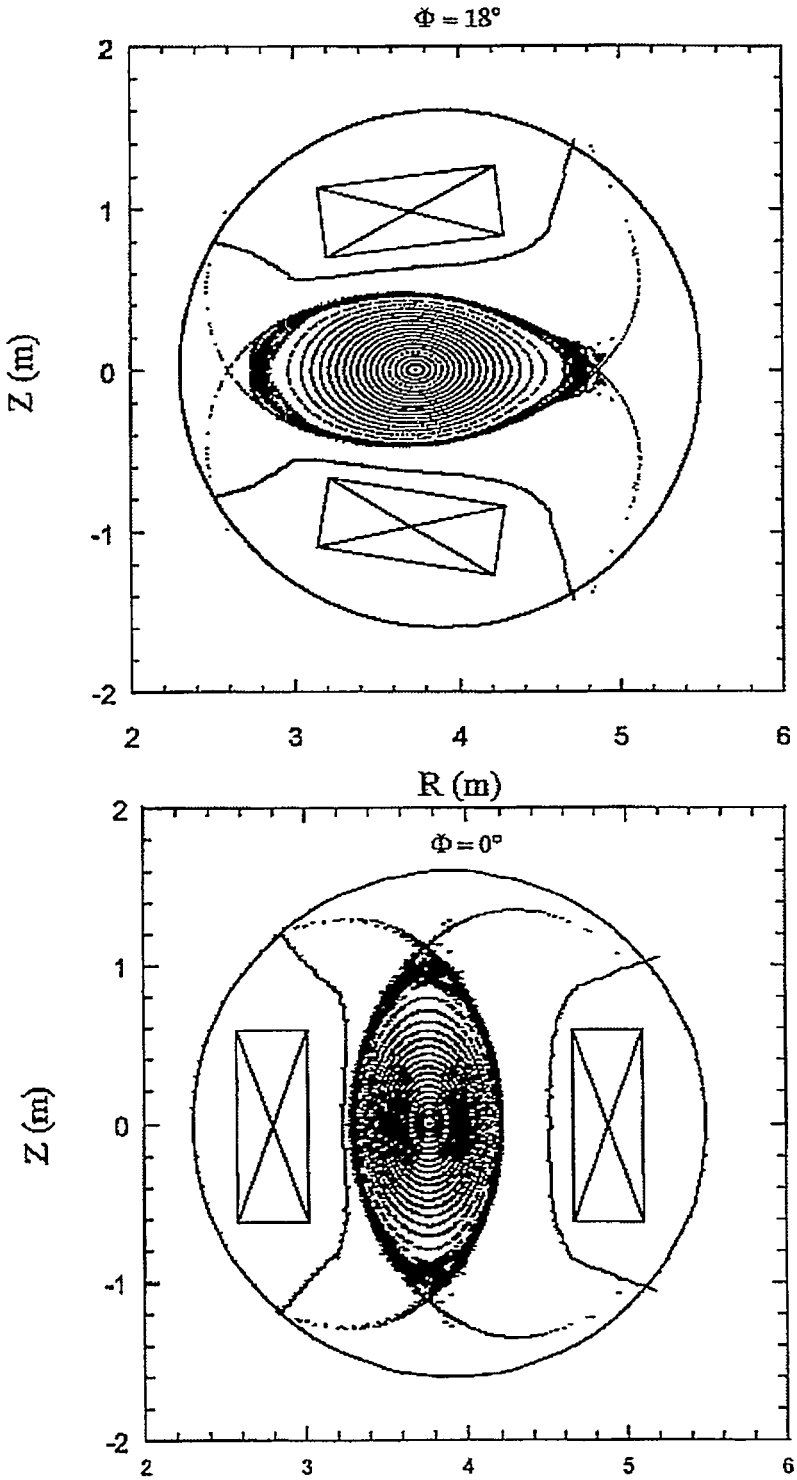

2.Simple View

Direction of Magnetic field

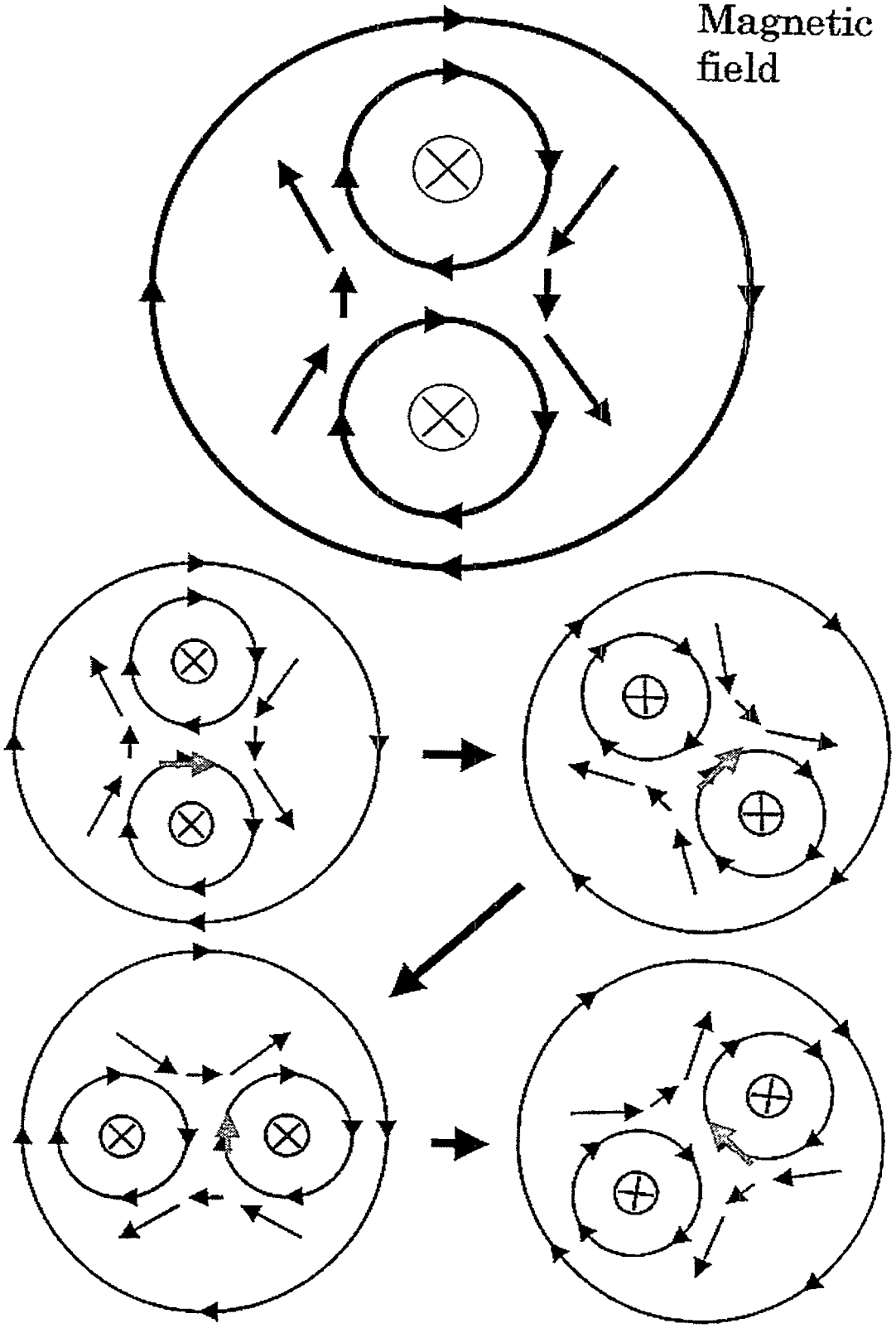

3.Structure of the magnetic line of helical device

3-1. Lagrangian of a charged particle in a magnetic field

$$L = \frac{1}{2}m\left(\dot{r}^2 + \left(r\dot{\varphi}\right)^2 + \dot{z}^2\right) + e\left(\dot{r}A_r + r\dot{\varphi}A_\varphi + \dot{z}A_z\right)$$

3-2. toroidal symmetry and Lagrangian invariant. (tokamak case)

$$L(r,\varphi+\Delta\varphi,z) - L(r,\varphi,z)$$
$$= \frac{\partial L}{\partial \varphi}\Delta\varphi + \frac{\partial L}{\partial \dot{\varphi}}\Delta\dot{\varphi} = 0$$

$$\frac{d}{dt}\left(mr^2\dot{\varphi} + erA_\varphi\right) = 0$$
$$P_\varphi = mr^2\dot{\varphi} + erA_\varphi = const.$$

3-3. Hamiltonian of a charged particle in a magnetic field

$$
\begin{aligned}
H &= P_r\dot{r} + P_\varphi\dot{\varphi} + P_z\dot{z} - L \\
&= \frac{1}{2}m\left(\dot{r}^2 + \left(r\dot{\varphi}\right)^2 + \dot{z}^2\right) \\
&= \frac{1}{2}\left(P_r - eA_r\right)^2 + \frac{1}{2}\left(P_z - eA_z\right)^2 + \frac{1}{2}\left(P_\varphi - erA_\varphi\right)^2
\end{aligned}
$$

magnetic surface function

$$\Psi = rA_\varphi$$

$$P_0 = P_\varphi = const.$$

$$H = \frac{1}{2}\left(P_r - eA_r\right)^2 + \frac{1}{2}\left(P_z - eA_z\right)^2 + \frac{1}{2}\left(P_0 - e\Psi\right)^2$$

To do the same, a magnetic surface function of a linear helical device can be obtained.

3-4. helical symmetry and Lagrangian invariant. (linear helical device case)

$$L(r,\varphi+\Delta\varphi,z+\Delta z)-L(r,\varphi,z)=\Delta L=0$$
$$\Delta\varphi=\alpha\Delta z$$

$$\Delta L=\frac{\partial L}{\partial\varphi}\Delta\varphi+\frac{\partial L}{\partial\dot{\varphi}}\Delta\dot{\varphi}+\frac{\partial L}{\partial z}\Delta z+\frac{\partial L}{\partial\dot{z}}\Delta\dot{z}=0$$

$$\frac{d}{dt}\left(\alpha mr^2\dot{\varphi}+\alpha erA_\varphi+m\dot{z}+eA_z\right)=0$$

$$P_0=\alpha mr^2\dot{\varphi}+\alpha erA_\varphi+m\dot{z}+eA_z$$
$$=\alpha mr^2\dot{\varphi}+m\dot{z}+e\left(\alpha rA_\varphi+A_z\right)=const.$$

Magnetic surface function of linear helical device

$$\Psi=\left(\alpha rA_\varphi+A_z\right)$$

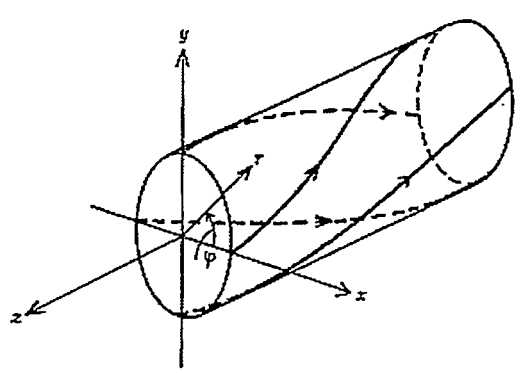

3-5. Magnetic potential ϕ

No electric current, stable condition

rot H = curl H =0 $\longrightarrow$ H=grad ϕ

Poisson equation

$$\nabla^2\phi = \frac{1}{r}\frac{\partial}{\partial r}\left(r\frac{\partial\phi}{\partial r}\right) + \frac{1}{r^2}\frac{\partial^2\phi}{\partial\theta^2} + \frac{\partial^2\phi}{\partial z^2} = 0$$

$$\phi = R(r)\Theta(\theta)Z(z)$$

Linear helical symmetry

$$\phi(r,\theta,z) = \phi(r, \theta+\Delta\theta, z+\Delta z) = \phi(r, \theta+\alpha\Delta z, z+\Delta z)$$

$$\frac{\partial\phi}{\partial\theta}\Delta\theta + \frac{\partial\phi}{\partial z}\Delta z = \left(\alpha\frac{\partial\phi}{\partial\theta} + \frac{\partial\phi}{\partial z}\right)\Delta z = 0$$

$$\alpha\frac{\partial\phi}{\partial\theta} + \frac{\partial\phi}{\partial z} = \alpha RZ\frac{\partial\Theta}{\partial\theta} + R\Theta\frac{\partial Z}{\partial z} = 0$$

$$\alpha\frac{1}{\Theta}\frac{\partial\Theta}{\partial\theta} + \frac{1}{Z}\frac{\partial Z}{\partial z} = 0$$

Each part should be a constant.

$$\frac{1}{\Theta}\frac{\partial\Theta}{\partial\theta} = il$$
$$\frac{1}{\alpha}\frac{1}{Z}\frac{\partial Z}{\partial z} = -il$$

$$\Theta = e^{il\theta}$$

$$Z = e^{-il\alpha z}$$

Poisson equation becomes,

$$\frac{1}{R}\frac{1}{r}\frac{\partial}{\partial r}\left(r\frac{\partial R}{\partial r}\right) - l^2\frac{1}{r^2} - (l\alpha)^2 = 0$$

$$\rho = l\alpha r$$

$$\frac{\partial^2}{\partial\rho^2}R + \frac{1}{\rho}\frac{\partial}{\partial\rho}R - \left(1 + \frac{l^2}{\rho^2}\right)R = 0$$

Bessel function I

$$R(\rho) = I_l(\rho) = I_l(l\alpha r)$$

Magnetic potential

$$\phi = I_l(l\alpha r)e^{il(\theta - \alpha z)} = I_l(l\alpha r)\sin(l(\theta - \alpha z))$$

General representation

$$\phi = B_0 z + \frac{1}{\alpha} \sum_{l=1}^{\infty} b_l I_l(l\alpha r) \sin(l(\theta - \alpha z))$$

Magnetic field

$$B_r = \sum_{l=1}^{\infty} l b_l I_l'(l\alpha r) \sin(l(\theta - \alpha z))$$

$$B_\theta = \sum_{l=1}^{\infty} \frac{1}{\alpha r} l b_l I_l(l\alpha r) \cos(l(\theta - \alpha z))$$

$$B_z = B_0 - \sum_{l=1}^{\infty} l b_l I_l(l\alpha r) \cos(l(\theta - \alpha z))$$

Vector potential

$$A_r = -\frac{1}{\alpha 2 r} \sum_{l=1}^{\infty} b_l I_l(l\alpha r) \sin(l(\theta - \alpha z))$$

$$A_\theta = \frac{B_0}{2} r - \frac{1}{\alpha} \sum_{l=1}^{\infty} b_l I_l'(l\alpha r) \cos(l(\theta - \alpha z))$$

$$A_z = 0$$

Magnetic surface

$$\psi = A_z + \alpha r A_\theta$$

$$= \frac{B_0}{2} r^2 - r \sum_{l=1}^{\infty} b_l I_l'(l\alpha r) \cos(l(\theta - \alpha z))$$

$$= const.$$

General representation

$$\phi = B_0 z + \frac{1}{\alpha} \sum_{l=1}^{\infty} b_l I_l(l\alpha r) \sin(l(\theta - \alpha z))$$

Magnetic field

$$B_r = \sum_{l=1}^{\infty} l b_l I_l'(l\alpha r) \sin(l(\theta - \alpha z))$$

$$B_\theta = \sum_{l=1}^{\infty} \frac{1}{\alpha r} l b_l I_l(l\alpha r) \cos(l(\theta - \alpha z))$$

$$B_z = B_0 - \sum_{l=1}^{\infty} l b_l I_l(l\alpha r) \cos(l(\theta - \alpha z))$$

Vector potential

$$A_r = -\frac{1}{\alpha 2 r} \sum_{l=1}^{\infty} b_l I_l(l\alpha r) \sin(l(\theta - \alpha z))$$

$$A_\theta = \frac{B_0}{2} r - \frac{1}{\alpha} \sum_{l=1}^{\infty} b_l I_l'(l\alpha r) \cos(l(\theta - \alpha z))$$

$$A_z = 0$$

Magnetic surface

$$\psi = A_z + \alpha r A_\theta$$

$$= \frac{B_0}{2} r 2 - r \sum_{l=1}^{\infty} b_l I_l'(l\alpha r) \cos(l(\theta - \alpha z))$$

$$= const.$$

$$\psi = A_z + \alpha r A_\theta$$
$$= \frac{B_0}{2} r^2 - r \sum_{l=1}^{\infty} b_l I_l'(l\alpha r) \cos(l(\theta - \alpha z))$$
$$= const.$$

(l is corresponded with a number of coils.)

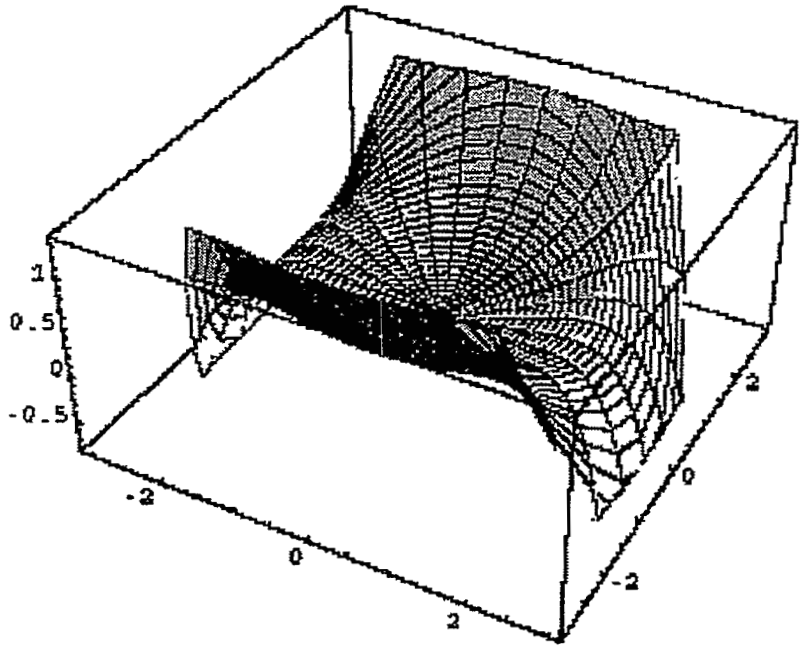

Magnetic Surface Function l=2,z=0

Equilibrium point (center) O-point

Equilibrium point (saddle) X-point

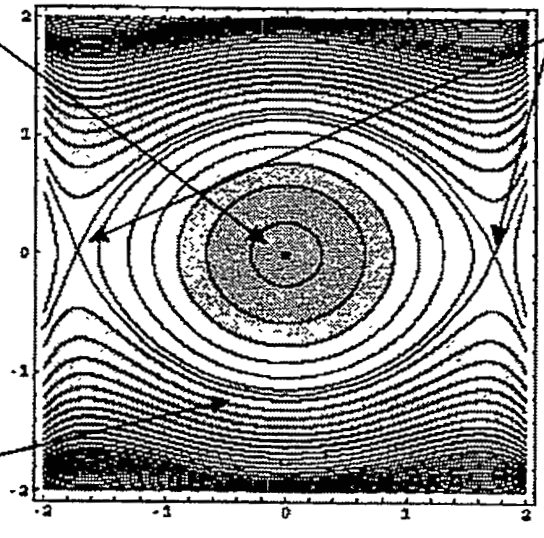

Separatrix

Contour plot

3-6. Magnetic surface of circular helical device

No symmetry!

No analytic magnetic surface function!

Consider:

Magnetic surface of linear helical device
+
perturbation

1) The X-point and the separatrix still remain?

No.
Separatrix breaks and ergodic (chaotic) structure appears.

2) The toruses around the O-point still remain?

YES.
KAM torus theory shows an existence of stable torus orbit.

4.Structure of the magnetic line at the edge and the divertor legs

4-1. two kinds of chaotic structure

1) Overlapping of magnetic islands.

Rational surface is unstable.
If the rational surface resonates with a perturbation field (error field), the rational surface splits and make magnetic islands.

If a width of the islands is greater than a distance between two resonated rational surfaces, the islands overlap, and magnetic lines make a chaotic structure.

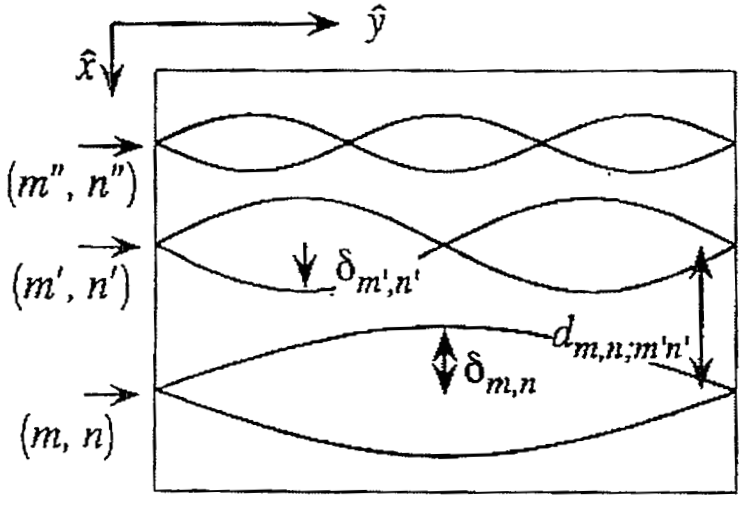

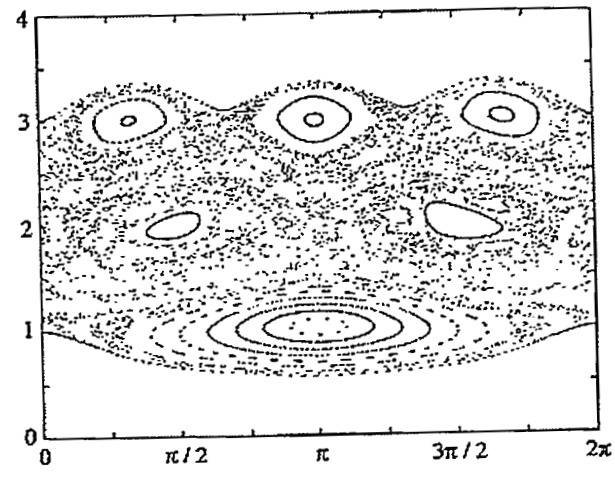

2) Deformation of torus and separatrix
(Whisker structure)

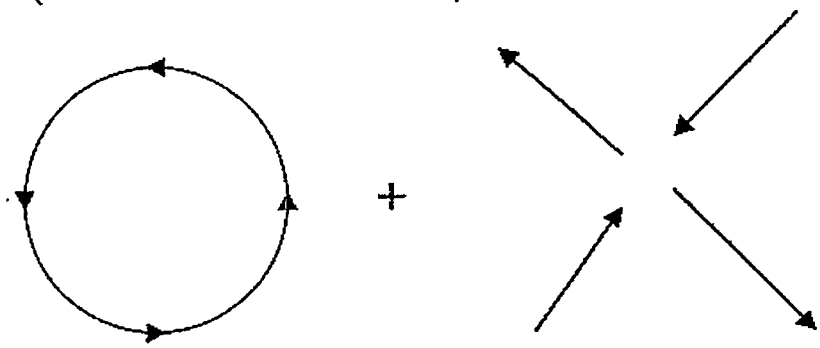

Torus Perturbation

Torus is pulled, folded up, and pushed.

So called baker mapping.

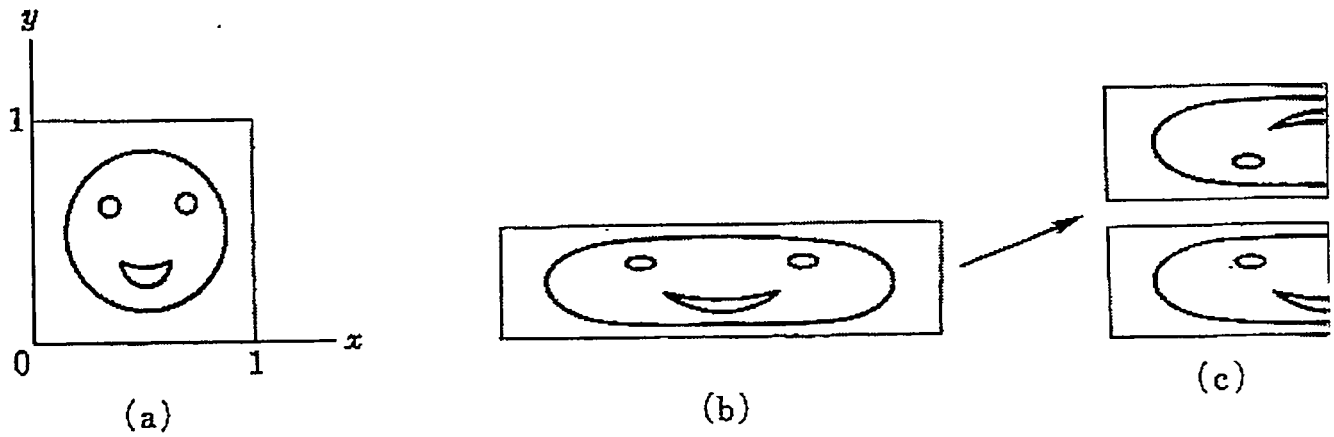

Moving of points

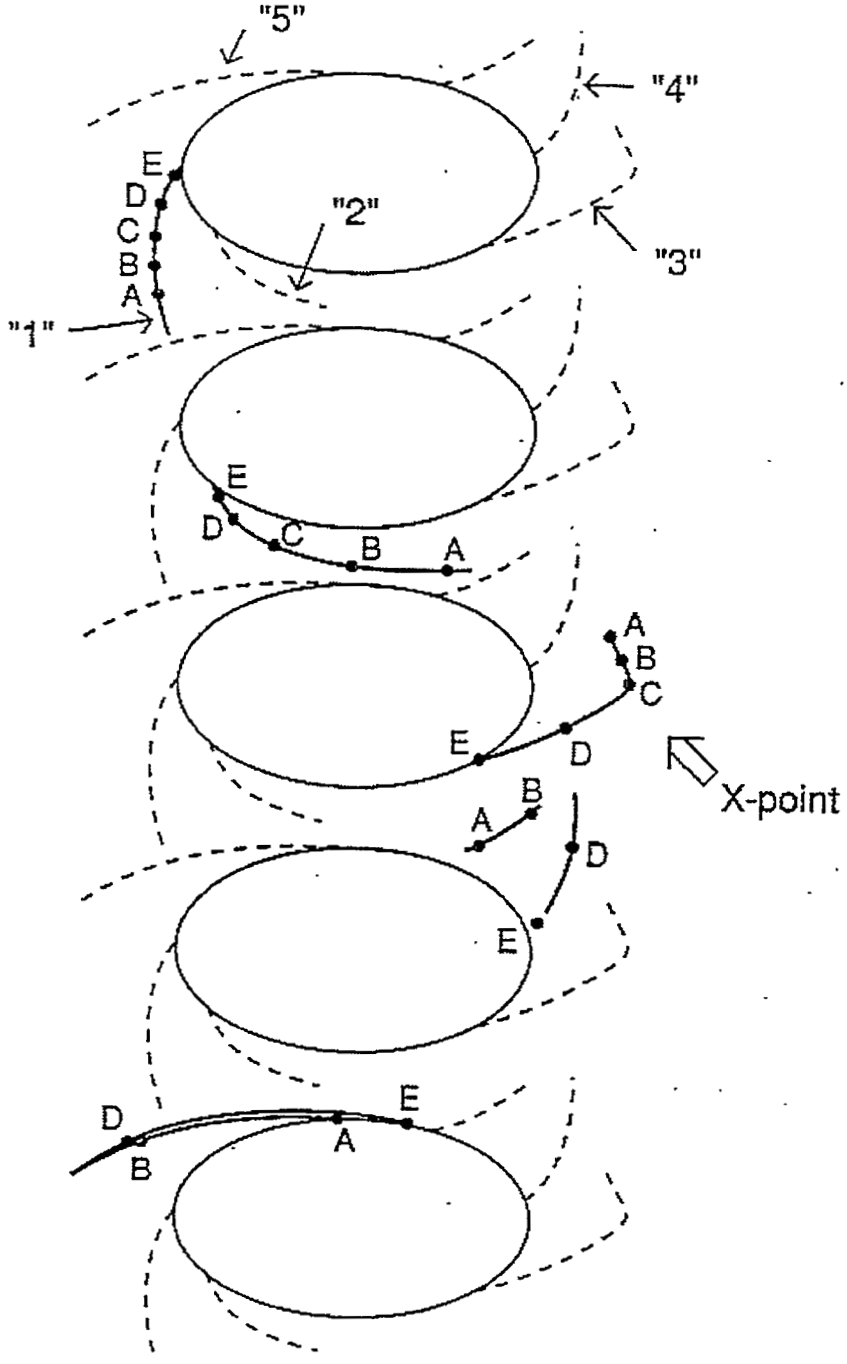

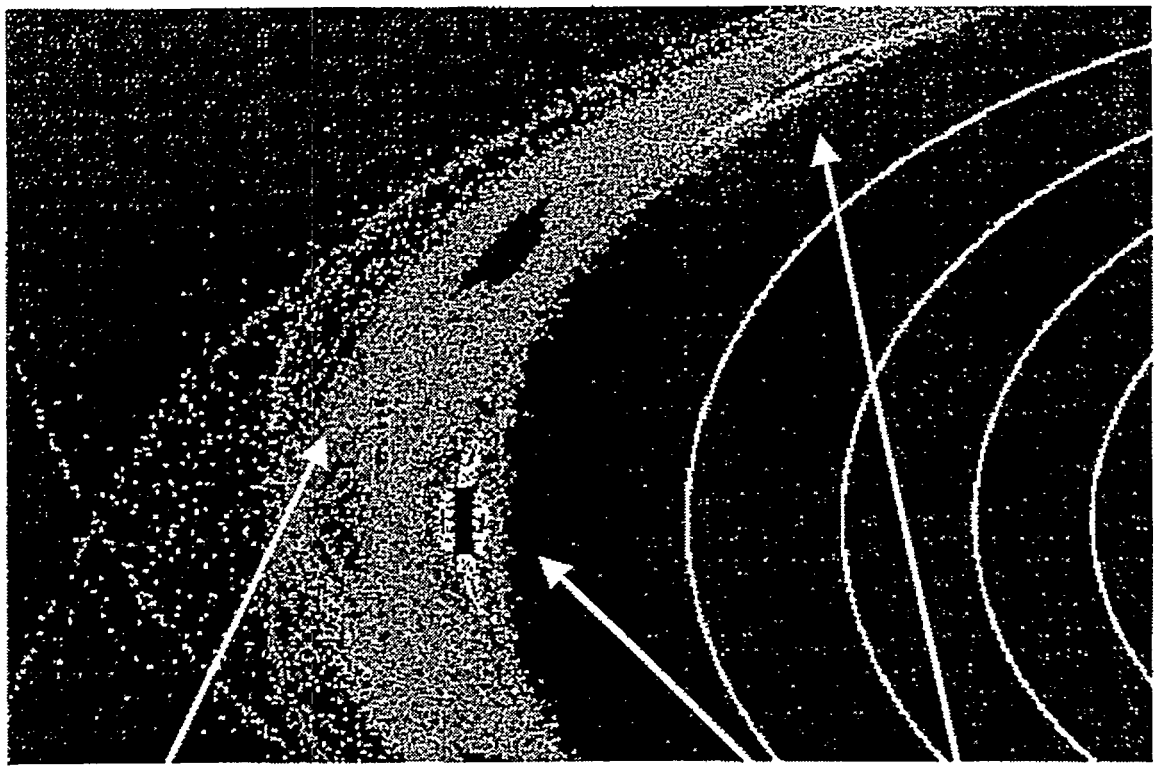

Whisker region

Natural
magnetic island

Experimental Setup ~ Langmuir Probe Array ~

NIFS

- 30 ch. Langmuir probe array which is set on a carbon tile is installed in the LHD from #1 inner diagnostics port.
- Probe tips are on the plane which is perpendicular to the helical coils.
- Spatial Resolution: 5 mm ~ 15mm
- Probe tips: Dome type (R 1 mm)
- The angle between the magnetic field line and the carbon tile surface is about 30 degree.

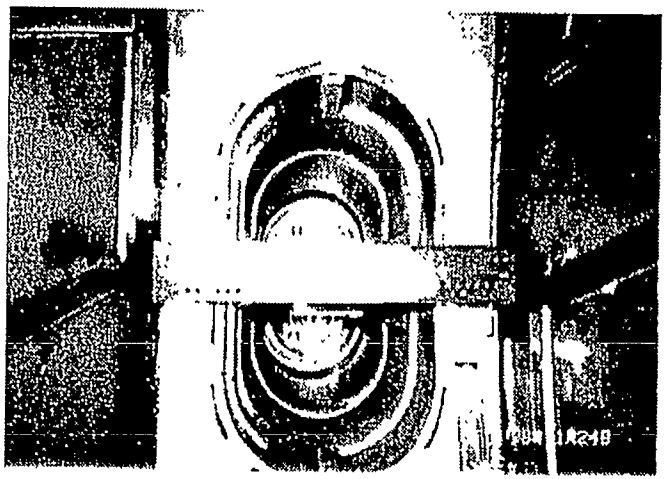

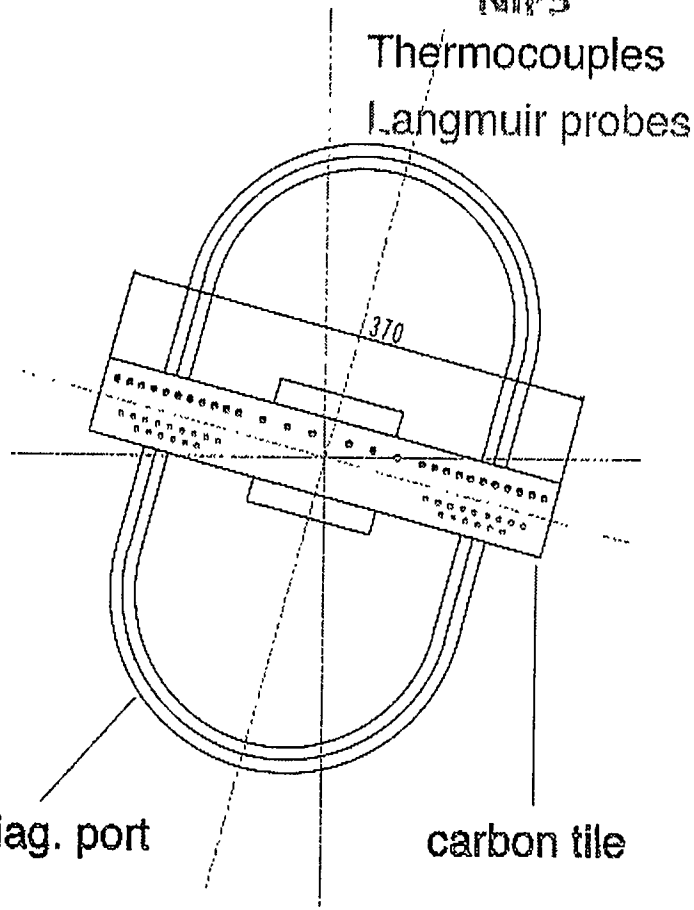

Particle Flux Profiles on the Divertor Plate

NIFS

- Measured particle flux (Γ_{div}) profiles are shown (⊙) for 3 discharges with different magnetic axes.
- Connection length profiles of the magnetic field line connecting to the divertor plate are also indicated.
- Connection lengths at the peaks of Γ_{div} are longer than 1000 m.
  → Much longer than those in tokamaks divertor.
- The peaks positions of Γ_{div} agree with the long magnetic fields' position.
- The width of the Γ_{div} profile is independent of the plasma parameter.
  it is considered to be restricted by magnetic sturcture.
  This result is agree with the previous calculation [1] qualitatively.

[1] N. Ohyabu, et al., Nucl. Fusion 34(1994) P.384.

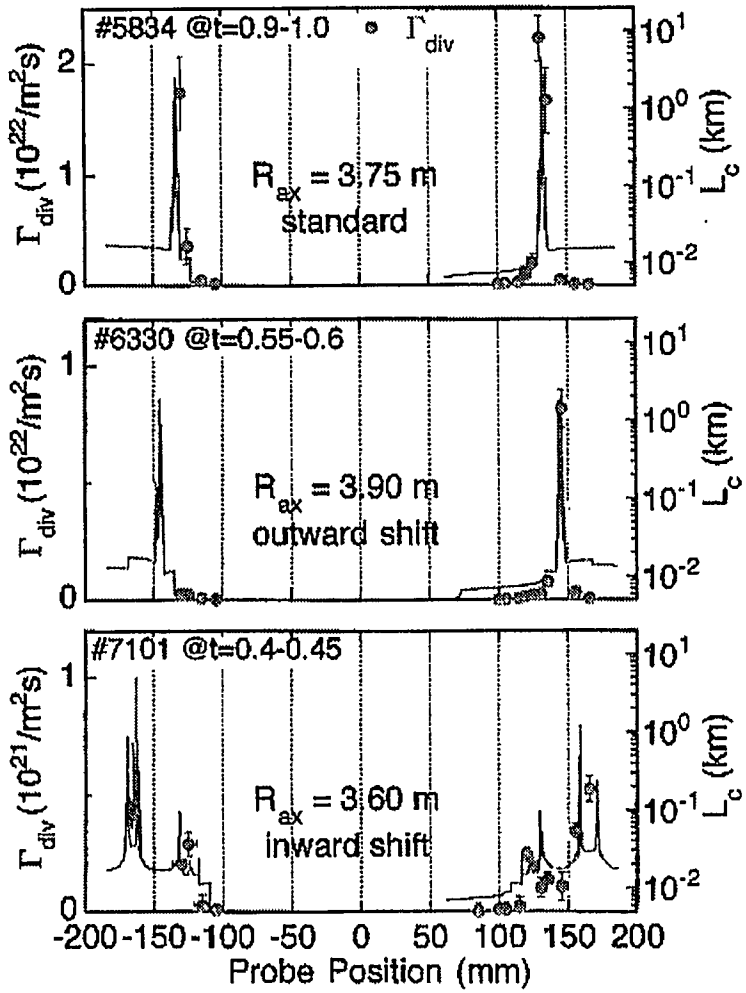

Schematic view of divertor leg

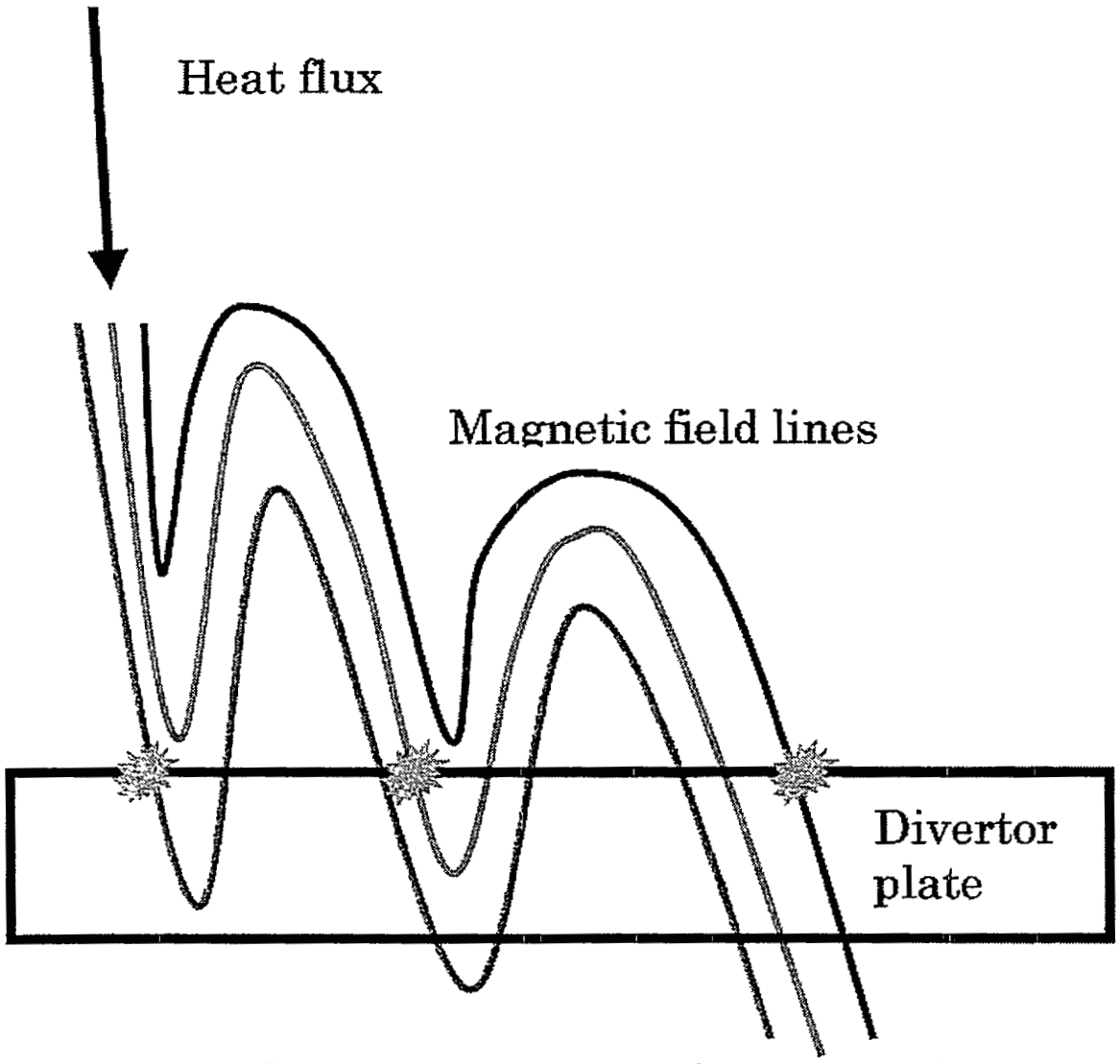

Because of special structure of magnetic field lines, hit points of plasma on divertor plate are discrete.

Asymmetry of heat flux

θ: direction of divertor plate
r: distance between center and cross point

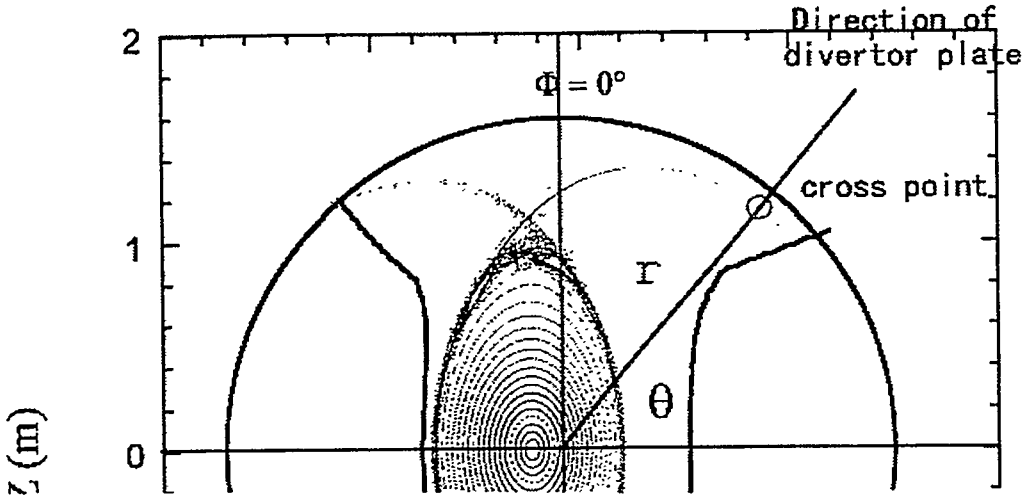

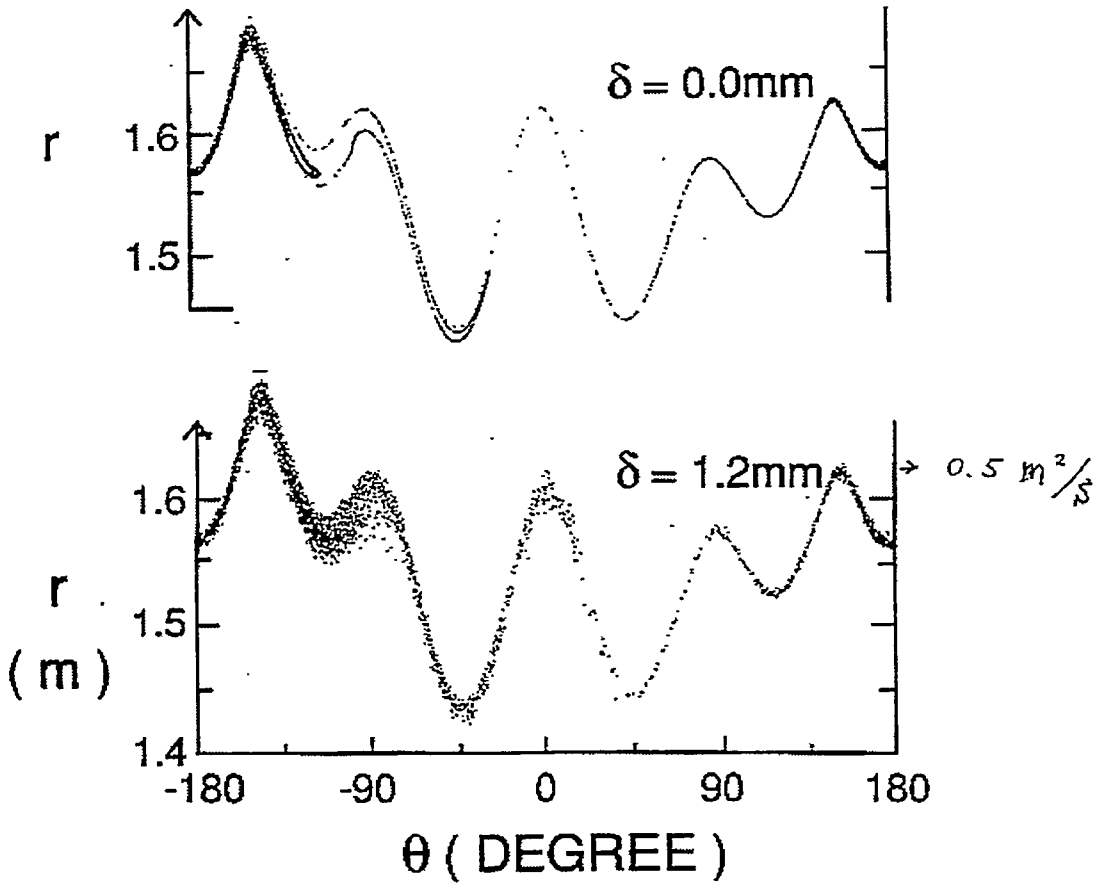

6.Conclusion

1) LHD has four divertor legs.

2) LHD has magnetic surface.

3) Structure of magnetic field at the edge of LHD plasma is chaotic.

4) Divertor legs have also complicated structure.

5) Because of the structure of magnetic field line, hit point on the divertor plate is discrete. And this structure has been observed experimentally at inside of the torus.

6) According to a Monte Carlo simulation, asymmetry of heat flux is predicted.

Particle Balance Modeling for Steady-State Magnetic Fusion Devices

- Effects of Plasma-Wall Interactions on the Global Particle Balance -

Presented at the US-Japan Workshop
Santa Fe, 11/1-11/4/99

Yoshi Hirooka

National Institute for Fusion Science, Japan

NIFS

4-reservoir particle balance model

- Core
  (1) Particle confinement loss: τ_p
  (2) External fueling gain
  (3) CX-particle gain from SOL
  (4)Wall recycling gas fueling gain

- SOL
  (1)Particle confinement loss: τ_{SOL}
  (2) Wall recycling gas fueling gain
  (3) CX-particle loss
  (4)External fueling gain
  (5)Gas ionization gain

- Gas
  (1) Wall recycling gas gain
  (2)Fueling loss
  (3) Pumping loss

- Wall
  (1) CX-particle implantation gain from SOL
  (2) Co-deposition gain

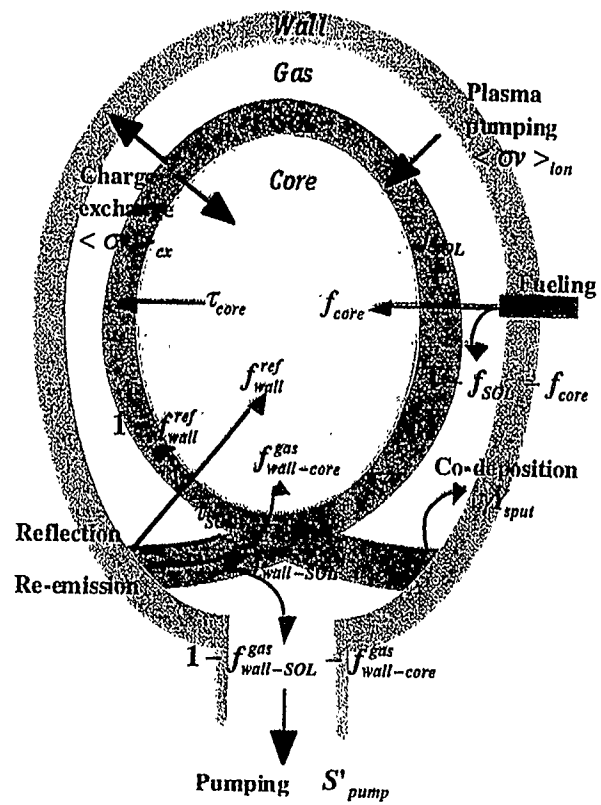

NIFS

Possible explanations of density decay during NBI-heating

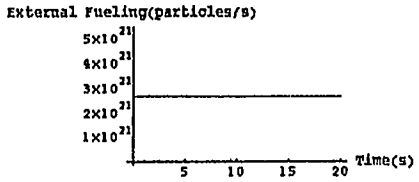

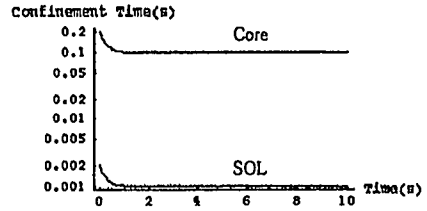

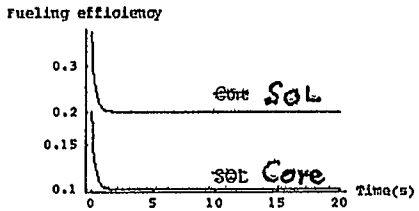

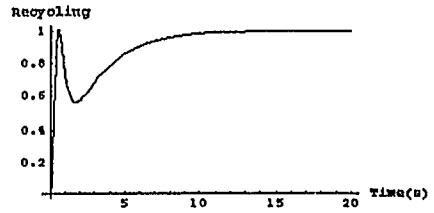

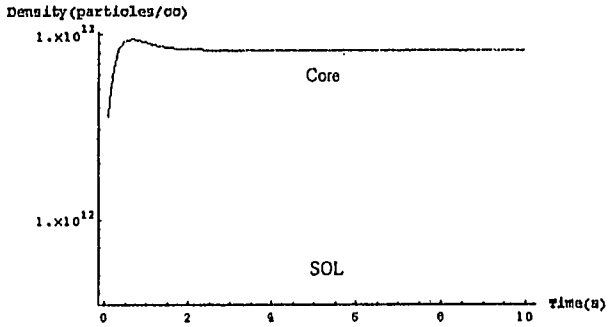

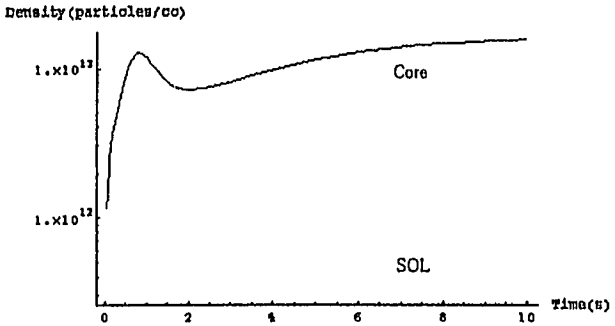

NIFS

A large pumping speed is needed to maintain the plasma density

Sp=10,000,000 liters/s

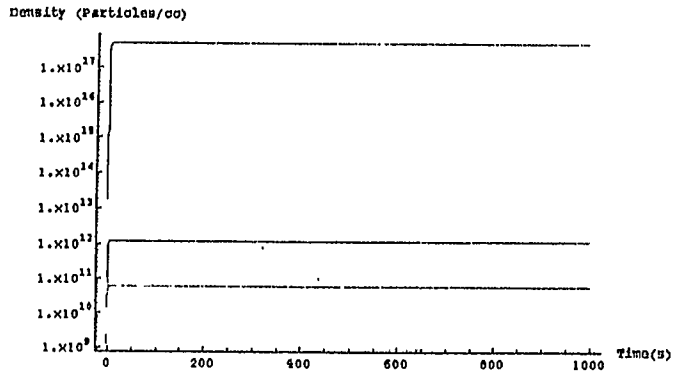

Sp=100,000 liters/s

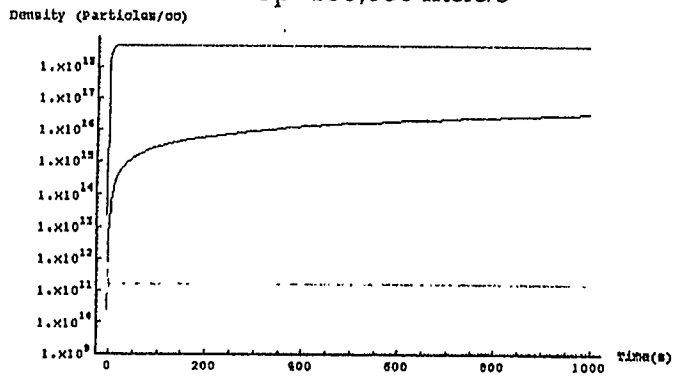

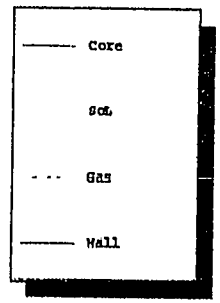

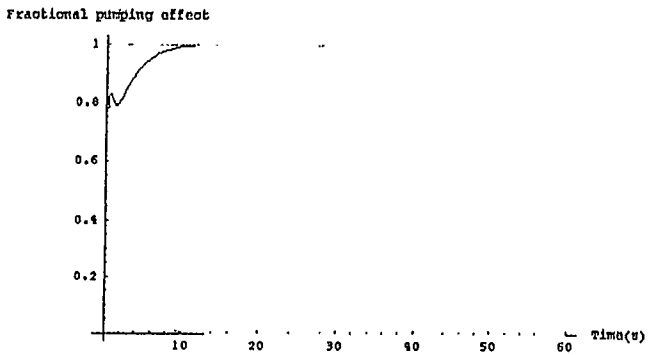

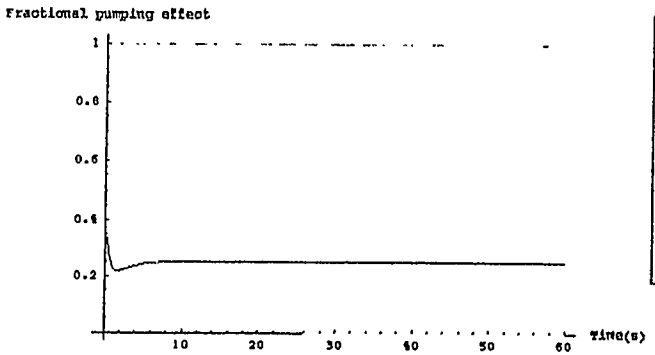

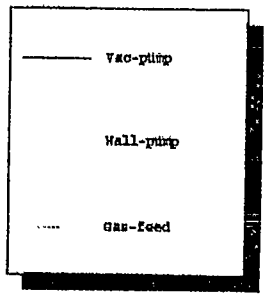

NIFS

Wall-pumping helps maintain the plasma density

Sp=1000,000 liters/s
Re=99%
Co-deposition: No

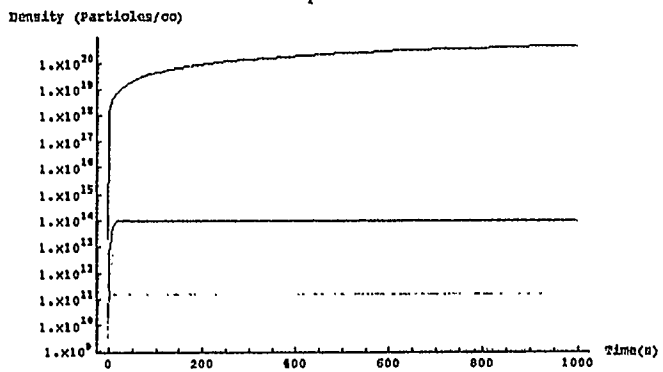

Sp=1000,000 liters/s
Re=99%
Co-deposition: Yes(40%)

a few grams of tritium

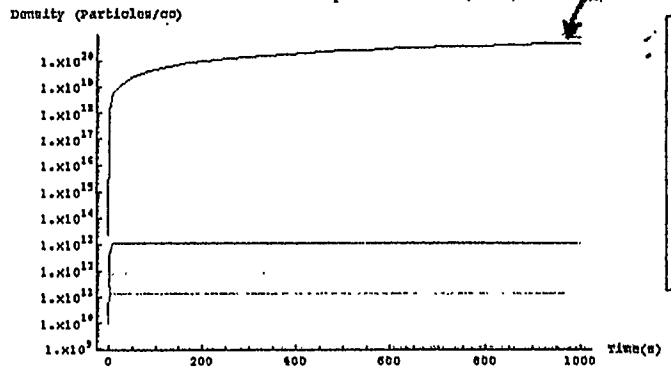

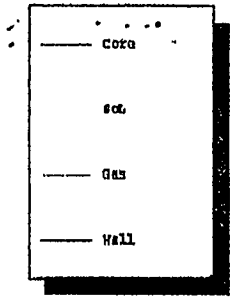

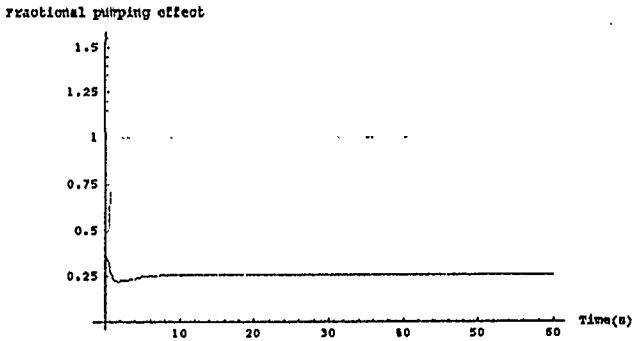

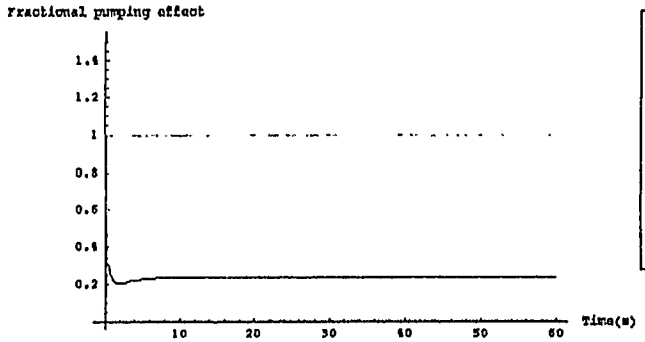

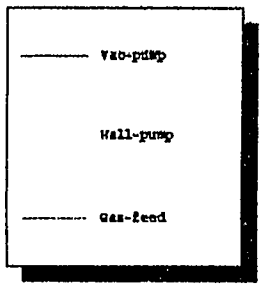

NIFS

What if cryo-pumps are saturated over a 1000 second discharge?

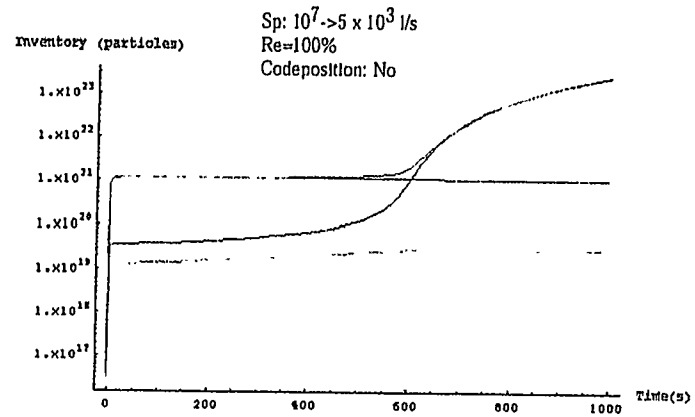

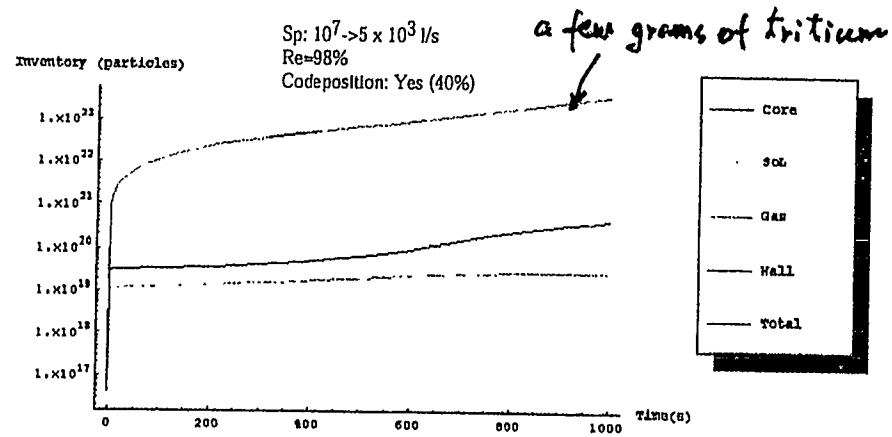

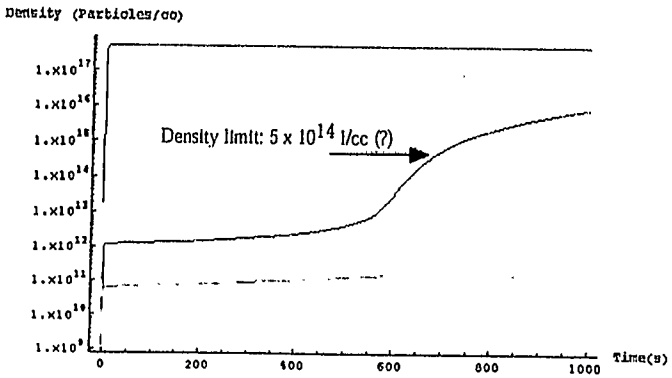

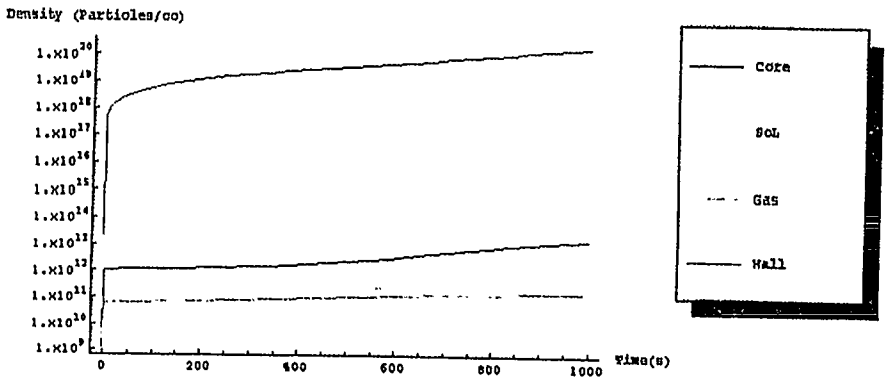

NIFS

Summary

- A zero-dimension particle balance model has been developed, assuming four reservoirs: core, SOL, gas, and wall.

- The model has successfully been applied to analyze the data on density decay, observed during NBI-heating in LHD and also in JT-60. Results indicated that PWI plays an important role.

- Model analysis has indicated that without wall pumping an extremely large pumping speed will be needed to maintain the plasma density for steady-state operation. However, one cannot fully take advantage of wall pumping because of tritium build-up.

- If cryo-pumps are saturated during a 1000 sec discharge, the plasma density will rise to the level the density limit may be exceeded.

NIFS

Summary of NSTX PFC Activities and Proposal for Liquid Metal Experiment in CDXU

R. Majeski, S. Luckhardt, R. Doerner, M. Finkenthal, PPPL
H. Ji, H, Kugel, D. Mansfield, D. Stutman, R. Woolley, University of California at San Diego
L. Zakharov and S. Zweben, Johns Hopkins University

Presented by:

Richard Nygren, SNLA

Liquid Lithium Wall Experiments in CDX-U

Presented by R. Kaita[a]

with R. Majeski,[a] S. Luckhardt,[b] R. Doerner,[b] M. Finkenthal,[c]
H. Ji,[a] H. Kugel,[a] D. Mansfield,[a] D. Stutman,[c] R. Woolley,[a]
L. Zakharov,[a] and S. Zweben[a]

[a]Princeton Plasma Physics Laboratory, Princeton University,
Princeton NJ 08543-0451

[b]University of California at San Diego, San Diego CA, 92093-0417

[c]Johns Hopkins University, Baltimore MD, 21218

18th IEEE/NPSS Symposium on Fusion Energy

Albuquerque, NM

October 25-29, 1999

Physics and technology issues to be studied

- Effects of fully non-recycling lithium target on plasma
  - Plasma current penetration and equilibrium control
  - Deuterium fueling and lithium impurity accumulation
  - Effects on plasma confinement and RF coupling/heating

- Effects of plasma on the liquid lithium surface
  - jxB forces on lithium during MHD activity and disruptions
  - Possible surface coatings such as lithium hydride

- Development of technology for liquid lithium targets
  - Long-term compatibility of vessel materials with lithium
  - Safe and efficient lithium handling and cleaning

PPPL

CDX-U has an extensive set of diagnostics

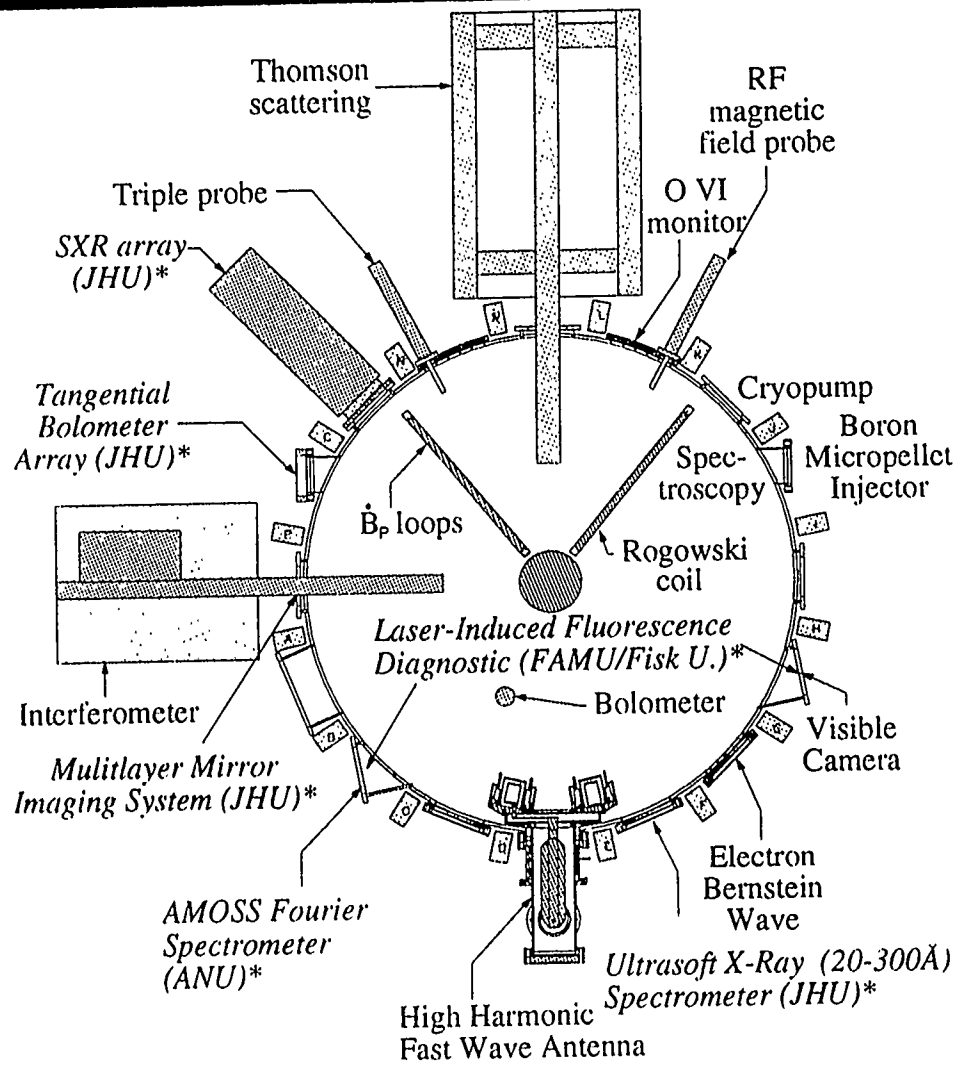

*Collaborator diagnostics

Various liquid lithium limiter schemes can be tested in CDX-U

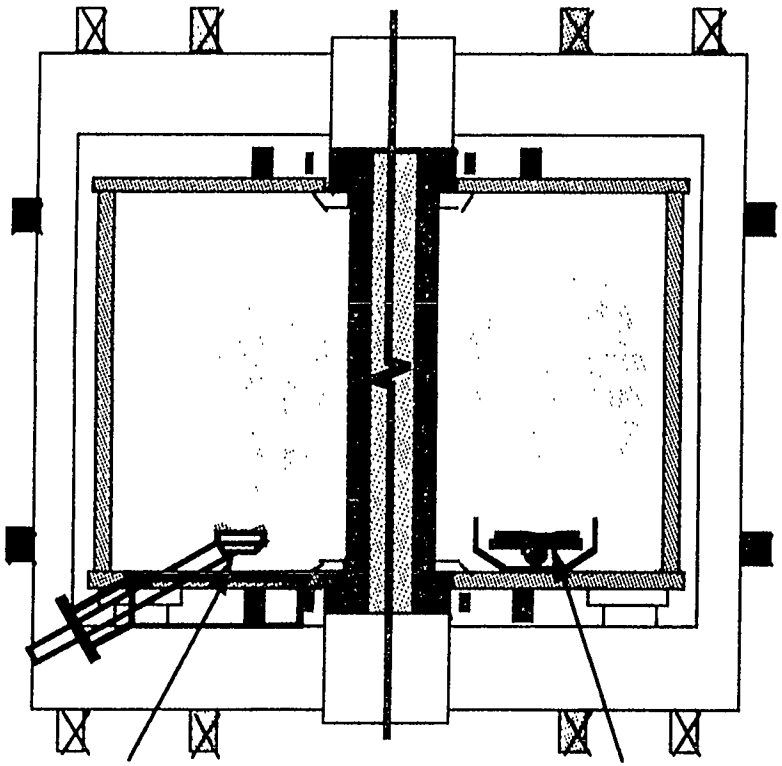

UCSD

PPPL

Concept for UCSD Liquid Lithium Limiter ("L3") on CDX-U

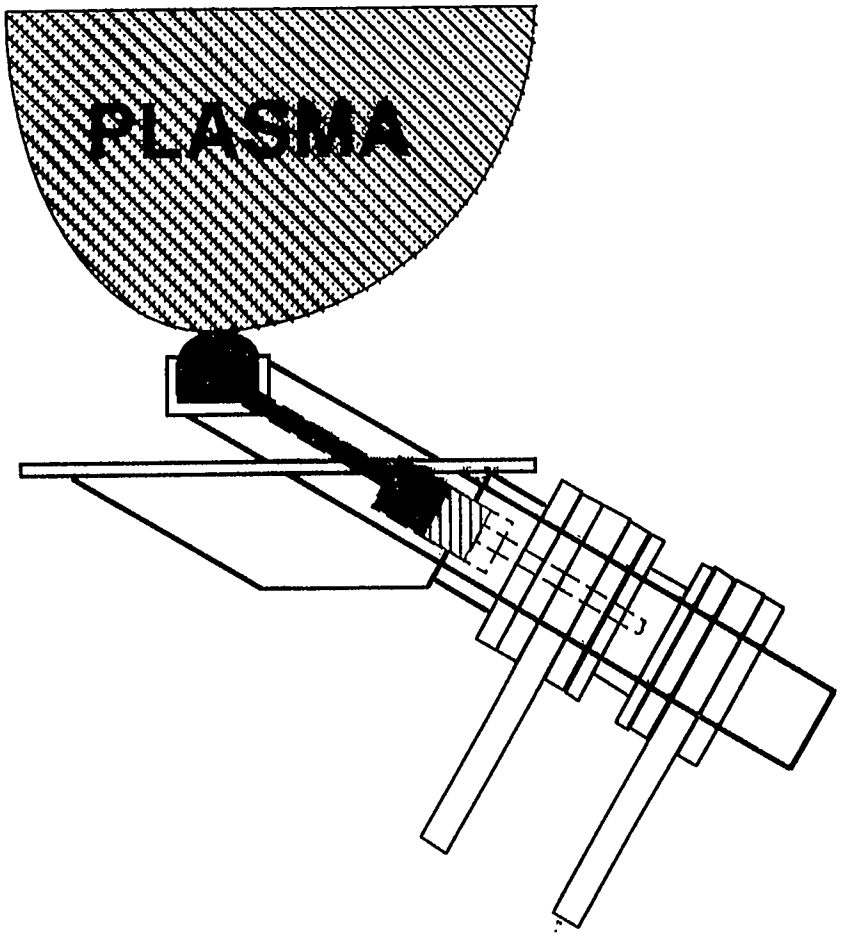

UCSD

PPPL

Interaction of liquid lithium and spherical torus plasmas can be studied in CDX-U

- $R_0 = 34$ cm
- $a = 22$ cm
- $A \equiv R_0/a \geq 1.5$
- $\kappa \leq 2$
- $\delta > 0.2$
- $B_t \leq 0.5$ Tesla (~0.5 sec)
  - CW fields at 1 kG
- Ohmic $I_p \leq 150$ kA
- $P_{auxilliary} \leq 200$ kW (rf)
- "Flat-top": 20-50 msec

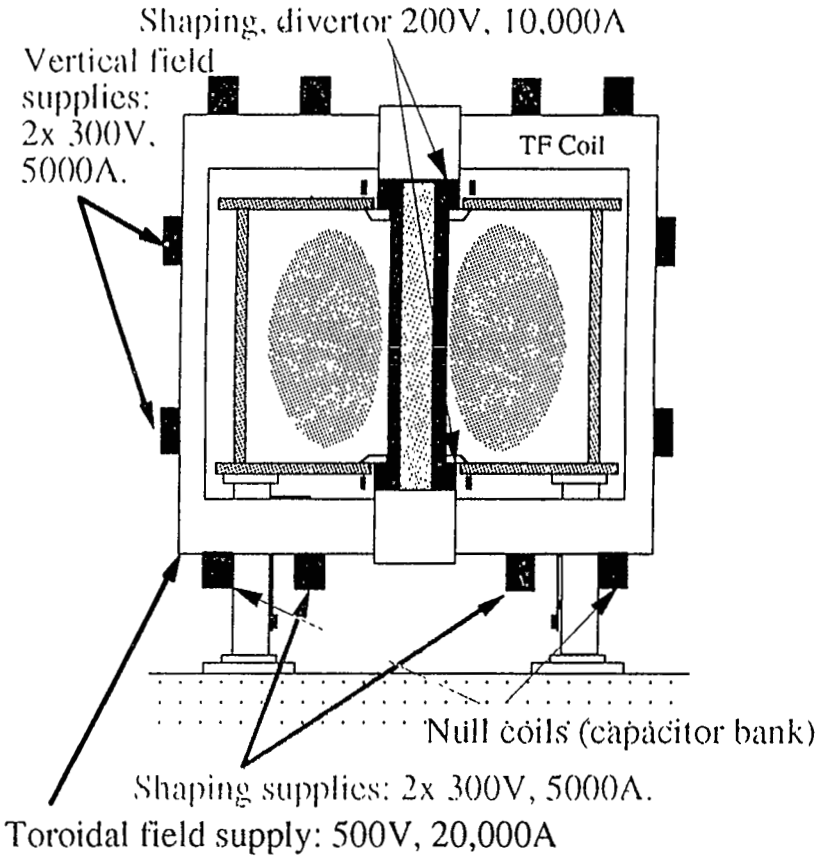

All programmable 12ϕ power supplies (18 MW).

Technology development for toroidal lithium target

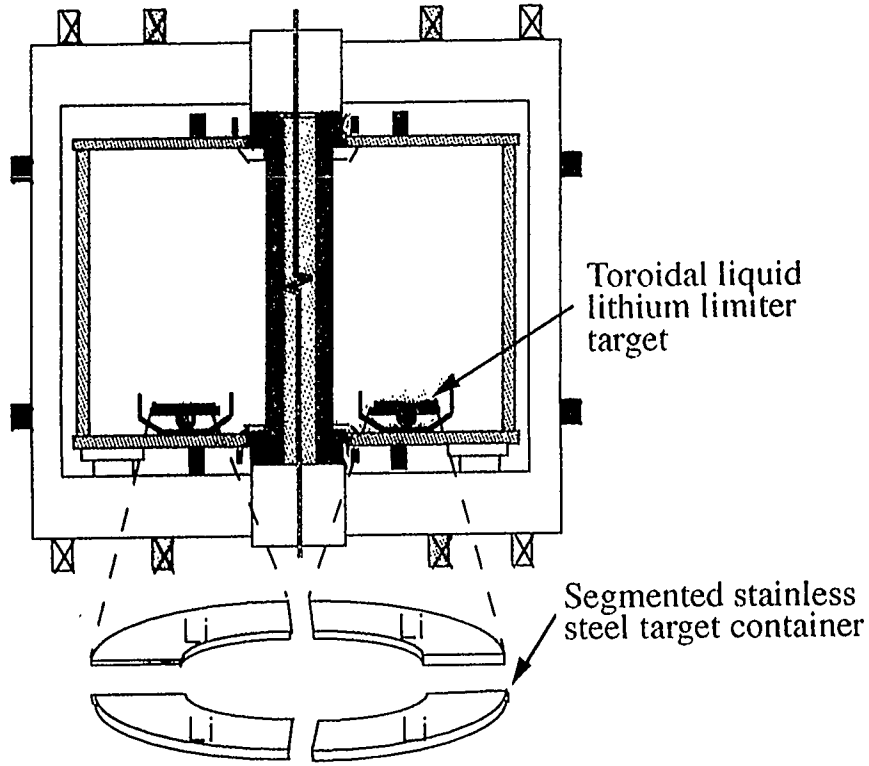

- Tight-fitting stainless steel sections supported on insulators
- Liquid lithium temperature controlled with internal heaters
- Lithium amount (1 liter) ≈ TFTR DOLLOP experiment

PPPL

Summary

- Liquid walls are a potentially "revolutionary" solution to generic MFE first-wall problems
- CDX-U is ideally suited for investigating critical liquid wall issues quickly and economically
- PPPL has the facilities and experience to perform these experiments in a safe and well-controlled manner
- CDX-U plus existing and planned liquid wall programs can lead to implementation on NSTX, Alcator C-Mod, etc.

PPPL

18th IEEE/NPSS Symposium on Fusion Engineering
Albuquerque, NM, October, 1999

Design of the Plasma Facing Components for the National Spherical Tokamak Experiment (NSTX)

P. L. Goranson
Oak Ridge National Laboratory

Presentation Outline

- **Overview**
- **PFC General Configuration and Requirements**
- **Centerstack Tile Design and Thermal Analysis**
- **Divertor Plate Tiles and Supports**
- **Carbon-Carbon Graphite Tradeoff Study**
  - Pull tests
- **Assembly Sequence** (time permitting)

Overview of Plasma Facing Component (PFC) Program

- Work was performed in the 1997 - fall 1998 time frame
- 3584 individual graphite tiles
- Required 279 engineering drawings on ProE
- ~96 different tile designs
- 112 diagnostic interfaces

Overall Configuration

- Center Stack Tiles
- Inboard Divertor plates and tiles
- Outboard Divertor plates, tiles and support rings
- Passive plates, tiles, support gussetts

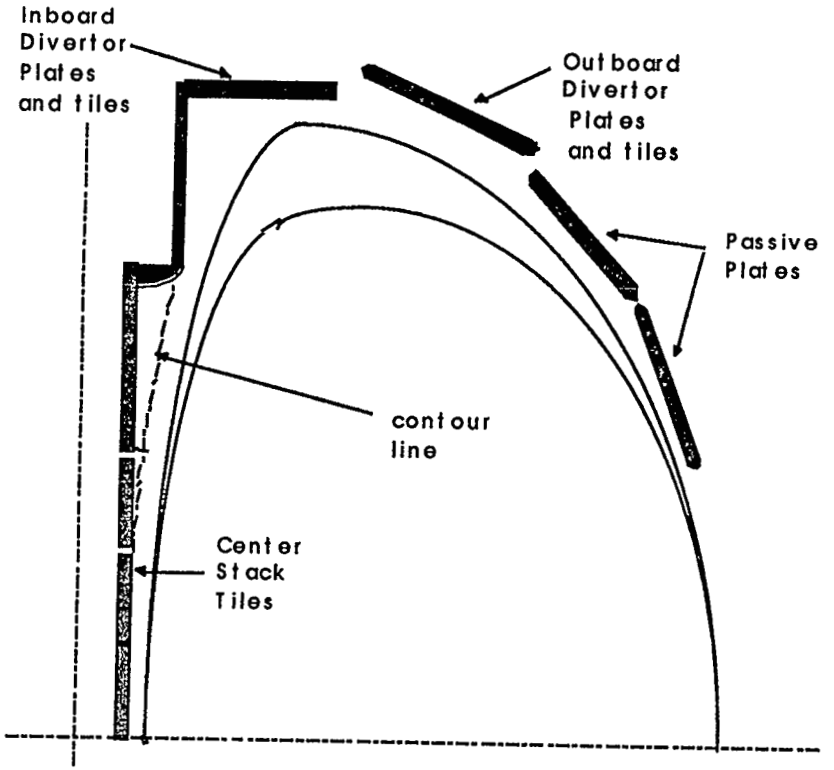

I-104

Center Stack prior to assembly

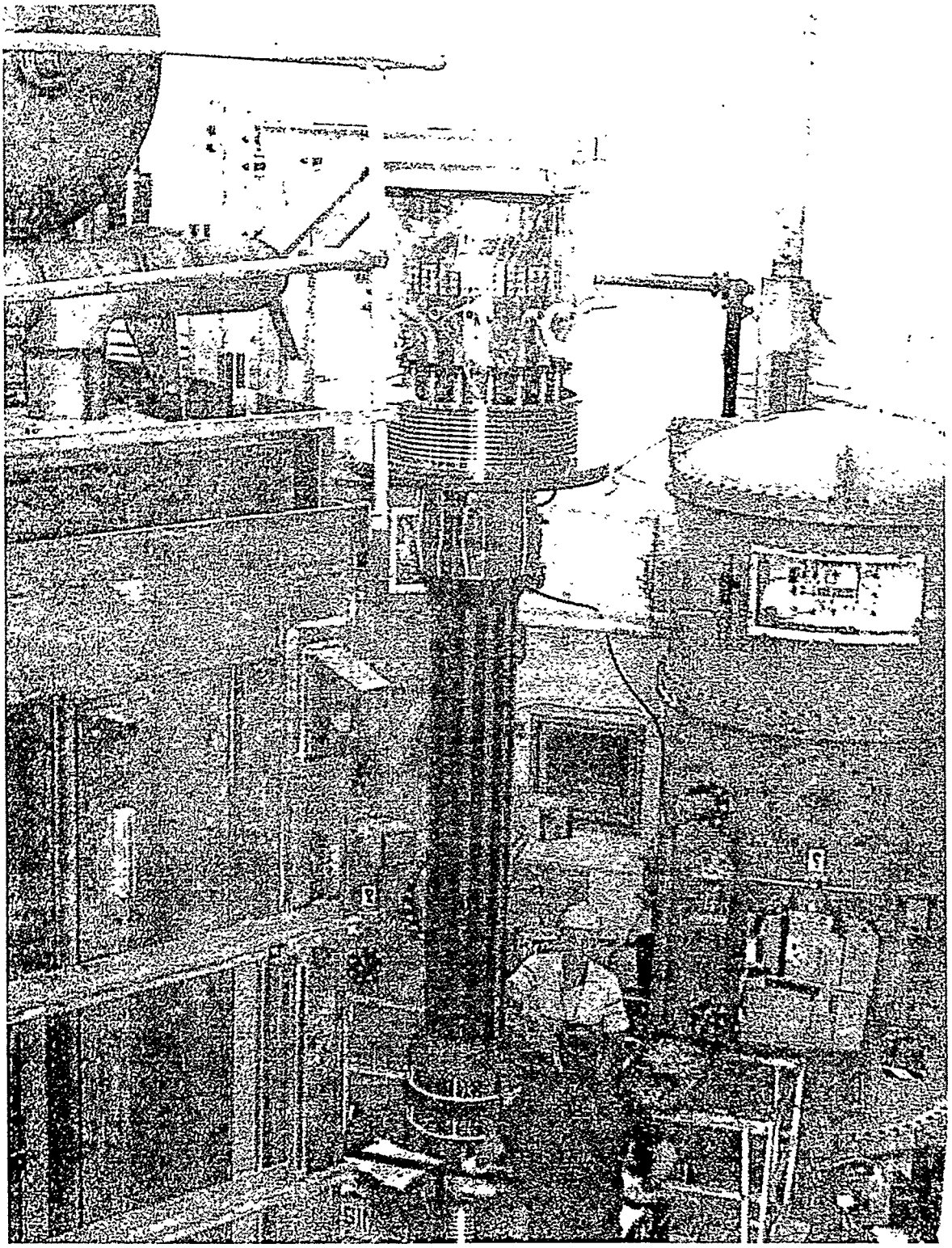

Center Stack installed in vessel

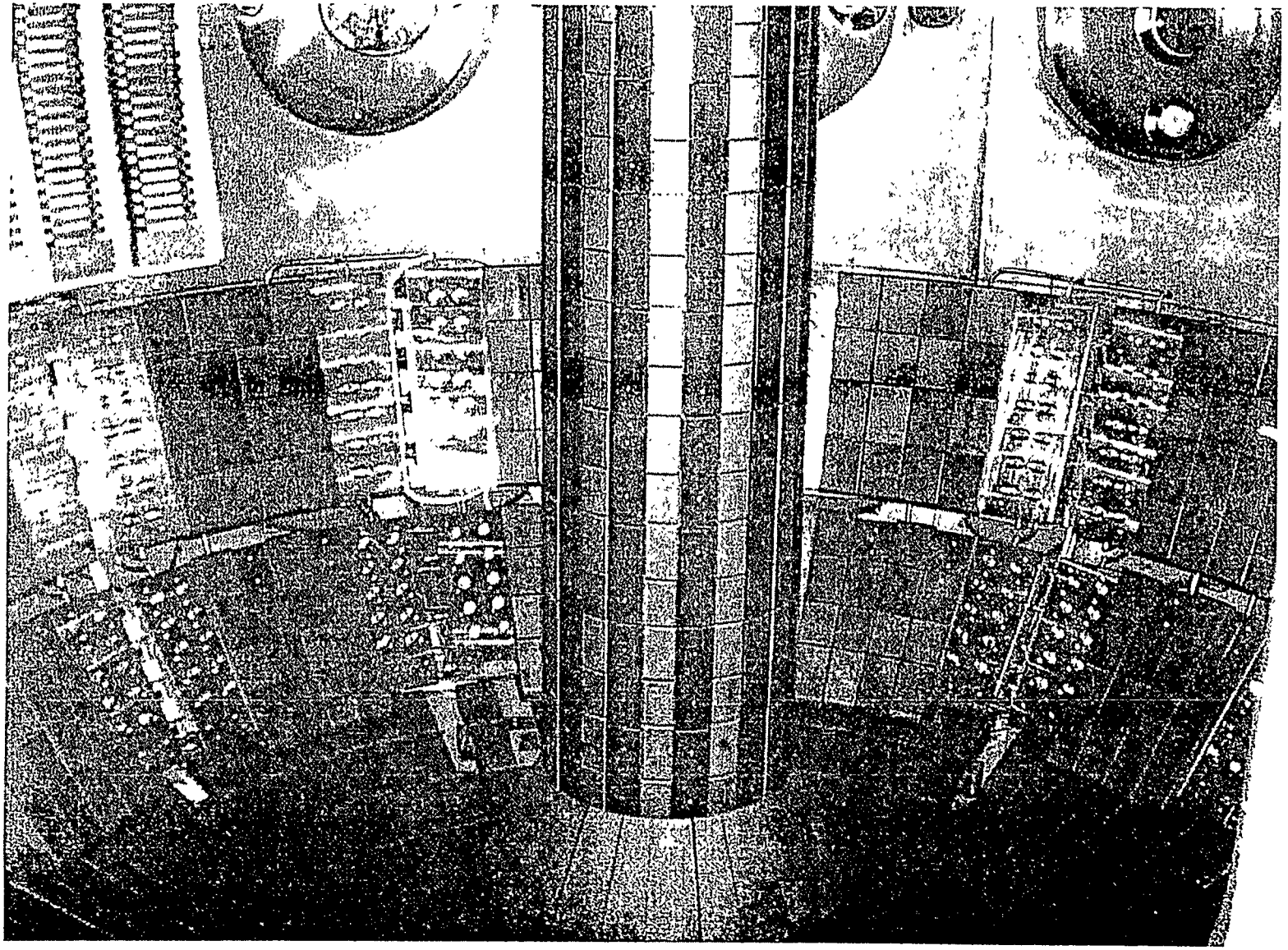

Closeup of lower Center Stack and divertor plates with tiles

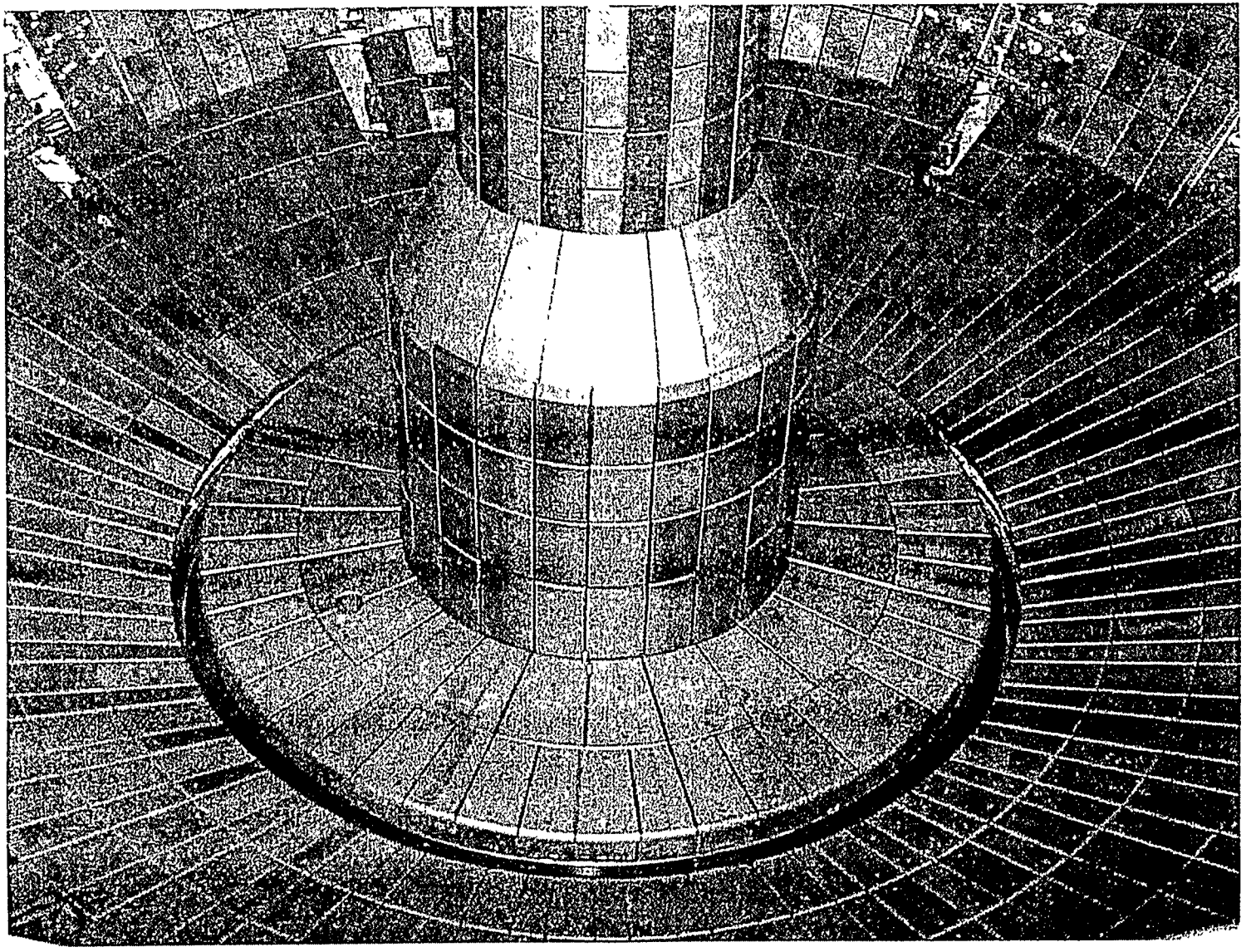

Upper divertor plates and passive plate brackets

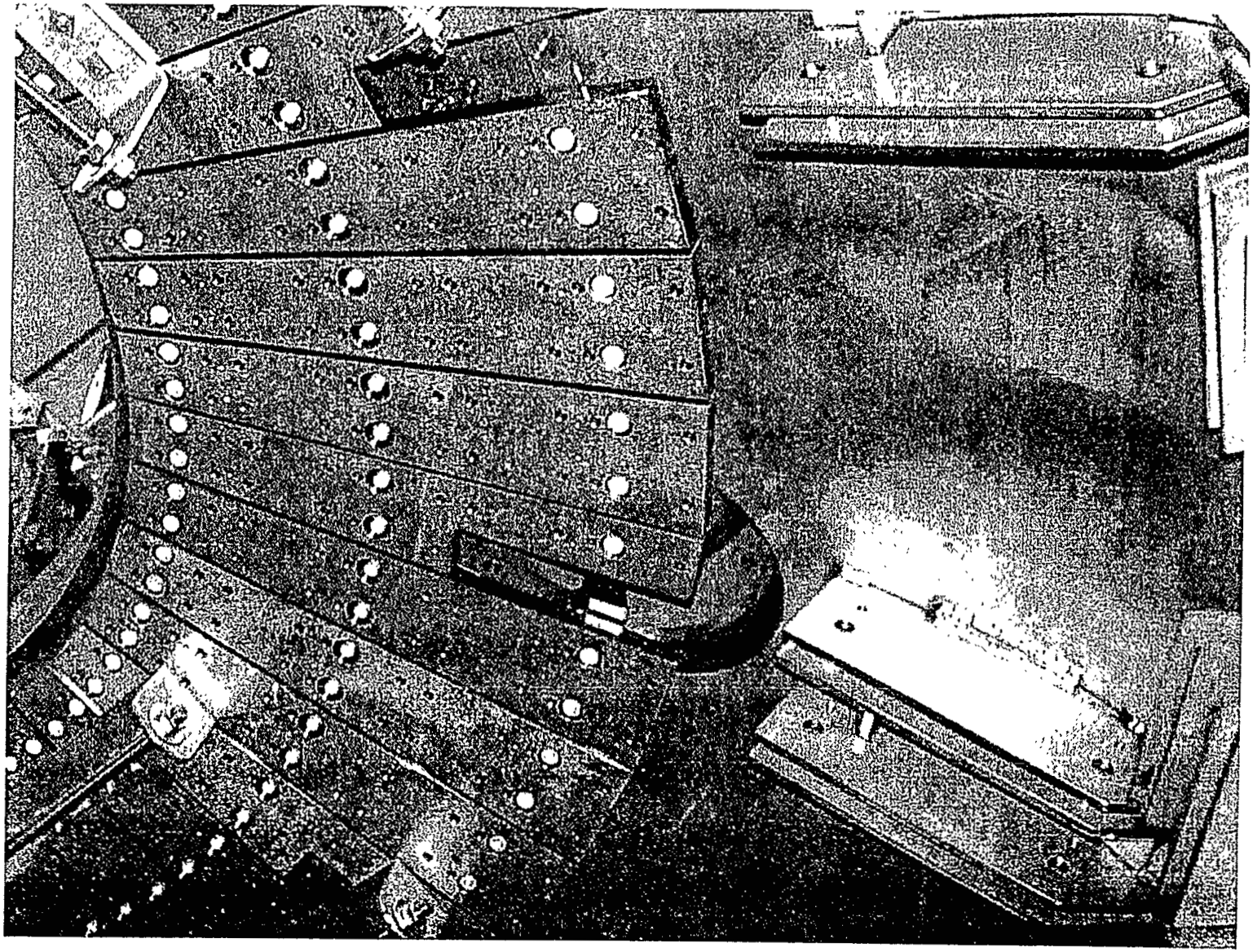

Upper divertor plates during installation process

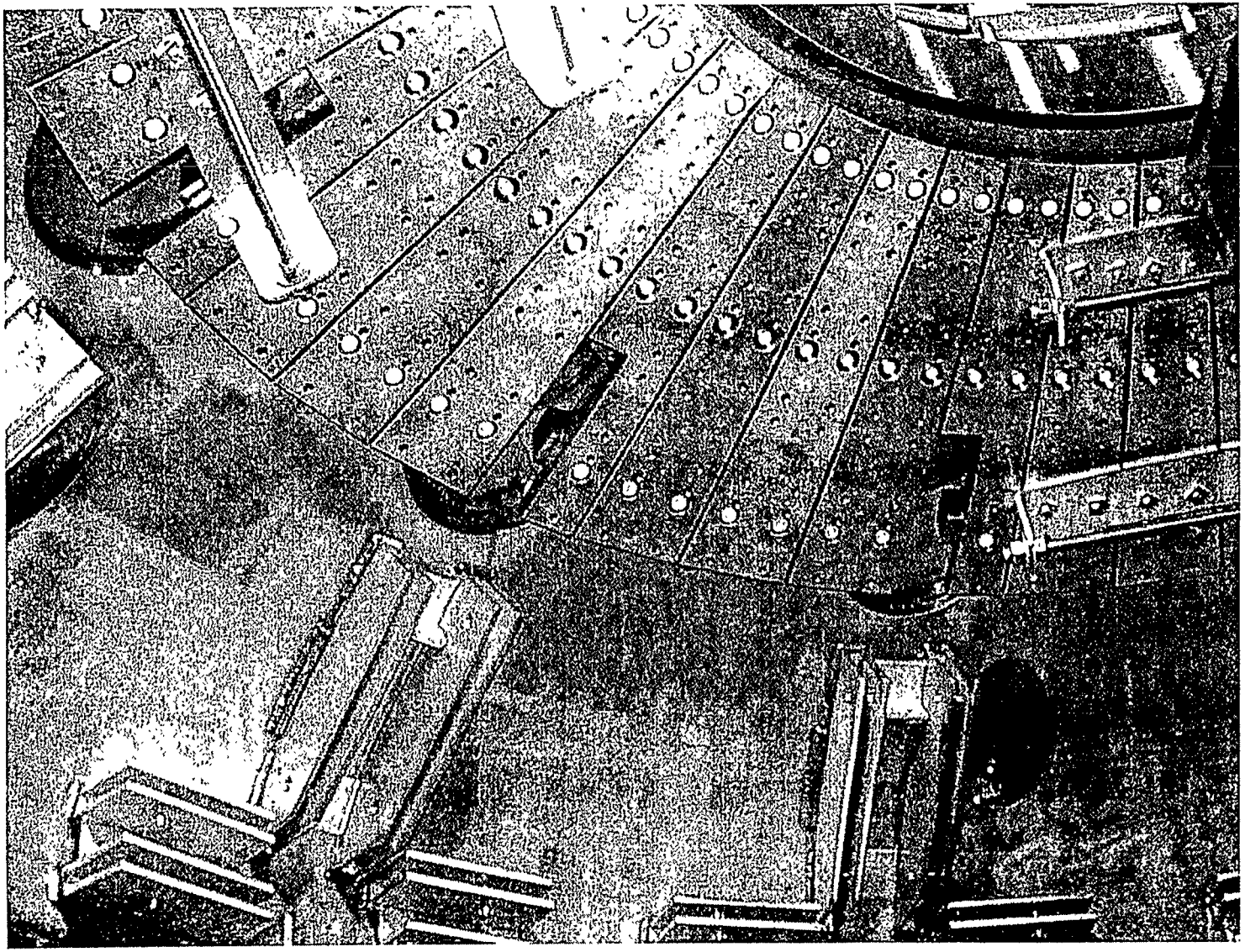

Interior view showing center stack and passive plates

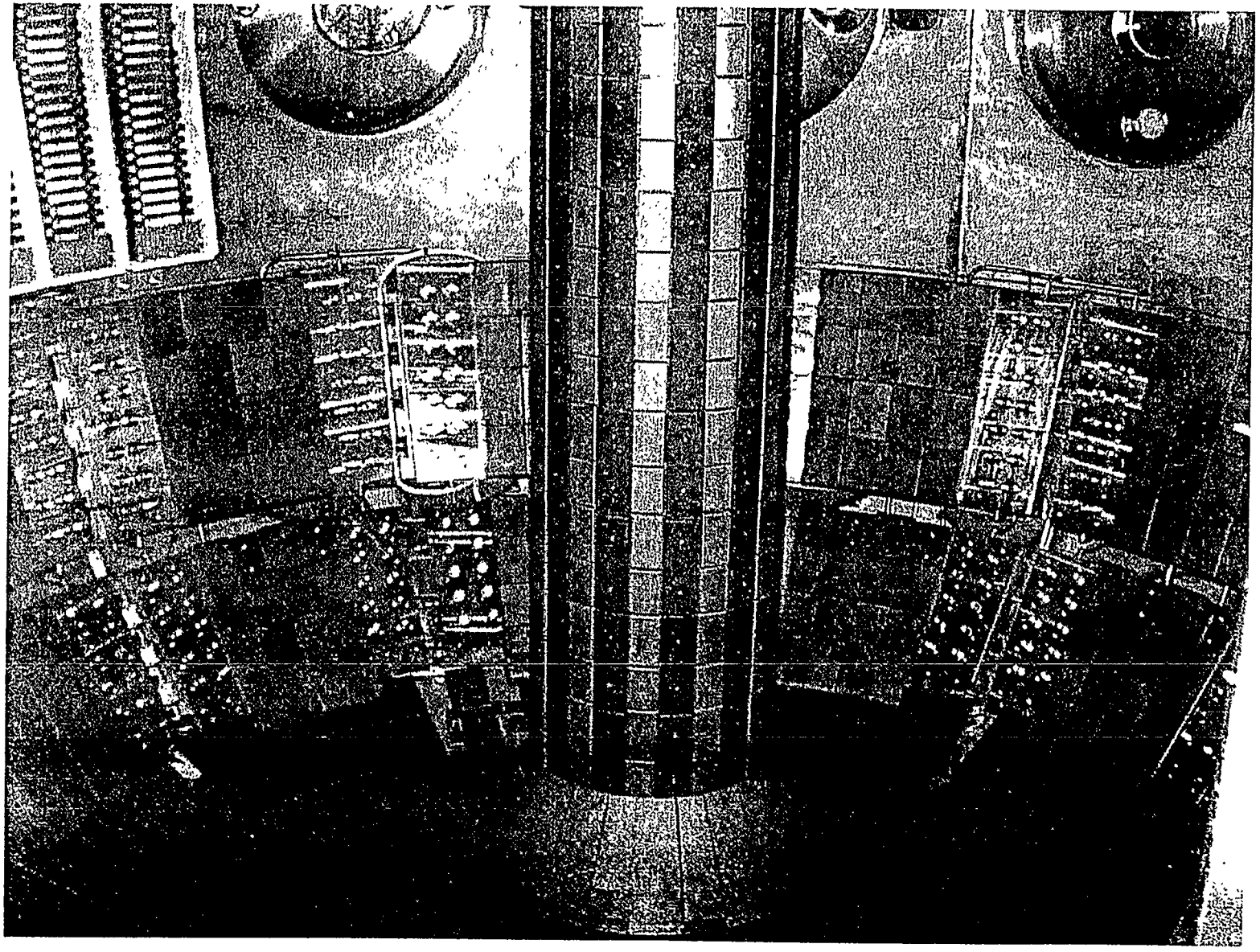

CSC Design Goals

- Total radial envelope 14 mm
  - including mounts, tiles, and thermal shielding
- Thermal isolation from CSC
- Two fasteners per tile
- Ability to remove single tile without removing all tiles
- Minimize CSC distortion due to attachment
  - too thin to tap
- Utilize existing graphite and carbon-carbon material
- and, of course, minimize cost and complexity

Requirements and Design Criteria - General

NSTX

- **Provide accurate placement of tiles**

  +/- 0.5 mm, tile-to-tile
  +/- 0.5 mm, tile surface to center stack cylinder or divertor surfaces
  (assume cylinder and divertor surfaces are concentric and aligned with magnetic flux surfaces)

- **React electromagnetic loads**
  - up to 75 psi on center stack tiles in compression
  - halo currents cause primary load

- **Provide for thermal expansion** of the tiles
  - tile peak surface temperature < 1200 C
  - tile temperature gradient up to 600 C

- **Limit thermal contact of center stack tiles with the cylinder**

- **Enhance thermal contact of divertor tiles and passive plate tiles with cooled divertor and passive plates**

Cross section through CSC Tile Assembly

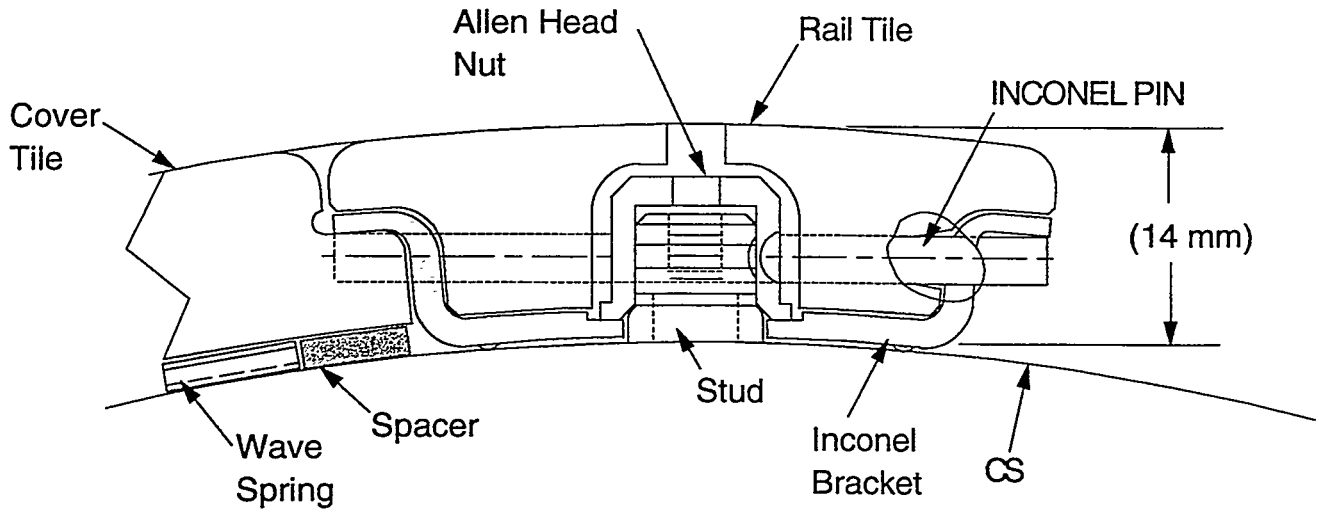

Center Stack Tile Design

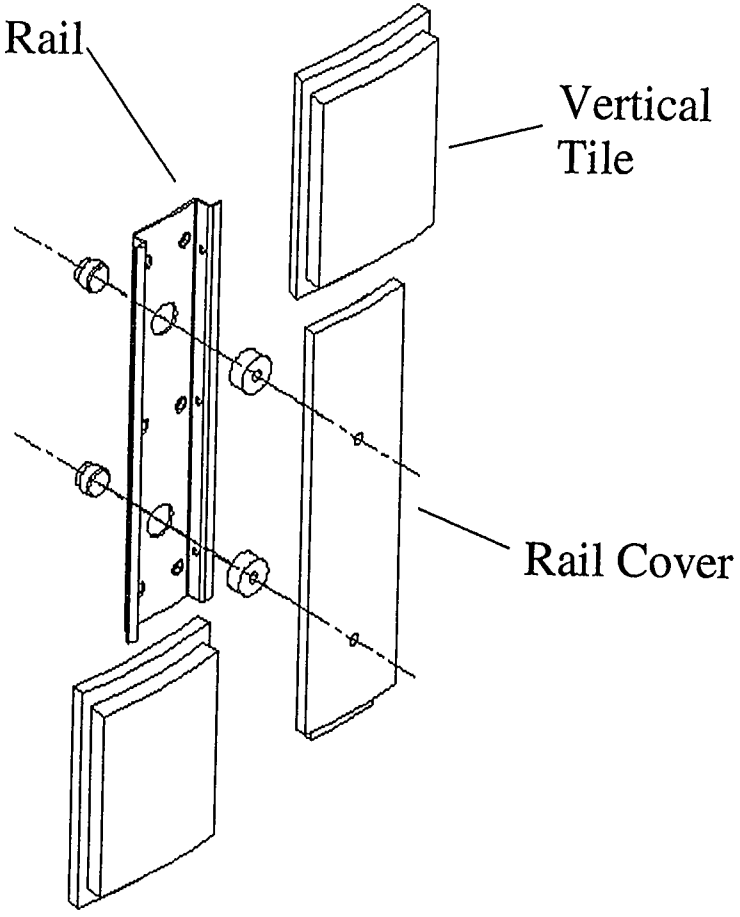

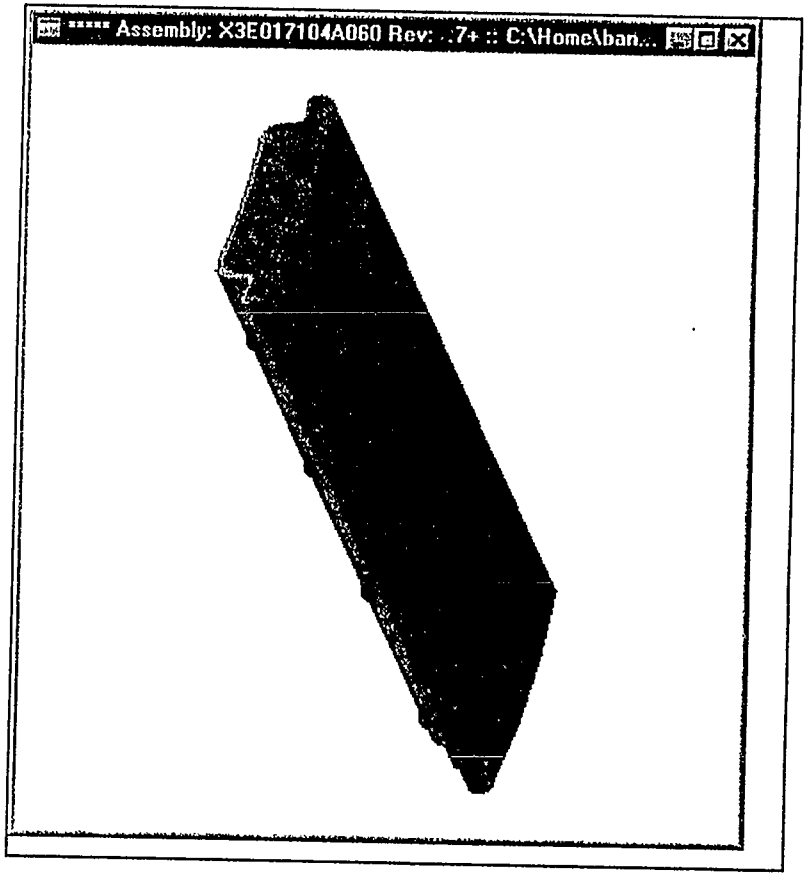

Center Stack Tile Design - Vertical Bolted Rail

Metallic rails with carbon covers clamp vertical rows of tiles

- Robust, all metal retainers
- Graphite tiles, FMI-4D carbon-carbon covers
- Good thermal expansion capability
- Fair, controlled thermal isolation
- Multiple fasteners per tile
- Relatively simple parts

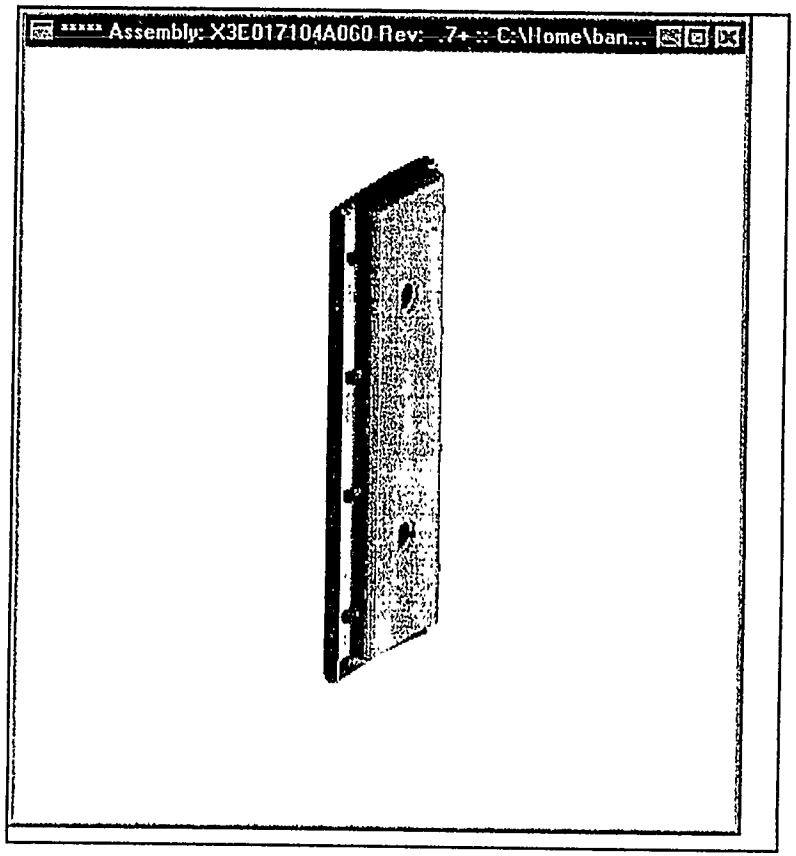

Center Stack Tile Design - Vertical Bolted Rail

Metallic rails with carbon covers clamp vertical rows of tiles

- Robust, all metal retainers
- Graphite tiles, FMI-4D carbon-carbon covers
- Good thermal expansion capability
- Fair, controlled thermal isolation
- Multiple fasteners per tile
- Relatively simple parts

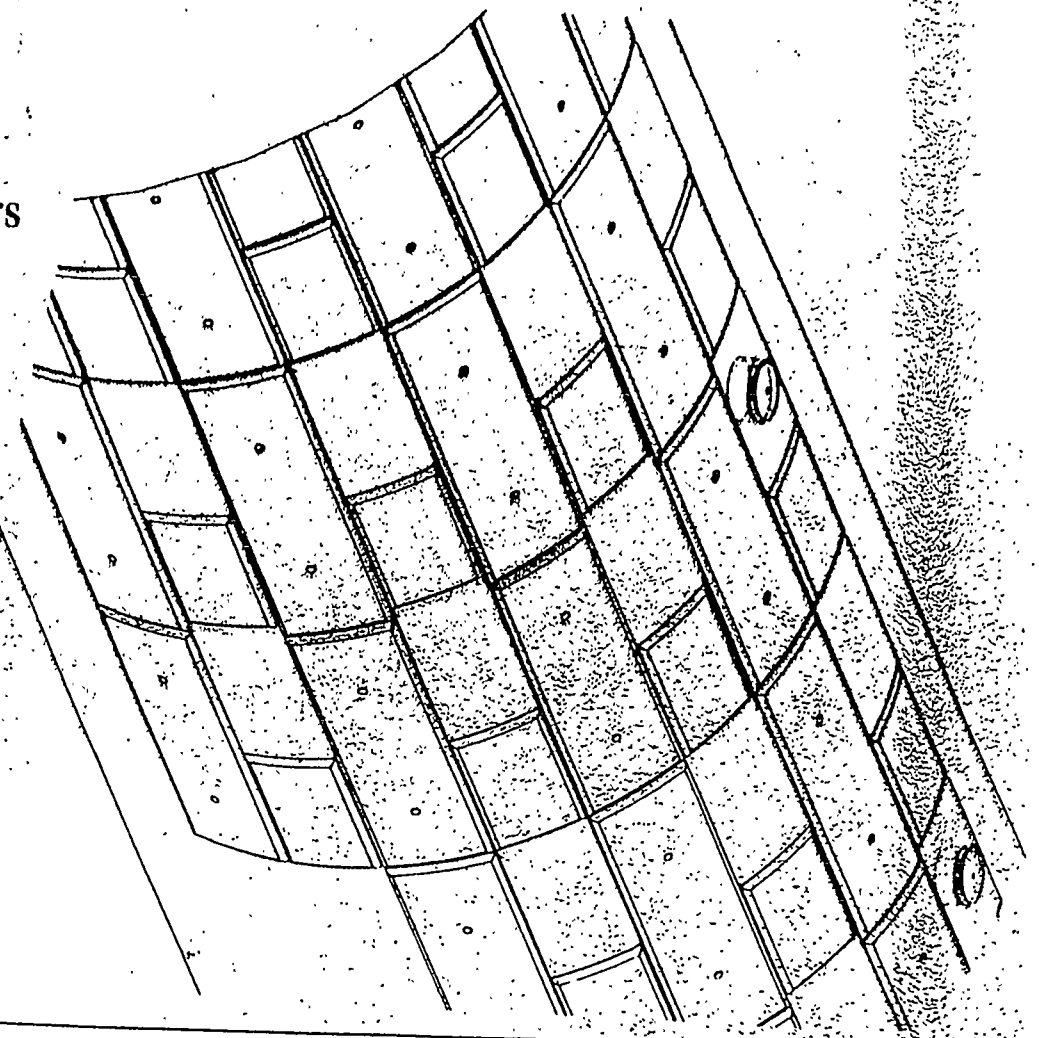

Center Stack Tile Design

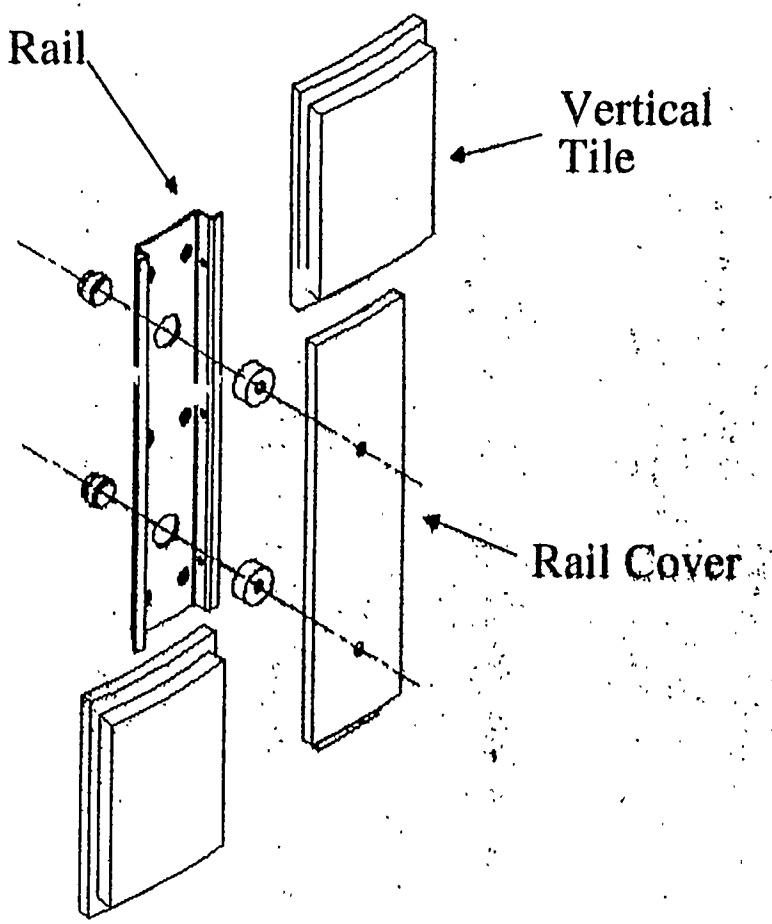

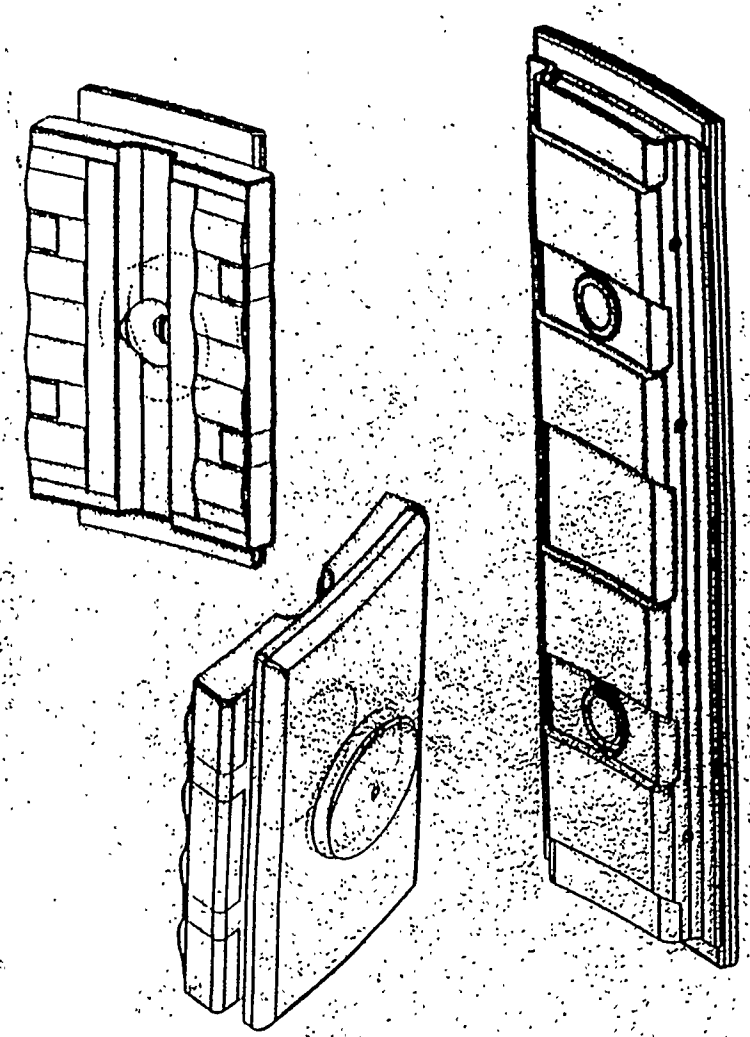

Requirements/Design Criteria - Thermal loads

NSTX

- Normal Operation, peak surface flux

  - Center stack ~ 200 W/cm^2 peak

  - Inboard divertor
    ~ 700 W/cm^2 for single null

  - OB divertor
    ~ 1100 W/cm^2 for $\lambda = 3$ cm
    ~ 1700 W/cm^2 for $\lambda = 1.5$ cm
    (peak from calc = 1400 W/cm^2)

  - Passive plates ~10 W/cm^2

- Disruption
  - Peak surface flux: TBD

- NBI shine (upgrade only)
  - Peak surface flux: TBD

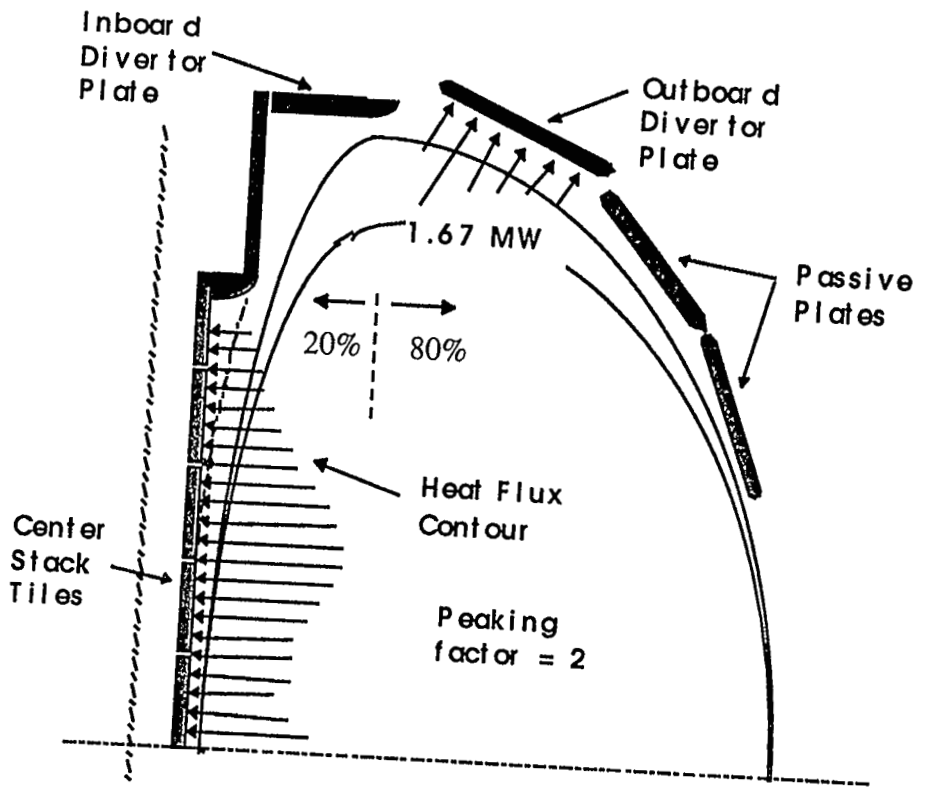

MSC/PATRAN Version 6.0 25-Jun-97 12:40:41
FRINGE: 5_sec_200W_composite, nr5.nrf01: Temperature -PATRAN 2.5

NSTX Center Stack Graphite Tile

Thermal Analysis

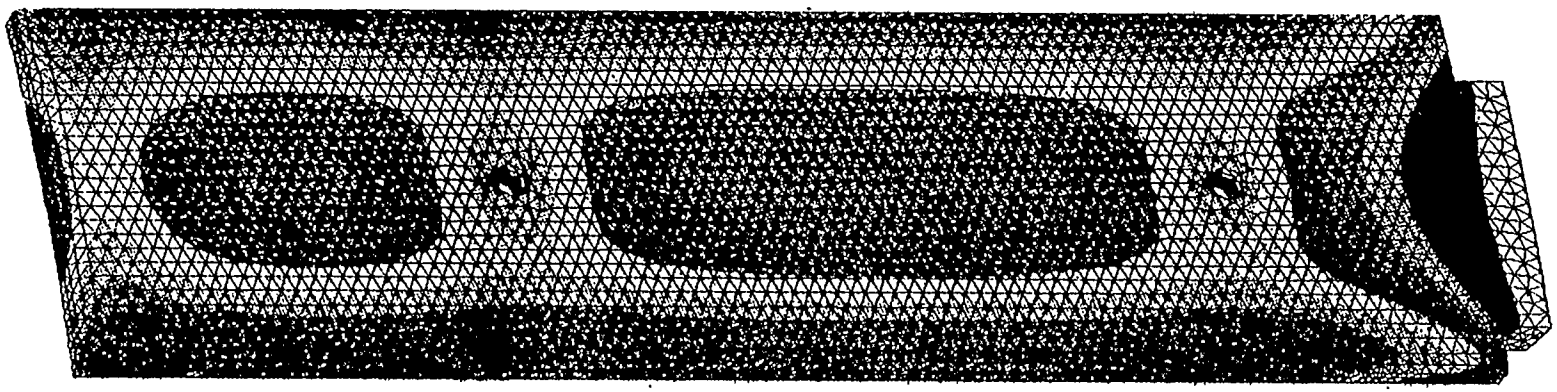

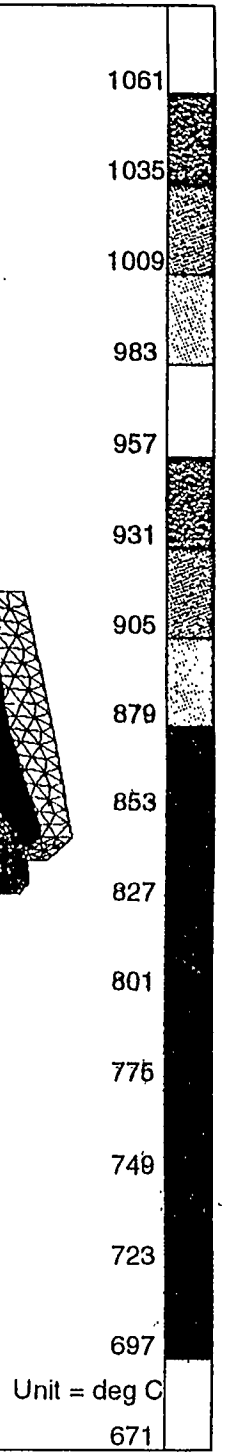

Tstart = 525 C
Qin = 200 watt/cm**2
Material: Graphite Composite

MSC/PATRAN Version 6.0 11-Apr-97 08:35:59
FRINGE: TIME: 9.0500000000D+02 SECONDS, nr66.nrf01: Temperature -PATRAN 2.5

NSTX Center Stack Graphite Tile

Thermal Analysis

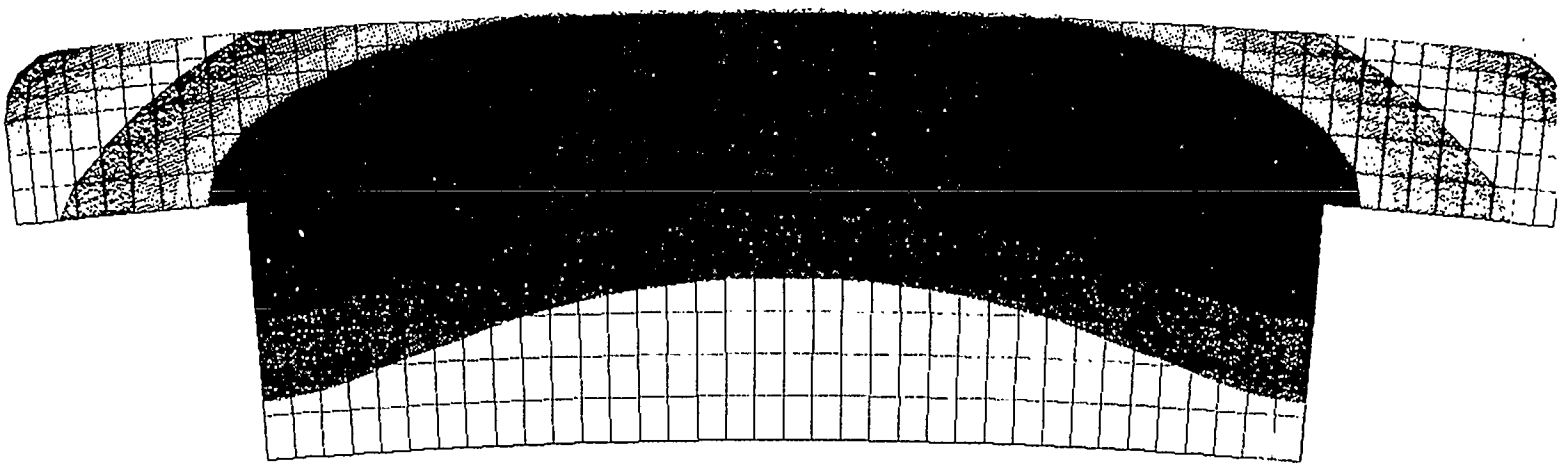

Tstart = 540 C

Qin = 320 Watt /cm**2

Center Stack Tile Thermal Analysis

- Tile initially evaluated with analytic solutions

  Tmax ~ 1200C for 320 W/cm^2 *applied for 5 seconds each 300 seconds*
  Temperature at end of cooldown ~ 540 C, after multiple pulses

- 2-D computer model indicated large gradient at end of overlap regions, in tile cover

  Tmax ~ 1650C for 320 W/cm^2

- 3-D model indicates overlap region dominates gradient, holes and counterbores for fasteners are not a problem

- Heat load of ~ 200 W/cm^2 will reduce max temperature to around 1200 C for POCO *or 1000 C for Allied Signal material*

- Heat transfer to centerstack casing less than 0.5 W/cm^2 (tiles at 700C, casing at 150C)

PASSIVE PLATE/OUTER DIVERTOR TILE MOUNT DESIGN

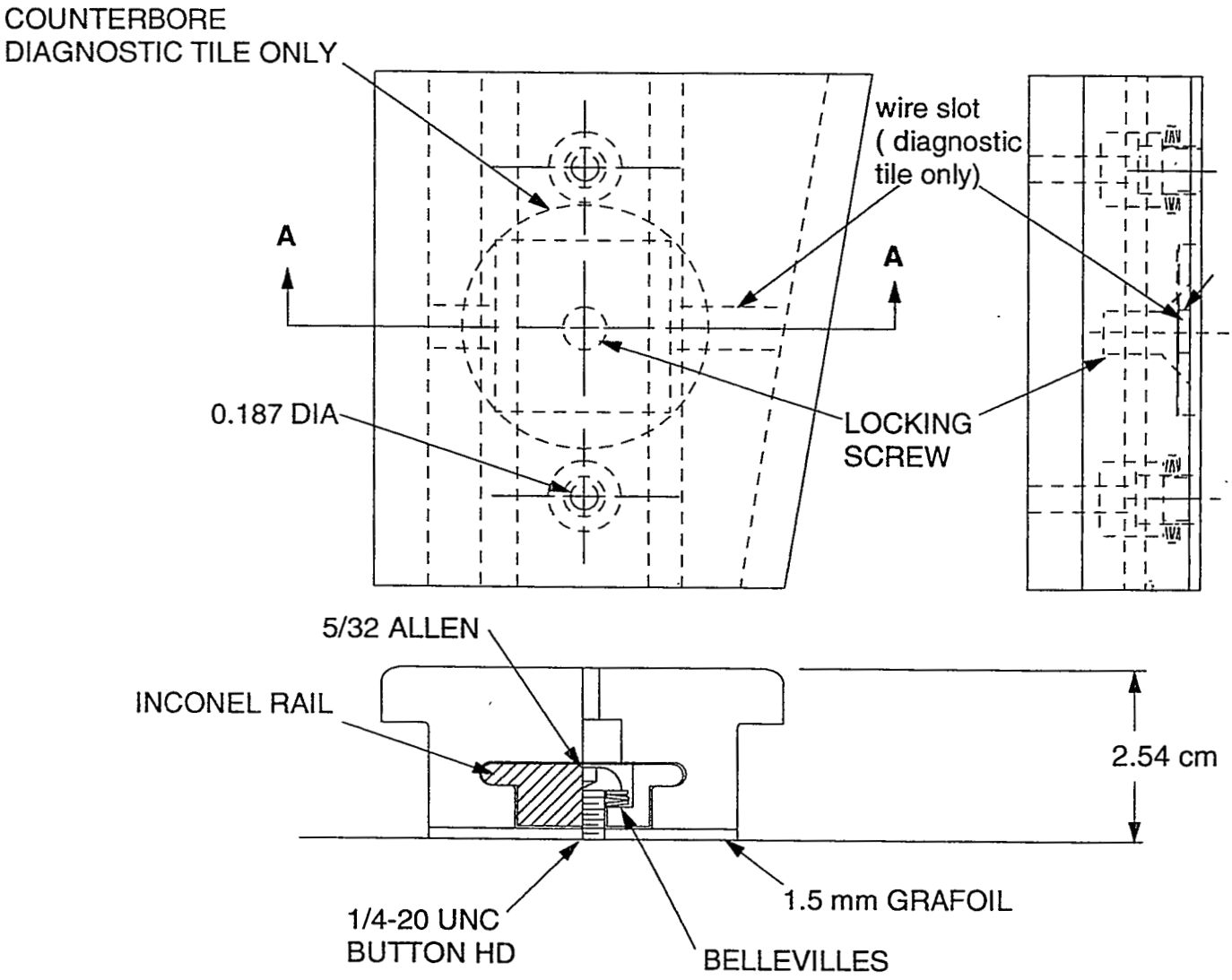

PULL TESTS

TEST CRITERIA

- Simulate worst case disruption load on CS tiles
- 100 psi distributed load
  equates to 300 lbs per pin
- Simulate as closely as possible baseline 4 pin configuration attachment

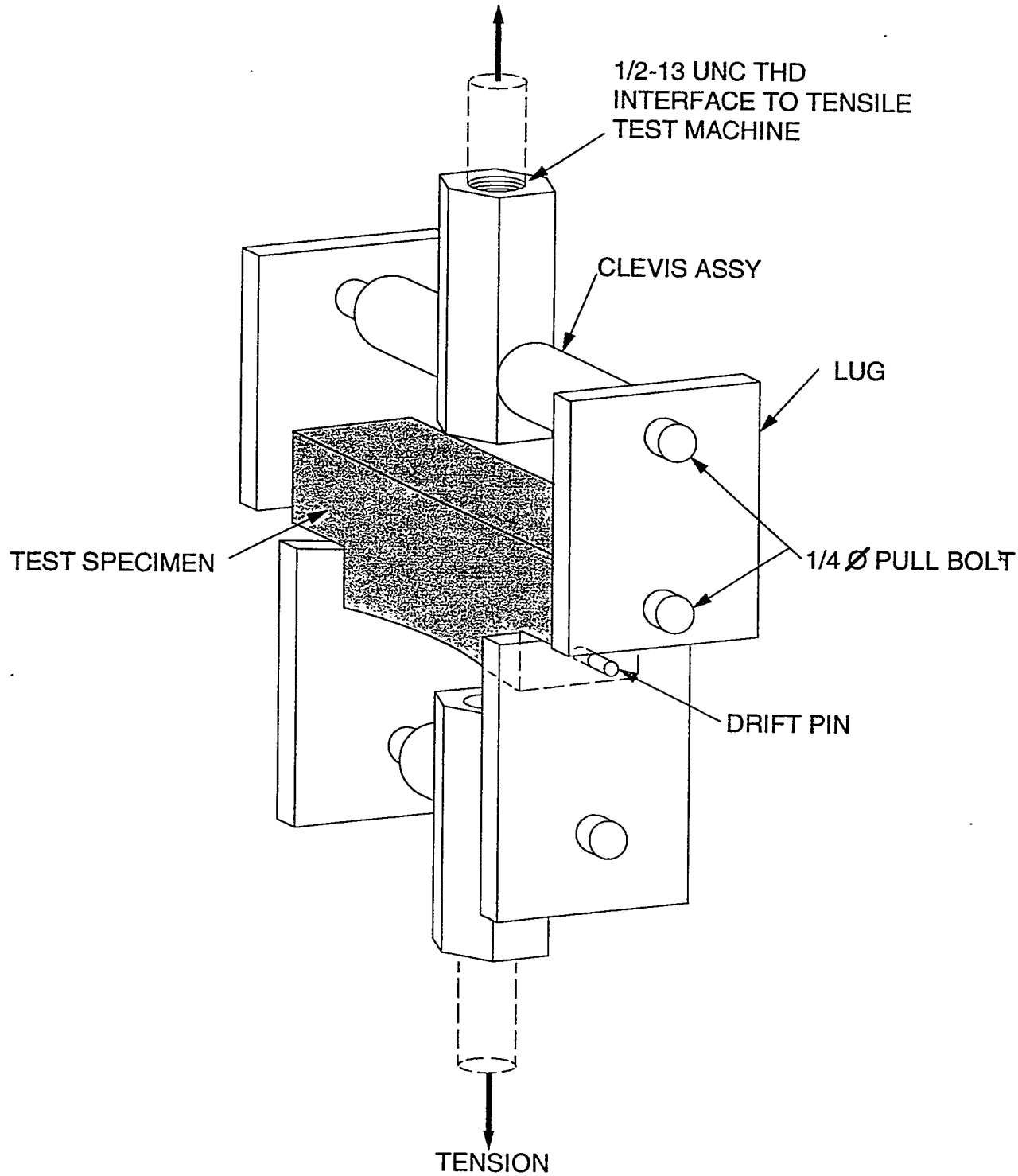

FIGURE 4 PULL FIXTURE

CENTER STACK PULL TESTS

PURPOSE

Test Series 1
Determine ultimate strength of baseline configuration and mechanism of failure(FMI material)

Test Series 2
Determine suitability of Allied Signal(AS) material, a more economical and more readily available material than FMI

- Quantify effect of using two pins instead of one
  strength expected to double, thereby giving safety margin required

- Study effect of using larger diameter pins with same centerline

Test Series 3
Determine the effect of grain orientation in the Allied Signal material.

1999, ~~Oct.~~ Nov. 1-4, US/Japan Workshop
Santa Fe, NM

In-vessel observation of JT-60U and its divertor modification

K. Masaki (JAERI)

- Divertor modification to the W-shaped divertor with in-out divertor pumping slots (Nov. ~ Dec. 1998)
- In-vessel observation (Nov. 1997, Nov. 1998)

JAERI

Background

On JT-60U, open divertor was modified to W-shaped divertor with inner divertor pumping slot in 1997. With the W-shaped divertor, reduction of carbon impurity was successfully confirmed using "puff and pump" in attached state and partially detached state with weak X-point MARFE. Long sustainment of ELMy H-mode and continuous helium exhaust were also demonstrated.

However, the W-shaped divertor only with the inner pumping was not effective in high density region, i.e. detached state, because the in-out asymmetry of particle flux changes to symmetry or inverse asymmetry. Therefore, confinement of the main plasma was not improved drastically.

To resolve these disadvantages, outer divertor pumping slot was added to the W-shaped divertor in December 1998.

JAERI

Structure of W-shaped divertor

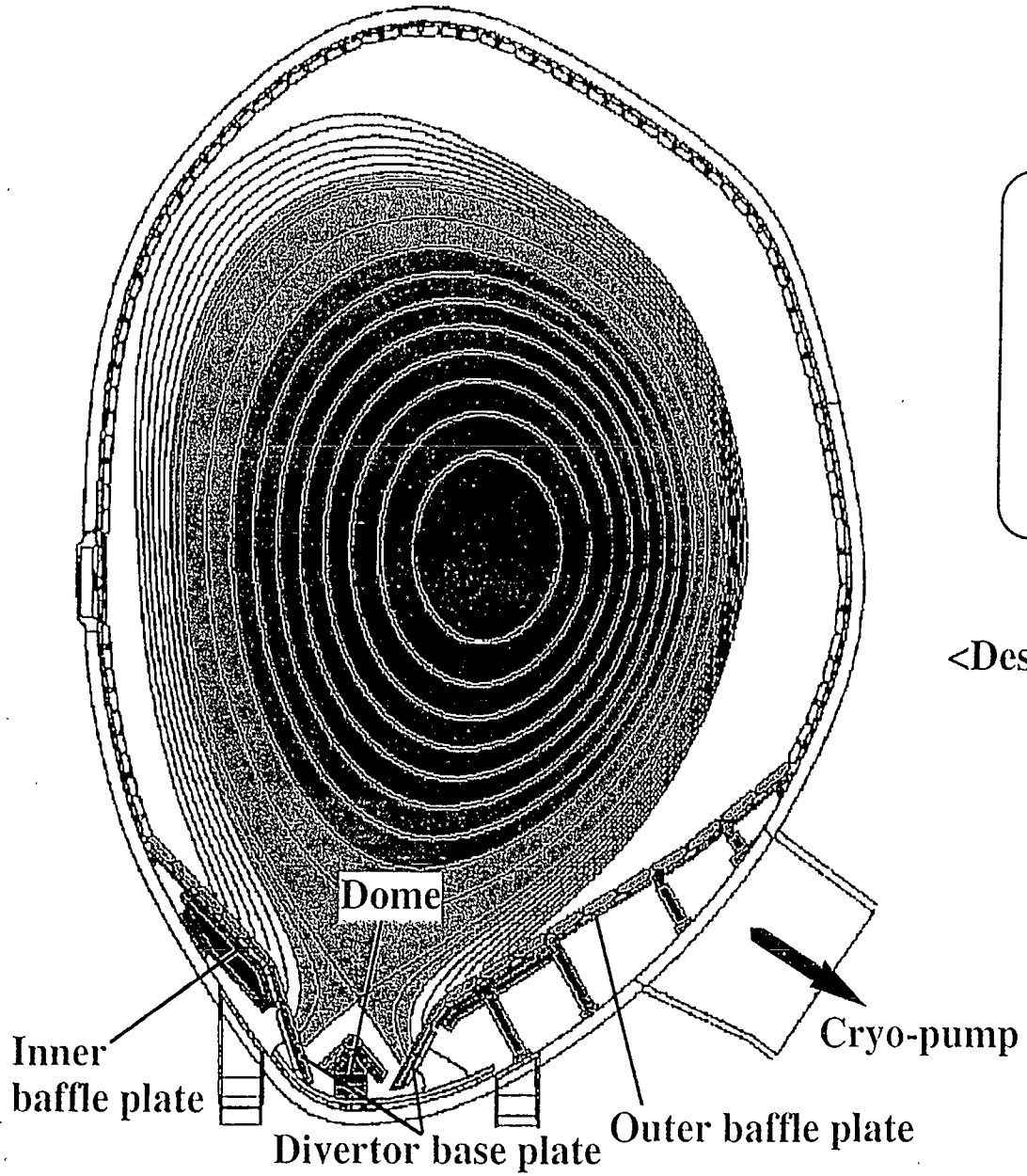

The W-shaped divertor consists of inclined targets, a dome in the private flux region, pumping from the private flux region.

<Design conditions>

Plasma current : 3MA

Toroidal magnetic field : 4T

Cryo-pump for divertor pumping
: three, 30m^3/s/unit (D_2, 0.1Pa, 300℃)

JAERI

Gas seal structure between dome and outer divertor

Removable gas seal structure

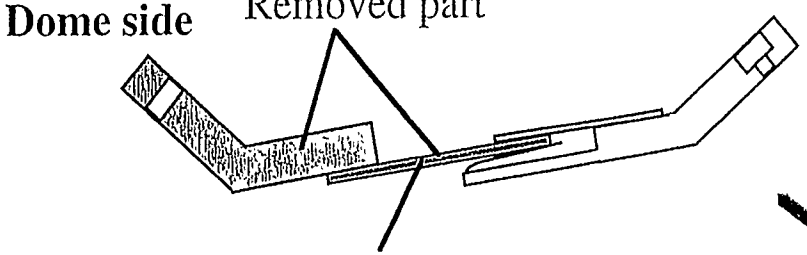

Sprayed ceramic (Al_2O_3) coating plate

This structure consists of inserted-sliding parts to allow thermal expansion and vibration during disruption. Gray plate were removed for outer divertor pumping slot.

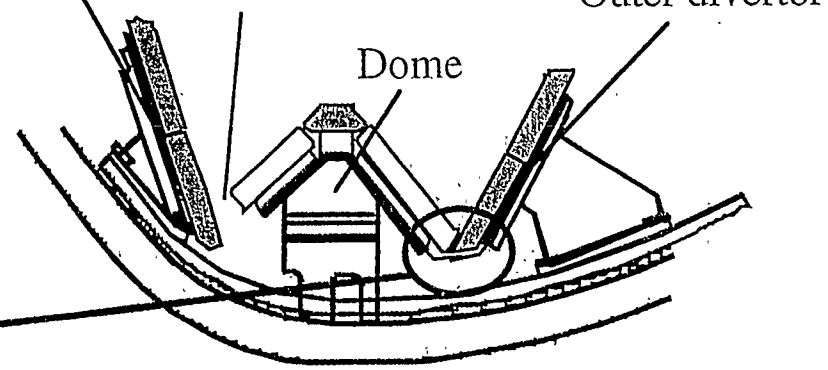

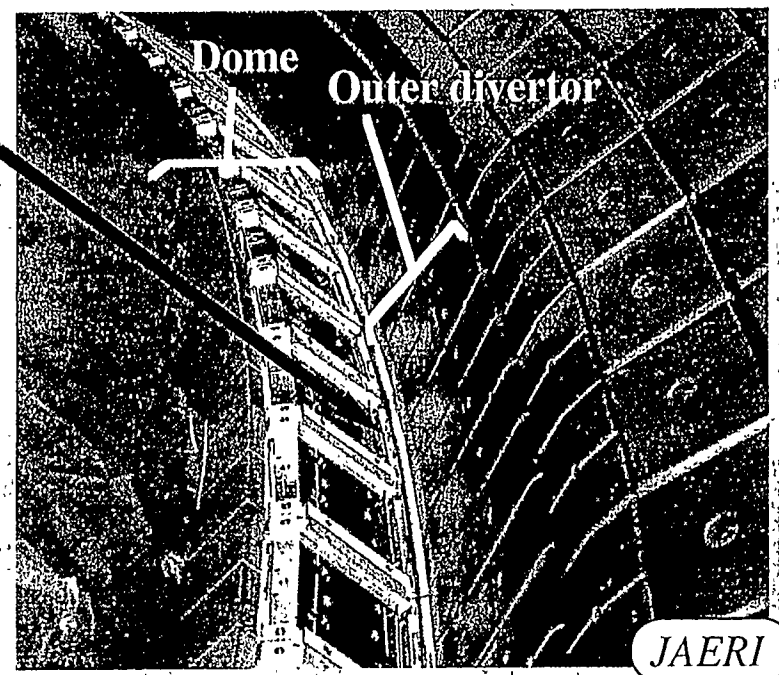

JAERI

W-shaped divertor with in-out divertor pumping slots

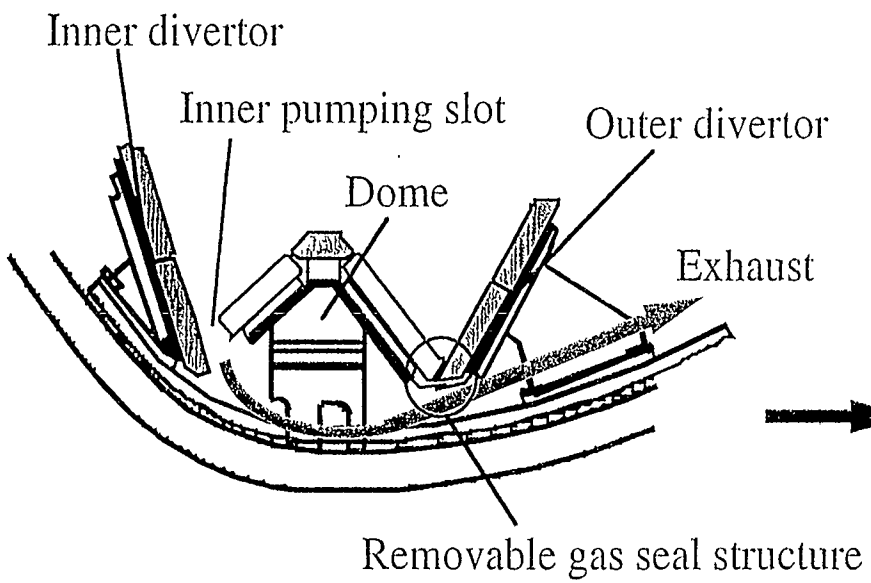

Previous W-shaped Divertor
(Jun. 1997 - Dec. 1998)

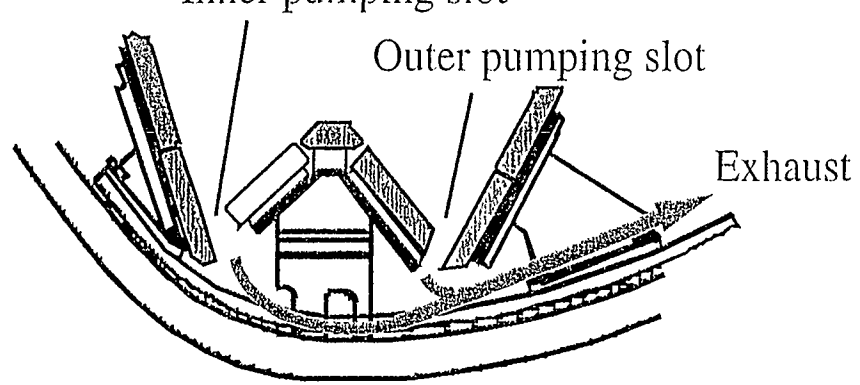

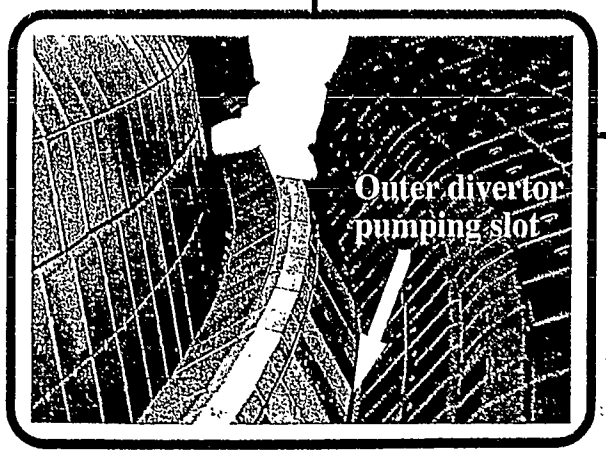

In order to have a wide variety of plasma configuration, all outer dome tiles were replaced with CFC tiles

JAERI

Dome (1 unit)

These tiles were tapered to avoid the heat concentration to the tile edge.

However, Some of the tiles protruded with installation error. All edges of the protruded tiles were re-shaped to be hidden for plasma particle flow.

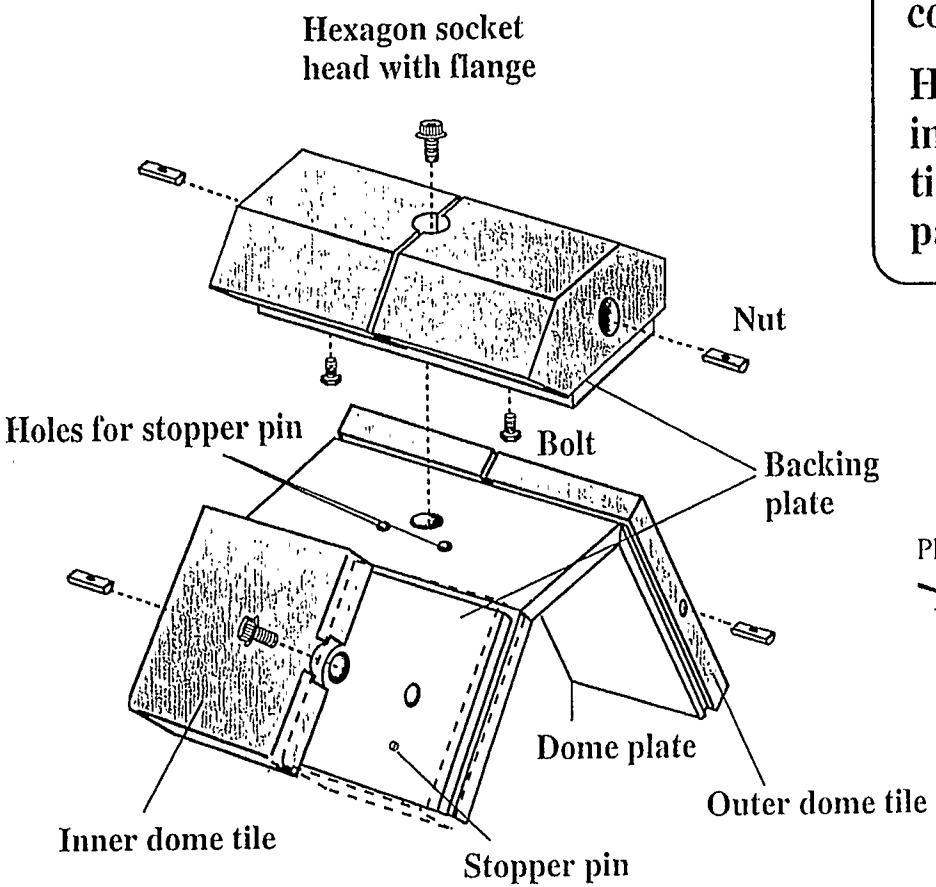

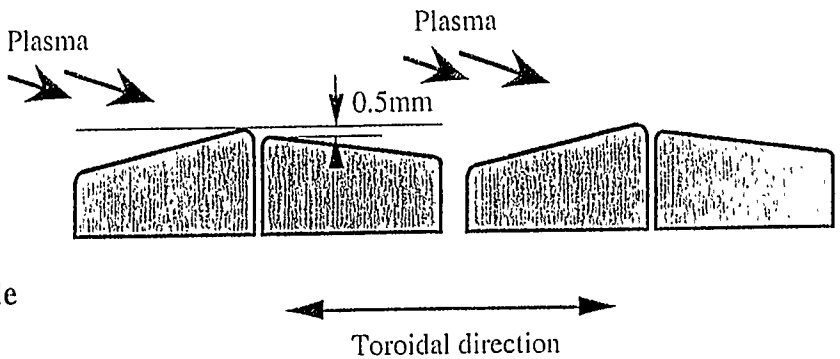

Total : 125 units

JAERI

Inner divertor (1 unit)

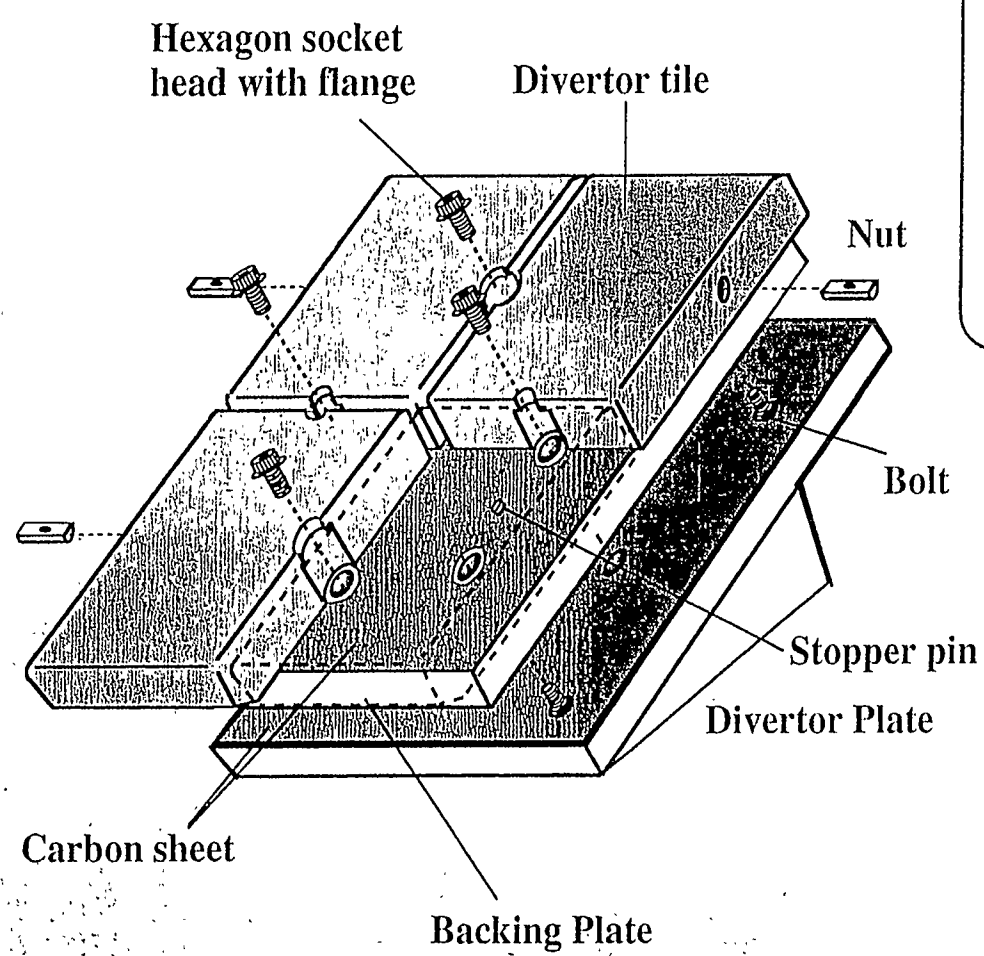

These divertor tiles were designed as the surface is circumscribed (inner divertor) and inscribed (outer divertor) in each circle of inner and outer divertor plates.

Moreover, these tiles were tapered to avoid the heat concentration to the tile edge.

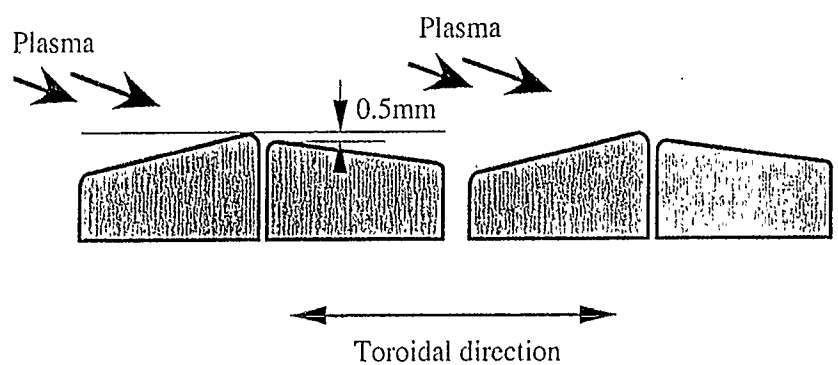

Inner divertor : 125 units
outer divertor : 125 units Total 250 units

JAERI

Experimental results

(1) Divertor pumping speed

$16 m^3/s$ (improving by 30 %)

(2) Improved efficiency of helium pumping

$\tau^*_{He} / \tau_E \sim 3$ in ELMy H-mode

ITER requirement : $\tau^*_{He} / \tau_E < 10$

(3) Reduction of L-H transition threshold power

Reduction of 30 %, low Zeff (~2)

These results indicate efficient divertor pumping of the W-shaped divertor.

JAERI

In-vessel observation of JT-60U

Deposit and erosion

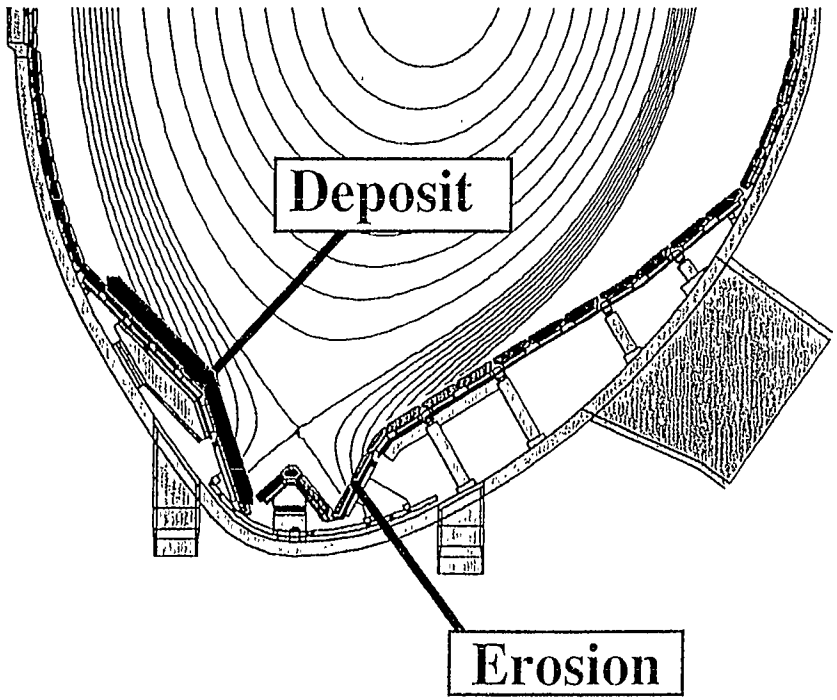

In-vessel observation in Nov. 1997

Deposits : Inside >> Outside

Erosion : Inside << Outside

In-vessel observation in Nov. 1998

Deposits : Inside > Outside

Erosion : reduced

Inside < Outside

JAERI

Damage of Armor tiles

Nov. 1997

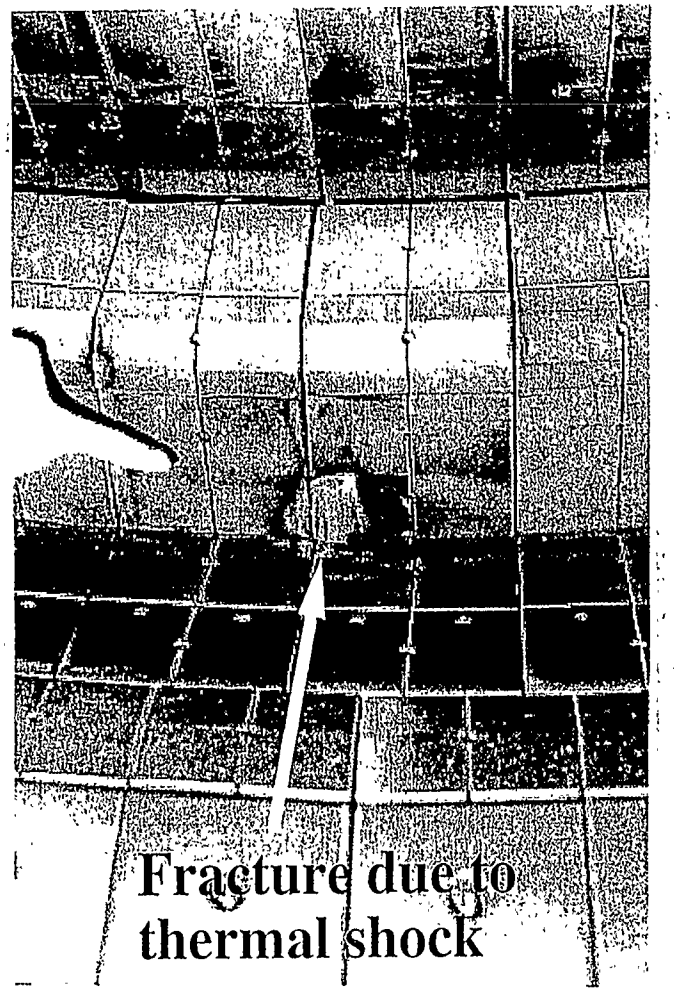

Nov. 1998

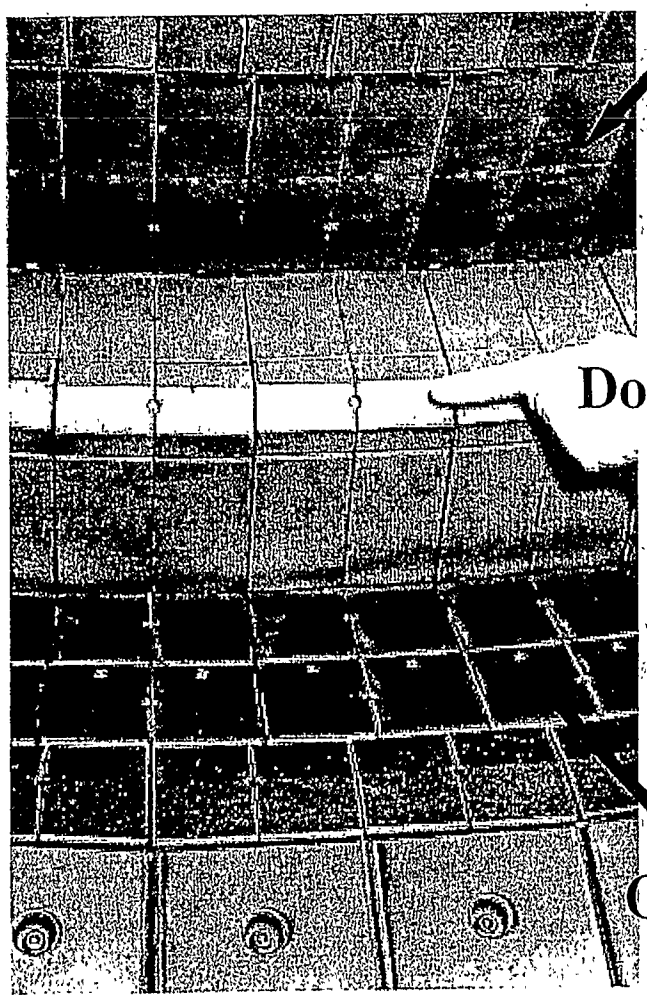

JAERI

Dust of the W-shaped divertor

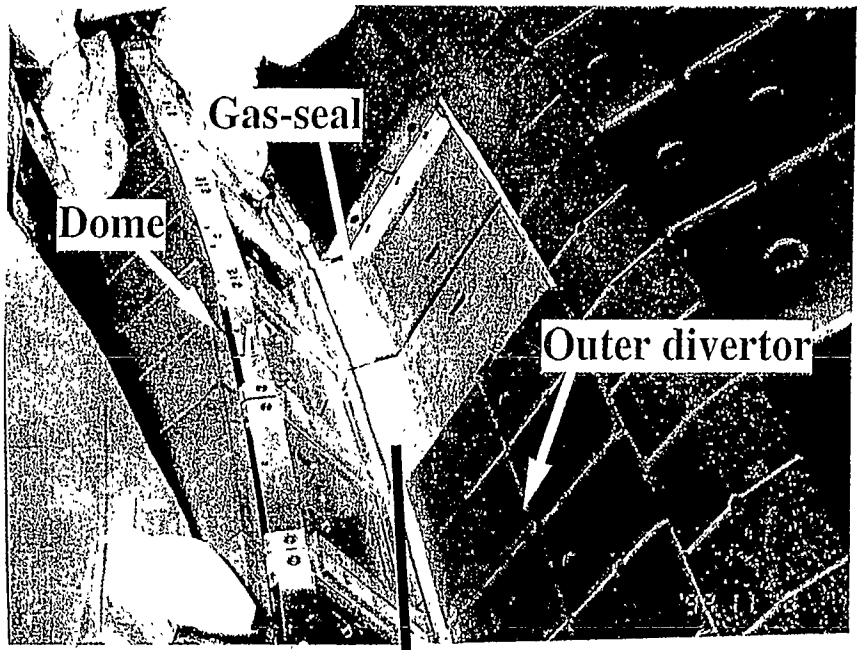

Dust on the gas-seal between dome and outer divertor
(collected in Nov. 1998)

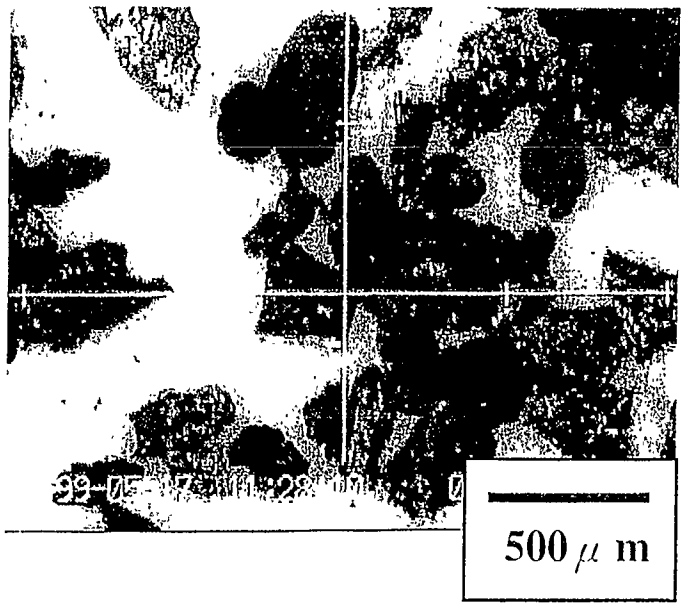

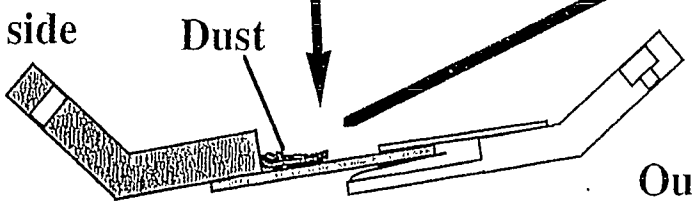

Gas-seal structure

JAERI

Dust on the gas-seal between dome and outer divertor

(collected in Nov. 1998)

×175

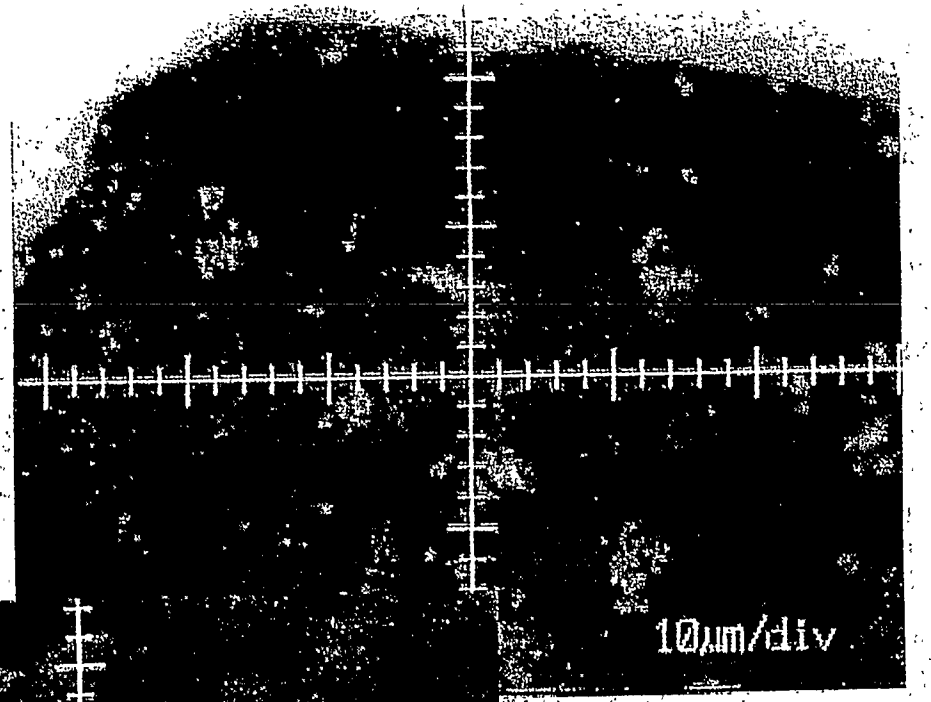

×1000

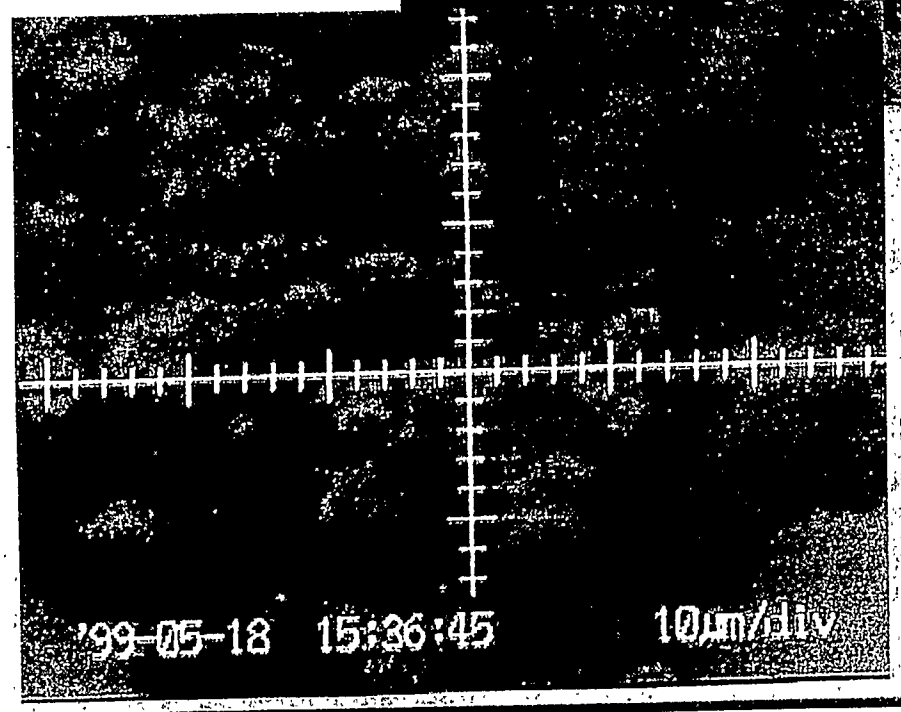

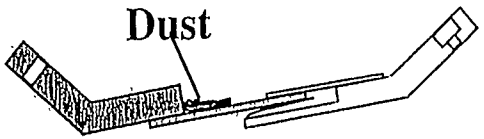

Gas-seal structure

JAERI

Surface of the outer dome tile

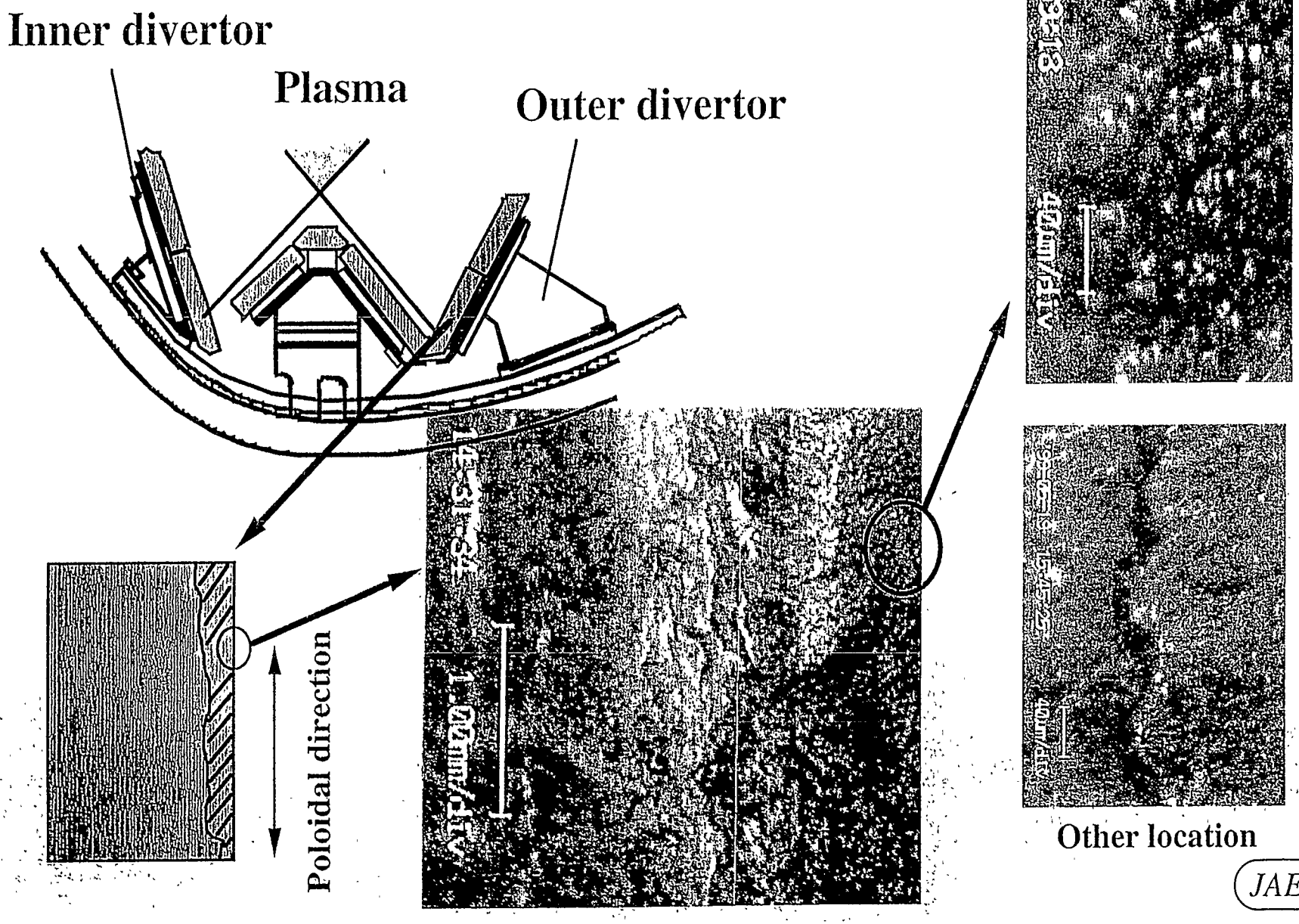

JAERI

Dust of the W-shaped divertor

(Observation by optical microscope)

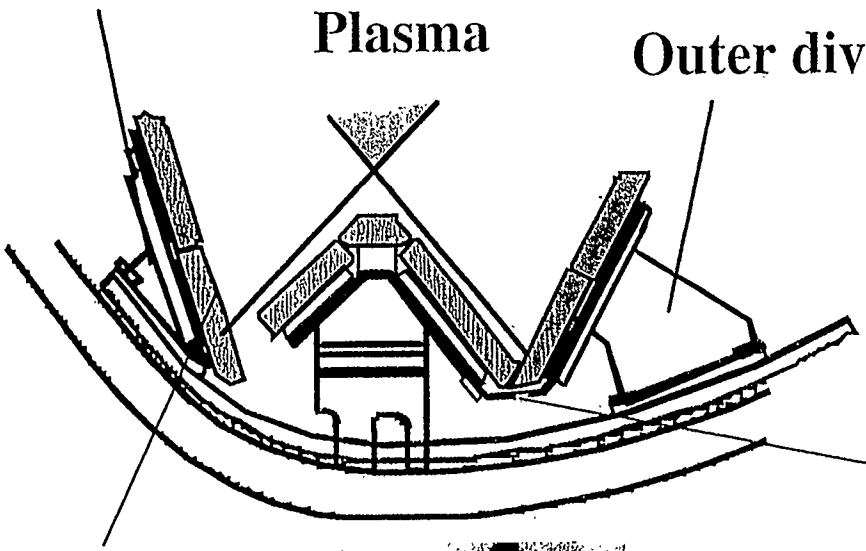

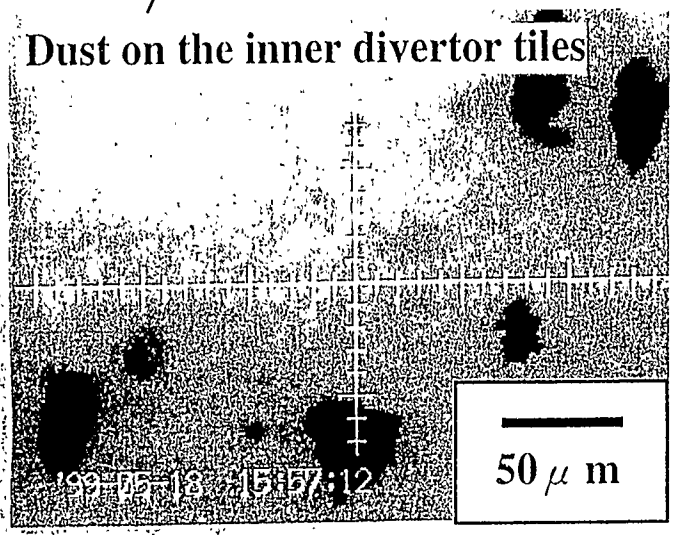

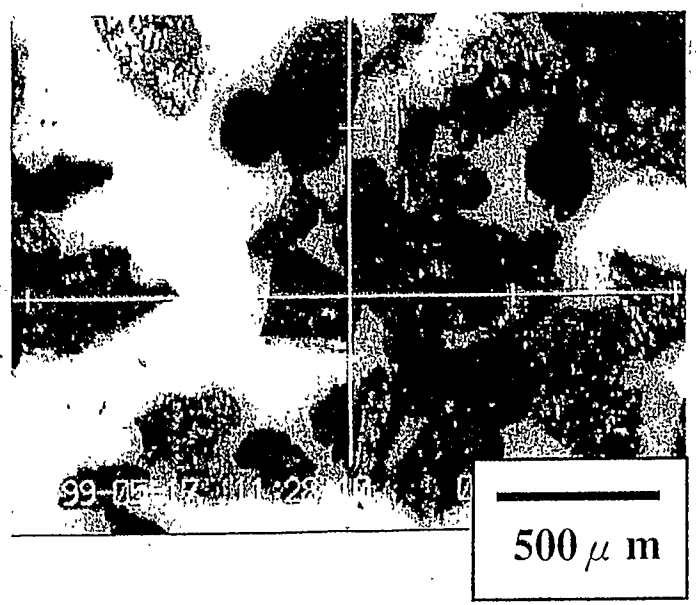

Dust on the gas-seal between dome and outer divertor

JAERI

Be-7 Poloidal Distribution of JT-60U W-shaped divertor

Be-7 : probably produced by B-10 (p, alpha) reaction

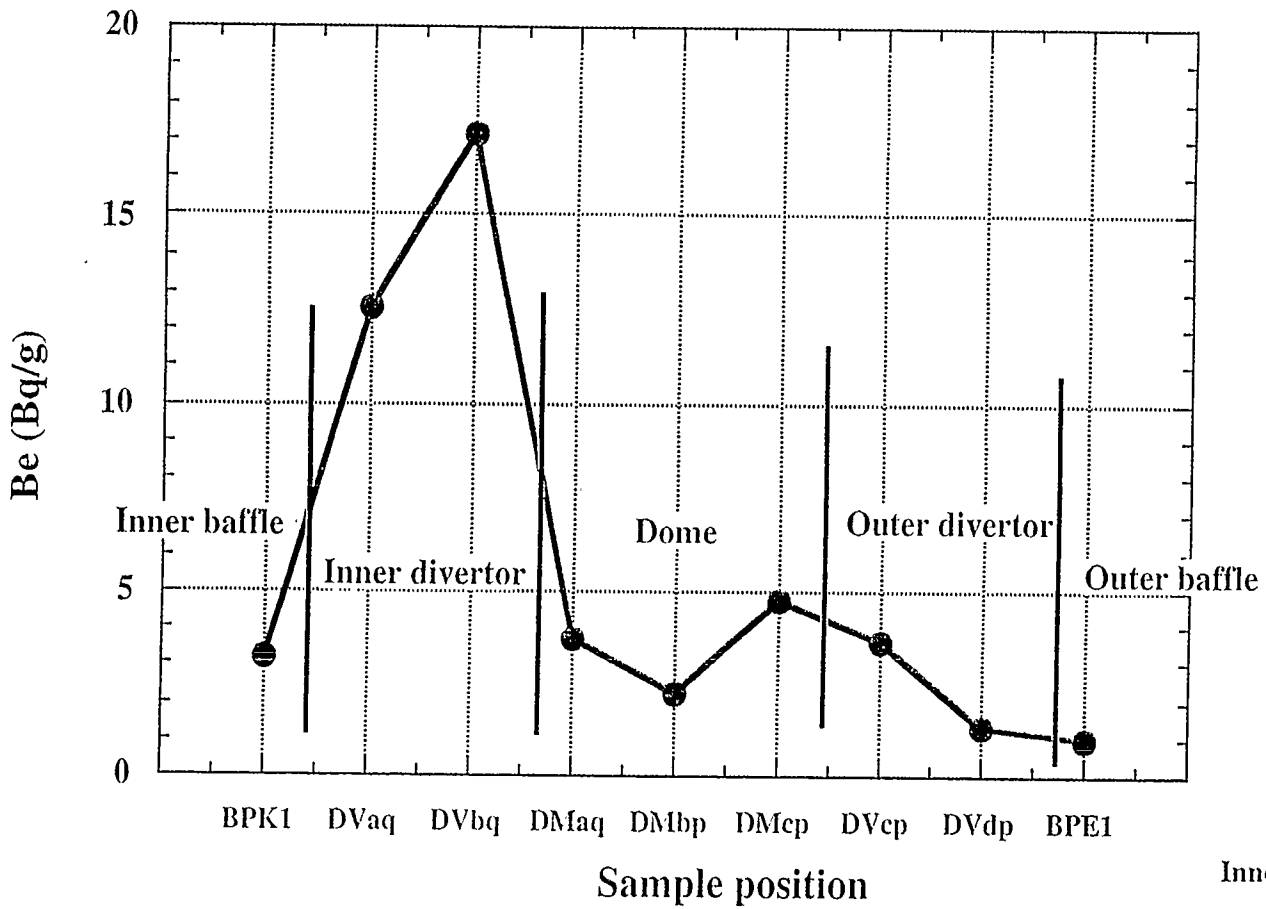

Sample tiles were removed in Nov. 1998.

Boronization was carried out in March 1998.

Boron source was only boron film formed by boronization.

No B_4C tiles.

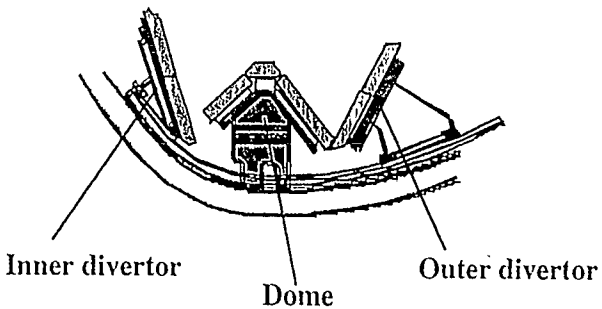

JAERI

Be-7 poloidal distribution

How Be-7 is produced in JT-60U is not precisely known. The best estimation is that it is produced by B-10 (p , alpha) reaction. The high energy protons come mainly from the D-D reactions and partly accelerated by ICRF heating.

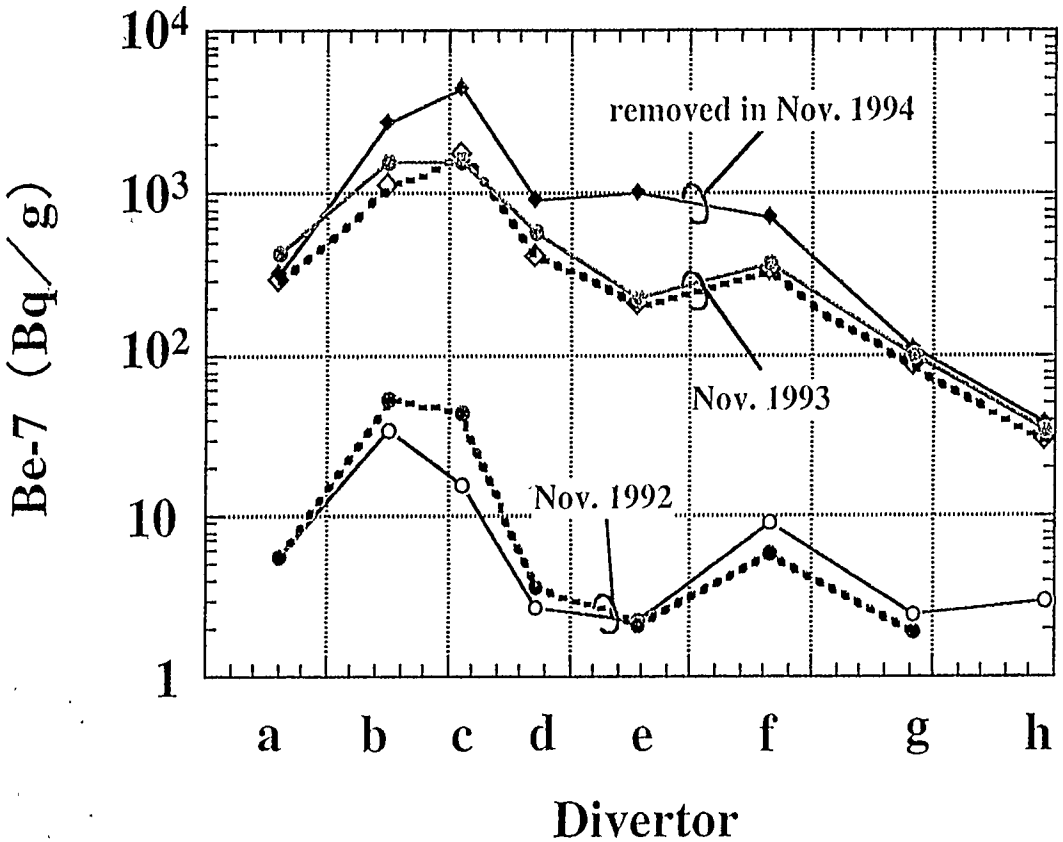

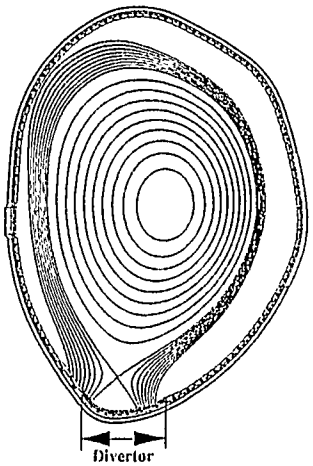

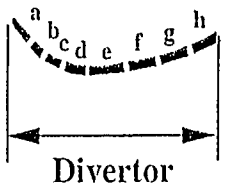

- B_4C tiles were installed
  <Dec. 1992>
  in divertor row-f

  <Dec. 1993>
  in divertor row-e
- Boronization using decaborane was also carried out about twice a year.

JAERI

Summary

Modification of W-shaped divertor to that with in-out divertor pumping slots was conducted in Dec. 1998 in order to improve plasma performance in detached state. With the modified W-shaped divertor, improved results have been obtained, and show efficient divertor pumping.

In-out asymmetry of deposit (inside > outside)

Erosion : inside < outside

In- out asymmetry of Be-7 distribution (inside > ouside)

Dust on the gas-seal :
~500 μ m、 small broken pieces of deposit layer

These results imply impurity transport from outer divertor to inner one ?

JAERI

Plasma Edge Studies – 2

RECENT RESULTS FROM DIMES

Clement Wong

for the DIMES team

D. Whyte, P. West, R. Bastasz, W. Wampler, J. Brooks

- Central Conductors
- Carbon Source
- DiMES-Li experiment
- Leading Edge Experiment
- Plan for Y2K

US-Japan Workshop on Plasma Surface Interactions and
High Heat Flux Components for Next Fusion Devices
November 1-4, 1999, Santa Fe, New Mexico

Sandia National Laboratories UCSD GENERAL ATOMICS DIII-D NATIONAL FUSION FACILITY SAN DIEGO

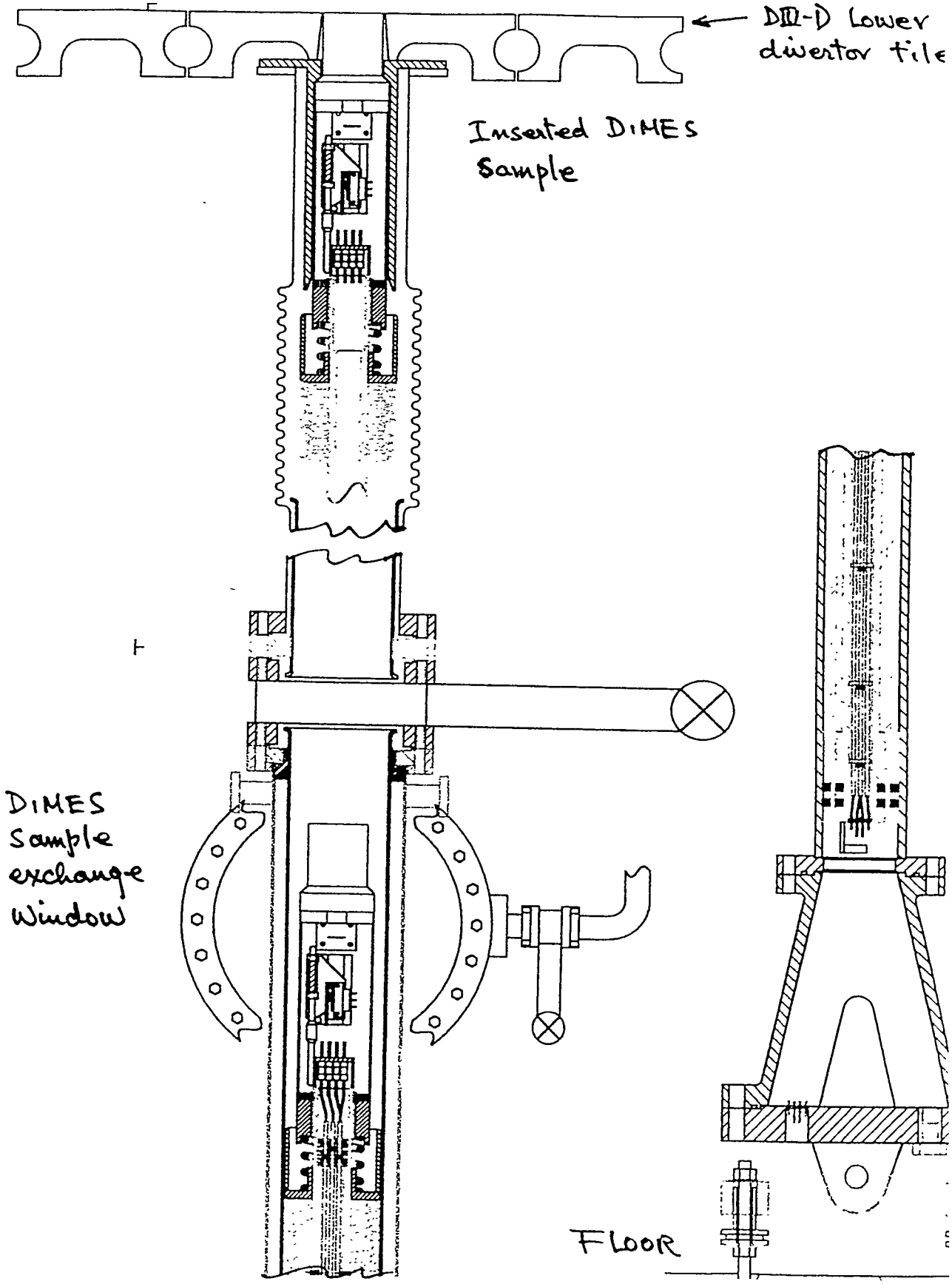
DIII-D Lower divertor tile
Inserted DIMES Sample
DIMES Sample exchange window
FLOOR

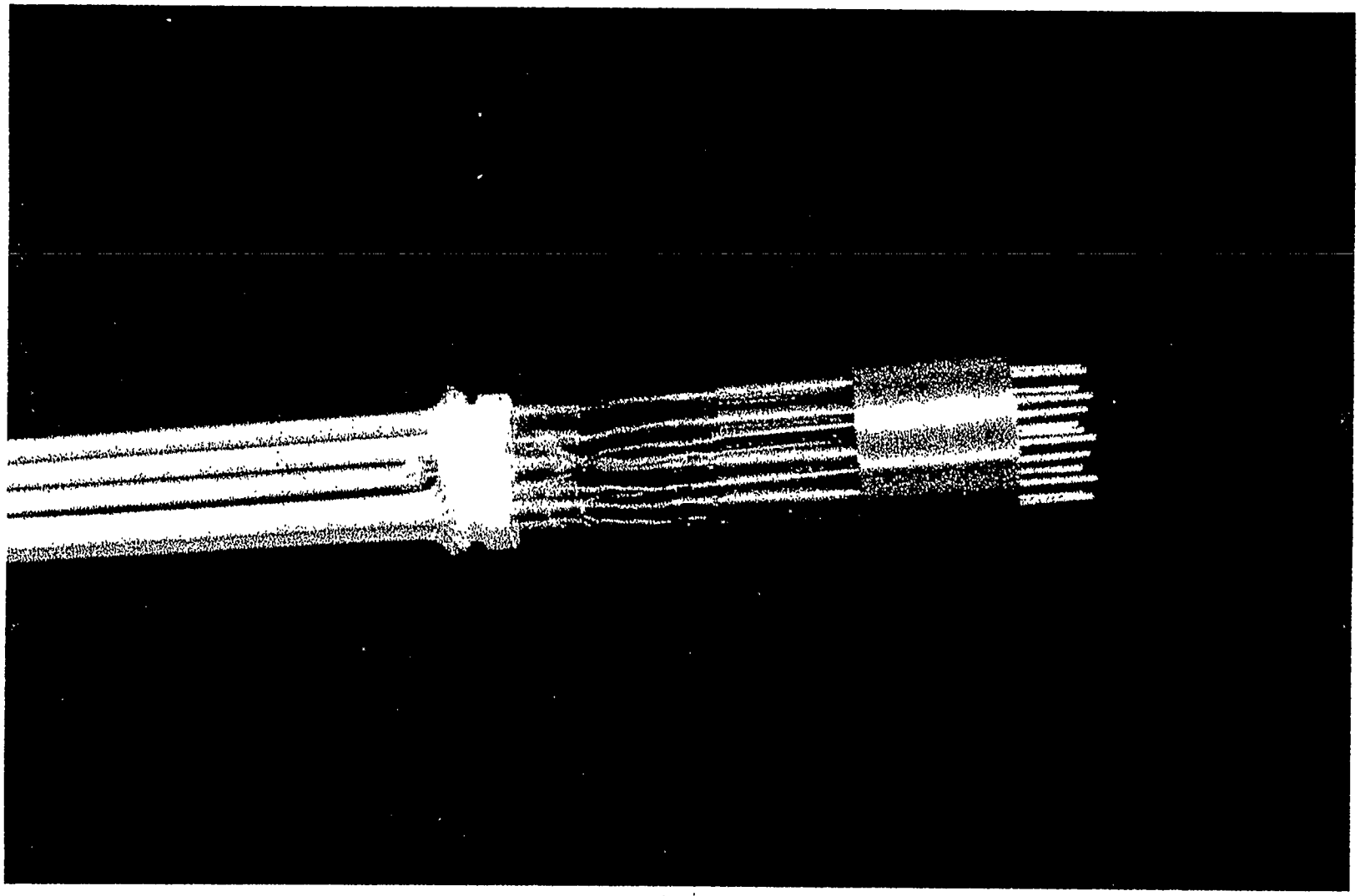

DIII-D
NATIONAL FUSION FACILITY
SAN DIEGO

GENERAL ATOMICS

240-98/rs

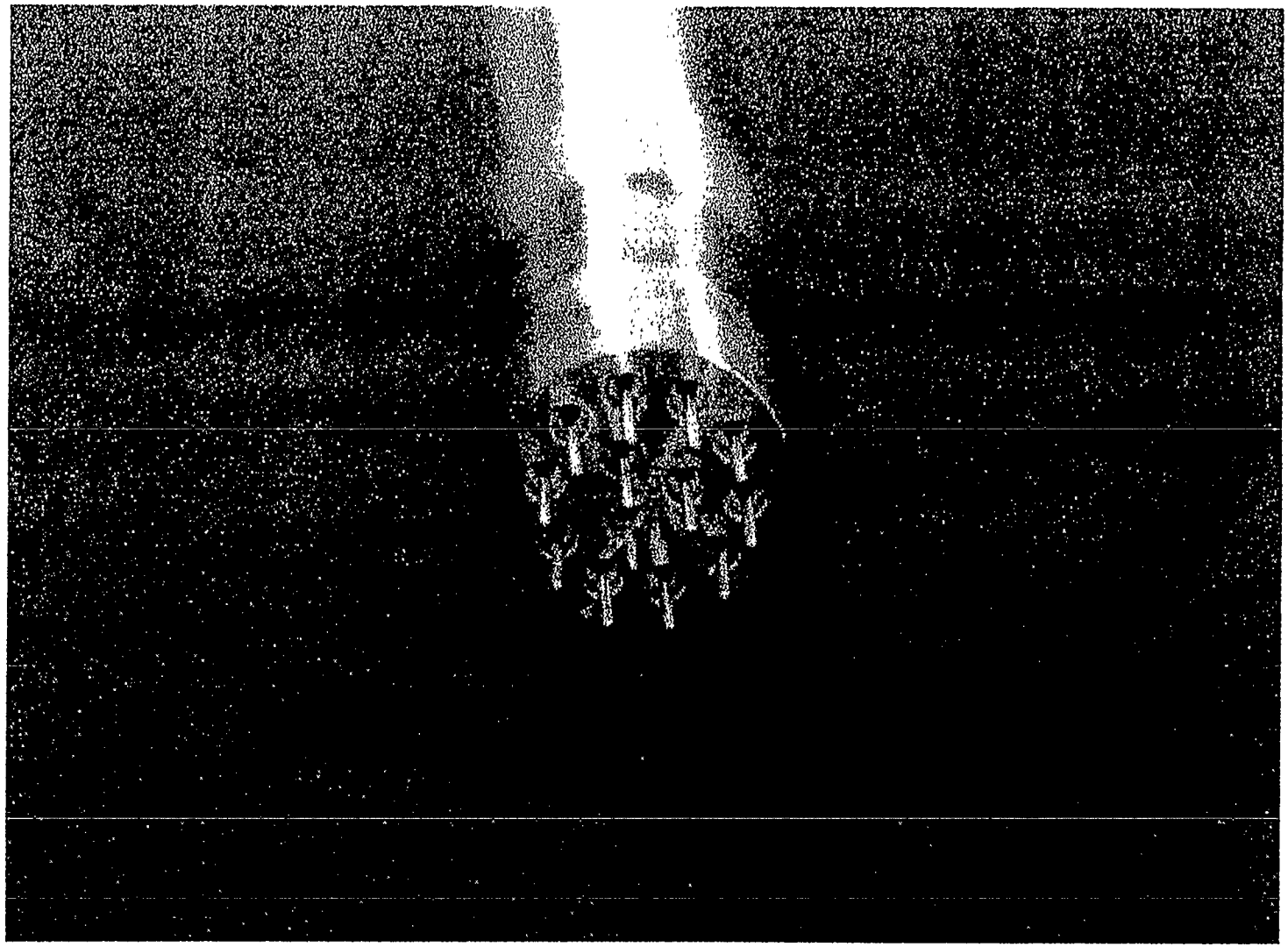

DIII-D
NATIONAL FUSION FACILITY
SAN DIEGO

GENERAL ATOMICS

240-98/rs

DIII-D

Divertor detachment eliminates net carbon erosion in the entire lower divertor! ...yet carbon density in core plasma remains constant?

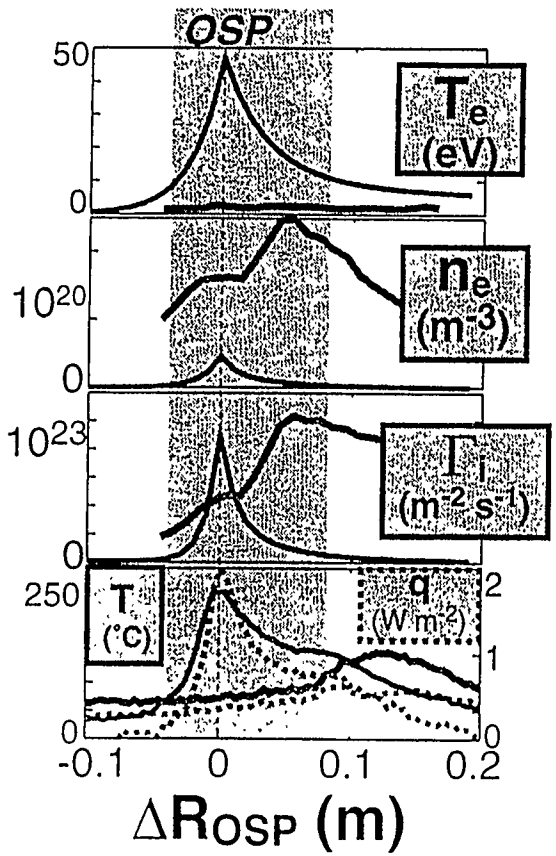

Attached vs. Detached

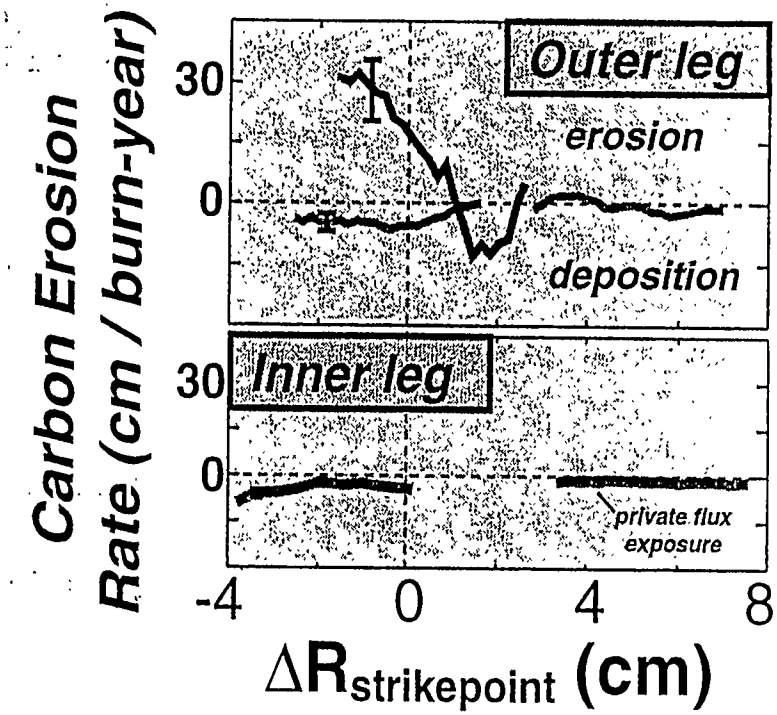

D_2 Torr L /s	I_p MA	P_{aux} MW	W_{th} MW	n_e/n_C $10^{19}m^{-3}$	f_C %
0	1.4	7.2	1.2	4 / .16	4
~100	1.35	6.9	0.9	10 / .15	1.5

Erosion & Transport of Lithium in the DIII-D Divertor

Motivation

- Advantages of liquid metal plasma-facing components (ALPS)
  - Self-healing surface (no net erosion).
  - Resilience to off-normal events like disruptions.
  - Enhanced heat and particle removal capabilities with flowing liquid surfaces.
  - Access low recycling / collisionality divertor plasma with strongly pumping lithium surface.
- Low Z of lithium provides great opportunity to study physics of divertor erosion (sputtering) and transport using visible spectroscopy in divertor.

Experiment

- Obtain detailed erosion and transport data on lithium in both solid and liquid state
  - Needs injected power and plasma shaping control (one day experiment)
  - Dedicated divertor spectroscopy for determination of lithium sputtering and transport.
  - Expect enhanced erosion at higher surface temperature due to evaporation.
  - Use new DiMES head that allows control of sample temperature.
  - Obtain detailed divertor plasma diagnosis for modeling.

DiMES Li-EXPERIMENT IN DIII–D

- Li sample assembly designed and fabricated at SNL-L
- Sample loaded with 0.25 mm Li-foil on SS holder
- PISCES Li results help to guide DiMES experimental details
- Ar sample transfer procedure developed
- HWA document approved by DIII-D
- Ist piggyback experiment performed
- 2nd experiment could be exposed to a low recycling ELM free H mode plasma
- Diagnostics and modeling efforts are being coordinated
- Heated sample assembly tested at SNL-L, DIII-D and will be utilized
- Benchmark modeling codes by studying Li transport from the DIII-D divertor

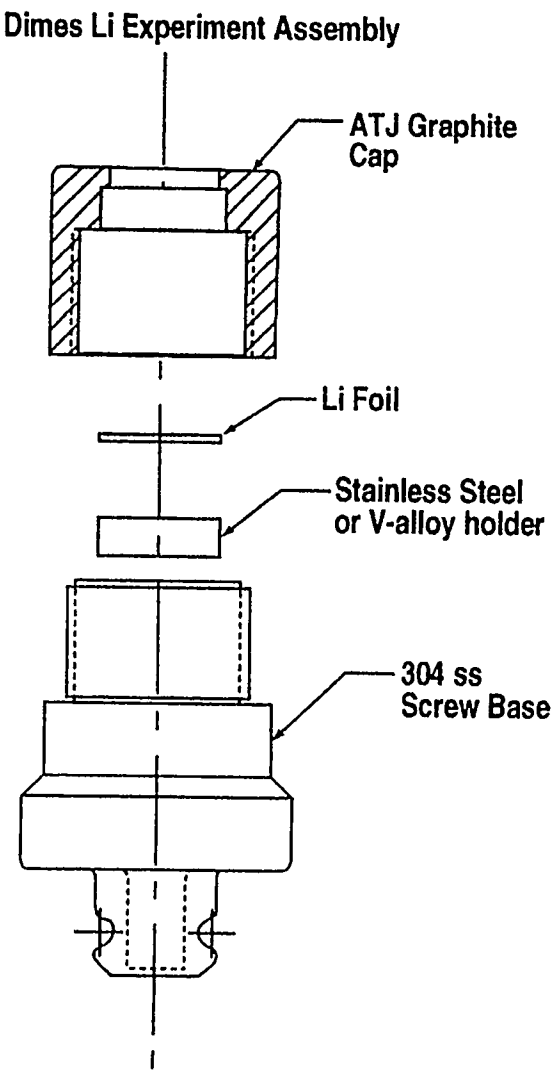

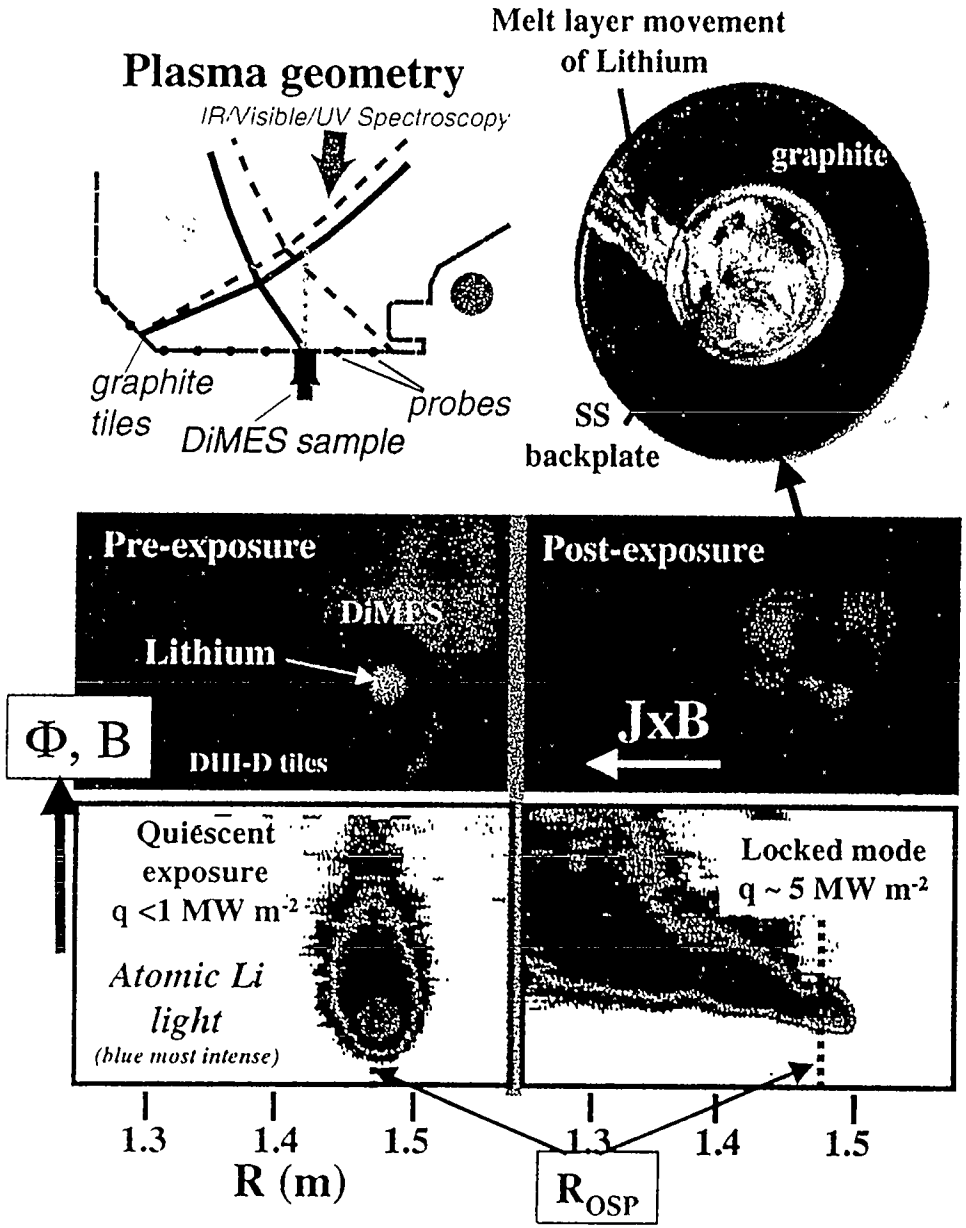

1st piggyback Lithium exposure in DIII-D / DiMES is a success

- Lithium surface remained pristine by using glove-box / Ar purge for transfer of sample.
- Quiescent outer strikepoint exposure shows expected neutral Lithium plume along B from physical sputtering.
- High heat flux exposure during locked-mode
  - Substantial melting of Li.
  - Apparent JxB movement of melt layer.
  - Removal of entire 0.25 mm Li thickness on portions of sample!

DiMES Leading Edge Experiment

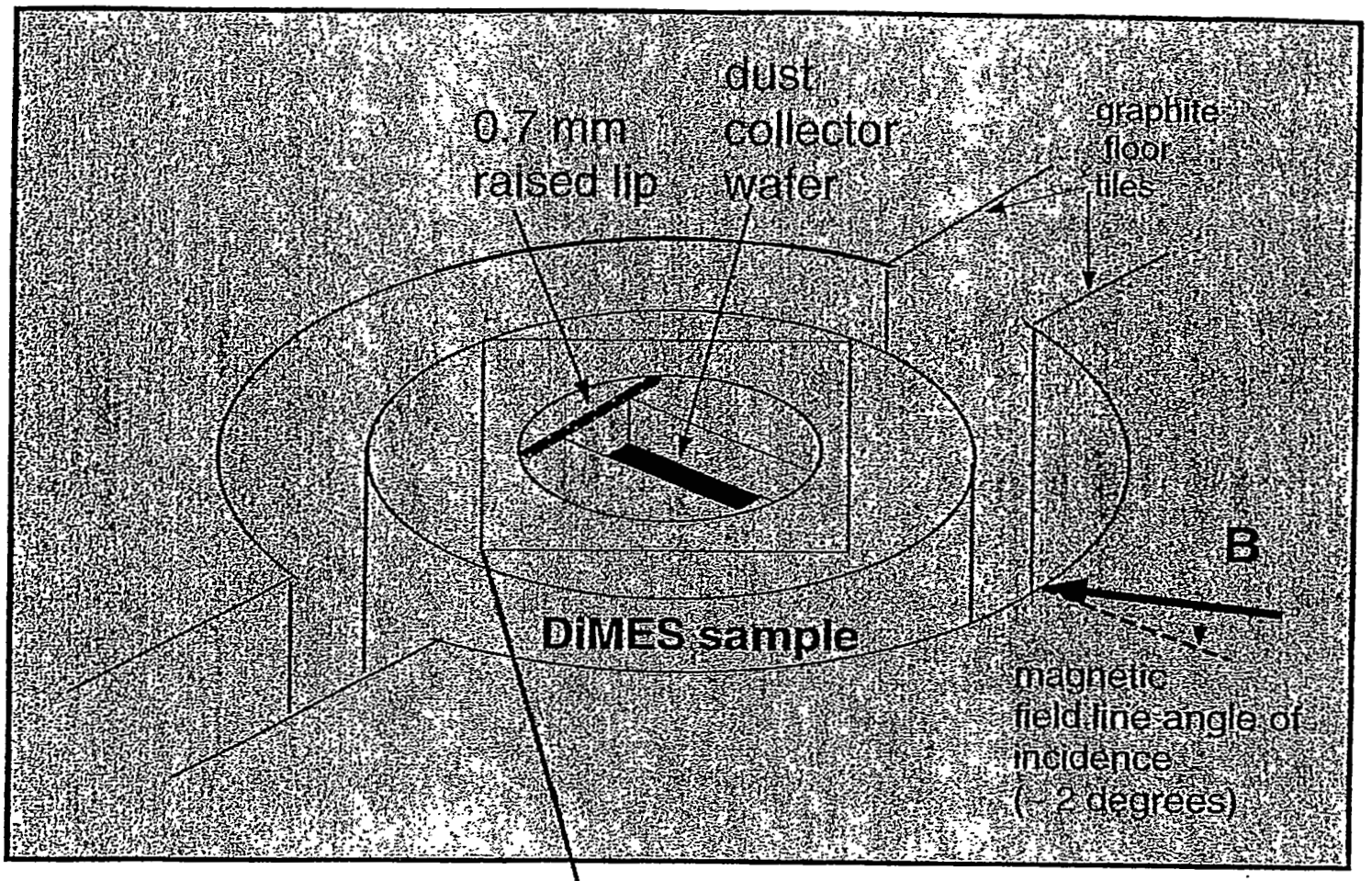

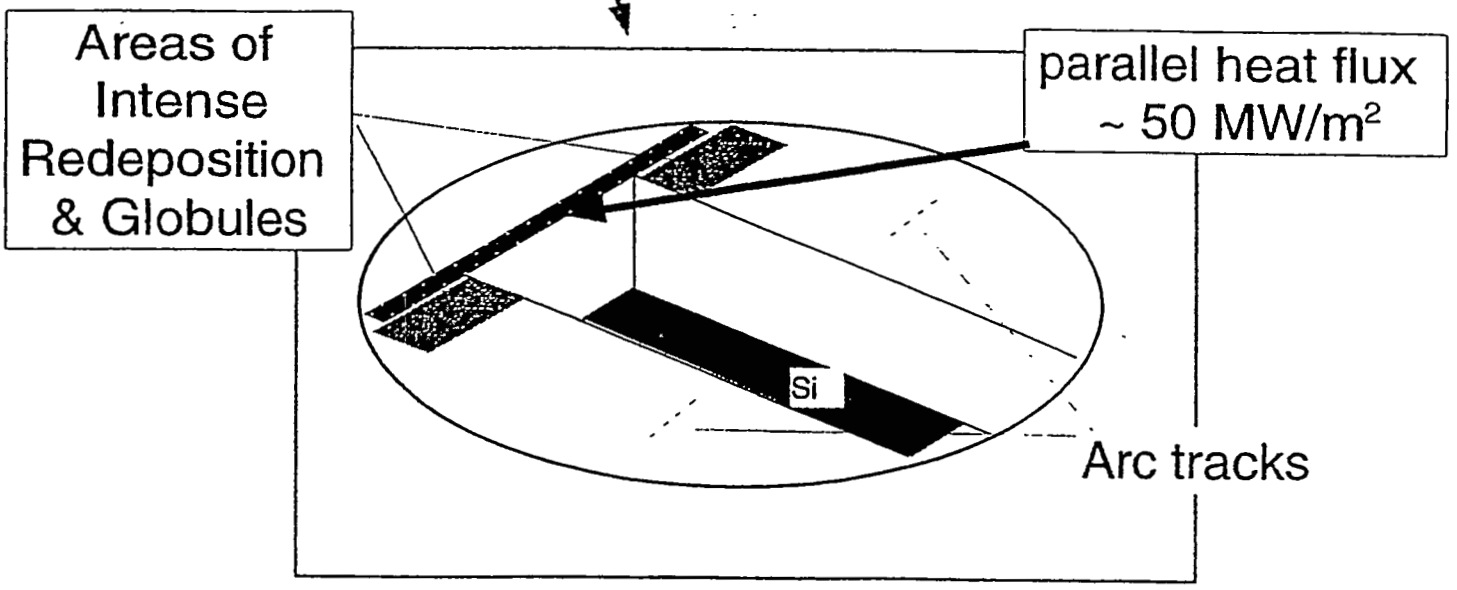

Combination of lithium and DIII-D divertor diagnostics provide a unique opportunity to study divertor transport of impurities

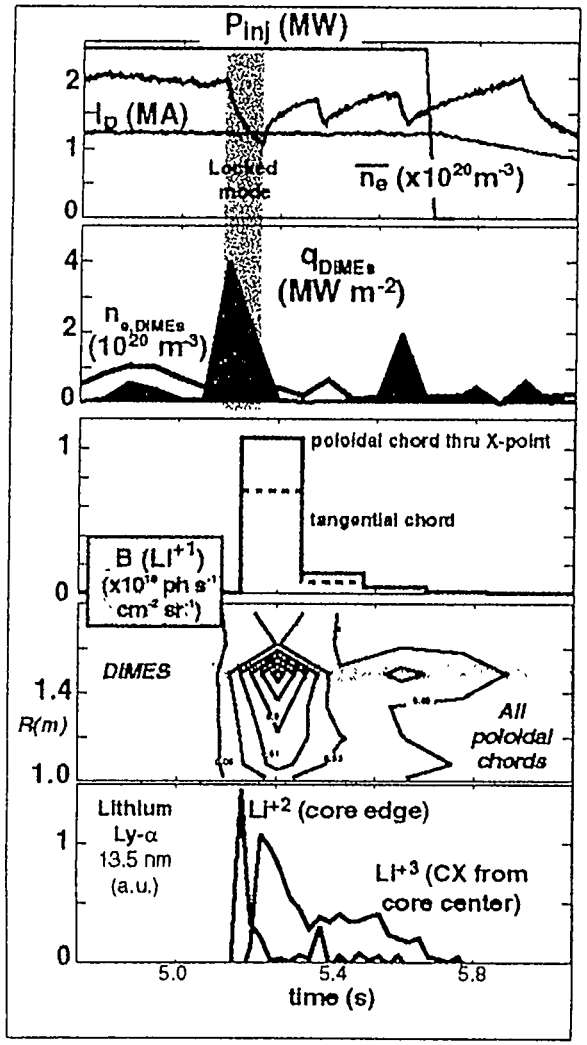

- Divertor visible diagnostics provide 2D mapping of both Li "divertor" charge states (i.e. neutral and singly ionized)
- Core UV spectrometer measures both edge and central core Li.
- Every charge state of Lithium is measured.

Lithium also provides unique opportunity to study erosion and transport in the <u>private flux</u> region.

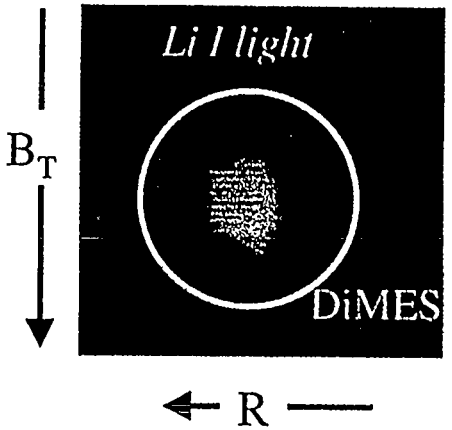

Uniform light pattern likely indicates spatially isotropic CX sputtering into dense and cold PF plasma

Proposed Y2K DiMES Experiments

Dedicated

- Lithium erosion and transport
- Effect of impurities on divertor erosion

Piggyback

- First-wall PMI *(during upper single-null experiments)*
  - charge-exchange diagnostics (hydrogen sensor) on DiMES
  - study formation / erosion of mixed material layers at first wall.
- Erosion properties of boronization layers
  - 1999 experiment showed higher than expected erosion rate.
  - Continue examination of boron's effect on carbon source.
- Contribution of arcing to divertor erosion
  - previous W film exposures showed ~100% of erosion from arcing
  - quantify frequency and consistency of arcing.
- Leading edge erosion
- Active monitoring
  - advanced langmuir probe development
  - smart tile development

Long Term Evolution of Graphite Tiles in DIII-D

D. Whyte, *UCSD*

for the DiMES & PISCES teams

C.P.C. Wong, W.P. West, R. Bastasz, W.R. Wampler,
J.N. Brooks, R. Doerner, S. Luckhardt, R. Conn

US-JAPAN WORKSHOP ON PLASMA SURFACE INTERACTIONS AND HIGH HEAT FLUX COMPONENTS FOR NEXT FUSION DEVICES

Sante Fe, NM November 1, 1999

DIII-D
NATIONAL FUSION FACILITY
SAN DIEGO

UC San Diego

Outline

- Background & Motivation
- History of chemical and total erosion yields in DIII-D lower divertor (1992- present).
- Effect of lower divertor carbon erosion yield on core plasma carbon contamination.
- Laboratory studies of DIII-D graphite tiles - effect of boronization on chemical erosion yield.
- Summary & discussion.

Background & Motivation

- Previous results suggest chemical erosion of carbon plays an **important** role in DIII-D
  - Helium plasmas: reduced carbon radiation in core and divertor.
  - UEDGE modeling: a "distributed" chemical carbon source (using University of Toronto Y_{chem}) provided radiation to induce detachment and match C spectroscopy.
- Previous results suggest that chemical erosion of carbon plays a **minor** role in DIII-D
  - CD-band emission not observed in divertor ($Y_{chem} < 10^{-3}$).
  - Divertor detachment, which eliminates physical sputtering, showed only carbon deposition in divertor (DiMES, PSI 98) ..total yield reduced by x100.

- Current carbon-based tokamaks show divertor erosion and tritium retention will seriously limit operations of next-step DT devices.

Divertor detachment eliminates net carbon erosion in the entire lower divertor! ...yet carbon density in core plasma remains constant?

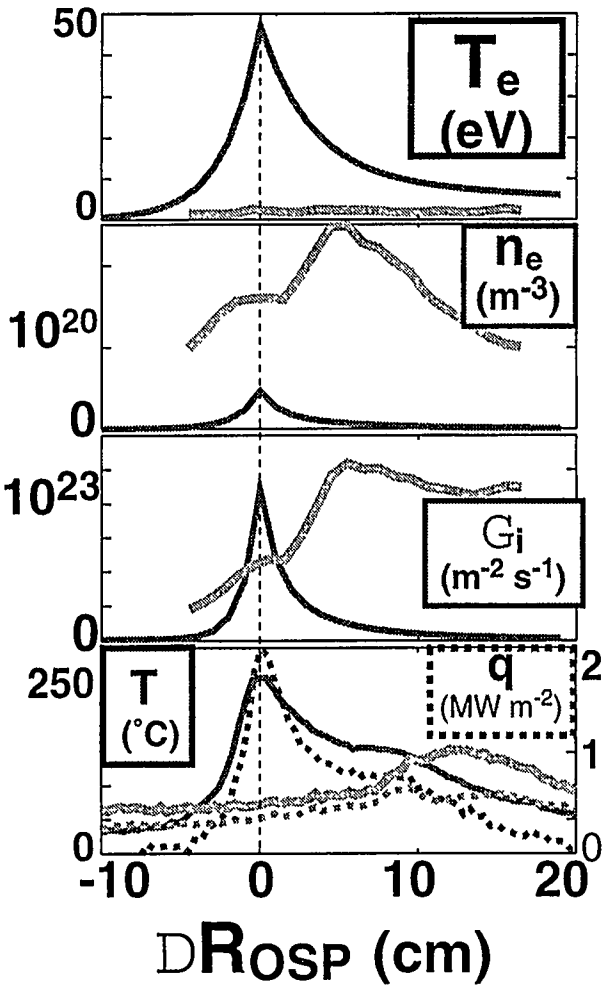

Attached vs. Detached

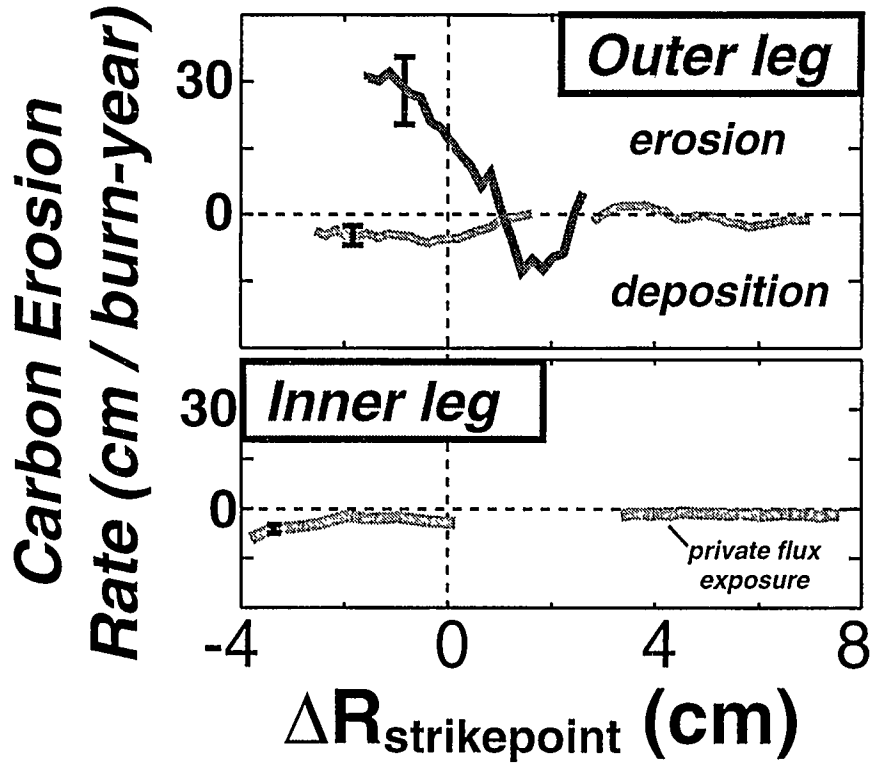

D_2 Torr L /s	I_p MA	P_{aux} MW	W_{th} MW	n_e/n_C $10^{19}m^{-3}$	f_C %
0	1.4	7.2	1.2	4 / .16	4
~100	1.35	6.9	0.9	10 / .15	1.5

Atomic and molecular spectroscopy suggest chemical erosion plays a minor role in DIII-D divertor.

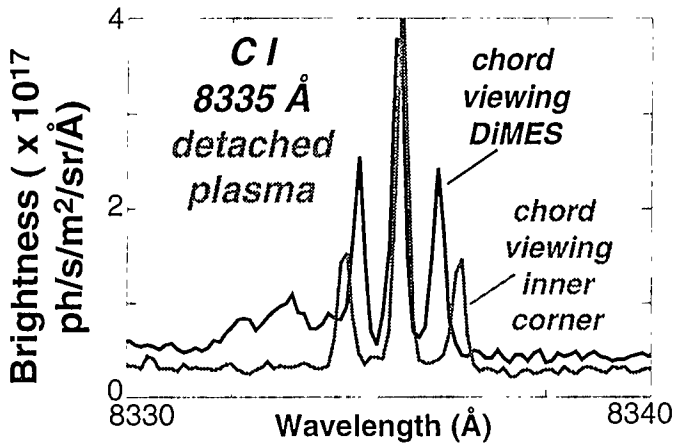

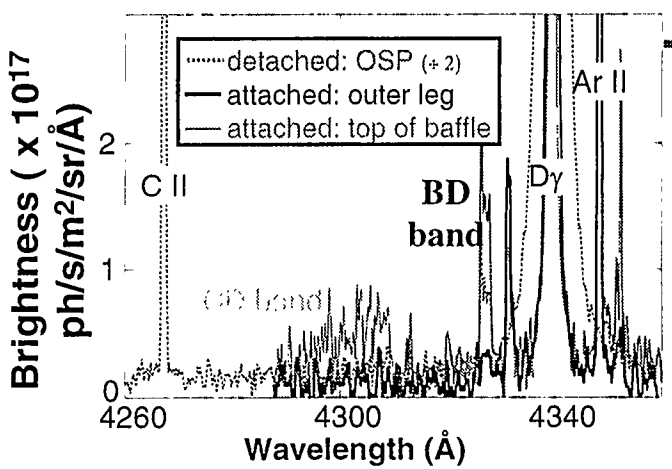

Atomic Carbon SXB ~ 300

Molecular Carbon (C_xH_y) DXB ~ 100

Assumption	Y_{chem}
Ions only	$\leq 10^{-3}$
Ions=neutrals	$\leq 10^{-4}$

Detached DiMES exp't

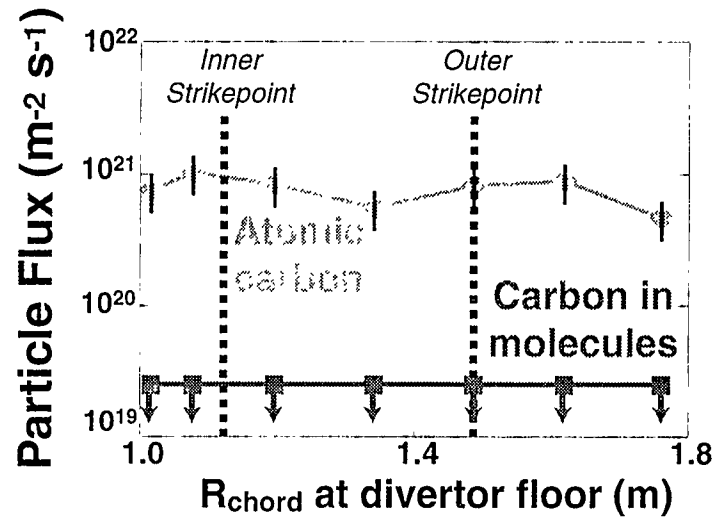

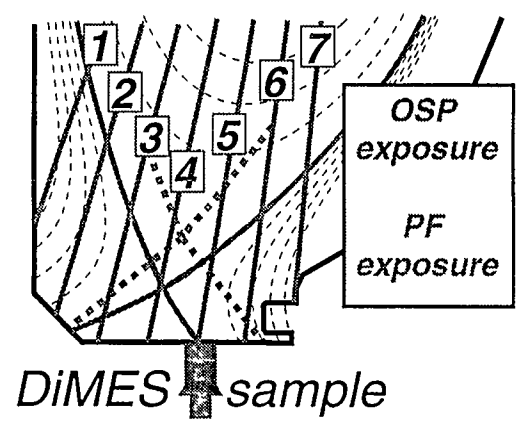

Based on carbon-based tokamaks' standard operation, erosion will severely limit operation of D-T burning device.

- **Pervasive in/out asymmetry.**
- **Outer divertor net erosion rate: > *10 cm / burn-year*!**
- **T trapping in erosion caused layers: ~ *1 kg / m² / burn-year*!**

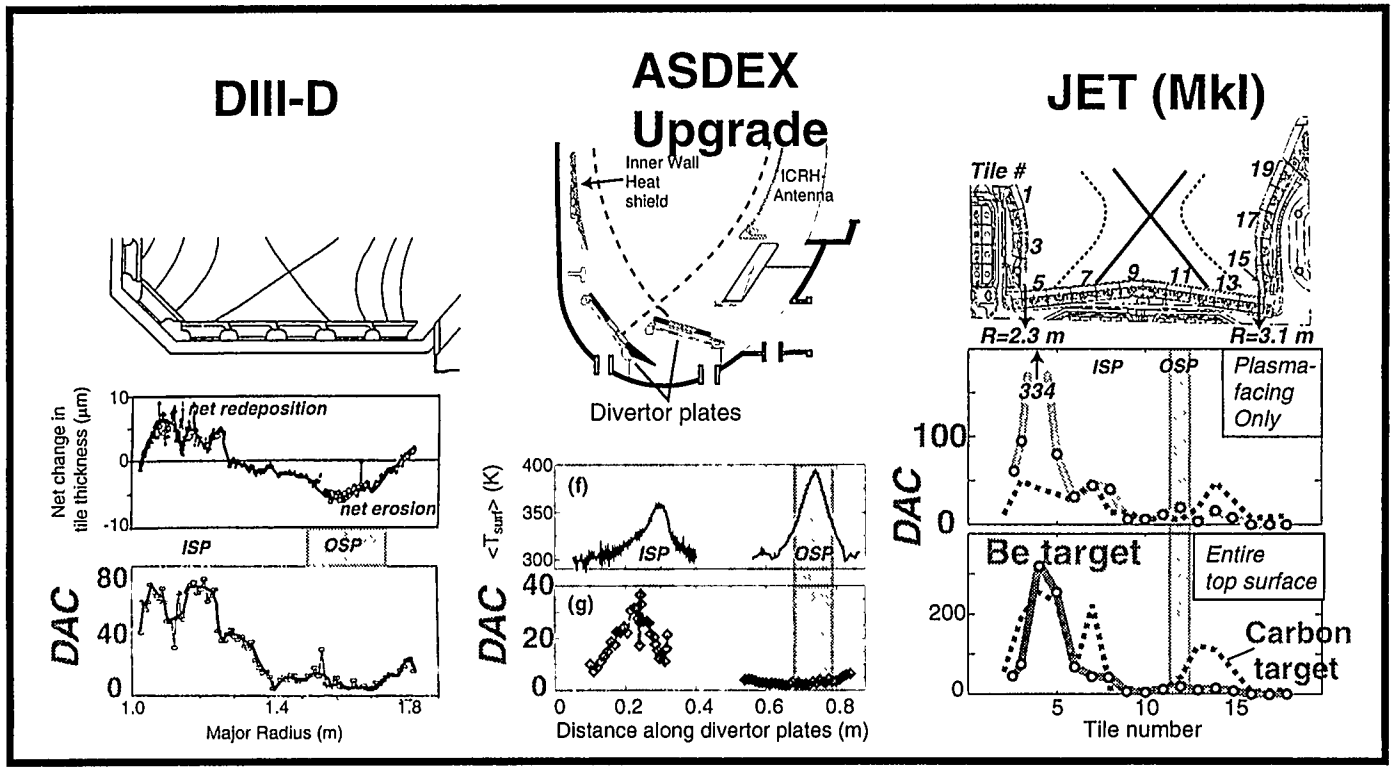

Poloidal erosion / redeposition patterns from 3 tokamaks: > 1 year of operations.
DAC: trapped D concentration

D.G. Whyte, et al. Nucl Fusion (1999).

History of chemical and total erosion yields in DIII-D lower divertor (1992- present).

Relative spectroscopy can be used to measure carbon erosion yields in situ

- Technique relies on S/XB (loss events per photon) and relative intensities:
  - Fairly insensitive to T_e and n_e.
  - Insensitive to photometric calibration.

- Chemical erosion yield

$$Y_{chem} = \frac{\Gamma_{C_x D_y}}{\Gamma_D} = \frac{B_{CD} \cdot D/XB_{CD}}{B_{D_\gamma} \cdot S/XB_{D_\gamma}}$$

- Total erosion yield

$$Y_{total} = \frac{(\Gamma_{C_x D_y} + \Gamma_{C_0})}{\Gamma_D} \propto \frac{B_{CII} \cdot S/XB_{CII}}{B_{D_{\alpha,\gamma}} \cdot S/XB_{D_{\alpha,\gamma}}}$$

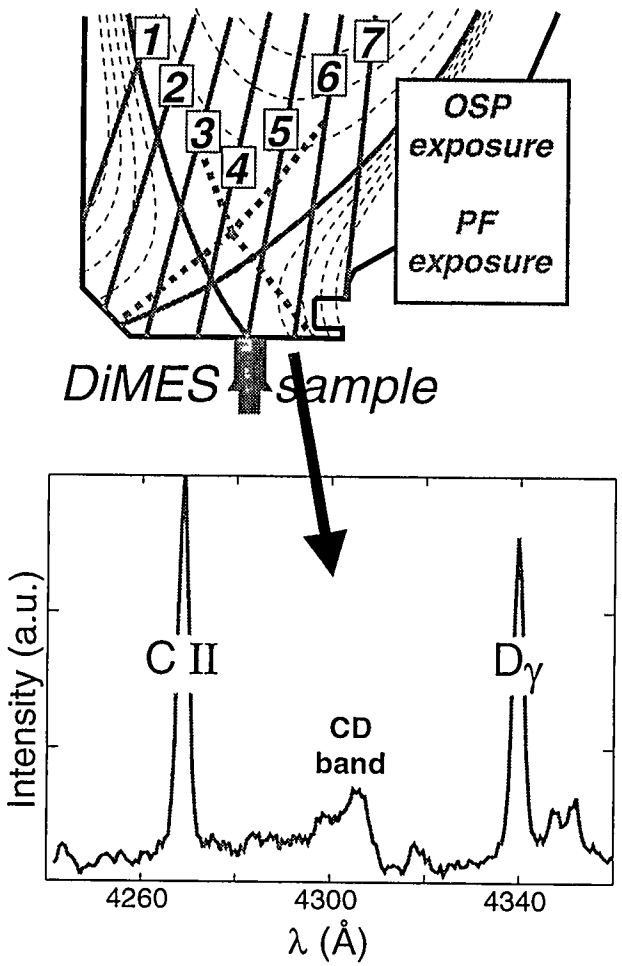

S/XB and D/XB values are fairly constant for attached plasma (T_e > 10 eV) conditions.

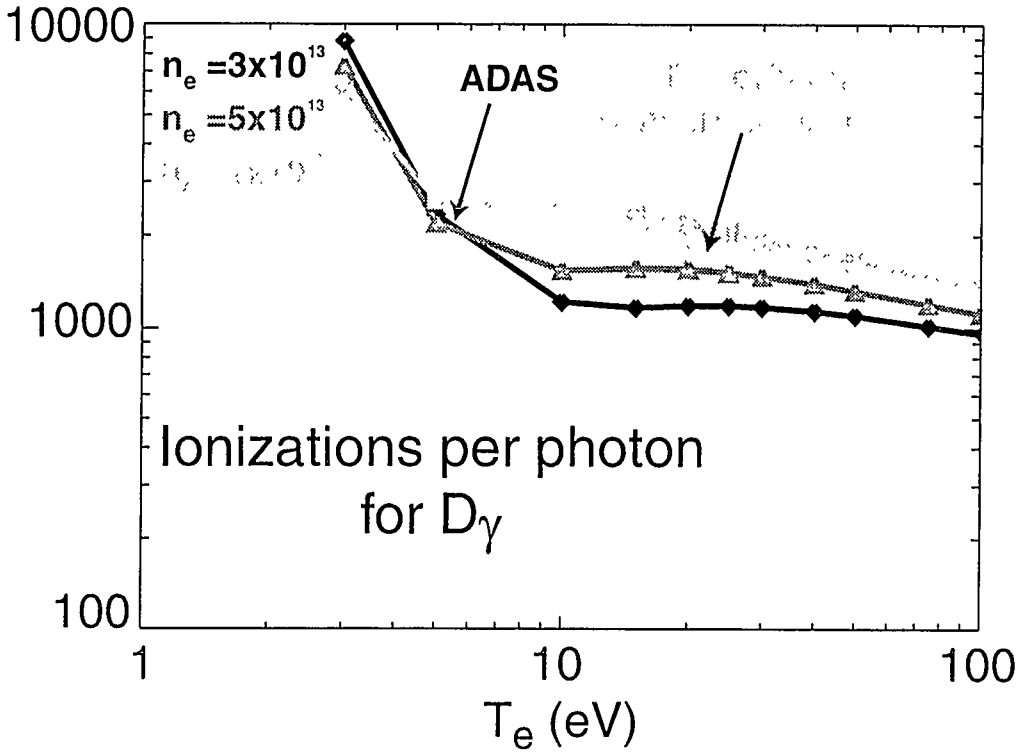

- Derived values for D_γ S/XB
  - Atomic rate calculations.
  - Experimental comparison to probes & DTS.
  - Agreement / scatter to within a factor of 2.
  - Assumes recycling ~ influx.

- D/XB is derived from controlled CD_4 injections:
  - **JET: D/XB ~40-50 for attached plasmas.**
  - **PISCES: D/XB ~50-100 for T_e > 10 eV.**

DIII-D tiles have accumulated ~2.5 μm of boronization layers & ~10^5 seconds (25,000 shots) of plasma exposure without significant alterations to lower divertor tiles.

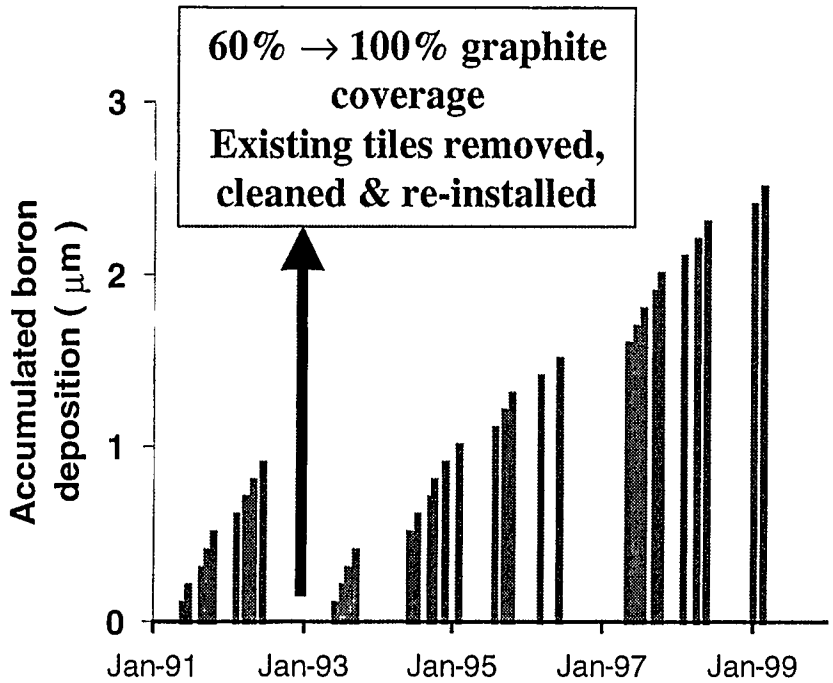

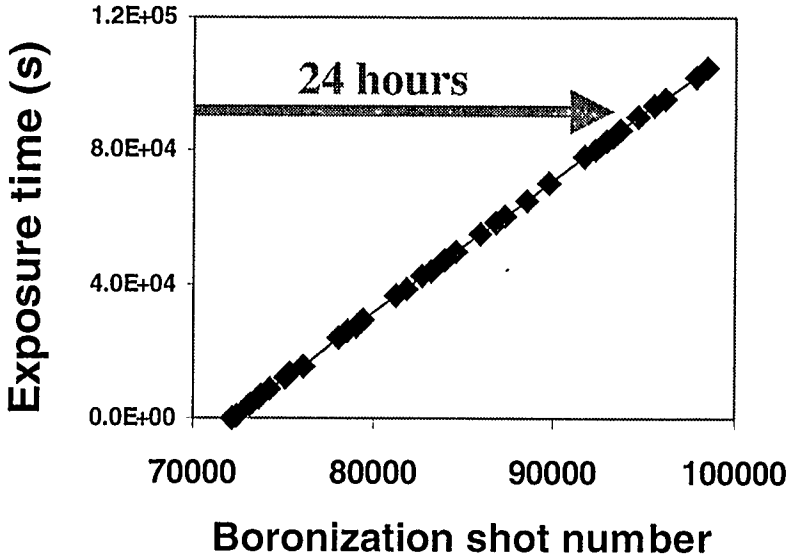

Single boronization = ~100 nm uniform B layer deposited

Graphite tiles are visibly altered by tokamak exposure.

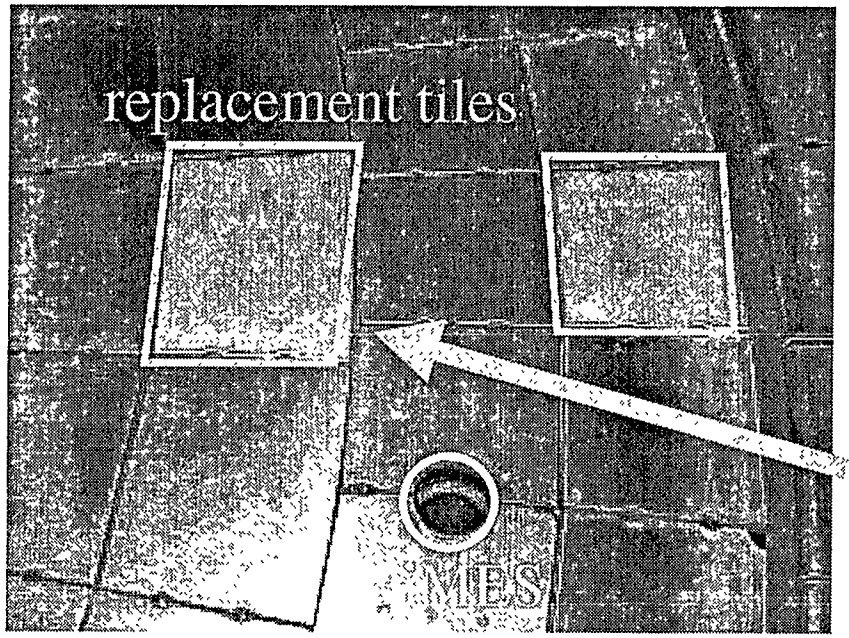

DIII-D Lower Divertor near DiMES (August 1998)

Plasma-exposed tile removed from DIII-D for PISCES exposure

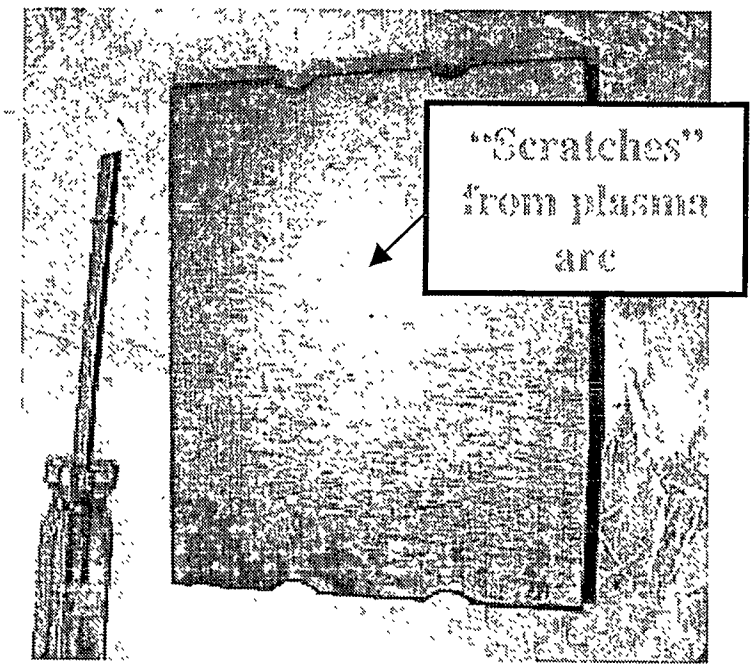

In 1992-1993, a single boronization would cause an immediate, but temporary, reduction in Y_{chem} and Y_{total}.

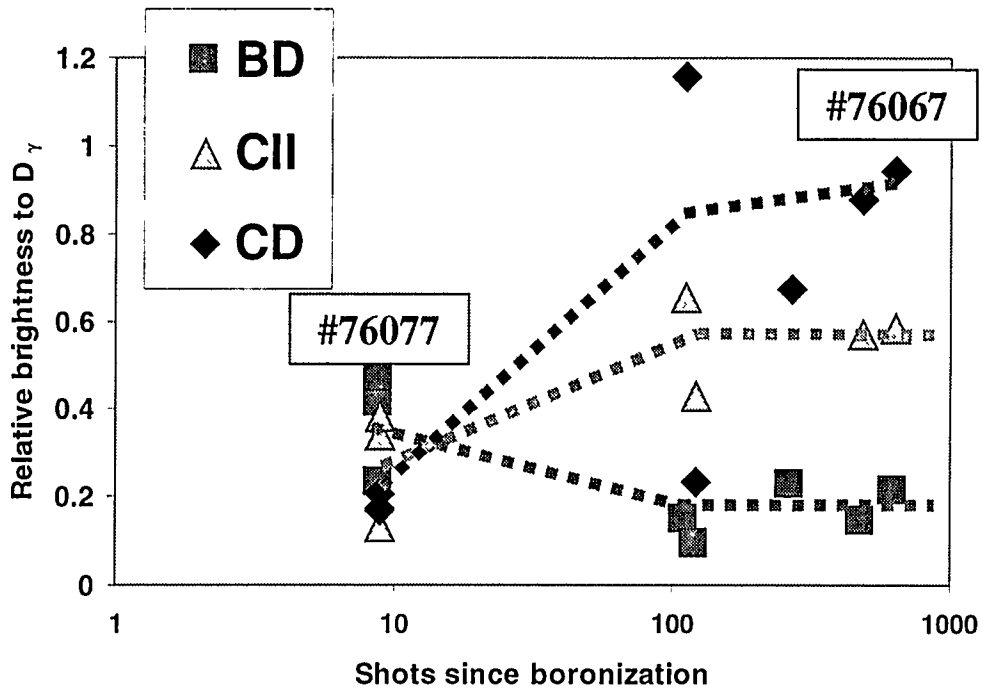

Averaged over lower divertor chords

- Direct comparison before and after boronization.
  - Y_{chem} reduced ~x4
  - Y_{total} reduced ~x2
- BD band reduced, but not eliminated by plasma exposure.
- Substantial removal of 100 nm boron layer consistent with measured OSP net erosion rates ~ 2 nm/s

Comparison of nearly identical plasmas show that Y_{chem} has decreased significantly in DIII-D since 1993.

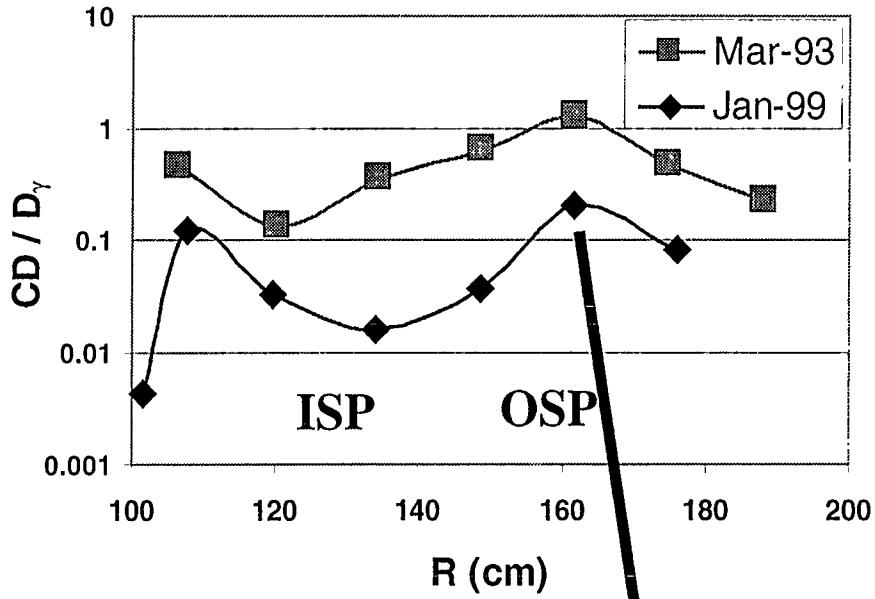

	#76952	#98042
I_p (MA)	1.5	1.4
n_e (cm^{-3})	7.6×10^{13}	6.8×10^{13}
P_{inj} (MW)	6.9	6.6
W_{dia} (MJ)	1.2	1.1

Spectra normalized to D_γ intensity & for different detector responses (intensified vs. non-intensified)

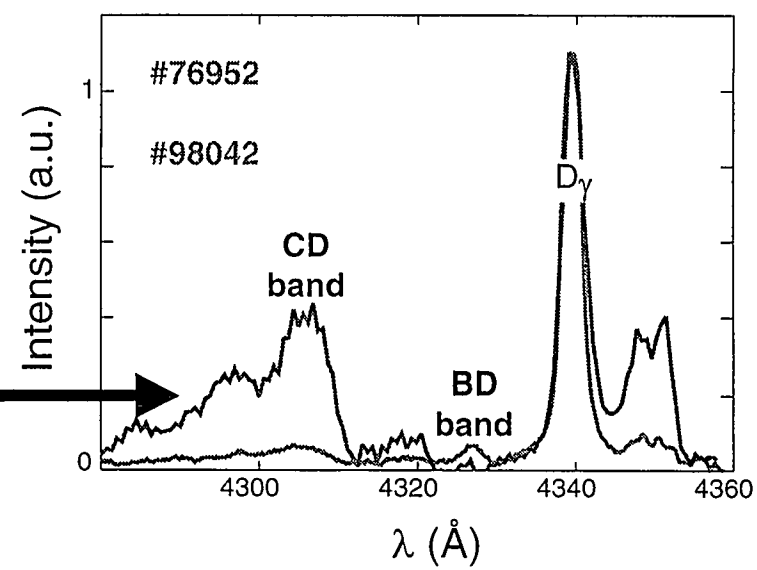

A database of lower divertor CD band spectroscopy (1992-1999) clearly shows a large reduction in Y_{chem}.

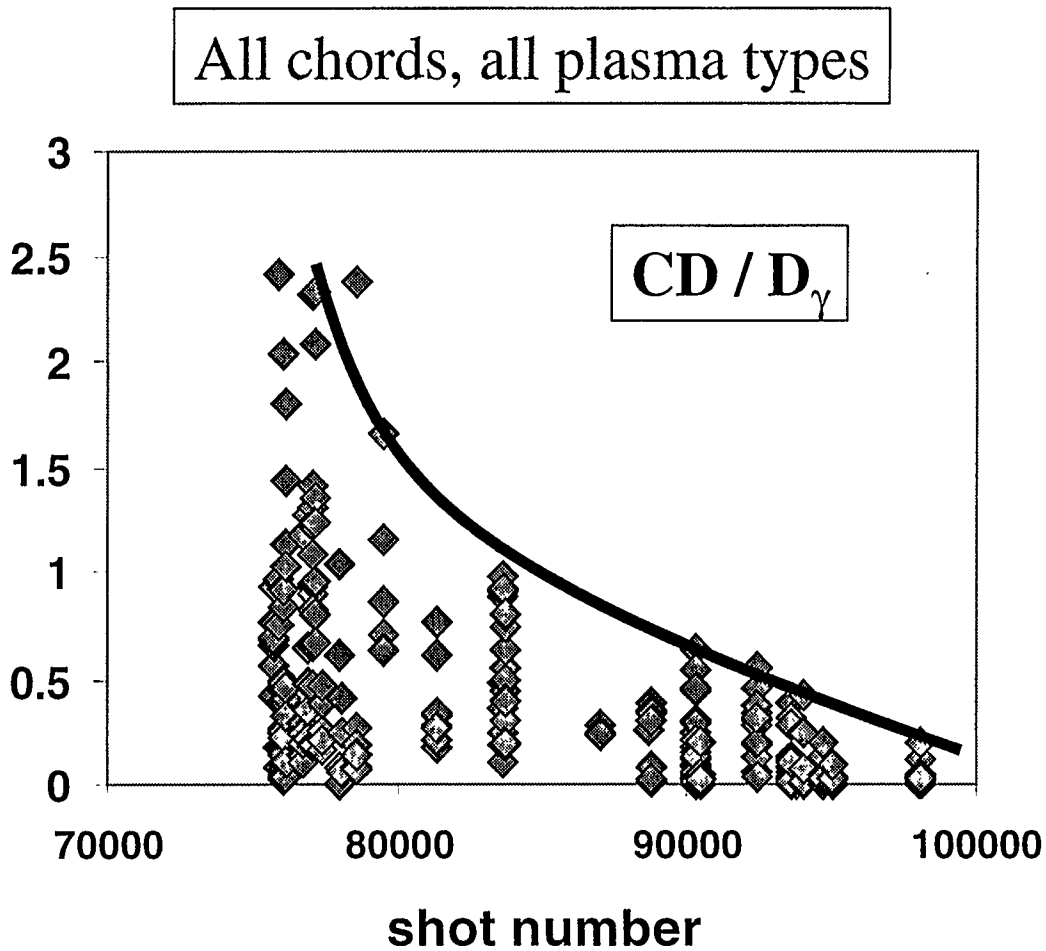

- Includes all discharges where spectrometer was tuned to 430 nm:
  - **LSN & DN**
  - **Ohmic, L, ELMy H**
  - **Attached & detached.**

Average lower divertor Y_{chem} for attached ELMy H-mode plasmas has gradually decreased a factor of 20 from ~2% to ~0.1% since 1992.

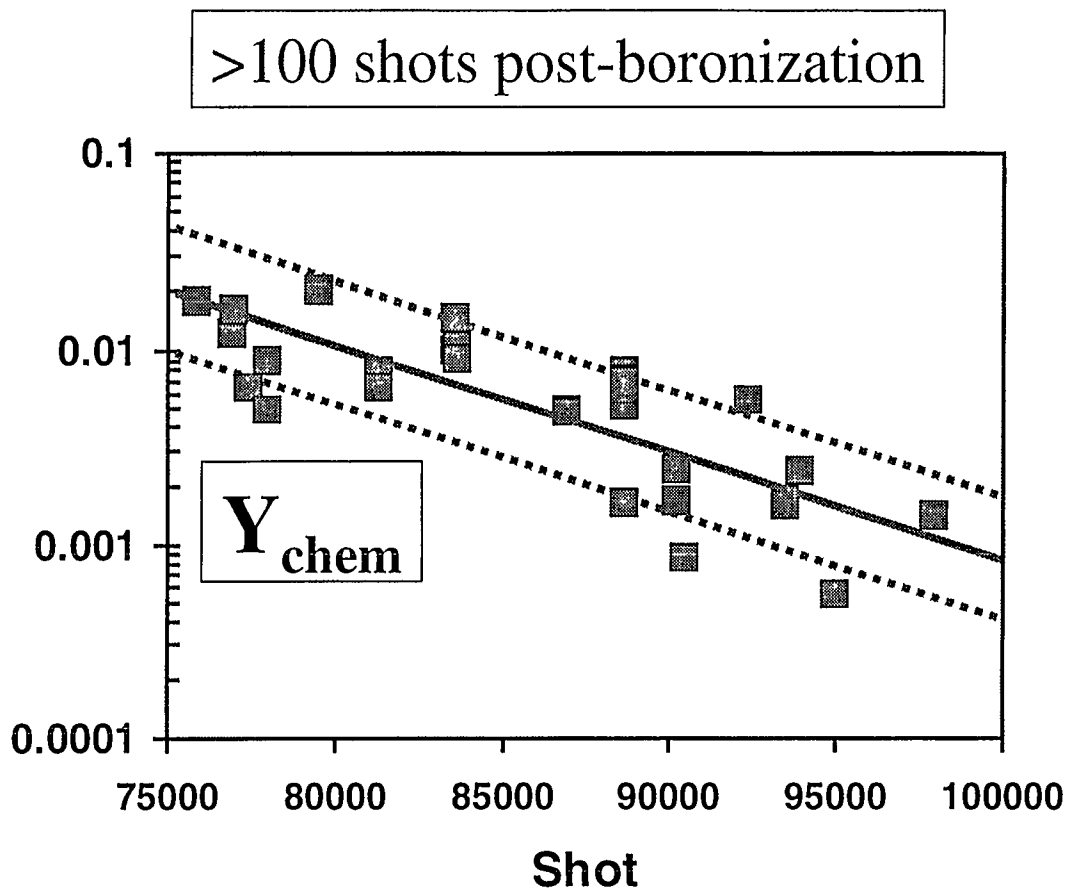

- Yield measurement fairly reliable since for attached divertor $T_e > 10$ eV:
  - **$D/XB_{CD} \sim 50$**
  - **$S/XB_{D\gamma} \sim 2000$**

$$Y_{chem} = \frac{\Gamma_{C_xD_y}}{\Gamma_D} = \frac{B_{CD} \cdot D/XB_{CD}}{B_{D_\gamma} \cdot S/XB_{D_\gamma}}$$

- Scatter in yield probably indicative of uncertainty in T_{plate}, Γ & S/XB .

Observed yield reductions are *not* due to any systematic "drift" of plasma parameters used in spectroscopy database.

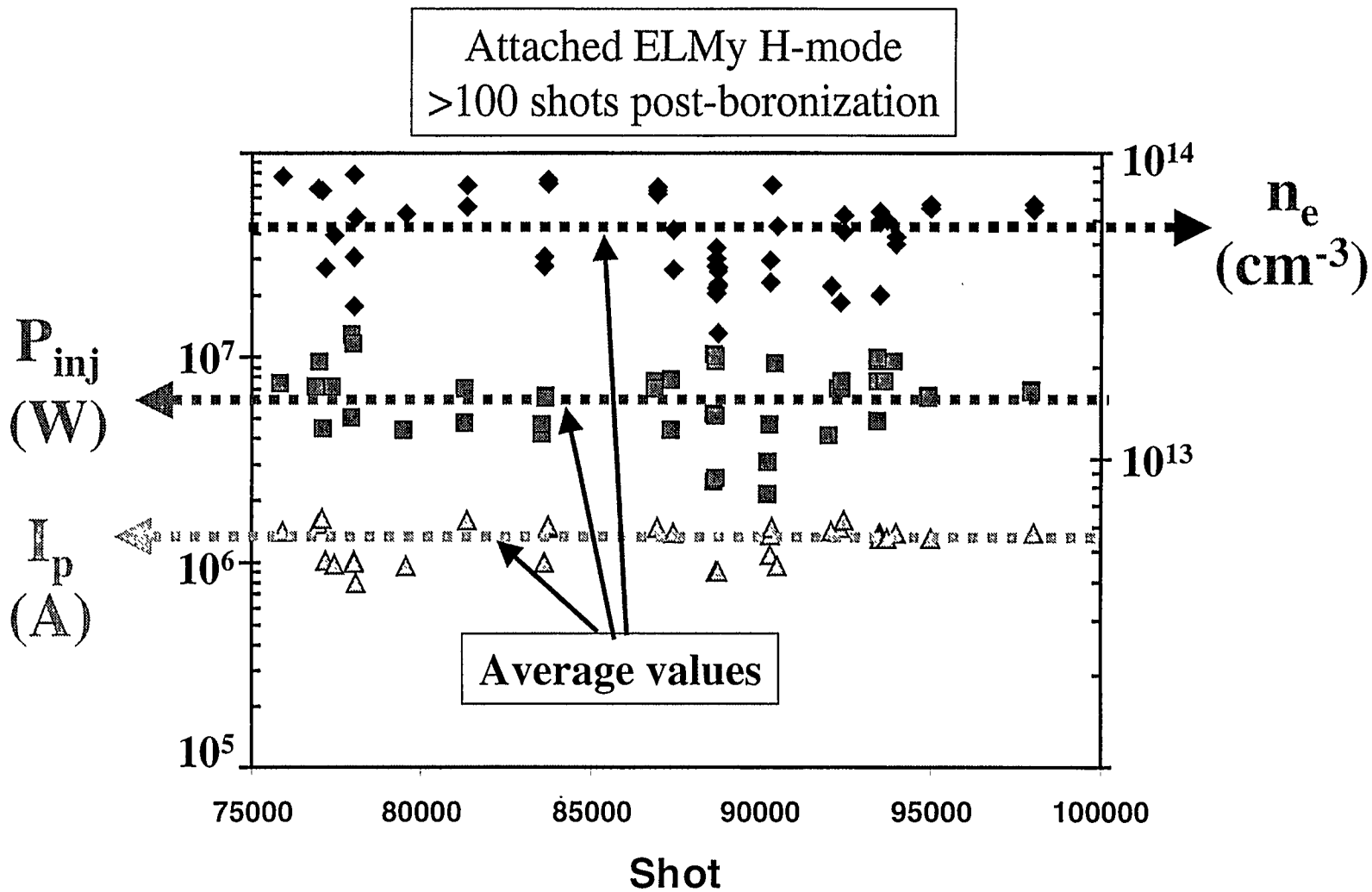

DIII-D tile evoluti

Y_{chem} reduction is even larger at ISP, consistent with plasma redeposition of both boron and carbon at the inner divertor leg reducing the yield.

Attached ELMy H-mode
>100 shots post-boronization

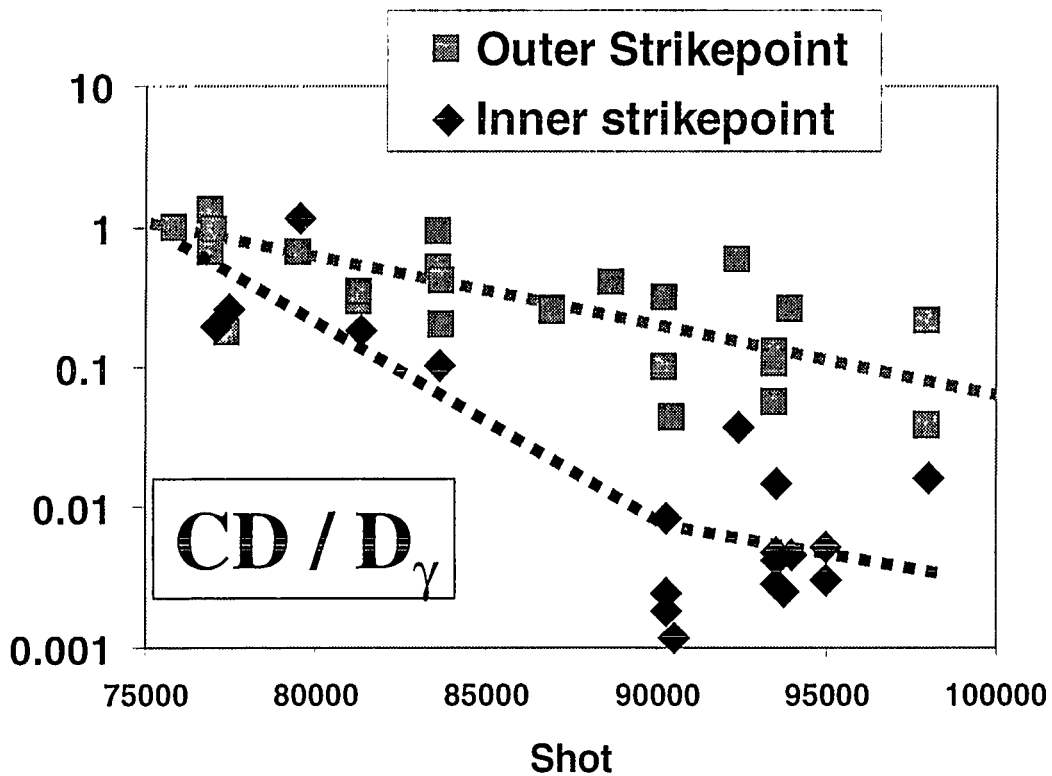

- Absolute yield comparison not available because of poor plasma diagnosis at ISP.

Smaller subset of detached plasmas show a lower erosion yield than attached plasmas, consistent with lower incident energy at tiles.

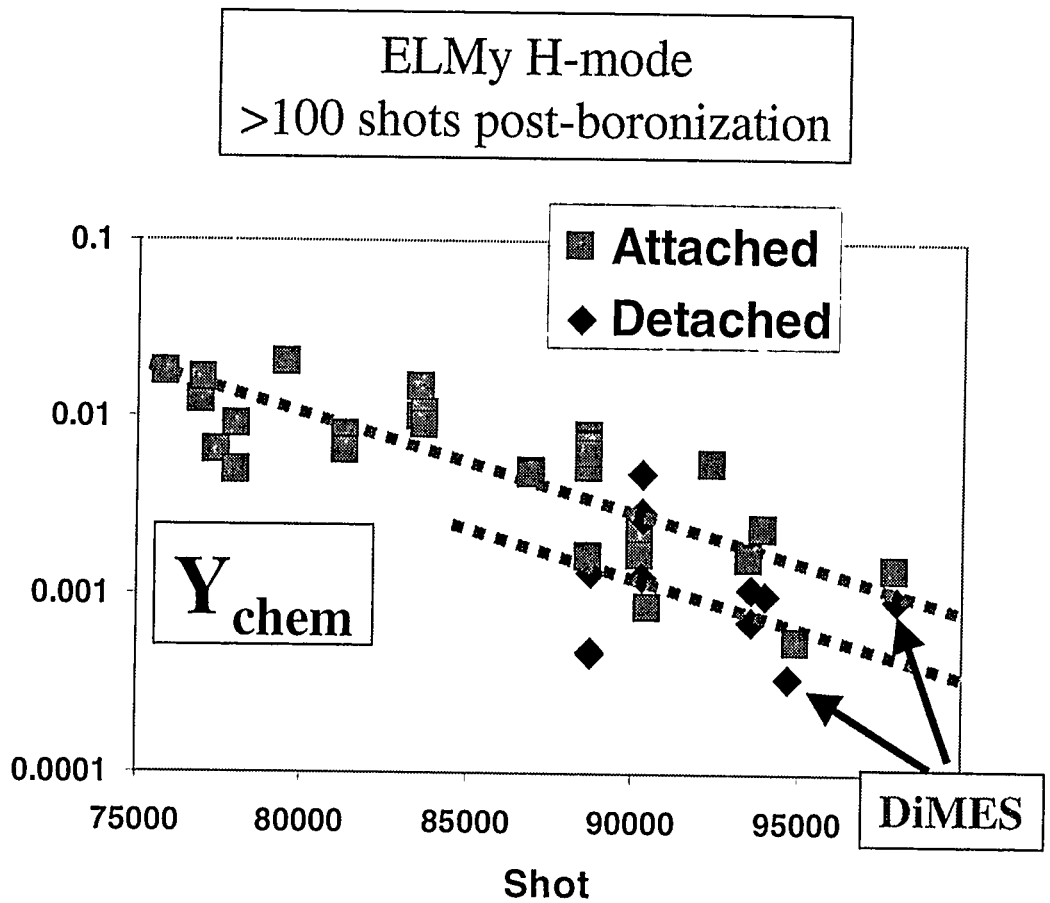

- Yield comparison depends on changes due to recombining divertor plasma ($T_e < 2$ eV):
  - **D/XB_{CD} ~ 20 (PISCES)**
  - **$S/XB_{D\gamma}$ ~ 350 (Experiment)**

$$Y_{chem} = \frac{\Gamma_{C_x D_y}}{\Gamma_D} = \frac{B_{CD} \cdot D/XB_{CD}}{B_{D_\gamma} \cdot S/XB_{D_\gamma}}$$

Simultaneous with the reduction in Y_{chem} of ~x10, the lower divertor Y_{total} has decreased ~x4.

Attached ELMy H-mode
>100 shots post-boronization
Maximum value in lower divertor

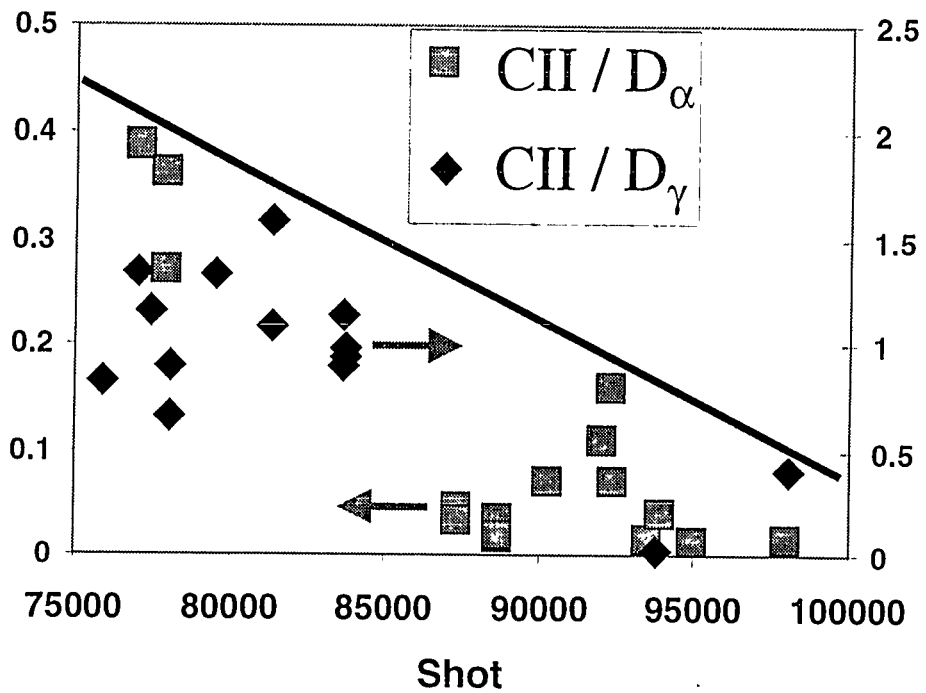

OSP spectra
Identical Shots
1993 & 1997

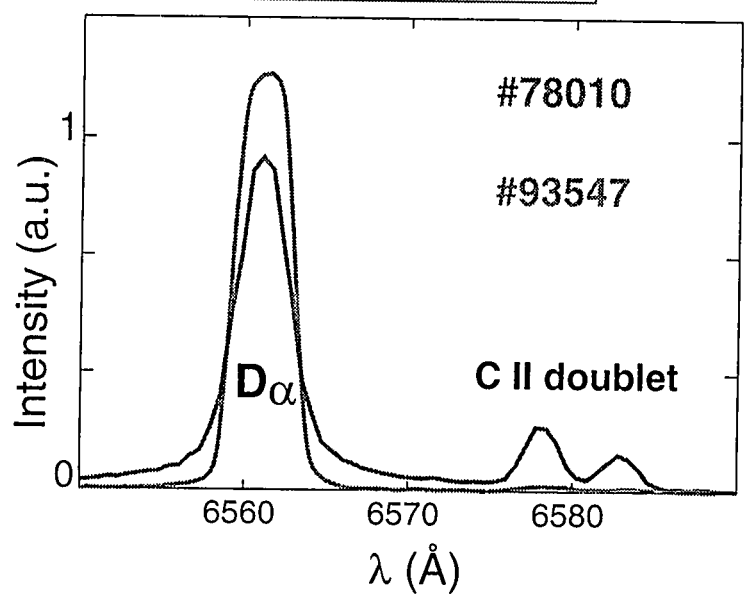

$$Y_{total} = \frac{(\Gamma_{C_x D_y} + \Gamma_{C_0})}{\Gamma_D} \propto \frac{B_{CII} \cdot S/XB_{CII}}{B_{D_{\alpha,\gamma}} \cdot S/XB_{D_{\alpha,\gamma}}}$$

Effect of lower divertor carbon erosion yield on core plasma carbon contamination

Despite the significant decrease in lower divertor yield / source, the core impurity content has not decreased.

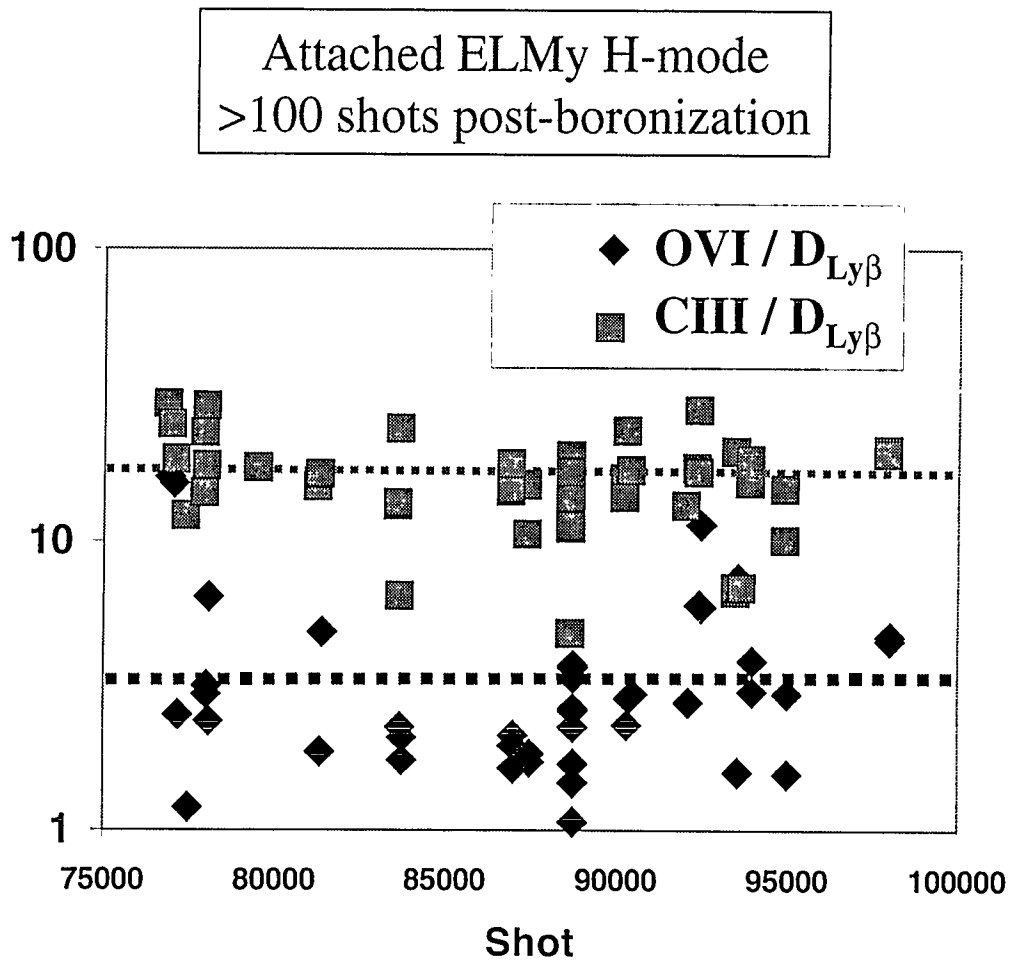

- Relative midplane XUV spectroscopy of impurity resonance lines:
  - CIII (977 Å)
  - OVI (1030 Å)
  - $D_{Ly\beta}$ (1025 Å)

- CER analysis not complete, but "casual" observation indicates no reduction in f_{Carbon} either.

Fractional radiated power, which is typically dominated by carbon, has not significantly decreased either.

Attached ELMy H-mode
>100 shots post-boronization

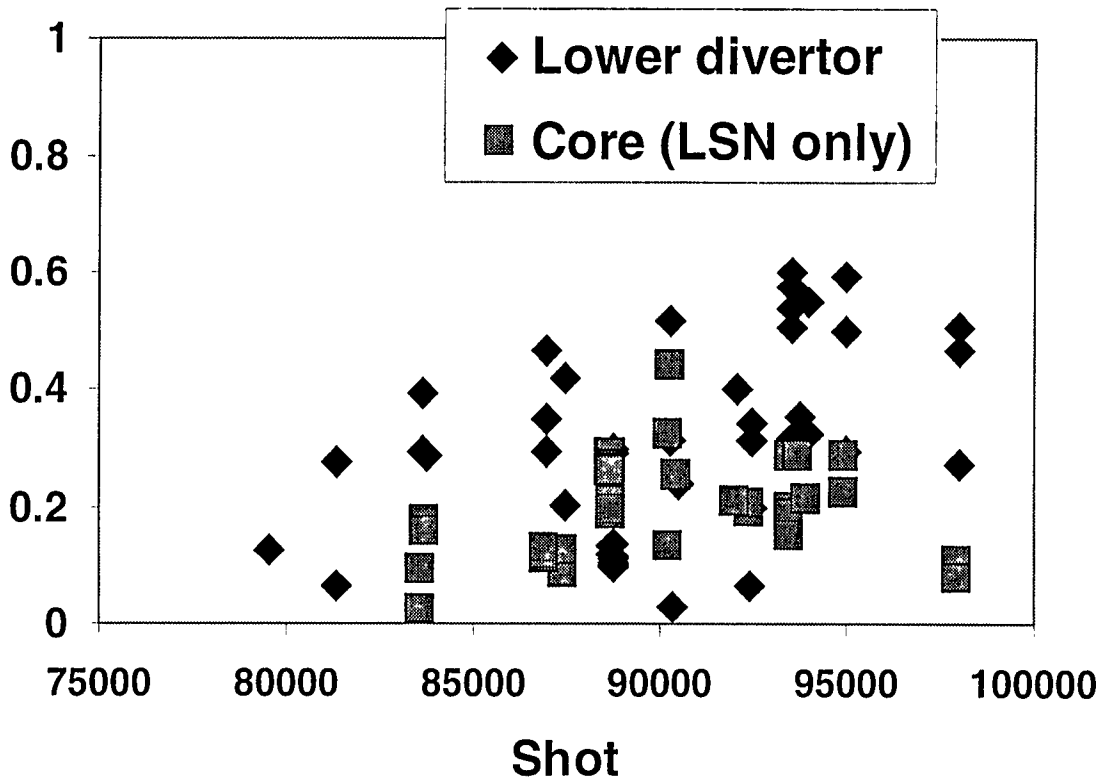

- Agrees qualitatively with midplane XUV spectroscopy results

The average BD band in the lower divertor has not changed significantly with accumulative boronizations.

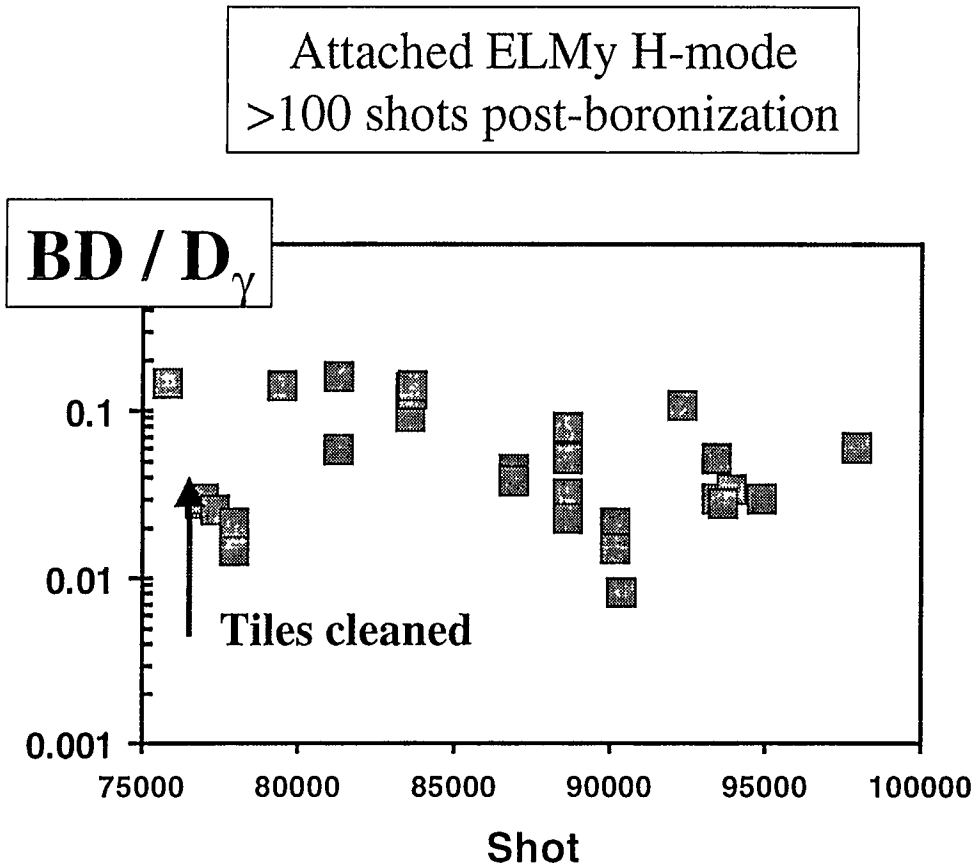

- BD band is a measurement of boron *chemical* erosion yield
  - **B II measurements would better indicate relative boron content…but rarely tuned to lines with spectrometer.**
  - **Results could indicate substantial boron-carbide bond formation, which would be resistant to chemical erosion.**

Summary: DIII-D Y_{chem} Study

- **Old** DIII-D results for Y_{chem} are in agreement with other tokamaks...
  - **JET:** Y_{chem} = 2 % T_{surf}=450K
  - **ASDEX-U:** Y_{chem} = 1-2 % T_{surf}=350K
  - **DIII-D (1992-93)** Y_{chem} ~ 2 % T_{surf}~400 K

- **...But present chemical and total yields are greatly reduced**
  - **DIII-D (1999):** Y_{chem} ~ 0.1% T_{surf}~400K
  - **DIII-D tile:** Y_{chem} = 0.16-0.4 % T_{surf}=600K (PISCES)

- Boronizations are the most likely cause for the Y_{chem} reduction
  - 30+ boronizations have applied ~2.5 microns of boron.
  - No major tile changes or clean-ups in lower divertor in over six years...both JET and ASDEX have refit lower divertor several times.

Summary on Y_{total} & Carbon sources

- Reduced Y_{chem} (and other effects?) have significantly reduced the measured total carbon outflux from the lower divertor.
  - Chemical erosion is now a minor player in lower divertor erosion with Y_{chem} ~0.1% << Y_{phys} ~1-5%.

- No simultaneous decrease in core carbon fraction is found. Two explanations are possible:

  1. Carbon ion SOL transport always adjusts to equilibrate thermal gradient vs. diffusive forces, making the source amplitude unimportant (preliminary UEDGE results show this effect).

  2. The divertor is the not the principal source of carbon in the core plasma (e.g. All Be divertor in JET had carbon as main core impurity).

Laboratory studies of DIII-D graphite tiles — effect of boronization on chemical erosion yield.

Plan: Use PISCES at UCSD to directly assess Y_{chem} of DIII-D divertor tiles

- Two DIII-D lower divertor tiles removed (Summer '98)
  - SEM and profilimetry revealed a >micron-depth low-Z deposition layer at the inner divertor.
  - ~800 discharges since last boronization.
  - Visual inspection shows a metallic-like surface substantially different than virgin ATJ graphite.

- Section of tile exposed in PISCES-B linear plasma device
  - Steady-state exposure with similar Γ and T_e to DIII-D divertor.
  - 30 eV incident energy fixed by target bias…minimal $Y_{phys.}$
  - In-situ surface analysis station.

PISCES-B Experimental Configuration

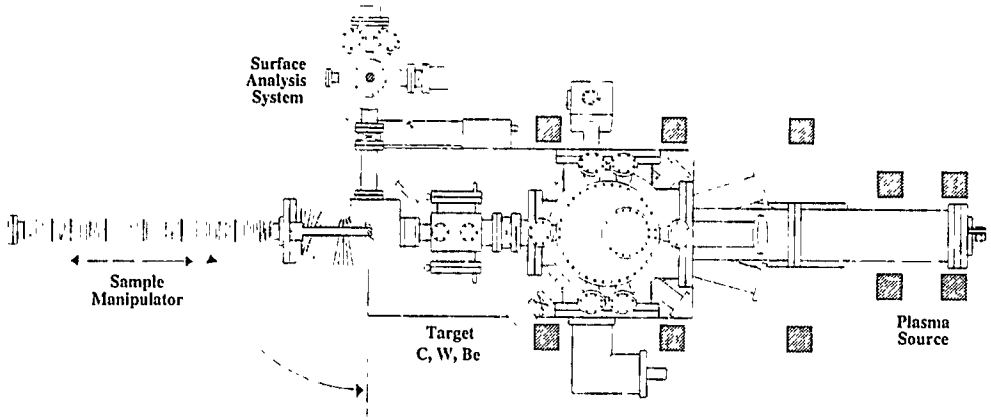

PISCES-B Linear Plasma Device

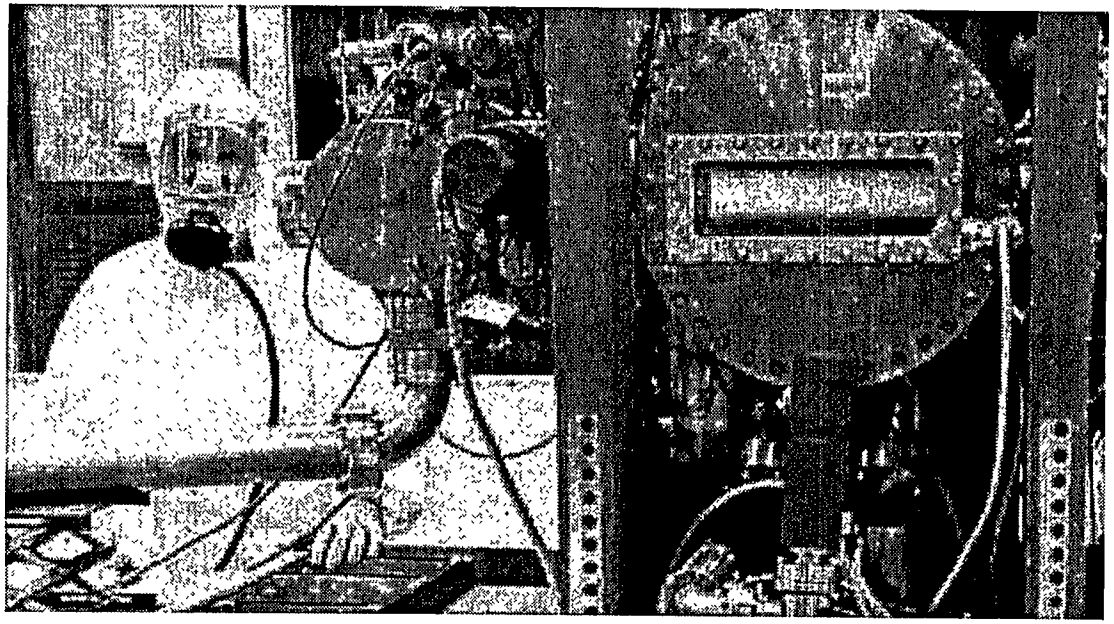

Y_{chem} Measurements on PISCES

- Weight loss of sample
  - net yield -> gross yield correction from modeling.
- CD band spectroscopy
  - Calibrated visible spectrometer.
  - Benchmarked with CD_4 puffing through target.

Calibrated CD_4 injection through PISCES target & High resolution spectroscopy provide detailed information about hydrocarbon transport & Y_{chem}

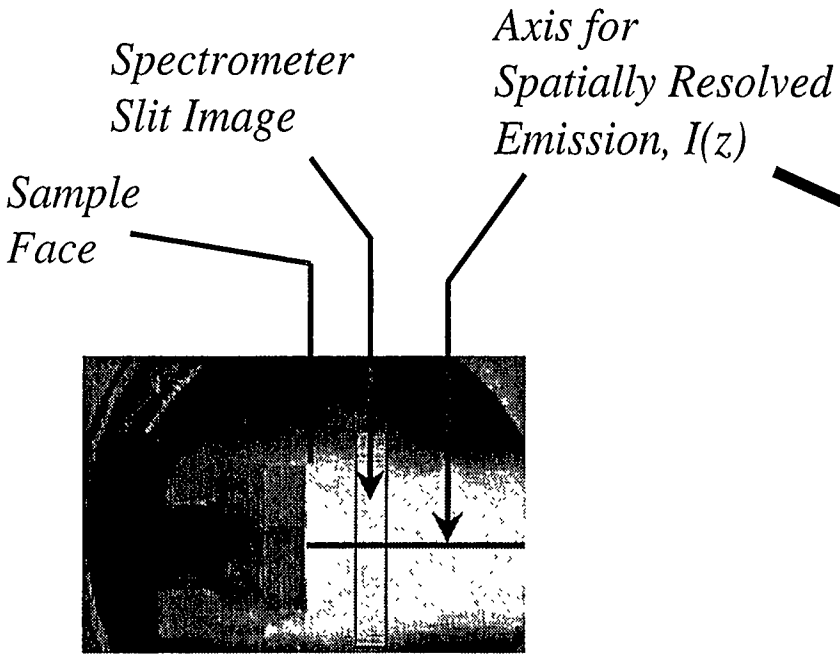

CD_4 injection

CD radical band (430 nm) axial profile

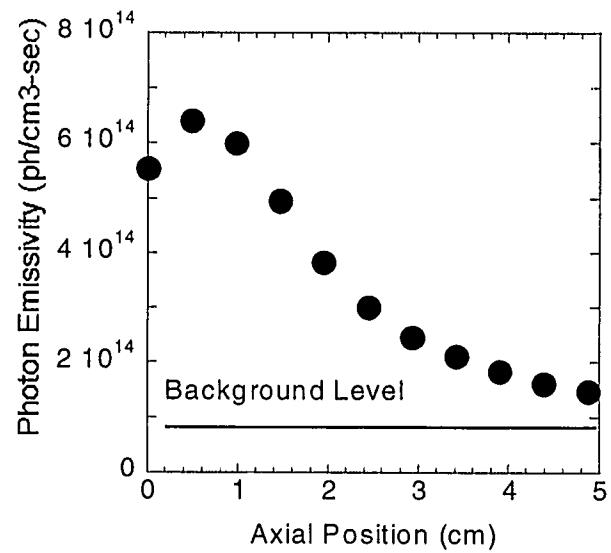

Summary of PISCES & UTIAS erosion tests on DIII-D tiles

- DIII-D CD-band molecular excitation rates measured
  - Apparent $Y_{chem} < 10^{-3}$ in DIII-D.
- Energy dependence: $Y_{chem} \propto E^{-(0.5-1)}$
- Surface composition
  - 5% boron initially on surface.
  - Y_{chem} **reduced x4** compared to virgin porous graphite.
  - < 10 minutes of plasma exposure removed most of the carbon from the surface!
- Flux dependence?: ***apparently not needed to explain low Y_{chem}.***
- Preliminary result from UTIAS indicates portion of DIII-D redep film is resistant to O_2 chemical removal

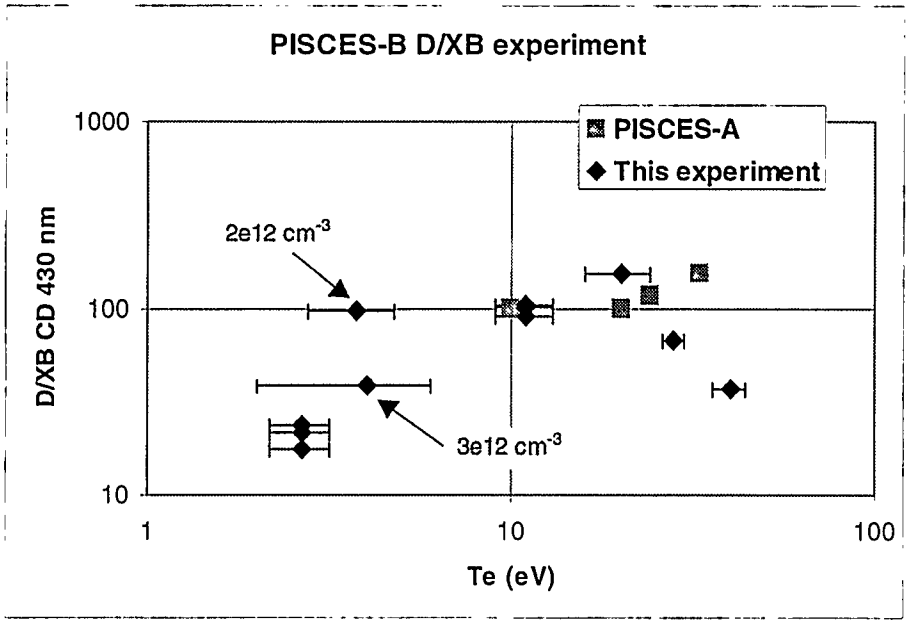

D/XB Measurements (Molecules / Photon ratio)

- D/XB~100 is a maximum.
- Reproduces previous result.

Implication:

- DIII-D CD-band spectroscopy used D/XB=100.
  ..but $T_e < 5$ eV in PDD.

- **Revised upper limit from CD-band spectroscopy:**
  $Y_{chem} < 3\text{-}4 \times 10^{-4}$

WBC Erosion Code Has Been Thoroughly Benchmarked Against PISCES Data.

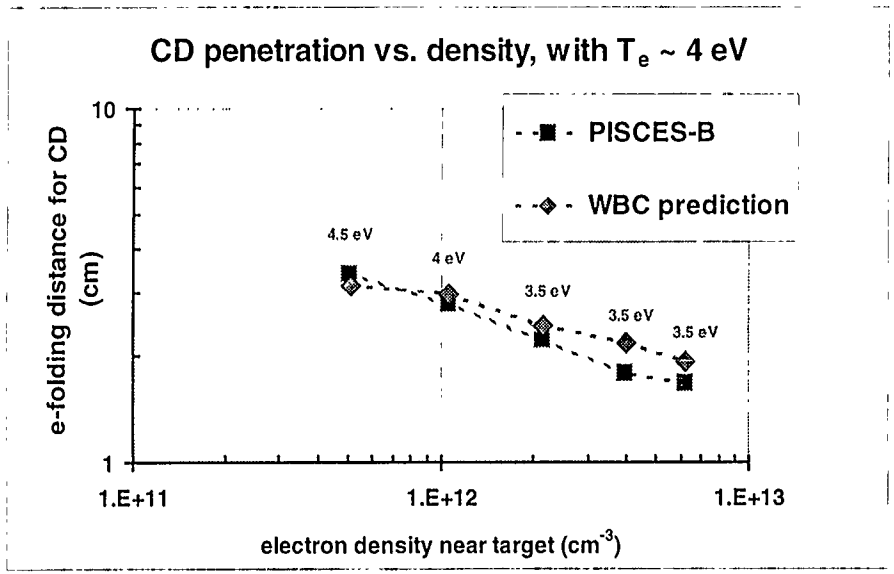

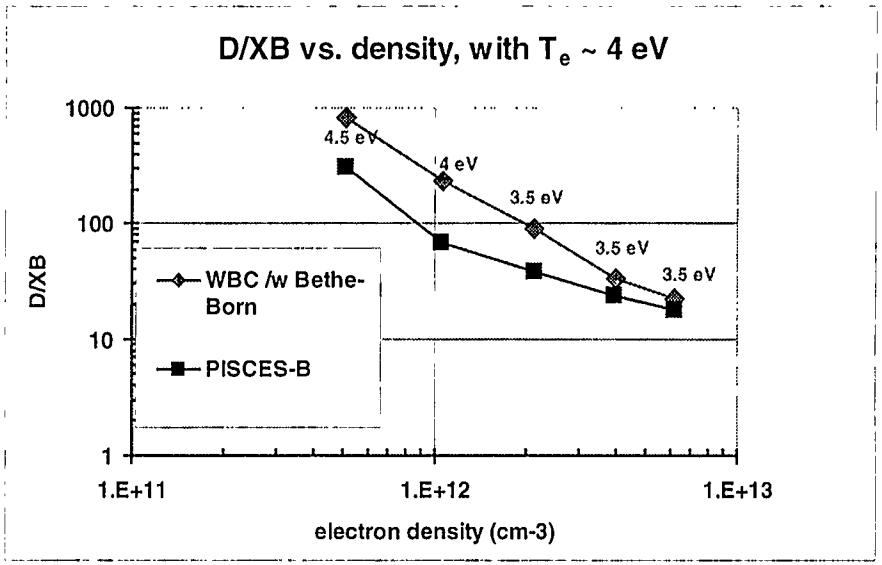

- WBC sub-gyro Monte-Carlo model (J. Brooks, ANL)
  - includes full dissociative reactions for CD_4.
- Model matches both CD penetration and photon efficiency.
  - Strongly non-linear penetration vs. n_e
  - Very large n_e dependence on D/XB for approx. constant T_e.
- Questions constant D/XB used in tokamak experiments during density scan

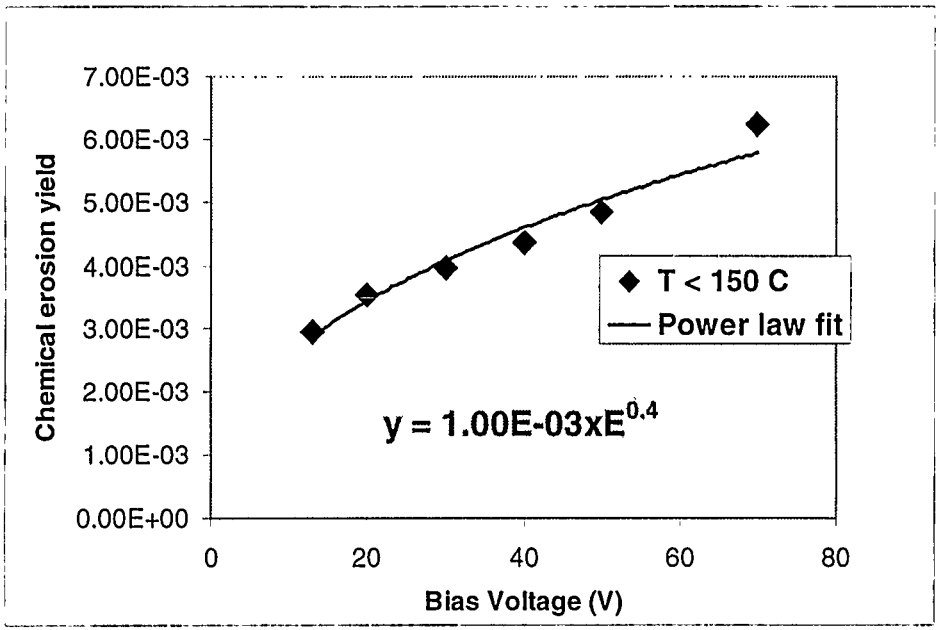

Energy dependence on Y_{chem}

$$Y_{chem} \propto E^{-0.4}$$

$$\Gamma = 10^{23}\ s^{-1}\ m^{-2}$$

$$T_e \sim 4\ eV$$

Different energy dependence on chemical erosion yield from one experiment to another.
PISCES data is more reliable in the sense that bias voltage is directly controlled...and all other exposure conditions are constant.

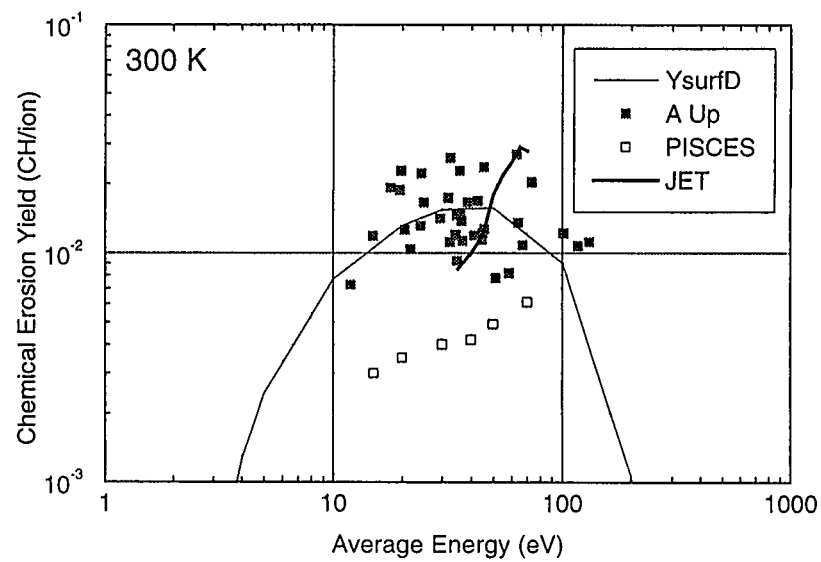

Auger surface analysis of DIII-D tile surface pre and post exposure on PISCES-B

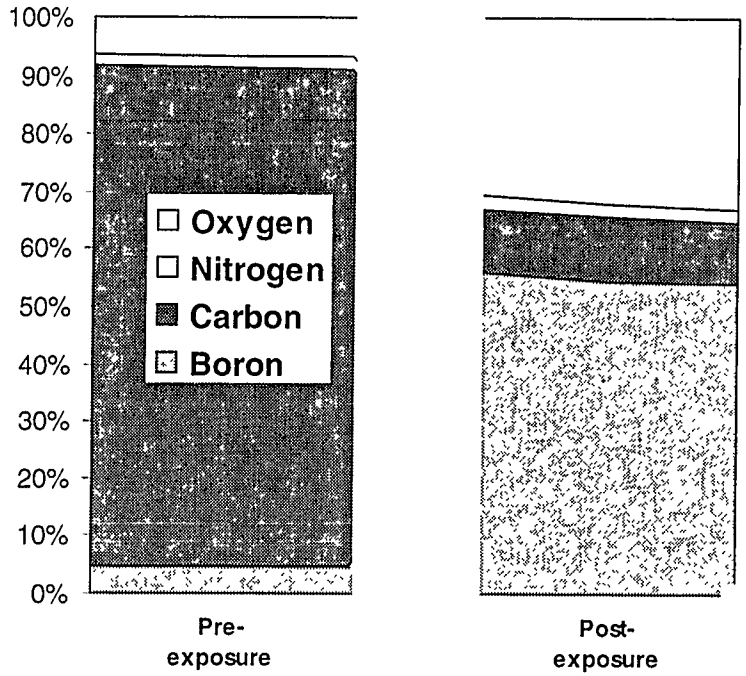

Exposure conditions:

$E = 30$ eV

$\Gamma = 10^{23}\ s^{-1}\ m^{-2}$

$T_e \sim 5$ eV

$n_e \sim 1.5 \times 10^{13}\ cm^{-3}$

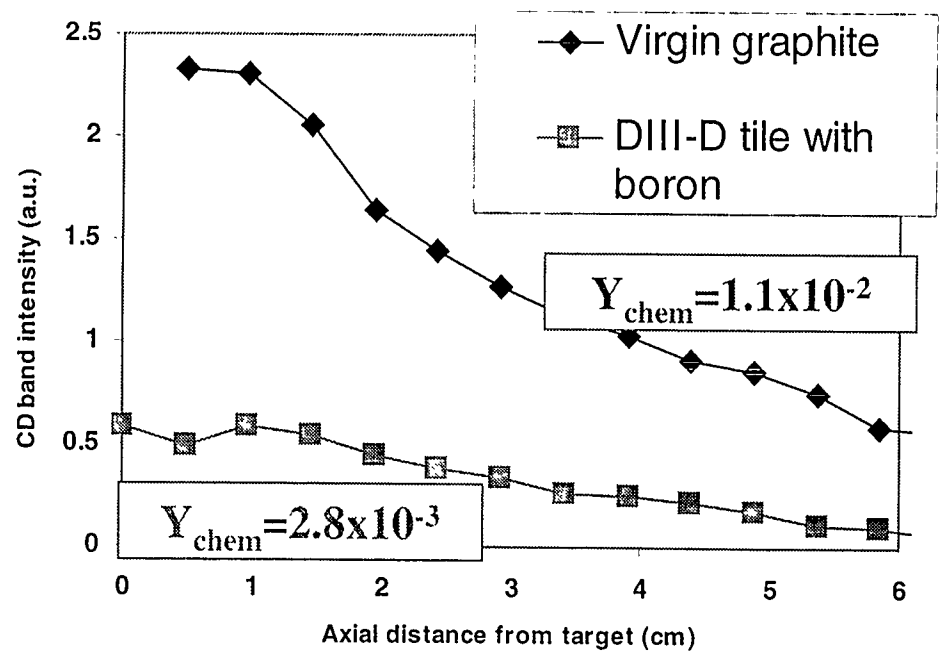

Discussion

- Chemical erosion in the lower divertor is NOT the source of carbon in detached plasmas.
  - Yet substantial atomic carbon radiation / flux is measured despite $T_e < 5$ eV, i.e. no physical sputtering?
  - Net erosion is eliminated everywhere in lower divertor!
- Strong indications that boronizations have substantially reduced the chemical and total effective yields of carbon in the DIII-D tokamak.
  - In-situ and laboratory experiments show Y_{chem} reduced ~4-10x compared to "virgin" graphite.
  - No need to invoke flux dependence as method of reduced Y_{chem}
- **Future work**
  - Test more tile samples (PISCES and UofT)
  - Remove more complete poloidal set of tiles during next vent?
  - Incorporate Y_{chem} into DiMES / WBC modeling & mixed material modelling

Discussion (continued).

- These results are very encouraging for the use of carbon in the "learning" phase of any next-step, high duty-cycle DT device.
  - Graphite is very forgiving of disruptions, ELMs, etc.
  - Detached plasmas necessary for power handling…Y_{phys}=0…
  - …But large Y_{chem} for graphite produces significant erosion / redeposition and Tritium retention.

- Based on the DIII-D results, ~24 hours of plasma exposure, including frequent boronizations, should condition graphite divertor tiles to obtain order of magnitude reduction in Y_{chem}.

DiMES tungsten sample exposure to detached OSP plasmas confirms net redeposition rate & suppression of net erosion.

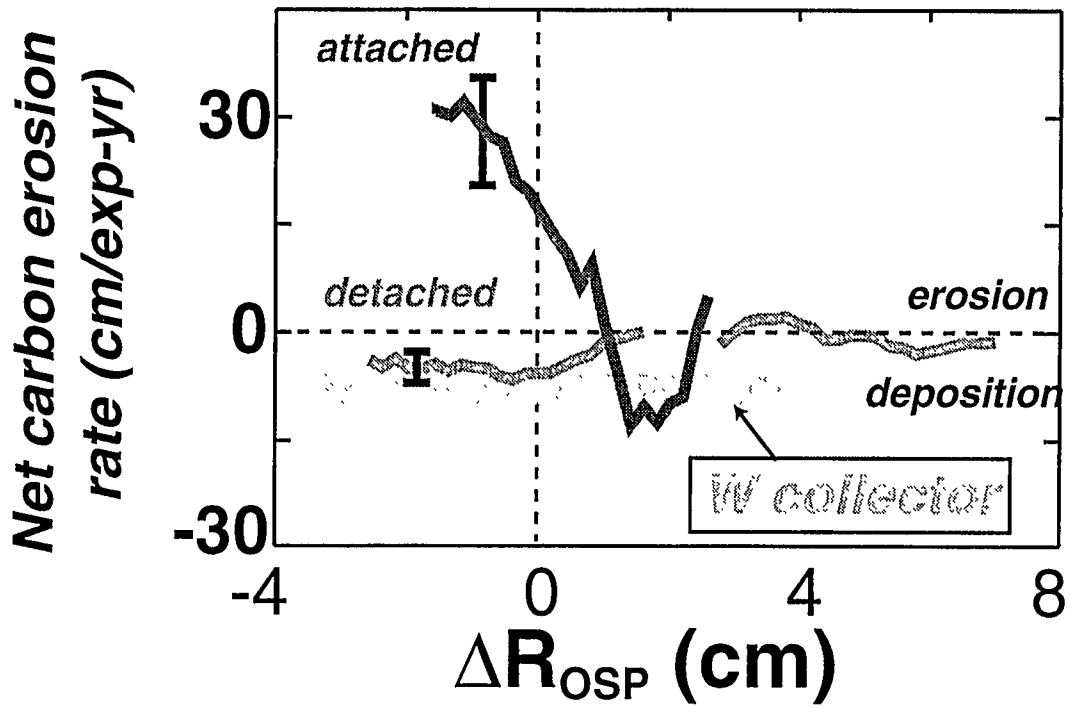

- Exposure conditions identical, except in W case:
  - f_{Carbon} ~x2 higher at 2.5% in core plasma.
  - R_{OSP} near R_{DiMES}, but not finely controlled.
- Uniform carbon layer of ~150 nm deposited onto W sample.
- No signs of arc traces.
- Redeposition rate increases with f_{Carbon}.

US-Japan workshop on Plasma surface interactions and high heat flux components for next fusion devices Nov. 1-4, 1999, Santa Fe, USA

W poloidal limiter experiments in TEXTOR-94

presented by T. Tanabe, *CIRSE, Nagoya University*

Cooperation with

M. Wada, *Doshisha University*

T. Ohgo, *Fukuoka University of Education*

K. Ohya, *Tokushima University*

M. Rubel, *Royal Institute of Technology*

V. Philipps, A. Huber, J. von Seggern, A. Pospieszczyk, B. Schweer & the TEXTOR team, *Juelich Research Center*

Scope of High-Z limiter Experiments at TEXTOR-94

- Continuation of poloidal limiter experiment. (Identification of the problem with the limiter usage.)
- Investigation of possible thermal shock of W layer on C. (Distribution of the heat absorption.)
- Heat transfer characteristics of limiter blocks.
- Investigation of particle emission and hydrogen recycling using twin-test-limiter. (Ta twin limiter)

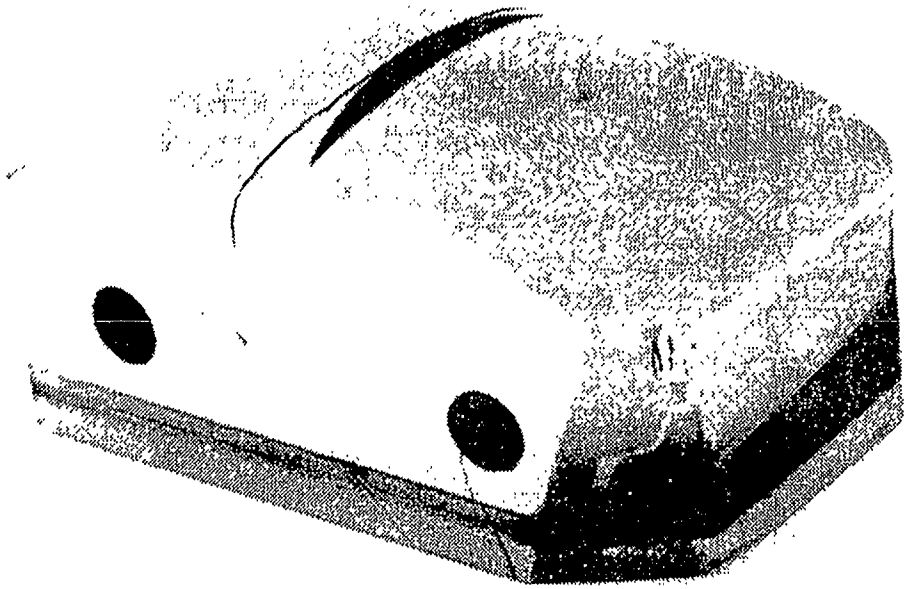

Fig.2 Photograph of damaged W test limiter.

Due to unintentional use below 450 K the limiter was cracked.

Thick carbon deposits at the front side and

a little melting at the front side corner are appreciable.

W poloidal limiter experiment

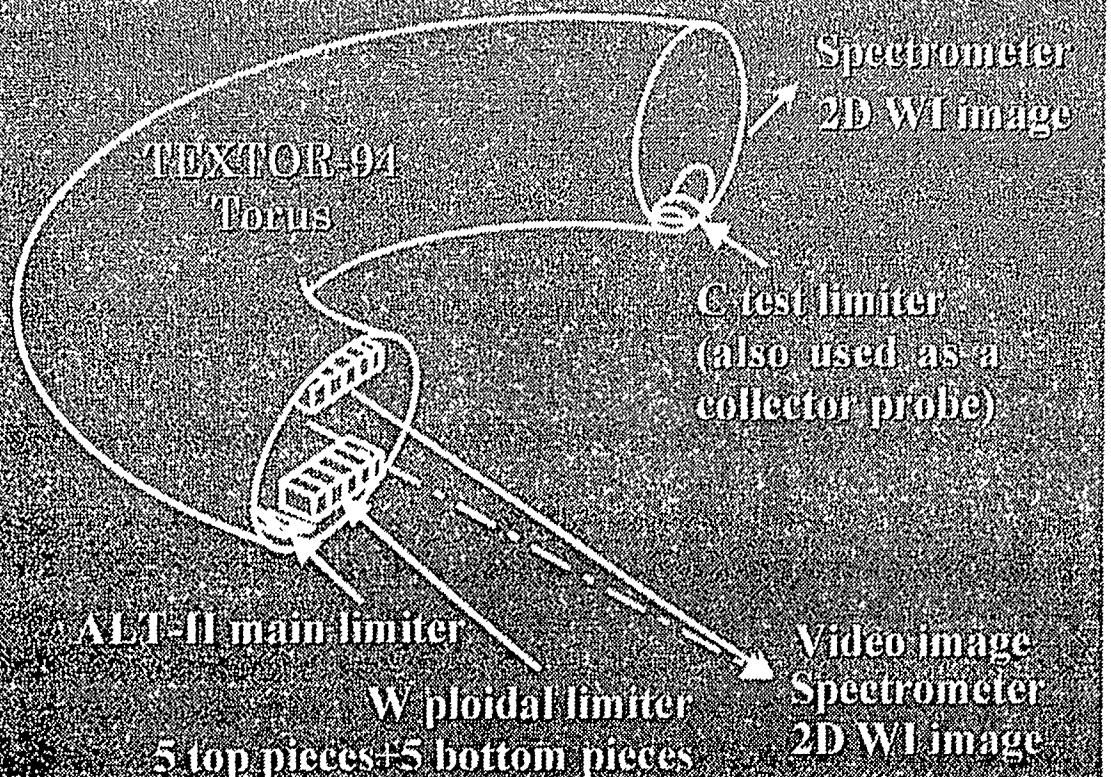

$S_{poloidal\ limiter} = 10 \times S_{test\ limiter}$

Dimensions in mm

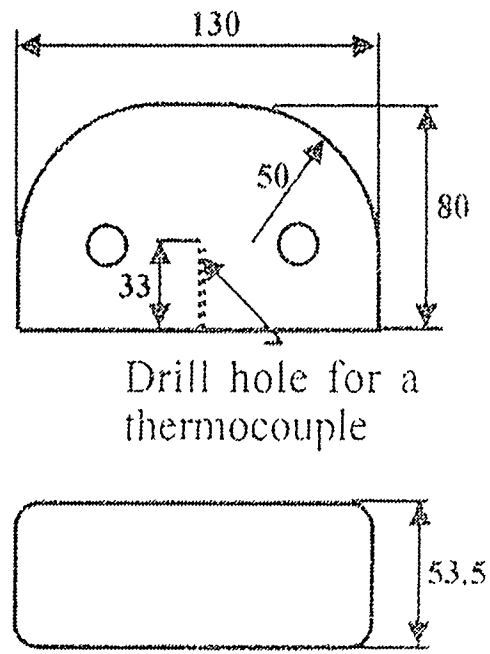

Poloidal W-limiter block
(Plasma-spray W coated C)

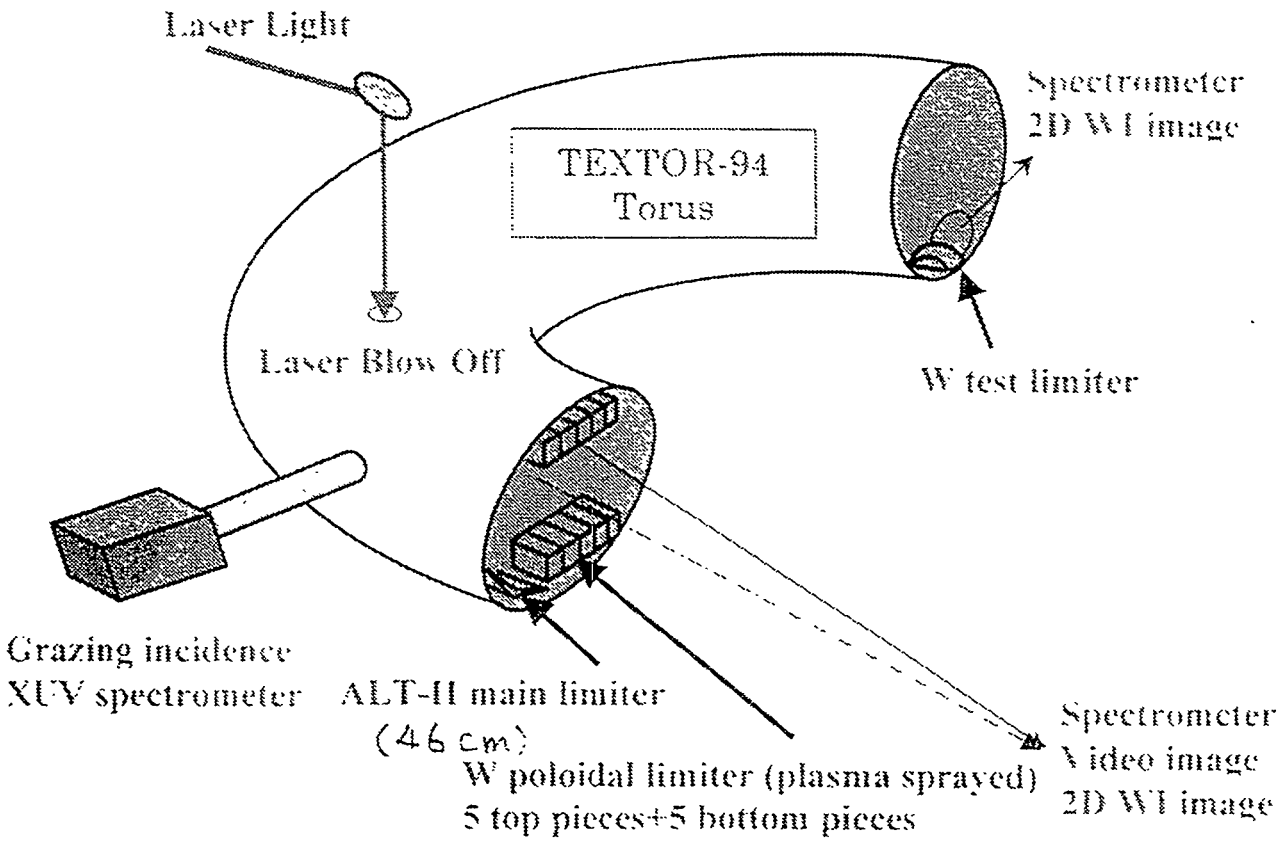

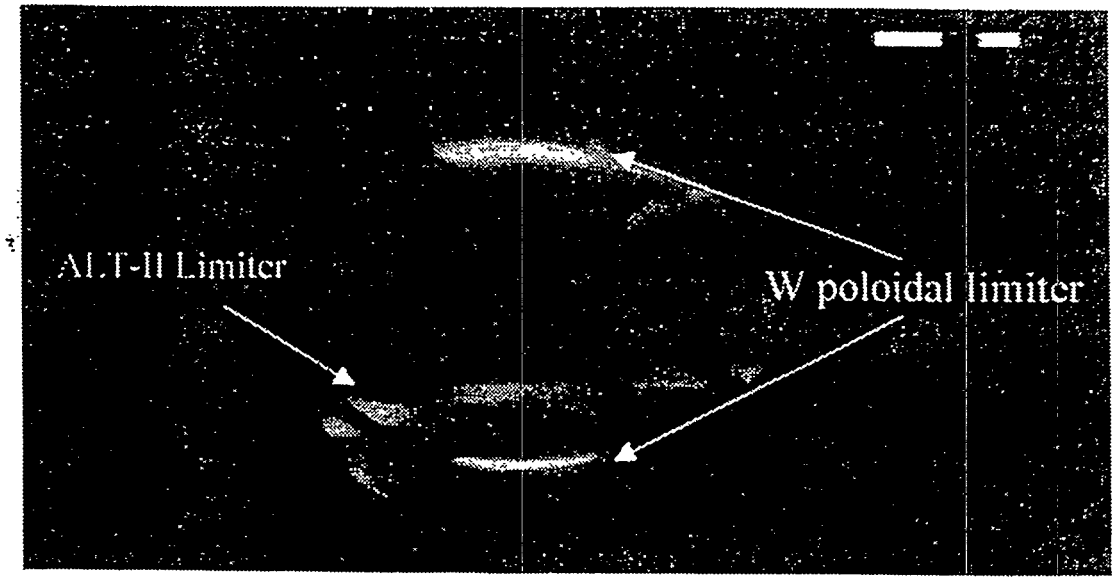

Video image

Fig.1 Schematically view of experimental setup in TEXTOR-94.

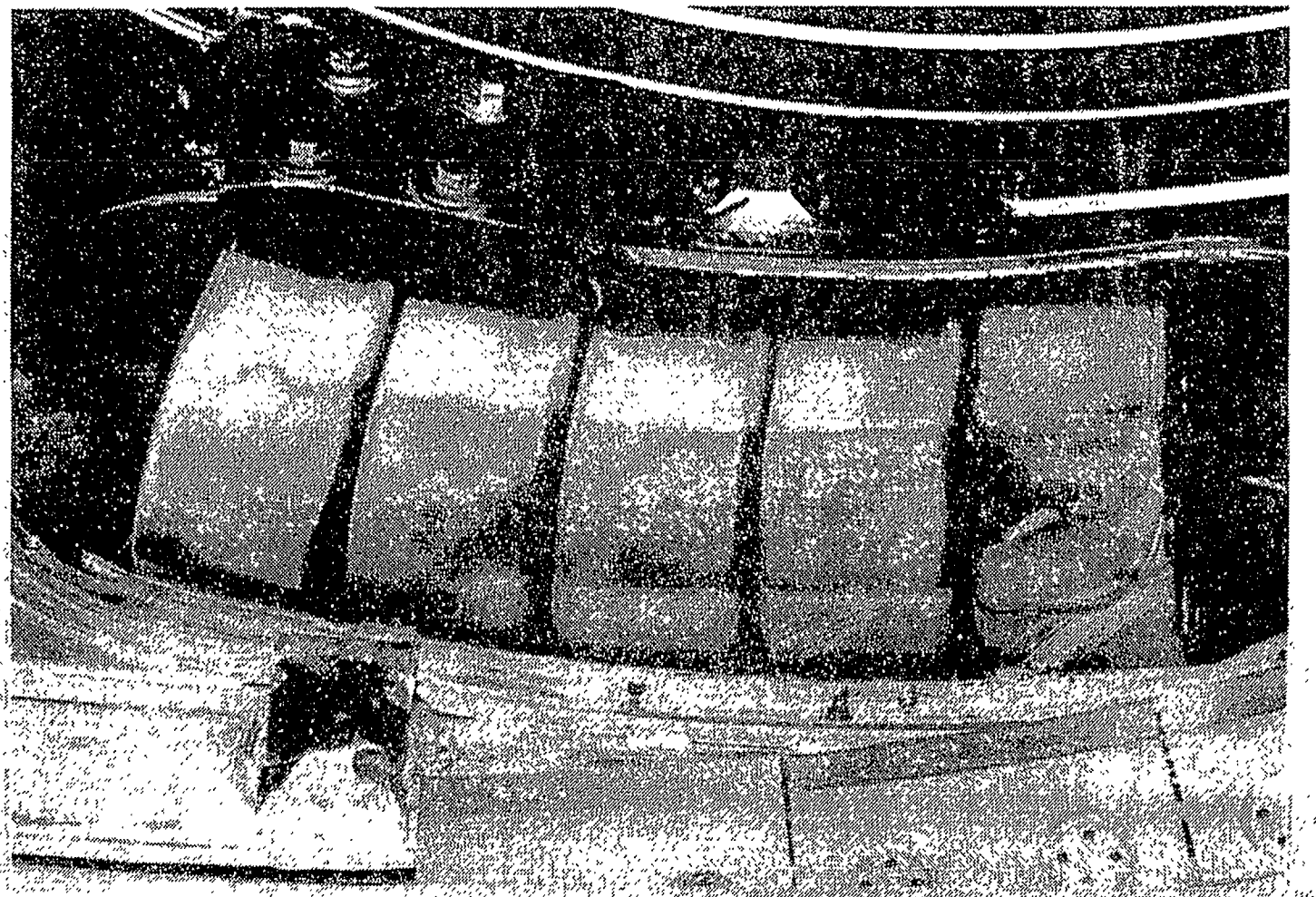

Discharge with a W-poloidal limiter

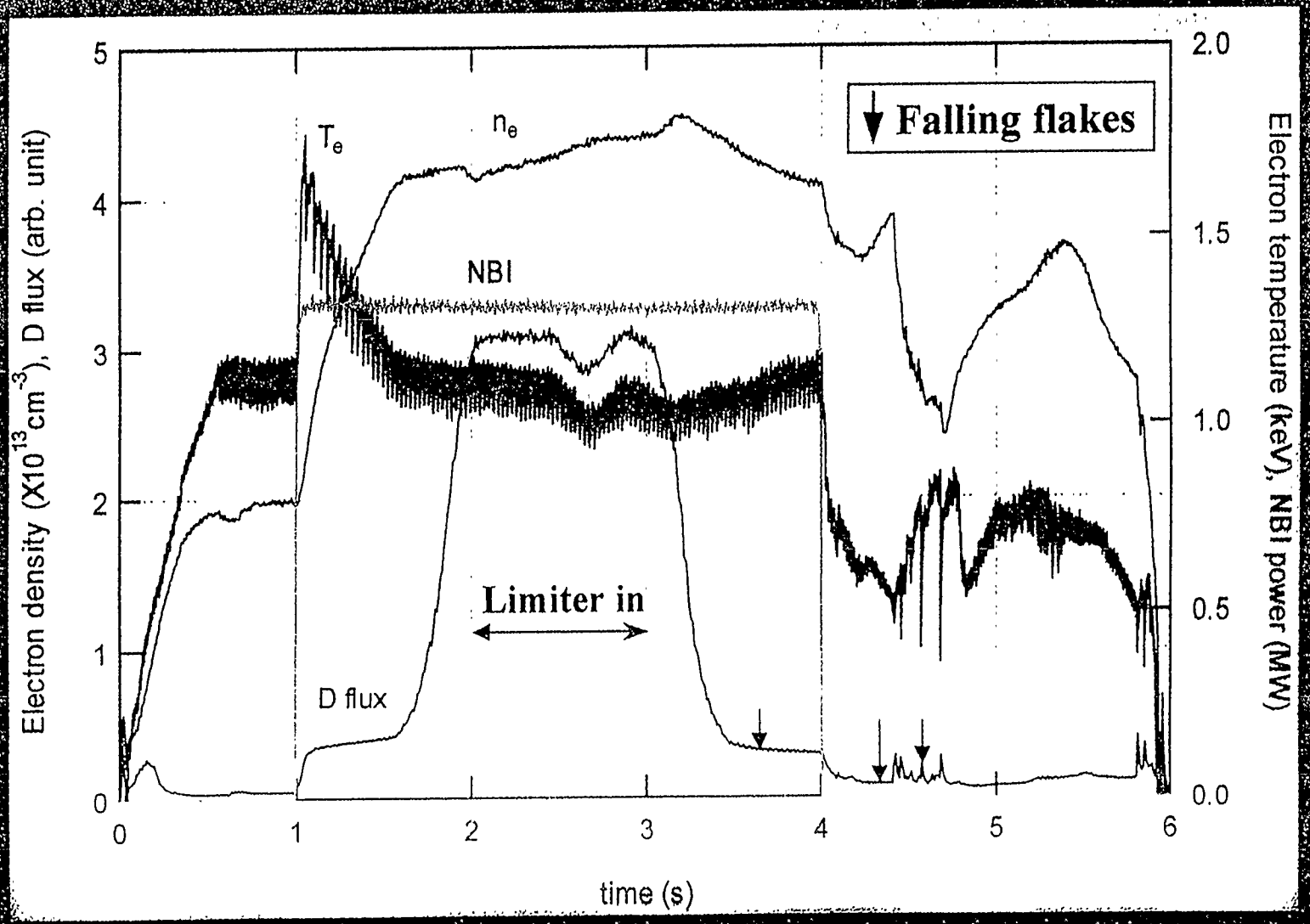

ポロイダルリミターが吸収する対流熱

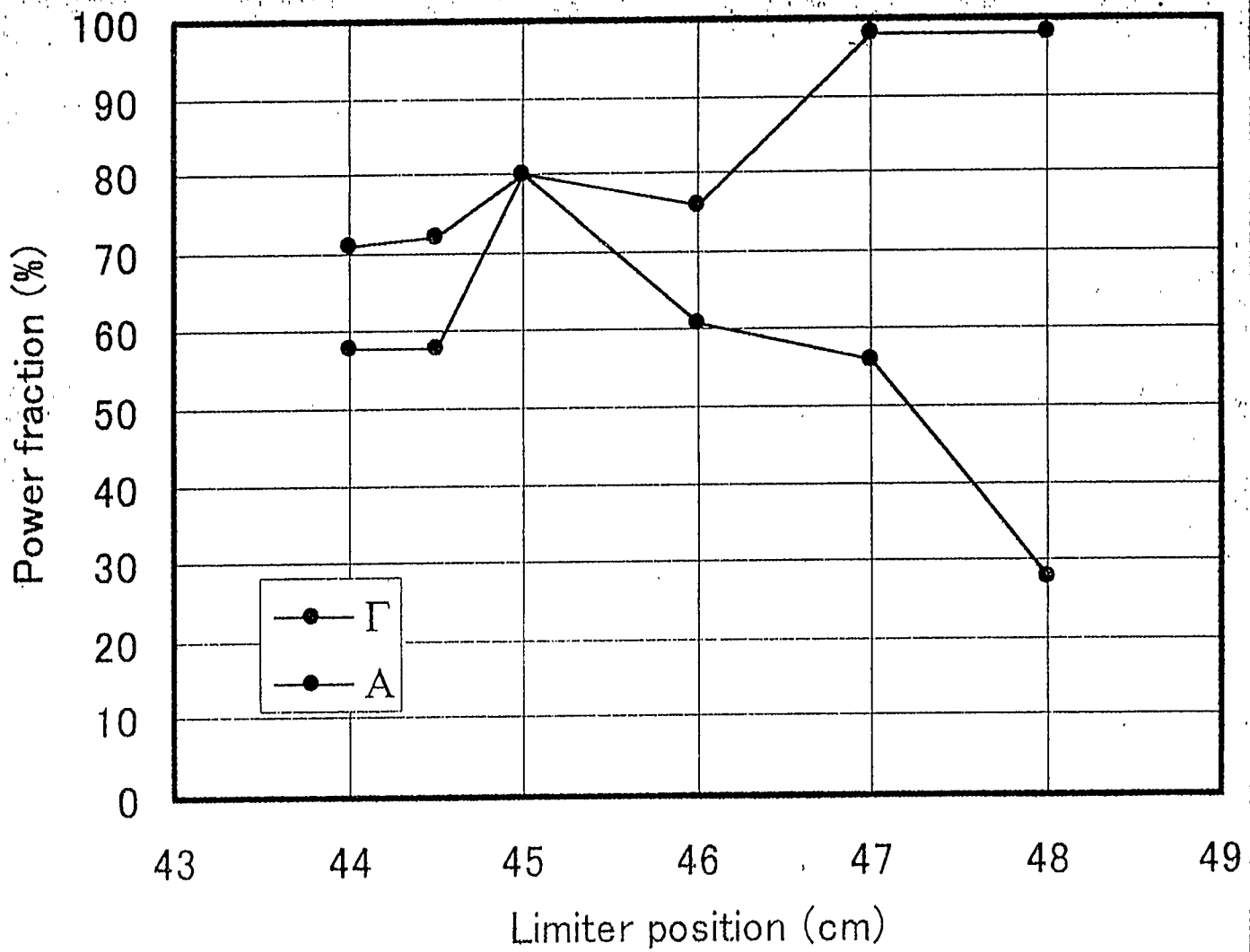

入熱と入射フラックス

入熱と入射D
フラックスはほ
ぼ比例関係

ALT-IIへの入
射フラックスが
減少しない。
(ポロナイゼー
ション実施時
には減少)

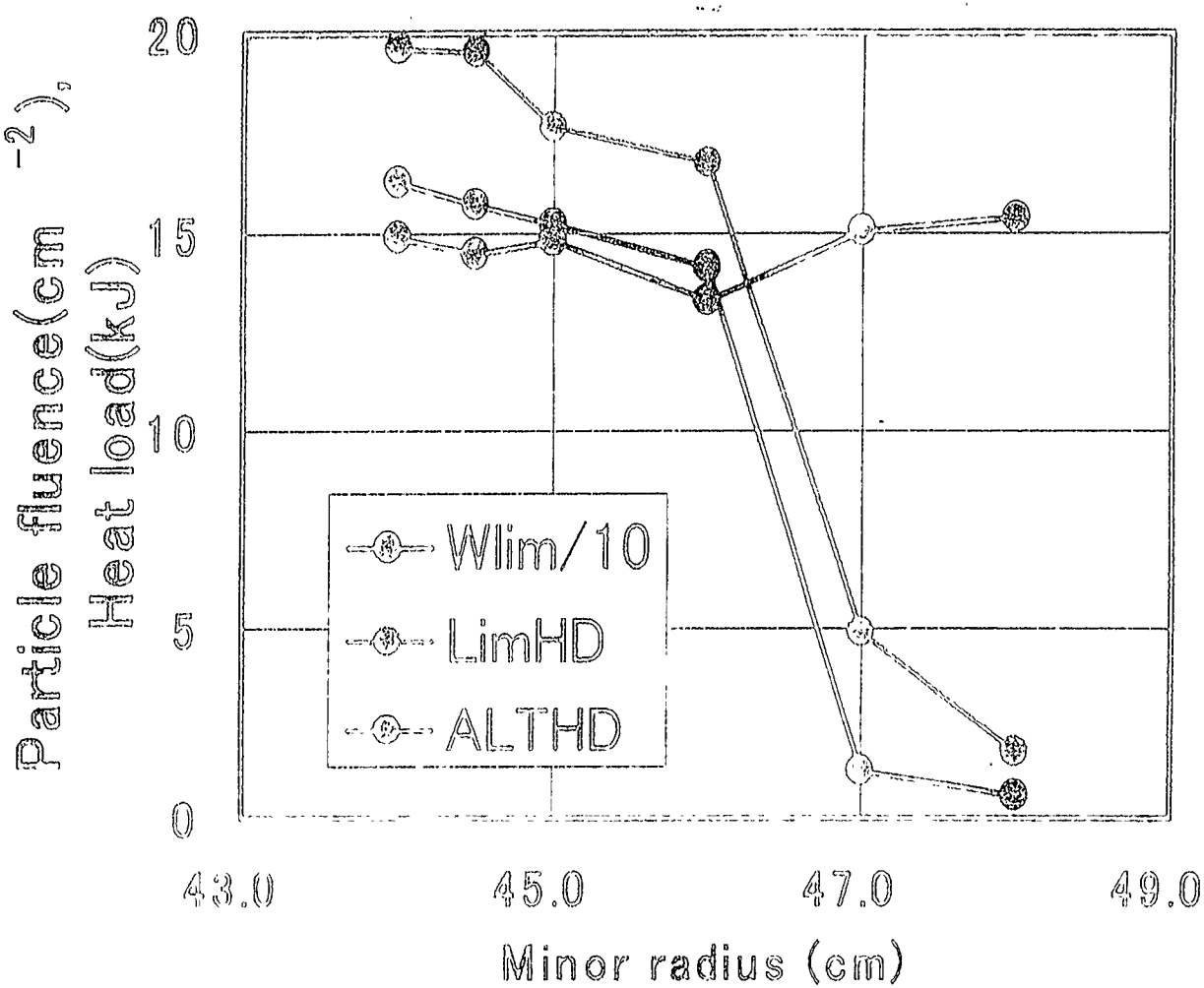

テストリミター入熱の変化

ALT-II位置＝テストリミター位置(46cm)より深い場所にポロイダルリミターが中心部に挿入されるとテストリミターへの入熱が減少

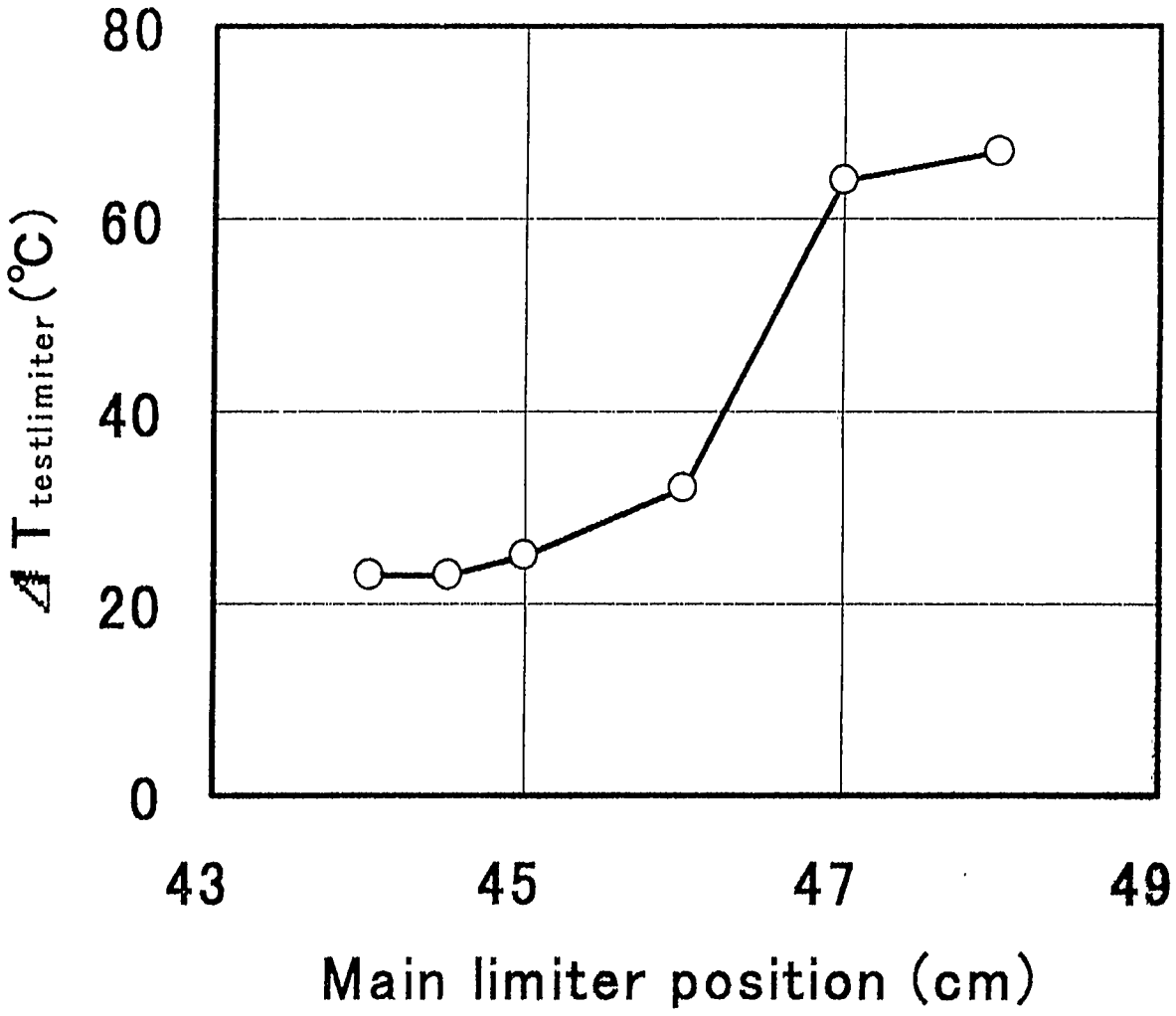

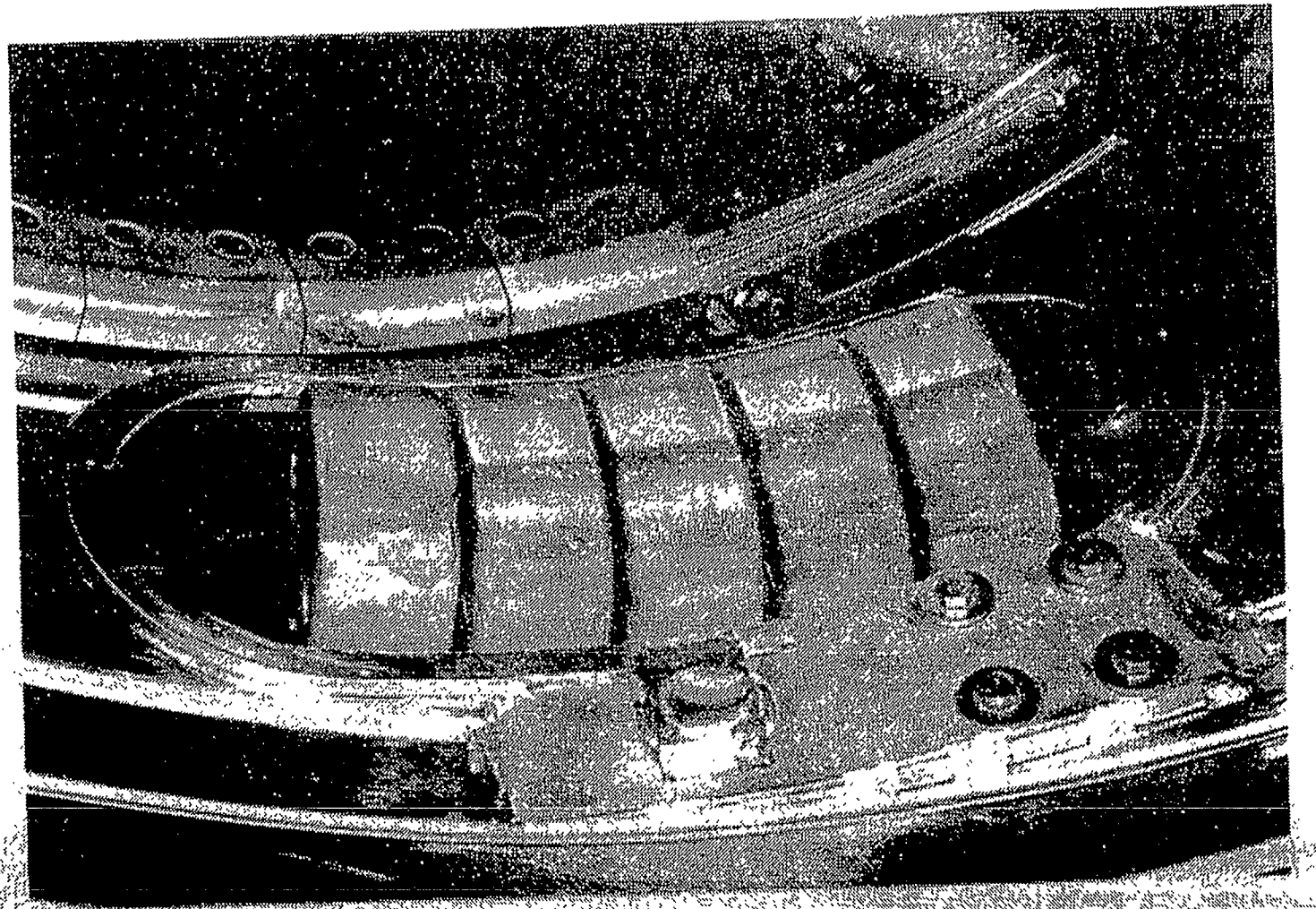

EURATOM-Assoziation
Institut für Plasmaphysik / Trilateral Euregio Cluster

ポロイダルリミターからのW放出

- WI強度が小さい.（特にテストリミターと比較して.）
- CDバンドスペクトルが計測される.（炭素層）
- 酸素ラインが強い.

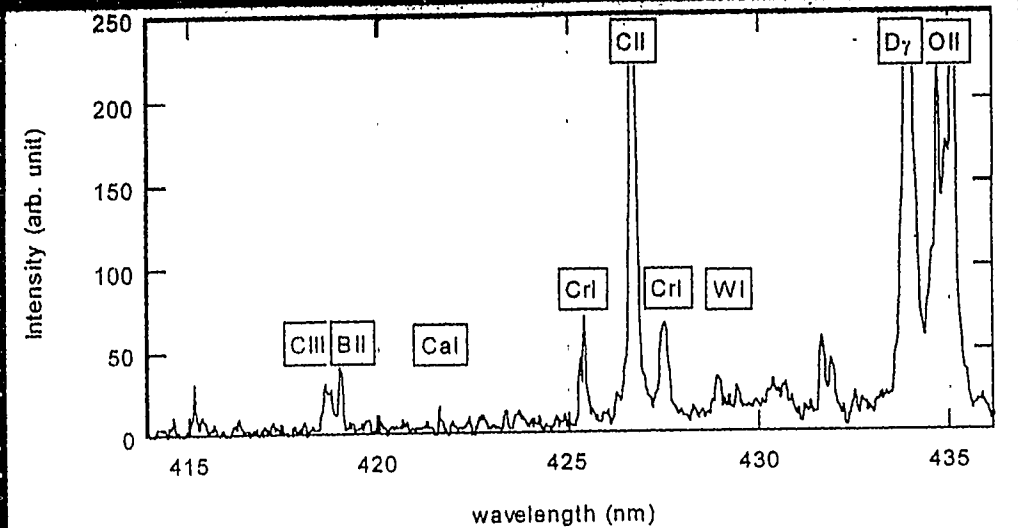

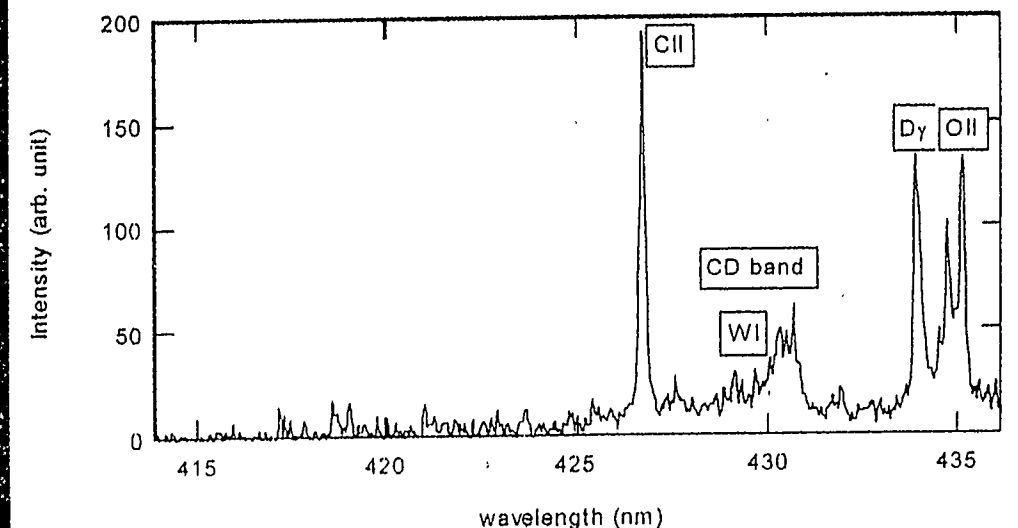

スペクトル比較

Test limiter

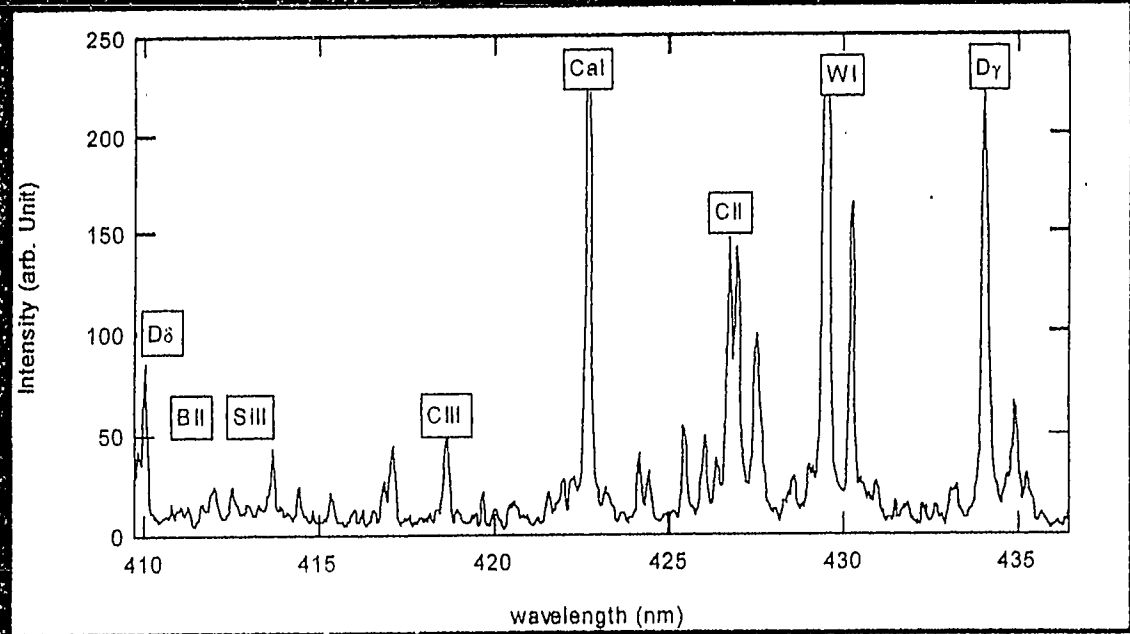

Poloidal limiter

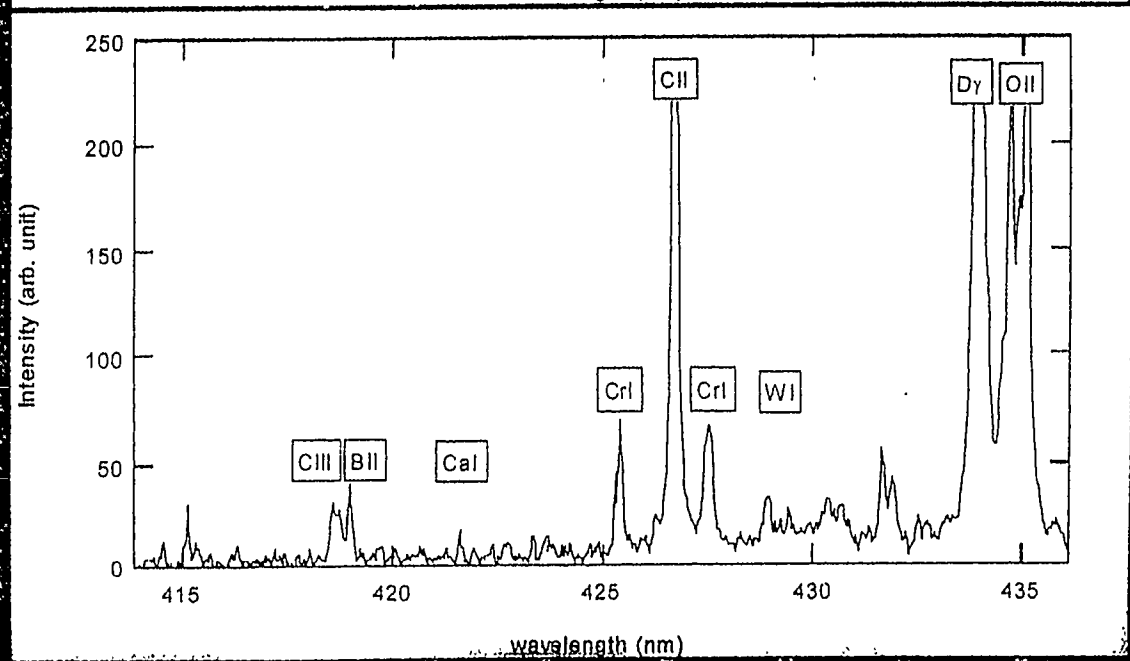

ポロイダルリミターからの軽元素放出

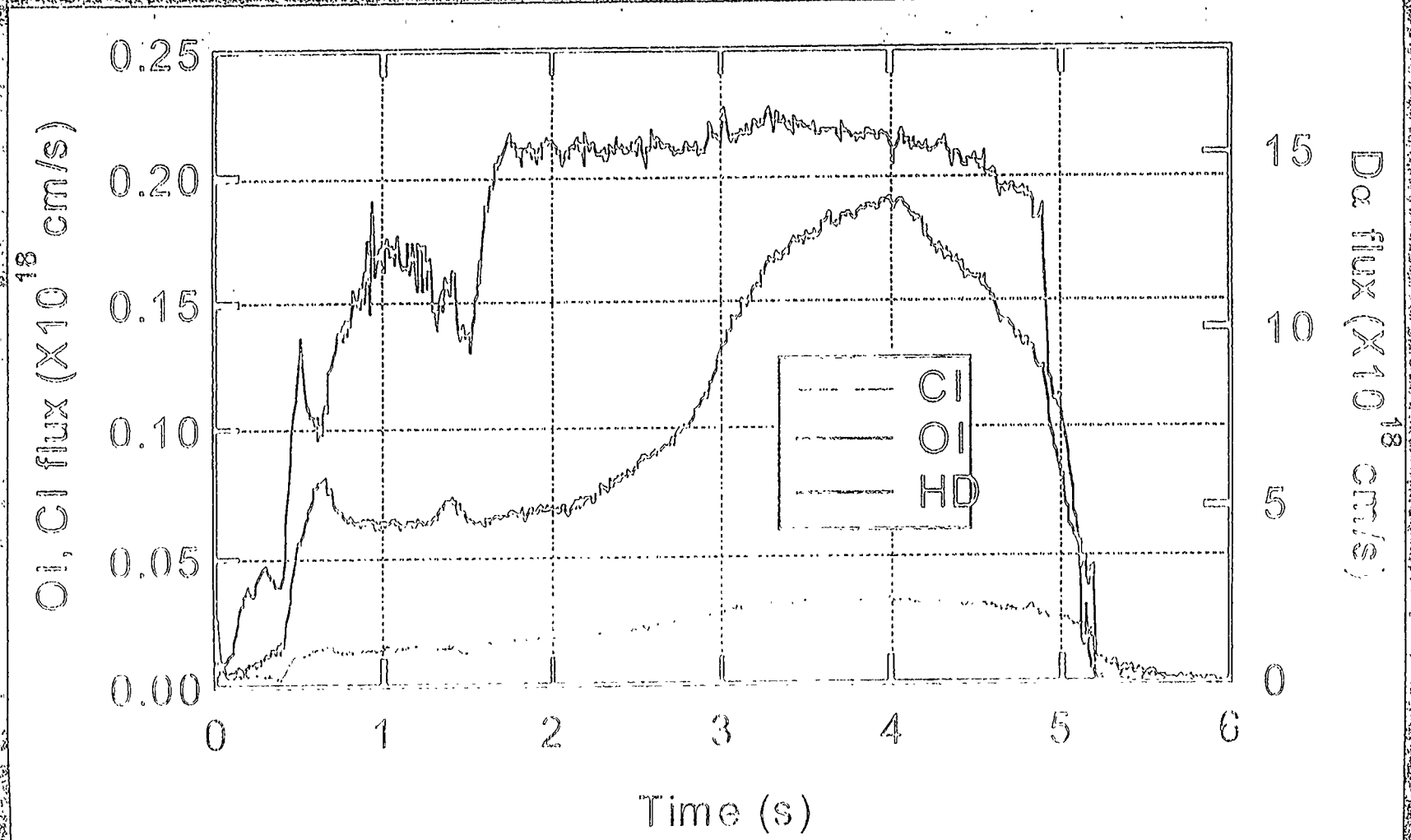

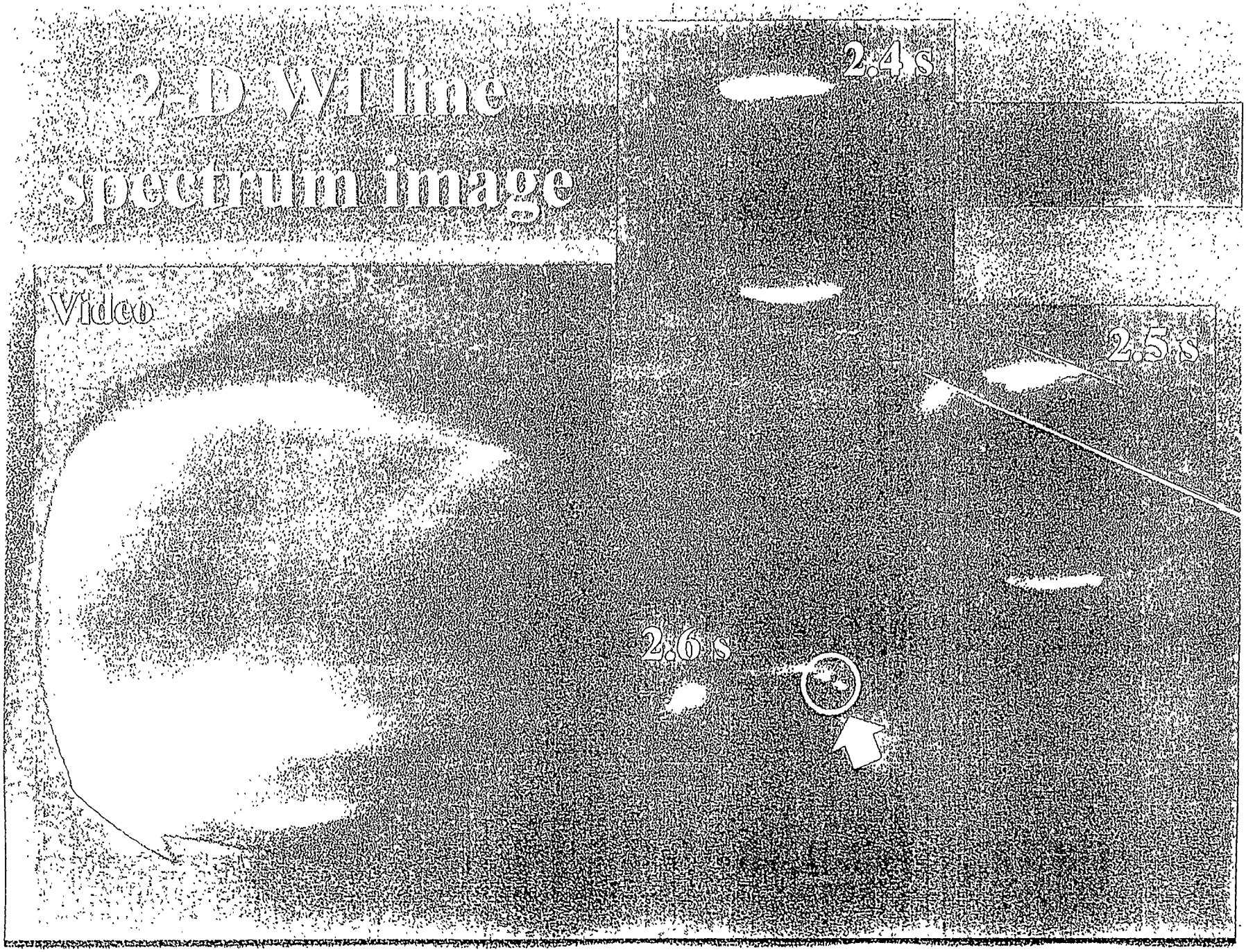
2-D VI line
Spectrum image
Video
2.4 s
2.5 s
2.6 s

Shot 79242

W flakes fell off from top limiter

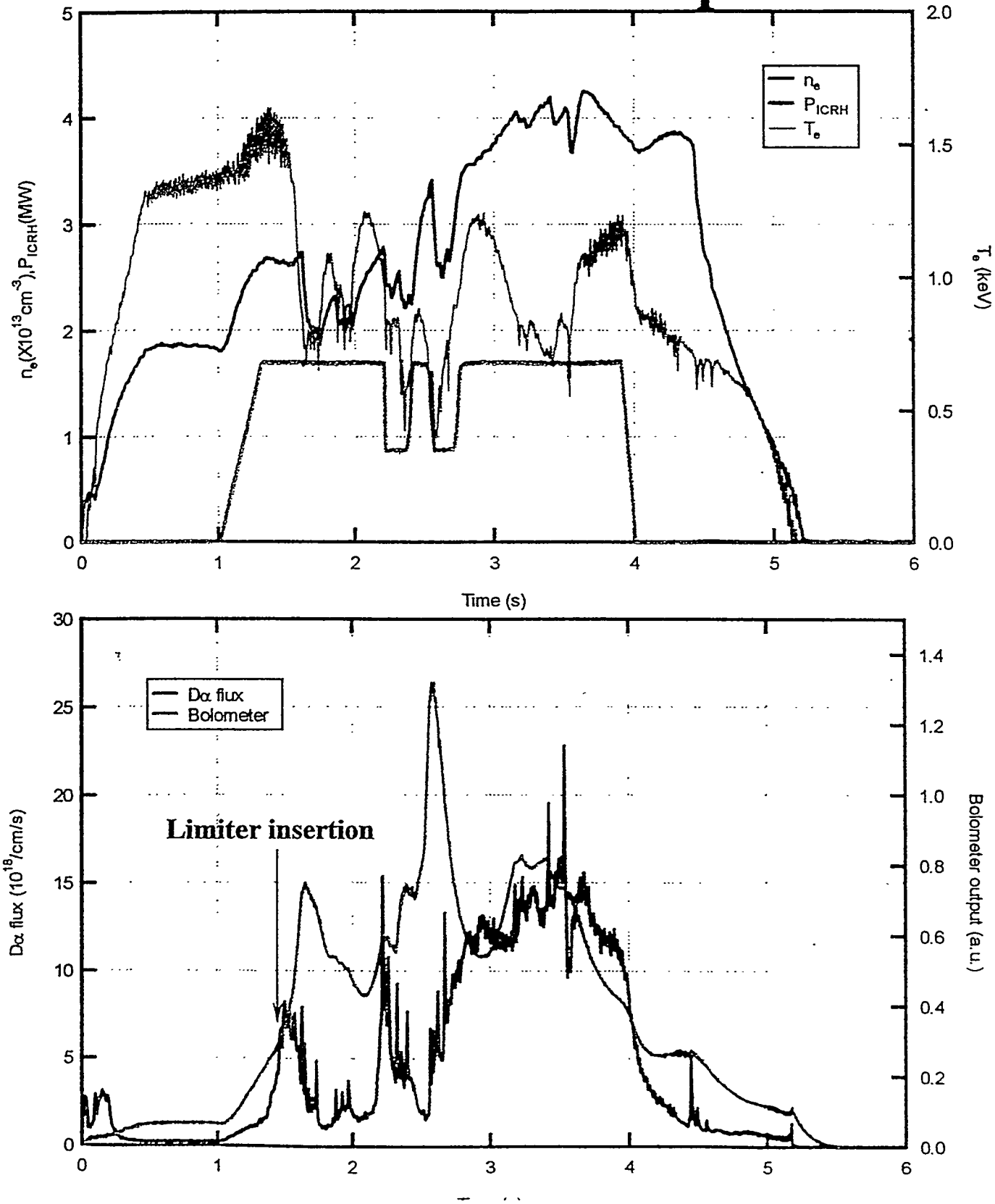

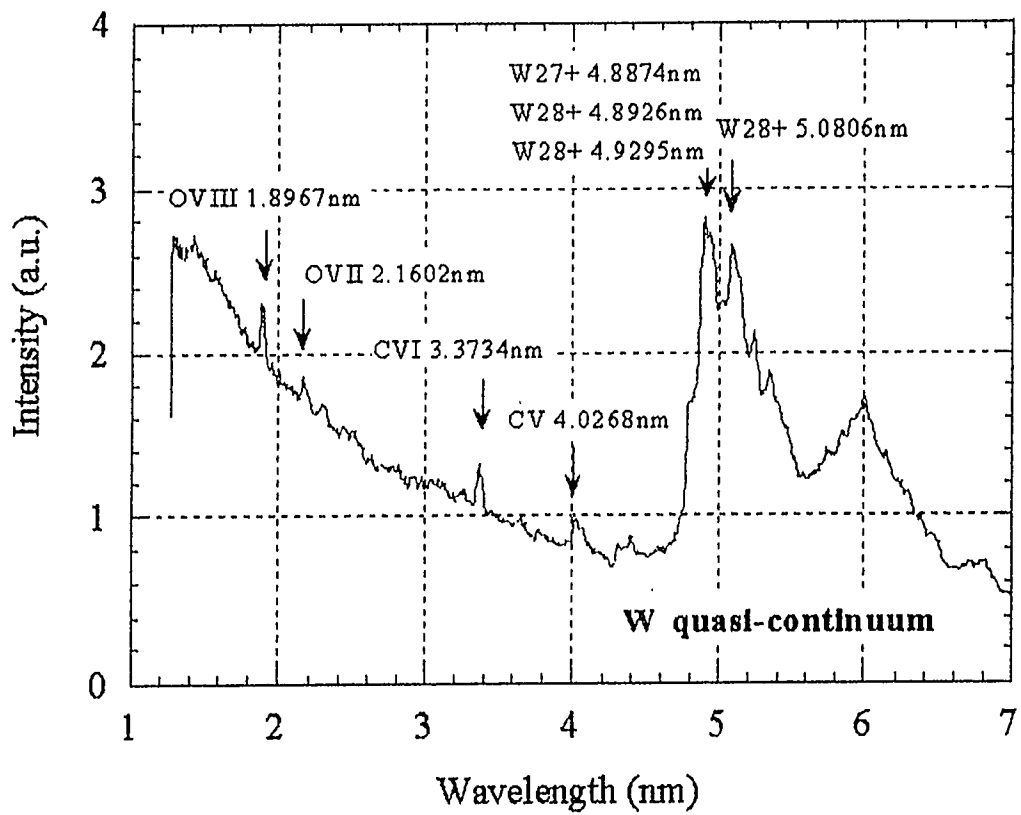
W27+ 4.8874nm
W28+ 4.8926nm
W28+ 4.9295nm
W28+ 5.0806nm
OVIII 1.8967nm
OVII 2.1602nm
CVI 3.3734nm
CV 4.0268nm
W quasi-continuum
Intensity (a.u.)
Wavelength (nm)
0
1
2
3
4
1
2
3
4
5
6
7

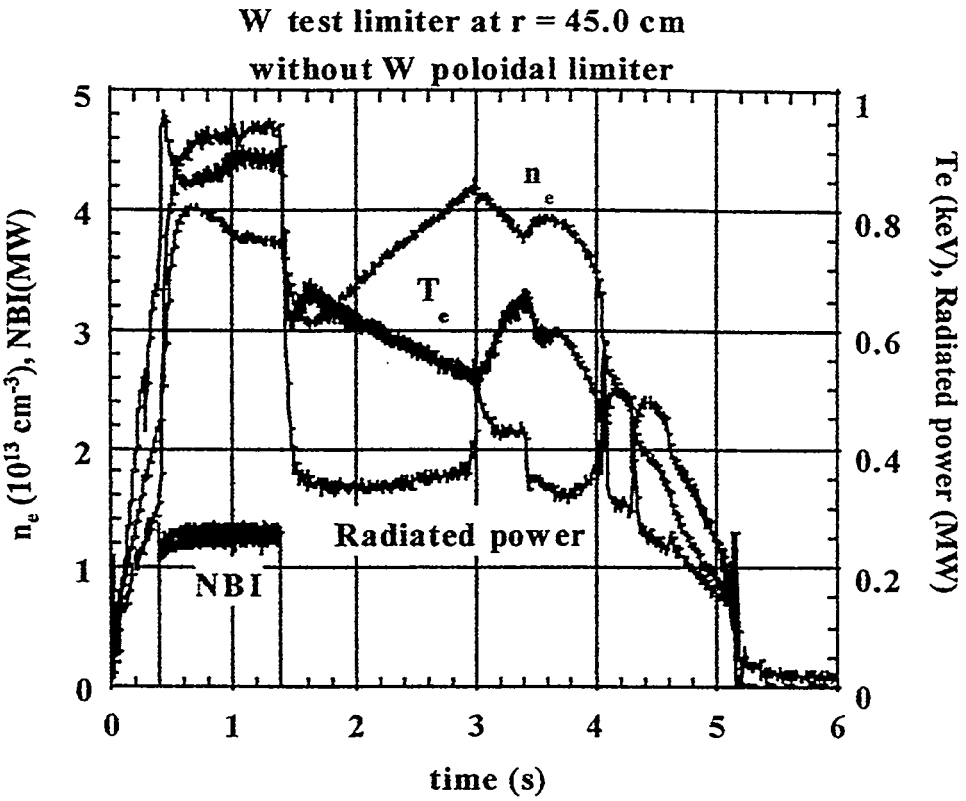
W test limiter at r = 45.0 cm
without W poloidal limiter
n_e (10^{13} cm^{-3}), NBI(MW)
Te (keV), Radiated power (MW)
n_e
T_e
Radiated power
NBI
time (s)

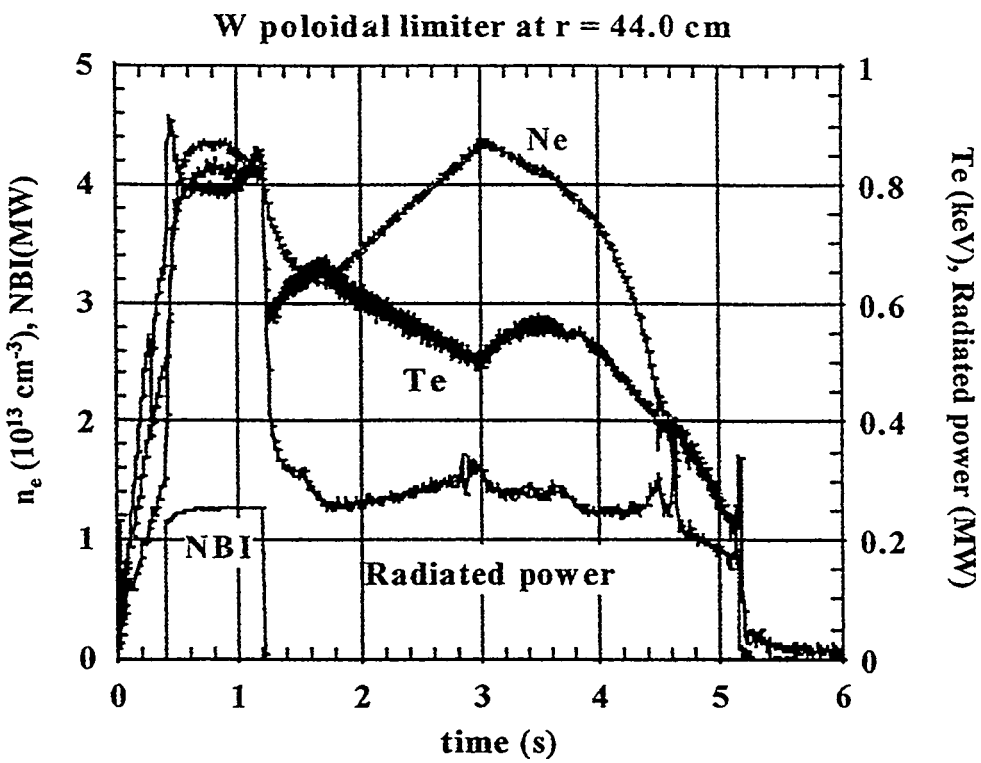
W poloidal limiter at r = 44.0 cm
n_e (10^{13} cm^{-3}), NBI(MW)
Te (keV), Radiated power (MW)
Ne
Te
NBI
Radiated power
time (s)

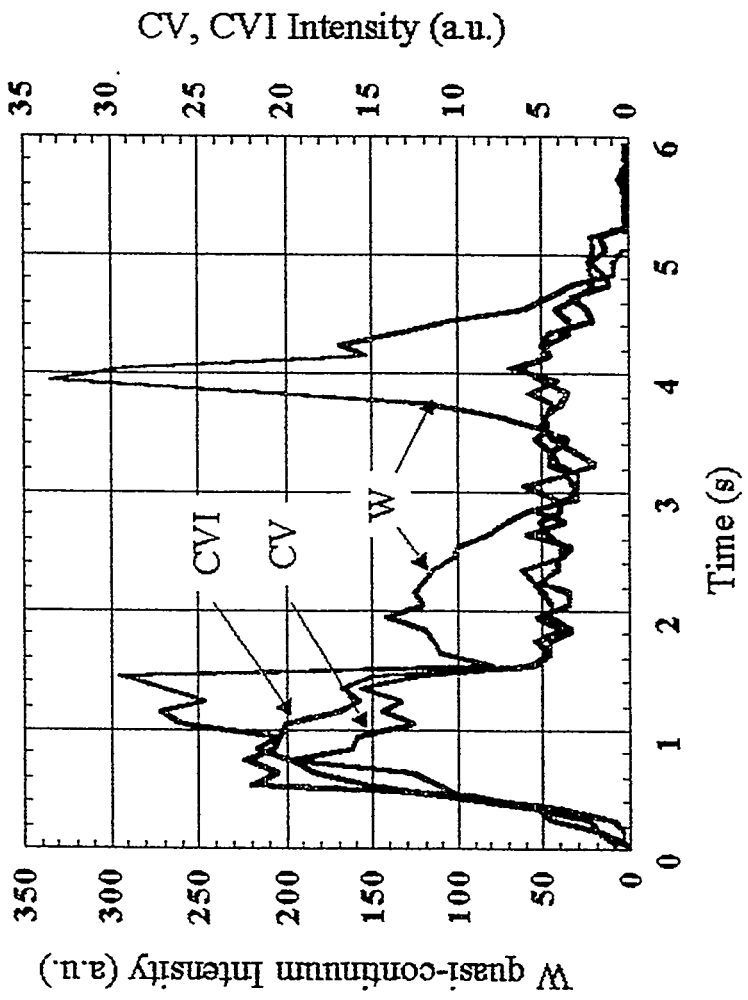
CV, CVI Intensity (a.u.)
35
30
25
20
15
10
5
0
CVI
CV
W
0
1
2
3
4
5
6
Time (s)
350
300
250
200
150
100
50
0
W quasi-continuum Intensity (a.u.)

#83359 - #83362
(r-test 46 cm)

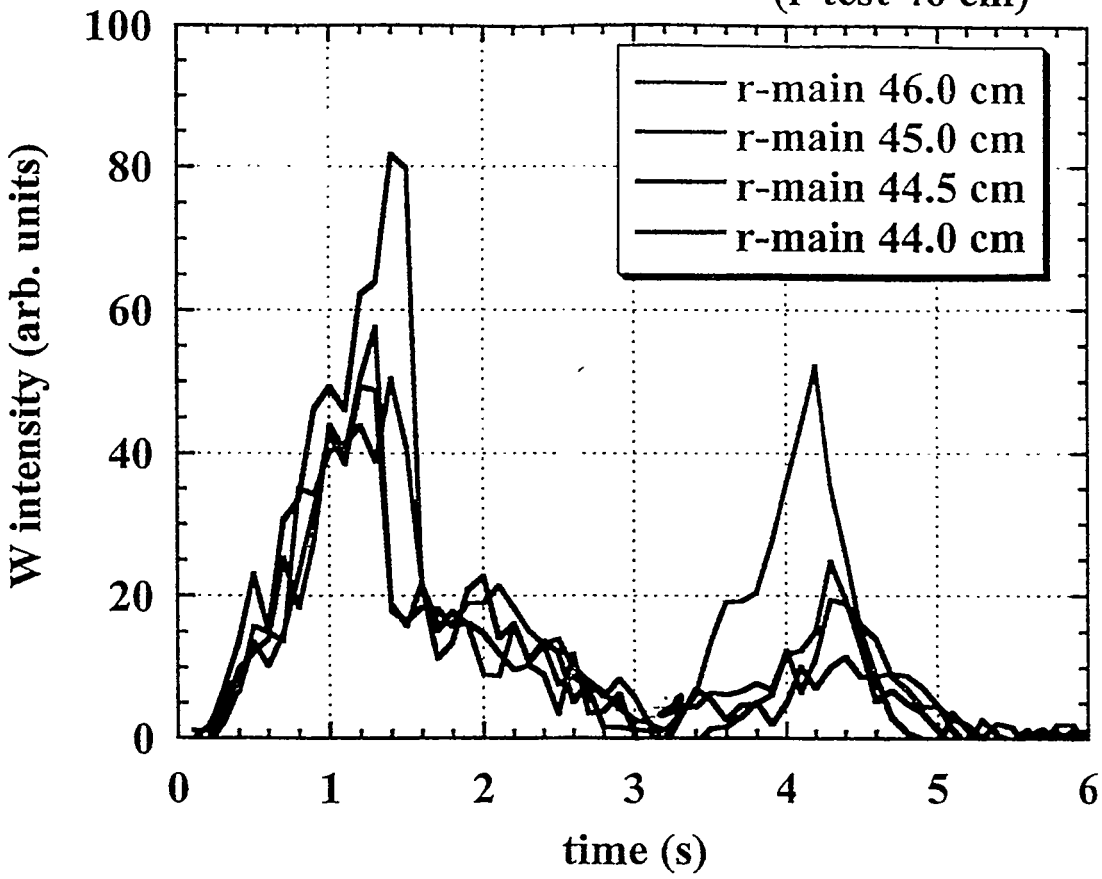

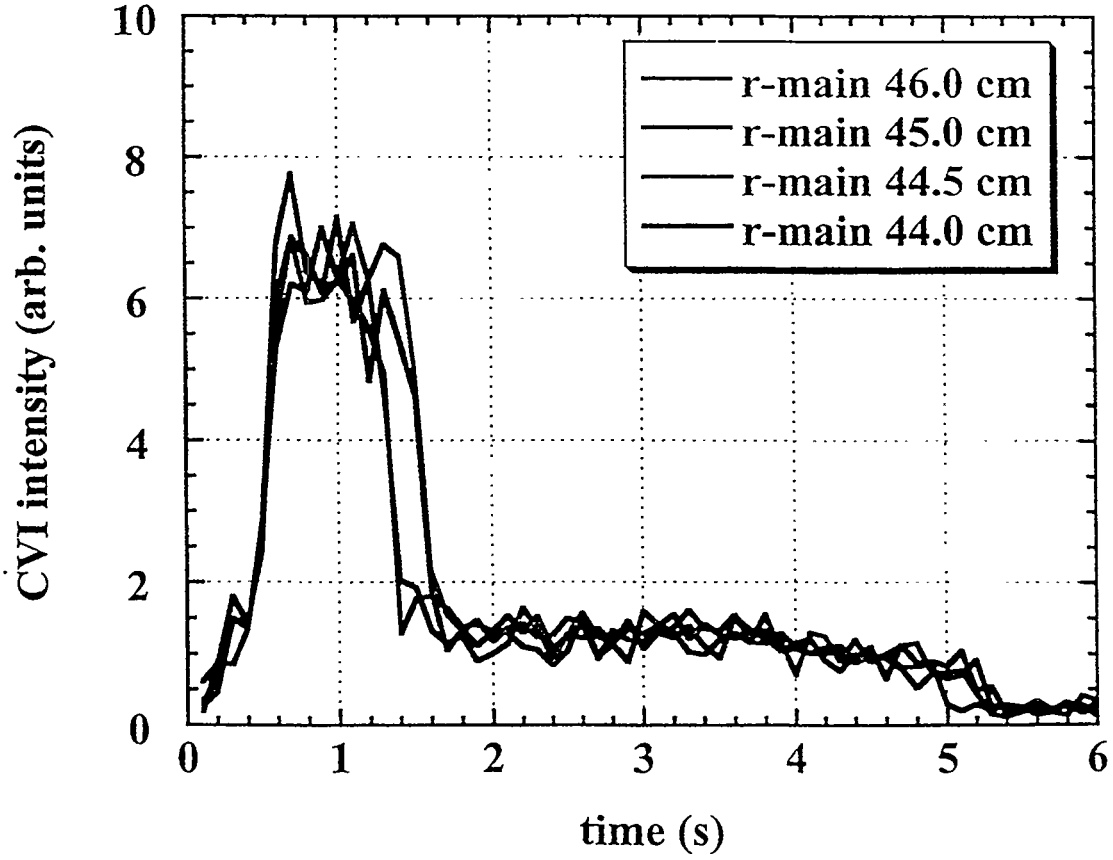

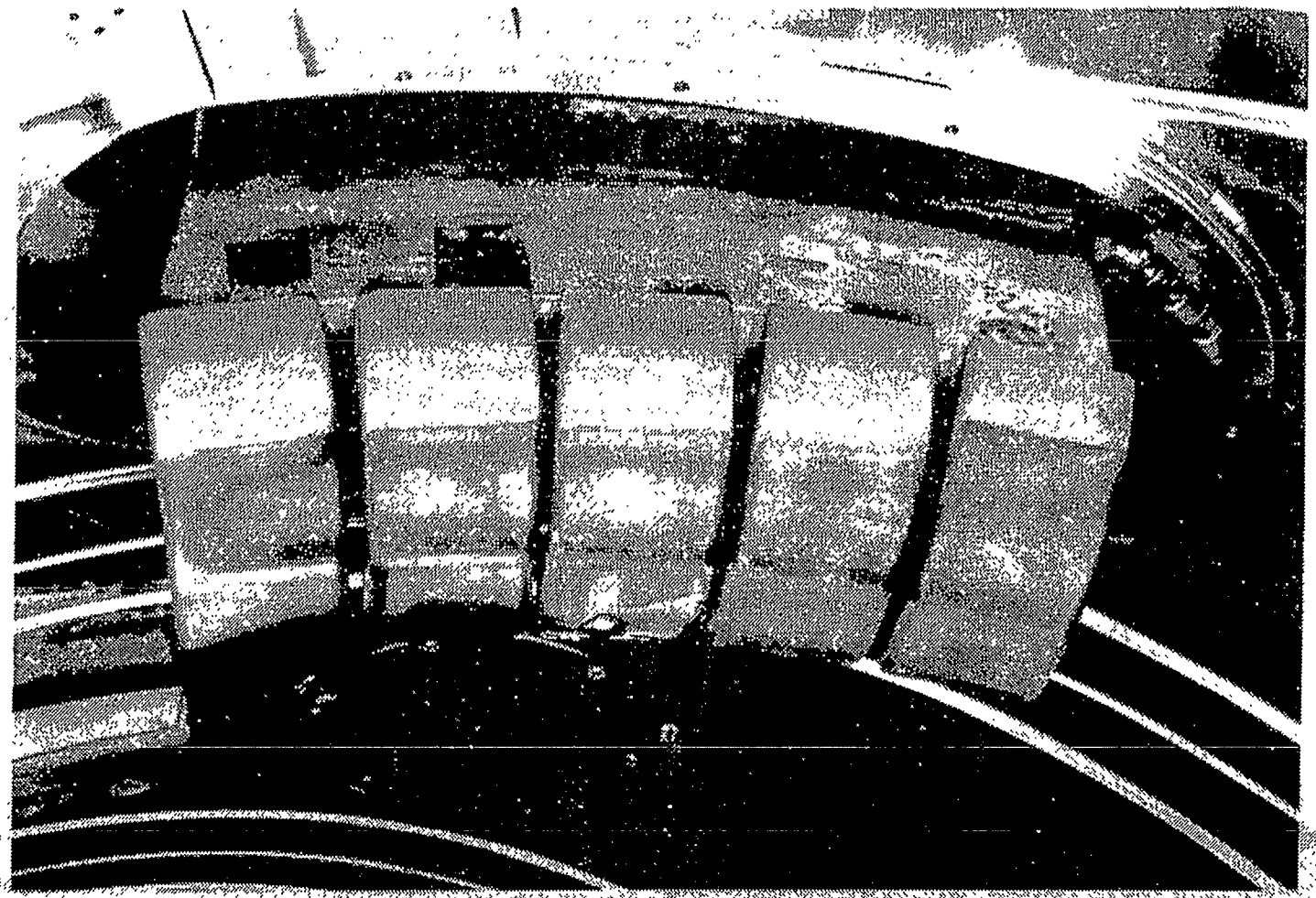

EURATOM-Assoziation
Institut für Plasmaphysik / Trilateral Euregio Cluster

Forschungszentrum Jülich

EURATOM-Assoziation
Institut für Plasmaphysik / Trilateral Euregio Cluster

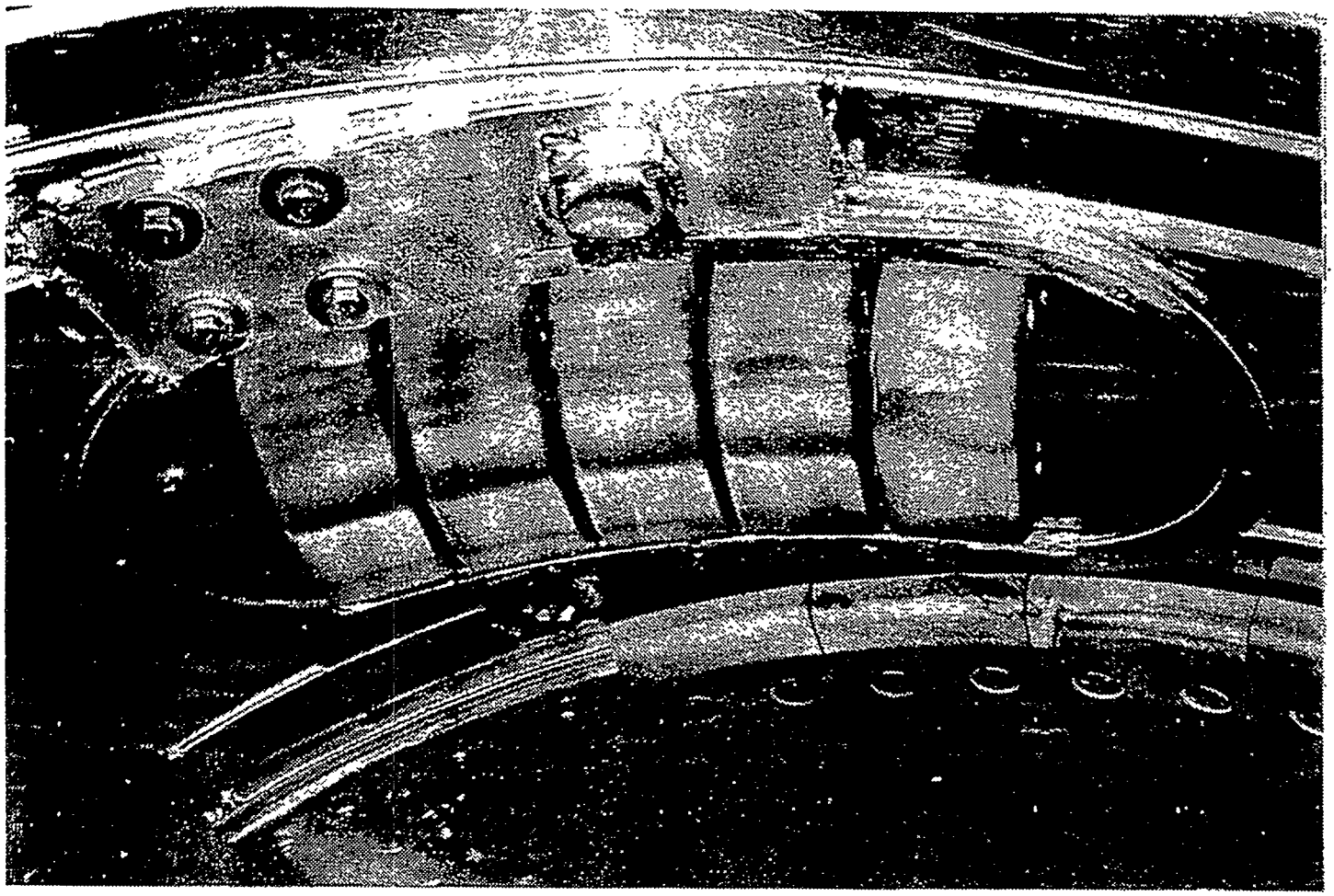

Main (general) conclusions

under condition of 60% of PMI occurring at W limiter with heavy carbon contamination

(1) W wall can sustain high temperature plasma

(2) No plasma collapse by runaway sputtering is observed

(3) Radiation from W in plasma center is very strong (if it accumulates)

(4) C and W are compatible as PFM

(5) PVD-W coated graphite may not be good solution

Once high temperature plasma is established, any materials can be PFM and maybe high Z helps edge cooling like Ne seeding and/or siliconization for RI mode. Of course the accumulation of high Z impurity, which is independent of the source, should be avoided. (For example; Saw-tooth activity helps)

Recommendation

Start-up with low Z limiter

Steady state operation with high Z divertor ?

Plasma Surface Interactions - 1

USA-JapanWorkshop on PSI and HHFC for next fusion devices

MEMBRANE PUMPING OF UPGRADED HELICAL DIVERTOR AT LHD: CONCEPT AND SIMULATION EXPERIMENTS

N. Ohyabu, Y. Nakamura, H. Suzuki, Y. Nakahara
National Institute for Fusion Science, Japan
A. Livshits, V. Alimov, A. Busnyuk, A. Samartsev, A. Doroshin
Bonch-Bruyevich University, Russia

Santa Fe, New Mexico, November 1-4, 1999

Contents

EXPERIMENTAL EVIDENCES OF SUPERPERMEABILITY

Physical experiments were carried out with thermal hydrogen atoms and fast ions using the atomic beam and ion beam technique.

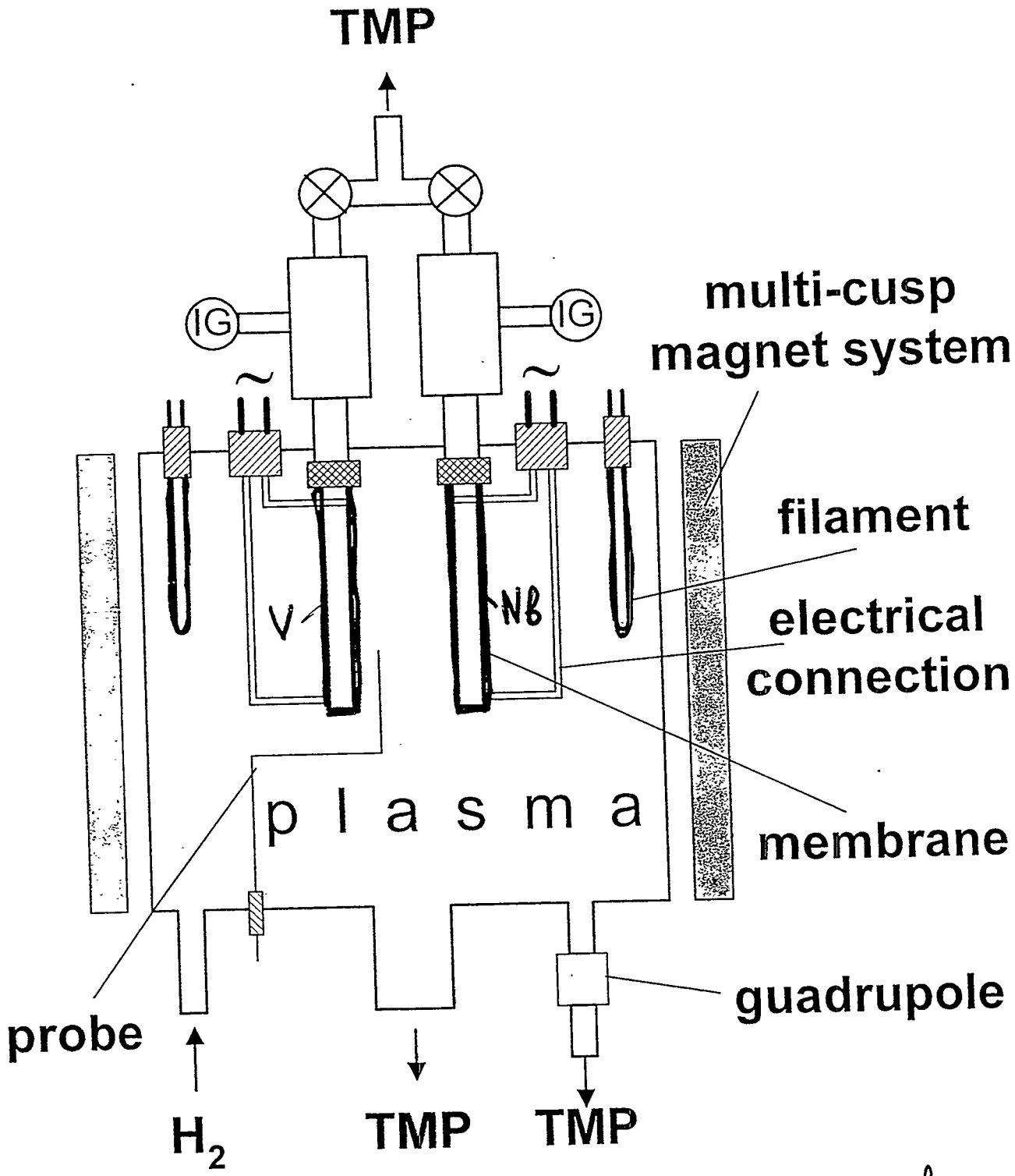

membranes
plasma
vacuum
operation mod

BIAS / ENERGY DEPENDENCE OF PERMEATION

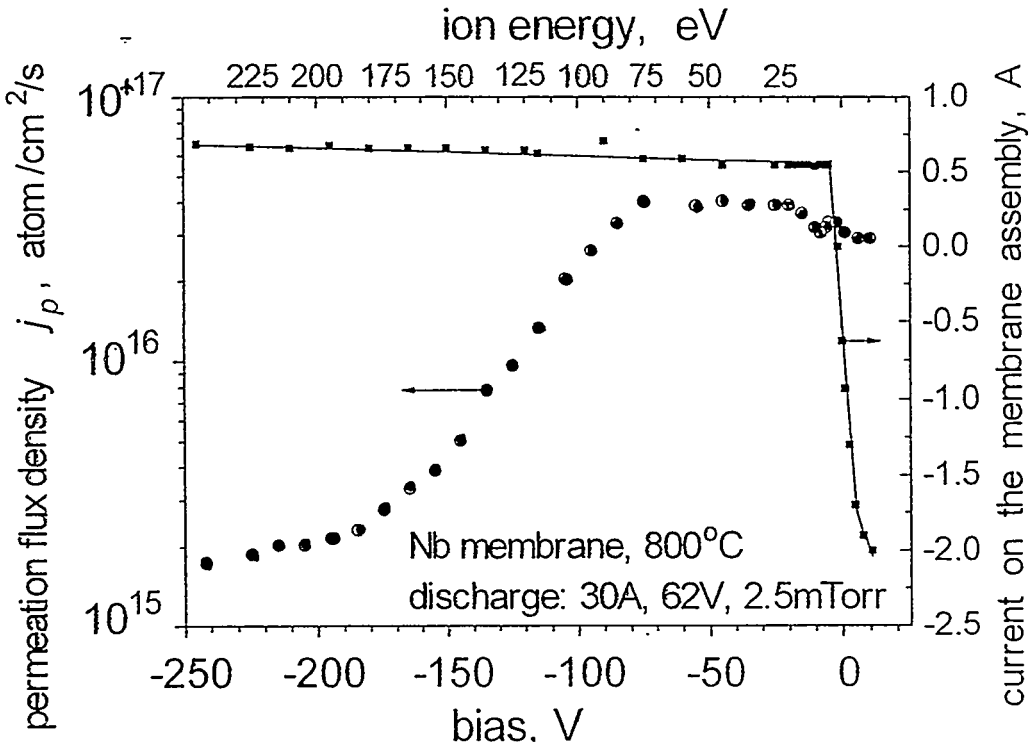

(A) *Input of ions*. One can see an effect of the cut-off of ions by a positive bias on the permeation flux density, j_p, though this effect is not quite clearly expressed because a small peculiarity in the j_p behavior superimposes in the vicinity of $U_b \approx 0$. The observed effect is in no disagreement with our expectancies, on taking into account that an input of ions into the incident flux density does not exceed 10% of a density of the H atom flux.

(B) *Plasma driven superpermeation*. The permeation flux density, j_p, remains constant, in the first approximation, over the bias range of $0 > U_b > -(60-70)$ V. ***Thus a stable ("spontaneous") plasma driven superpermeation*** **that has been found at the floating potential** ***keeps at ion energies of up to 60 – 70 eV.***

Examples of the possible employment of permeation and absorption technique for active particle control

>>>

Short-way separation of D/T and He

He is supposed to be pumped by cryopumps in the existing ITER Project. We were suggesting to install a superpermeable membrane along the pumping duct walls. The membrane can isolate a major part of D/T mixture before the cryogenic panels, automatically compress D/T by a few orders of magnitude, purge it of any impurities including He, and return back into the fueling system. If the membrane is installed far enough from the divertor, D/T mixture, when reaching it, will mainly consists of thermal molecules that have to be converted again into suprathermal particles, e.g. into thermal atoms. That may be done either at a hot metal surface (an atomizer) or in a gas discharge. As it has been shown basing on the results of model experiments, a membrane system of quite a reasonable size and with a fairly moderate power consumption may isolate more than 99% of D/T, drastically reducing its freezing up at the cryogenic panels.

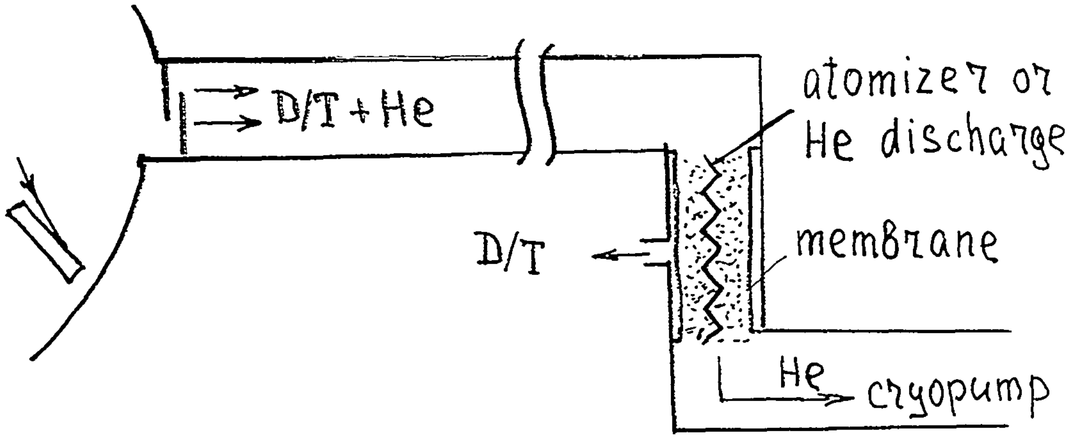

APPLICATION OF SUPERPERMEATION AND ENHANCED ABSORPTION IN LHD

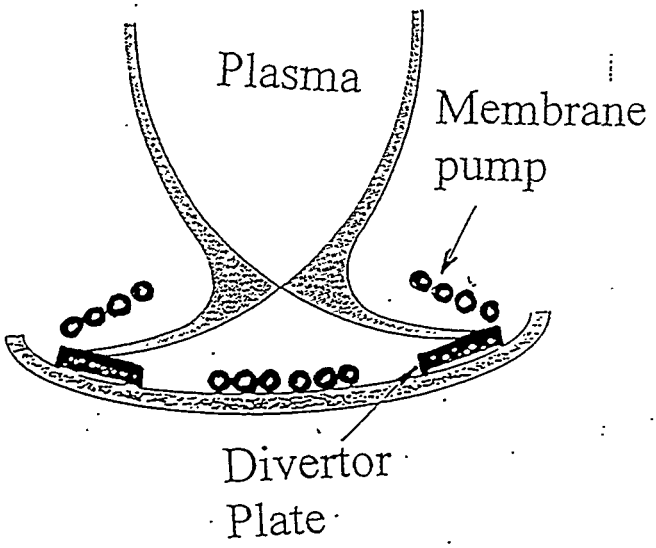

Helical Divertor

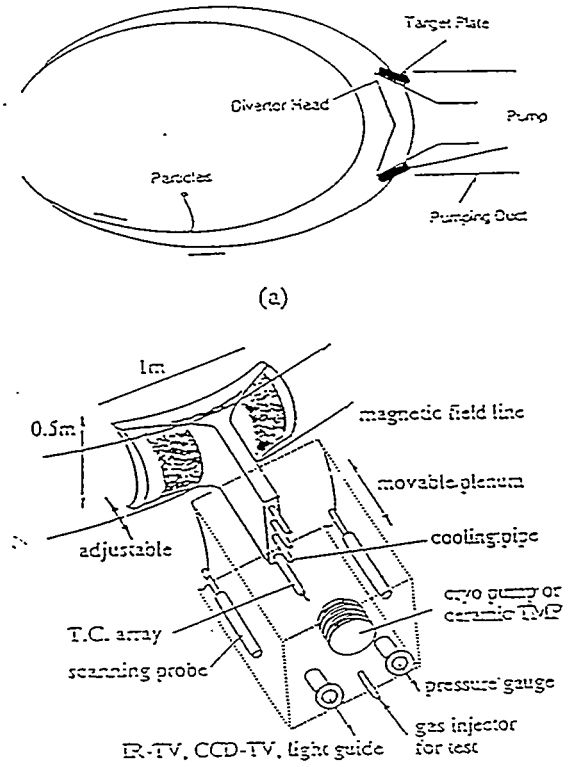

Local Island Divertor

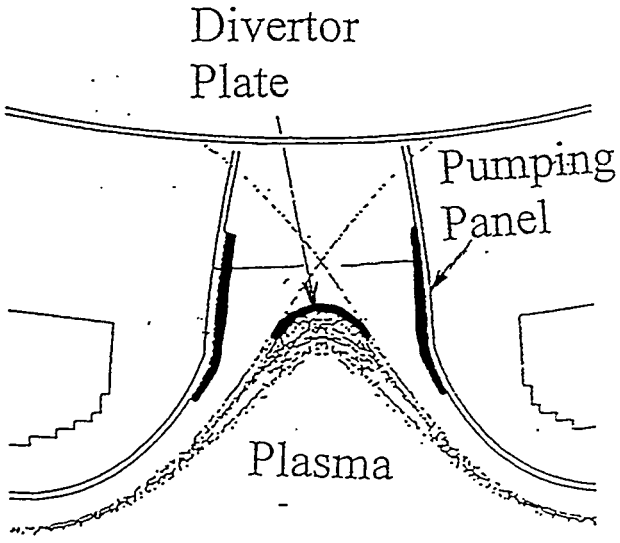

Upgraded Helical Divertor

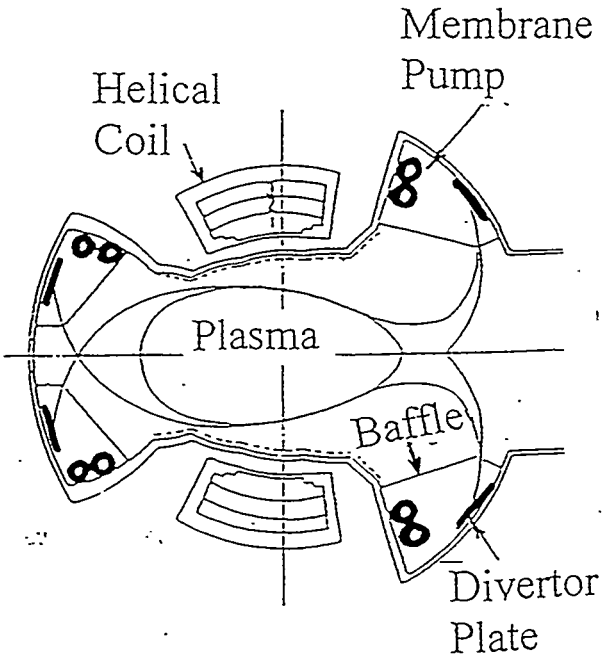

Closed Helical Divertor

UPGRADED HELICAL DIVERTOR

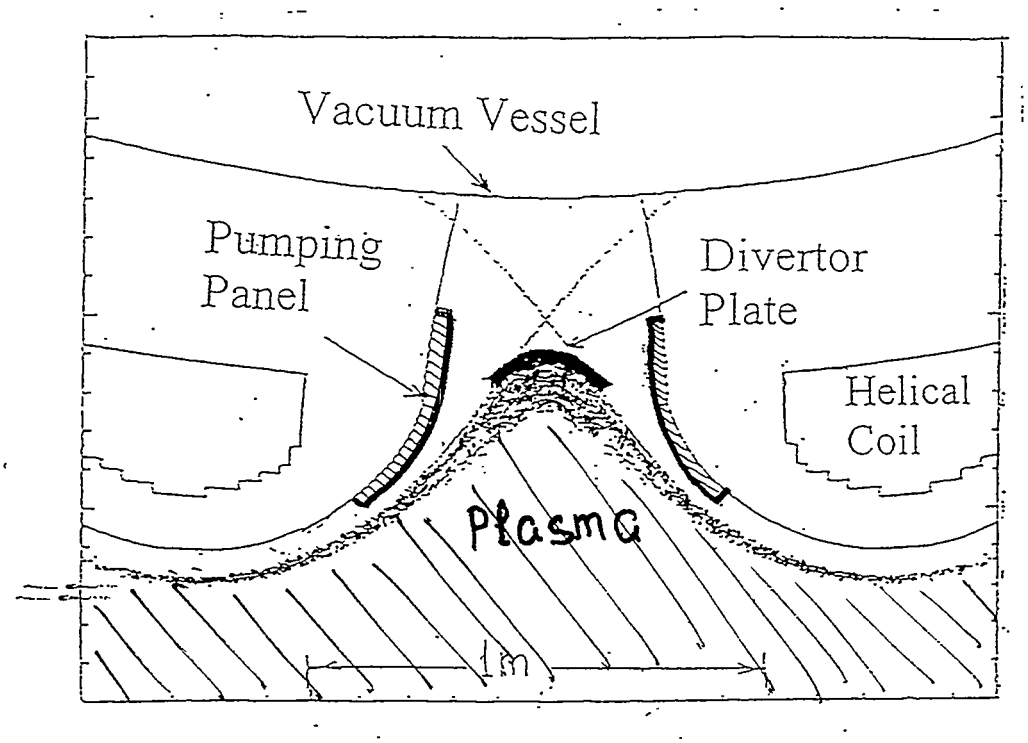

The main goal of **the** upgraded divertor is reaching **of highest core plasma parameters (temperature) due to the low recycling regime** (the "high temperature operation regime") ***to be provided by effective pumping.***

The idea of pumping consists in removing of the CX atoms generated by the plasma from particles re-emitted by the divertor plate with using either a membrane or an absorption pumping panel. It is believed that 10-20% of all the hydrogen particles re-emitted by the divertor plate may be pumped in such a way.

UPGRADED HELICAL DIVERTOR

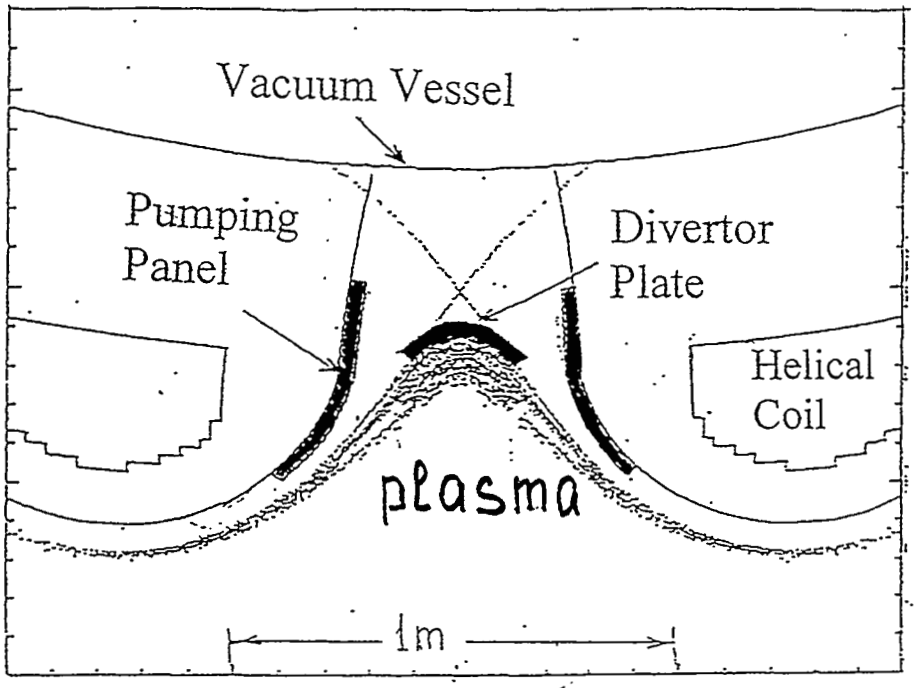

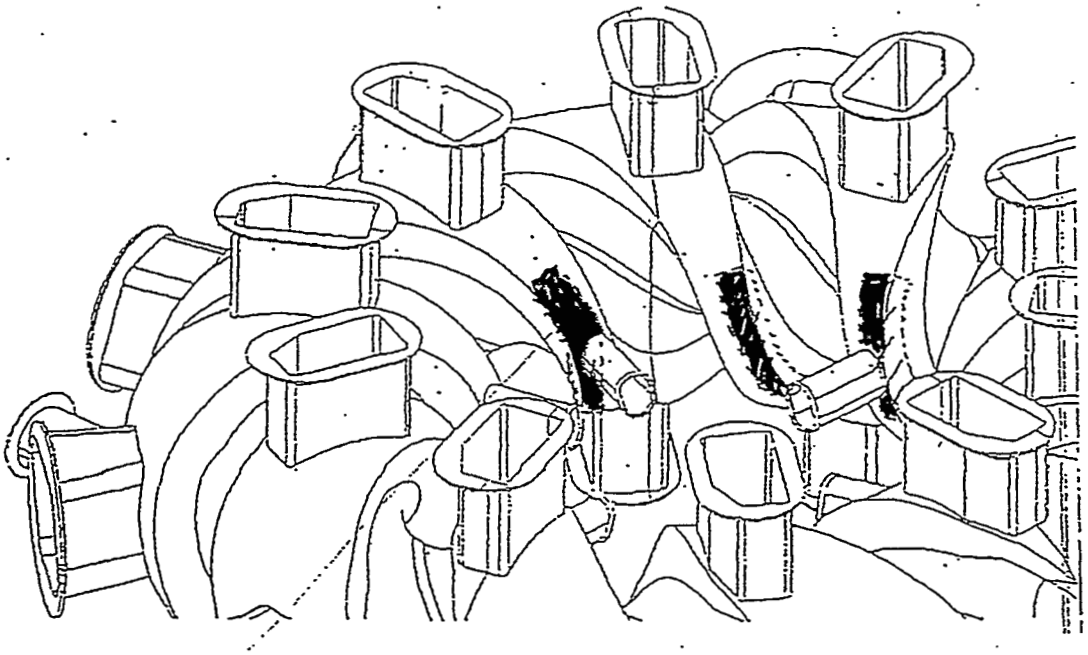

UPGRADED HELICAL DIVERTOR

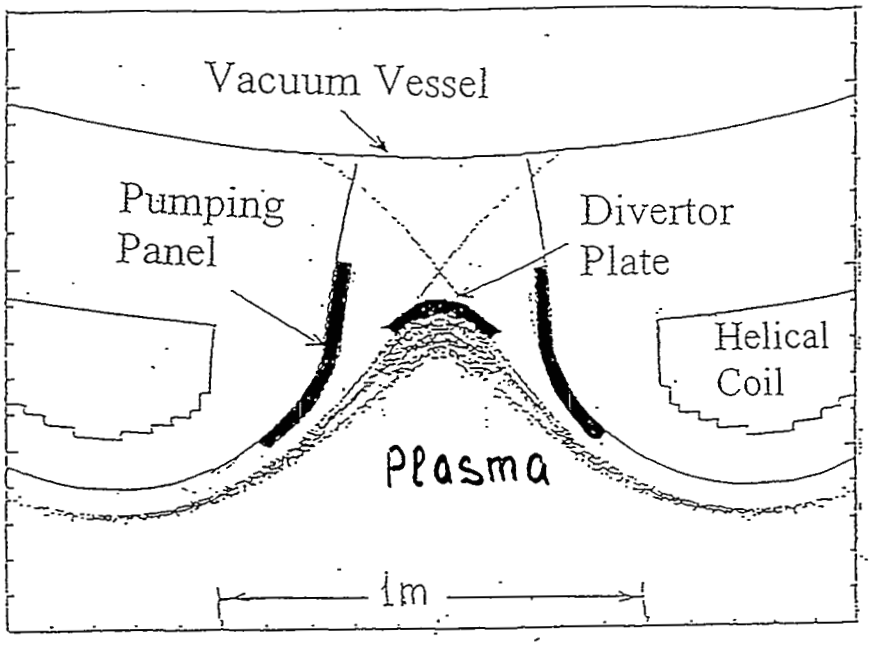

Pulse regime: shot is 10s, pause is 300s
CX flux density: $\approx 4\ 10^{15}$ $cm^{-2}s^{-1}$ (averaged over area)
CX atom energy: $\approx$ 2keV
Heat flux during the shot: $\approx$1.3 $W/cm^2/s$ (averaged over area)
Carbon flux to the panel during the shot:
< 1.5 $10^{14} C/cm^2/s$ in the most unfavorable places (according to the preliminary estimates), i.e. no more than 1 monolayer for the shot.
Net carbon deposition rate is supposed to be zero: it is supposed that sputtering by the CX atoms will predominate over the carbon deposition.
Magnetic field is 3T

Total area of pumping panels: $\approx 20\ m^2$

Short way separation of D/T and He with a membrane system installed in pumping duct

There is neither sputtering nor deposition of carbon here. Several *membrane systems combined with an atomizer with* a pumping speed of about 1000 l/s were successfully tested, and there are no fundamental limitations on fabrication of a system of any required size.

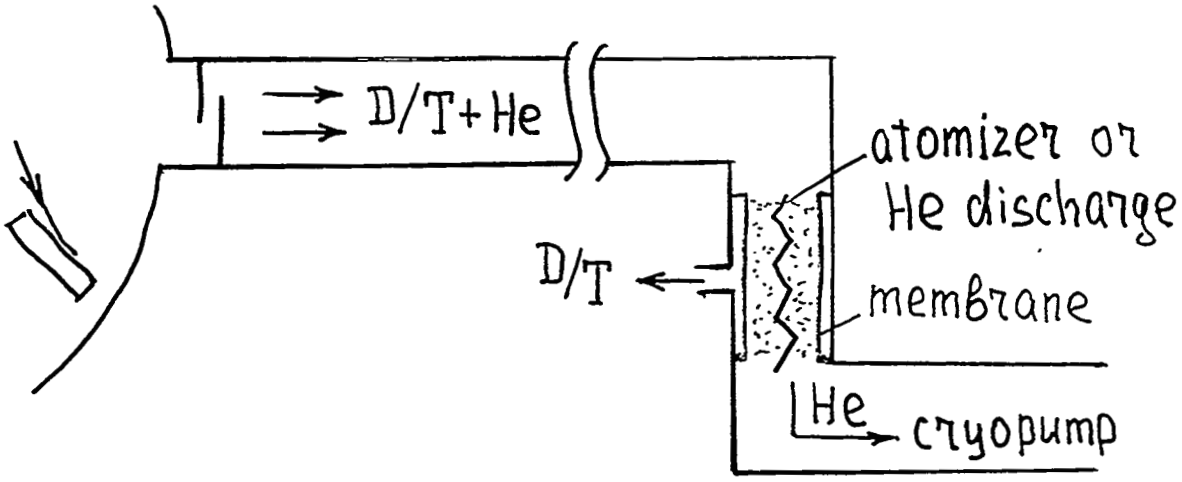

A *membrane system combined with a gas discharge* (instead of atomizer) seems to us being even more promising. A work in this direction is being carried out by Dr. Bacal's group. Since D/T will be evacuated by the membrane, He is expected to be the main gas, and therefore He discharge with a small concentration of H should be tested. Dr. Notkin will touch upon this point in his presentation.

Superpermeation technology of this type might be included in the ITER Project which is under reviewing now.

Requirements for the permeation/absorption panels for particle control

What physical factors possibly may damage superpermeation?

It was theoretically and experimentally shown that, under conditions of interest, **radiation enhanced diffusion** does not in fact affect superpermeation and enhanced absorption and neither does **reemission induced by energetic hydrogen**. At the same time, **sputtering of the plasma facing surface** and **the growth of a polyatomic carbon film** may present a real problem.

<u>**Sputtering of plasma facing surface**</u>. If a superpermeable membrane is initially symmetrical and if nothing has been undertaken to dynamically maintain the impurity monolayer, sputtering of only the membrane upstream side will result in the development of an unfavorable asymmetry and in an ensuing degradation of superpermeation (as well as in a dramatic decrease of enhanced absorption). This phenomenon have been observed many times in ion beam and plasma experiments.

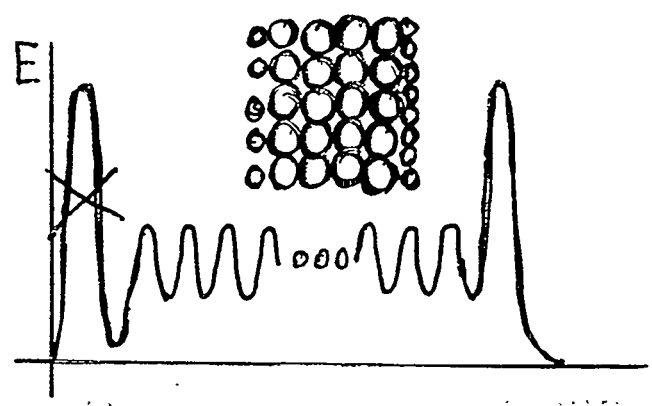

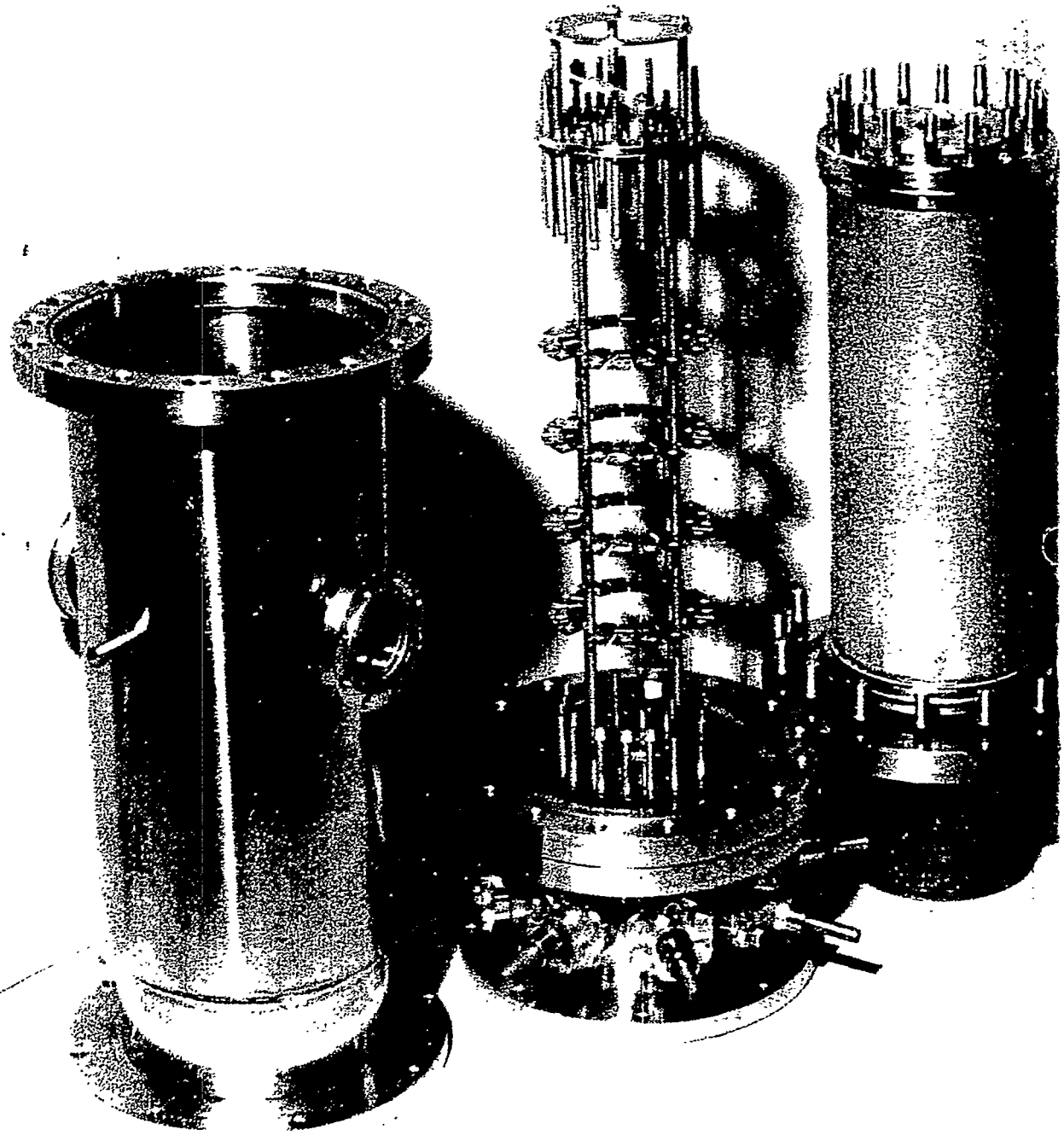

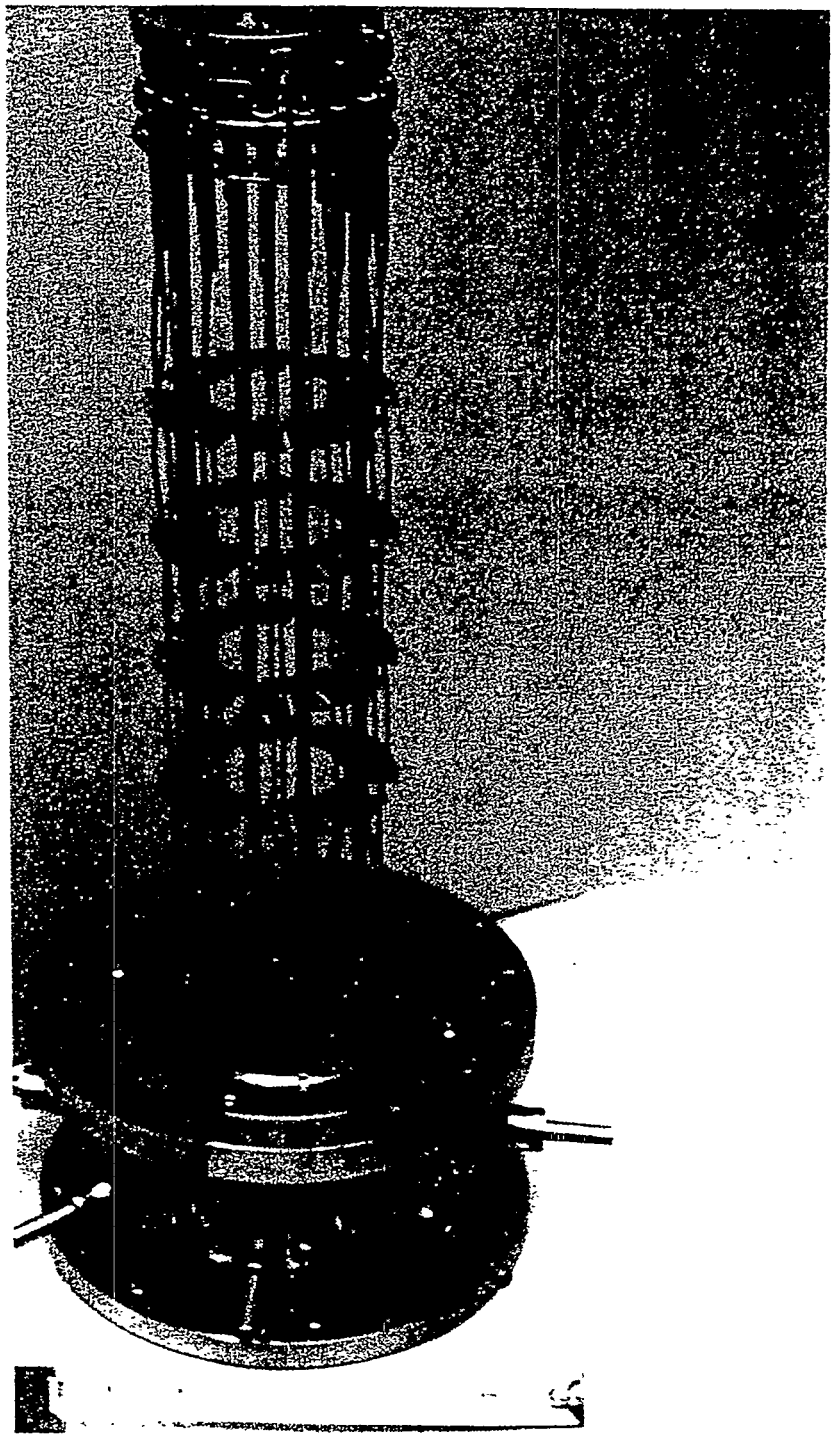

PUMPING SPEED AND PERMEATION FLUX DENSITY

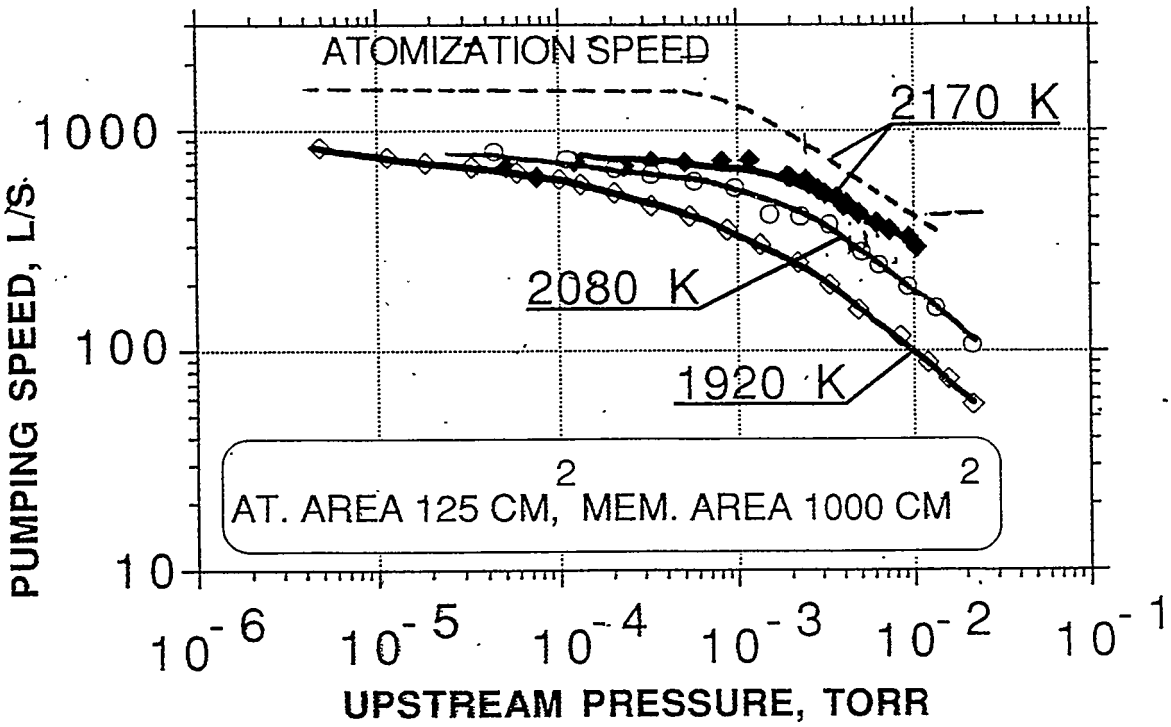

The pumping speed curve is really parallel to the atomization speed curve. This means that membrane permeation itself does not depend on the pressure and flux density over the whole investigated pressure range, *i.e. the membrane remains superpermeable up to the highest flux density and pressure investigated*.

Membrane in a high recycling divertor

The situation seems to be rather favorable here too: the low temperature divertor plasma must not physically sputter the pumping panel. On the other hand, the dense divertor plasma will capture the sputtered carbon atoms preventing the surface from the deposition of carbon.

Membrane in a low recycling divertor (Upgraded helical divertor for LHD)

Situation is more problematic here. CX atoms of keV scale energy will sputter the pumping panel. The low density divertor plasma is expected to be rather "transparent" for the sputtered C atoms and so C will reach the pumping panel.

Thus two problems have to be solved, if one wants to employ the superpermeation technique under conditions of such a kind:

- *Superpermeable membranes being able to preserve a favorable asymmetry in spite of sputtering should be developed.*
- *The conditions and regimes for the superpermeable membrane operation under the carbon flux should be found.*

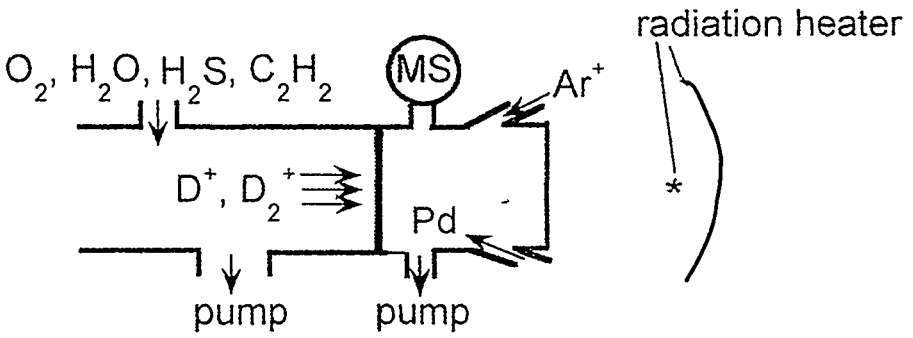

Scheme of ion beam experiment with a Nb membrane where Pd could have been deposited in situ at the membrane downstream side preliminary cleaned by Ar^+ ion beam.

The membrane might be heated by an external source of light through the glass window. The chemical state of upstream side might have been in situ controlled by admitting chemically active gases in the course of ion bombardment.

Effect of the deposition of Pd
on the Nb membrane downstream side

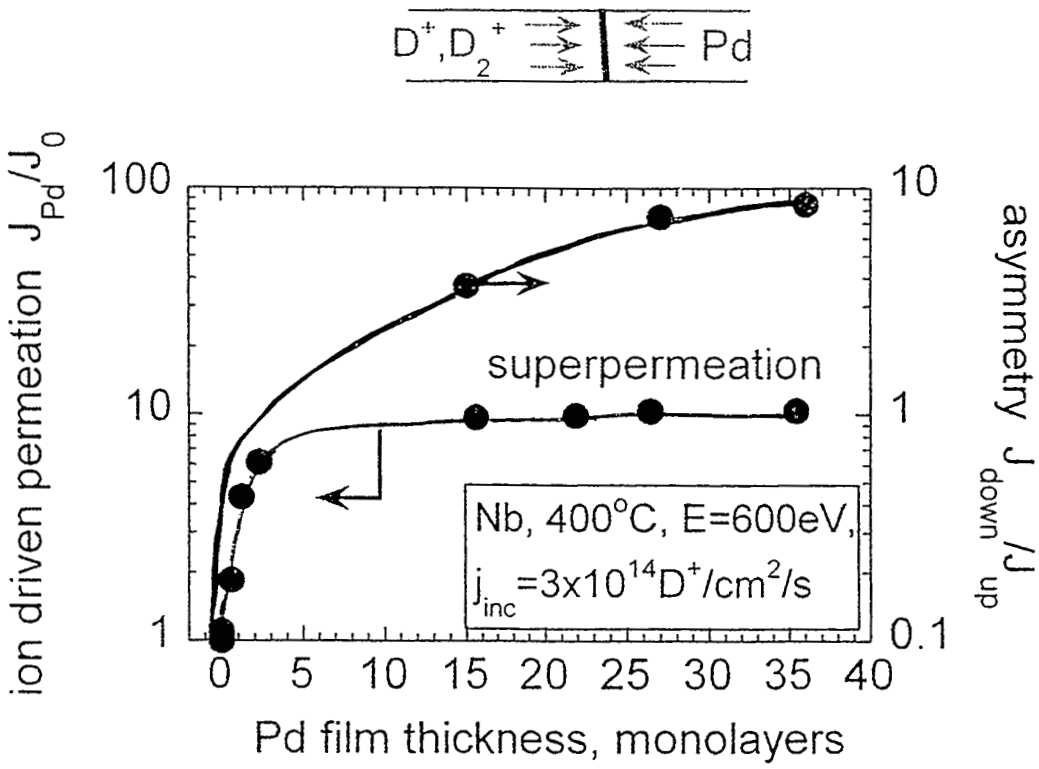

Pd deposition results in an about tenfold increase of ion driven permeation due to the increase of membrane asymmetry; as a result superpermeation is reached in spite of sputtring in UHV.

An independent measurement of the membrane asymmetry has shown its hundredfold increase from a very unfavorable magnitude (0.1) to a rather favorable one (10) despite the permanent sputtering.

When the Pd film thickness reaches a few tens of monolayers the film remains stable and no repeated deposition is required, if temperature does not exceed 500-600°C.

The main reason of the effect of Pd is that Pd surface can be easily maintained clean (in contrast to Nb surface), and the clean surface ensures a very much facilitated desorption of absorbed hydrogen.

Combined effect of S at the upstream side and Pd at the downstream side on the Nb membrane asymmetry and molecule permeation

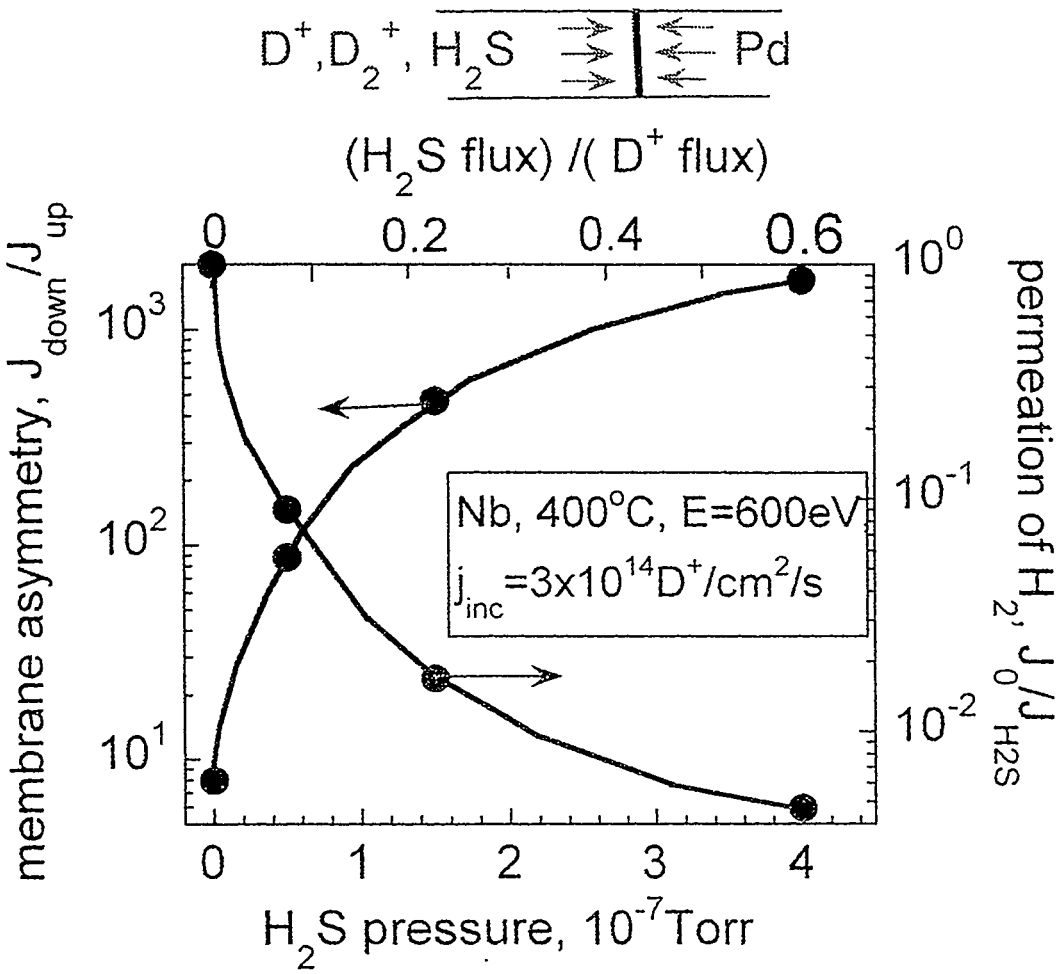

The presence of H_2S at the membrane upstream side in combination with a Pd coating at the downstream side results in an asymmetry increase and in the supression of molecule permeation by orders of magnitude.

H_2S is an "exotic" species for fusion devices but H_2O, O_2 and C_2H_2 have a similar effect. Perhaps B or Be also may be acting in a similar way?

Plasma-Membrane Test Device with a Graphite Target

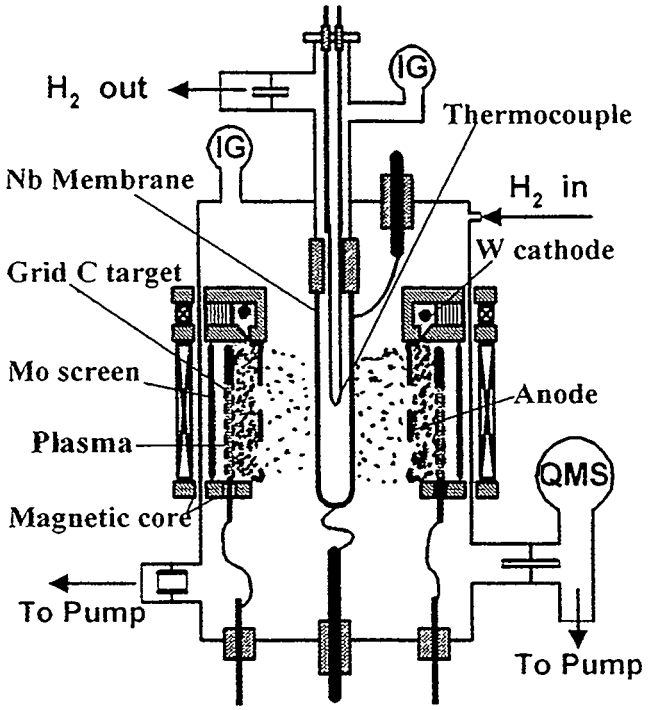

Hydrogen plasma surrounds a resistively heated tubular Nb membrane. The plasma generated by a discharge with hot W cathode. A resistively heated grid target made of graphite contacts the plasma, surrounding it from the outside.

Two main groups of suprathermal hydrogen particles are impinging on the membrane: *thermal* atoms, and the *energetic* atoms originating from ion neutralization at the target. An additional flux of energetic ions could have been obtained by membrane biasing.

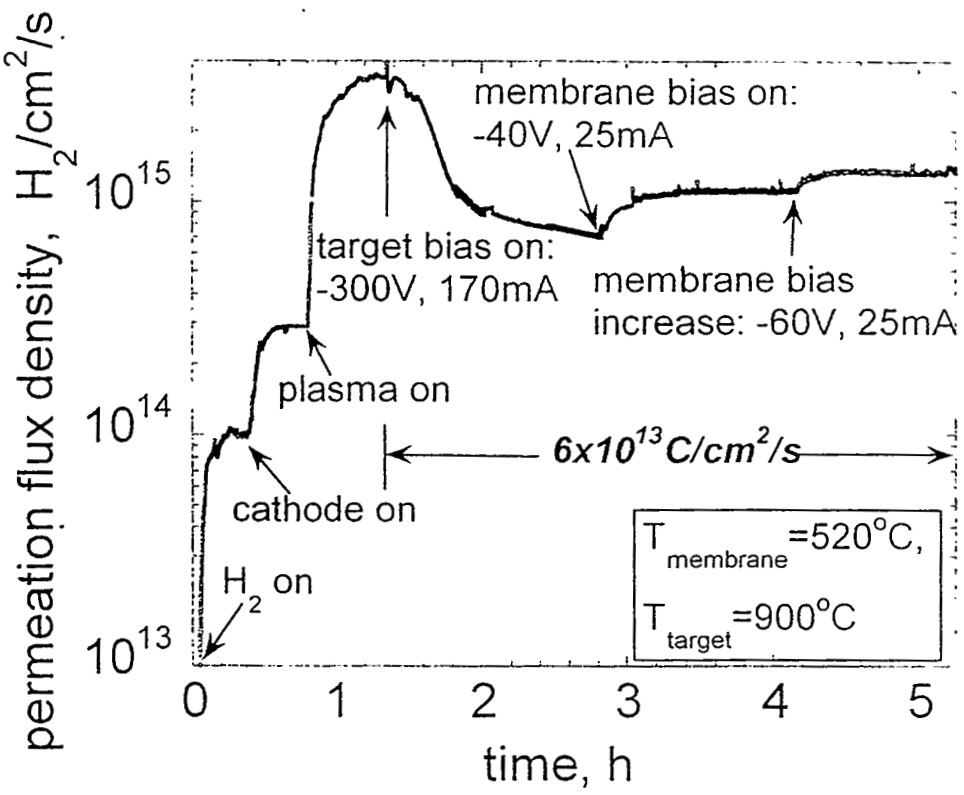

Even though energetic (about 100 eV) reflected H atoms were getting at the membrane alongside of C, the permeation started decreasing due to blocking of the surface by polyatomic C film.

To intensify the C removal, a low-voltage bias was applied to *the membrane*, so that the energy of ions falling onto the membrane increased to a few tens of eV and the total flux of energetic hydrogen increased about 2 times. In point of fact, the permeation decrease was stopped, and a stable permeation was reached and was keeping during the whole observation time. Thus this experiment directly demonstrates that *stable superpermeation may exist even under the high carbon flux, if hydrogen flux ensures a sufficient rate of carbon removal.*

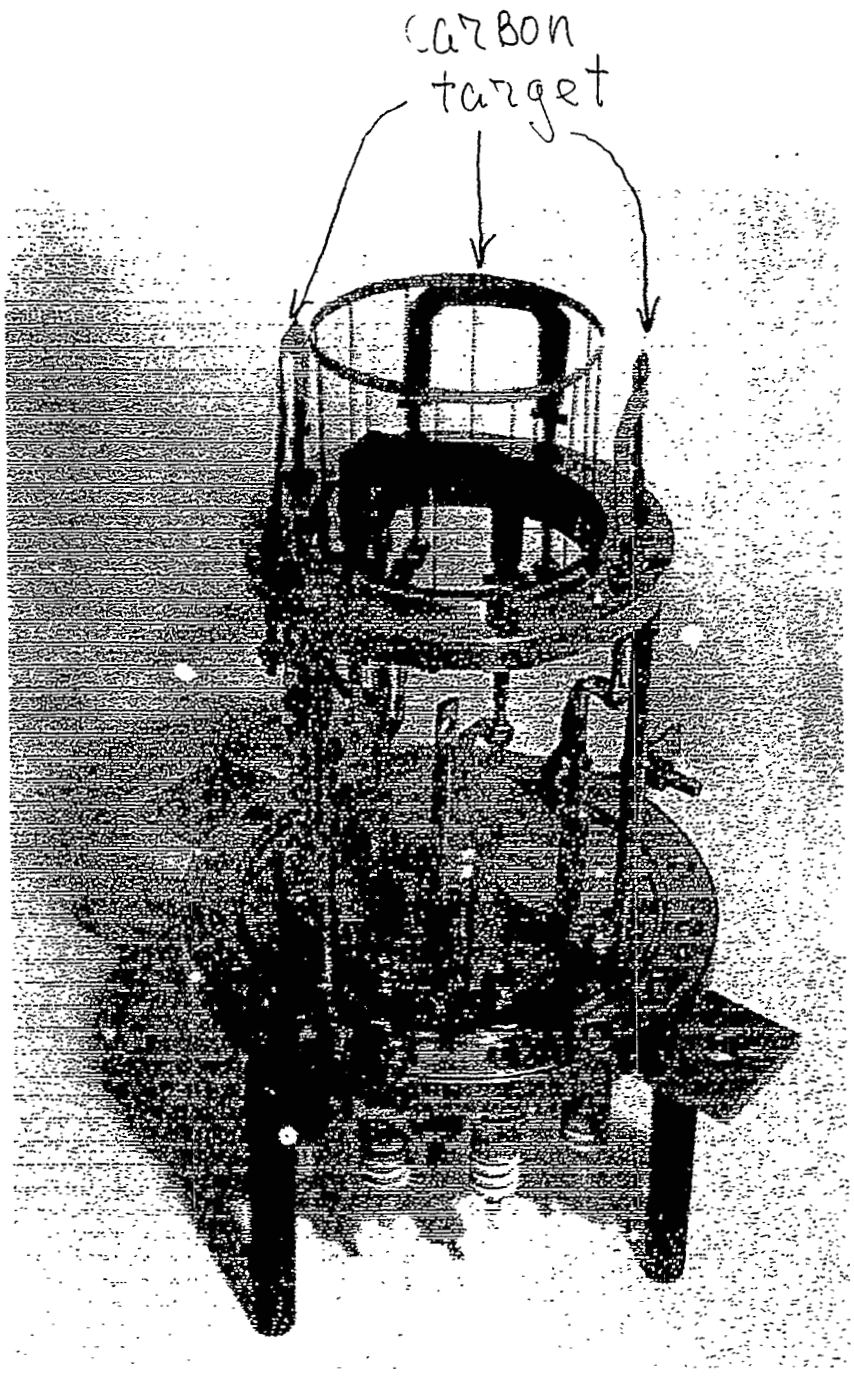

Fig. 4

Plasma generator anticathode, in assembly with the heated part of carbon target and with the anode, mounted at the lower flange of vacuum vessel. Electrical leads with flexible insertions connecting the carbon elements to the vacuum feedthroughs can be seen.

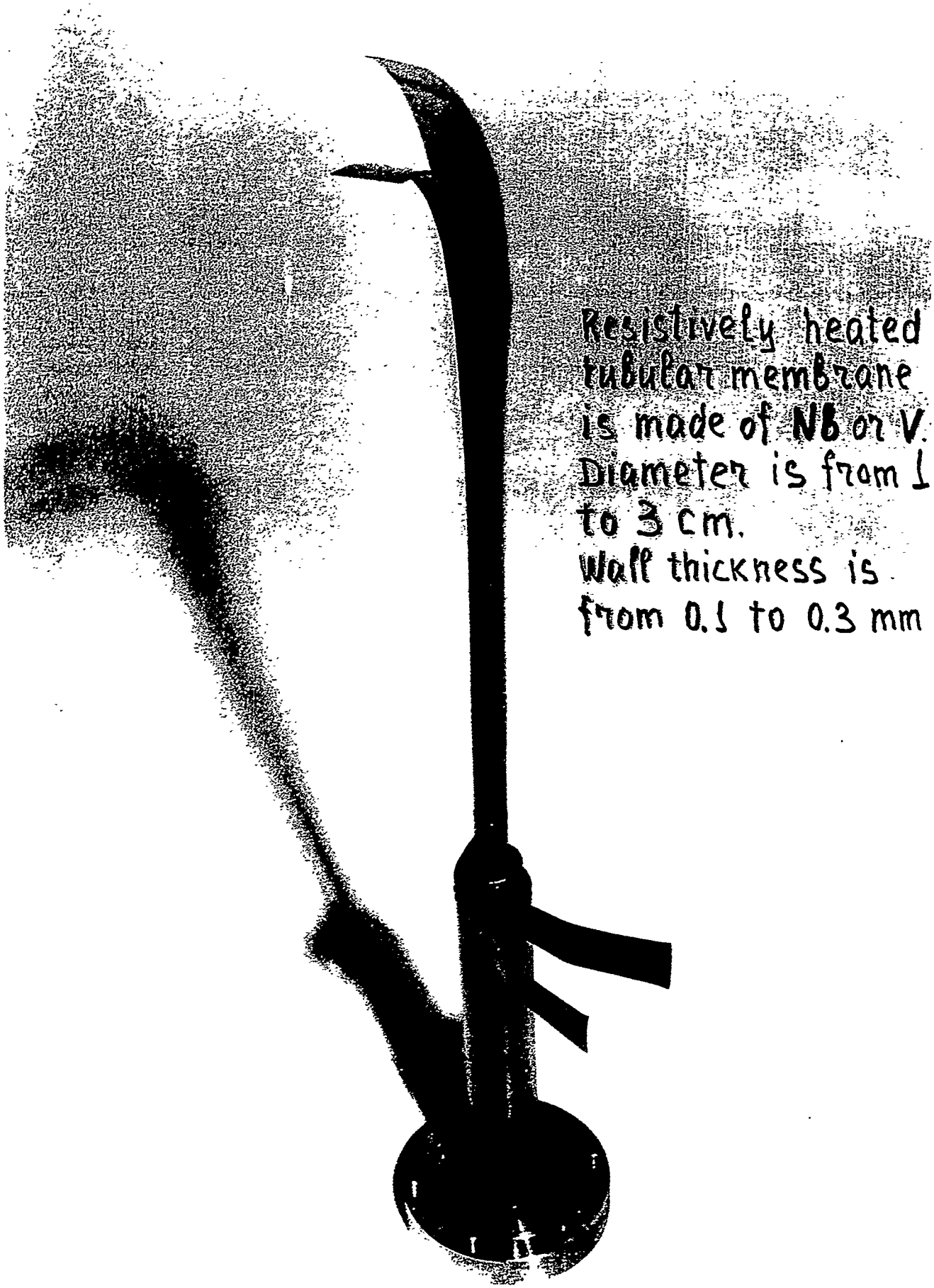
Resistively heated
tubular membrane
is made of Nb or V.
Diameter is from 1
to 3 cm.
Wall thickness is
from 0.1 to 0.3 mm

Temperature dependence of the rate of production of carbon-containing species

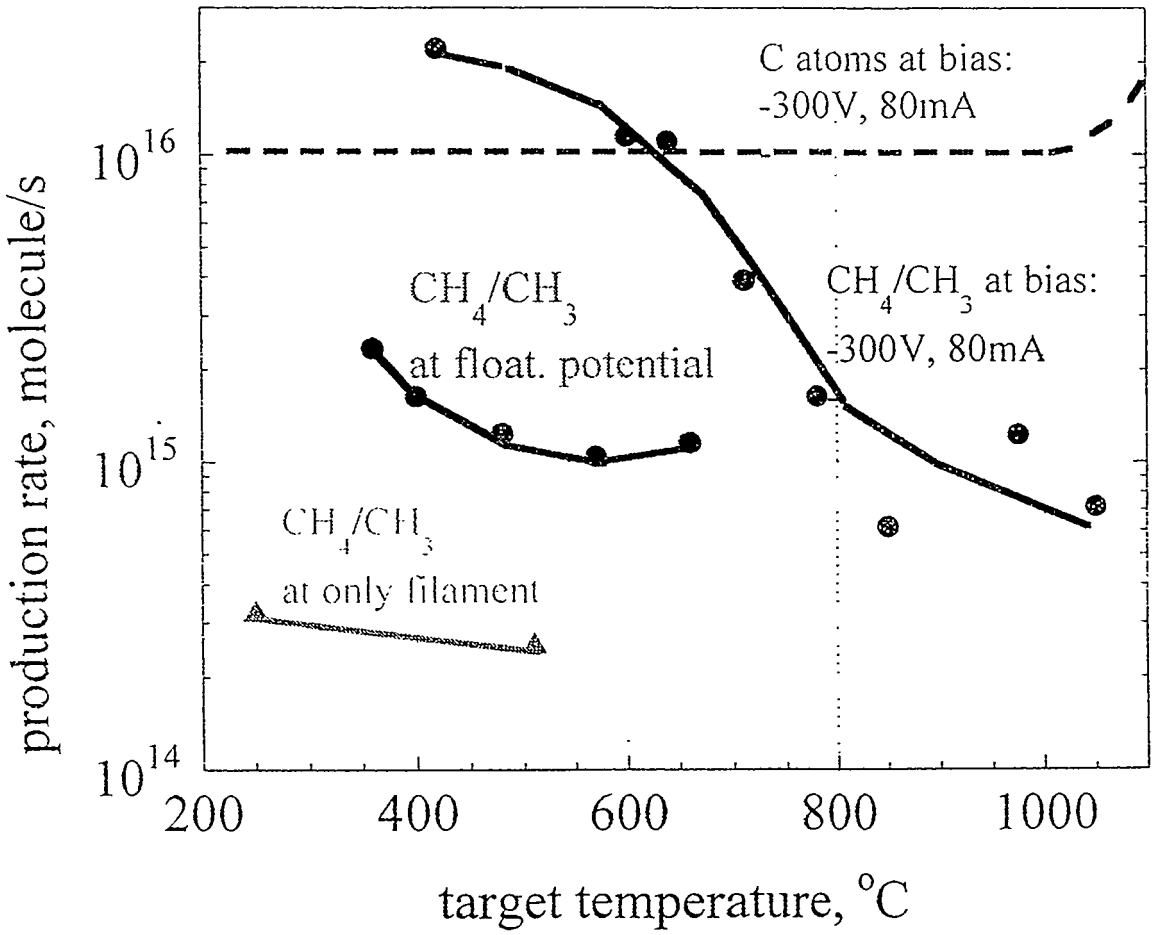

One can vary the fluxes of hydrocarbons and C atoms over wide ranges to give domination to ones or the others by means of controlling target bias and temperature.

Temperature dependence of permeation from the C contaminated H-plasma

(C flux is about $3x10^{12}Ccm^{-2}s^{-1}$)

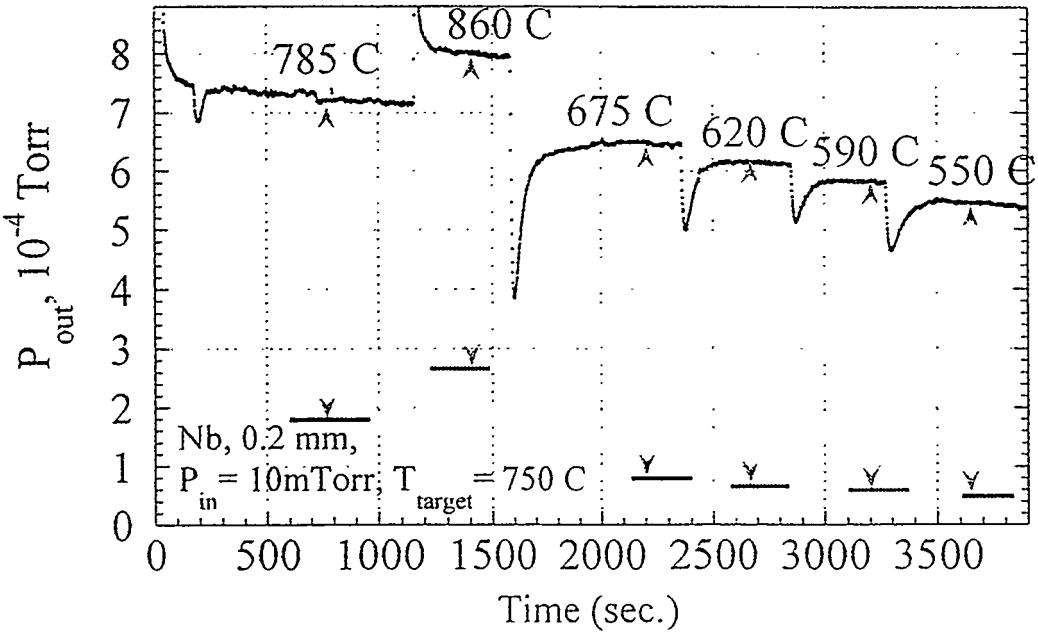

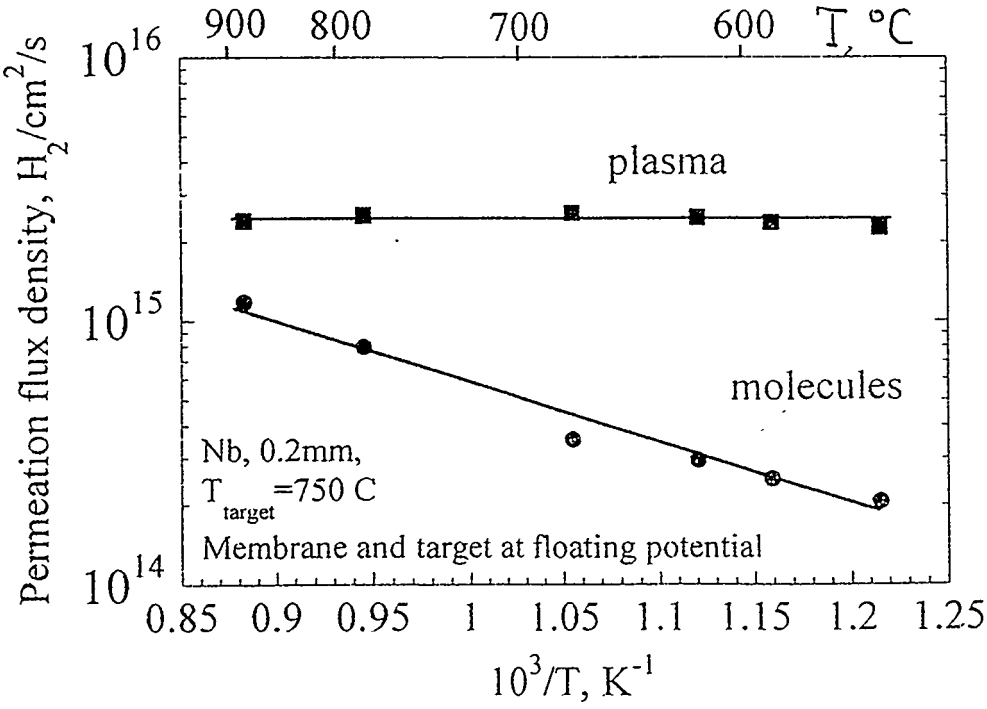

The role of carbides of the Group Va metals.

Although membrane biasing can remove C film, membrane heating at $T = 1000\text{-}1200\ ^{\circ}C$ was usually employed to restore the due state of superpermeable membrane after C deposition. Carbon will not be removed from the sample at such temperatures, and therefore it must be diffusing into bulk metal. Thousands of C monolayers are transported in this way inside metal during a typical experimental campaign to exist only in the form of carbide there (C solubility in Nb is negligible). In fact, a layer-by-layer AES analysis of extracted samples discovered a ~1 μm (!) near-surface NbC/Nb_2C layer. So one has to conclude that, unlike the modifications of pure C (graphite, a:C-films, diamond-like films), ***NbC (and perhaps VC, TaC as well) do not stop hydrogen transport in the superpermeation regime.*** Hence: (1) the surface barrier inhibiting hydrogen reemission keeps at Nb transformation into NbC (perhaps due to an oxicarbide monolayer), and, (2) a very low level of permeation barrier E_b inherent to Nb is conserved in NbC.

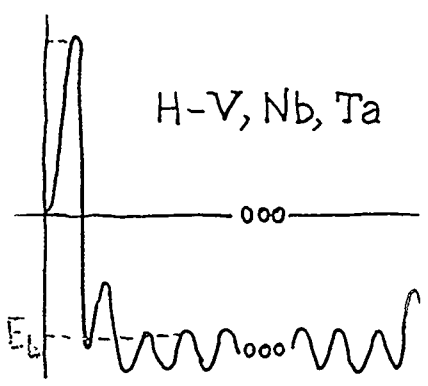

CONCLUSIONS

- Surface composition of PFM is responsible for the large scale effects on hydrogen absorption, permeation and reemission; these effects may be employed for the active particle control in fusion devices.
- There are sufficient physical grounds right now to employ the permeation technique for the short way separation of D/T and He and for the particle control in *high recycle* divertors.
- An employment of permeation/absorption technique in a *low recycle* divertor looks rather attractive but more problematic because of sputtering and possible deposition of carbon.
- It is experimentally shown that superpermeable membrane may keep its favorable asymmetry under the sputtering even under UHV conditions.
- It is experimentally demonstrated that at definite conditions superpermeable membrane may steadily operate under concurrent flows of suprathermal hydrogen and C.
- In contrast to modifications of pure C, NbC (VC, TaC) does not inhibit hydrogen trasport in the superpermeation regime.

Wall Pumping in LHD

H.Suzuki
National Institute for Fusion Science

Topics

Pumping System of the LHD

Devices

Basic Parameters

Results of 2nd Campaign

Analysis of typical shot (Shot 12550)

Conclusion

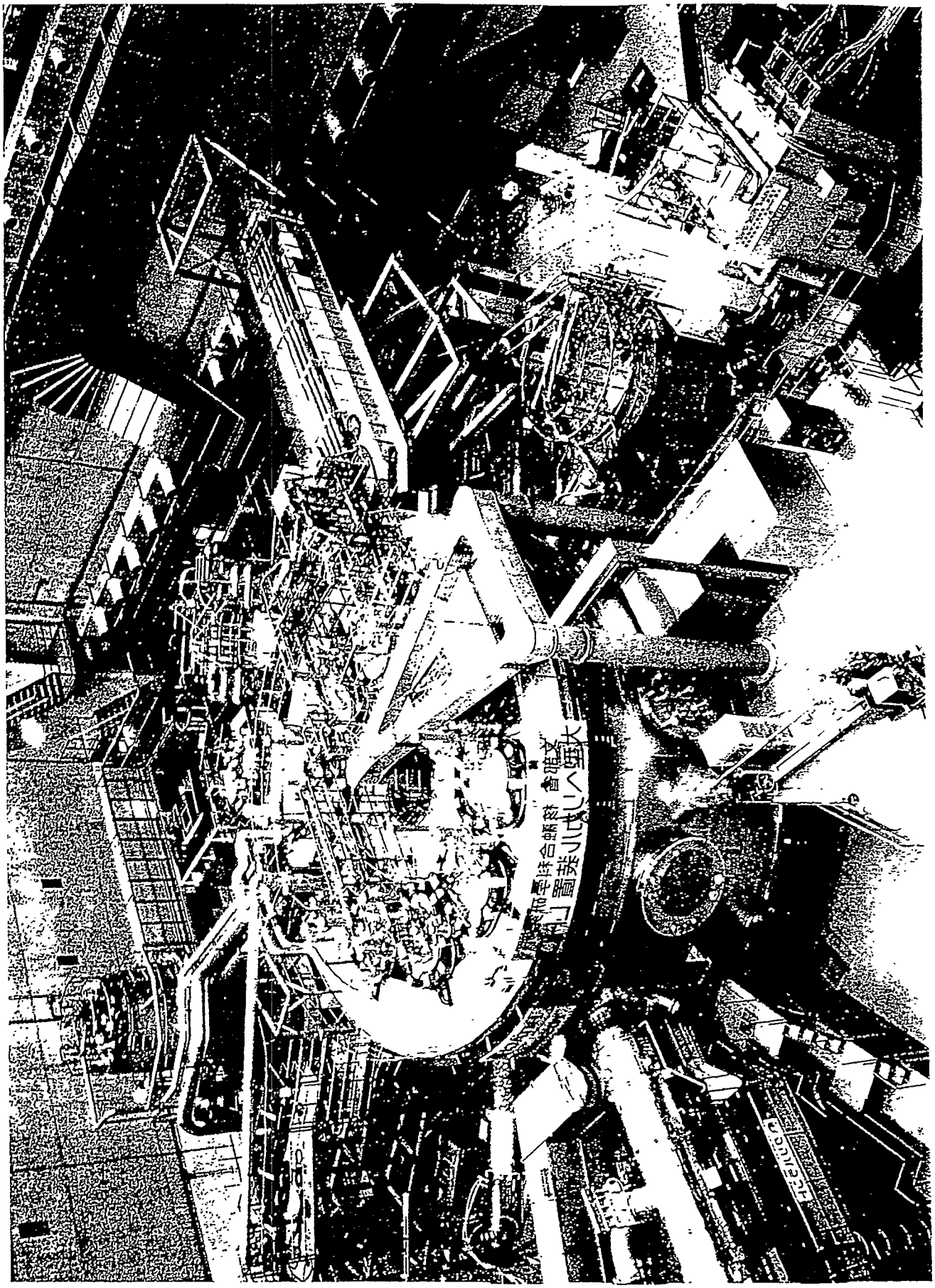
「国際学生合唱祭 合唱交流」
大阪センチュリーシンフォニー
HILTON

Vacuum Vessels

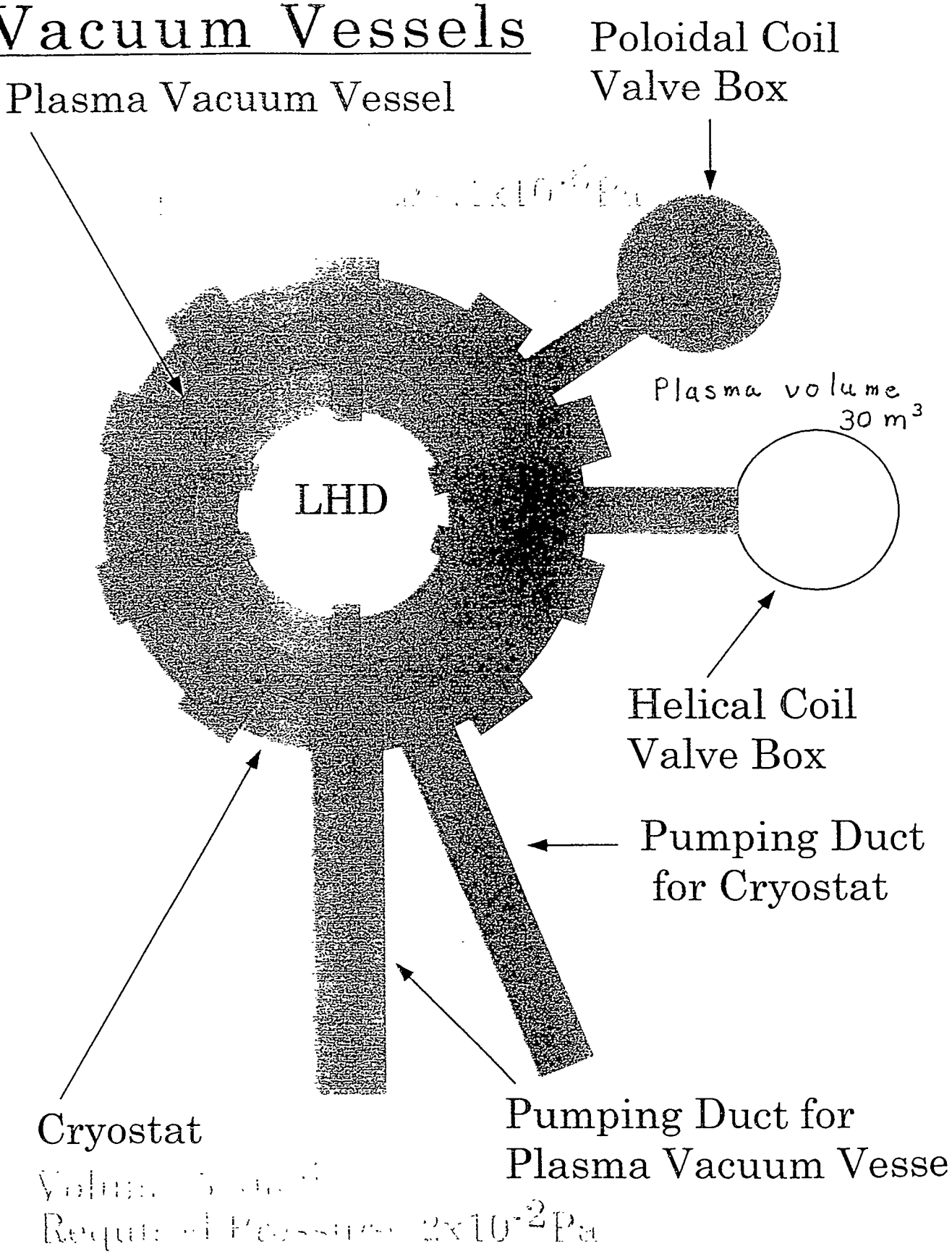

Measurement

for monitoring

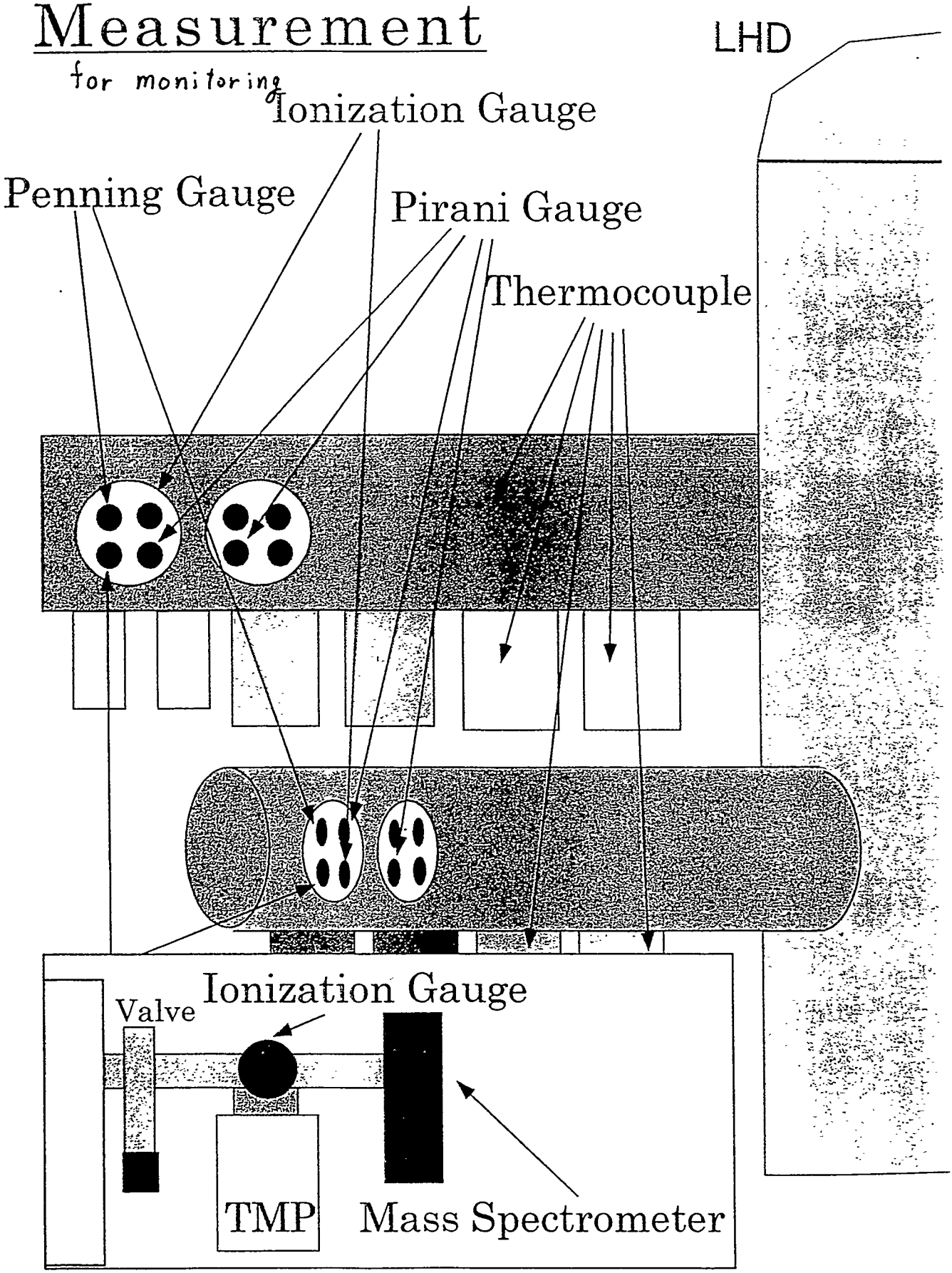

Pumps

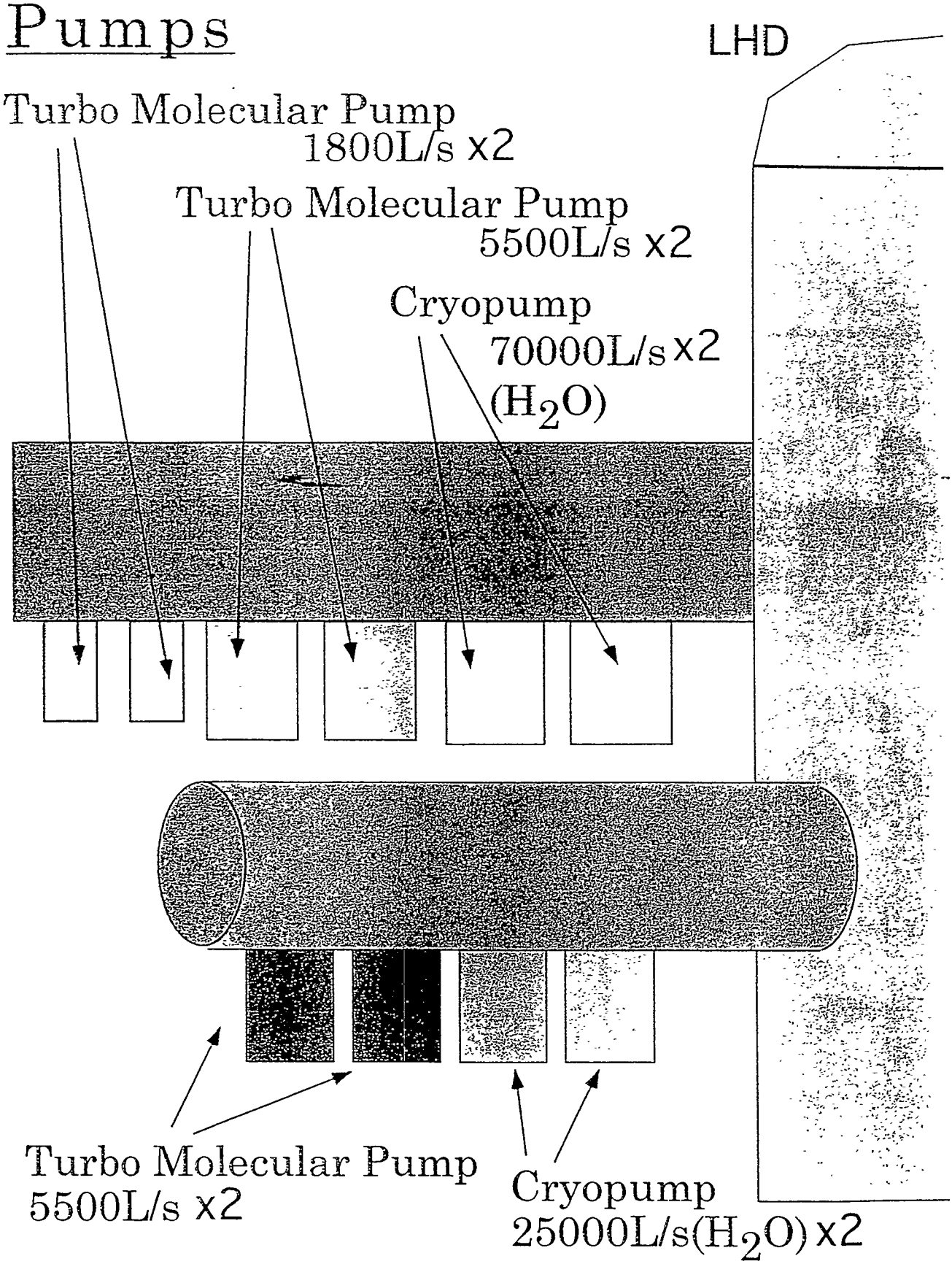
LHD
Turbo Molecular Pump
1800L/s x2
Turbo Molecular Pump
5500L/s x2
Cryopump
70000L/s x2
(H_2O)
Turbo Molecular Pump
5500L/s x2
Cryopump
25000L/s(H_2O) x2

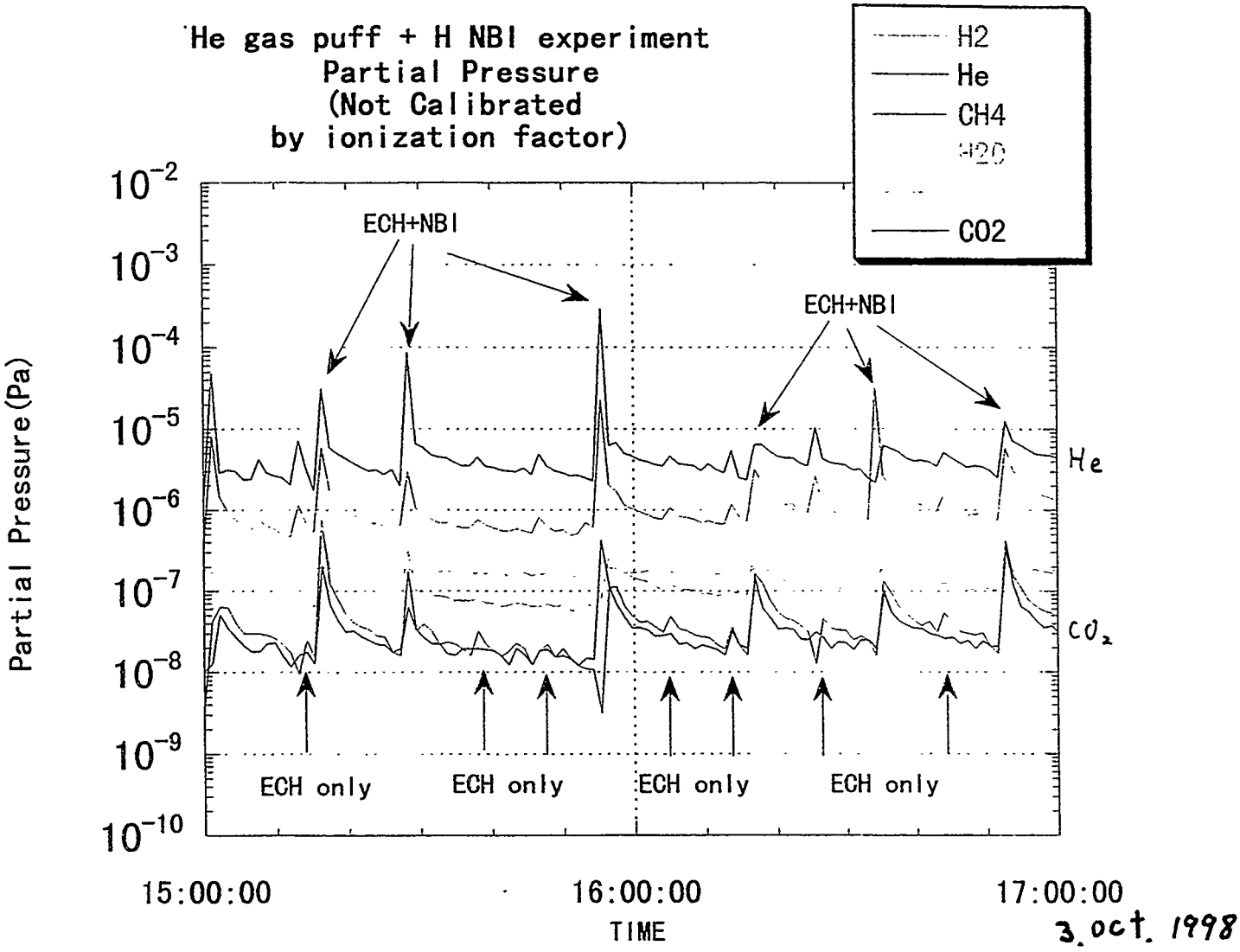

ECH 1 : 90 kw x 160 ms
ECH 2 : 140 kw x 200 ms
ECH 3 : 200 kw x 200 ms

NBI 1 : 1000 kw x 400 ms
NBI 2 : 670 kw x 150 ms

Devices

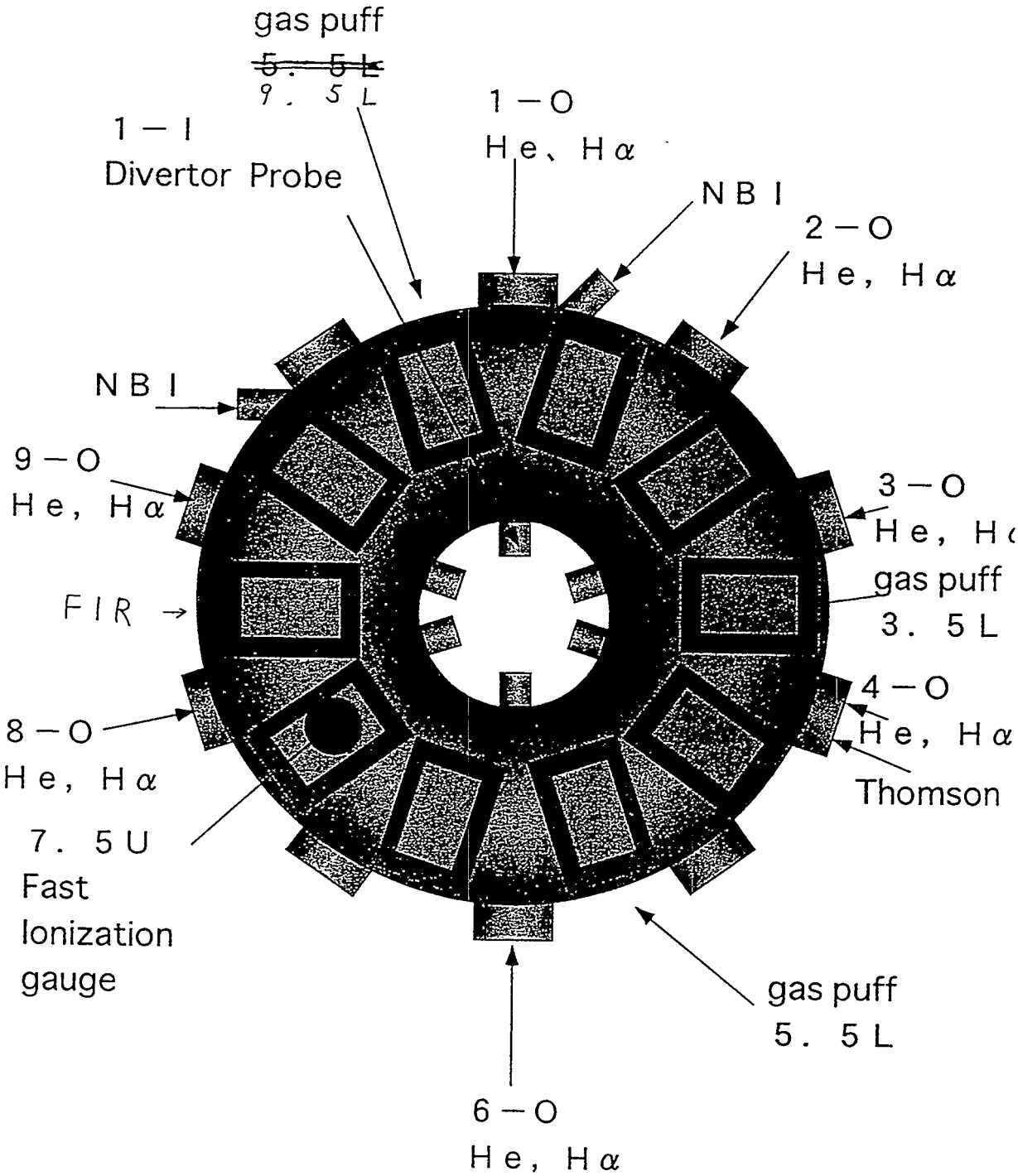

(LHD Top Viiew)

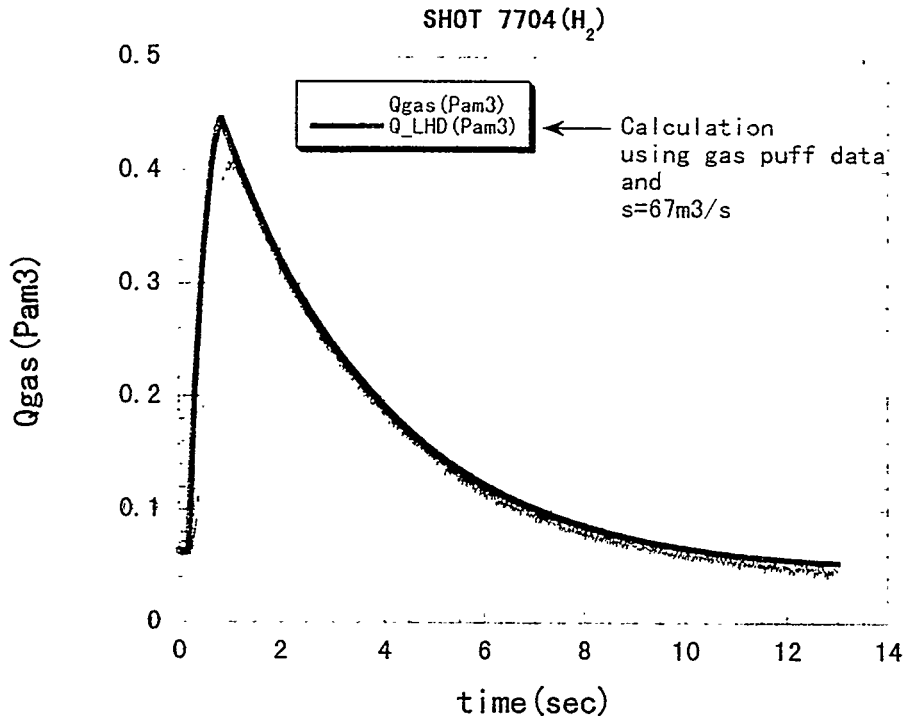
SHOT 7704 (H_2)
Qgas (Pam3)
Q_LHD (Pam3)
Calculation
using gas puff data
and
s=67m3/s
Qgas (Pam3)
time (sec)
0.5
0.4
0.3
0.2
0.1
0
0
2
4
6
8
10
12
14

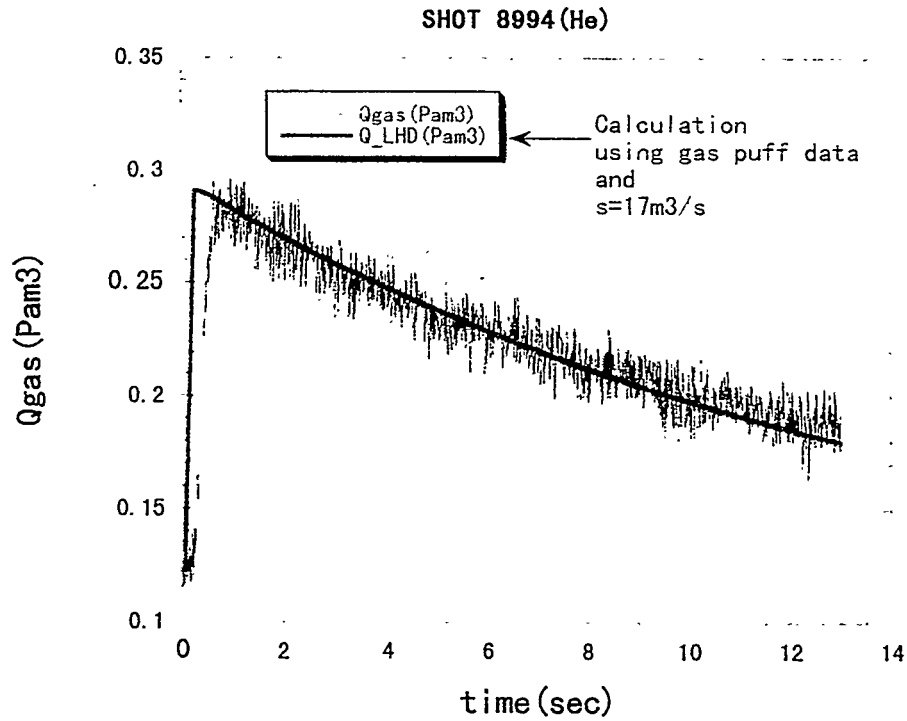
SHOT 8994 (He)
Qgas (Pam3)
Q_LHD (Pam3)
Calculation
using gas puff data
and
s=17m3/s
Qgas (Pam3)
time (sec)
0.35
0.3
0.25
0.2
0.15
0.1
0
2
4
6
8
10
12
14

Basic Parameters

Plasma Vacuum Vessel Volume : 210m^3

Plasma Vacuum Vessel Surface Area : 730 m^2
(Stainless Steel)

NBI Armor Tile area: 1.5m^2 x 2
(Carbon)

Divertor Plate area: 30m^2 (1680 tiles, 1000kg)
(Carbon) (3rd campaign)

Plasma volume 30m^3

Puff Piezo Valve : 5Pam^3/s, 50Pam^3/s, 100Pam^3/s

Effective Pumping Speed

66.7m3/s (hydrogen gas)
16.7m3/s (helium gas)

Mixture gas

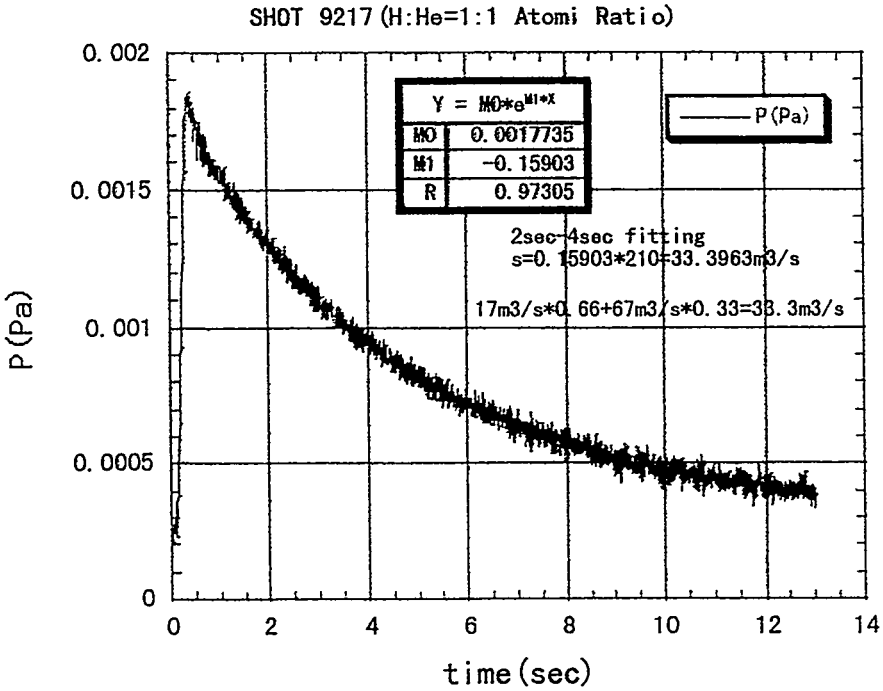

Atomic ratio
Hydragen atom; Helium Atom=1:1

Molecular ratio
Hydragen atom; Helium Atom=1:2

S=33.3963m^3/s (fitting)

67m^3/s*0.33+17m^3/s*0.~~33~~=33.3m^3/s
66

Ti Getter

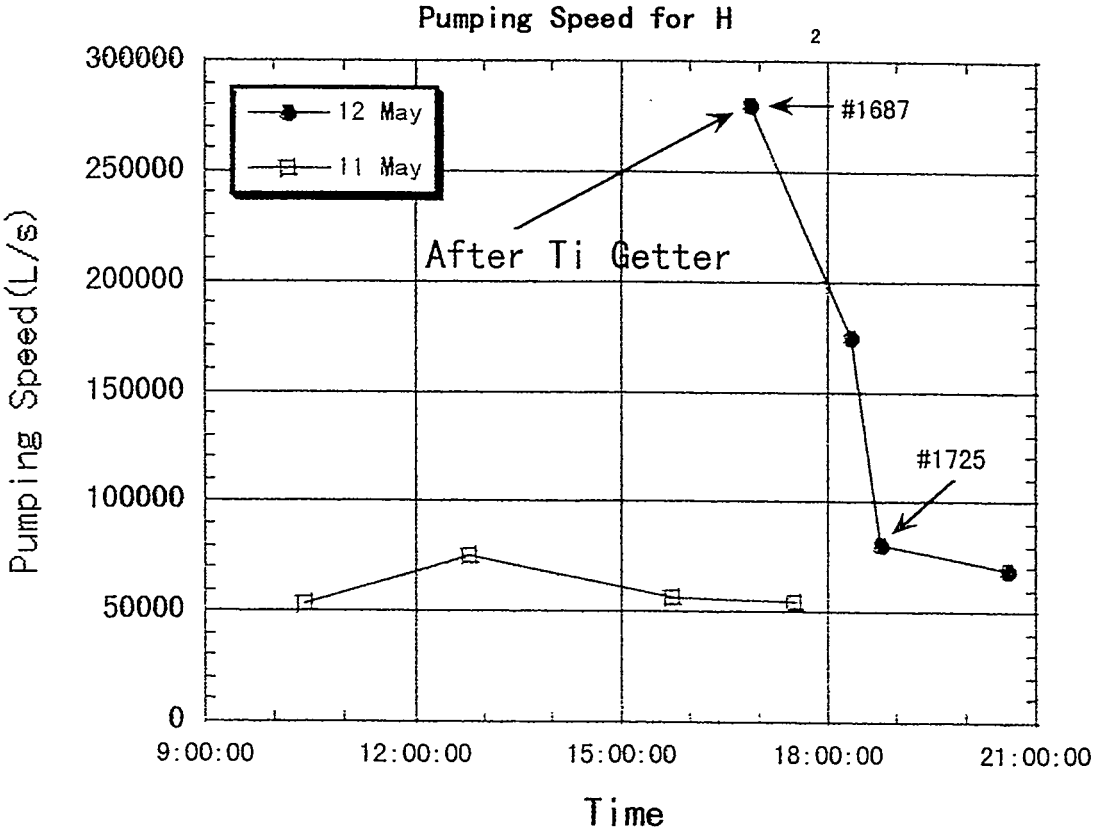

After Ti gettering, 280000L/s of pumping speed has been observed. But, effect of Ti getter for pumping hydrogen gas has decreased soon.

H_2 shot

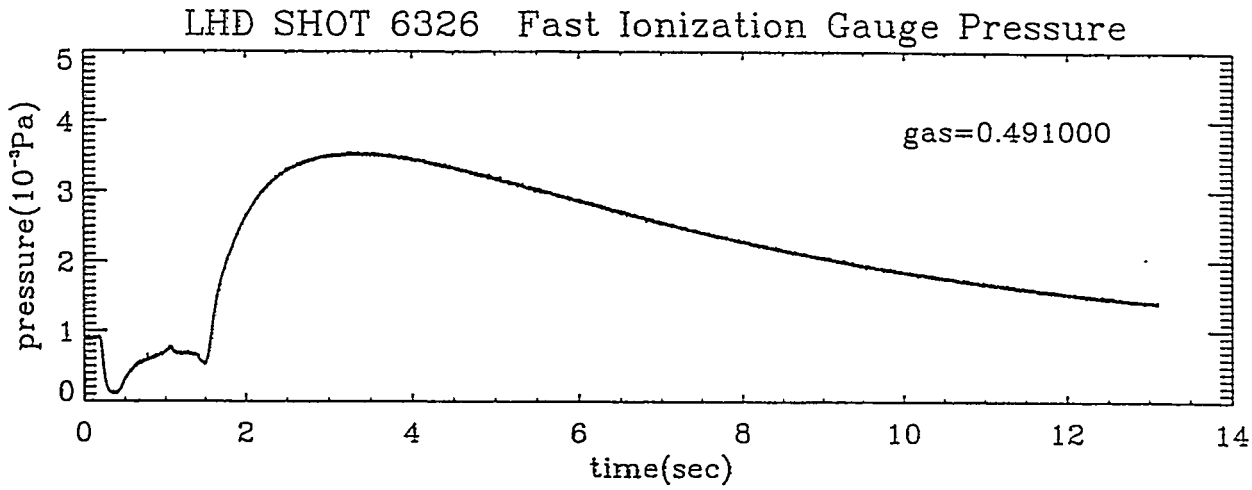
LHD SHOT 6326 Fast Ionization Gauge Pressure
gas=0.491000
pressure(10^{-3}Pa)
time(sec)

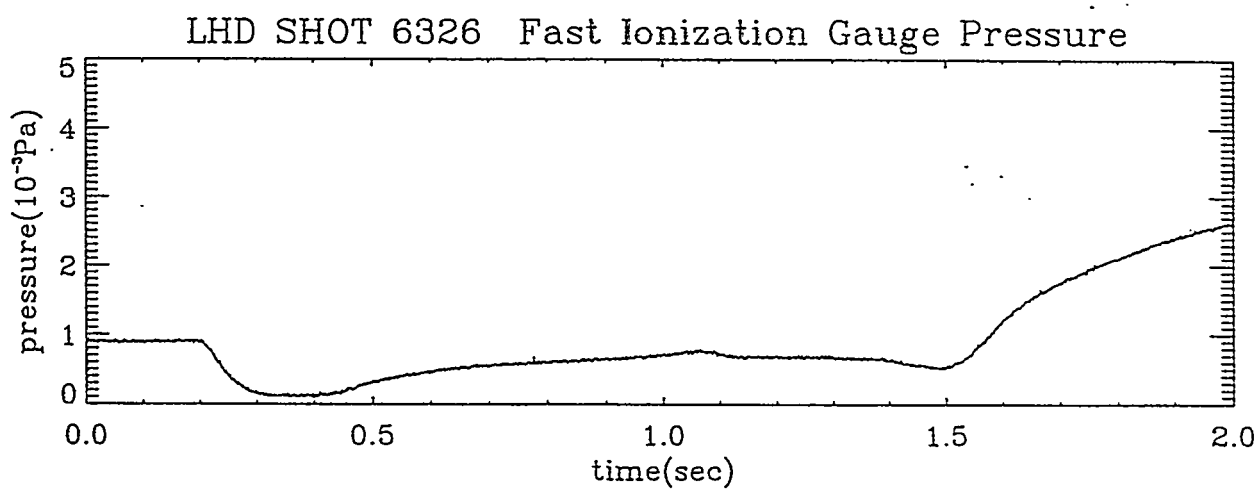
LHD SHOT 6326 Fast Ionization Gauge Pressure
pressure(10^{-3}Pa)
time(sec)

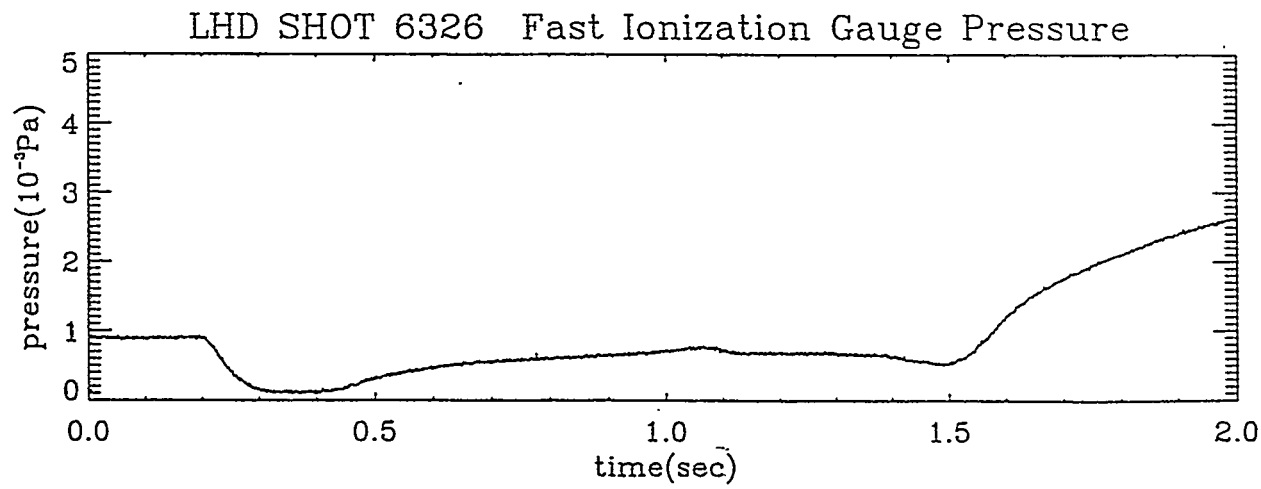
LHD SHOT 6326 Fast Ionization Gauge Pressure
pressure(10^{-3}Pa)
time(sec)

He shot

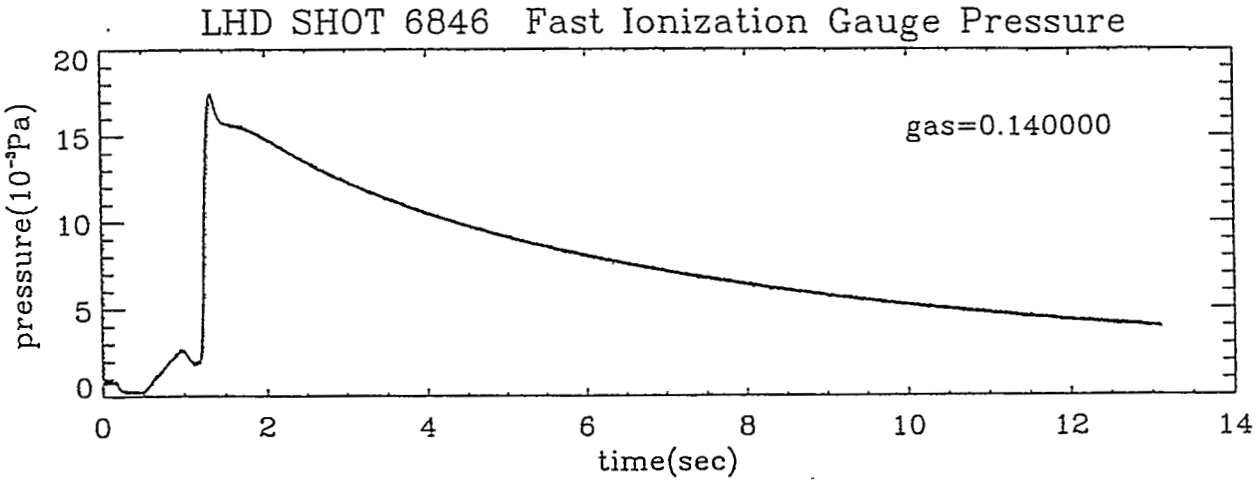
LHD SHOT 6846 Fast Ionization Gauge Pressure
gas=0.140000
pressure(10^{-3}Pa)
time(sec)
0
5
10
15
20
0
2
4
6
8
10
12
14

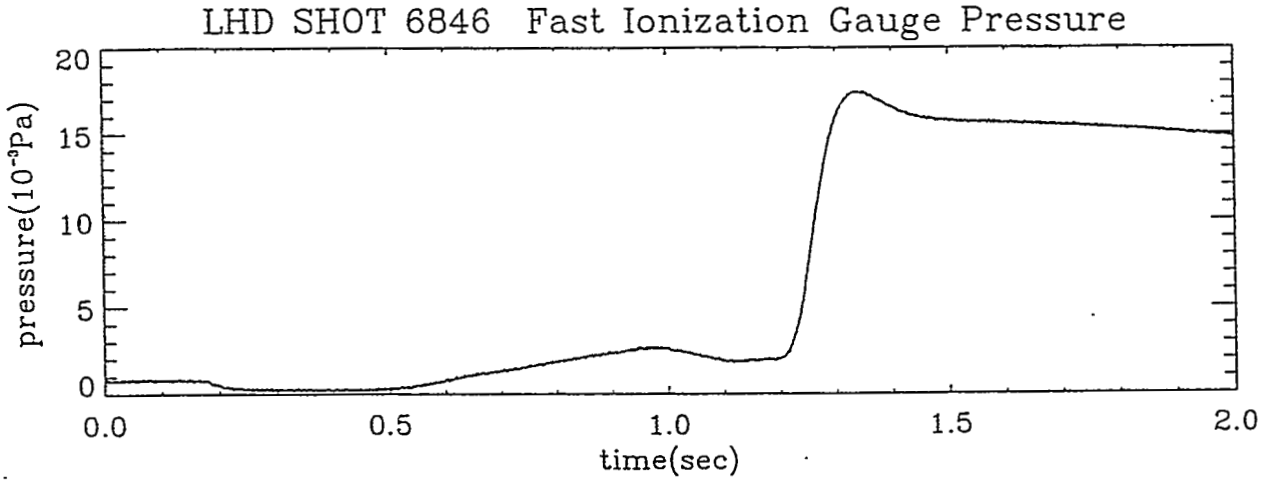
LHD SHOT 6846 Fast Ionization Gauge Pressure
pressure(10^{-3}Pa)
time(sec)
0
5
10
15
20
0.0
0.5
1.0
1.5
2.0

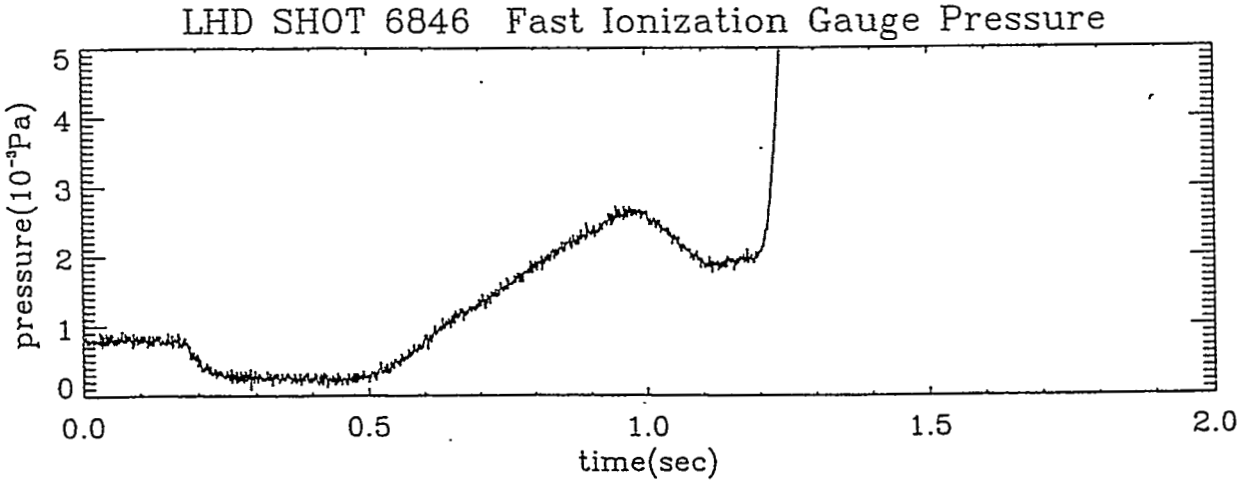
LHD SHOT 6846 Fast Ionization Gauge Pressure
pressure(10^{-3}Pa)
time(sec)
0
1
2
3
4
5
0.0
0.5
1.0
1.5
2.0

Same gas puff condition

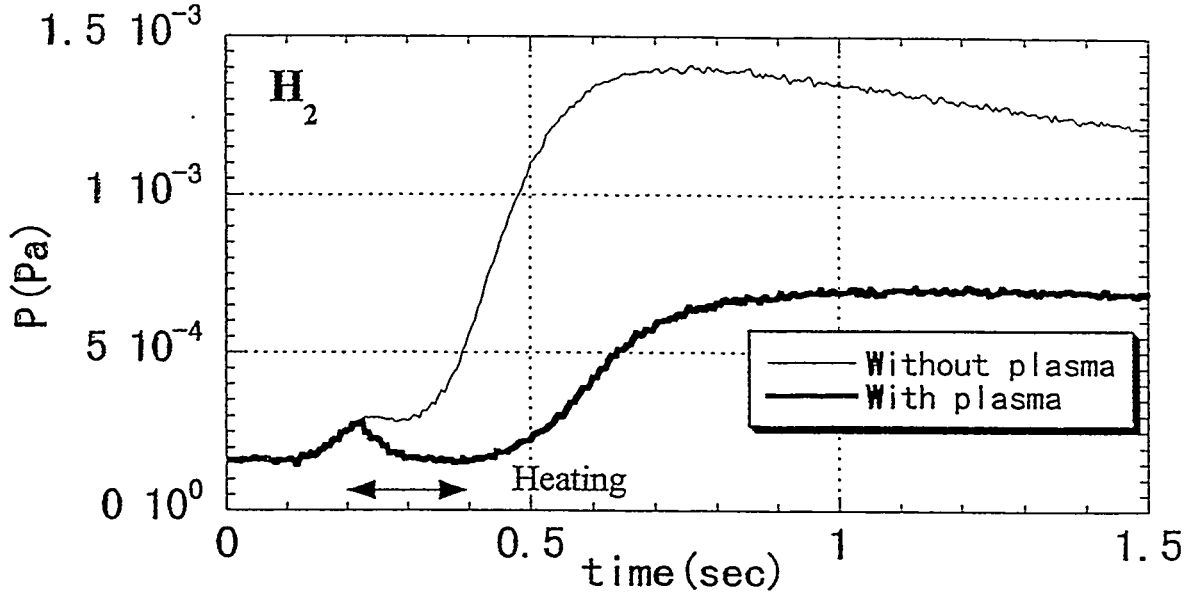

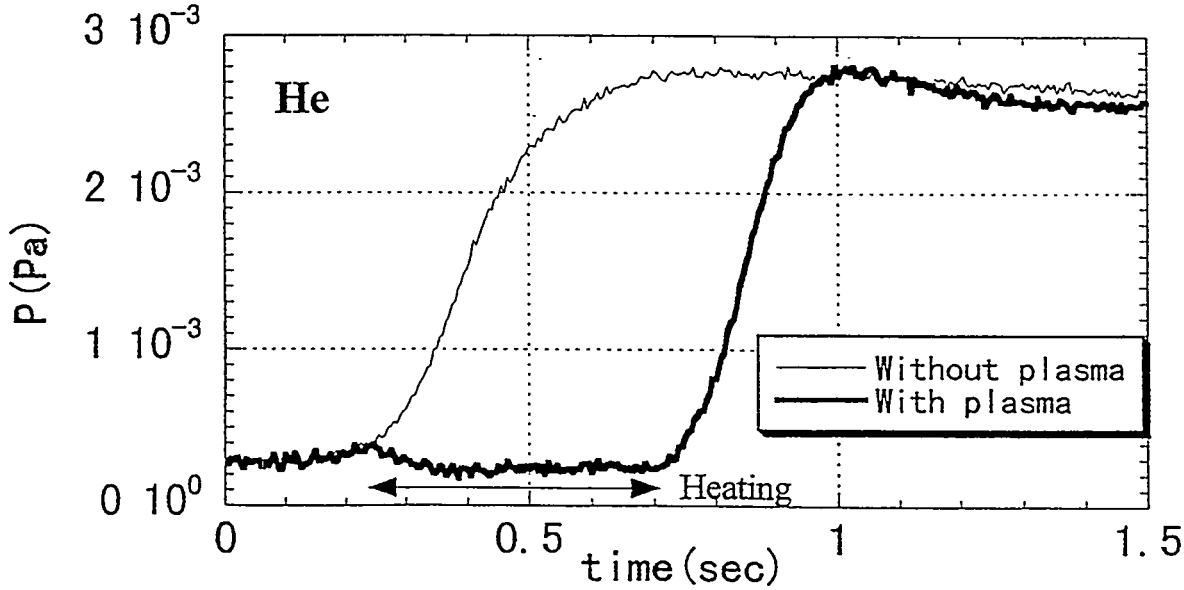

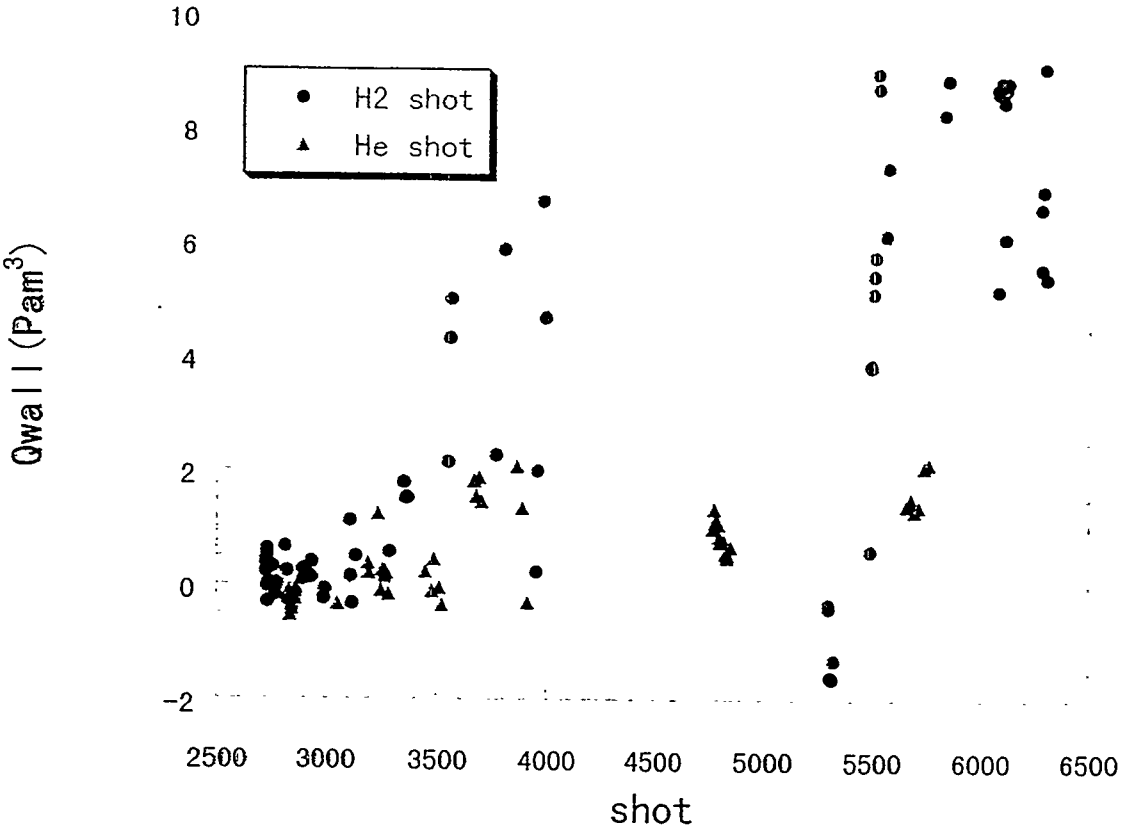
H2 shot
He shot
Qwall (Pam3)
shot
10
8
6
4
2
0
-2
2500
3000
3500
4000
4500
5000
5500
6000
6500

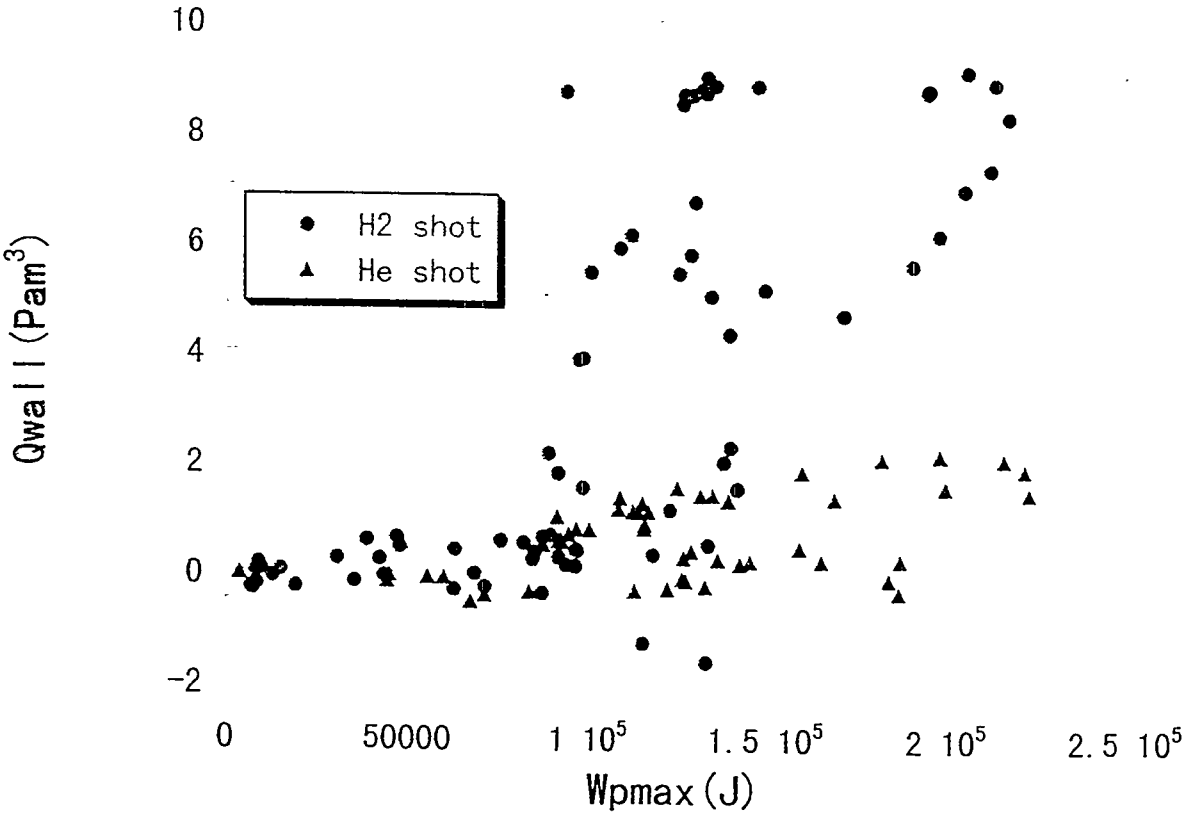
H2 shot
He shot
Qwall (Pam3)
Wpmax (J)
10
8
6
4
2
0
-2
0
50000
1 10^5
1.5 10^5
2 10^5
2.5 10^5

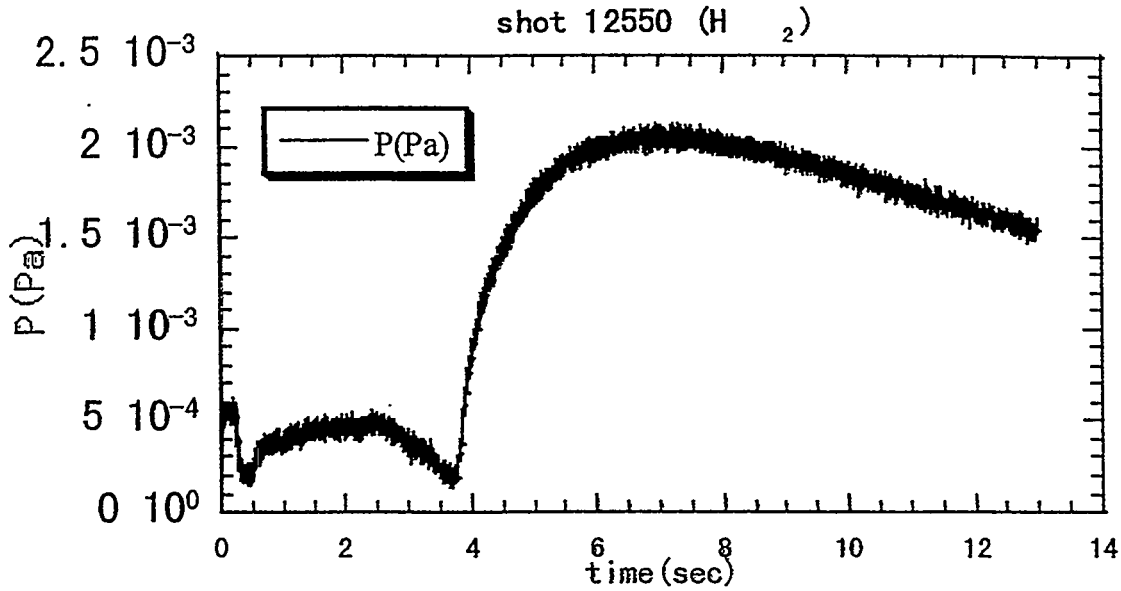

$$Q_{LHD} = \int_0^{\tau} Q_{in} - Ps\, dt$$

$$Q_{gas} = P * V_{vessel}$$

$$Q_{plasma} = nl / l * V_{plasma}$$

K12550

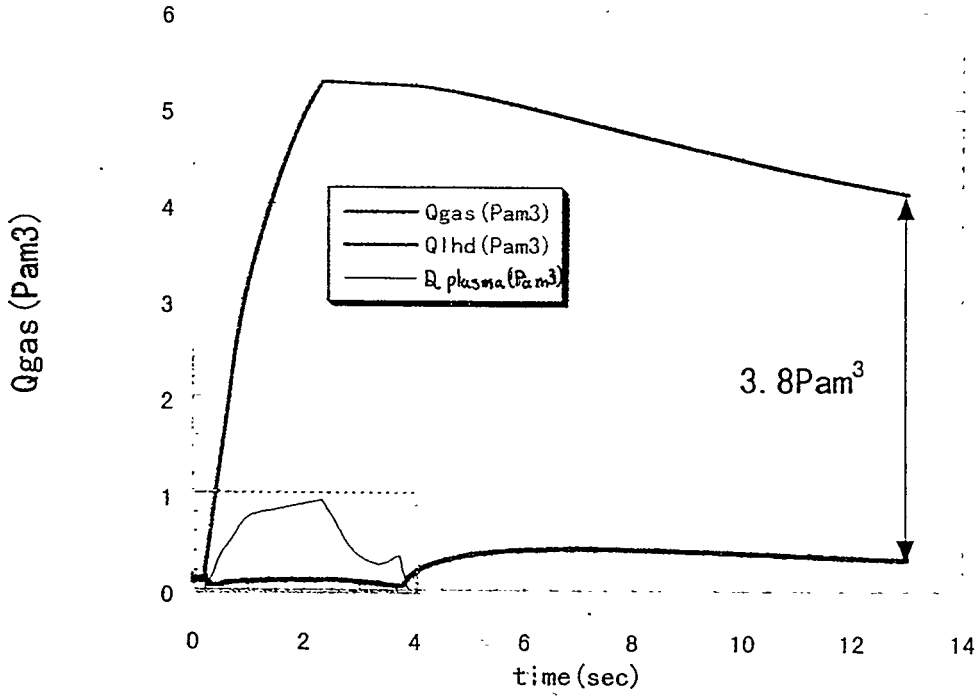

$\frac{3.8\ Pa \cdot m^3}{4\ s}$

$\sim 1\ Pa \cdot m^3/s$

$1/10^{-3}\ Pa\ m^3$

$\sim 1000\ Pa\ m^3/s$

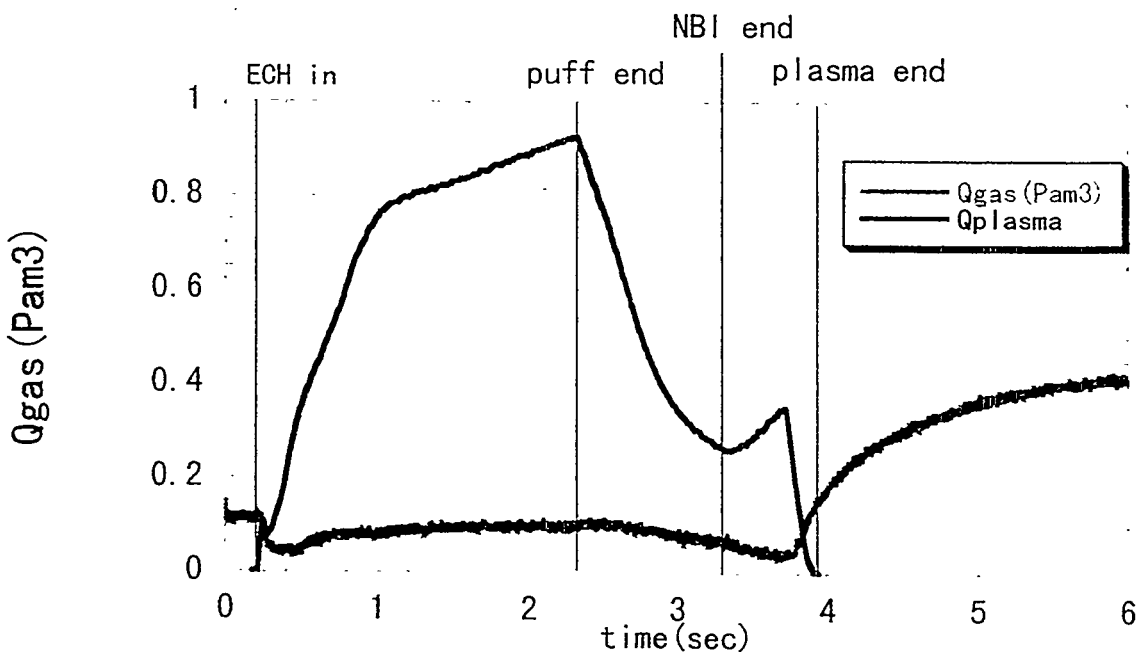

$69\ m^3/s$

(H_2)

$$N_{total} = N_{gas} + N_{wall}$$

$$\Gamma_{wall\_in} = vnSA = v\frac{N_{gas}}{V}SA$$

v : thermal velocity
S : sticking parameter
A : area
V : volume

$$\Gamma_{wall\_out} = \alpha N_{wall} = \frac{N_{wall}}{\tau}$$

$$\frac{dN_{gas}}{dt} = \Gamma_{wall\_out} - \Gamma_{wall\_in}$$
$$= \frac{N_{total}}{\tau} - \left(\frac{1}{\tau} + \frac{vSA}{V}\right)N_{gas}$$

Ntotal=const.

$$N_{gas}(t) = N_{gas}(t=\infty) + \left(N_{gas}(t=0) - N_{gas}(t=\infty)\right)e^{-\frac{N_{total}}{N_{gas}(t=\infty)\tau}t}$$

Ntotal=qt

$$N_{gas} = \frac{qVt}{V+\tau vSA} - \frac{q\tau V^2}{\left(V+\tau vSA\right)^2} + \frac{q\tau V^2}{\left(V+\tau vSA\right)^2}e^{-\frac{V+\tau vSA}{\tau V}t}$$

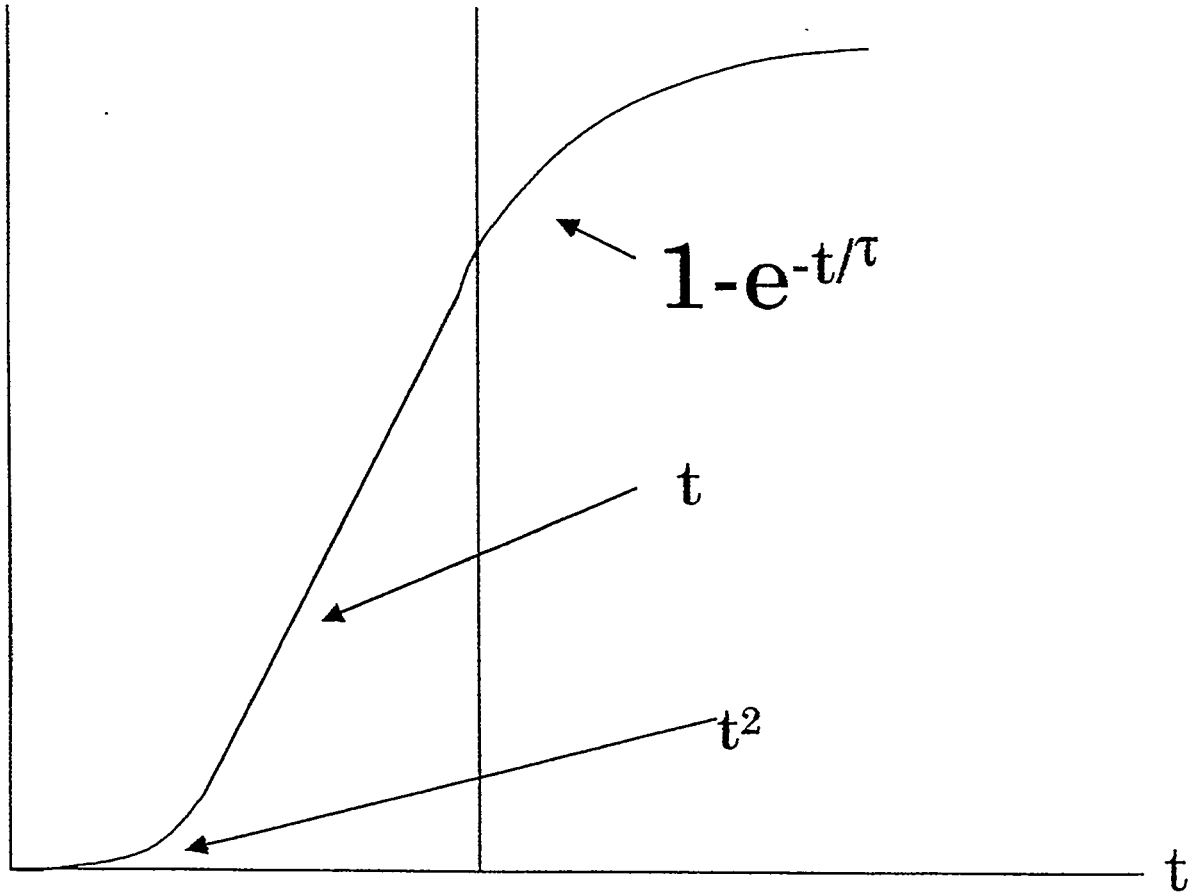

Puff off

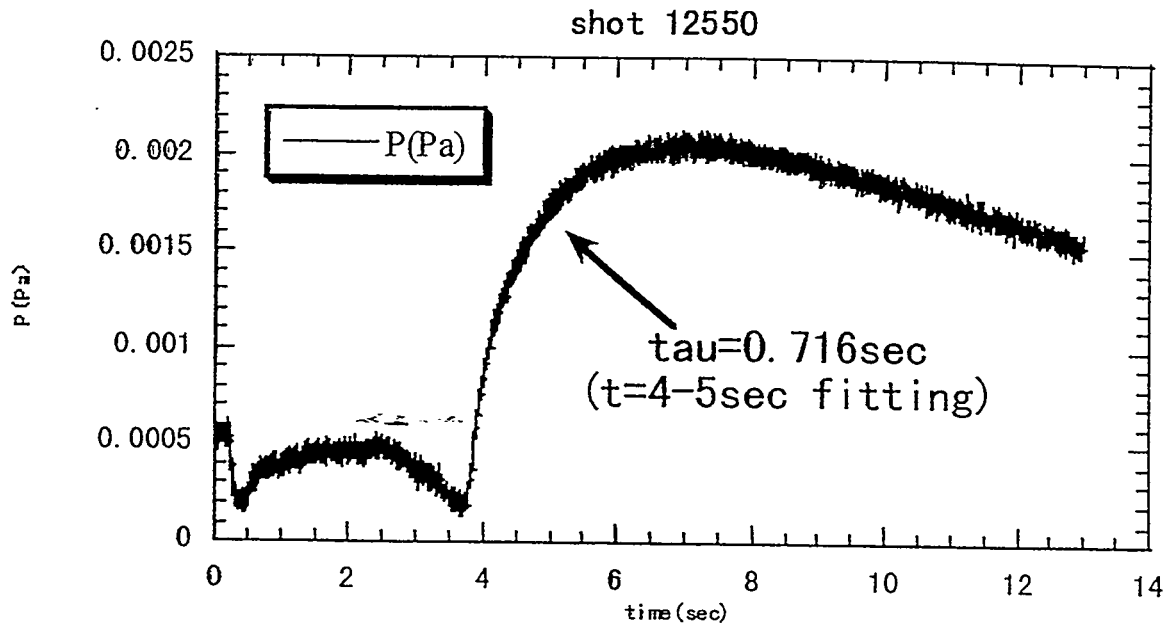

Simple absorption on a surface

$$\frac{1}{\tau} = \frac{1}{\tau_0}\exp\left(-\frac{E}{RT}\right)$$

τ_0 : frequency of thermal oscillation, 1e-13sec

E: 6300J/mol(H_2 case)

T : 300K

τ=1.2e-12 sec

NOT simple absorption on the surface.

Implantation and diffusion determine the time constant

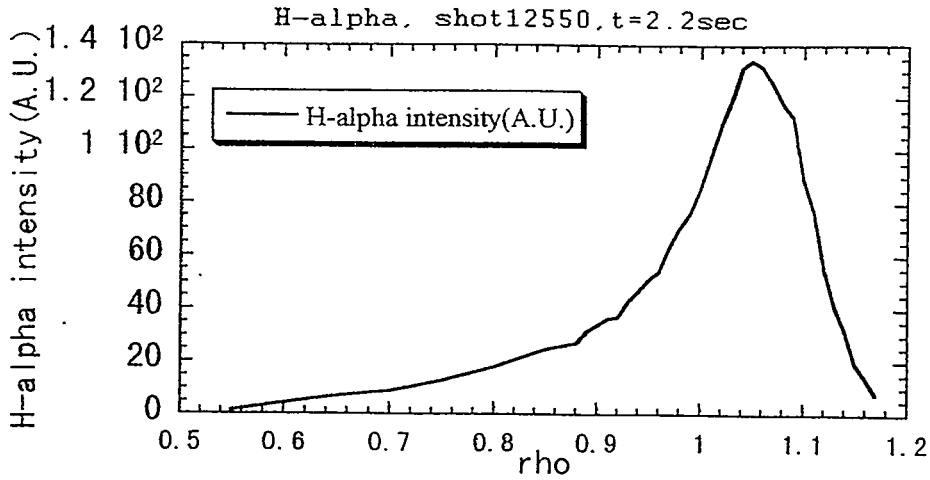
H-alpha, shot12550, t=2.2sec
H-alpha intensity(A.U.)
H-alpha intensity(A.U.)
rho

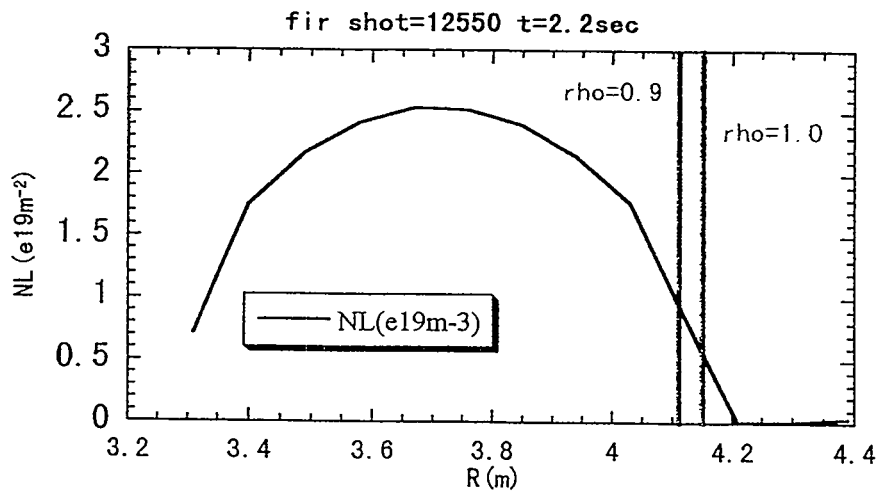
fir shot=12550 t=2.2sec
rho=0.9
rho=1.0
NL(e19m-3)
NL(e19m-2)
R(m)

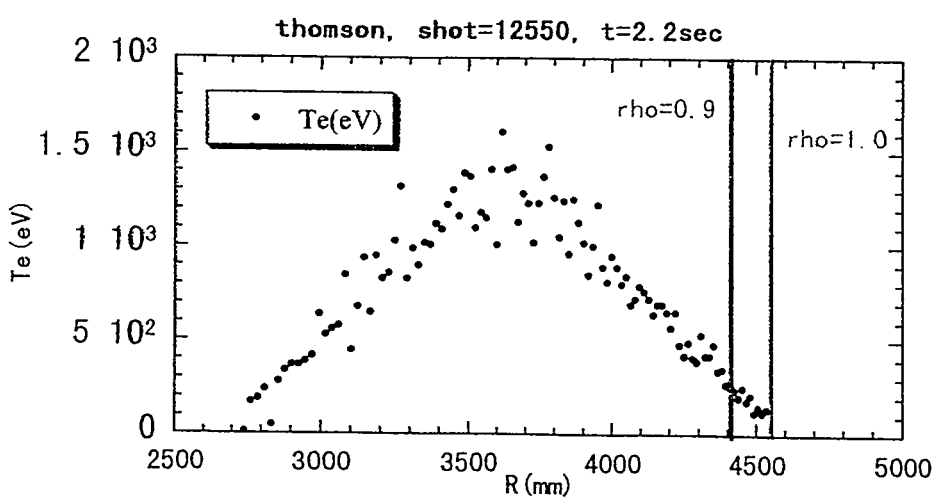
thomson, shot=12550, t=2.2sec
Te(eV)
rho=0.9
rho=1.0
Te(eV)
R(mm)

Conclusion

1) Neutral gas pressure has been measured by FIG.

2) Using particle balance, wall pumping effect has been observed in hydrogen plasma experiments.

3) In helium plasma experiments, wall pumping effect is none or very few.

4) In most hydrogen plasma discharge case, more than a half of input hydrogen atoms have been implanted in the wall.

5) A part of implanted hydrogen atoms have released with a time constant of 0.5-1 sec. However, most of implanted hydrogen atoms have stay in the wall.

Investigation of plasma-liquid surface interactions in PISCES-B

presented by:
R. Doerner

For the PISCES-B Materials Research Group:
R. P. Doerner, D.G. Whyte, R. W. Conn, A. A. Grossman, S. C. Luckhardt, R. Seraydarian, and F. C. Sze

US-Japan Workshop on Plasma-Surface Interactions and High-Heat Flux Components for Next Fusion Devices,
Santa Fe, New Mexico,
Nov. 1-5, 1999.

UC SanDiego

PISCES (Plasma-Interaction with Surface Component Station)

- Linear plasma device dedicated to PMI studies.
- Steady-state plasma conditions.
- Complete impurity and plasma diagnostics.
- Plasma impurity control.

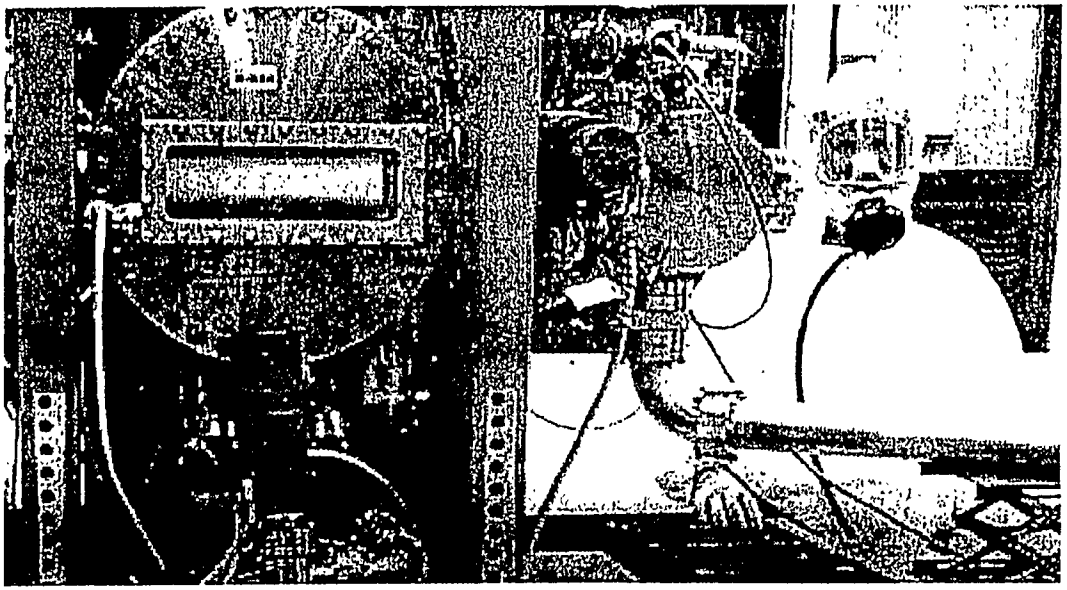

Measurements during PISCES plasma exposures include several cross-checks of diagnostics which increases the level of confidence in the results.

- erosion determined by weight loss, absolutely calibrated optical line emission and residual gas mass spectrometry

- plasma parameters measured with reciprocating Langmuir probe, sample bias current and optical spectroscopy

- impurity concentration by optical spectroscopy, mass spectrometry and post-exposure surface analysis (AES, SIMS, XPS)

- optical measurements of neutral e-folding length and Doppler shifts of eroded material verify calculations of redeposition fraction

- sample temperature measured with IR pyrometers and thermocouples

UC SanDiego

Several benefits are available from flowing walls.

- can accommodate high power loads
- wall becomes self-healing
- ability to easily recover from off-normal events
- tritium accumulation in wall material is minimized
- may be able to control recycling from wall material

Two liquid materials have been investigated in PISCES-B.

Lithium and Gallium

UC San Diego

There are several important scientific reasons for investigating the plasma interaction behavior of lithium*.

- melting point of Li (180°C) enables the study of the solid to liquid transition
- high vapor pressure allows investigation of evaporation vs. sputtering phenomena
- Li is easily diagnosed in the plasma and has a large database in plasmas
- non-recycling behavior of D on Li modifies boundary conditions and alters plasma solutions (i.e. high edge plasma temperature, TFTR?)
- secondary-ion yield may approach unity for alkaline metals (i.e. negligible erosion)
- useful to understand 'pure' Li interactions with plasma before moving on to study Li alloys interaction with plasma

* even if a different material choice is ultimately made for a power plant

UC SanDiego

Sputtered ions cannot escape the material surface due to the plasma sheath and will, therefore, not contribute to erosion.

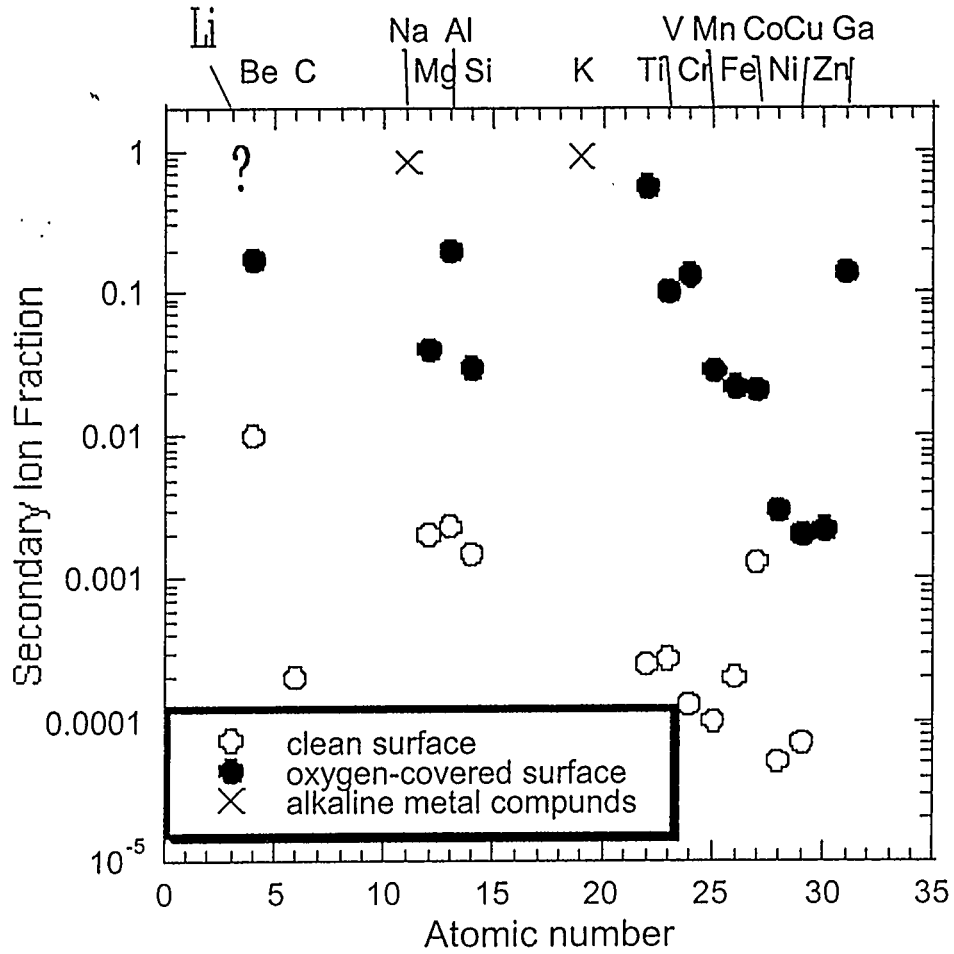

Data taken from A.R. Krauss and D.M. Gruen, JNM 85&86 (1979) 1179.

UC SanDiego

Temperature dependence of surface binding energy [Guggenheim model] causes increased physical sputtering at high temperature as predicted by TRIM.SP

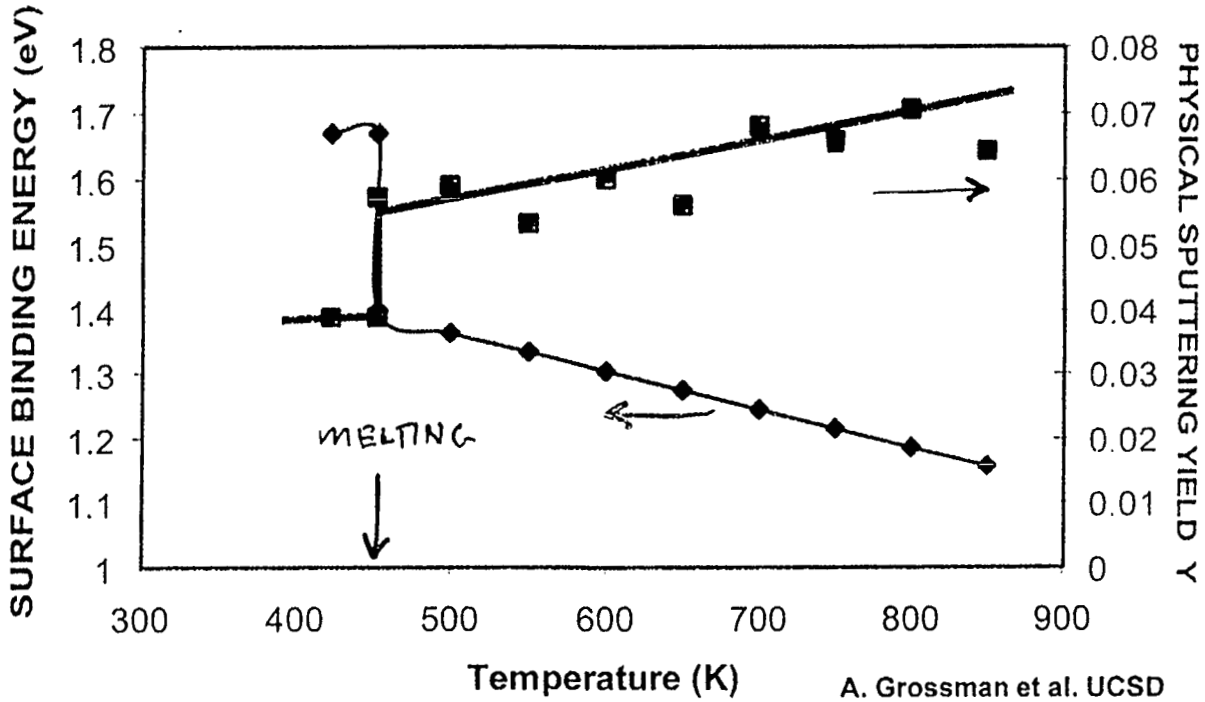

A. Grossman et al. UCSD

Lithium samples are prepared and transported in an argon atmosphere and installed with an argon purge of PISCES-B. Before plasma exposure samples still contain a lithium-oxide surface. AES shows lithium samples after exposure are clean.

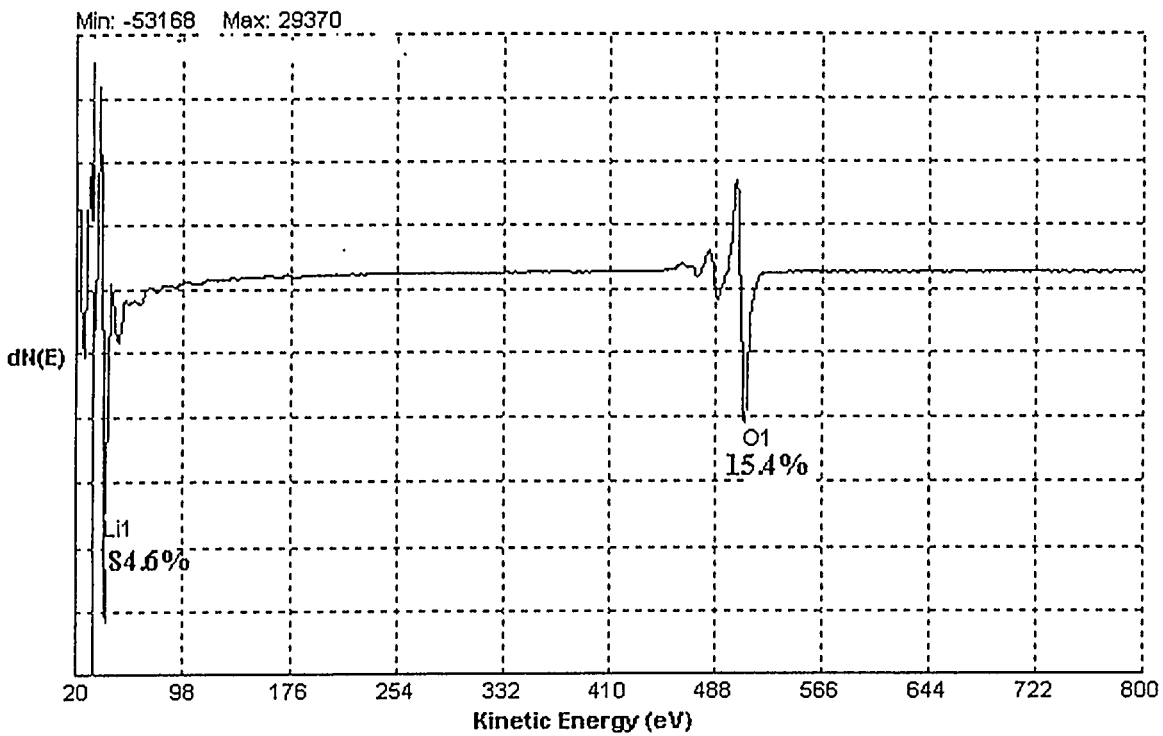

UC San Diego

Plasma interactions with liquid-lithium samples overwhelms most diagnostics (including the human eye).

Deuterium plasma interacting with solid lithium

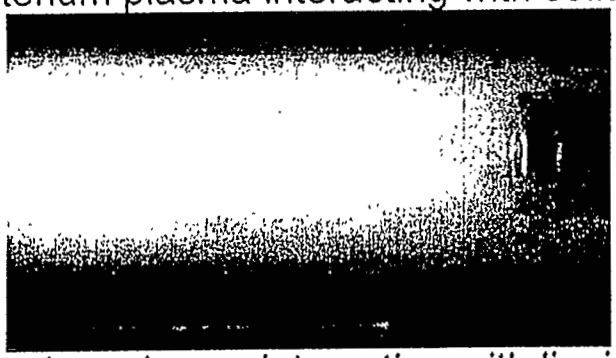

Deuterium plasma interacting with liquid lithium

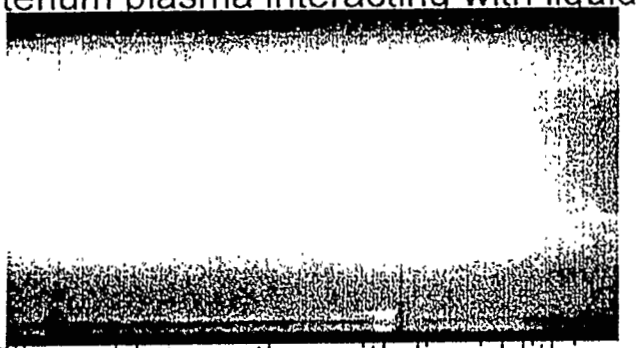

Filtered interaction with liquid lithium

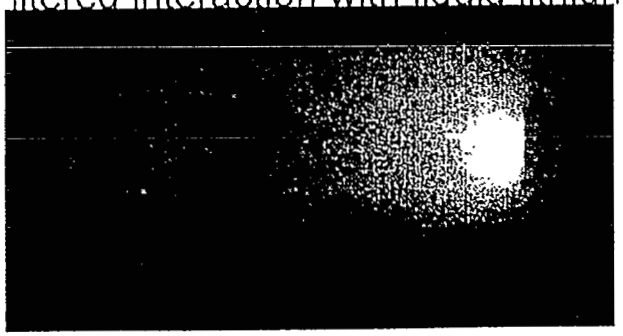

UC San Diego

Helium sputtering (@75eV) of both solid and liquid lithium shows good agreement between weight loss and spectroscopic data.

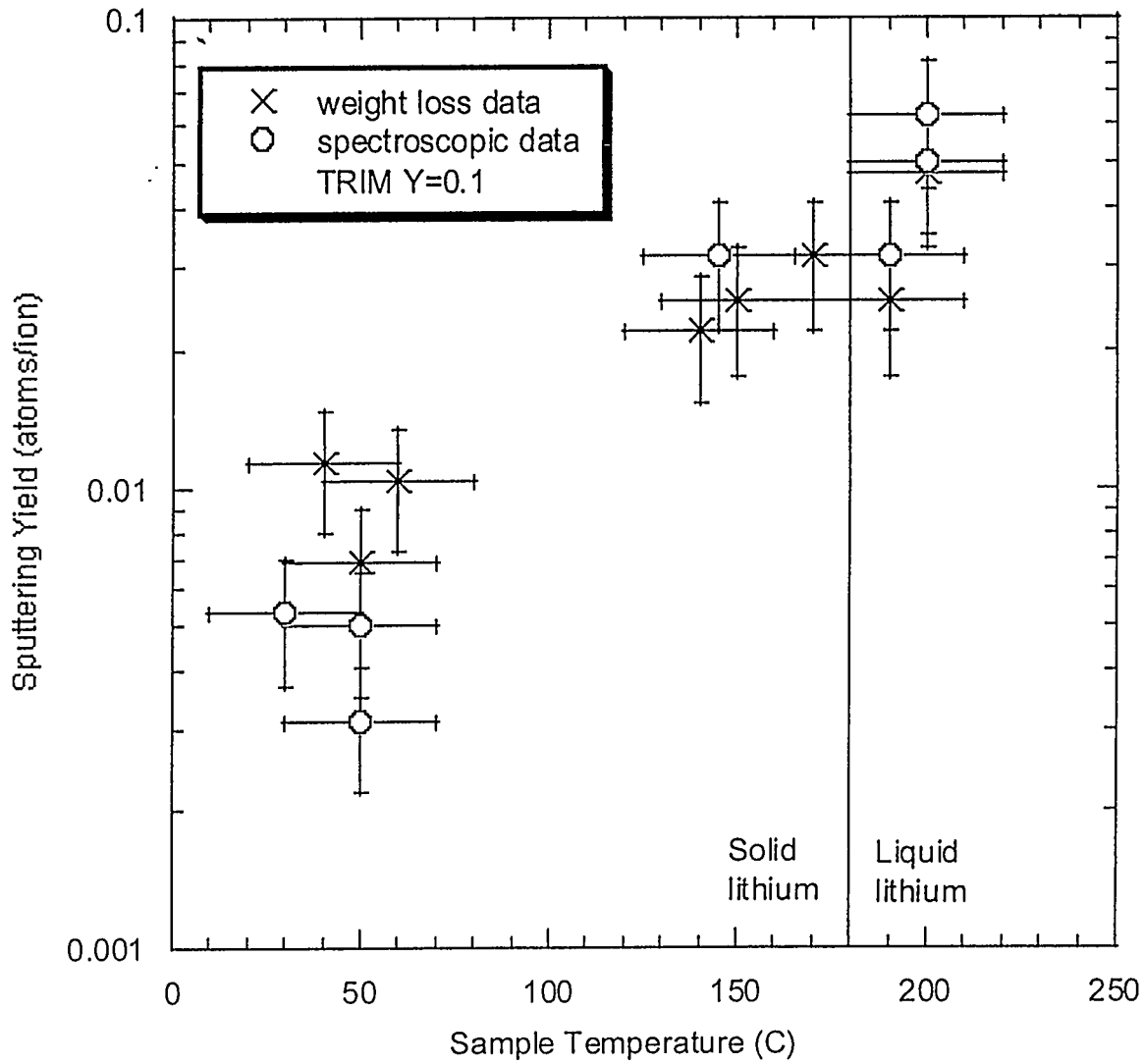

UC San Diego

Differences between weight loss and spectroscopic erosion yields may indicate the importance of chemical/surface cleanliness effects during 50eV D^+ plasma bombardment of lithium samples.

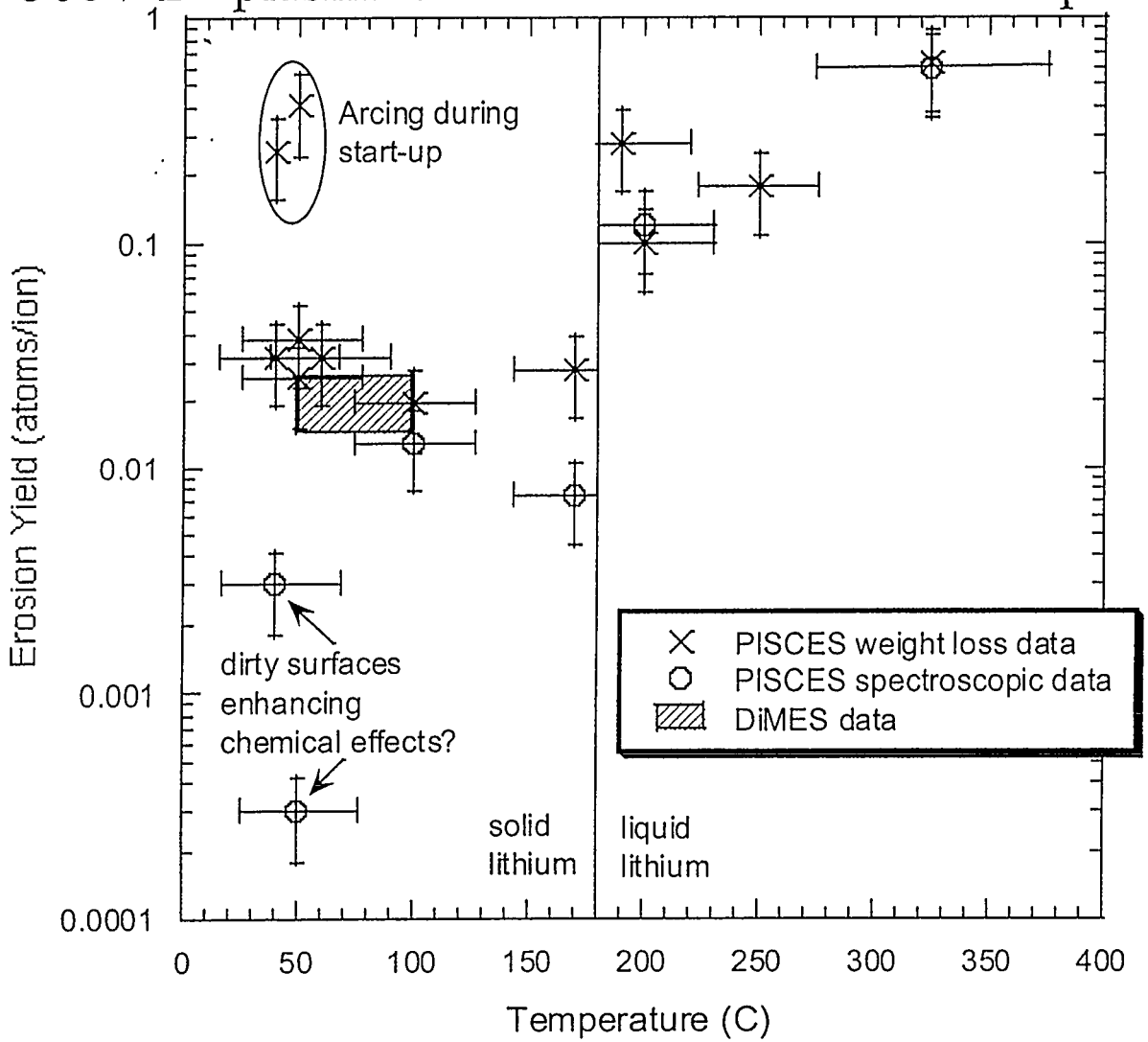

UC San Diego

Surface morphology changes indicate a chemical erosion mechanism acting during deuterium plasma bombardment of lithium samples. Mass and optical spectroscopy show no evidence of LiD, Li_2, Li_2O or LiOD.

Li surface before plasma exposure

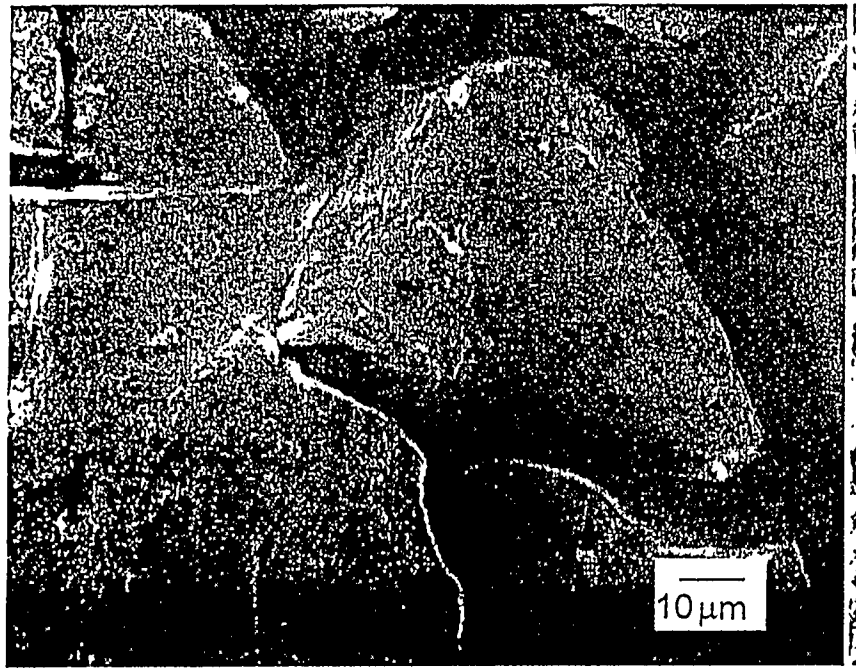

Li surface after plasma exposure @ 50C

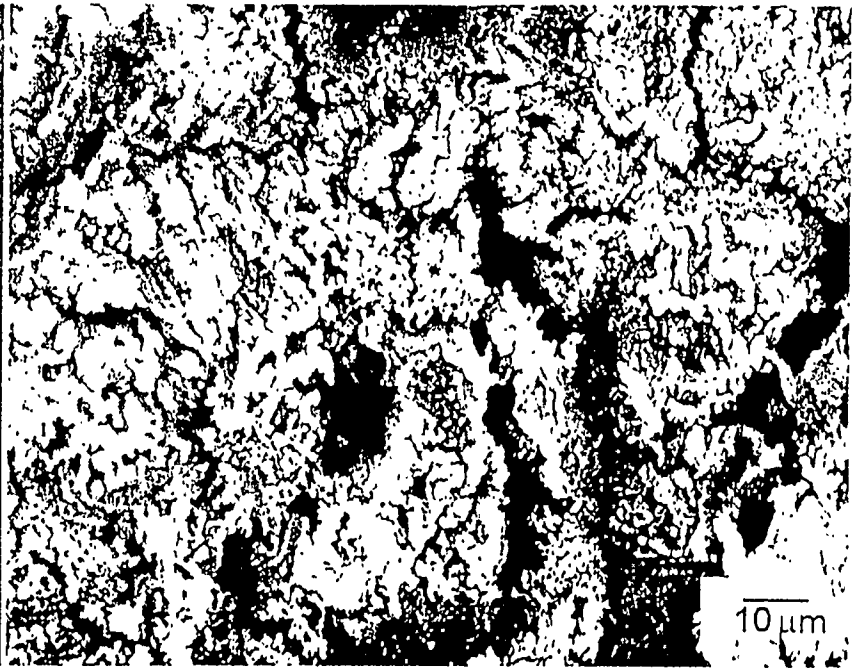

UC San Diego

Gallium offers several different material properties relevant to a fusion power plant scenario.

- low vapor pressure increases operating temperature window
- very small amount hydrogen isotope retention, strong recycling
- liquid at room temperature
- chemically inert to most plasma impurities

UC San Diego

Spectroscopic and weight loss measurements from exposure of liquid gallium to deuterium plasma, are in reasonable agreement to TRIM calculations of deuterium ion sputtering of solid gallium.

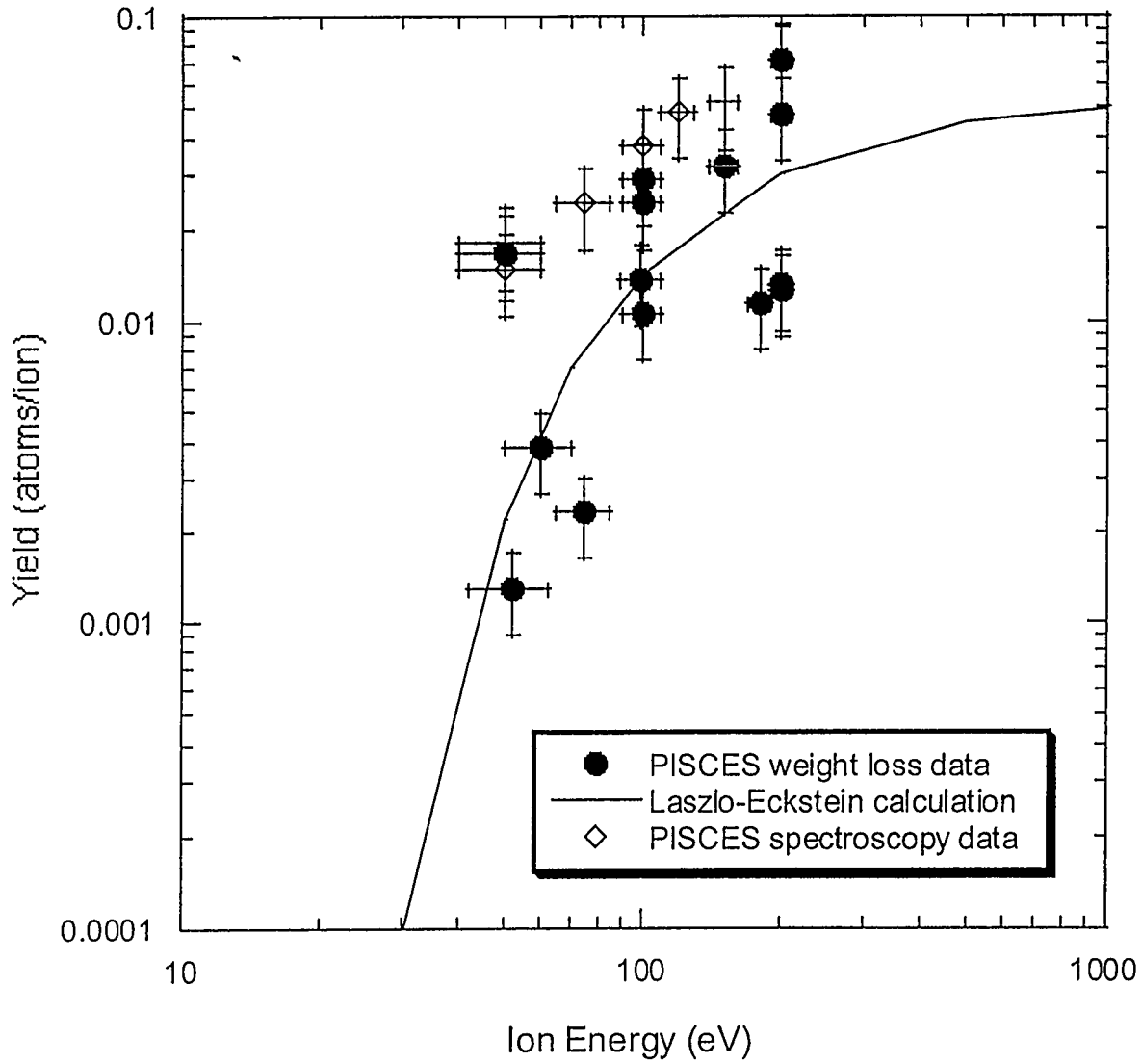

UC San Diego

Deuterium retention in liquid gallium is independent of temperature and fluence (saturates at a very low value = 5×10^{-6} D/Ga).

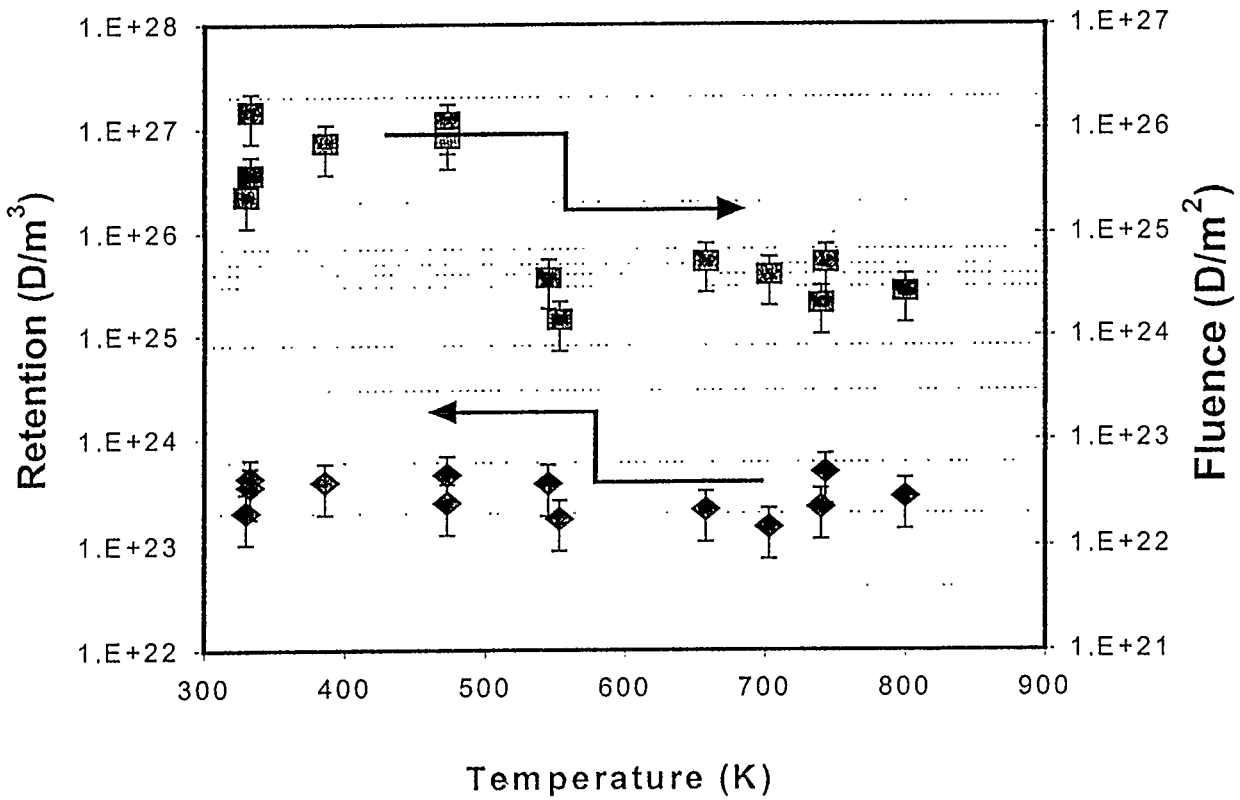

UC San Diego

Future plans include several modifications that will improve the confidence in results obtained during plasma-liquid interaction research performed in PISCES-B.

- modify sample holders to allow TC penetration directly into lithium sample
- modify a sample manipulator to incorporate radiative heating of samples (sample exposure temperature will become independent of plasma parameters)
- use D_α monitor to measure deuterium recycling from samples during plasma exposure
- obtain SnLi alloy to begin evaluation
- evaluate safety implications of exposing flibe to plasma in PISCES-B

November 1-4 1999, St. Francis Hotel, Santa Fe, New Mexico, USA
US-Japan Workshop on Plasma Surface Interactions and High Heat Flux Components for Next Fusion Devices

Impact of Mixed Material Deposition on Plasma Surface Interaction

N. Yoshida, Takeshi Hirai, M. Miyamoto, T. Fujiwara, K. Tokunaga, S. Itoh and the TRIAM group

Research Institute for Applied Mechanics, Kyushu University, Japan

Contents

Introduction

Characterization of the plasma facing surface is very important to understand :

- hydrogen recycling
- tritium retention
- impurity control, etc

We have reported that the plasma facing surface of the TRIAM-1M, all metal devices, are covered by the metallic deposited layer, which is completely different from the original surface in chemical composition and crystal structure.

Present Work

- Further analysis of microstructure and thermal stability of the deposited material.
- Retention and desorption of hydrogen

Surface probe experiments

■ Tokamak device: TRIAM-1M.

R=0.84m, axb=0.12x0.18m

Mo limiters
Mo divertor plates
SS304 vacuum vessel
Hydrogen plasma, limiter config.

■ Plasma parameters.

- Shot No.; #64995-#65026
- I_P; 20~25kA
- P_{LHW};~20kW (2.45G Hz)
- n_e; ~$2x10^{18}$ m^{-3}
- T_i; 1.5~2.5keV
- Duration; 31.5min. (31shots)

■ Specimens.

Thin foil specimens (SS304, W)
Specimen temperature ; R.T.

■ Probe position.
At the E-side in the SOL.

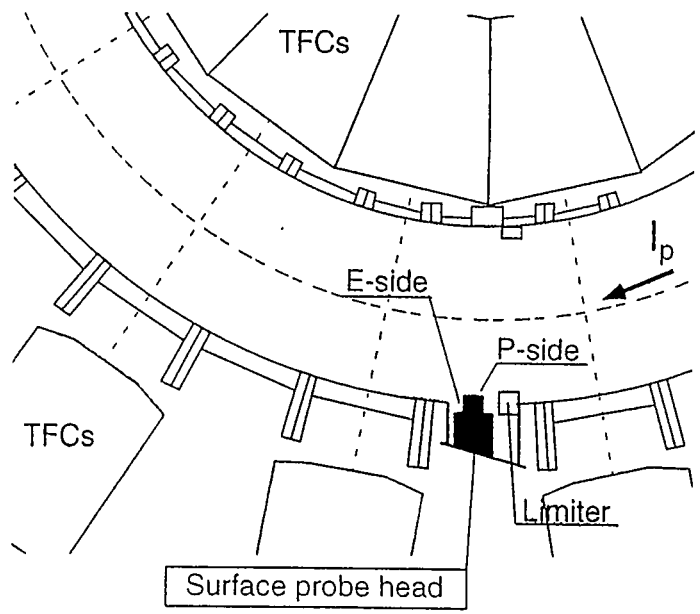

Probe head was inserted horizontally from the outside of the torus

Chemical composition of Deposition

■ Chemical composition of depo. by EDS analysis.

Depo. on Cu, in June 1995

Fe, Cr, Ni, Mo were detected

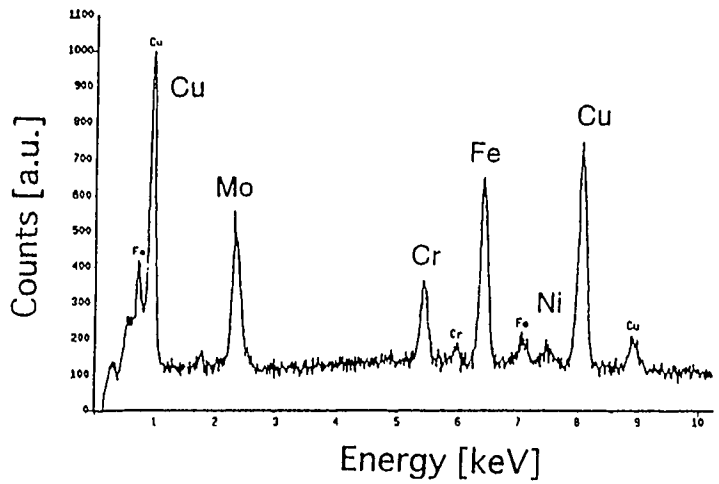

Depo. on W, in Nov. 1997

Only Mo was detected

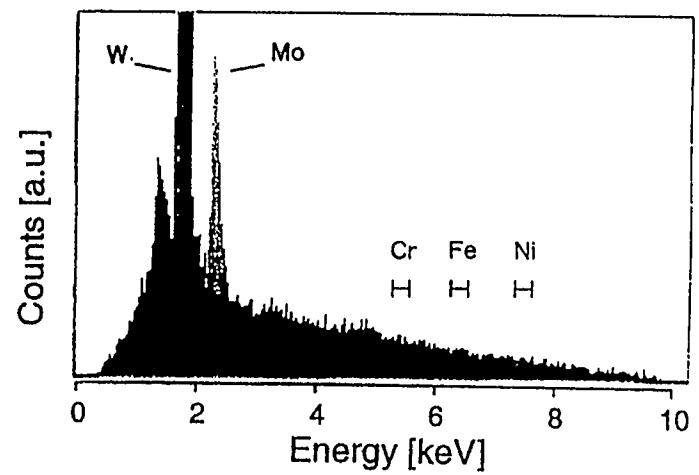

Fe, Cr, Ni (SS) : vacuum vessel

Mo : limiters and divertor plates(since spring 1995)

•••> Composition had changed between the two campaigns.

Inner surfaces have been gradually covered with Mo deposition as a result of PSI after Mo area had expaned (Mo divertor installed in 1995).

Microstructure of Depo. obtained from TRIAM-1M

■ TEM observation of Depo. (EDs and dark field images)

Depo. in TRIAM-1M ••••• 1-2nm fine grains, fcc.

Mo-depo. in a vacuum($<10^{-4}$Pa) ••••• ~20nm-size grains, bcc.

Microstructure was different.

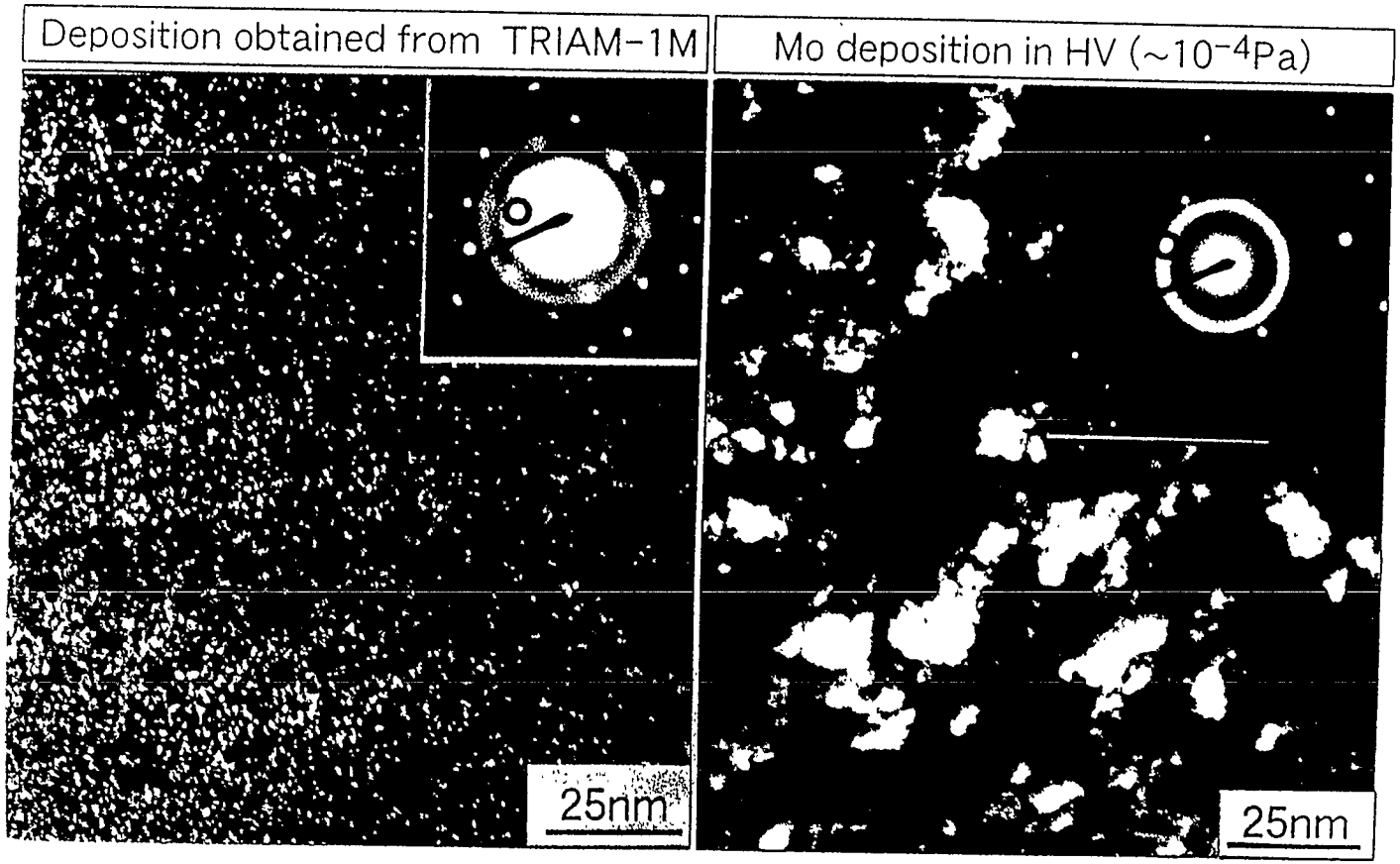

White contrast shows individual grain on Bragg condition

The deposition condition in TRIAM-1M; the depo. rate of Mo, flux of Hydrogen and Oxygen

■ Mo deposition rate and hydrogen, oxygen particle-flux.

● Mo deposition rate.

(the mean depo. rate) = (total Mo atoms•••RBS) / (duration)

$=4.2\times10^{18}$ atoms/m^2s

● Hydrogen flux (by Ion sound velocity).

$n_e \approx 10^{17} m^{-3}$, T_e=17eV, $C_s=6\times10^4$ m/s

$\Gamma_H=6\times10^{21}$ ions/m^2s

● Oxygen flux (by O concentration & H flux).

$n_O / n_H = (1\sim2)\times10^{-2}$

$\Gamma_O \approx 6\times10^{19}$ ions/m^2s

(Γ_H) / (Mo depo. rate) = $6\times10^{21} / 4.2\times10^{18} \approx 1.4\times10^3$

(Γ_O) / (Mo depo. rate) = $6\times10^{19} / 4.2\times10^{18} \approx 1.4\times10^1$

Co-deposition with Hydrogen and/or Oxygen, and Mo.

Vacuum Deposition (VD) Experiments

VD as simulation of deposition process in TRIAM-1M

- Deposited material.

  Mo (depo. rate=~1.2×10^{19}Mo/m^2s)

- Substrate materials;

  Stainless steel (SS304)

- Substrate Temperature; R.T.

- Deposition conditions.

  - High vacuum ($P<10^{-4}$Pa)
  - Gas leaking conditions

  Hydrogen ; Main component of plasma

  $P_{H2}=10^{-3}$Pa, 10^{-2}Pa (Γ_H/Γ_{Mo}= 1.8×10^1, 1.8×10^2)

  Oxygen ; Impurity in plasma

  $P_{O2}=5\times10^{-4}$Pa, 5×10^{-3}Pa (Γ_O/Γ_{Mo}= 2.3, 2.3×10^1)

- Observation; TEM observation.

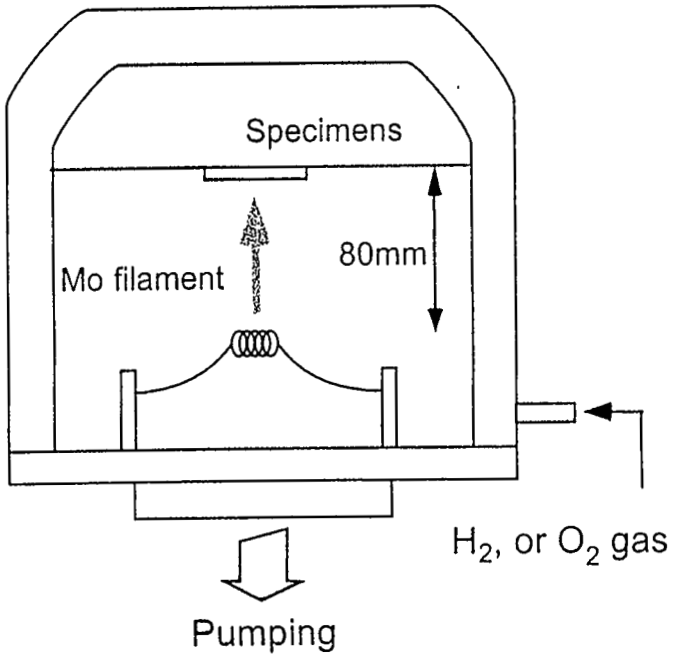

In TRIAM-1M

Γ_H/Γ_{Mo}Å 1.4×10^3

Γ_O/Γ_{Mo}Å 1.4×10^1

Microstructures of Mo-depositions

■ **TEM observation : ED and DF images.**

Mo-depo. in O_2 (P_{O2}=5x10^{-3}Pa) ; fine grains with fcc
<•••• similar to the deposition in TRIAM-1M

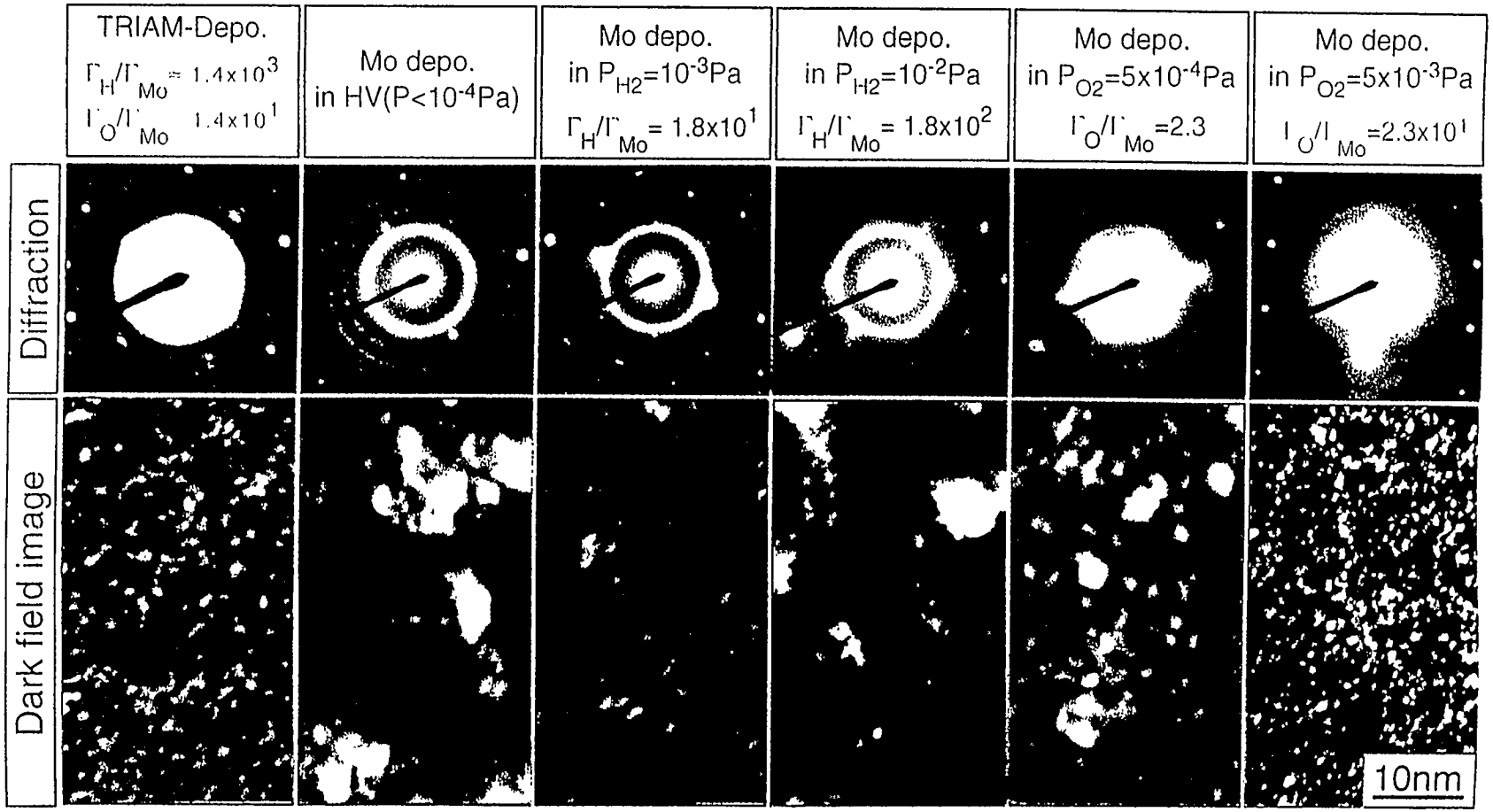

White contrast shows individual grain on Bragg condition

Thermal stability of Mo-deposition in O_2

■ Isochronal annealed Mo depo. (every 100K, for 10 min.)

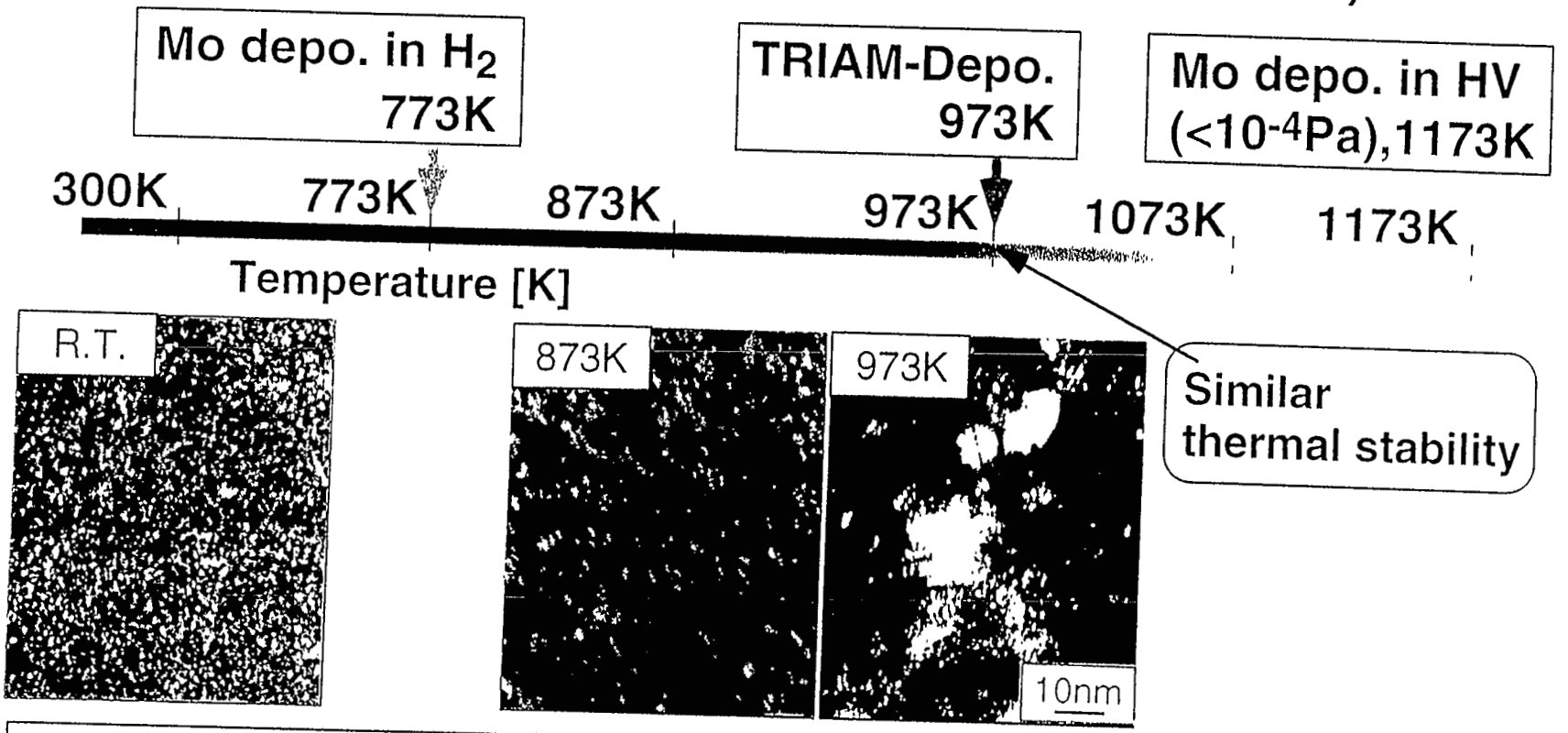

● Mo depo. in O_2 ≈ the deposition obtained from TRIAM-1M.
Microstructure, crystalline structure, thermal stability.

••••>O slightly(1-2%) contained in plasma determined the microstructure. ••••> Co-deposition with O and Mo.+H

Thermal desorption spectrometry (TDS)

- Specimens
  - Mo depo. in O_2(P_{O2}=5x10^{-3}Pa)...about 50nm-thick
  - SS304
  - Mo
- D implantation
  - Implanted ion ; 6keVD_3^+(2keVD^+...implanted range < 30nm)
  - Implanted temperature ; R.T.
  - Implanted D ; 3x10^{21}D/m^2
- Thermal desorption spectrometry (TDS)
  - Ramping temperature; R.T. ~ 1080K
  - Ramping rate ; 1K/s
  - Detected mass ; m/e=3(DH), 4(D_2), 19(DHO), 20(D_2O)
    - <••••• Gases associated with deuterium
  - Quantifyed by He standard leak

Microstructure of implanted Co-deposition

Micro cavities were formed in the H-implanted co-deposition.

• • • > Micro cavities could be good trapping sites for hydrogen.

• • • > Micro cavity formation is a possible mechanism of high retention rates of the deposition.

Bright field images of Co-deposition implanted with 4keVH_2^+ 7.2x$10^{21}m^{-2}$

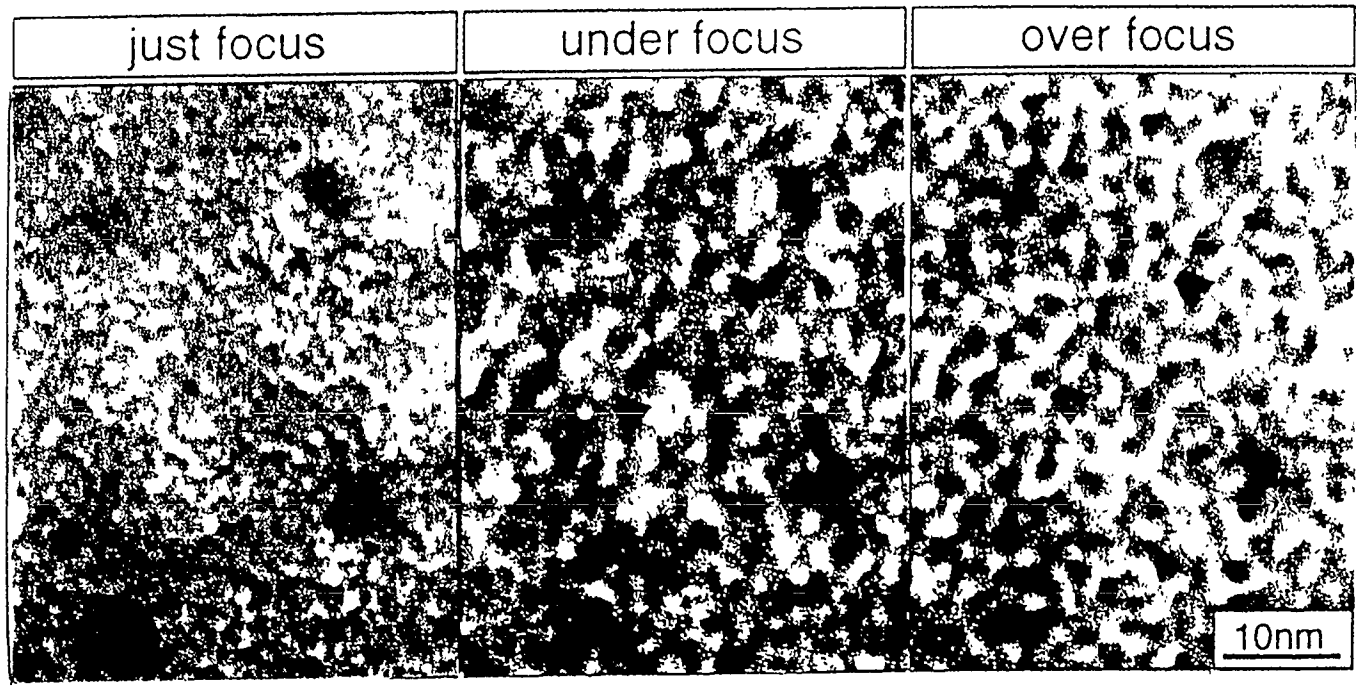

Blistering and Flaking of Deposited Layer

Blistering and flaking of the deposited layer occurs for both TRIAM-1M and H ion irradiated vacuum deposited layers.

Flaking of the deposited layer must be a mechanism of dust formation with a large amount of hydrogen.

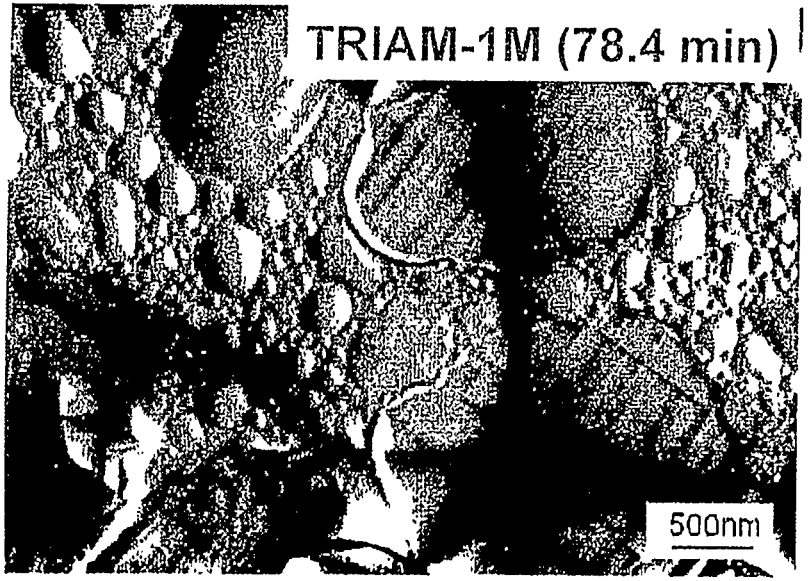

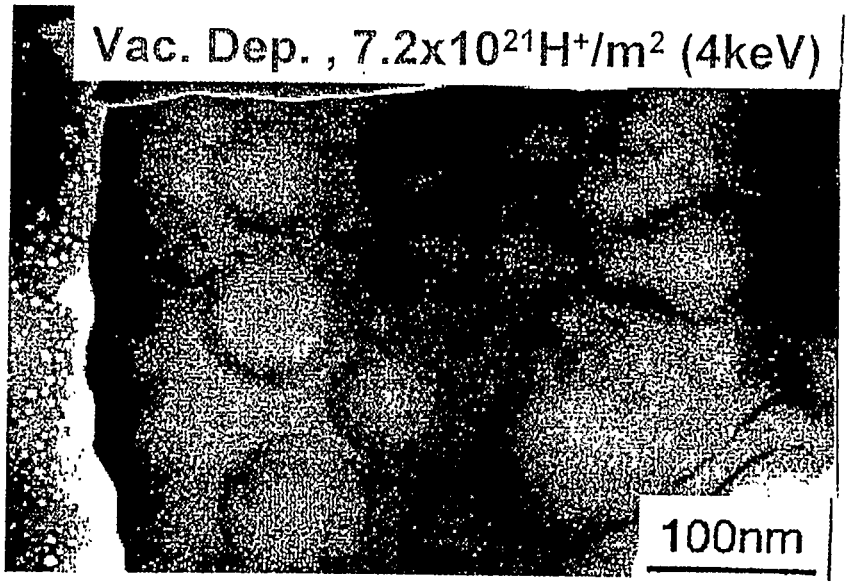

Schematic Drawing of defective Mo-depo.

1nm- grains, Defective structure, Cavities, Containing gas atoms

Disordering atoms near grain boundaries may play a role for good trapping site for implanted-D.

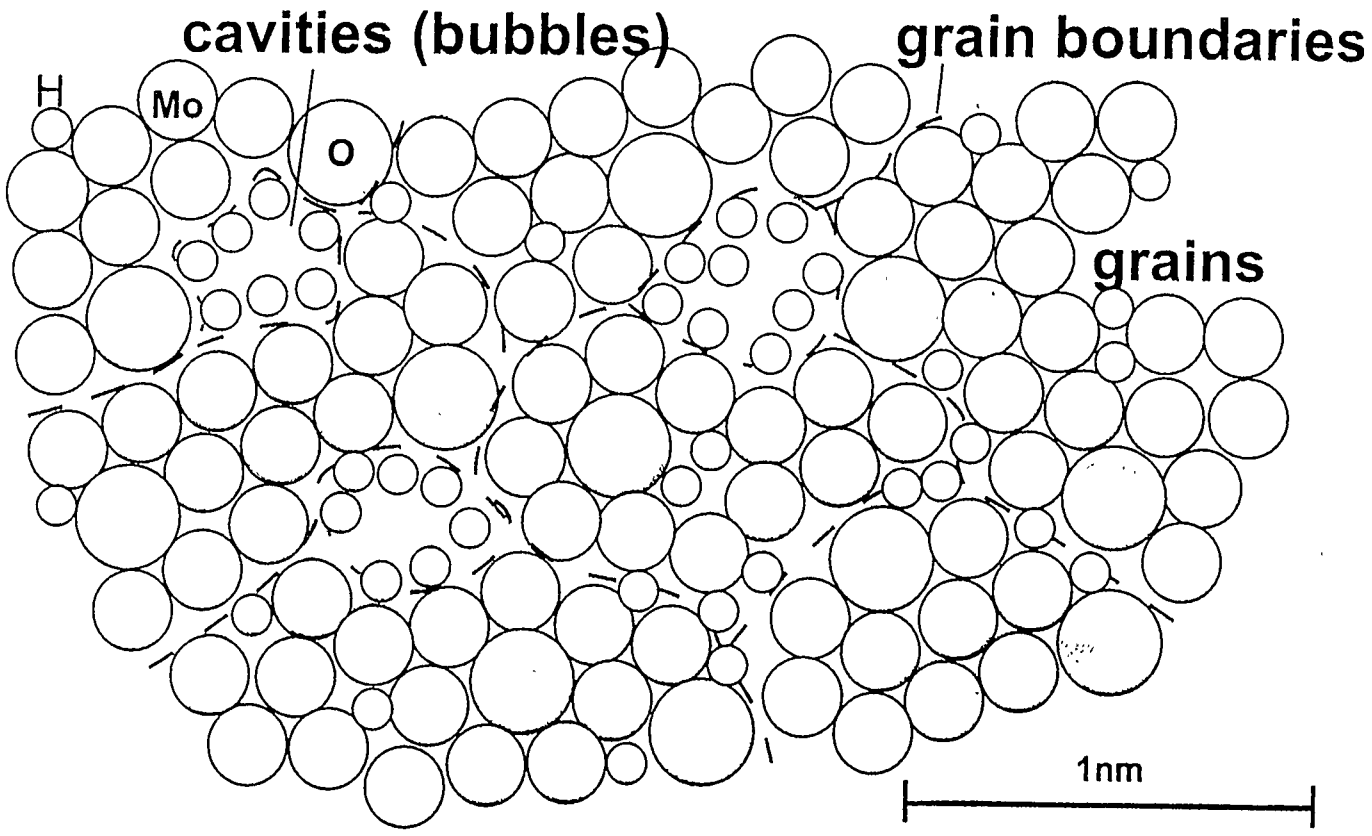

Deuterium retention

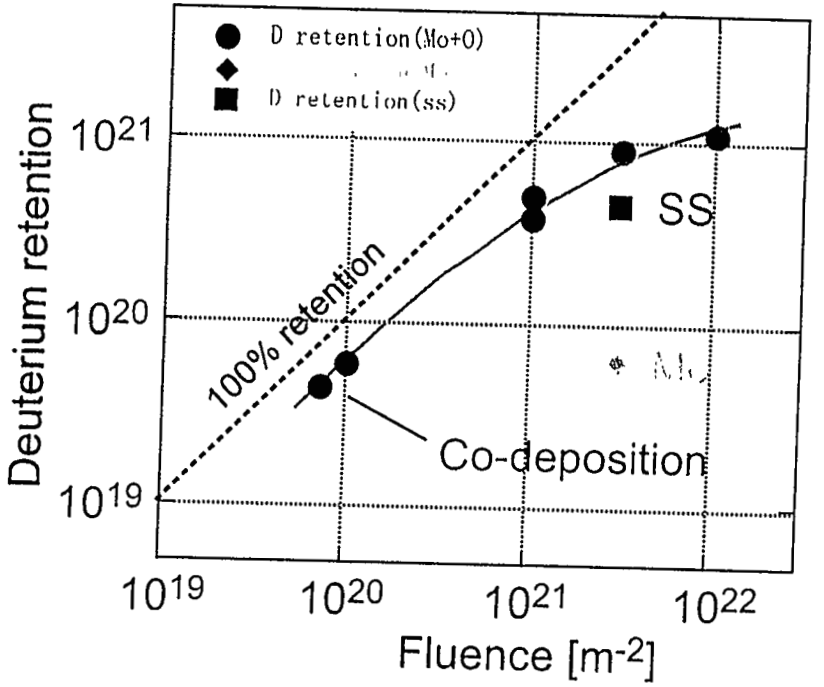

■ Fluence dependence of retention
(D as D_2, DH, D_2O, DHO)

Retention of D in Mo-depositon is much larger than those in Mo and SS.

Co-deposition with O increase the retention of H, even if PFMs such as Mo with low H retention were used.

Desorption of D_2 and D_2O

- Implanted D desorbed as D_2 and D_2O.

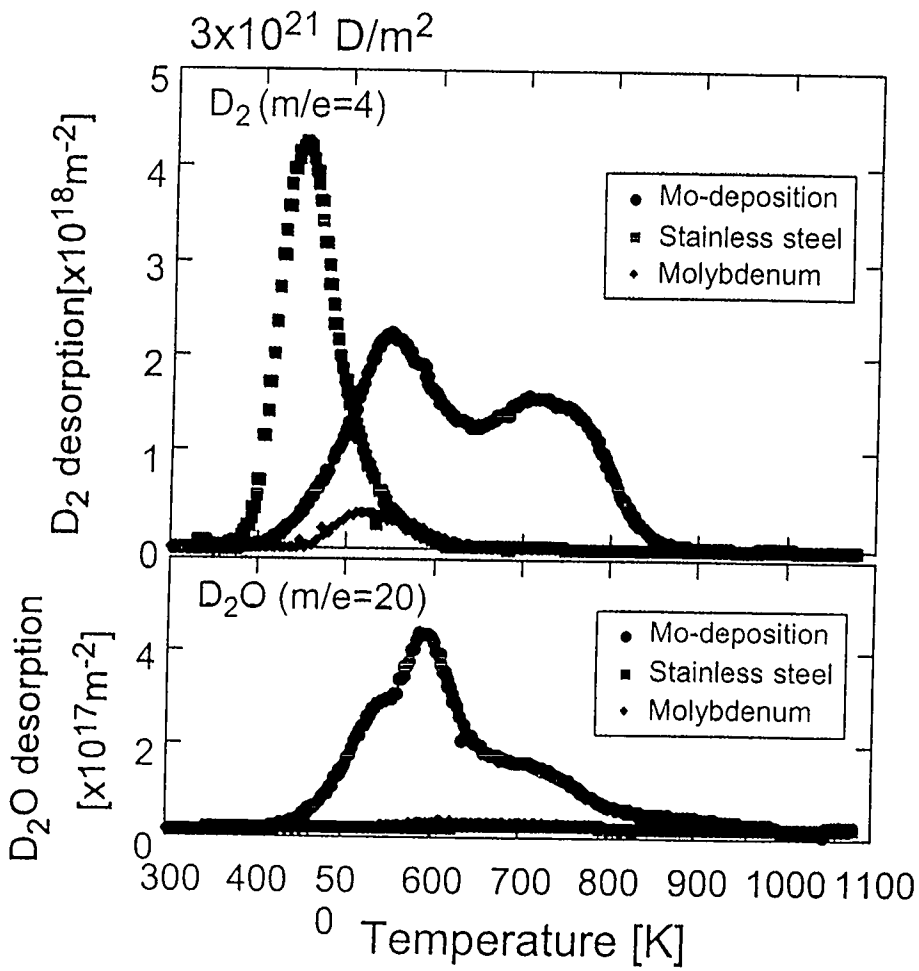

D_2•••>

(at least) 2 stages at 550K and 700K in Mo-depo.

D_2 desroption is different from those of Mo bulk or SS.

D_2O•••>

large desorption from Mo-depo.

negligible D_2O desorption from Mo bulk and SS.

Deuterium Retention

The numbers show the retention rates.
($3x10^{21}$ D/m^2)

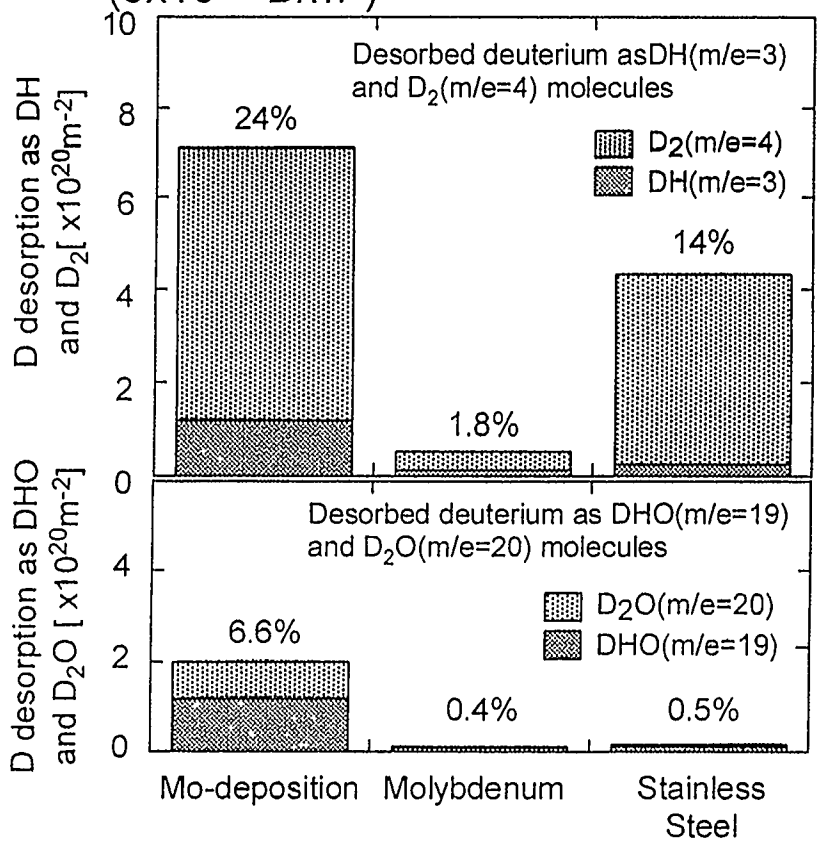

■ **Desoption of D**

D is reteined in Mo-depoition layer as D_2 (DH) and D_2O(DHO)

Much largerer amount of D is retained in Mo-depositon than those in normal Mo and SS

D/Mo=0.35
O/Mo=0.04

Strong retention of H in co-deposited layer of metallic impurities and O may be a commen phenomenon in may kind of metals such as W.

Summary

The mixed material deposition in TRIAM-1M were examined. Vacuum-deposited Mo were also examined to make clear the nature of the material and impacts on hydrogen retention.

- The inner surface of the TRIAM-1M was covered with the mixed material of Mo, O and H.
- The material has very defective structure. Its grain size is only about 1 nm and the crystal sturucture is fcc. Co-deposition with O determines this spetial structure.
- The mixed material shows strong retention of D at room temp.. D is desorbed as D_2 (DH) or D_2O(DHO) between 400K and 900K.
- Dense cavities were formed by hydrogen irradiation. They could act as strong trapping sites for hydrogen.
- The deposited layer is flaked by hydrogen irrradition. This may be a mechanism of hydrogen saturated dust formation in the TRIAM-1M.
- Present results show the formation of mexed material deposition is impotant issue even for metal devices. Due to its defective structure hydrogen retention is much higher than the normal metal surface.

Future Plane

- Influence of substrate temperature
  Microstructure may change at elevated temperatures.

- Laboratory experiments of Mo deposition in H and D atmosphere.
  ➡ *Estimation of co-deposition of D.*

- Effects of keV-energy range He injection.
  This may enhance hydrogen retention and exfoliation of the deposited layer.

U.S. – Japan Workshop : Santa Fe : November 1–4, 1999

Deployment of Active Probes and H-sensors in DIII–D

R. Bastasz* for the DiMES Team

*Sandia National Laboratories
Livermore, California

email: bastasz@sandia.gov

DiMES in DIII–D

"Divertor Materials Evaluation System"

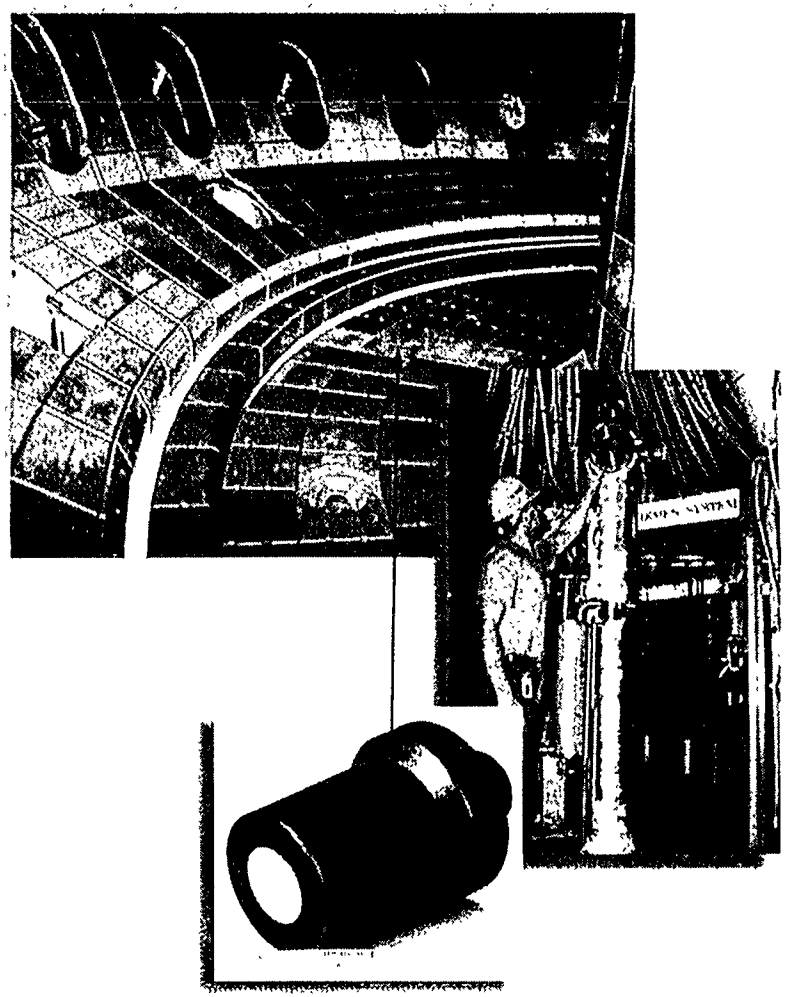

inserts and retrieves samples

provides controlled exposures to DIII-D plasmas

supports both passive and active probes

A DiMES Centenary: The hundredth DiMES sample has been made!

DiMES: Divertor Materials Evaluation System

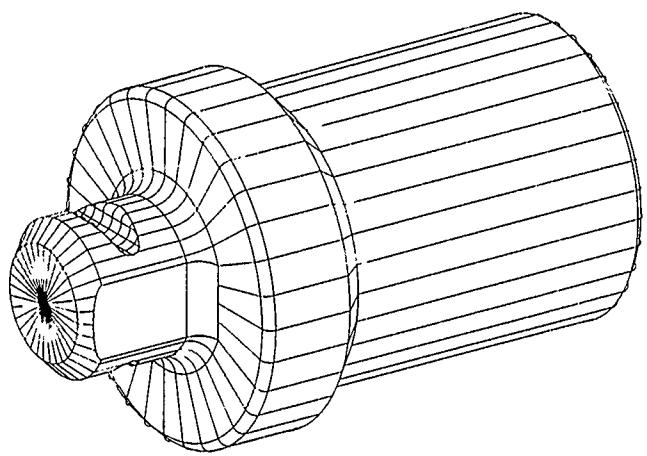

Materials exposed in DiMES:

Al, B_4C, Be, C, Si, Mo, V, W...

Some DiMES statistics:

- 1990: 1st sample made
- 1999: 100th sample made.
- 8 sample face designs have been built and used.
- 12 PMI studies based on DiMES data published.
- DiMES collaborators include 5 U.S. and 2 foreign groups.

DiMES samples can now be actively monitored and controlled.

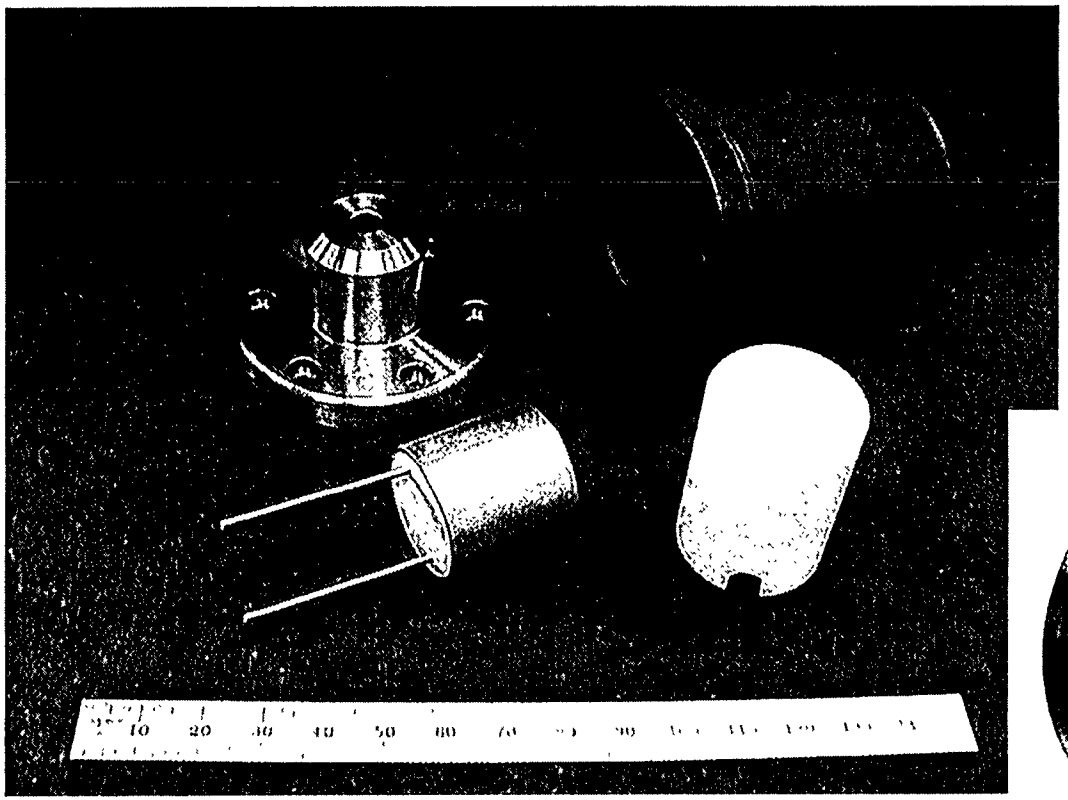

Sample with isolated tungsten insert for arcing studies.

↓

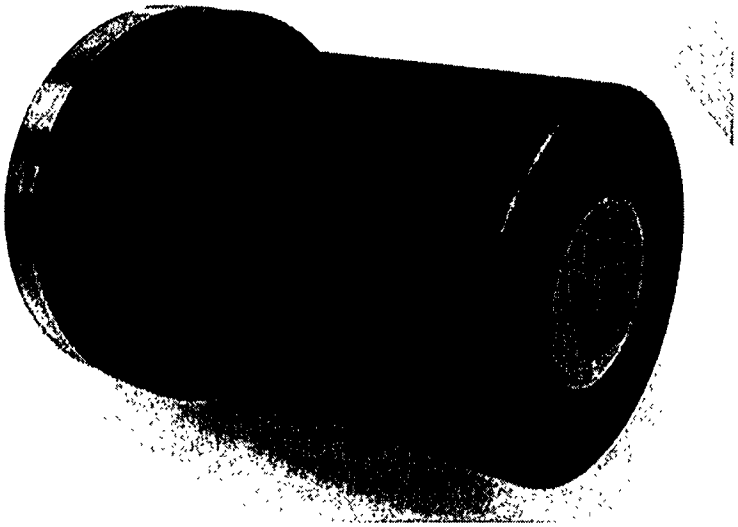

↑

Sample with internal heater for erosion/deposition studies.

Heated DiMES sample

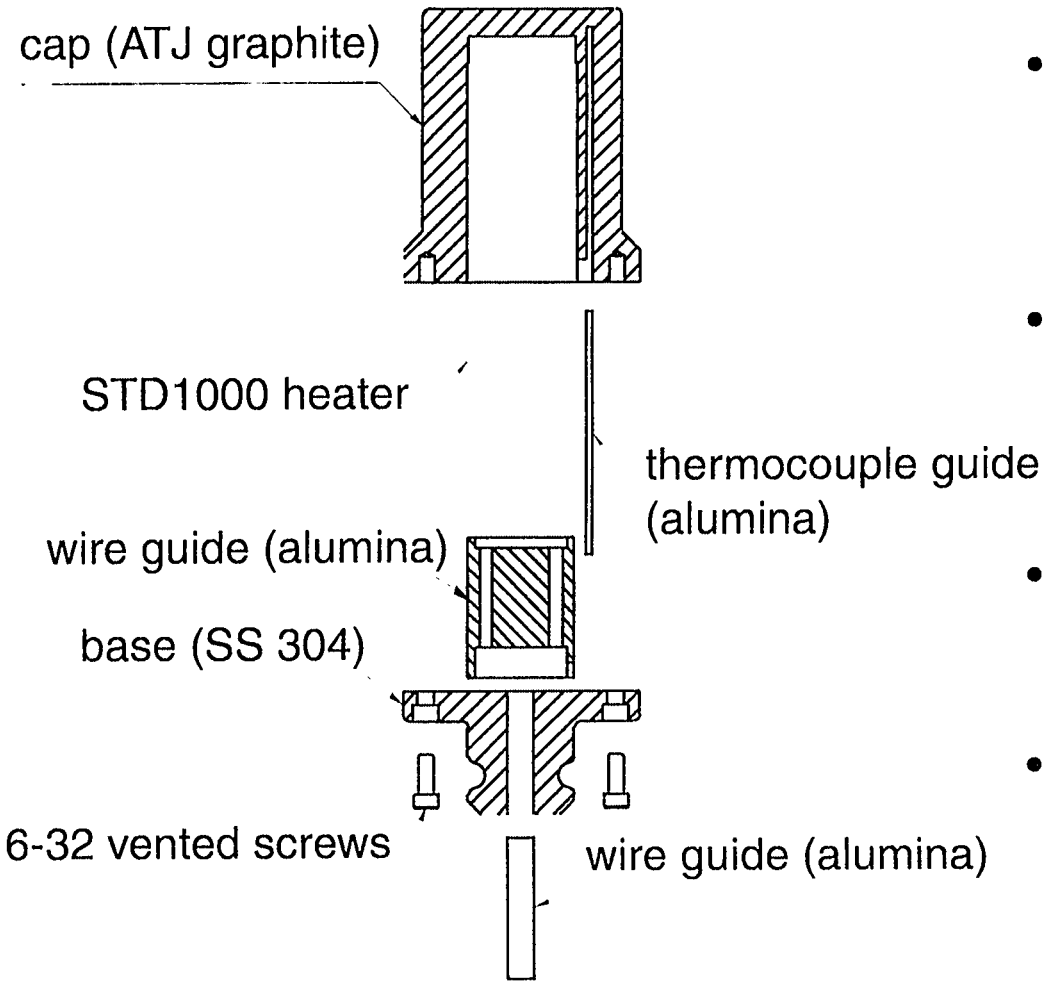

- Design is based on the already approved Langmuir probe head.
- All parts are vacuum compatible.
- Cap can be customized and is replaceable.
- Heater rated for 200 W power.

Fixture for testing heated DiMES sample in vacuum.

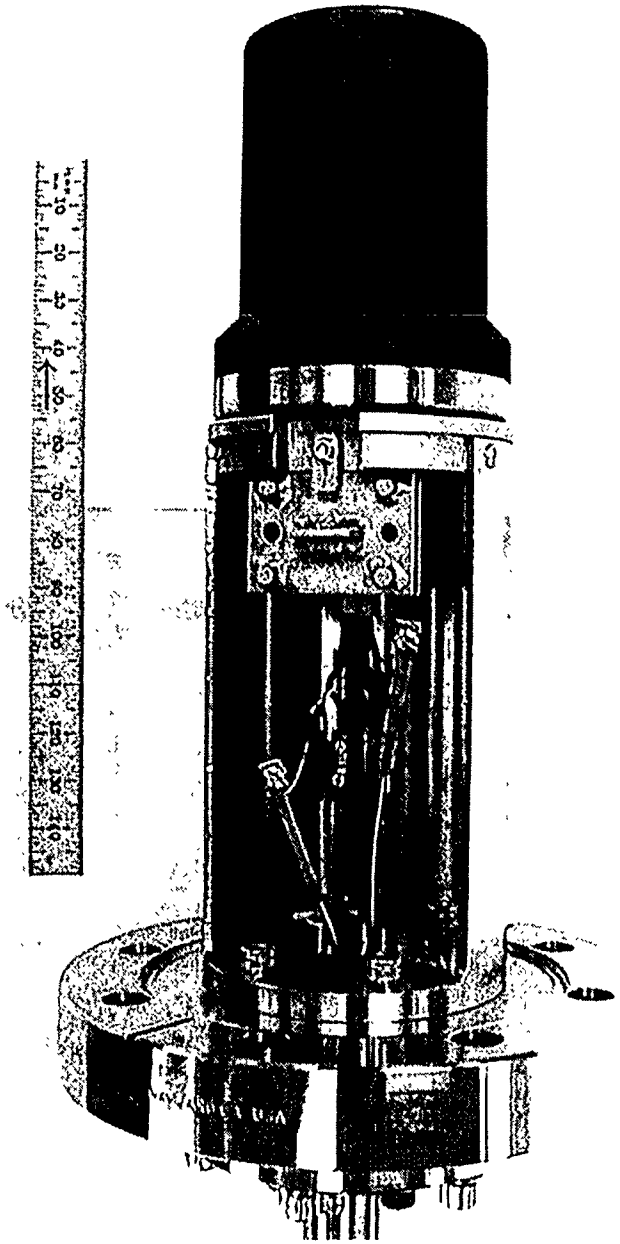

- 50 W power (5 V @ 10 A) heats probe to 380 °C.
- Probe baked out in vacuum before use.

Electrically monitored tungsten DiMES sample

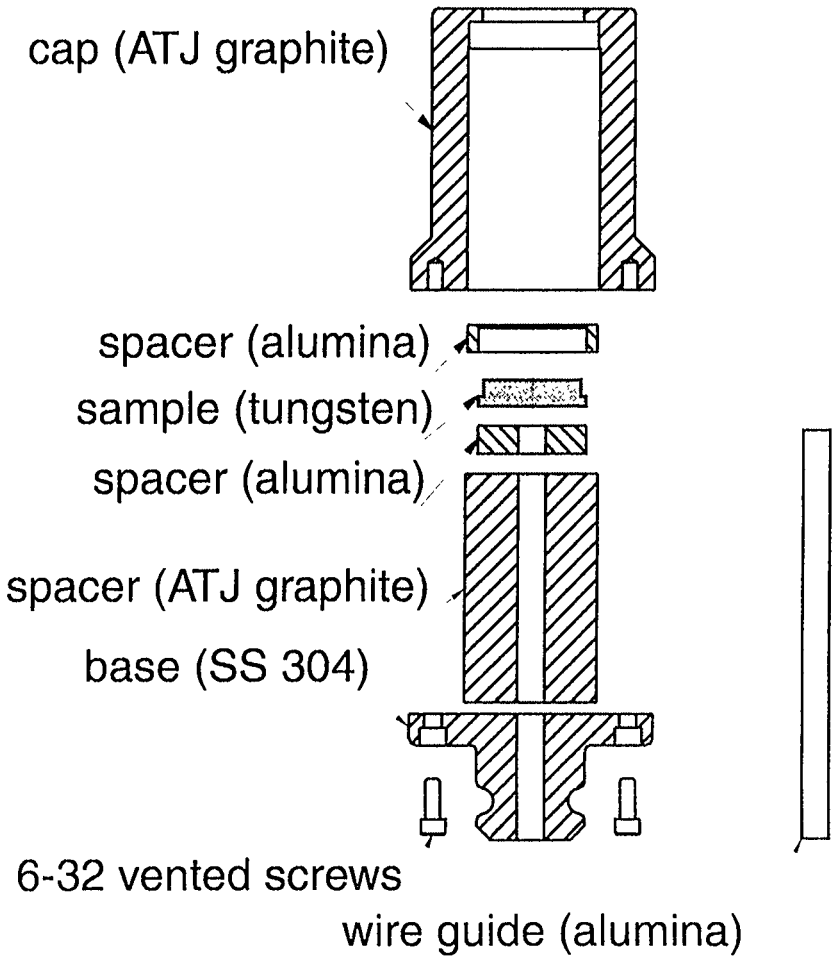

- Design is similar to previous sample probes.
- All parts are vacuum compatible.
- Sample is fully isolated and is replaceable.
- Monitor wire is spot welded to sample.

Ideas for a DiMES sample with lithium

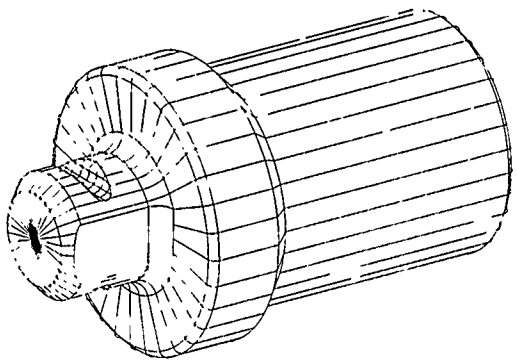

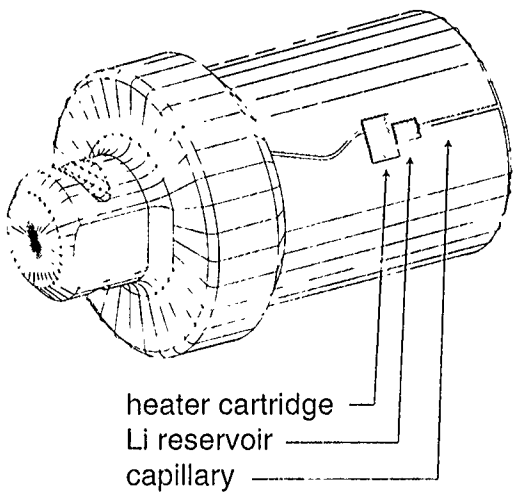

A. The simplest approach is to coat a sample with a Li film.

B. A thin Li foil could be used as an insert.

C. A heated Li reservoir could be placed inside.

- Sample needs to be handled in glove bag.
- He conditioning needed to clean off oxide.

A DiMES probe with a lithium metal insert was exposed to the DIII-D divertor plasma.

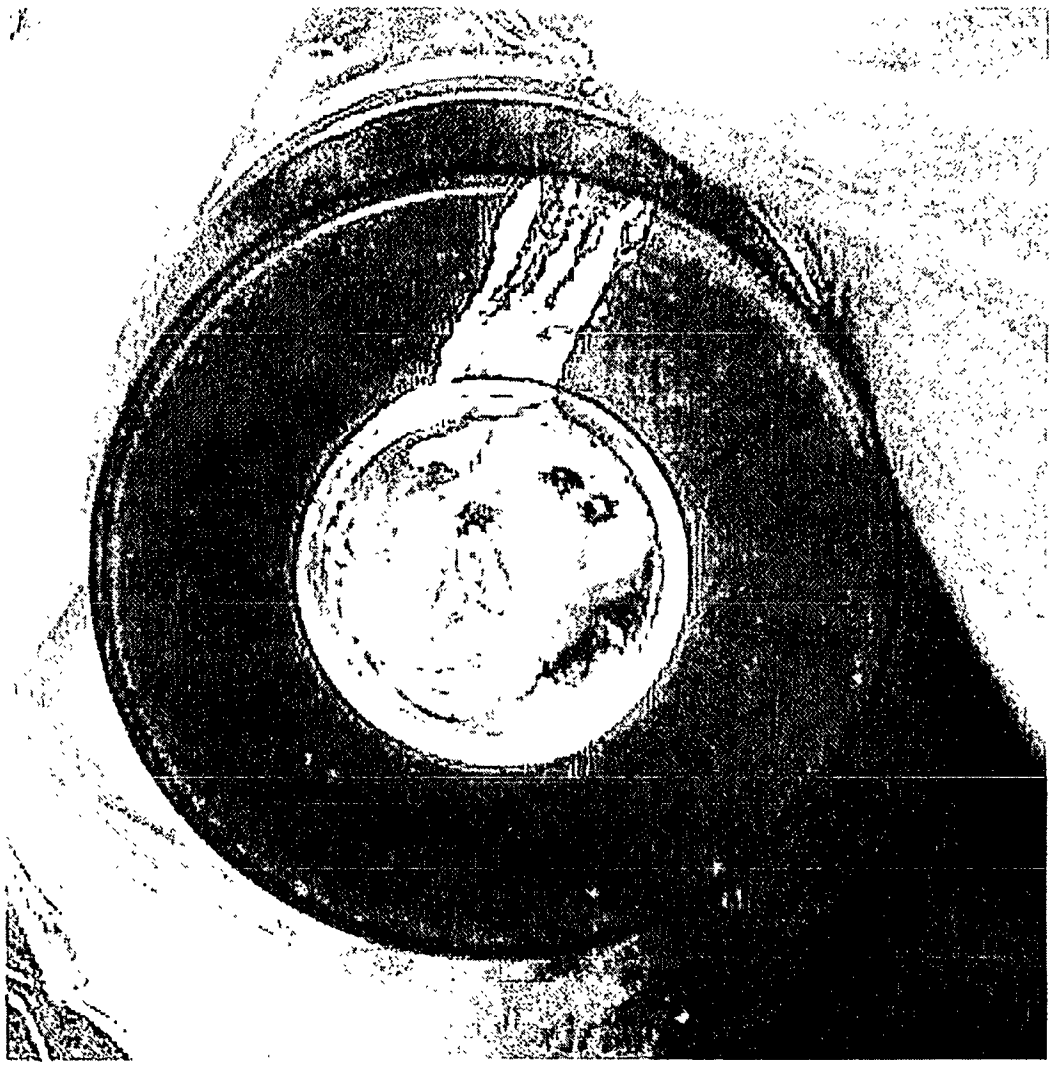

- DiMES #105 had a thin lithium disk mounted on center (2.5 cm diameter, 0.25 mm thickness).
- Probe was exposed to four plasma shots (100082, 83, 86, 87).
- OSP was set on DiMES for 0.5 s/shot during 1-source ELMy H-mode.
- Molten lithium spread across probe face radially inward.

Hydrogen Microsensors

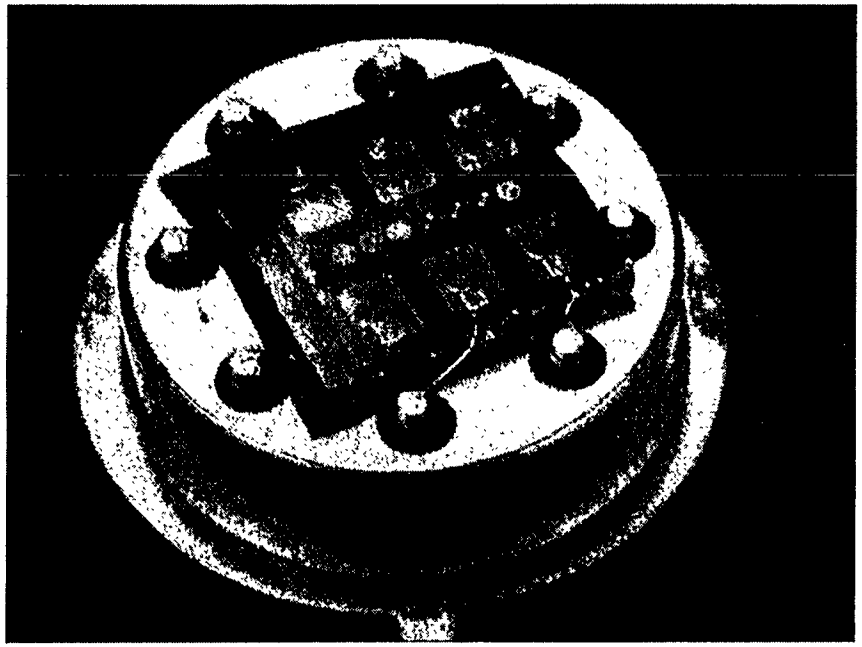

6 element H sensor array on a Si chip

- Sandia has developed solid-state chemical sensors that monitor hydrogen in a variety of environments.
- Hydrogen microsensors are small, robust, low-power devices, which have fast response and high sensitivity.

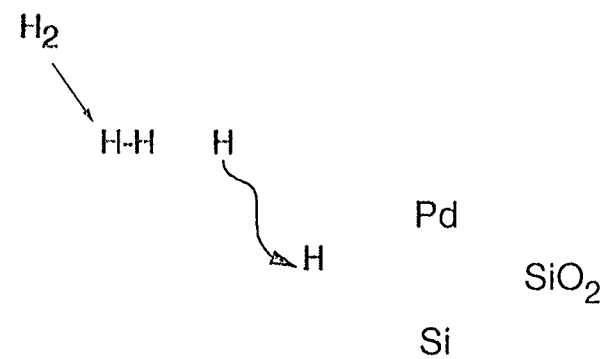

- The sensors detect hydrogen using a catalytic metal gate incorporated into a MIS device.

Hydrogen Microsensors: theory of operation

- Atomic hydrogen

1 - filters quickly through metal
2 - traps near interface
3 - alters barrier height
4 - affects electron flow across junction.

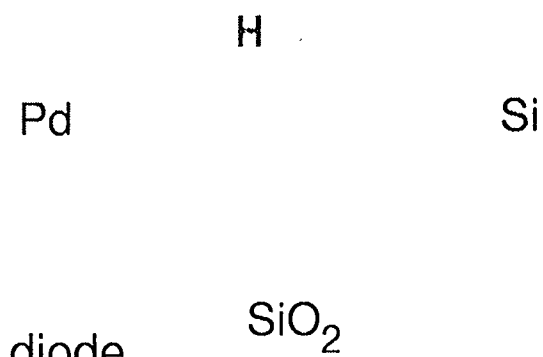

- Example: a reverse-biased tunnel diode

$$\phi_b \doteq \phi_m - \chi$$

$$I_r = A e^{-\phi_b/kT}$$

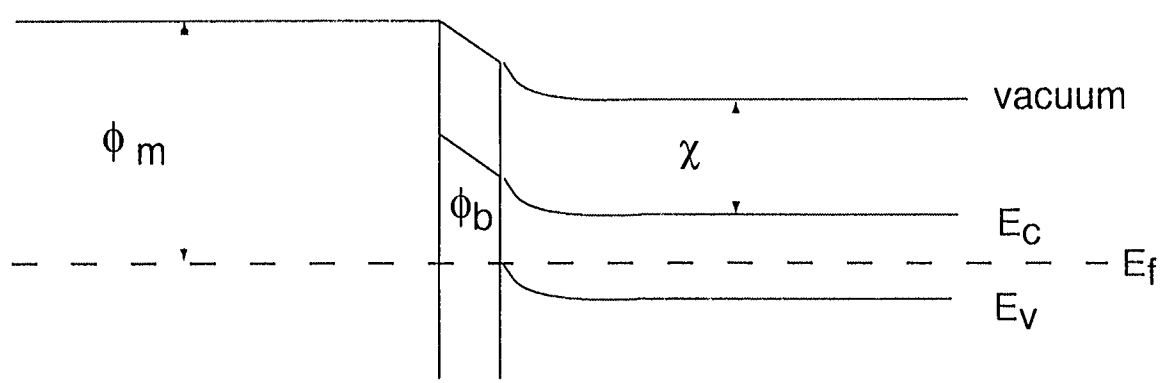

small barrier height change => large device response

Hydrogen Microsensor Properties

- Package size: $\approx$5 mm
- Power needs: $\approx 10^{-6}$ W
- Operating temperature: 25–200°C
- Detected species: H, D, and T
- Maxmium sensitivity: $\approx 10^{11}$ H/cm^2
- Response time: $\approx$10 ms.

Hydrogen Microsensors: An advanced PMI diagnostic

- Hydrogen microsensors are:
  - small solid-state devices
  - compatibile with tritium, neutrons, and X-rays
  - remotely controlled and maintained.
- Hydrogen microsensors can:
  - monitor the particle flux to chamber walls
  - measure the energy of impinging particles
  - study spatial and directional anisotropies.

Planned DiMES active probe use in year 2000.

- Heated DiMES sample for PMI studies with lithium.
- Electrically monitored tungsten DiMES sample for arcing studies.
- Hydrogen microsensor for charge-exchange neutral studies.

US-Japan workshop on Plasma surface interactions and high heat flux components for next fusion devices Nov. 1-4, 1999, Santa Fe, USA

Plasma Wall Interactions observed by Balmer lines emission in TPE

T. Tanabe, K. Shimada, *Nagoya University*
T. Venhaus and R. Causey, *Sandai National Laboratory*

Motivation:

⇒ Can we rely on hydrogen recycling by H α measurements?

Background:

⇒ Emission of excited atoms and molecules
⇒ Atomic reemission at elevated temperatures
⇒ High reflection coefficient at high Z materials

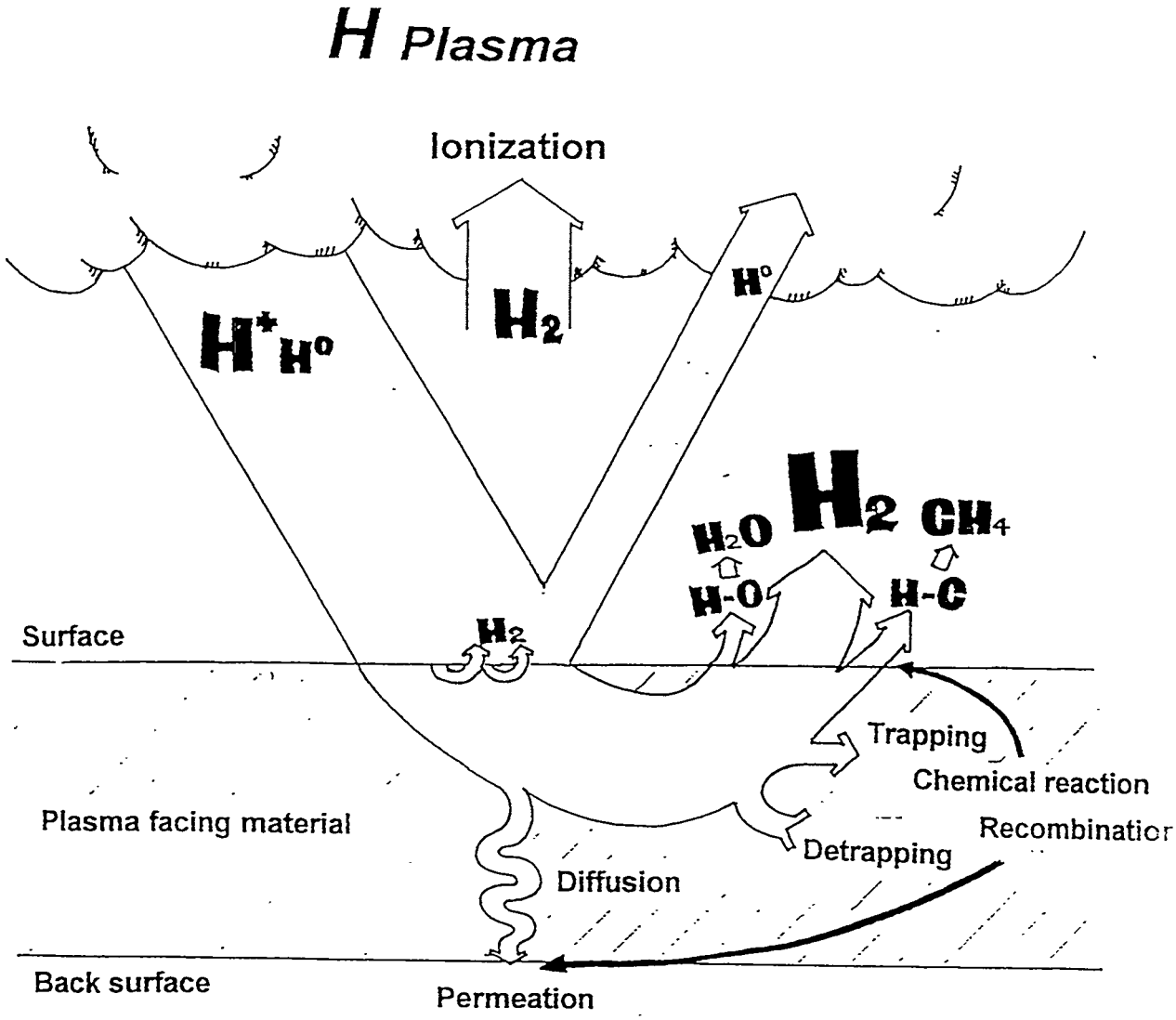

In a simple model, the hydrogen recycling in the steady state at the first wall could be assumed to be 1.0 irrespective of the target temperature. Because the first wall should be saturated after the long exposure to the plasma, and released flux (reemission plus reflection) from the wall should be equivalent to the incident flux. This argument, in which only particle balance between plasma and materials is taken into account, is somewhat misleading, because energy and momentum balance between plasma and materials is out of concern.

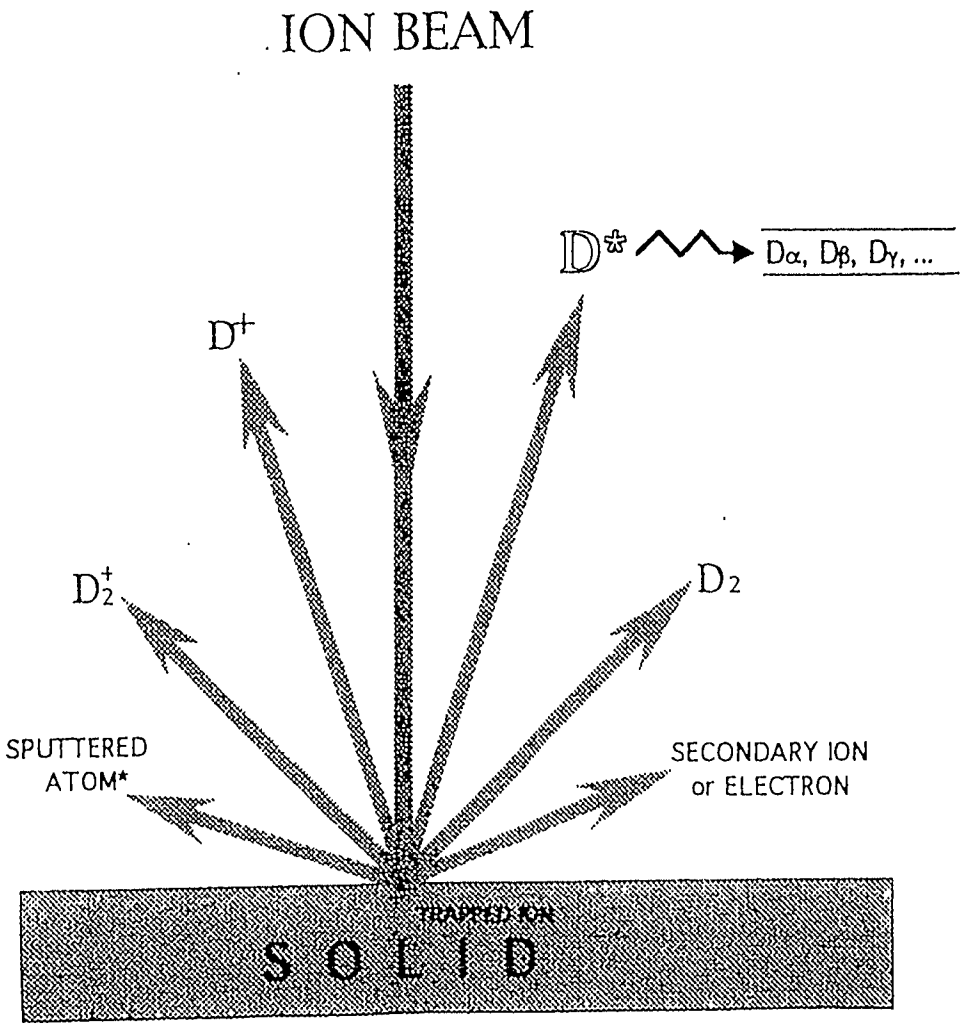

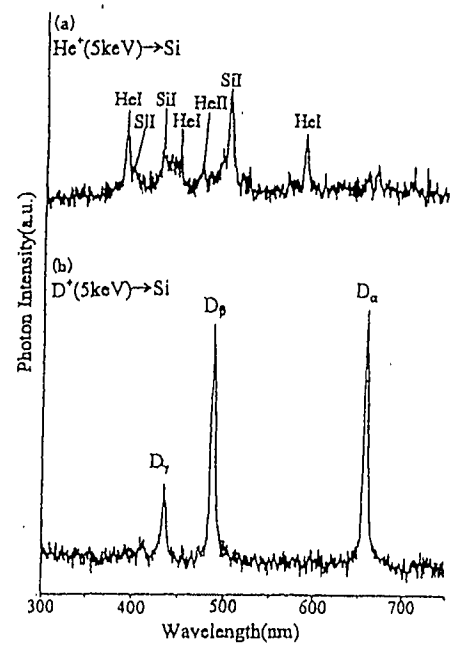

Reflection as an excited atom and reemission as an exited molecules are very important at higher temperature, while dynamic retention (retention under plasma exposures) becomes very small and less important in hydrogen

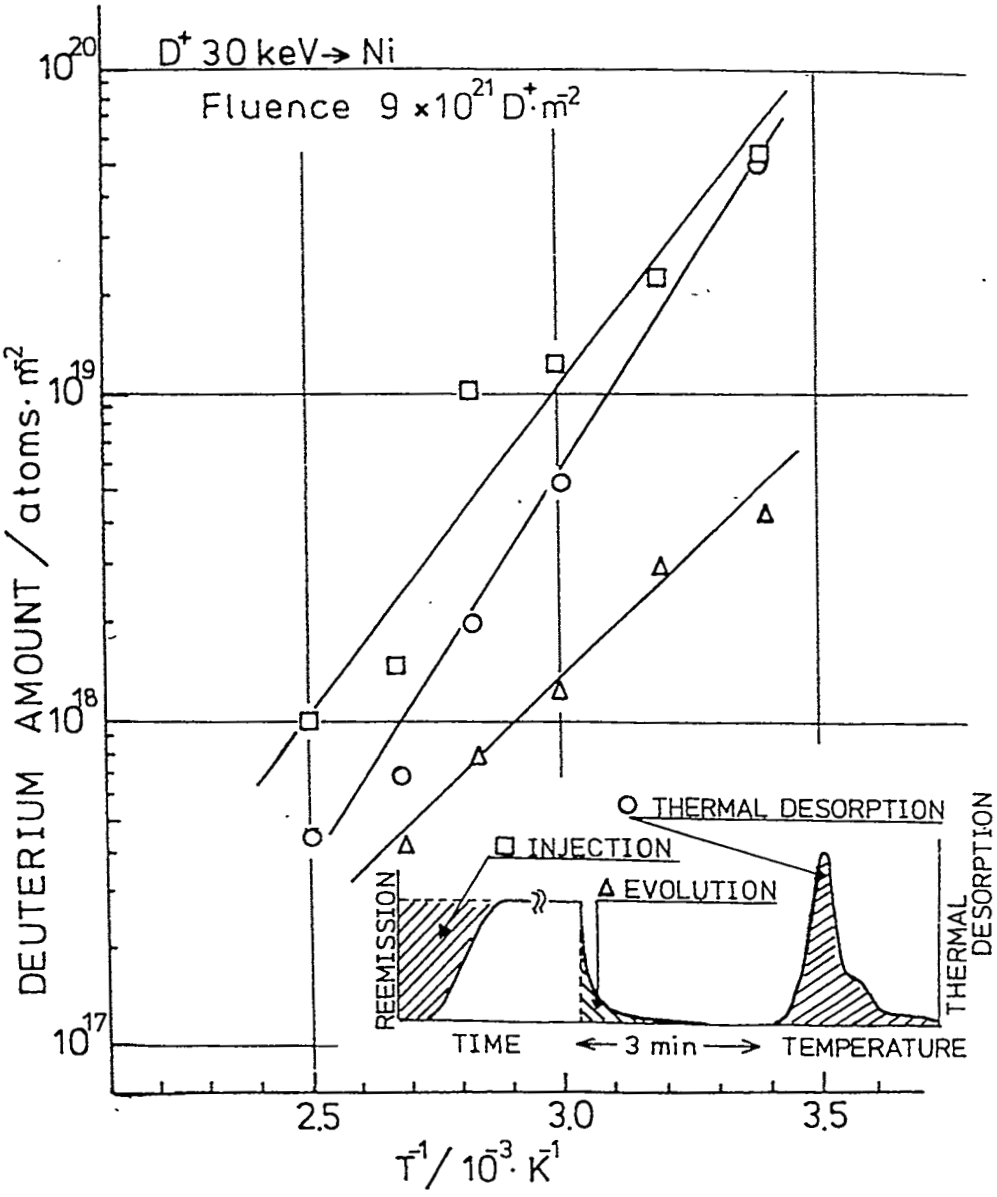

At low temperatures (near RT) most of the retained hydrogen in the target wall is not released without heating. Hence, thermal desorption has been one of the most powerful technique and applied to examine the hydrogen retention in the first wall. With increasing the target temperature, however, spontaneous release of the retained hydrogen after stopping the injection of hydrogen increases. At elevated temperatures, only very tinny amount of hydrogen is retained even during the exposure (dynamic retention) and most of them is spontaneously released after stopping the exposure. In this respect we can not rely on the wall pumping for obtaining low recycling regime as

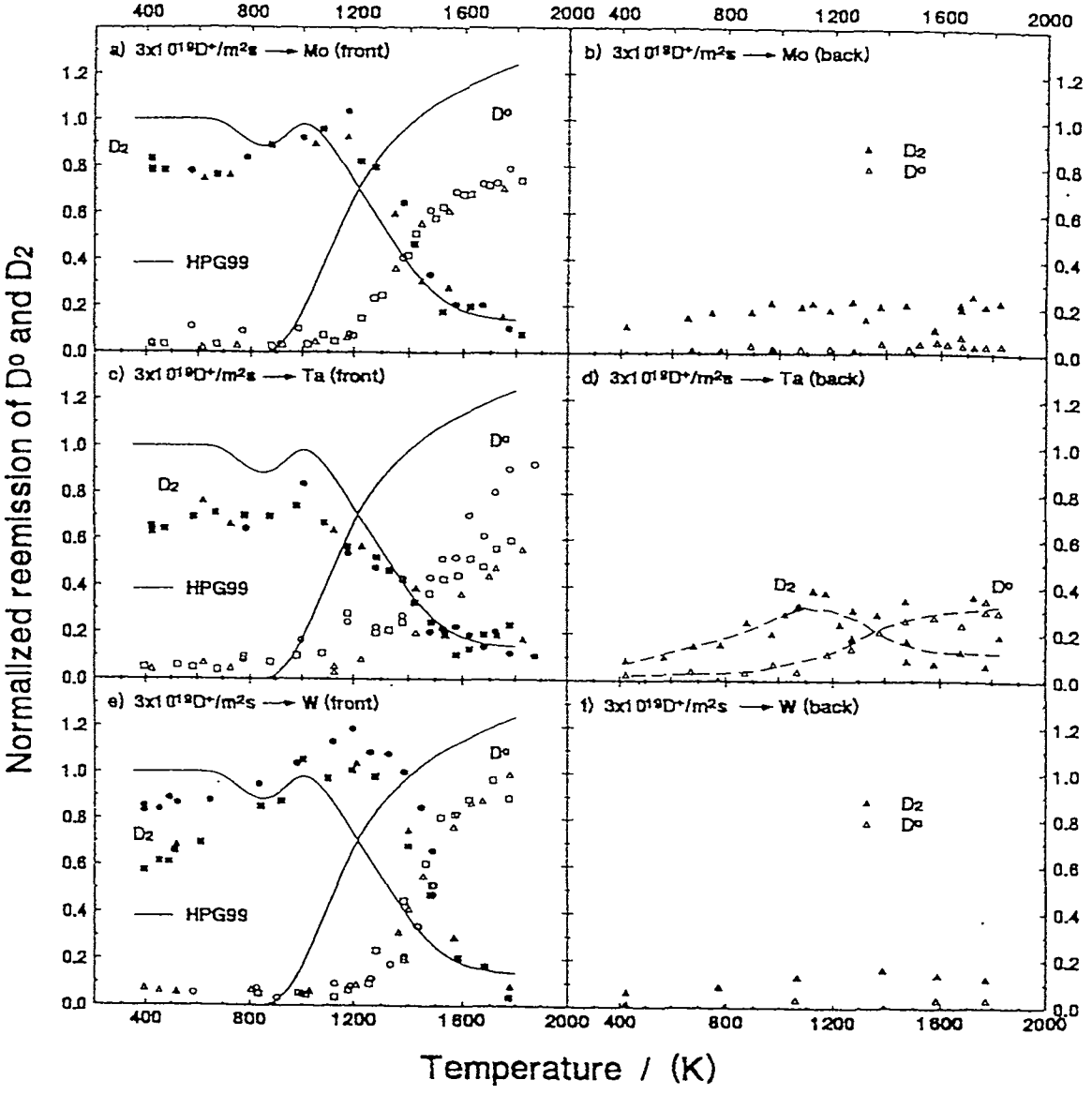

Fig. 2. Steady-state reemission of atoms and molecules as a function of sample temperature for (a, b) Mo, (c, d) Ta and (e, f The reemission data were normalized by setting a single normalization constant for all three specimens based on the average v of the molecular reemissions at ~ 1000 K; thus the normalized value of the sum of the molecular reemission from both surfac 1000 K is 1 ± 0.1. Solid symbols are for D_2 and open symbols are for D°. Different symbol shapes represent data taken on diffe days, in order of open then closed circles, open then closed squares and open then closed triangles. The cumulative flu associated with each data set is approximately (2–3) × 10^{23} D/m^2. The solid lines correspond to reemission results for pyro graphite [3].

Atomic reemission is dominant at elevated temperatures

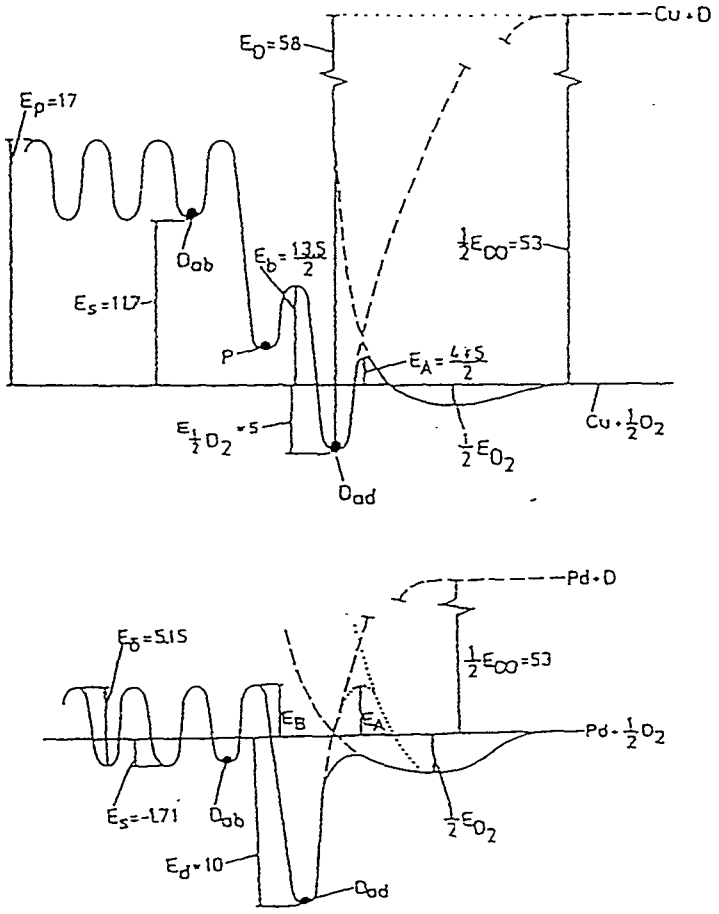

(a)One dimensional potential energy diagram for D_2 and D for (a) Cu (an endothermic hydrogen occluder and (b) Pd (an exothermic hydrogen occluder). All energies are in kcal/mol per D atm
(after Comsa, Surf. Sci. Repts.5(1985)145)

The reemitted hydrogen molecules are not necessarily equilibrated thermodynamically with the surface temperature of the target but are often in excited states vibrationally and/or rotationally. Higher is the target temperature, the more the reemitted molecules are in the excited states. Some of injected hydrogen is directly reflected. Not a small amount of the reflected particles is in electrically excited states and even

Journal of Nuclear Materials 266-269 (1999) 138-145

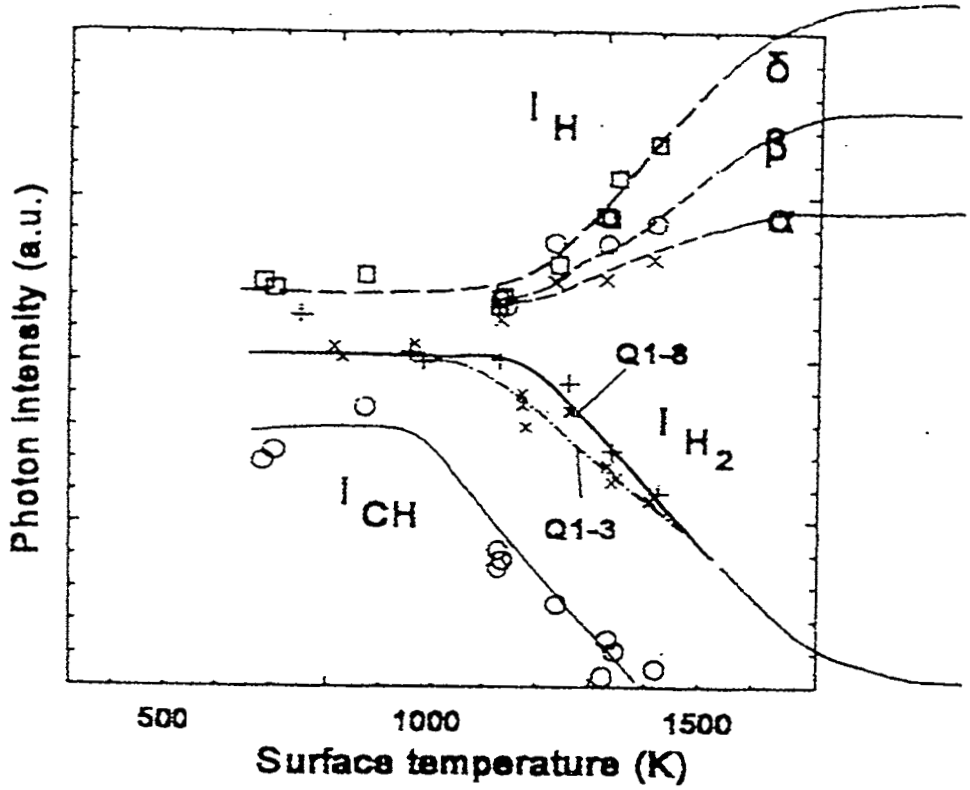

Fig. 3. Variations of the H_2-, CH-, and $H_{\delta,\beta,\alpha}$-emission (□,○,× resp.) as a function of the limiter temperature in the Ohmic part of the discharge (uniform heating). A smaller sum of individual Q_i-components is represented by (x).

Quite recently it has been confirmed in TEXTOR that some of the released particles from the wall are in excited states vibrationally and rotationally. The dominance of atomic reemission from graphite target above 1300K is another example.

The behavior of these excited particles in the boundary plasma must be significantly different from that of the ground state which has been assumed for the recycling particles from the wall in most of the model calculations.

Twin Limiter Experiment

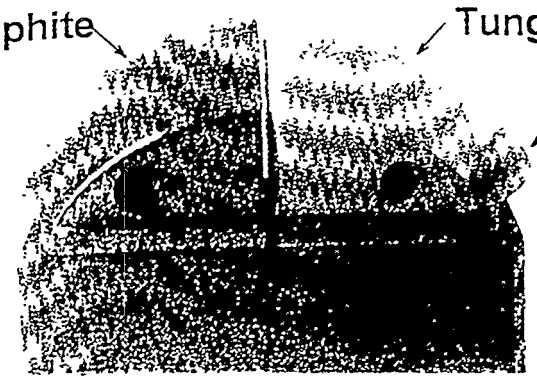

Layer Thickness
about $3 \times 10^{17} C/cm^2$
after 8 shots
1nm /sec
C/D ≈ 0.1

Institut für Plasmaphysik / Trilateral Euregio Cluster, EURATOM-Assoziation

Hydrogen recycling and retention

After 10 shots hydrogen desorbed from surface is larger than C-side of the twin limiter

Heating

Chemical sputtering

similar penetration length (Carbon & Hydrogen)

suppression of chemical sputtering?

Comparison with other elements

Ta-C twin limiter

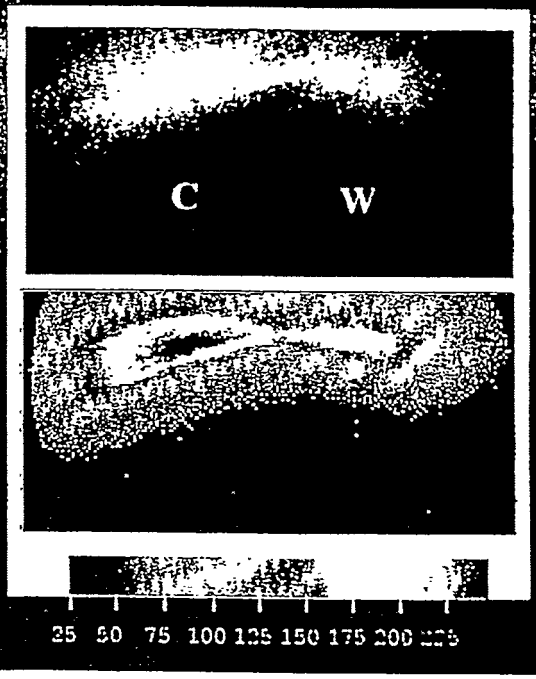

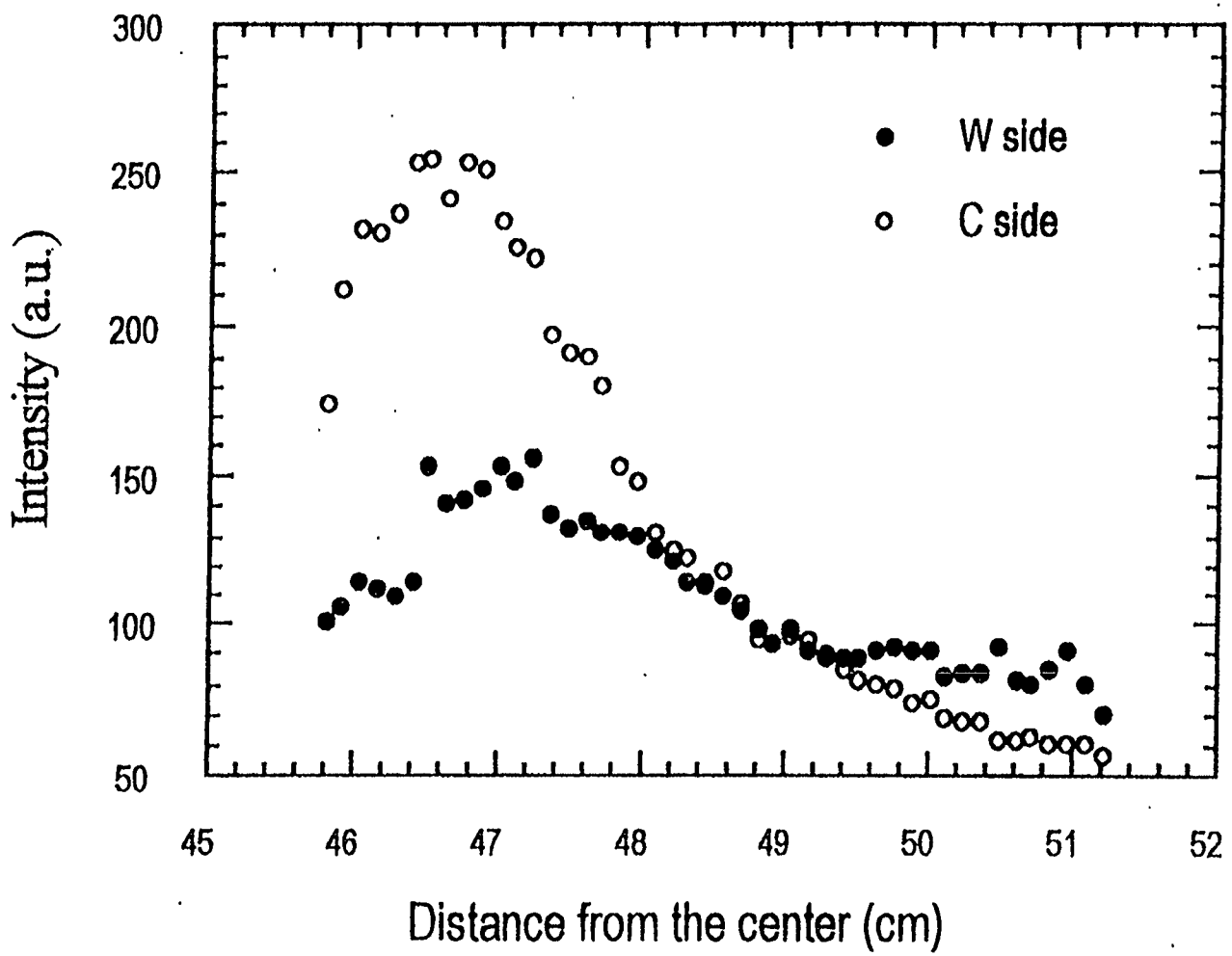

Fig.5 Comparison of D α intensity decay in front of the limiter between C and W sides

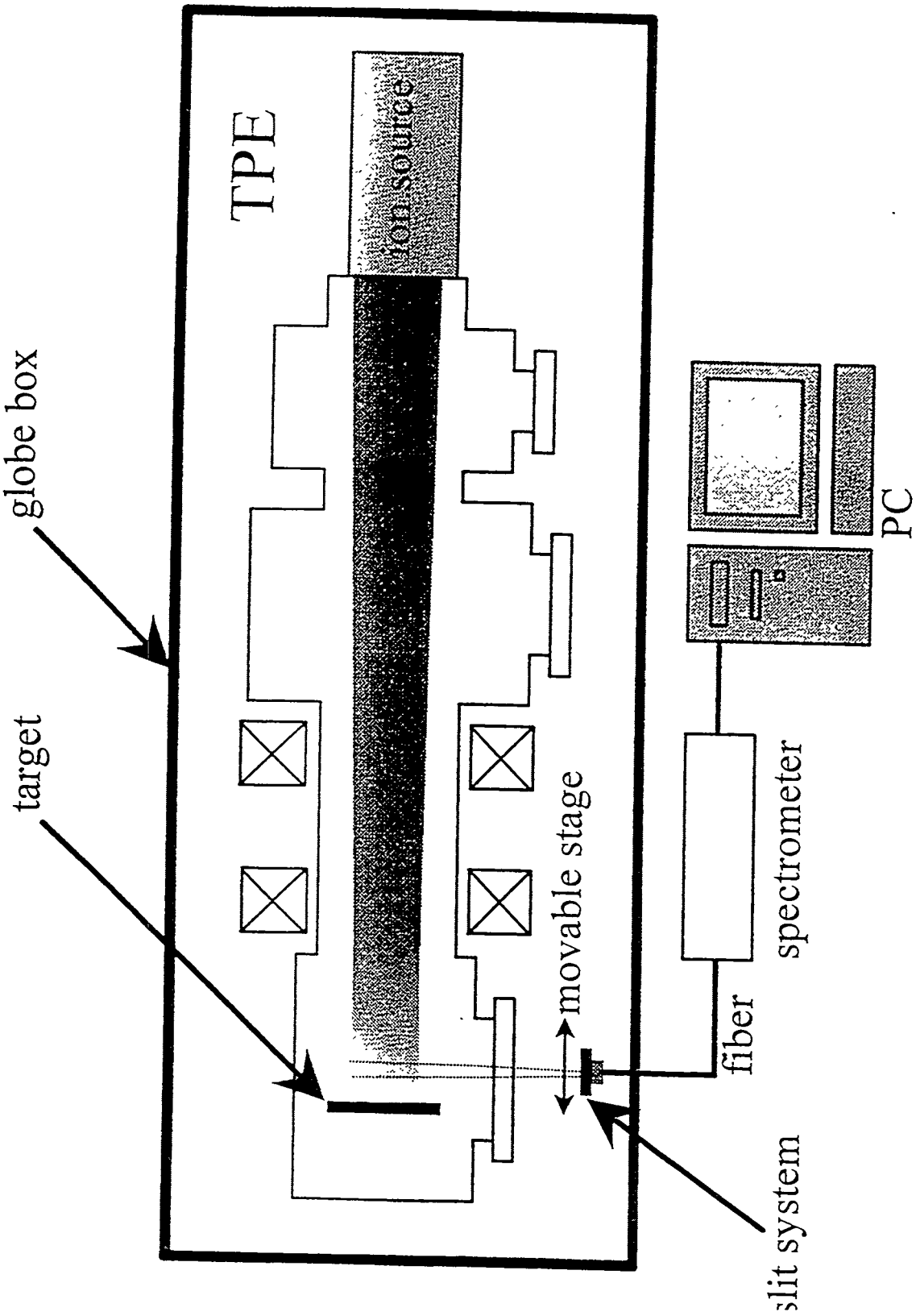
globe box
target
TPE
ion source
movable stage
fiber
spectrometer
PC
slit system

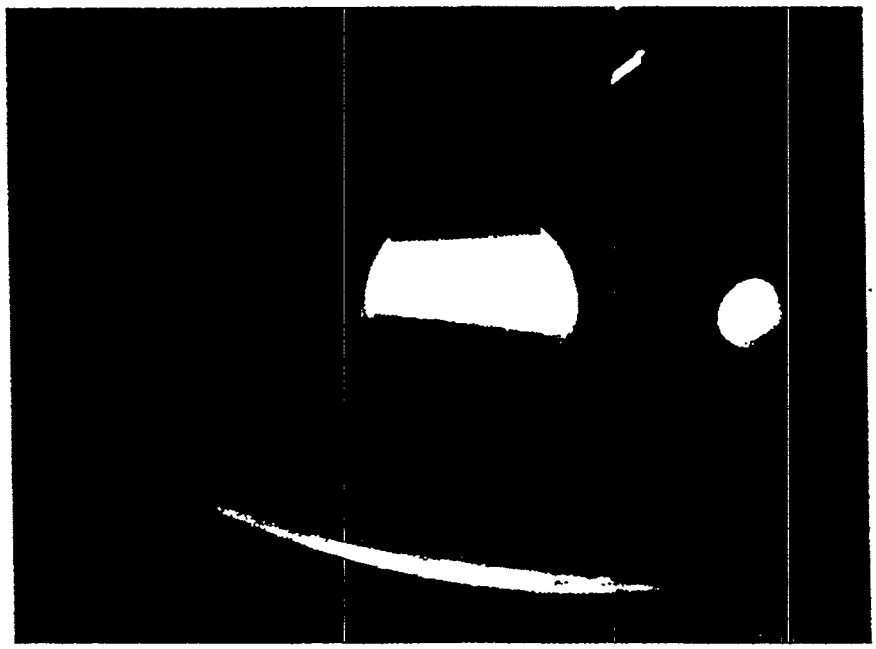

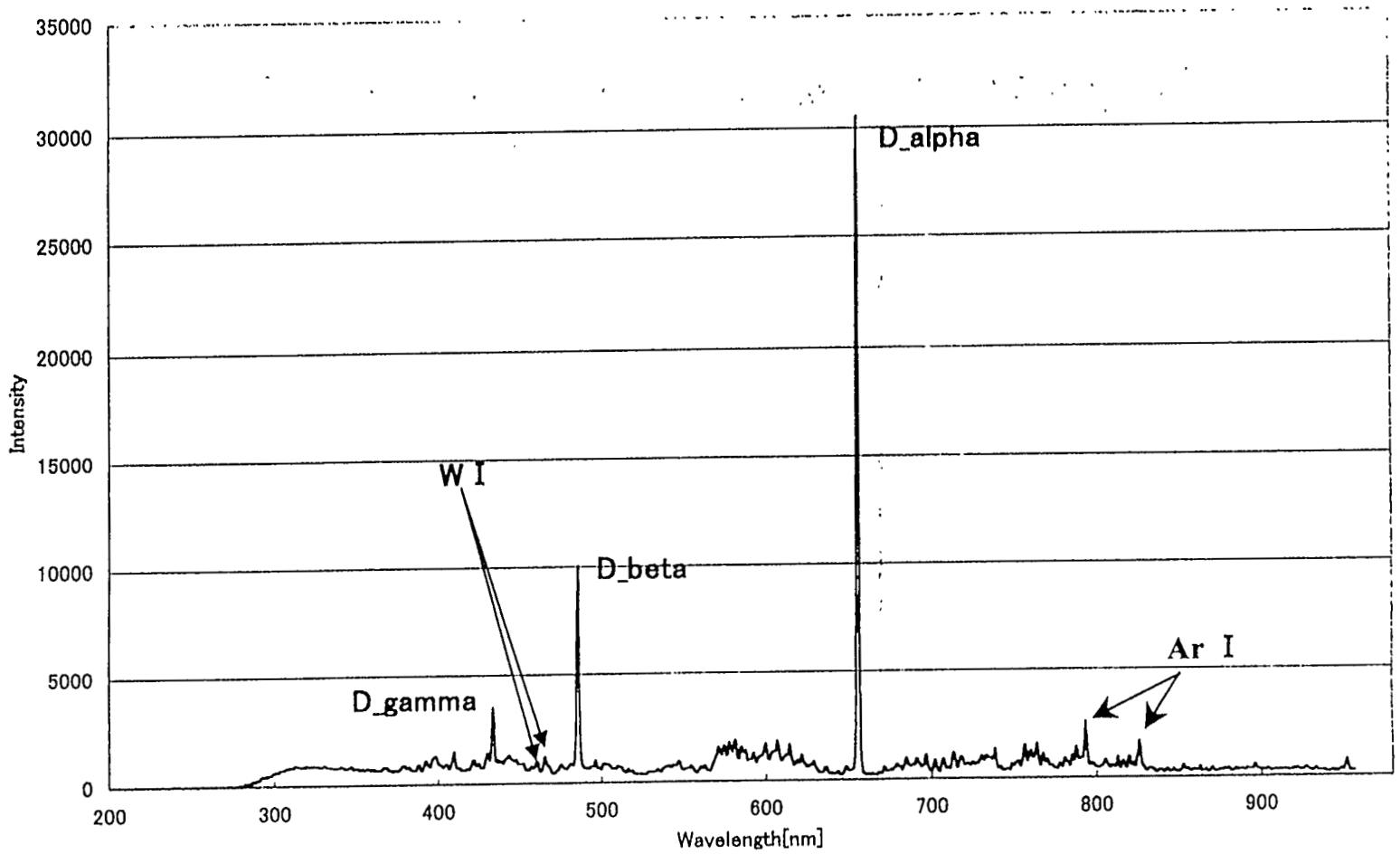
35000
30000
25000
20000
15000
10000
5000
0
Intensity
200
300
400
500
600
700
800
900
Wavelength[nm]
D_alpha
W I
D_beta
Ar I
D_gamma

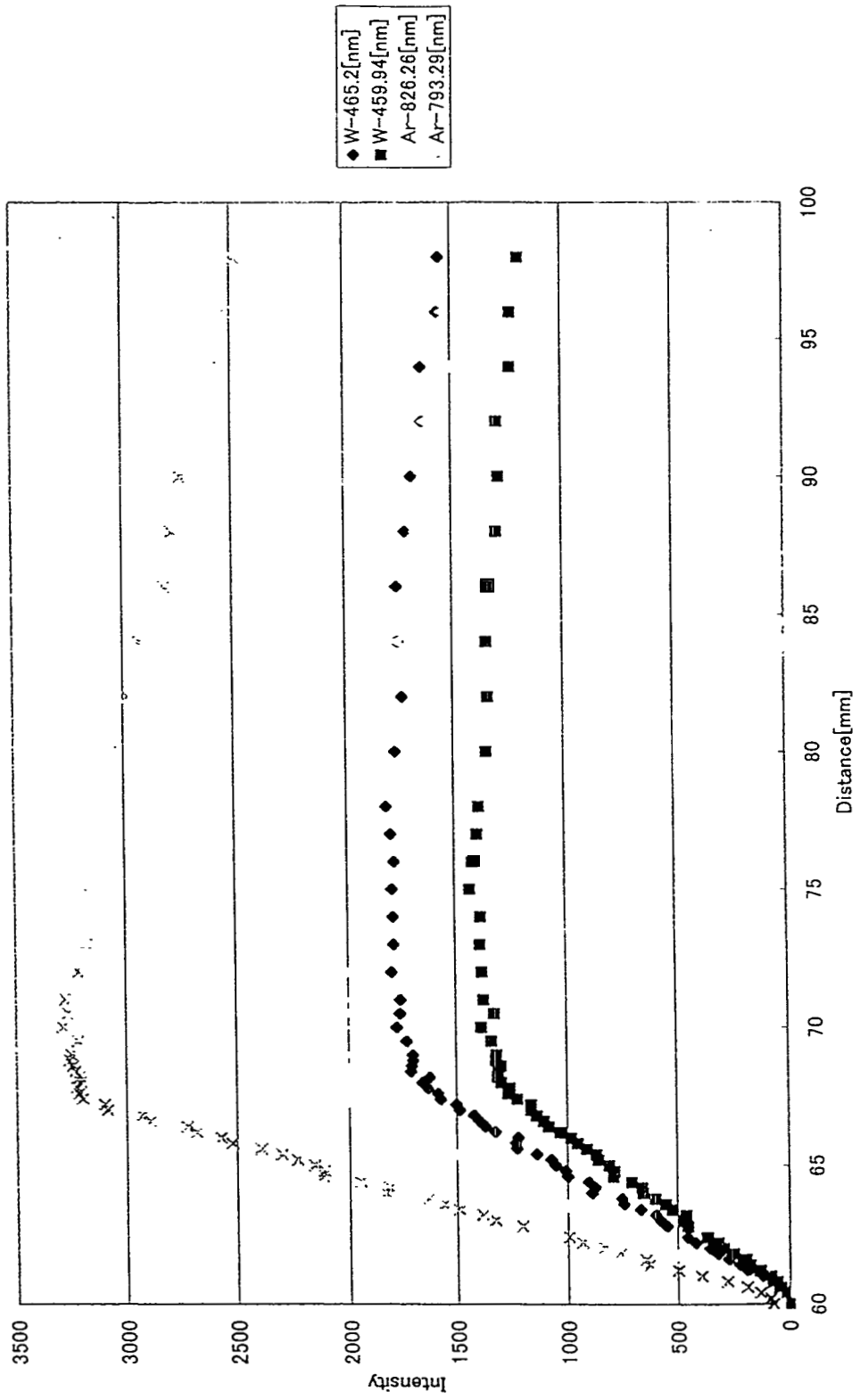
W-465.2[nm]
W-459.94[nm]
Ar-826.26[nm]
Ar-793.29[nm]
Intensity
3500
3000
2500
2000
1500
1000
500
0
60
65
70
75
80
85
90
95
100
Distance[mm]

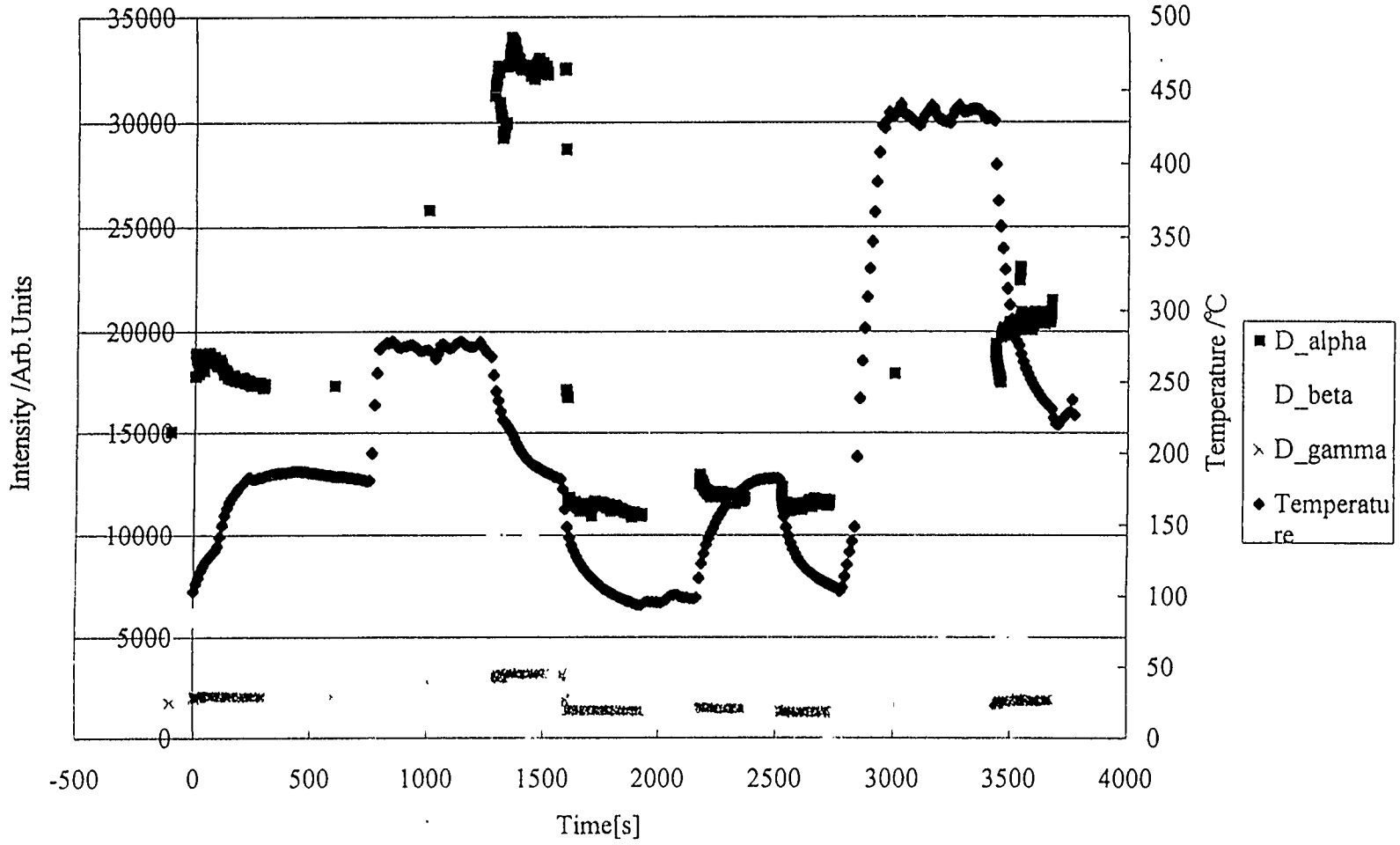
35000
30000
25000
20000
15000
10000
5000
0
Intensity /Arb.Units
500
450
400
350
300
250
200
150
100
50
0
Temperature /°C
-500
0
500
1000
1500
2000
2500
3000
3500
4000
Time[s]
D_alpha
D_beta
D_gamma
Temperatu re

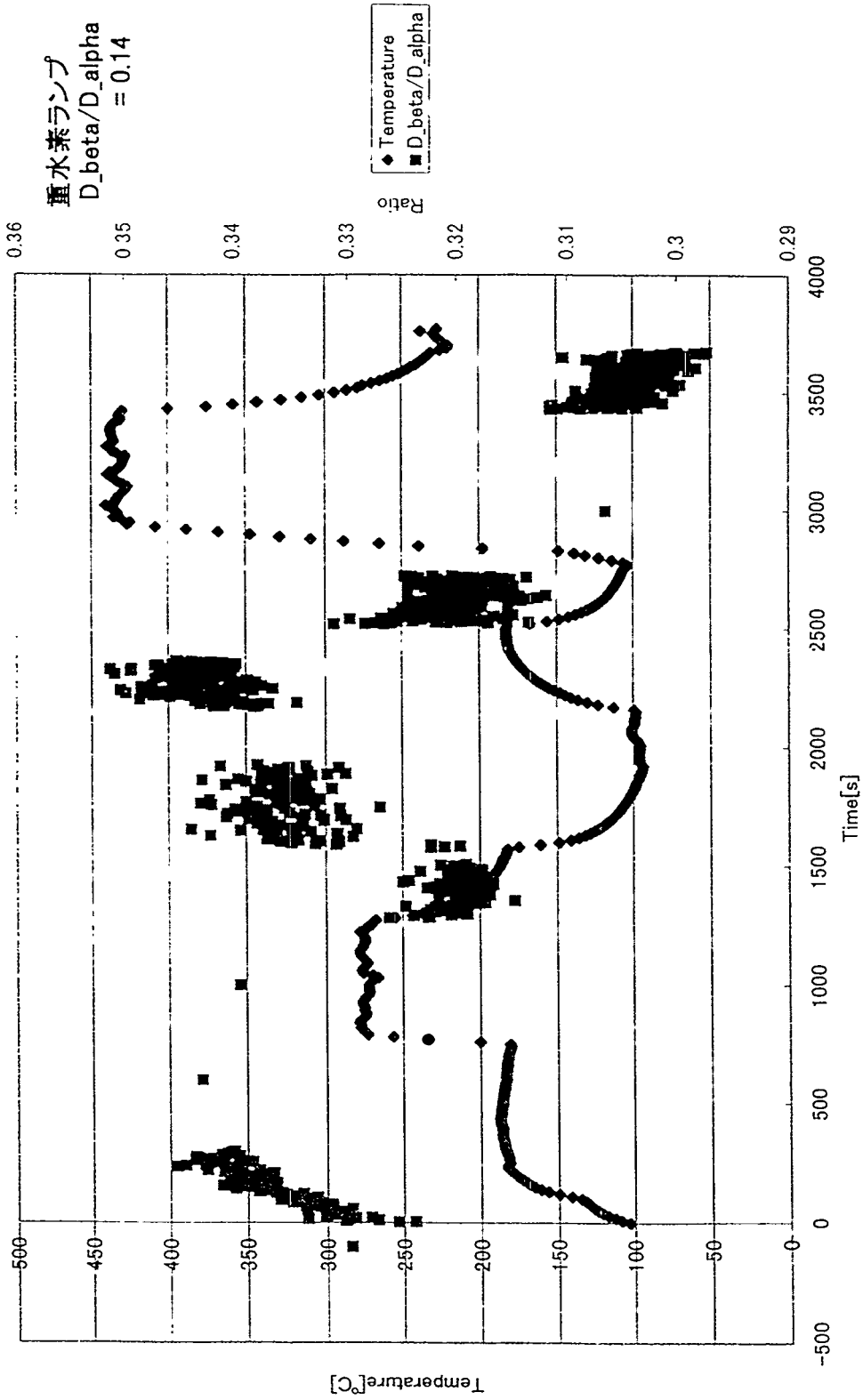
重水素ランプ
D_beta/D_alpha
= 0.14
Temperature
D_beta/D_alpha
Ratio
0.36
0.35
0.34
0.33
0.32
0.31
0.3
0.29
500
450
400
350
300
250
200
150
100
50
0
-500
0
500
1000
1500
2000
2500
3000
3500
4000
Time[s]
Temperature[°C]

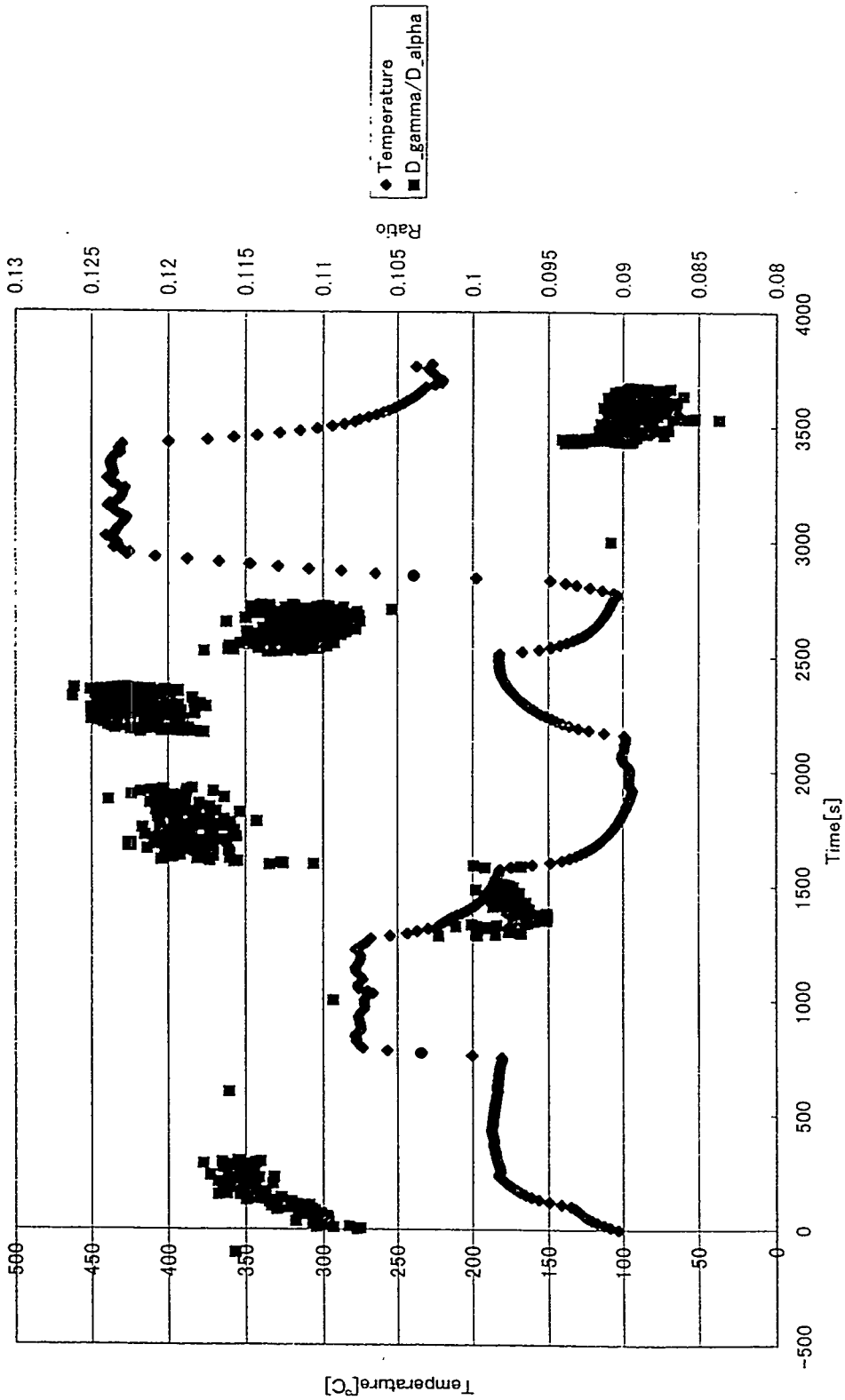
Temperature
D_gamma/D_alpha
Ratio
0.13
0.125
0.12
0.115
0.11
0.105
0.1
0.095
0.09
0.085
0.08
500
450
400
350
300
250
200
150
100
50
0
Temperature[°C]
-500
0
500
1000
1500
2000
2500
3000
3500
4000
Time[s]

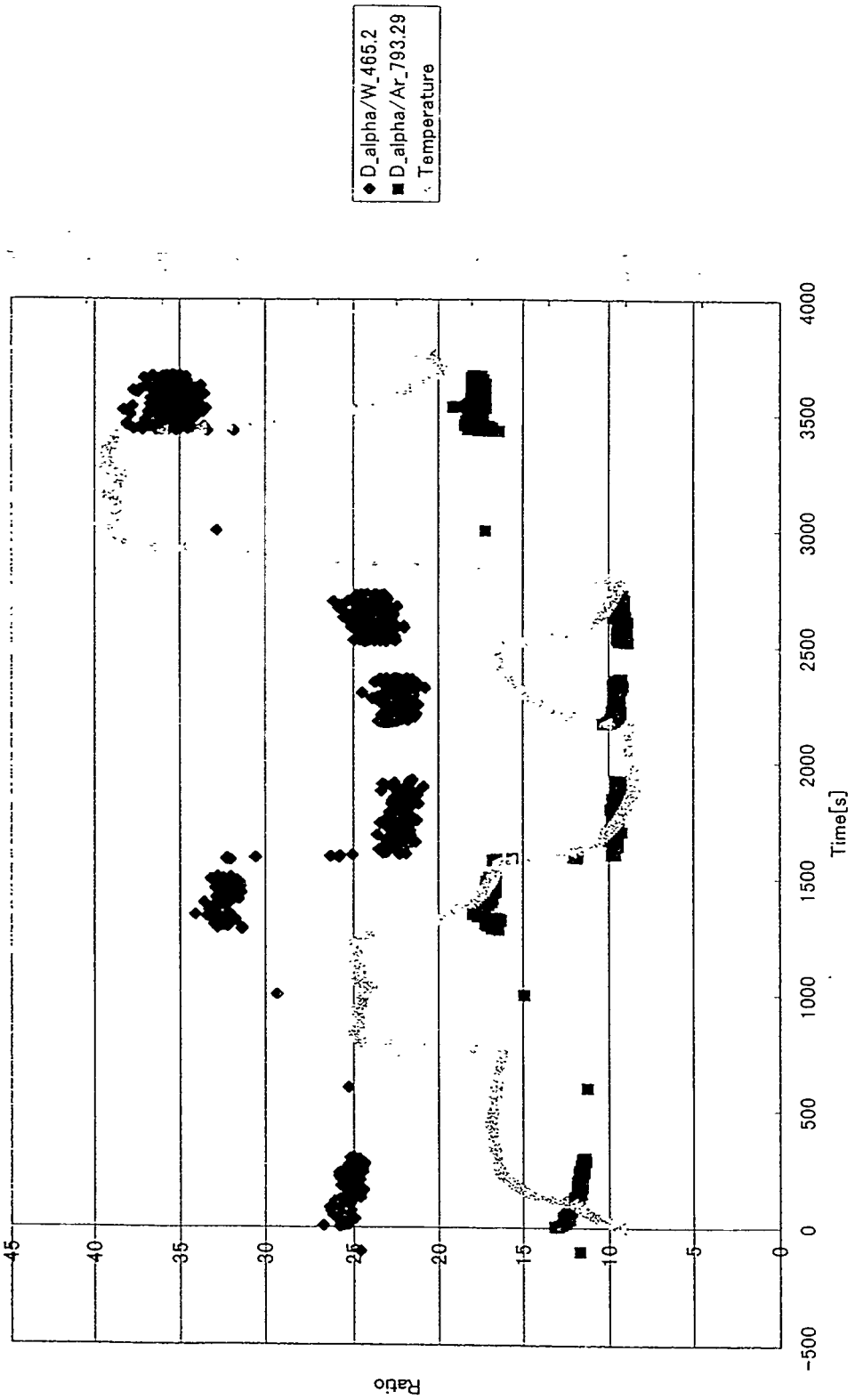
D_alpha/W_465.2
D_alpha/Ar_793.29
Temperature
Ratio
Time[s]
45
40
35
30
25
20
15
10
5
0
-500
0
500
1000
1500
2000
2500
3000
3500
4000

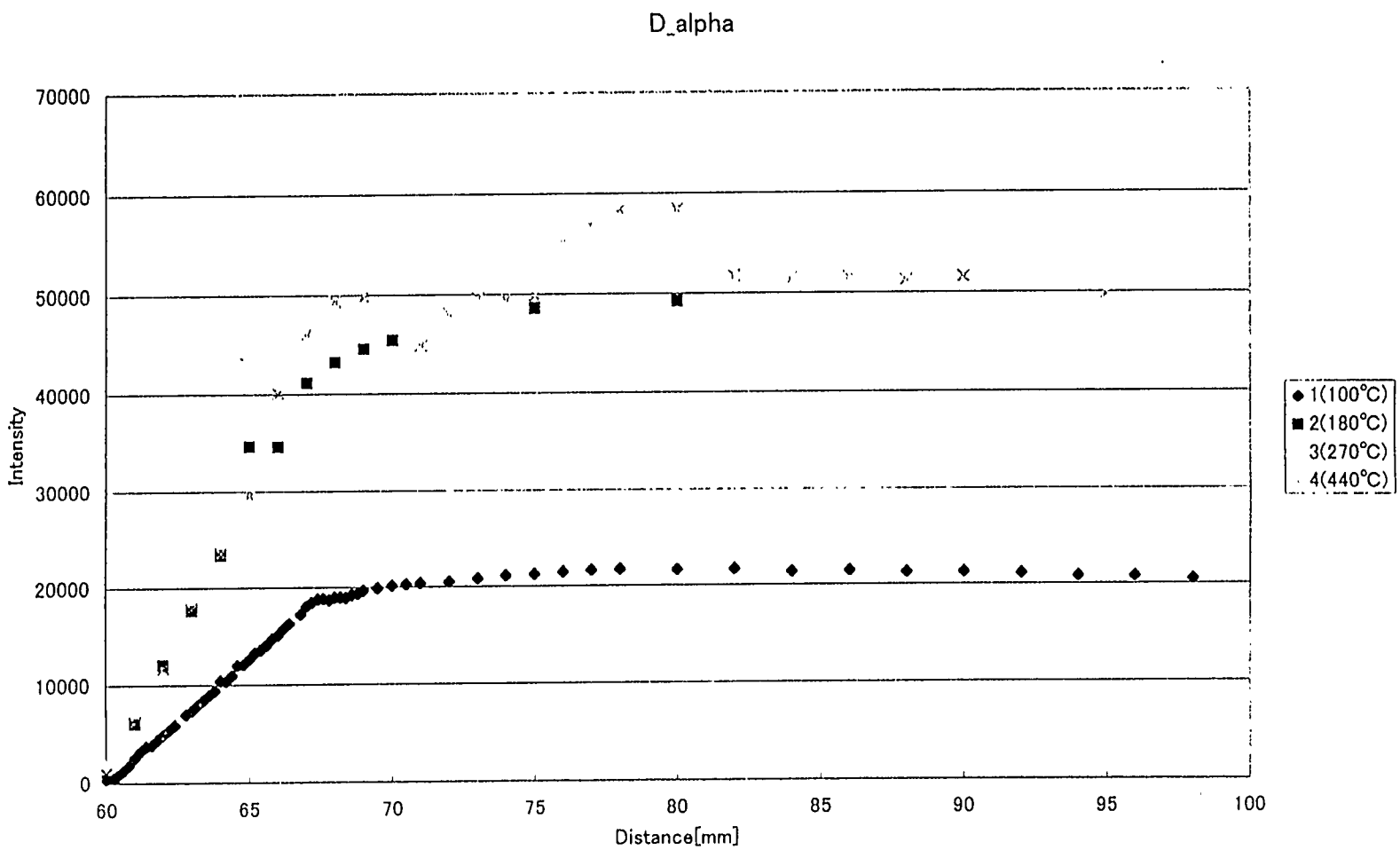
D_alpha
70000
60000
50000
40000
30000
20000
10000
0
Intensity
60
65
70
75
80
85
90
95
100
Distance[mm]
1(100°C)
2(180°C)
3(270°C)
4(440°C)

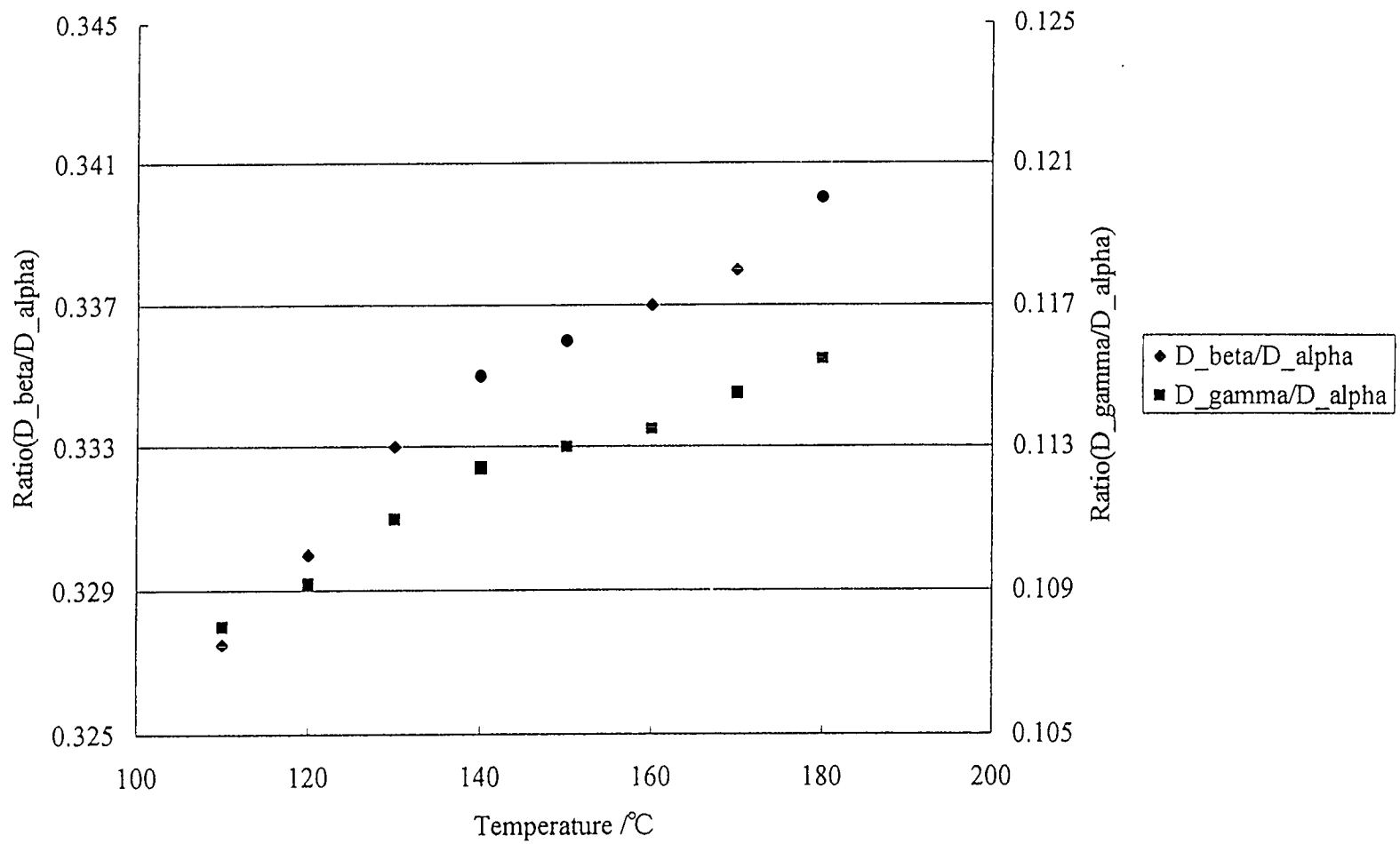
0.345
0.341
0.337
0.333
0.329
0.325
Ratio(D_beta/D_alpha)
0.125
0.121
0.117
0.113
0.109
0.105
Ratio(D_gamma/D_alpha)
100
120
140
160
180
200
Temperature /℃
D_beta/D_alpha
D_gamma/D_alpha

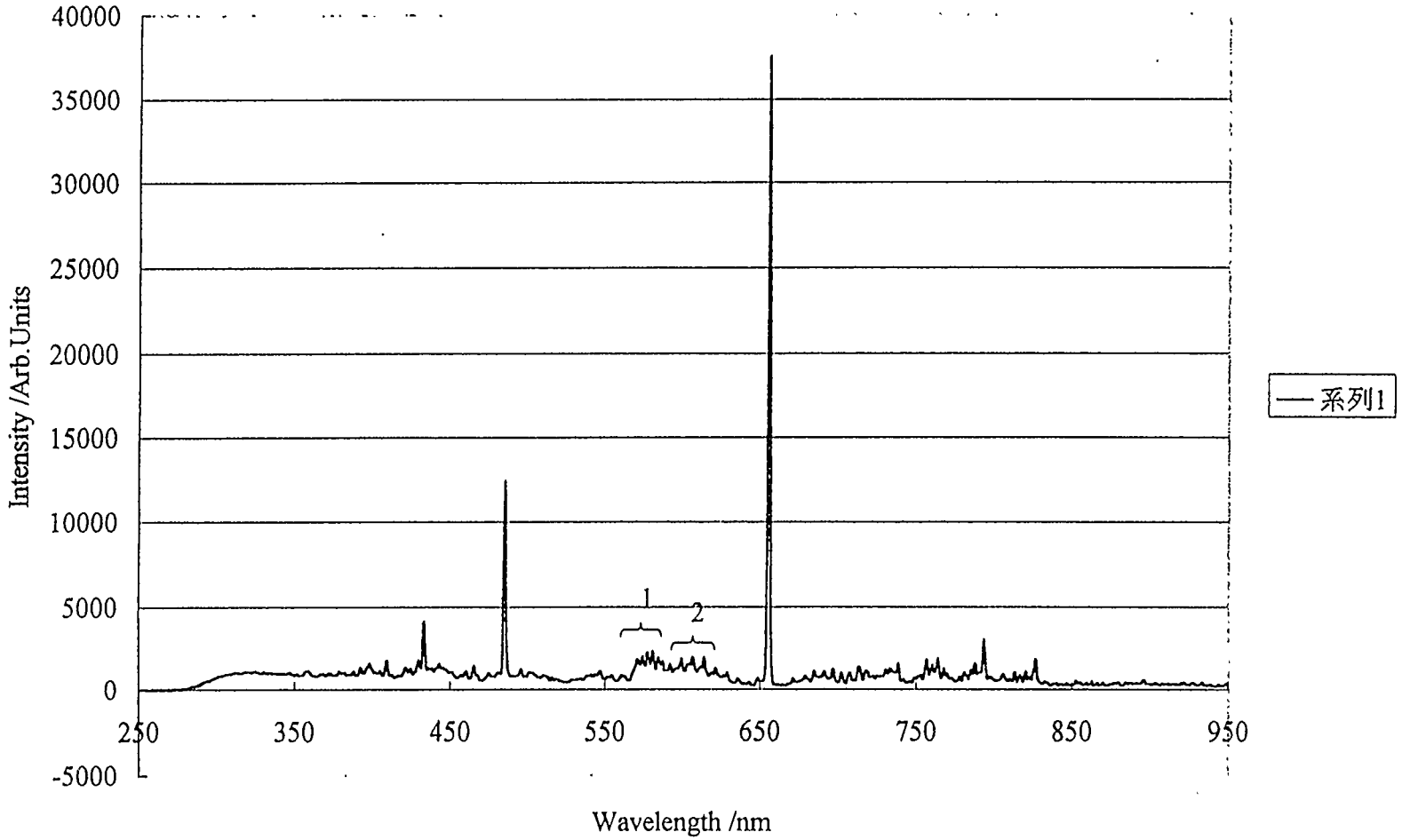
40000
35000
30000
25000
20000
15000
10000
5000
0
-5000
Intensity /Arb.Units
250
350
450
550
650
750
850
950
Wavelength /nm
1
2
系列1

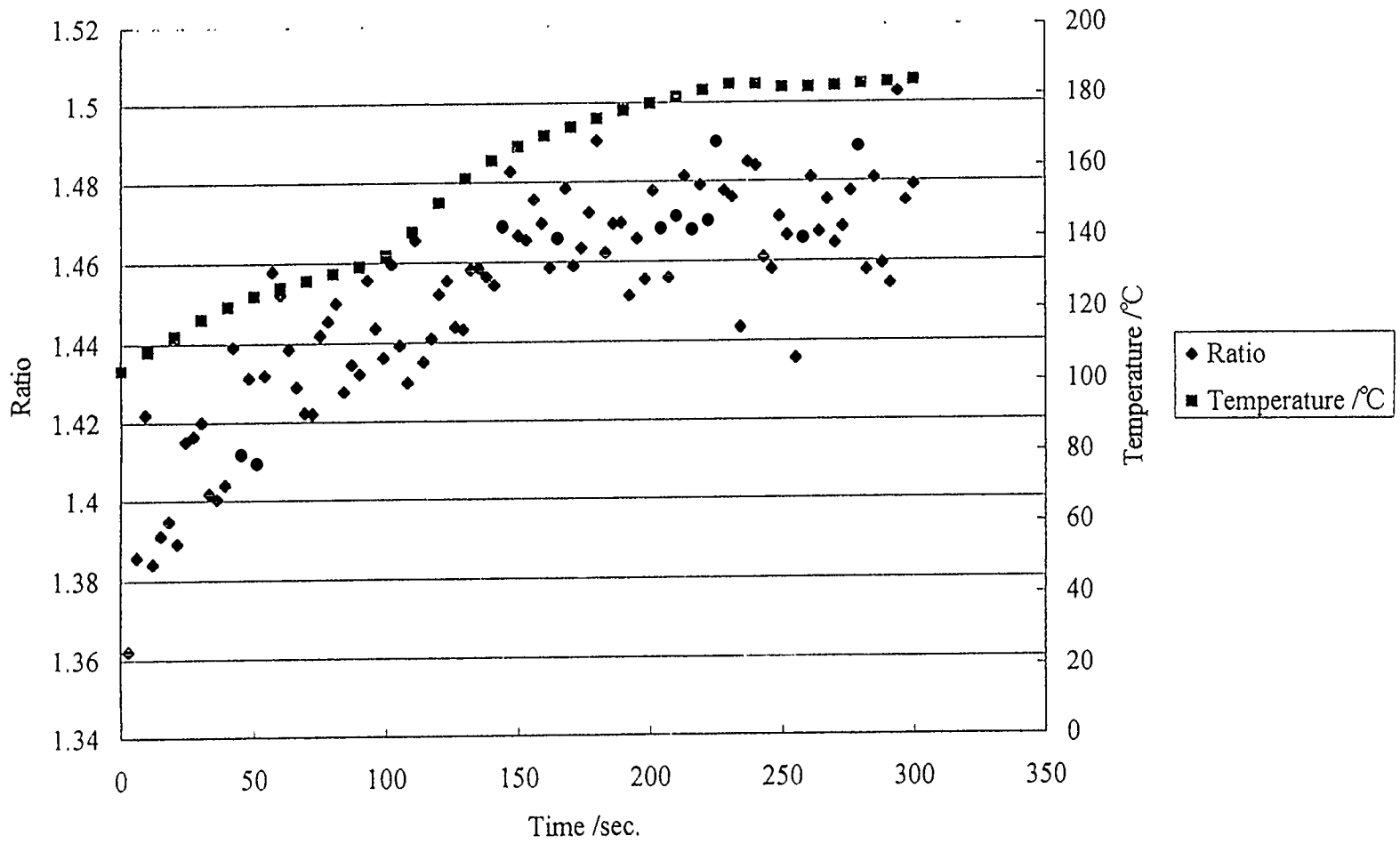
1.52
1.5
1.48
1.46
1.44
1.42
1.4
1.38
1.36
1.34
Ratio
200
180
160
140
120
100
80
60
40
20
0
Temperature /℃
0
50
100
150
200
250
300
350
Time /sec.
Ratio
Temperature /℃

Tanabe's View for future hydrogen recycling

At high temperature divertor plate (1000K like ITER), hydrogen recycling in the boundary plasma would be quite different from those observed in the present tokamak machines operated with low temperature divertor.

(i) 100% hydrogen recycling regime would be very easily attained, which would require another operational scenario without wall pumping.

(ii) the fractional energy return from recycled hydrogen to the plasma would be much higher than that of the present tokamak, which, in turn, would varies characteristics of hydrogen recycling properties.

Chemical sputtering with high flux ion beam

M.Isobe,Y.Ueda, Y.Ohtsuka, M.Nishikawa

Osaka University, Japan

III-122

1999 US-Japan Workshop on PSI and HHF Components in Next Fusion Devices

Nov. 1 - Nov. 4 in Santa Fe

Supra-high Temperature Engineering Laboratory
Graduate School of Engineering, Osaka Univ.

Target of This Work

1. Construction of erosion database of chemical sputtering of carbon based materials (isotropic graphite, C/C composite, boron doped graphite, and Si doped graphite) under high flux ($>10_{20}$ $m_{-2}s_{-1}$) and low energy (< 5keV) conditions. Until now, no database exist for these parameter range.

2. Making comprehensive erosion models for chemical sputtering in high flux regime.

High Flux Irradiation Test Stand

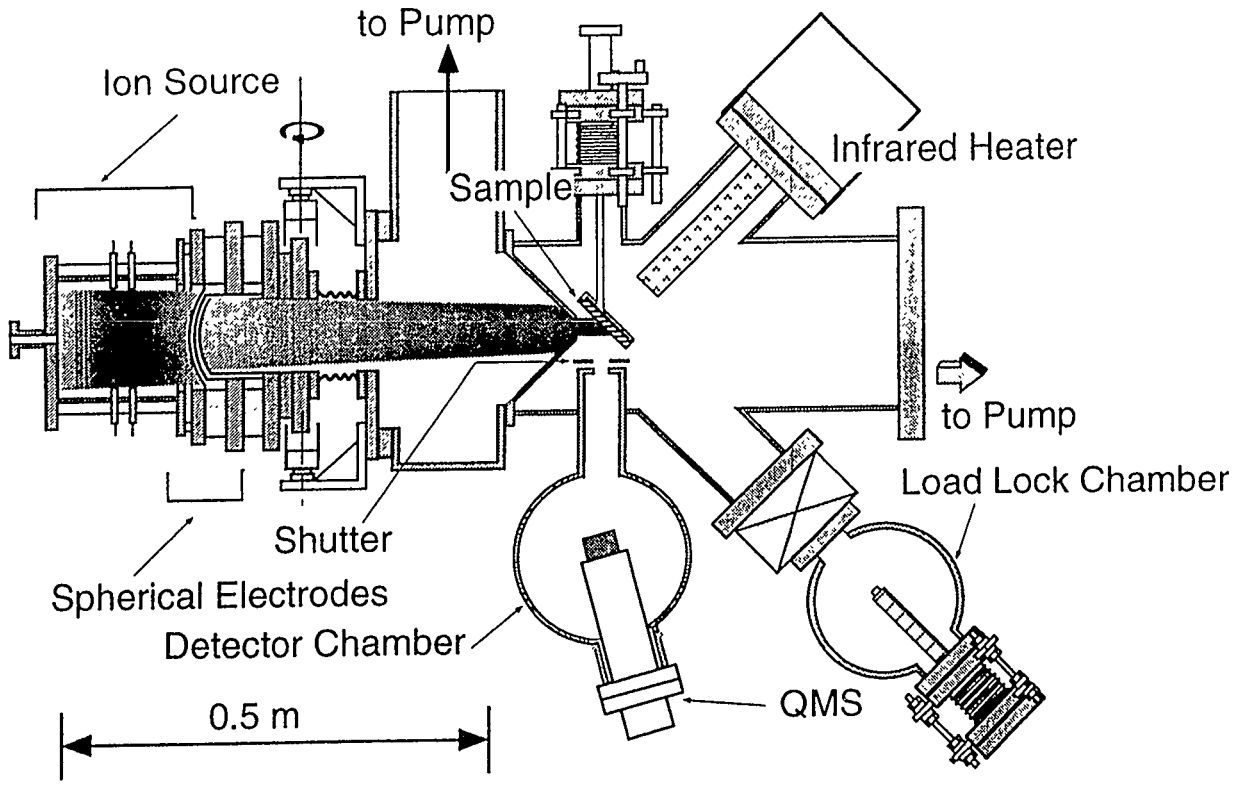

Surface temperature
IR thermometer

Sample

Size: 20 x 20 x 5 mm3

Materials (Toyo Tanso):
IG-430U
CX-2002
GB series
(B content 0%-20%)
SiC doped graphite

Beam aperture:
12 x 8 mm2

Supra-high Temperature Engineering Laboratory
Graduate School of Engineering, Osaka Univ.

Beam Specification

Ion Source

Bucket source --Arc discharge with thermionic cathodes

Electrodes---Spherical electrode

Effective diameter : 14 cm, Radius of curvature : 50 cm

Gas ---D_2 : 5 - 10 mTorr, Ar : 5 mTorr

Beam Characteristics

Energy : ~ 5 keV

Power density : 3.5 MW/m^2 (D), 1.2 MW/m^2 (Ar)

Flux : 1.0 x 10^{22} D/m^{2}s, 1.5 x 10^{21} Ar/m^{2}s

Impurities : 2~3% (mainly Oxygen)

Pulse length : 4 sec

Duty : ~ 5%

Elimination of Background

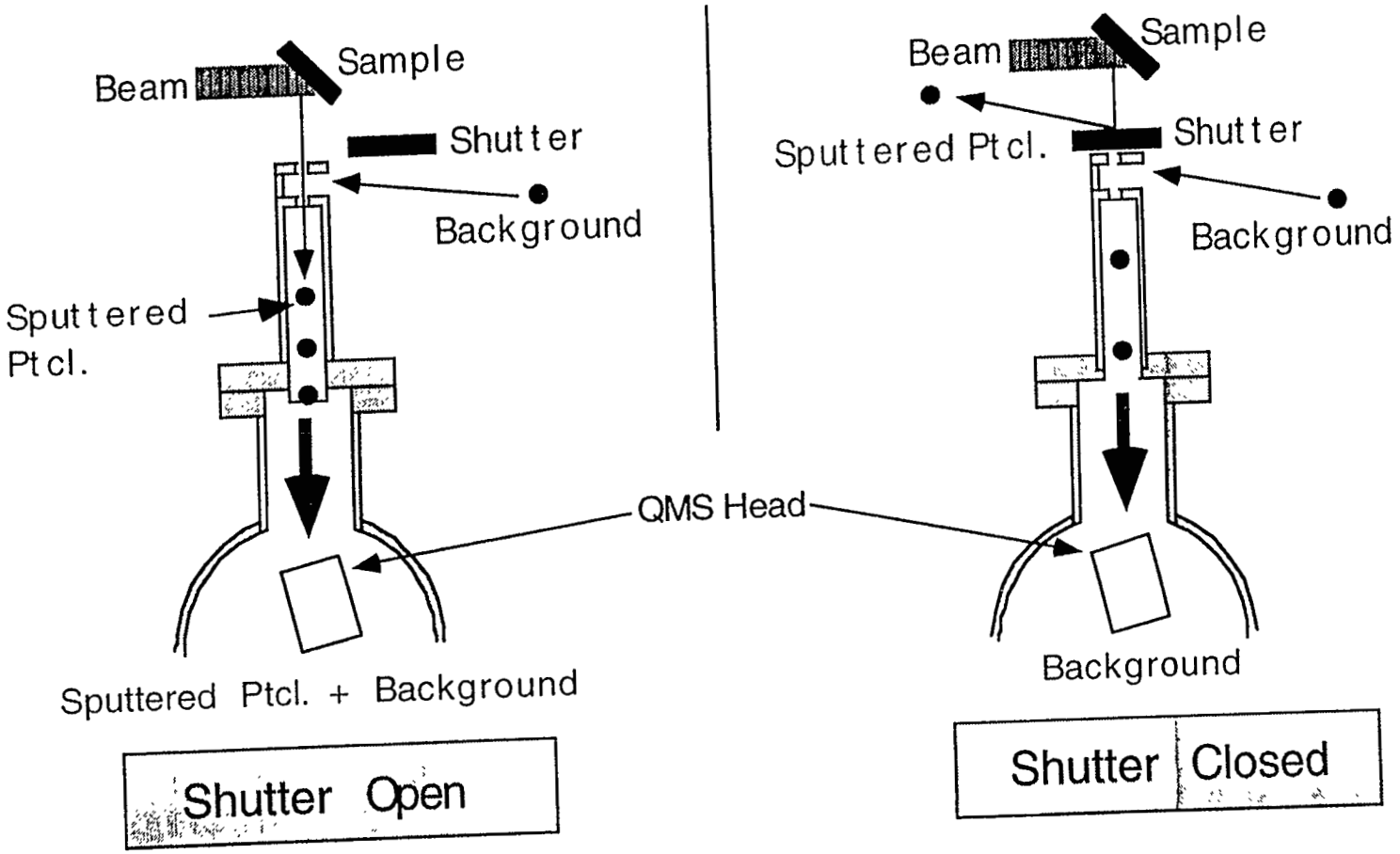

Typical QMS Signal and Temperature

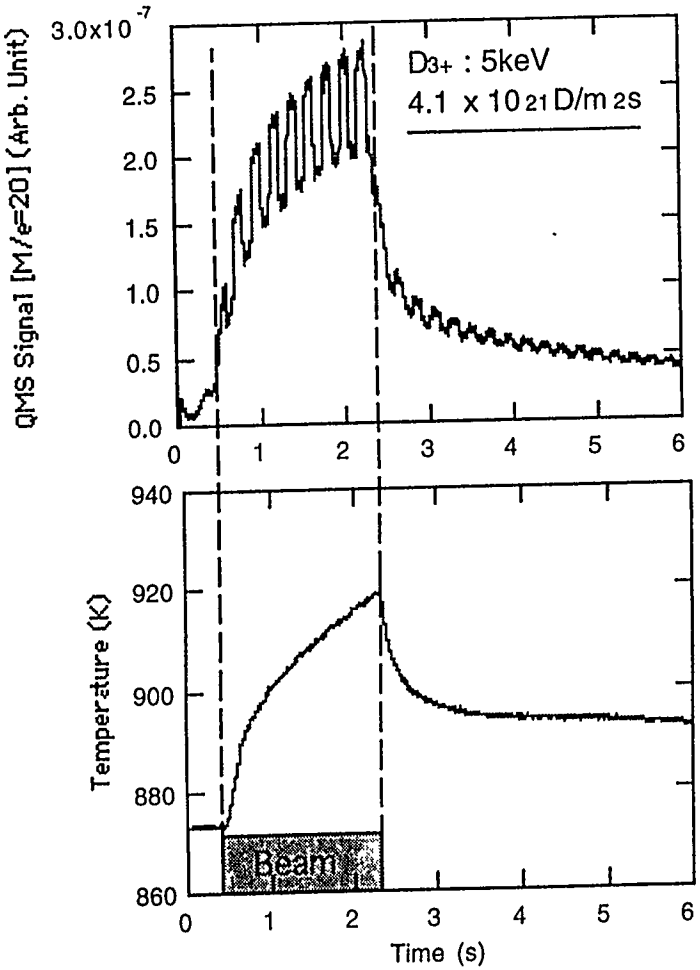

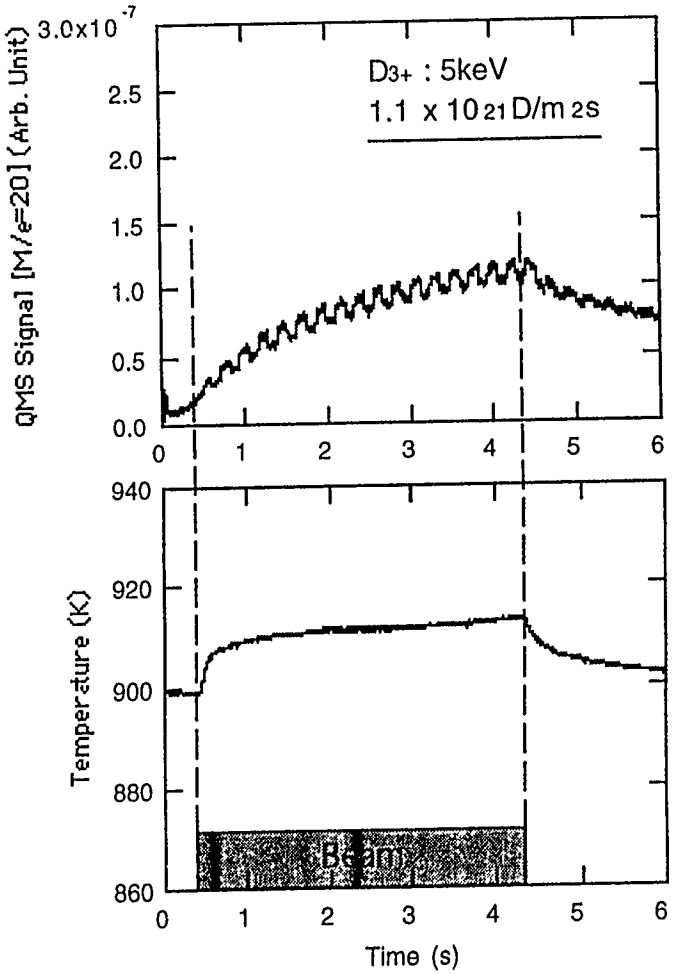

Temperature Dependence of Methane Yield for Isotropic Graphite (IG-430U)

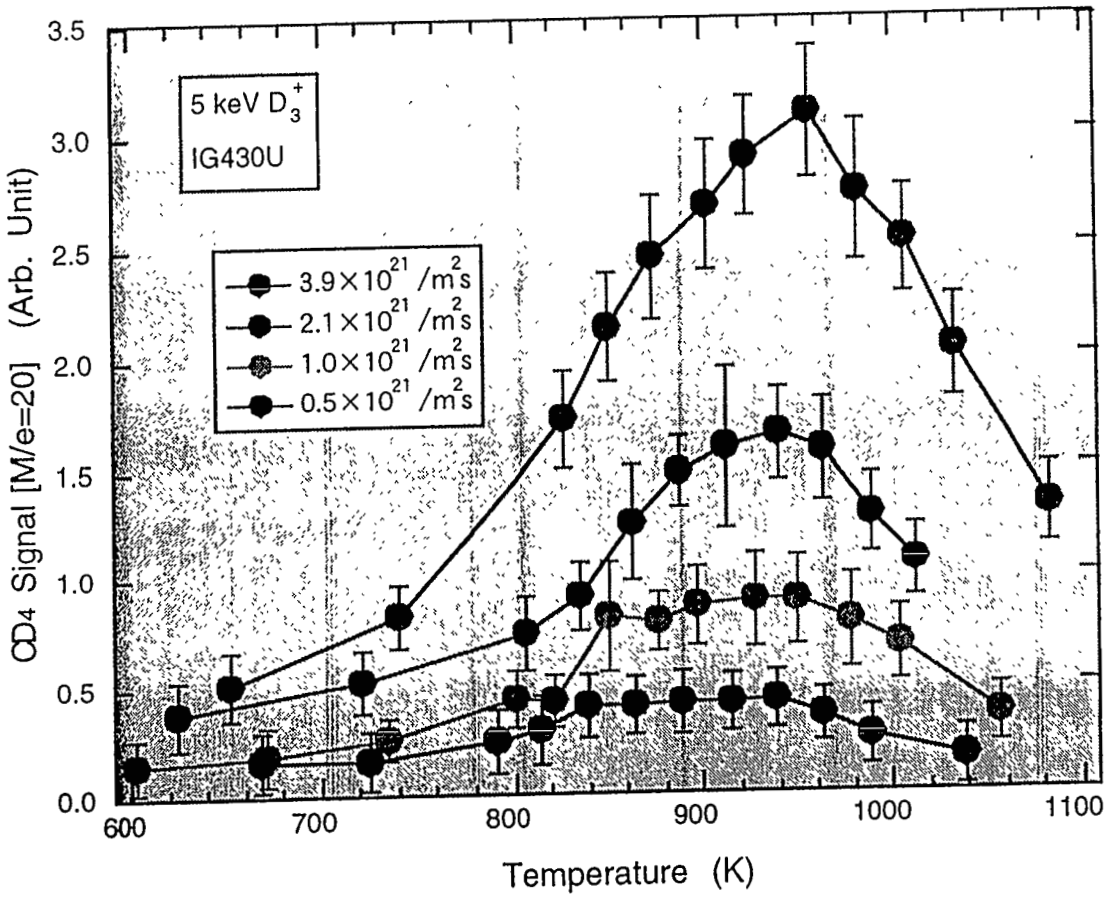

Peak temperatures range from 900 to 950 K (max 1000 K for CX2002).
The peak temperatures increase with flux.

Supra-high Temperature Engineering Laboratory
Graduate School of Engineering. Osaka Univ.

Chemical Sputtering of Boron-doped graphite

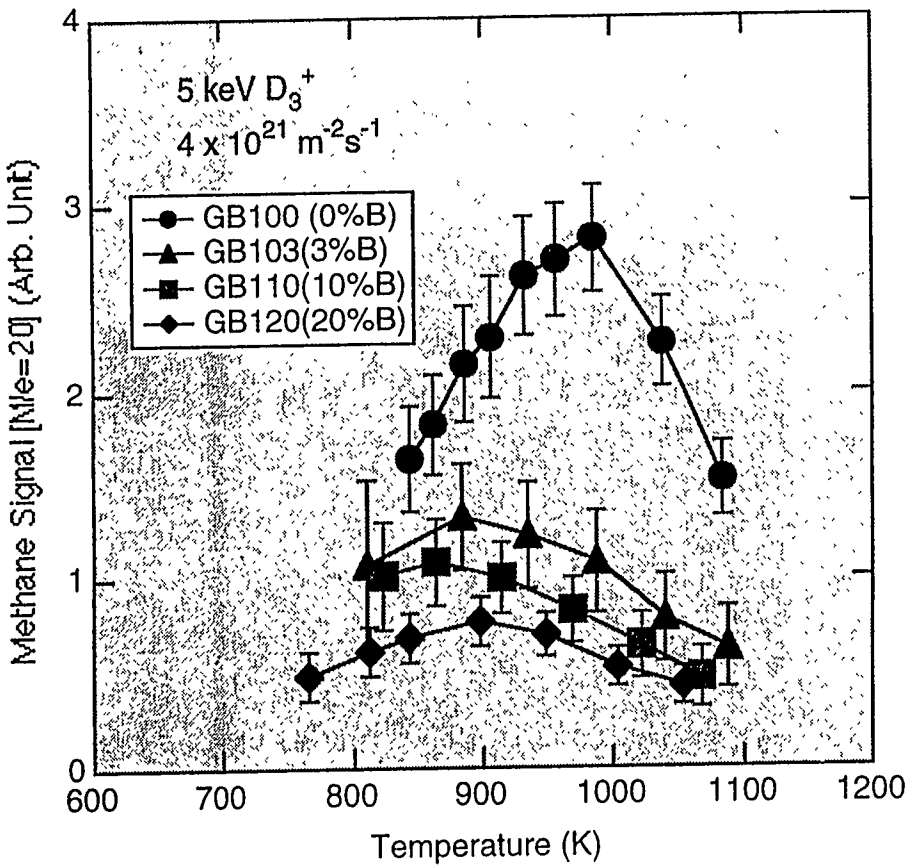

Reduction of methane signal by a factor of 3 - 4 is observed, which is similar to that of low flux experiments (4.5 keV H_3^+, 10^{19} $m^{-2}s^{-1}$)[1].

[1] Hino et al., J. Nucl. Mater. 211 (1994) 30.

Supra-high Temperature Engineering Laboratory
Graduate School of Engineering, Osaka Univ.

Chemical Sputtering of Si-doped graphite

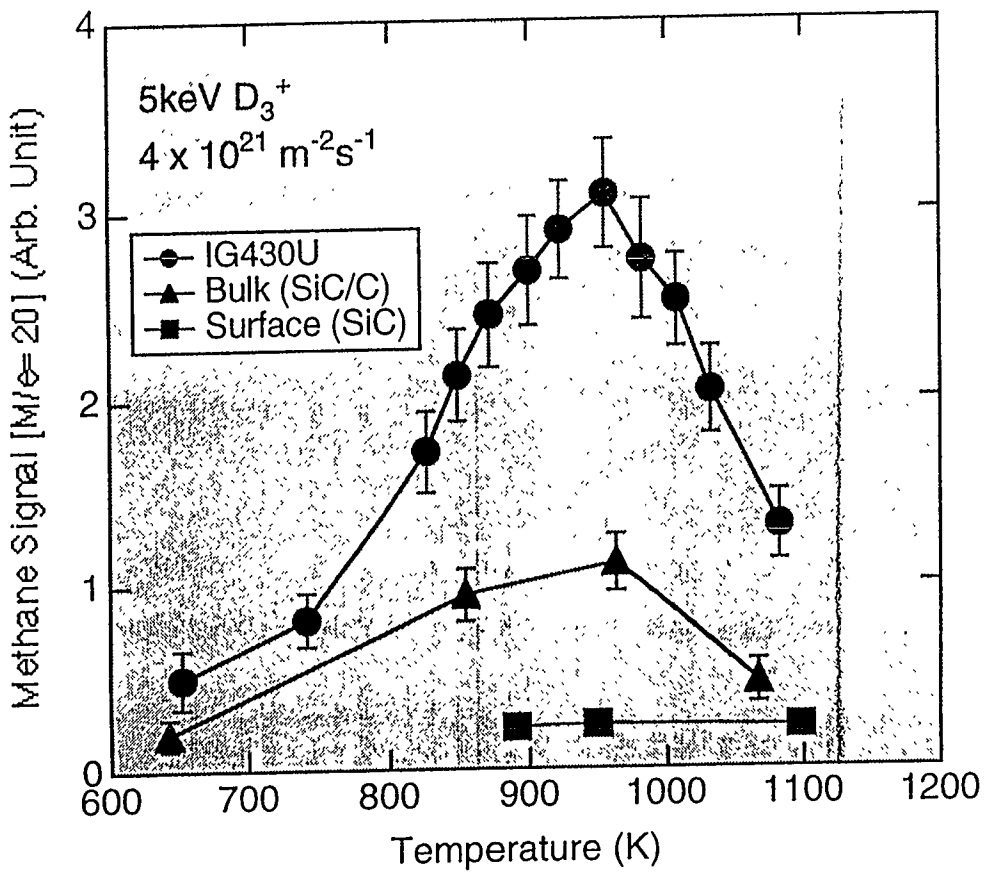

Si/C (Surface) = 0.46/0.54
Si/C (Bulk) = 0.16/0.84

Chemical sputtering of Si-doped graphite (Si/C~1) are almost suppressed in high flux regime.

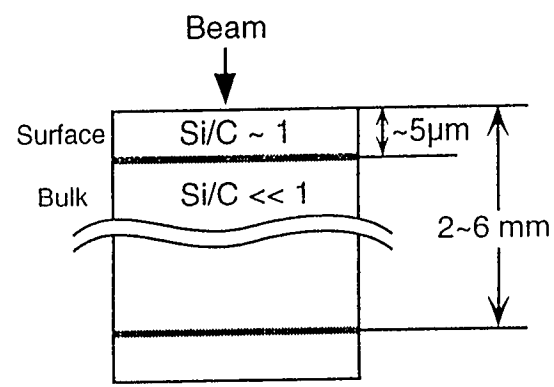

Structure of Si-doped Graphite

Bulk data were taken after presputtering by Ar beam (depth ~ 10μm).

Supra-high Temperature Engineering Laboratory
Graduate School of Engineering. Osaka Univ.

Flux Dependence of Methane Yield

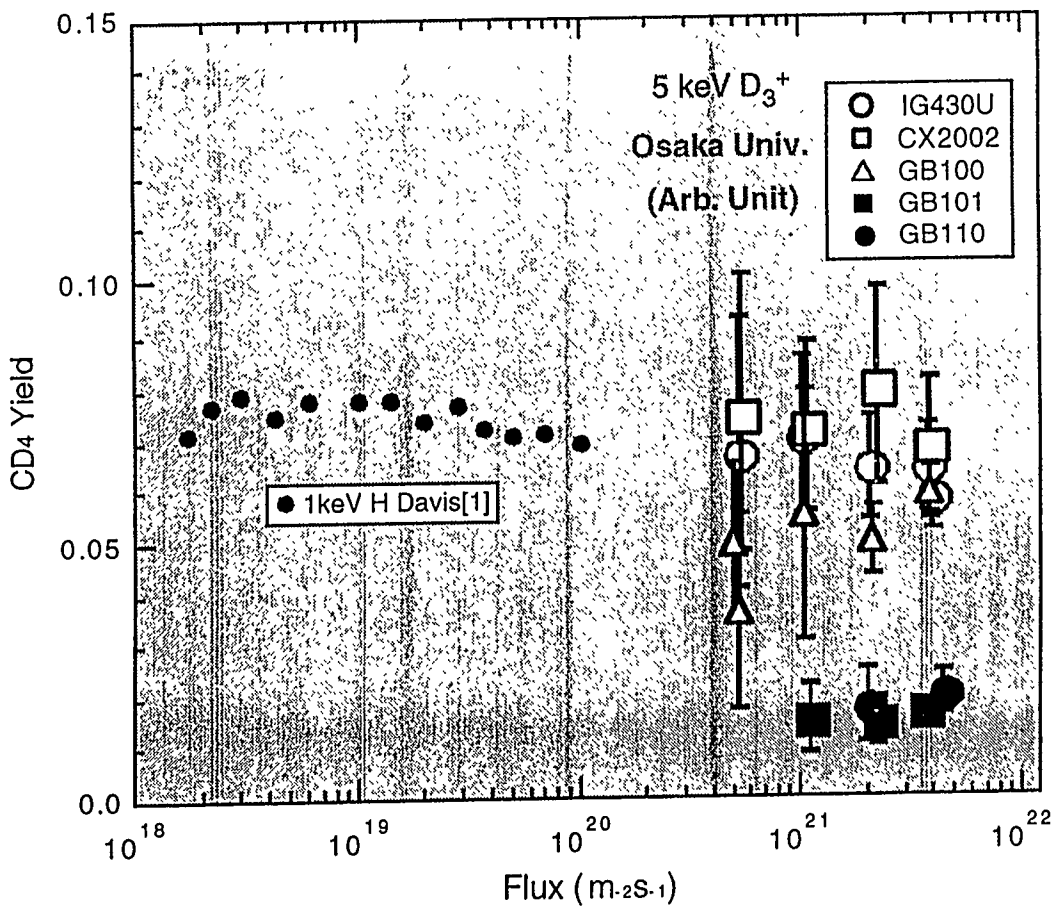

In our high flux regime, methane yield shows no significant flux dependence, which is similar to the low flux results.

[1] J. Davis et al., J. Nucl. Mater. 145&147 (1987) 417.

Supra-high Temperature Engineering Laboratory
Graduate School of Engineering, Osaka Univ.

Flux dependence of peak temperatures

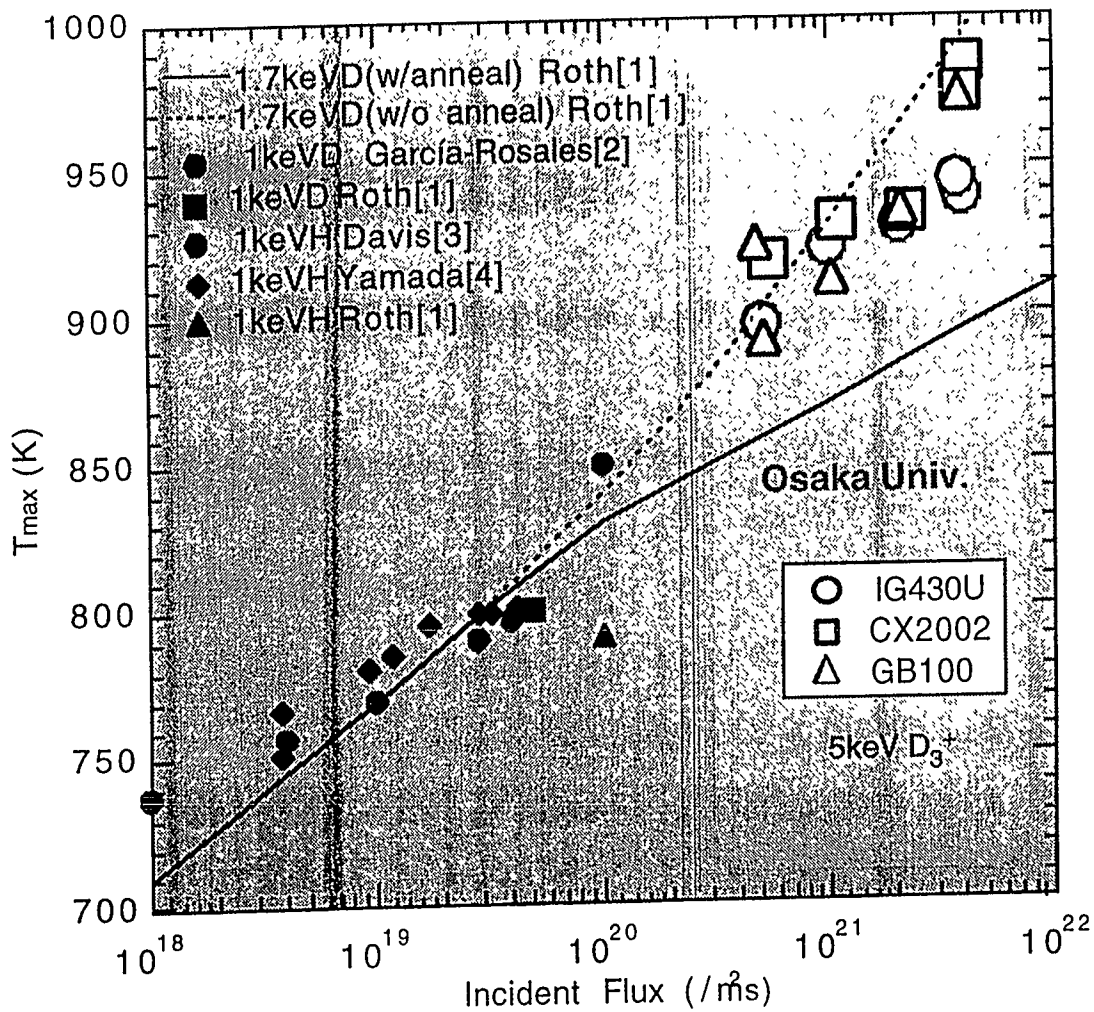

Peak temperatures T_{max} of pure graphite (IG-430U, CX2002, and GB100) increase with flux.

Tmax range between 900 K and 1000 K, which was not observed in the previous experiments.

Our data seem to be consistent with Roth model (C=1, no annealing term).

[1] J. Roth et al., Nucl. Fusion 36 (1996) 1647.
[2] C. García-Rosales et al., J. Nucl. Mater. 196-198 (1992) 574.
[3] J. Davis et al., J. Nucl. Mater. 145-147 (1987) 417.
[4] R. Yamada, J. Nucl. Mater. 145-147 (1987) 359.

Chemical Sputtering Model for a-C/H film

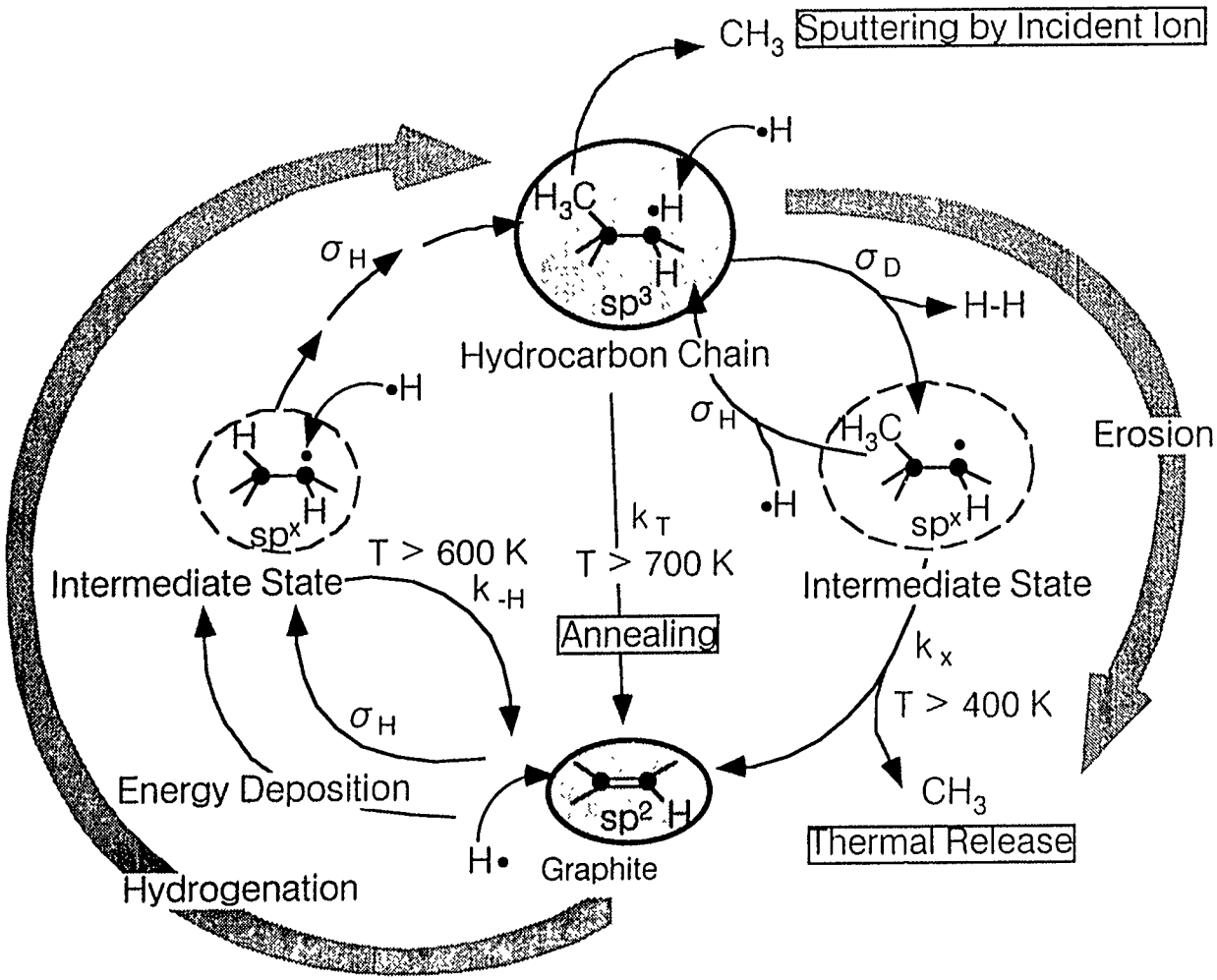

A. Horn et al.
Chem. Phys. Lett.
231 (1994) 193.

J. Roth et al.
Nucl. Fusion
36 (1996) 1647.

B. Mech et al.
J. Appl. Phys.
84 (1998) 1655.

Model of Chemical sputtering by Roth

Model Expression

$$Y_{tot} = Y_{phys} + Y_{therm}(1 + D\,Y_{phys}) + Y_{surf}$$

chemical sputtering (high energy) — surface sputtering (<100eV)

$$Y_{therm} = C^{sp^3} \frac{0.033 \exp\left(-\frac{E_{therm}}{kT}\right)}{2\times10^{-32}\Phi + \exp\left(-\frac{E_{therm}}{kT}\right)}$$

$$C^{sp^3} = \frac{C\left[2\times10^{-32}\Phi + \exp\left(-\frac{E_{therm}}{kT}\right)\right]}{2\times10^{-32}\Phi + \left[1 + \frac{2\times10^{29}}{\Phi}\exp\left(-\frac{E_{rel}}{kT}\right)\right]\exp\left(-\frac{E_{therm}}{kT}\right)}$$

$$C = \frac{1}{1 + 3\times10^{-23}\Phi}$$ Hydrogenation time

$$C = \frac{1}{1 + 3\times10^{7}\exp\left(-\frac{1.4}{kT}\right)}$$ Annealing

Possible reason for the reduction of methane yield in high flux regime (by Roth)

J. Roth et al., Nucl. Fusion 36 (1996) 1647.
J. Roth, J. Nucl. Mater. 266-269 (1999) 51.

Supra-high Temperature Engineering Laboratory
Graduate School of Engineering. Osaka Univ.

Methane Yield by Roth's model

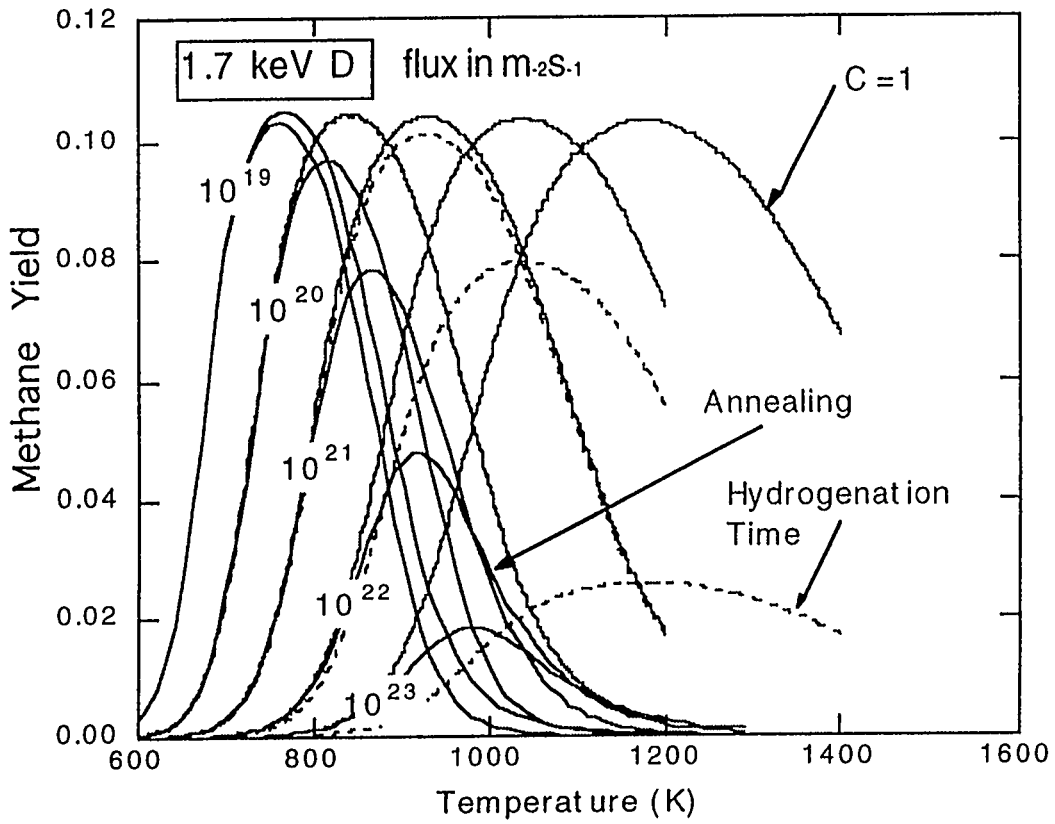

Reference: J. Roth, J. Nucl. Mater. 266-269 (1999) 51.

Supra-high Temperature Engineering Laboratory
Graduate School of Engineering, Osaka Univ.

Conclusion

1. Methane yields of pure graphite (IG-430U, CX 2002, and GB100) at peak temperatures are almost independent of irradiation flux, which is similar to low flux beam results ($< 10^{20}$ $m^{-2}s^{-1}$).
2. Peak temperatures increase with flux and range between 900 K and 1000 K for pure graphite,which is roughly 150 K higher than low flux results. These high peak temperatures over 900 K have not observed in all other experiments including plasma simulators and tokamaks. Our results show that the annealing effect introduced by Roth to a chemical sputtering model is insignificant.
3. The factor of 3 - 4 reduction of methane signal of B-doped graphite was observed compared with pure graphite, which is similar to low flux results.
4. Chemical sputtering of Si-doped graphite (Si/C~1) are suppressed in our high flux regime.

Supra-high Temperature Engineering Laboratory
Graduate School of Engineering. Osaka Univ.

Max-Planck-Institut
für Plasmaphysik

Dynamic Target Behaviour due to Ion Bombardment

W. Eckstein

Max-Planck-Institut für Plasmaphysik,
EURATOM Assoziation,
Boltzmannstr. 2, D-85748 Garching

TRIDYN (dynamic TRIM.SP)

based on vektorised TRIM.SP

amorphous target

binary collision approximation

Monte Carlo program

necessary for all targets with more than one component

and nonvolatile projectiles

all collisional effects are taken into account

diffusion, segregation und chemical effects are neglected

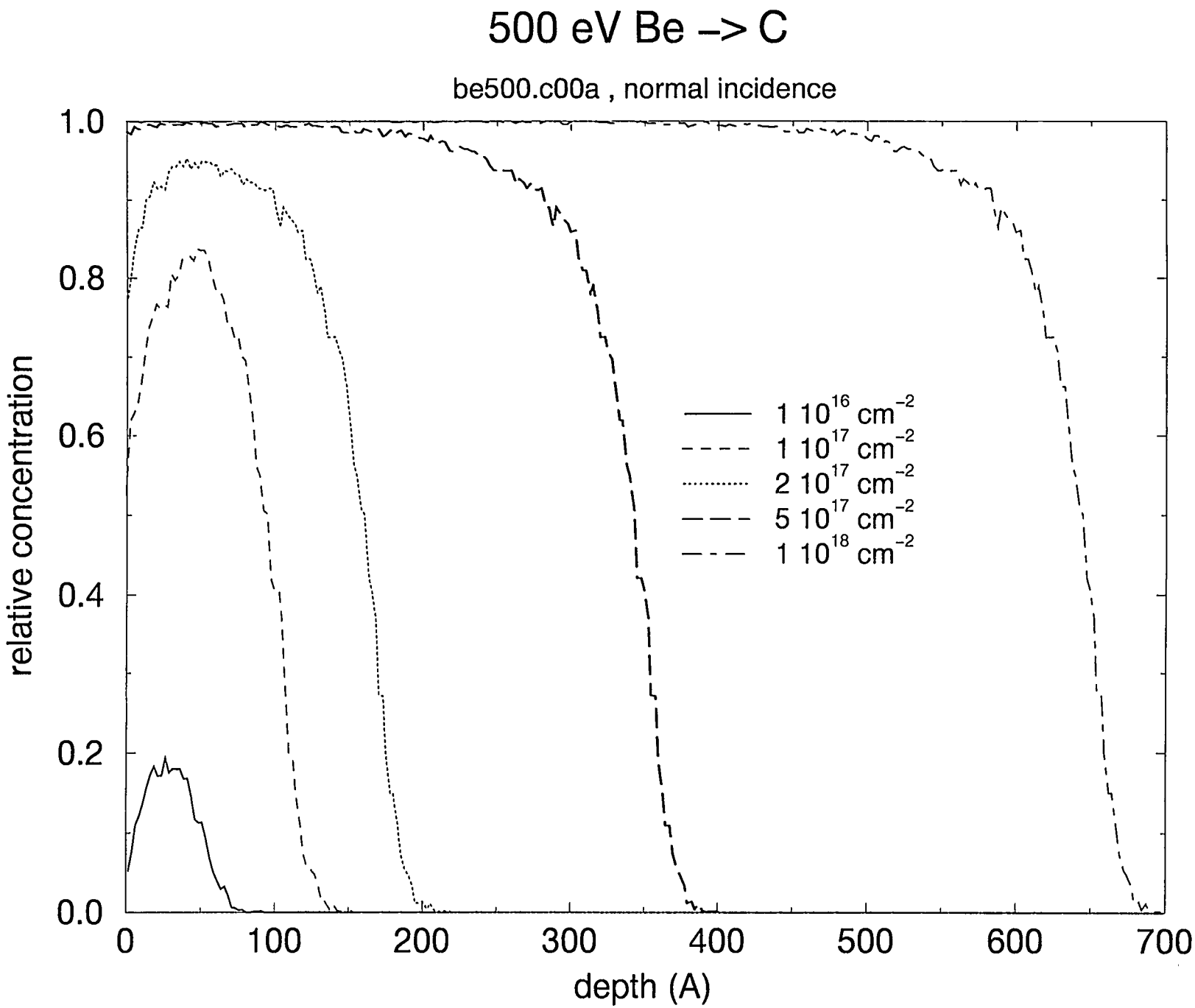
500 eV Be -> C
be500.c00a , normal incidence
relative concentration
depth (A)
1.0
0.8
0.6
0.4
0.2
0.0
0
100
200
300
400
500
600
700
1 10^16 cm^-2
1 10^17 cm^-2
2 10^17 cm^-2
5 10^17 cm^-2
1 10^18 cm^-2

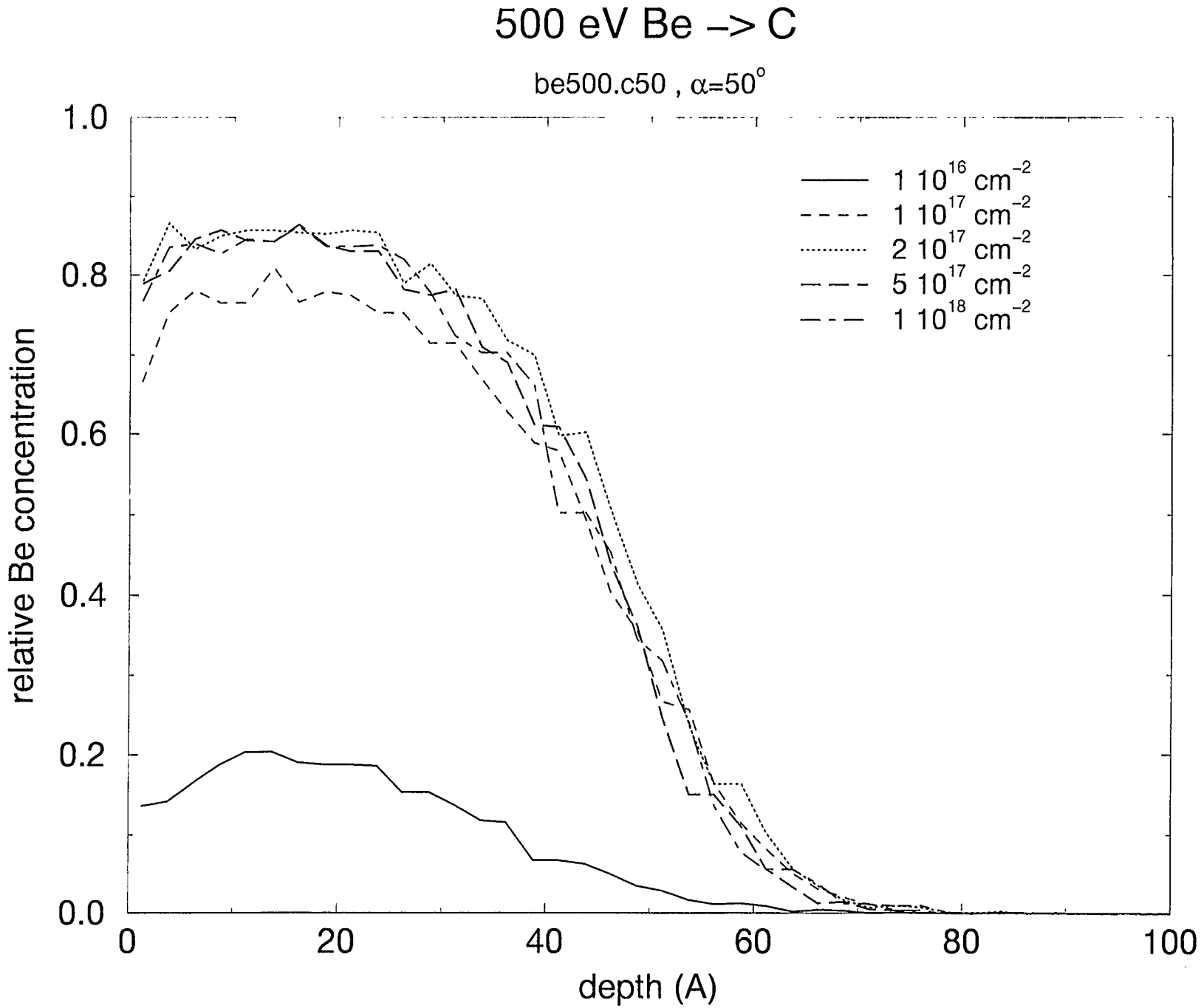
500 eV Be -> C
be500.c50 , α=50°
1.0
0.8
0.6
0.4
0.2
0.0
relative Be concentration
0
20
40
60
80
100
depth (A)
1 10^16 cm^-2
1 10^17 cm^-2
2 10^17 cm^-2
5 10^17 cm^-2
1 10^18 cm^-2

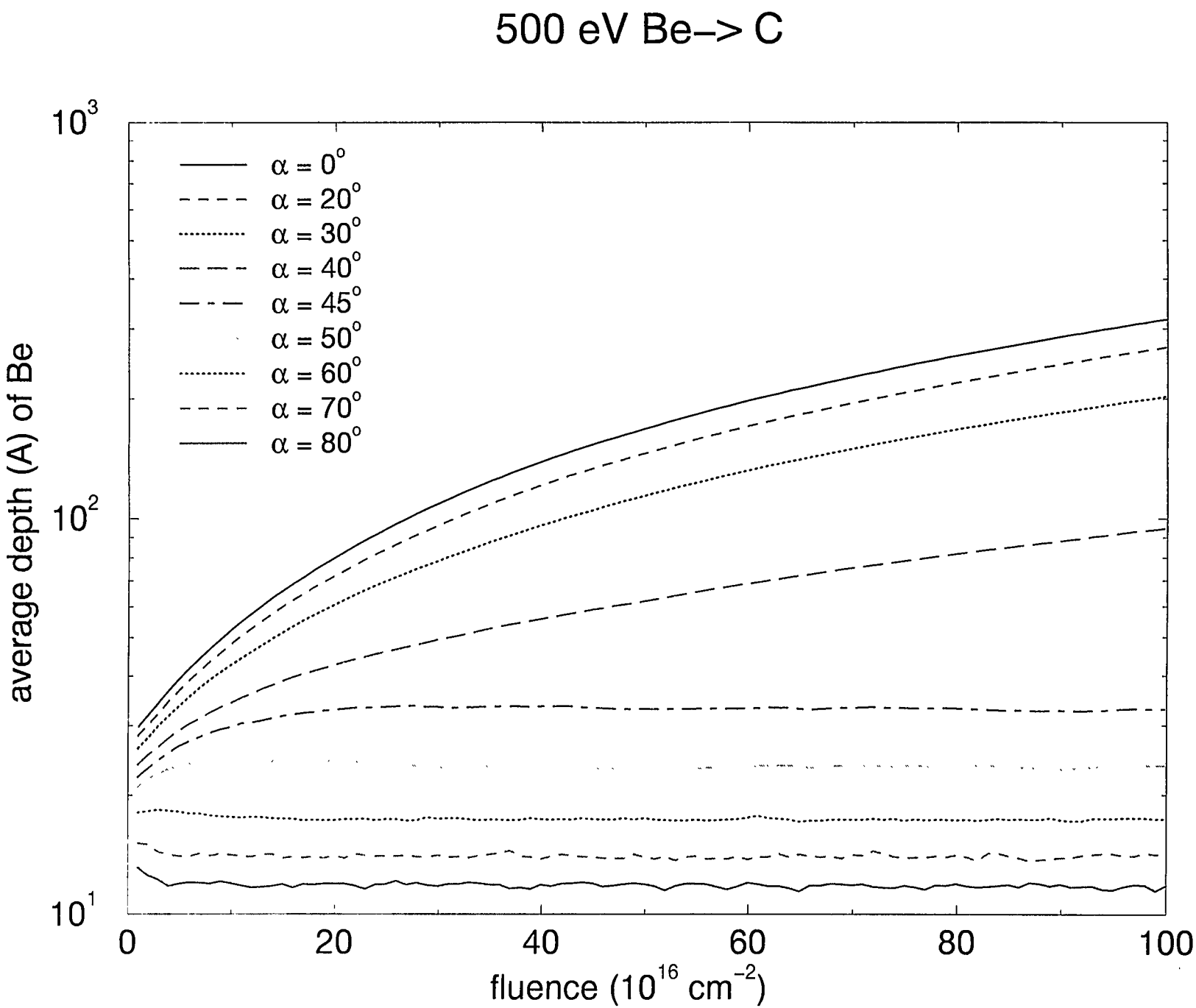
500 eV Be–> C
α = 0°
α = 20°
α = 30°
α = 40°
α = 45°
α = 50°
α = 60°
α = 70°
α = 80°
average depth (A) of Be
fluence (10^16 cm^-2)
10^3
10^2
10^1
0
20
40
60
80
100

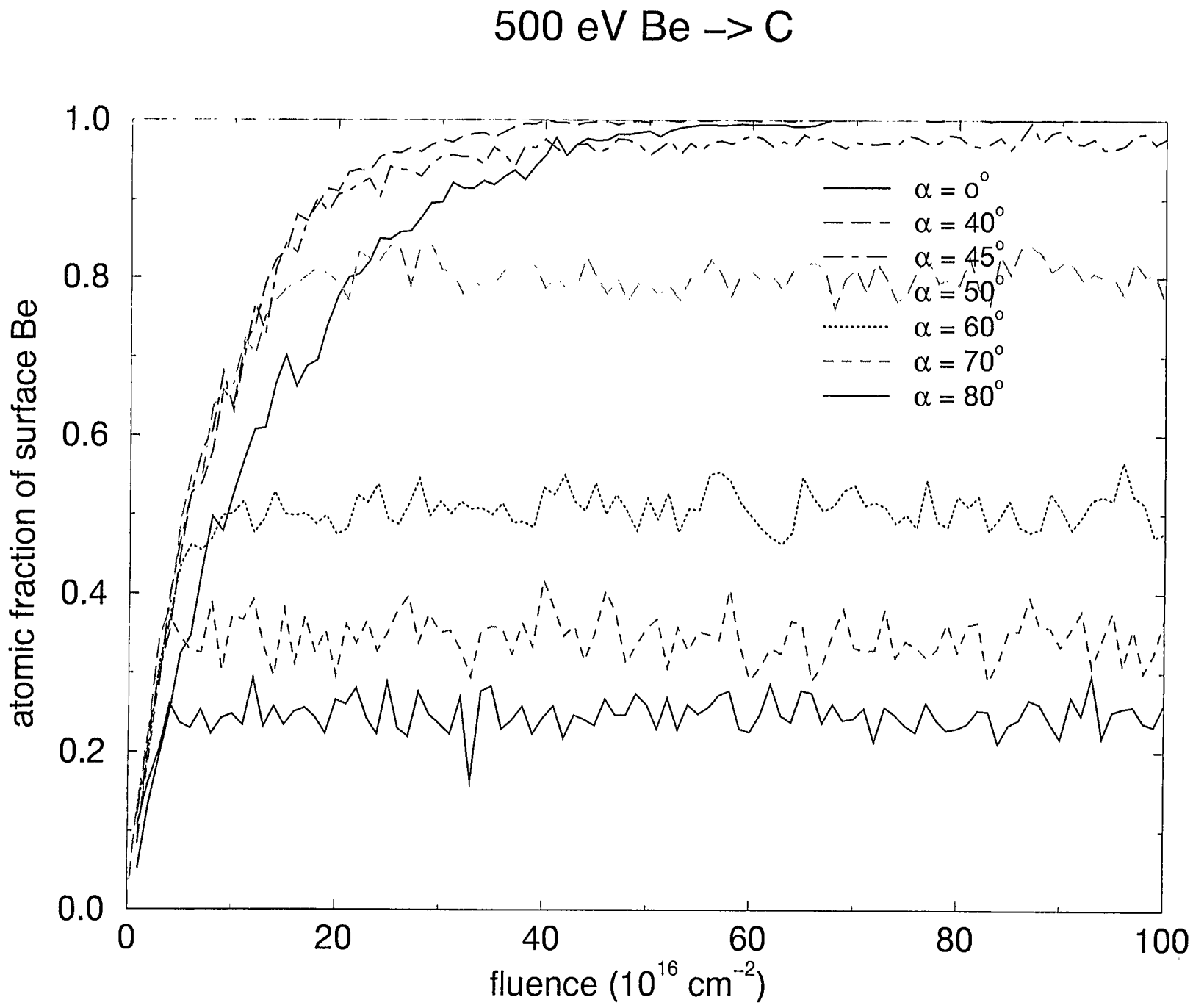
500 eV Be -> C
atomic fraction of surface Be
fluence (10^{16} cm^{-2})
0.0
0.2
0.4
0.6
0.8
1.0
0
20
40
60
80
100
α = o°
α = 40°
α = 45°
α = 50°
α = 60°
α = 70°
α = 80°

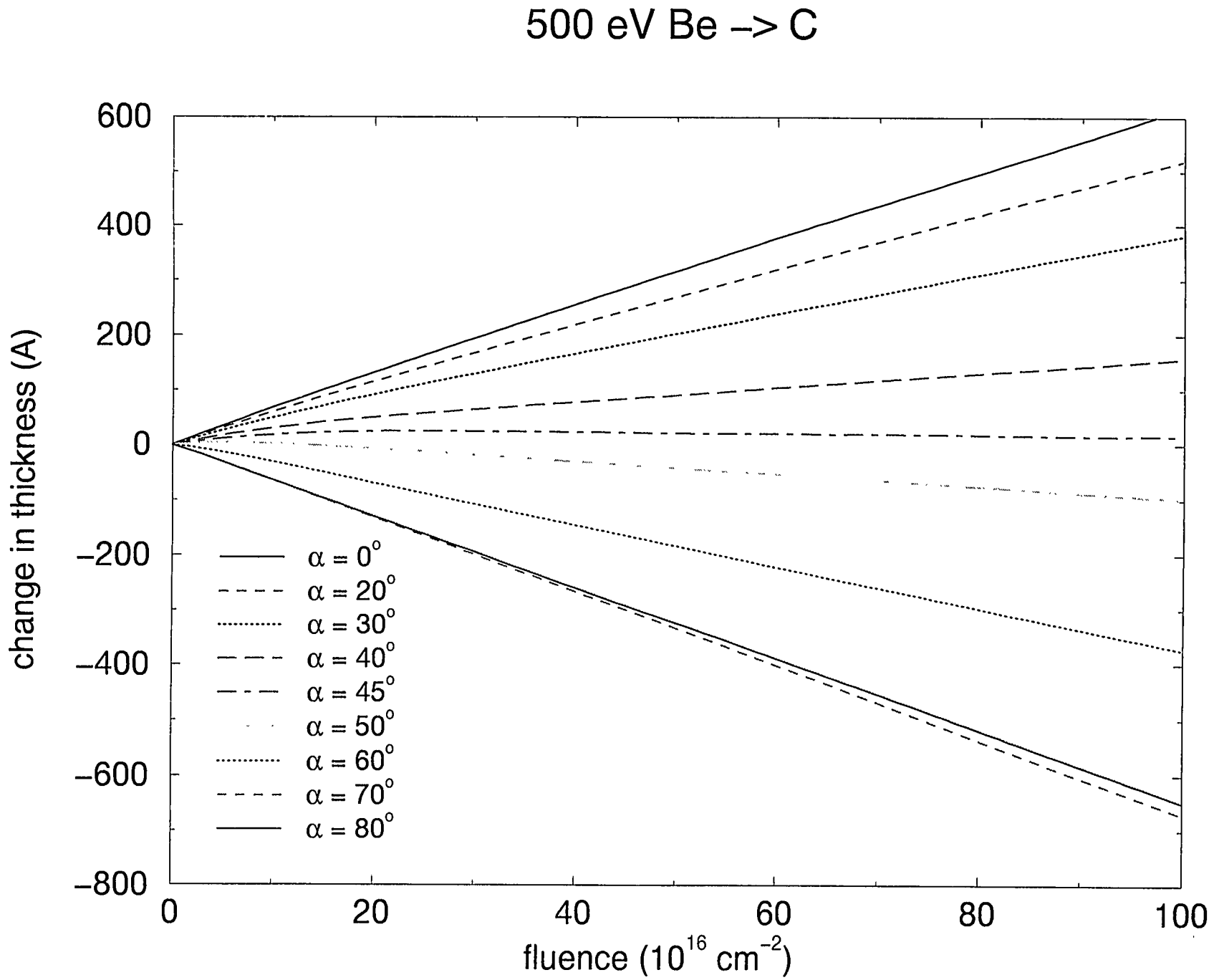
500 eV Be –> C
600
400
200
0
–200
–400
–600
–800
change in thickness (A)
0
20
40
60
80
100
fluence (10^{16} cm^{-2})
α = 0°
α = 20°
α = 30°
α = 40°
α = 45°
α = 50°
α = 60°
α = 70°
α = 80°

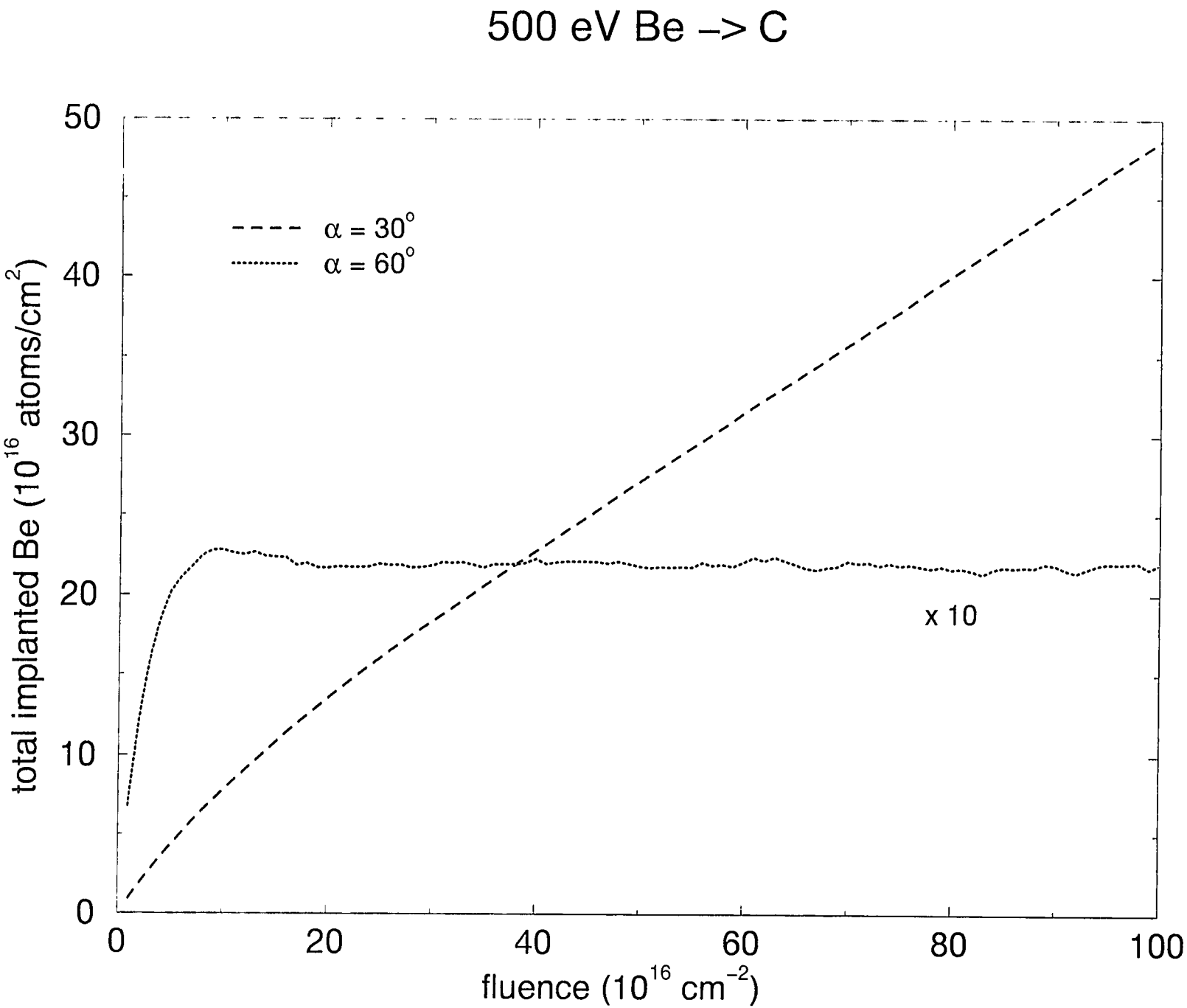
500 eV Be -> C
α = 30°
α = 60°
x 10
total implanted Be (10^{16} atoms/cm^2)
fluence (10^{16} cm^{-2})
0
10
20
30
40
50
0
20
40
60
80
100

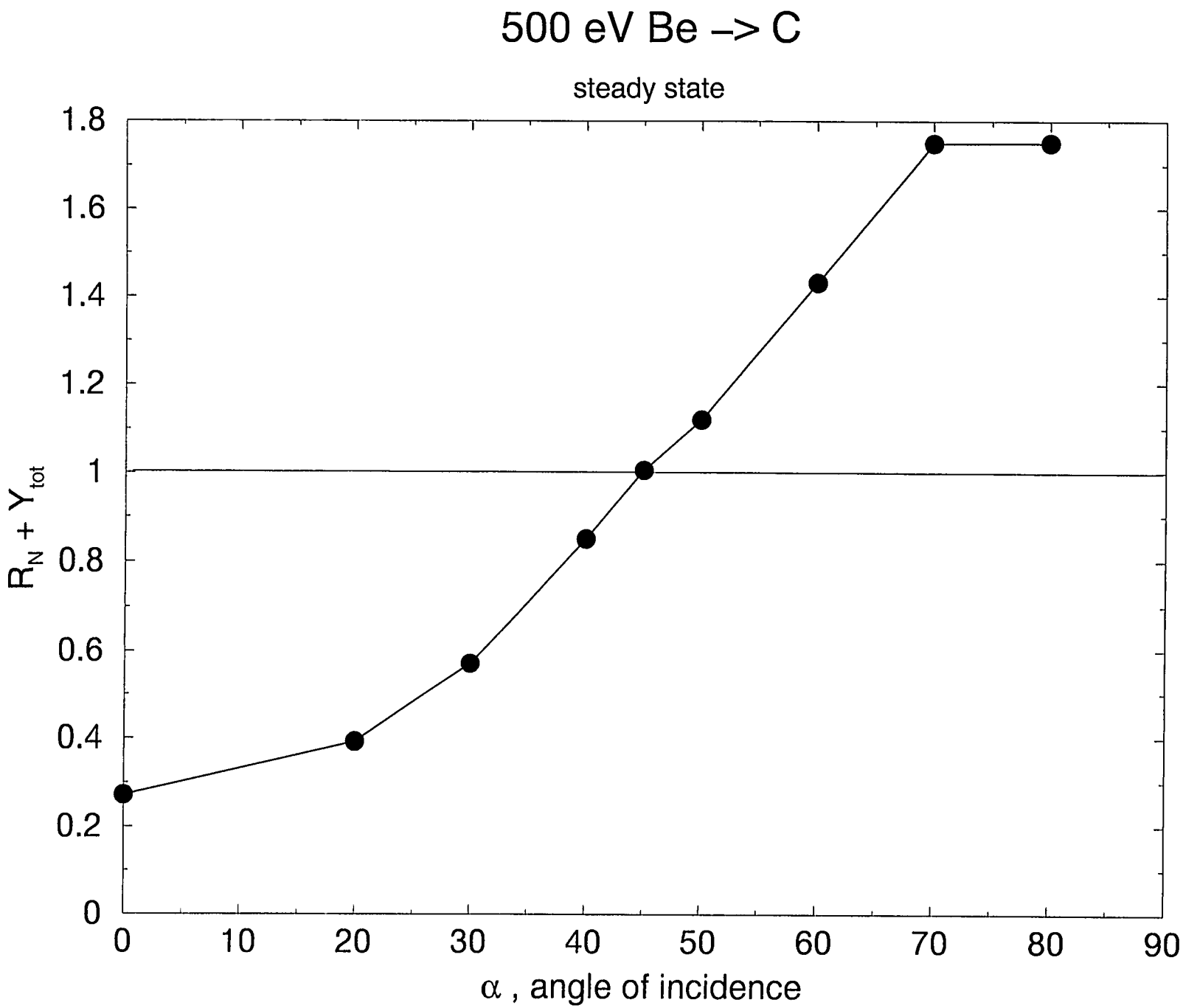
500 eV Be –> C
steady state
1.8
1.6
1.4
1.2
1
0.8
0.6
0.4
0.2
0
$R_N + Y_{tot}$
0
10
20
30
40
50
60
70
80
90
α , angle of incidence

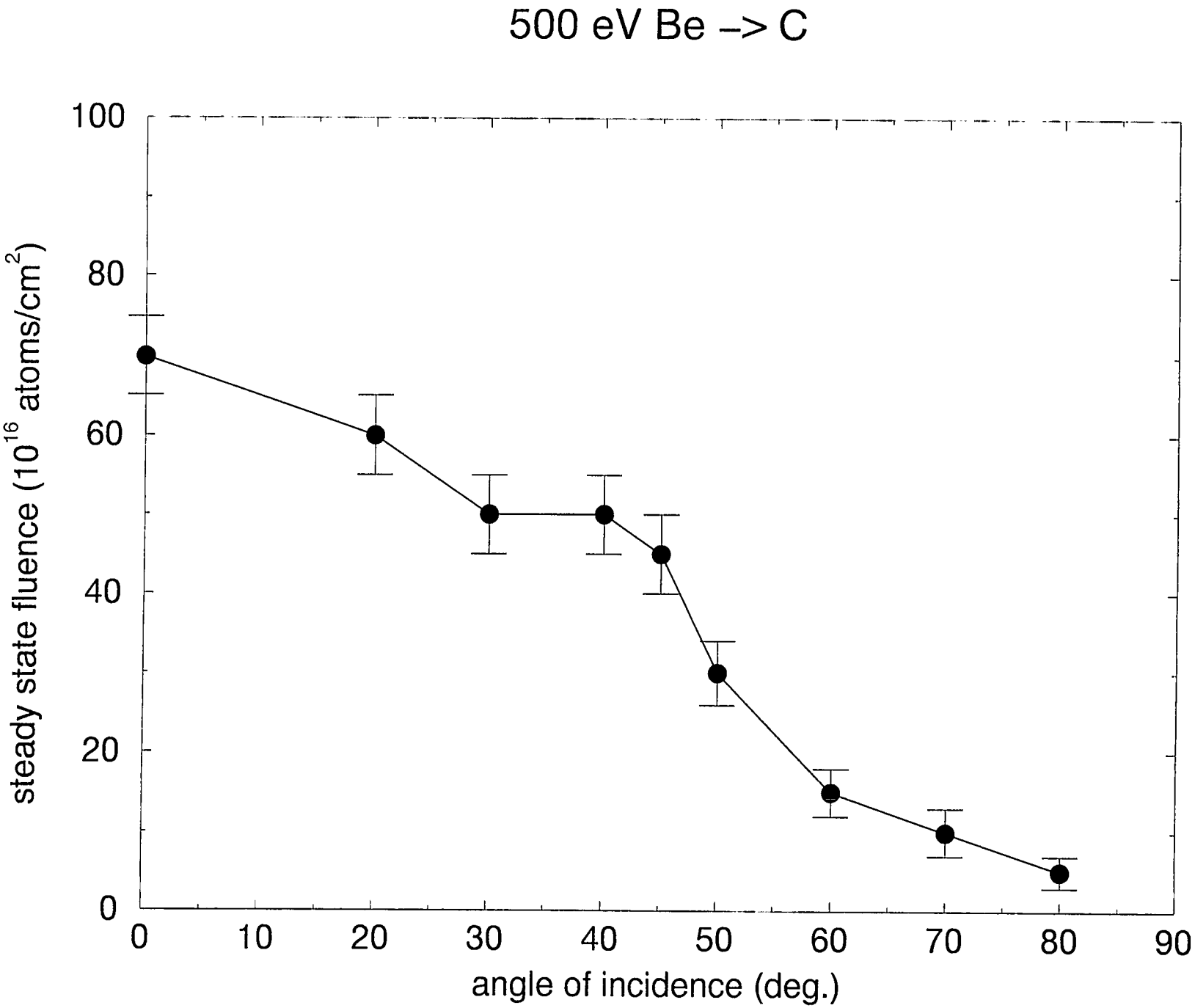
500 eV Be -> C
steady state fluence (10^{16} atoms/cm^2)
angle of incidence (deg.)
0
20
40
60
80
100
0
10
20
30
40
50
60
70
80
90

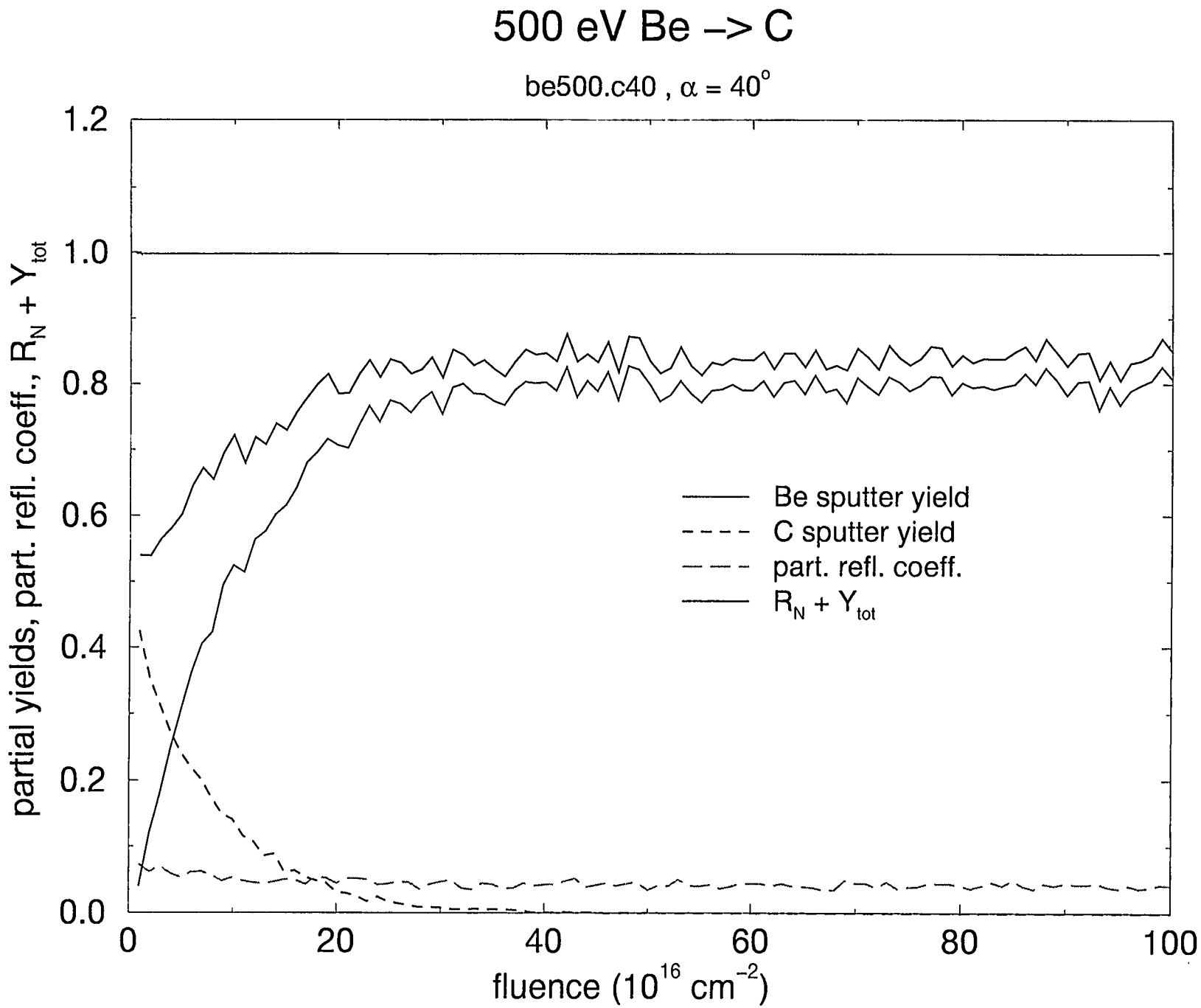
500 eV Be -> C
be500.c40 , α = 40°
partial yields, part. refl. coeff., $R_N + Y_{tot}$
fluence (10^{16} cm^{-2})
0.0
0.2
0.4
0.6
0.8
1.0
1.2
0
20
40
60
80
100
Be sputter yield
C sputter yield
part. refl. coeff.
$R_N + Y_{tot}$

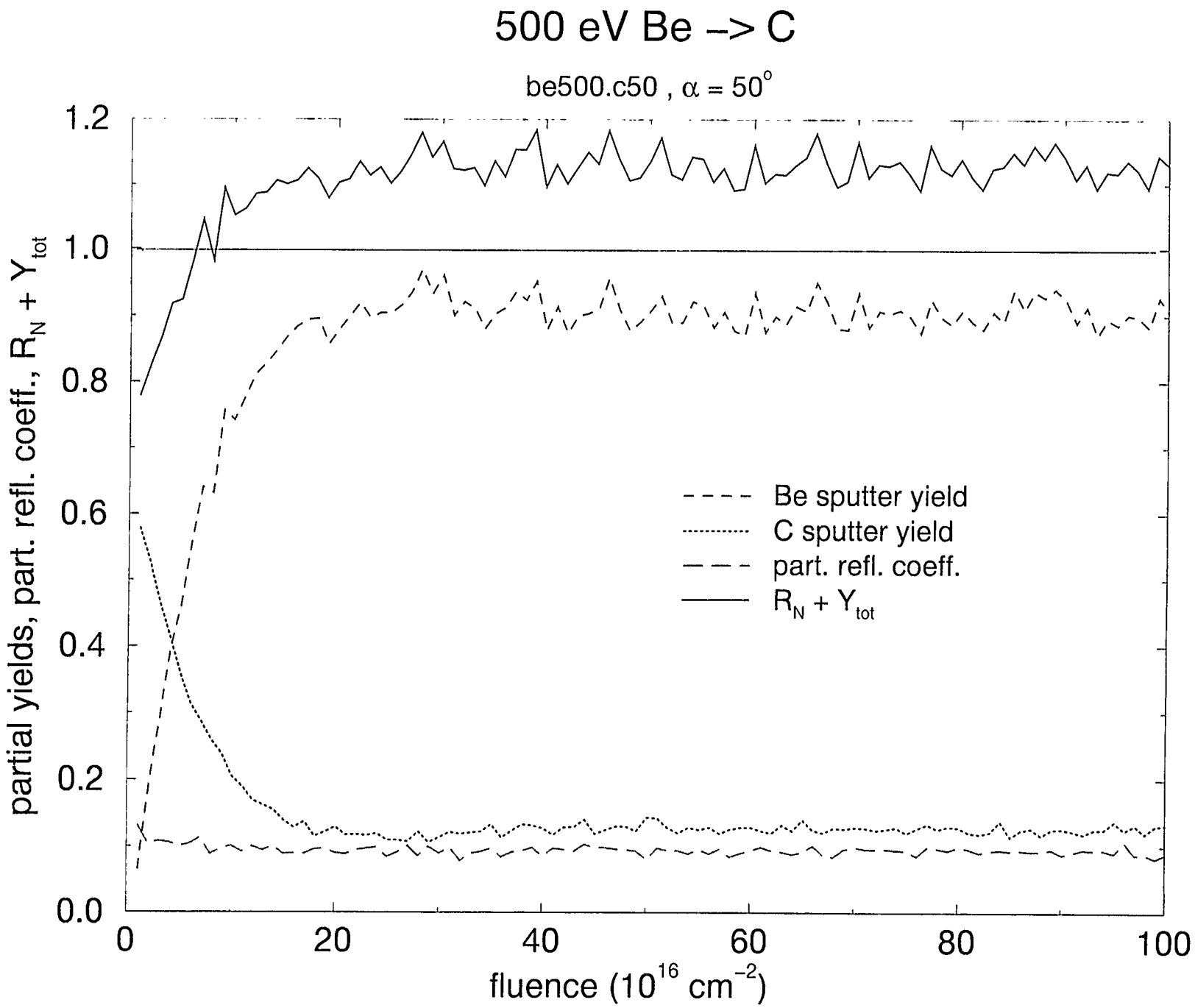
500 eV Be –> C
be500.c50 , α = 50°
partial yields, part. refl. coeff., $R_N + Y_{tot}$
fluence (10^{16} cm^{-2})
0.0
0.2
0.4
0.6
0.8
1.0
1.2
0
20
40
60
80
100
Be sputter yield
C sputter yield
part. refl. coeff.
$R_N + Y_{tot}$

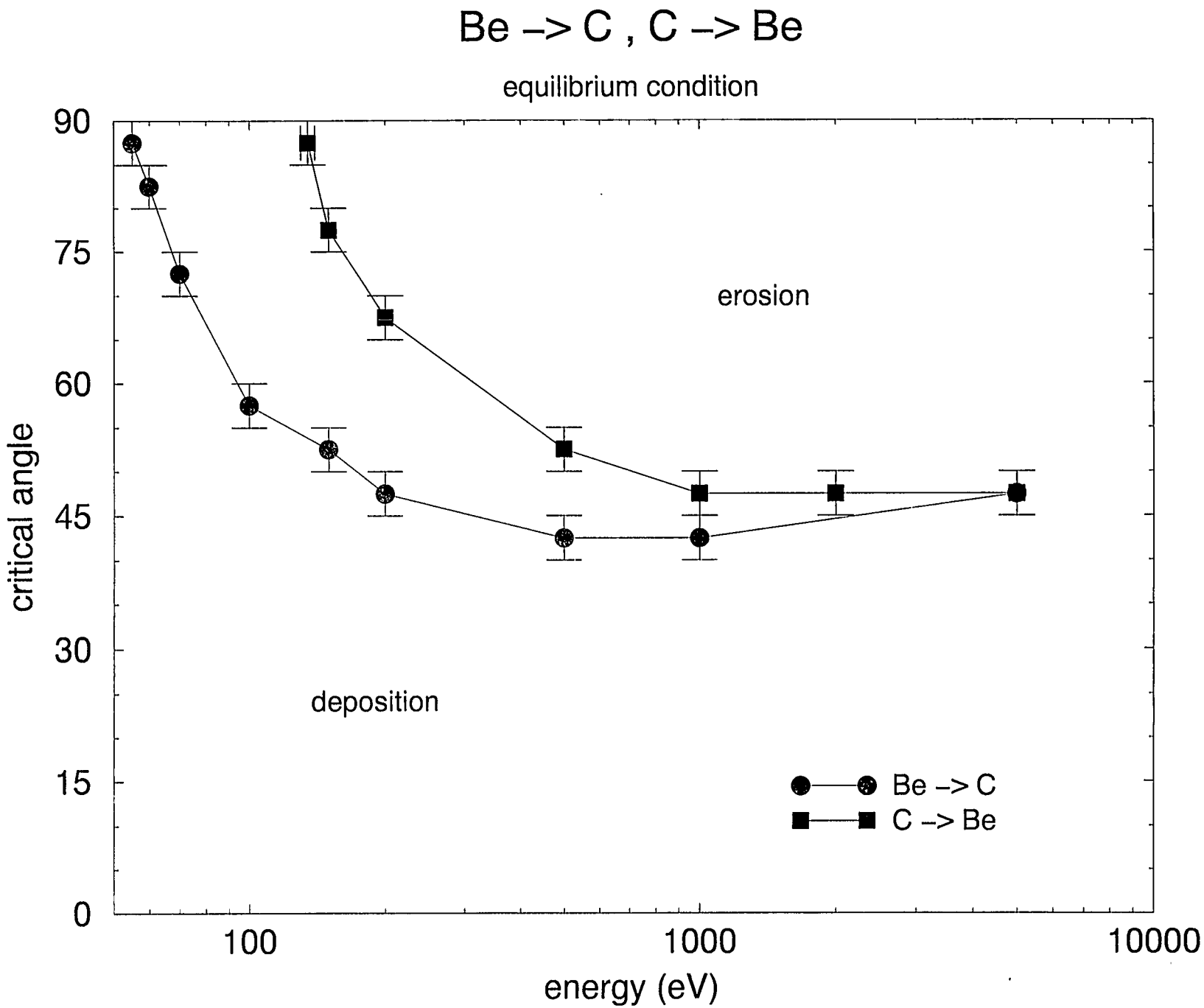
Be -> C , C -> Be
equilibrium condition
90
75
60
45
30
15
0
critical angle
erosion
deposition
Be -> C
C -> Be
100
1000
10000
energy (eV)

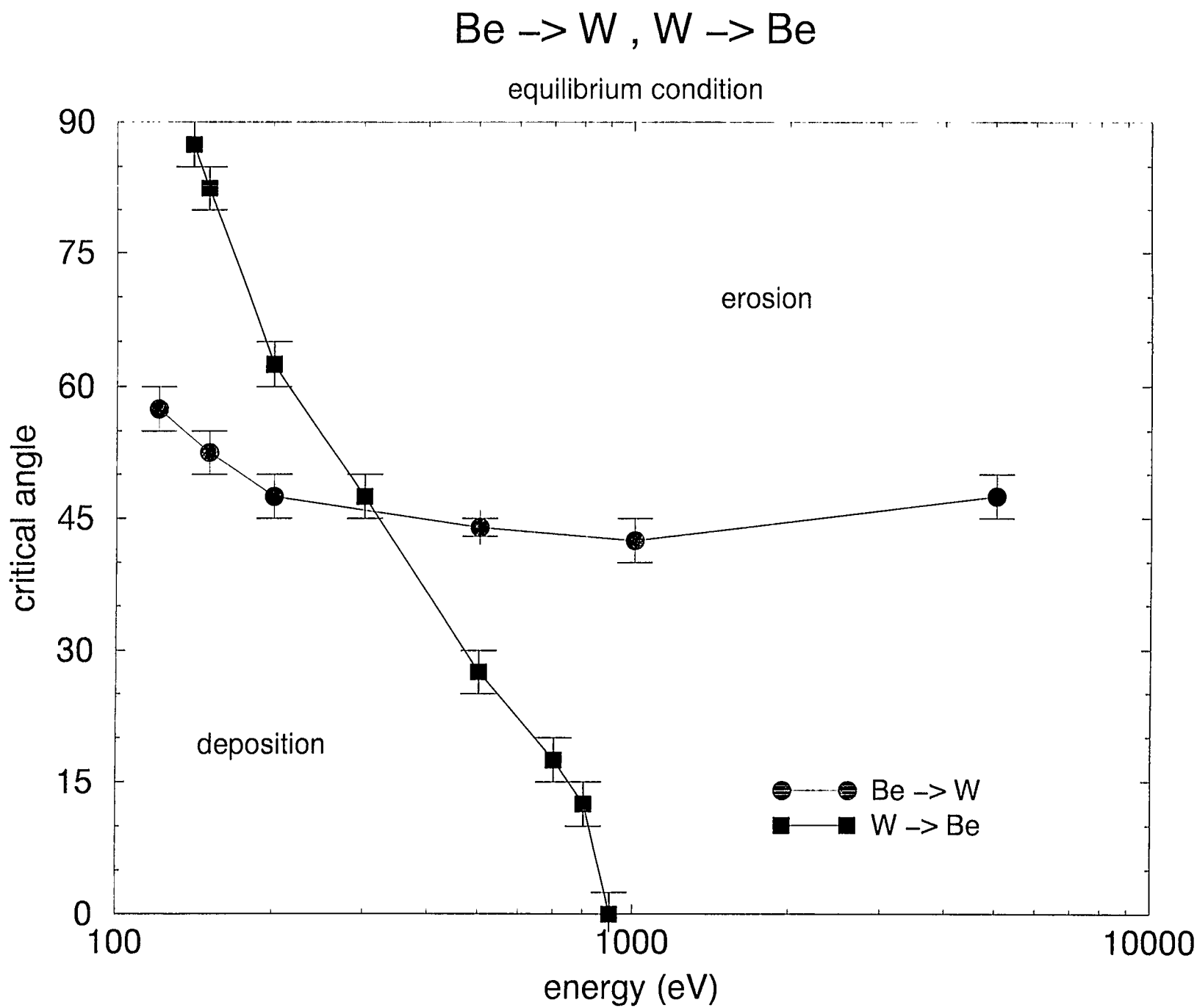
Be -> W , W -> Be
equilibrium condition
critical angle
energy (eV)
erosion
deposition
Be -> W
W -> Be
90
75
60
45
30
15
0
100
1000
10000

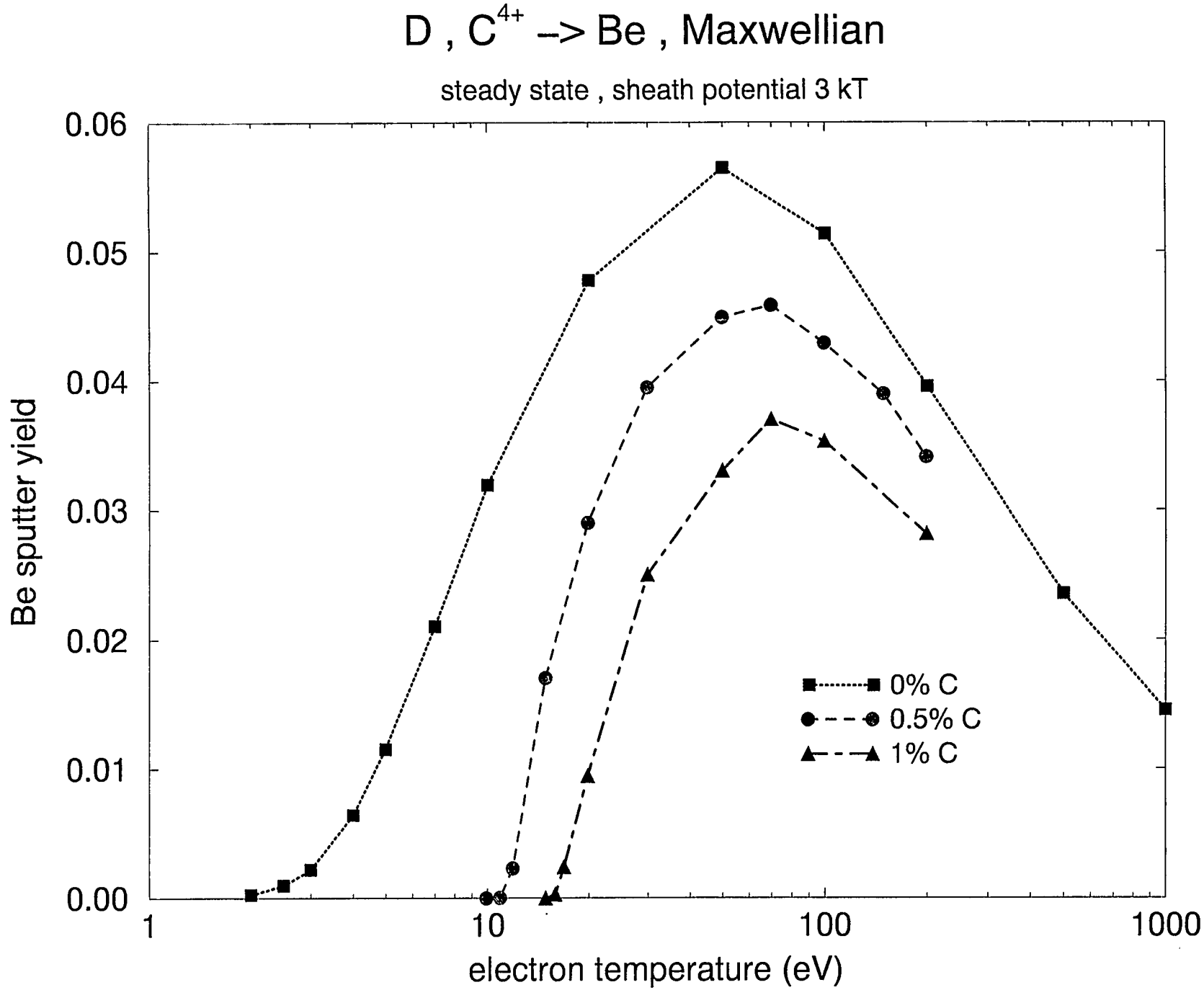
D , C4+ –> Be , Maxwellian
steady state , sheath potential 3 kT
Be sputter yield
0.06
0.05
0.04
0.03
0.02
0.01
0.00
1
10
100
1000
electron temperature (eV)
0% C
0.5% C
1% C

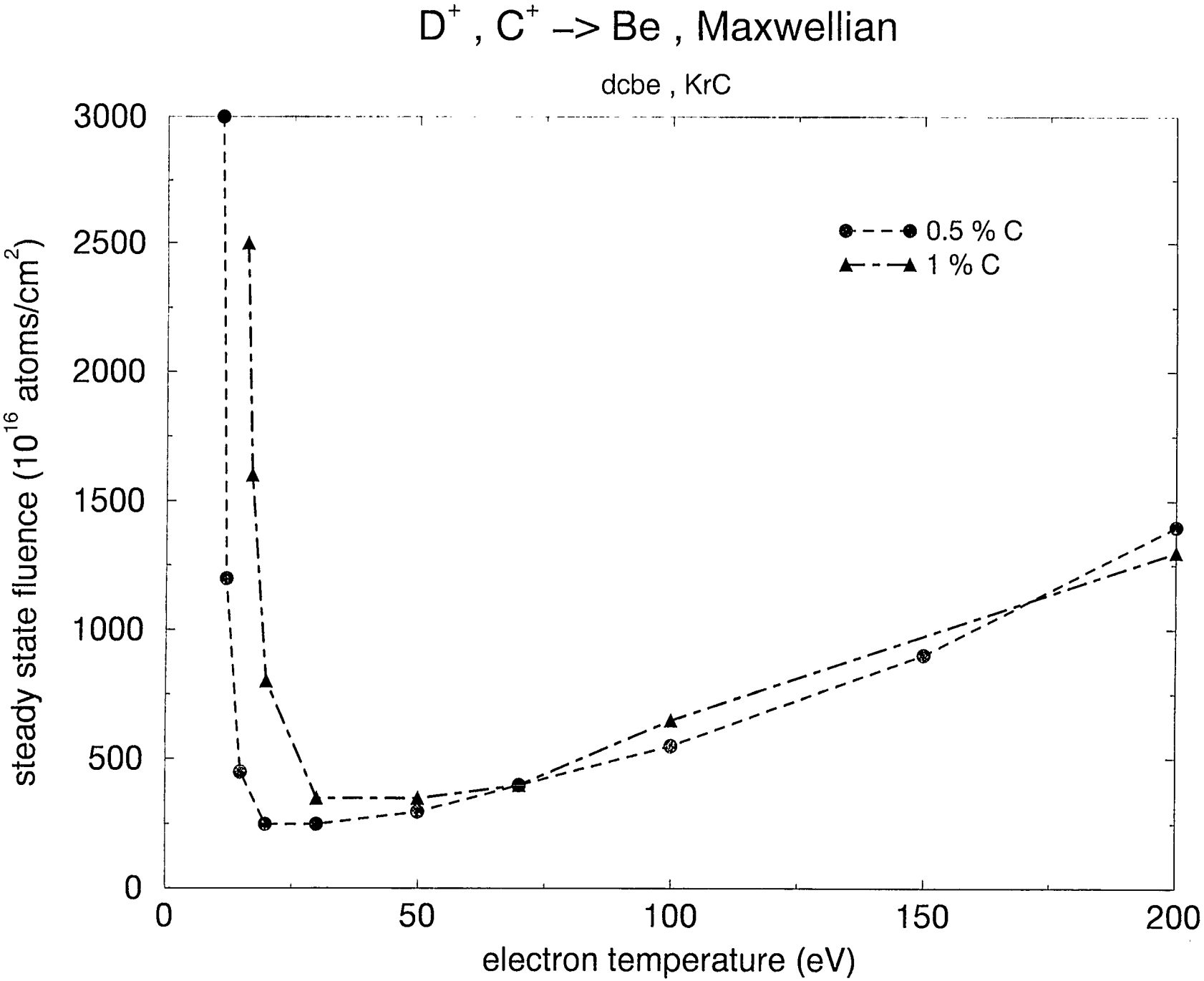
D+ , C+ –> Be , Maxwellian
dcbe , KrC
0.5 % C
1 % C
steady state fluence (10^16 atoms/cm^2)
electron temperature (eV)
0
500
1000
1500
2000
2500
3000
0
50
100
150
200

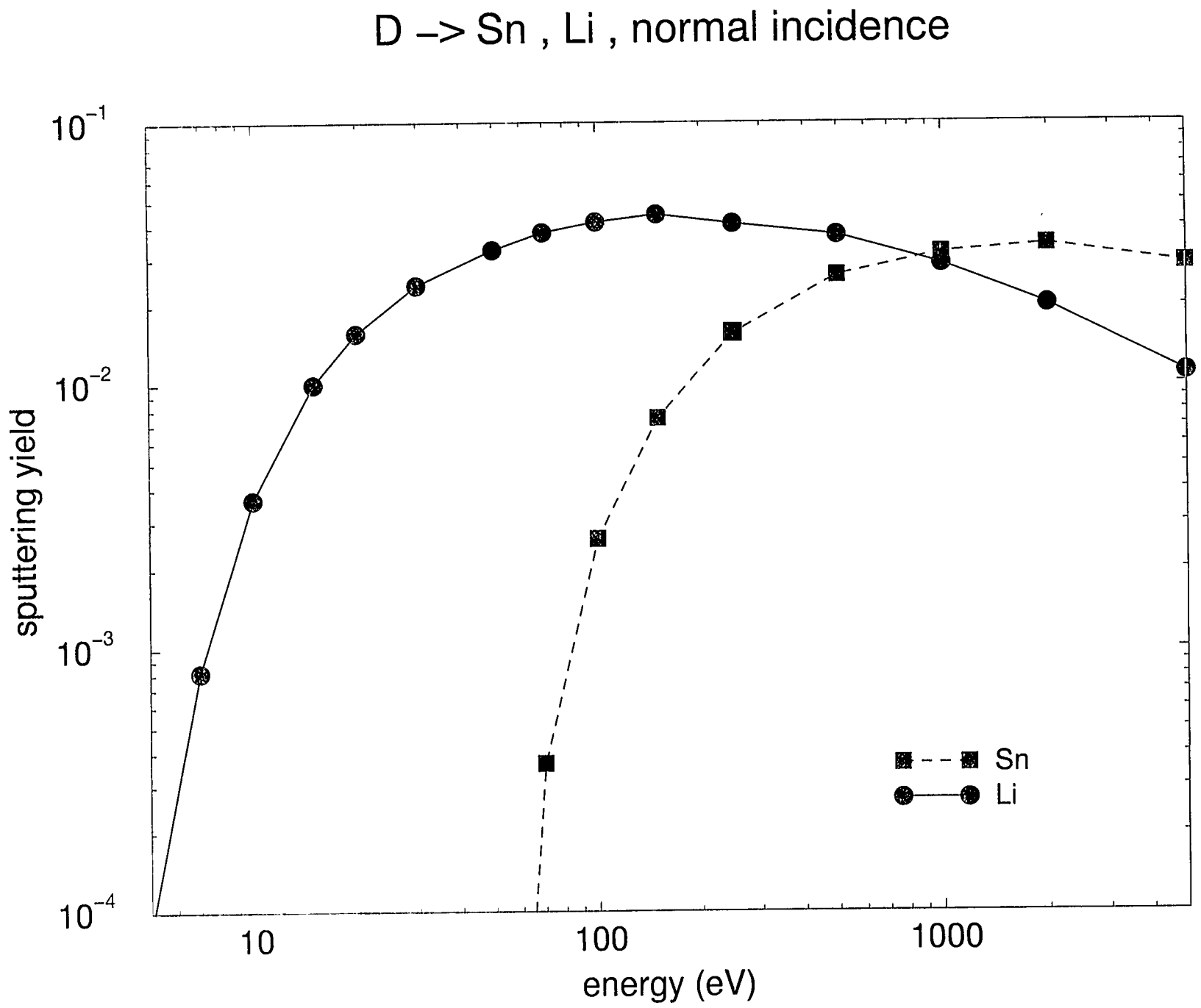
D –> Sn , Li , normal incidence
sputtering yield
10^{-1}
10^{-2}
10^{-3}
10^{-4}
10
100
1000
energy (eV)
Sn
Li

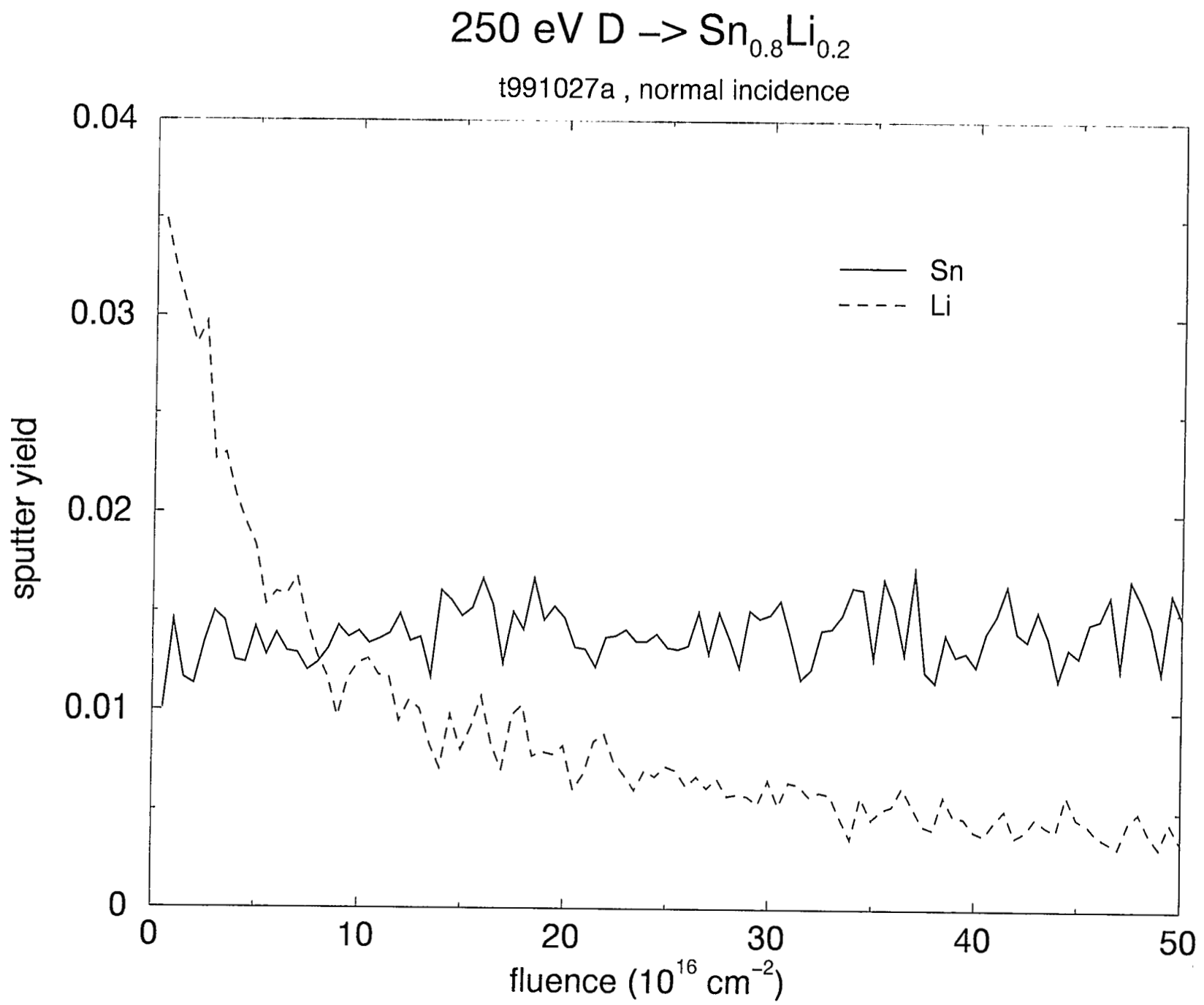
250 eV D –> $Sn_{0.8}Li_{0.2}$
t991027a , normal incidence
Sn
Li
sputter yield
0.04
0.03
0.02
0.01
0
0
10
20
30
40
50
fluence (10^{16} cm^{-2})

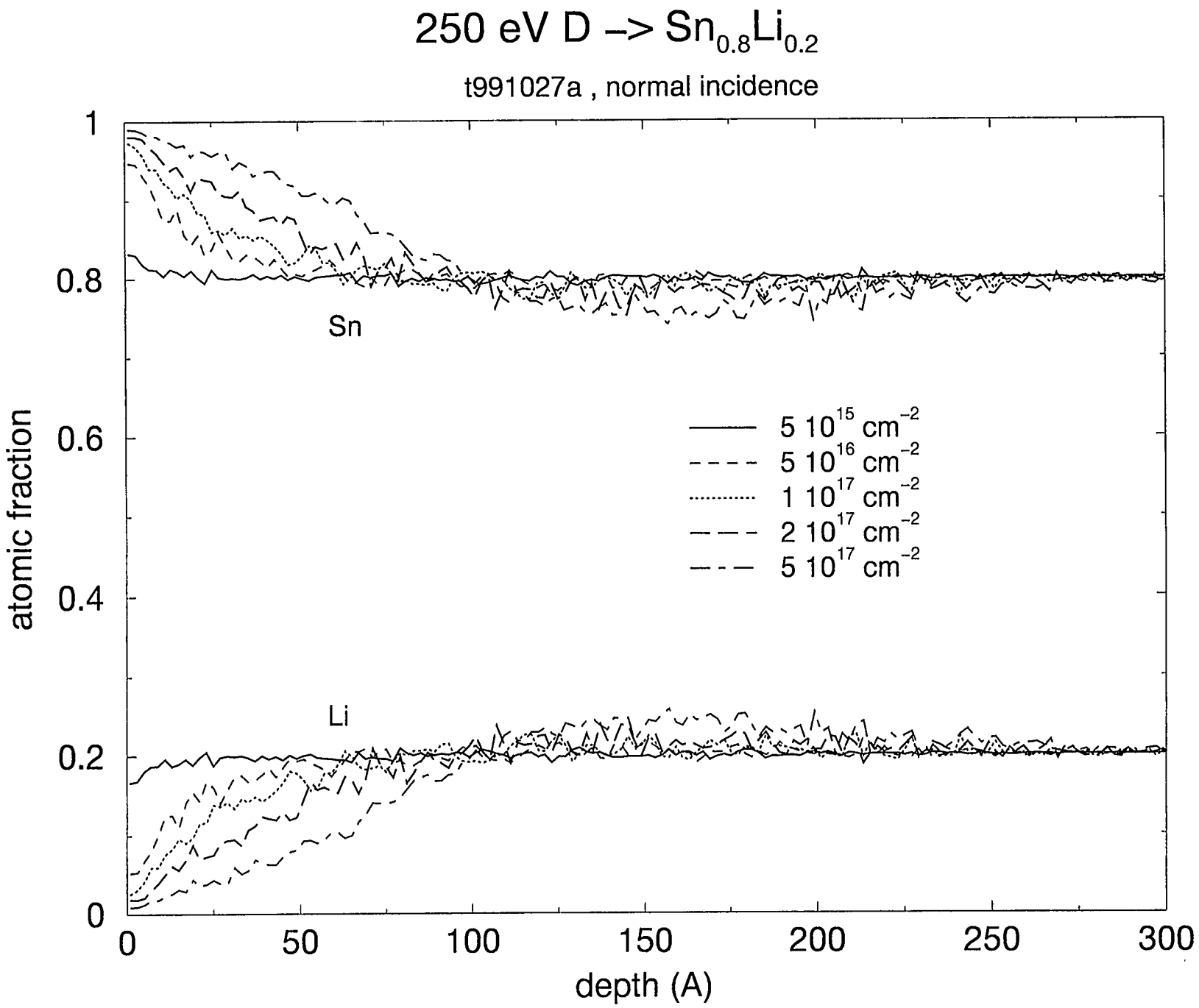
250 eV D -> $Sn_{0.8}Li_{0.2}$
t991027a , normal incidence
atomic fraction
depth (A)
Sn
Li
5 10^{15} cm^{-2}
5 10^{16} cm^{-2}
1 10^{17} cm^{-2}
2 10^{17} cm^{-2}
5 10^{17} cm^{-2}
0
0.2
0.4
0.6
0.8
1
0
50
100
150
200
250
300

Retention of Deuterium and Tritium in Alcator C-Mod

W. R. Wampler
Sandia National Laboratories, Albuquerque, NM 87185-1056

C. H. Skinner
Princeton Plasma Physics Laboratory, Princeton, NJ 08543

C. S. Pitcher, B. LaBombard, B. Lipschultz and C. Fiore
MIT Plasma Science and Fusion Center, Cambridge, MA 02139

1999 US-Japan Workshop on Plasma Surface Interactions
and High Heat Fulx Components for Next Step Fusion Devices
Santa Fe, NM, November 1-4, 1999

Introduction

- D T retention in tokamaks is dominated by two mechanisms, implantation and codeposition. Implantation saturates but codeposition continues and eventually dominates retention in tokamaks with carbon plasma-facing components (PFC's). In long-pulse tritium fueled machines this high long term retention would produce unacceptably high in-vessel tritium inventories.
- Alcator C-Mod has molybdenum tiles on the inner wall and divertor and no carbon PFC's and therefore should have low codeposition and low long term fuel retention.
- Here we present the first experimental study of long term retention of deuterium and tritium in C-Mod.

Experiment

- 22 Mo tiles were exposed to ~ 1090 deuterium plasmas in C-Mod, then analyzed for retained D and T
- Typical plasma conditions during exposure: n_e~1-5 x10^{20}/m^3, I_P=0.6-1.2 MA, B_T=3-8 T, duration1 sec, heating up to 5 MW.
- Boronization was used to reduce Mo impurities in the plasma.
- Tile analysis techniques:
  - D measured by $^3He(D,p)^4He$ nuclear reaction analysis (NRA),
  - B measured by $^{11}B(p,^4He)^8Be$ NRA,
  - Surface composition, erosion/deposition by RBS,
  - Tritium coverage within ~ 0.5μm from beta emission.

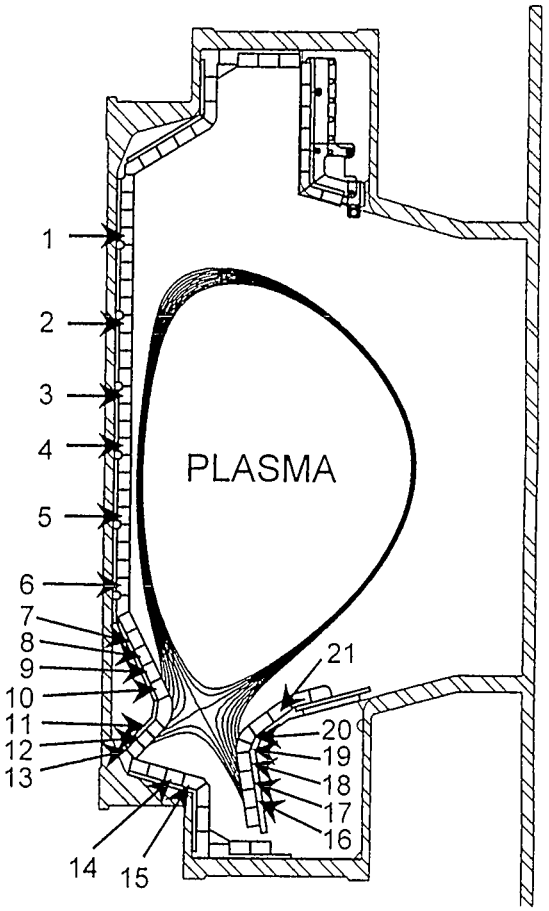

Results

- A boron film ~ 1μm thick is present from boronization.
- Net erosion only at the OSP where boron and ~ 0.1 μm of Mo have been eroded.
- Most of the deuterium is on the wall of the main plasma chamber.

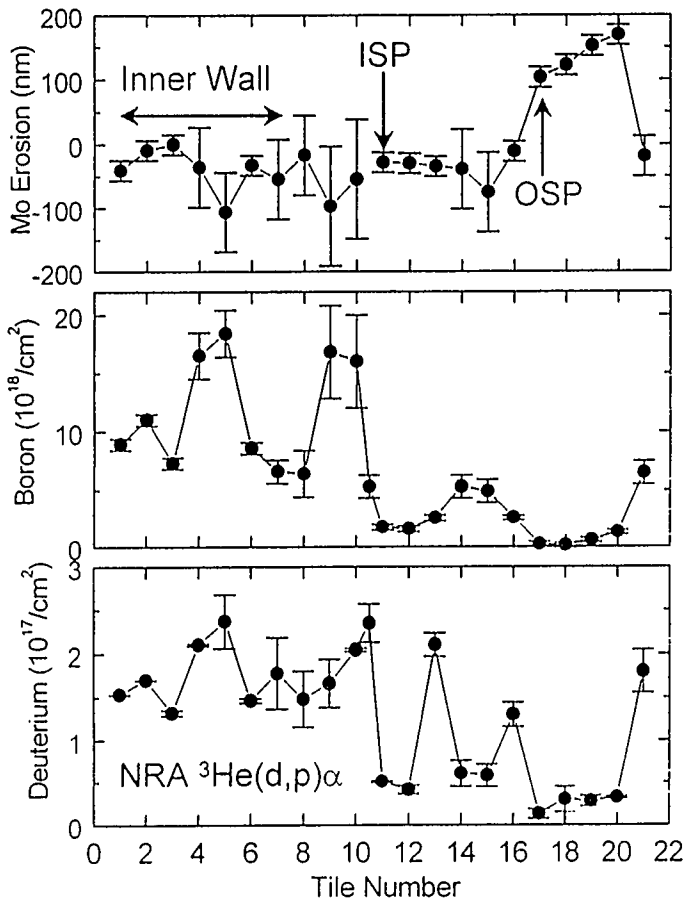

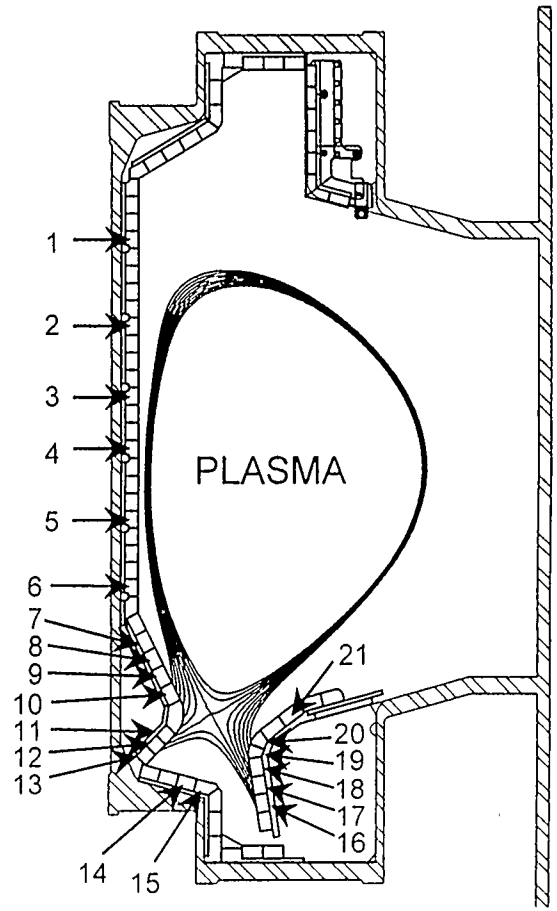

Deuterium Retention

The increase in D inventory in C-Mod during the campaign was estimated from the measured D coverage on the tiles, assuming D coverage is toroidally symmetric and similar on inner and outer wall of main chamber.

Region:	D coverage (10^{21} D/m^2)	Area (m^2)	D Inventory (10^{21} atoms)
Main chamber wall	1.8±0.4	16.5	30±7
Inner strikeplate	1.0	0.25	0.25
Private flux region	0.6	0.42	0.25
Outer strikeplate	0.5	0.50	0.25

- D is in the boron layer at a coverage consistent with implantation. In regions of net erosion (OSP) D retention is low.
- **In-vessel D inventory is 0.1 gram on the main chamber wall and 0.0025 gram in the divertor.**
- This D inventory is ~100 times greater than the quantity of D in a typical plasma, and can strongly affect fueling of individual plasmas. However, retention of implanted D saturates after several plasmas and will not result in large long term D inventories.

Tritium Retention

- During the run campaign **8.7×10^{15} tritium atoms were produced** by D(D,p)T reactions in C-Mod plasmas, determined by measurements of neutrons from the $D(D,n)^3He$ reaction.
- Measurements of tritium beta surface emission rate from the C-Mod tiles show tritium coverage is less than the detection limit of 10^8 T/cm^2.
- Measurements of D & T coverage give T/D < 5×10^{-10}.
- **Tritium retained < 1.5×10^{13}T** = (3×10^{22} D) x (5×10^{-10} T/D)
- **Tritium retained / Tritium produced < 0.002**.
  This is ~100 times lower than tokamaks with carbon PFC's.

Summary of DT Retention in C-Mod

- D retention is mainly on the main plasma chamber wall due to implantation into a boron surface layer. This mechanism should saturate early in the run campaign.
- The low D retention in the C-Mod divertor shows that D retention by codeposition is low.
- The fraction of tritium retained in C-Mod is ~100 times smaller than in other tokamaks with carbon PFC's, consistent with implantation rather than codeposition being the dominant mechanism for fuel retention in C-Mod.

CX neutrals in the main plasma chamber, What effects do they have?

Wall:

1. DT inventory
2. Erosion

Plasma:

1. Fueling
2. ***Sputter impurities which radiate energy***
3. ***Cool the plasma edge and degrade energy confinement***

Alcator C-Mod

CX neutral flux is high,
10^{22} - 10^{23} /s or
~ 10^{21} - 10^{22} /m^{2}s.
Higher than the flux of ions into the divertor.

Density of gas at P = 1mTorr is similar to density of plasma.

Energetic CX neutrals from the plasma return from the wall as low energy neutrals.

Multiple charge-exchange conducts heat from the plasma boundary, lowers the edge temperature and and degrades energy confinement.

In tokamaks with carbon PFC's He discharge conditioning removes D from the wall, giving lower CX flux, higher edge temperatures and better energy confinement.

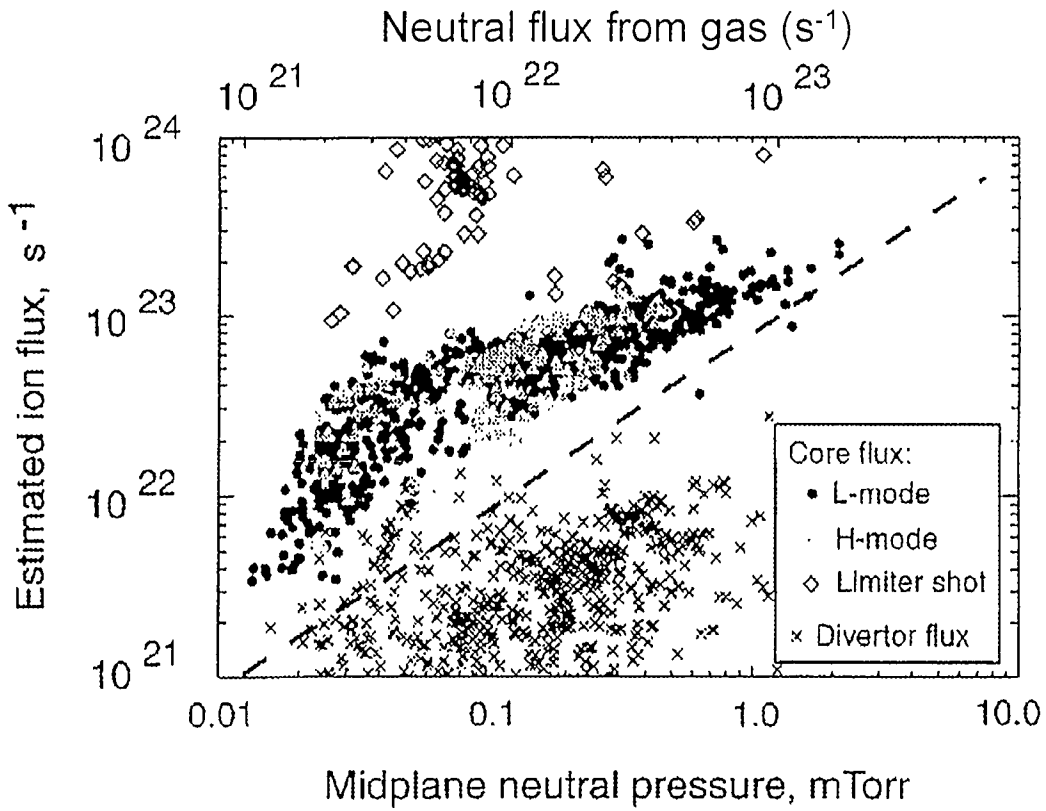

Flux of ions out of the plasma, derived from midplane D_α brightness, is plotted against the midplane gas pressure. Cross symbols show the estimated flux of ions entering the divertor chamber. *These data indicate that the main chamber recycling fluxes greatly exceed the flux if ions into the divertor.*
M.V. Umansky et. al., Physics of Plasmas 5 (1998) 3373

CX Neutral Energy Spectrum

High flux at low energy (< 100 eV) determines fuel recycling,
Lower flux at higher energy causes sputtering.

In C-Mod boronization reduces radiated power loss
which is mainly due to Mo impurities (Greenwald et. al., Nuclear Fusion **37** (1997) 793).
This is suggests sputtering of Mo by CX neutrals as an impurity source.

Conclusion:

Low-Z wall material may be necessary to avoid plasma impurities due to sputtering by CX neutrals.

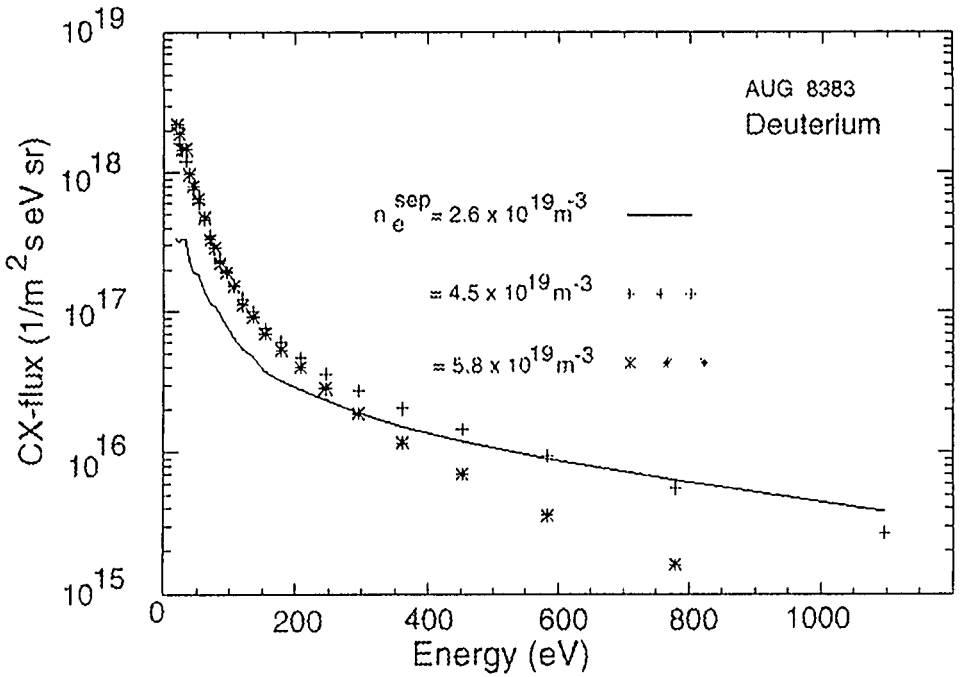

Energy spectrum of CX neutrals in ASDEX Upgrade.
H. Verbeek et. al., Nuclear Fusion 38 (1998) 1789.

Alcator C-Mod

Higher edge temperature gives a higher temperature gradient in the core, i.e. better energy confinement.

Higher edge temperature is achieved through reduced fuel recycling at the edge.

Suggestion:

Reduced recycling, and therefore better energy confinement, should be achieved by pumping in the divertor and fueling by pellet injection or neutral beams, not gas puffing.

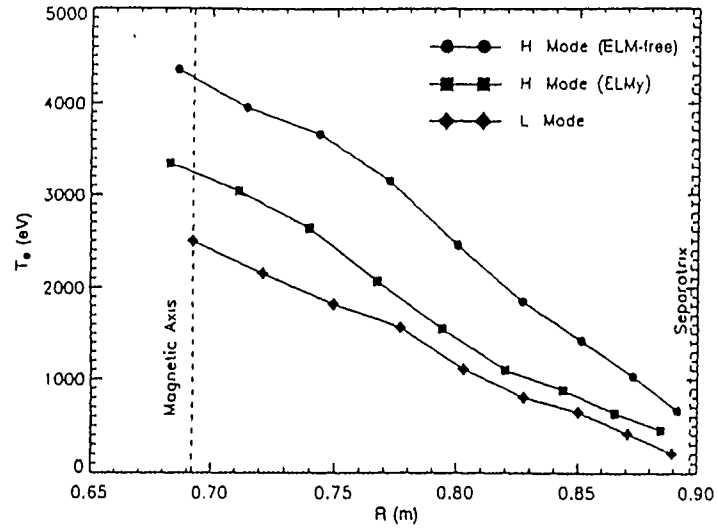

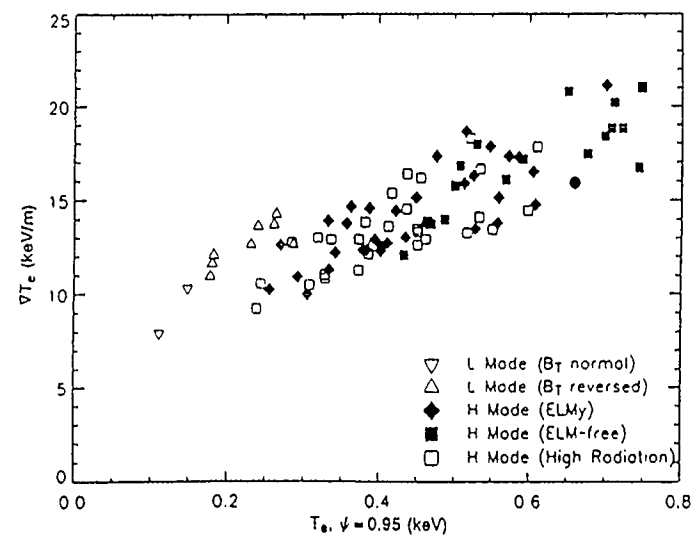

FIG. 16. ∇T_e in core versus $T_e(\psi = 0.95)$. The gradient is a spatial average taken between the outer edge of the sawtooth region and the beginning of the transport barrier

Plasma Surface Interactions – 2

HYDROGEN RETENTION IN CARBON AND TUNGSTEN

A.A. Haasz, J.W. Davis and M. Poon
University of Toronto

INTRODUCTION

Low divertor plasma temperatures have renewed interest in heavy metals for plasma-facing materials.

C and W are planned for use in the divertor region of ITER.

Of special interest are the hydrogen transport- and trapping-properties of tungsten.

- **What is the tritium inventory?**
- **What is the tritium reemission and permeation?**
- **What is the effect of C on the W surface on these processes?**

OBJECT OF PRESENTATION

- Brief overview of D retention data for:
  - graphite,
  - tungsten;

- Planned experiments on H retention and permeation.

(a) Apparatus:

- Mass-analyzed ion accelerator
- Thermal desorption spectroscopy [TDS]
- Nuclear Reaction Analysis [NRA]

(b) Specimens:

Carbon
- Pyrolytic graphite
- Monocrystal carbon
- EK98 [porous isotropic graphite]
- CKC graphite doped with B, Si, Ti, W

Tungsten
- Pure [polycrystalline, 99.95 wt%] tungsten foils [25 μm and 0.25 mm thick; annealed at T > 1470 K for 1 h]

C^+ implanted into W ***[Fig. 1]***

- C^+ implanted into the near-surface of pure W [25 μm thick W foil]

(c) Procedure:

- Implantation:
  - Specimens were implanted with D_3^+
  - For C^+ implantation into W, the C^+ flux was ~ $5x10^{18}$ C^+/m^2s
- Specimen heating during implantation:
  - For the results presented here, graphite specimens were kept at room temperature
  - W specimens were heated via a ceramic heater clamped behind the specimen.
- Temperature was measured with pyrometer [for desorption] and thermocouple [for implantation].
- Nuclear Reaction Analysis (NRA) was performed at McMaster University [Macaulay-Newcombe].
  - $D(^3He, ^4He)p$ nuclear reaction analysis
- Thermal Desorption Spectroscopy (TDS)
  - Specimens were heated to 1700-1900 K
  - Temperature ramping rate was 10 to 20 K/s
  - D retained in specimen was found from QMS signals for D_2, HD, and CD_4.

D RETENTION RESULTS: GRAPHITE

(a) *Pure Graphite:* *[Fig. 2]*

- Specimens: monocrystal, PyG, EK98, CKC-ref (undoped)

- All non-reflected D is retained in the various types of graphite studied until the implantation zone is saturated.

- Subsequently, the fluence dependence of retention depends on *specimen structure*.

(b) *Doped Graphite:* *[Fig. 3]*

- Specimens: CKC doped with B, Si, Ti, W

- Subsequent to reaching saturation of the implantation zone, specimens with different dopants exhibit different fluence dependence for D retention.

- One cannot rule out, however, the possibility that *specimen structure* may be controlling the observed fluence dependence behaviour.

(c) *Energy and Temperature Dependence:*

- Higher implantation energy leads to higher retention.
- Higher temperature leads to lower retention.

D RETENTION RESULTS: TUNGSTEN

(a) Pure Tungsten: (300 K) *[Figs. 4, 5]*

- D retention tends to saturation at fluences >10^{23} D/m^2.
- Same saturation is seen for 300, 500 and 1,000 eV D^+.
- D distribution peaks [NRA] are seen for 500 eV and 1 keV D^+ at 300 K implantation, but the peaks are well beyond the implantation range. *[NRA:Fig. 6]*

(b) Pure Tungsten: (500 K) *[Fig. 5]*

- NRA measurements of 500 eV D^+ at 500 K show much smaller near-surface D peaks.
- Similar D concentrations are seen on the front and back surfaces: ~ 0.1 at%.
  ***** evidence of diffusion through the bulk*****
  [NRA:Fig. 6]
- Good agreement is seen with TDS data.
- At high fluences, the trapped levels rise well above the 300 K values with no sign of saturation; this is consistent with diffusion-limited trapping (slope = 0.5).
- At fluences >10^{24} D/m^2, evidence of surface blistering is seen.
  [Fig. 7]

RESULTS: C^+-implanted W: Low C^+ Fluence: 10^{21} C^+/m^2

(a) 1 keV C^+ implanted at 300K: *[Fig. 8]*

XPS/3nm: significant amounts of graphitic C (21%) and WC (11%)

RBS: ~ ½ of the implanted C is near the surface; it is possible that > 10% WC exists beyond the top 3 nm

– At **low** D^+ fluences [500 eV D^+ at 300K & 500 K], D retention is much lower than the pure W case

– At D^+ fluences > 10^{24} D/m^2, D retention tends to the pure W level.

(b) 1 keV C^+ implanted at 500K: *[Fig. 9]*

RBS: less C is seen on the surface (compared with 300K implantation), suggesting the possibility of significant C diffusion into bulk.

– At 300K, D retention is similar to the pure W case for all fluences.

– At 500K, D retention levels appear to be ~ half of the corresponding pure W case for all fluences.

Possible explanation: C diffusion into the bulk W occupies trapping sites, which would otherwise be available to D.

RESULTS: C^+-implanted W: High C^+ Fluence: 10^{22} C^+/m^2

(a) 1 keV C^+ implanted at 300K: *[Fig. 10]*

XPS: ~ 48% graphitic C; < 3% WC in top 3nm
RBS: >½ of the implanted C is near the surface;
Possibly ~ 19% WC just below the W-C interface (beyond the XPS range);
Also seen, is a tail of ~ 2 at% C extending 170 nm into the specimen, indicating C diffusion.

With D implantation also at 300K:

– and ~ 10^{22} D^+/m^2 fluence, D retention is similar to that of graphite [~ $2x10^{21}$ D/m^2];

– for > 10^{22} D^+/m^2 fluence, retention is similar to pure W.

(b) 1 keV C^+ implanted at 500K: *[Fig. 10]*

RBS: similar to high-fluence C implantation at 300K;
~ 1 at% C extending 300 nm into the bulk.

With D implantation also at 500K:

– The D retention behaviour is consistent with the hypothesis that initially a graphite layer controls the retention;

– then, the graphitic C is sputtered by D^+, leaving a surface W-C layer, leading to enhanced recycling and a much lower D retention [dip in the curve in Fig. 10];

– eventually, the C from the surface WC (within D^+ range) will be preferentially sputtered, leading to increasing retention with D^+ fluence [Fig. 10];

– however, the C that has diffused deeper than the D^+ range, cannot be sputtered away by D^+, and therefore, the pure-W behaviour is not reproduced.

FUTURE PLANS

(a) Hydrogen Retention:

– Continue retention studies with C-W system using our dual-beam accelerator [D^+ and C^+].

(b) Hydrogen Permeation:

– Combine our permeation apparatus and **single-beam** accelerator for D permeation studies.

– C and D can be implanted *sequentially* into W by using C^+ and D^+ beams.

– C and D can be implanted *simultaneously* into W by using a $CD_{3,4}$ beam.

TRVMC May 25, 1999 2:21:02 PM

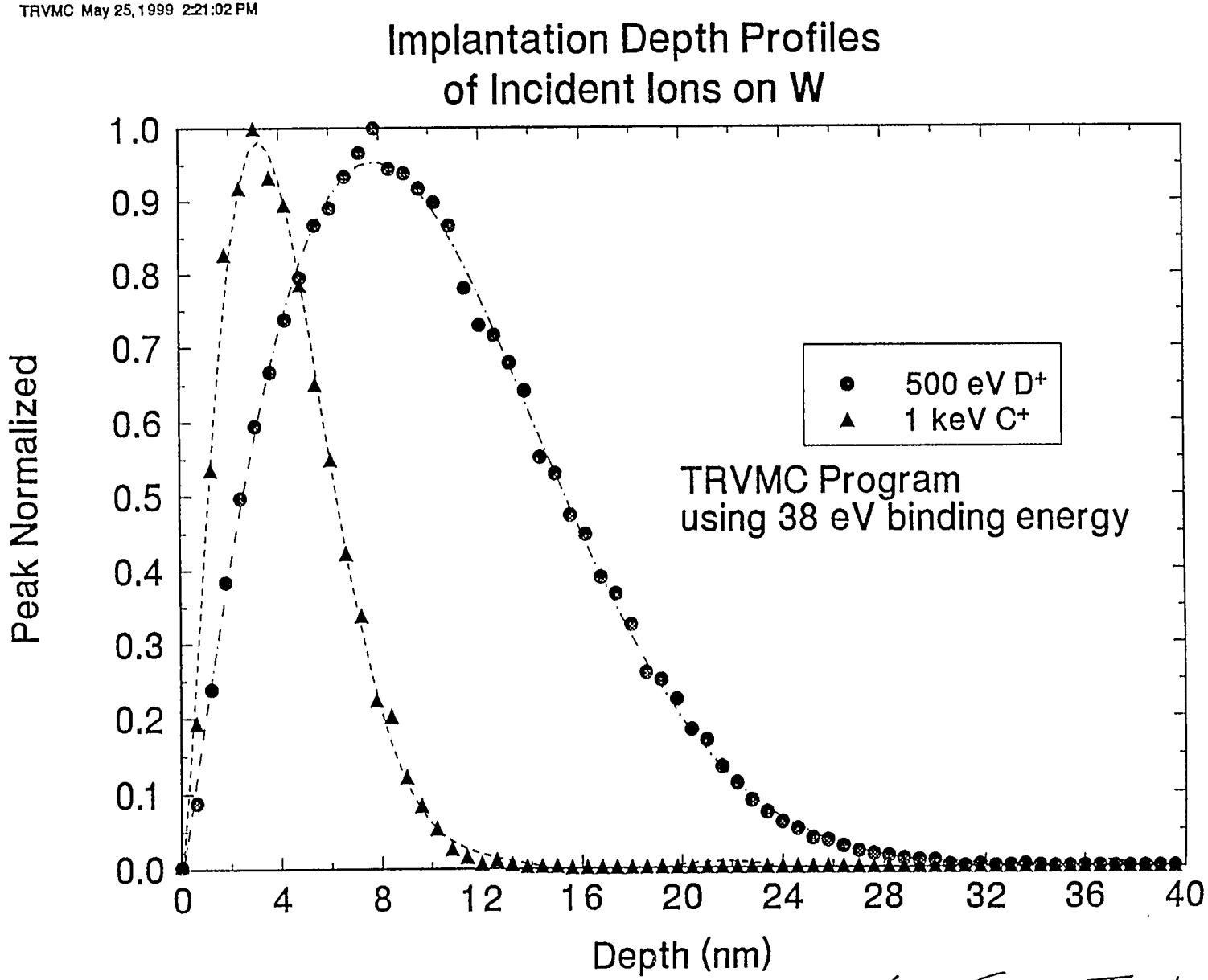

Haasz et al Fig. 1

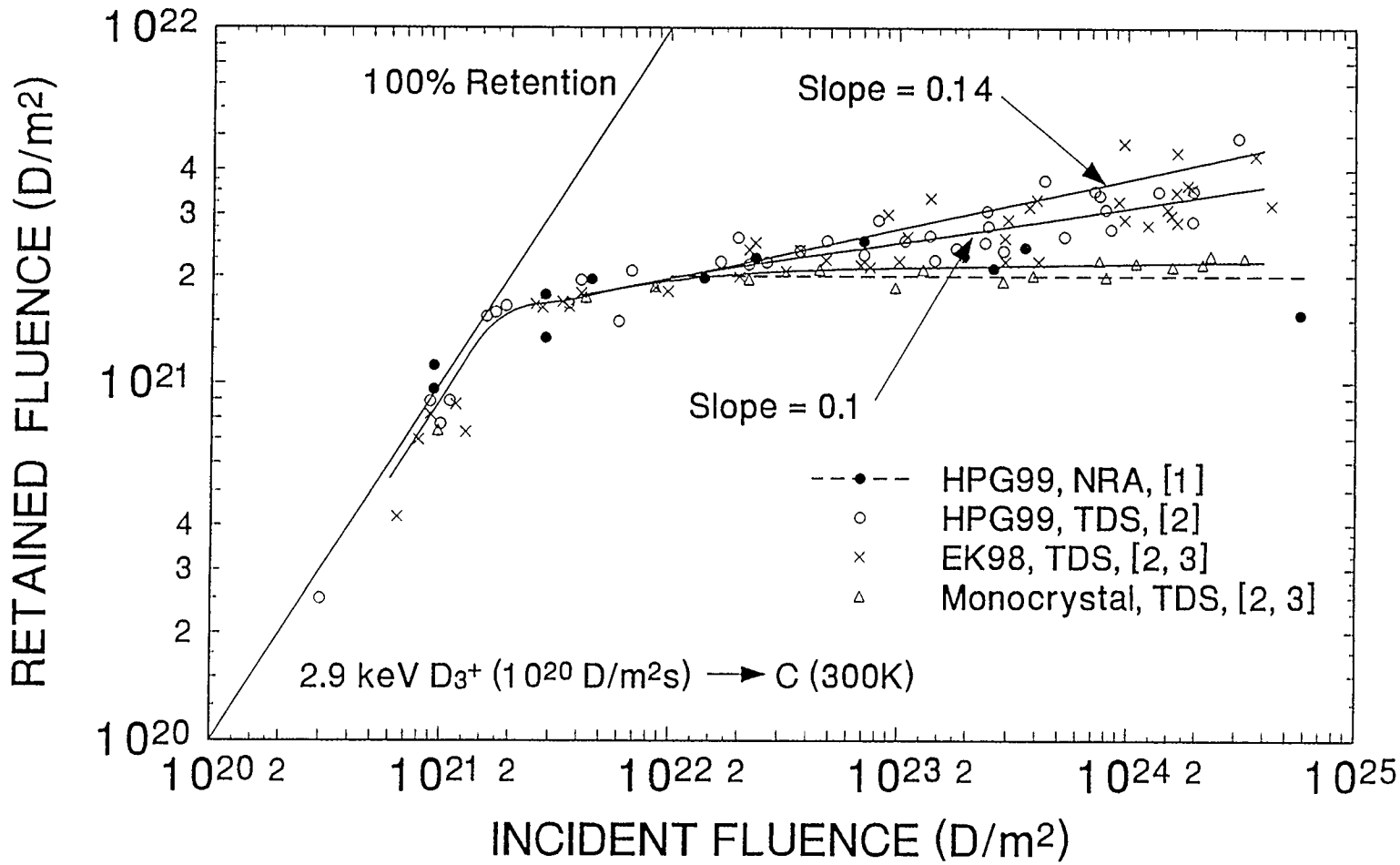

Haasz et al, Fig 2

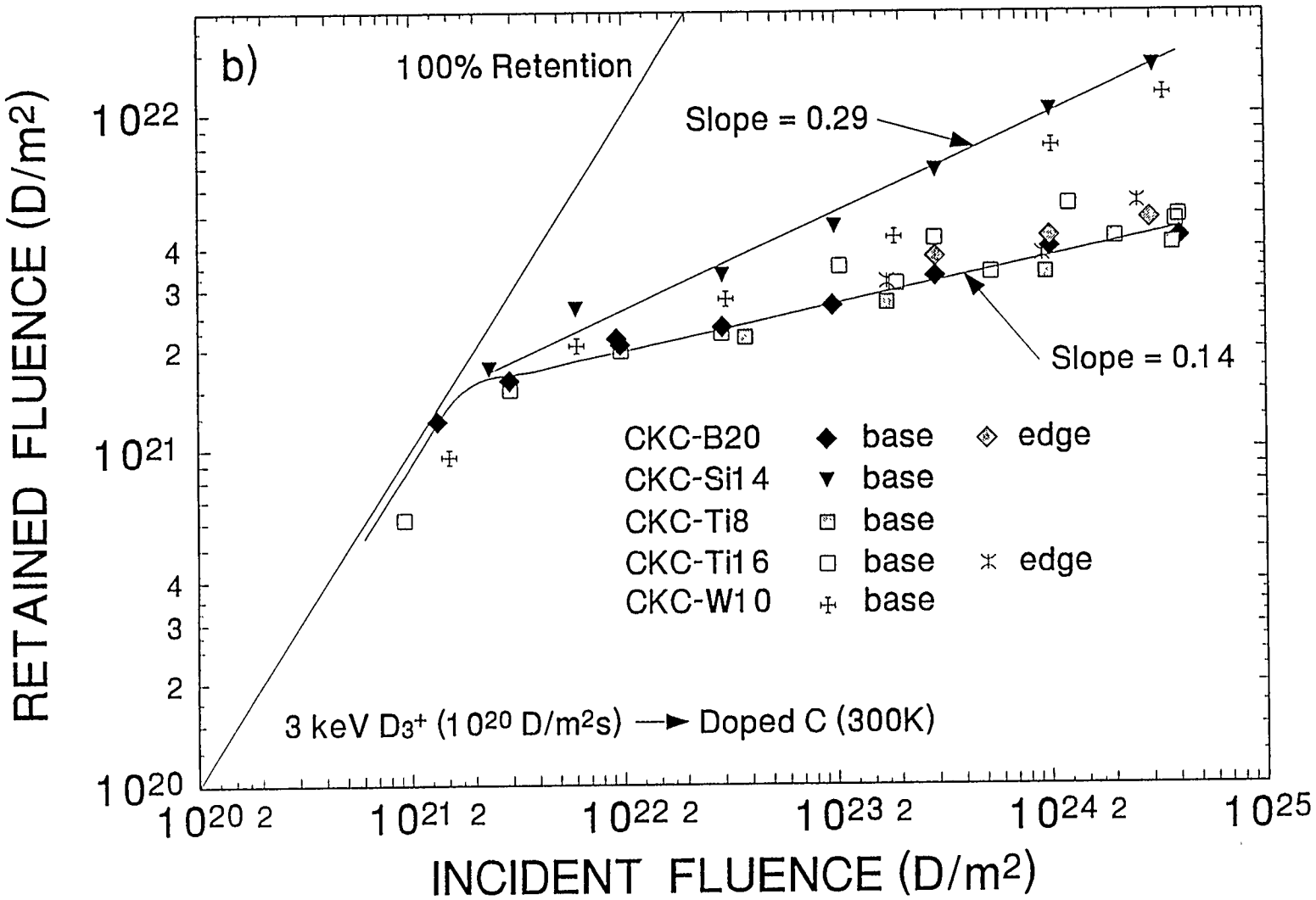

Haasz et al, Fig 3

Haasz and Davis, J. Nucl. Mater. 241-243 (1997) 1076

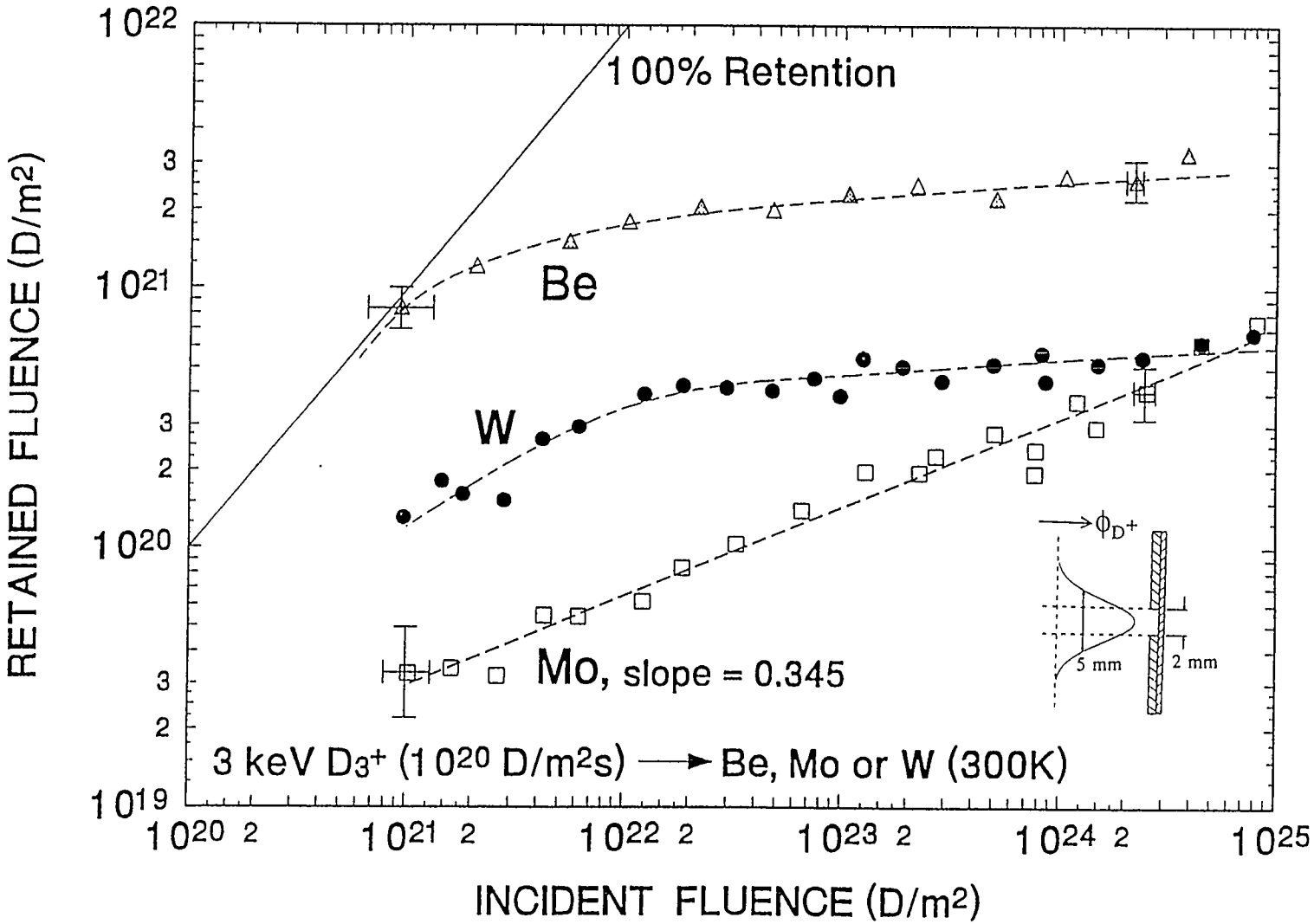

Haasz et al Fig 4

Haasz et al., J. Nucl. Mater. 258-263 (1998) 889

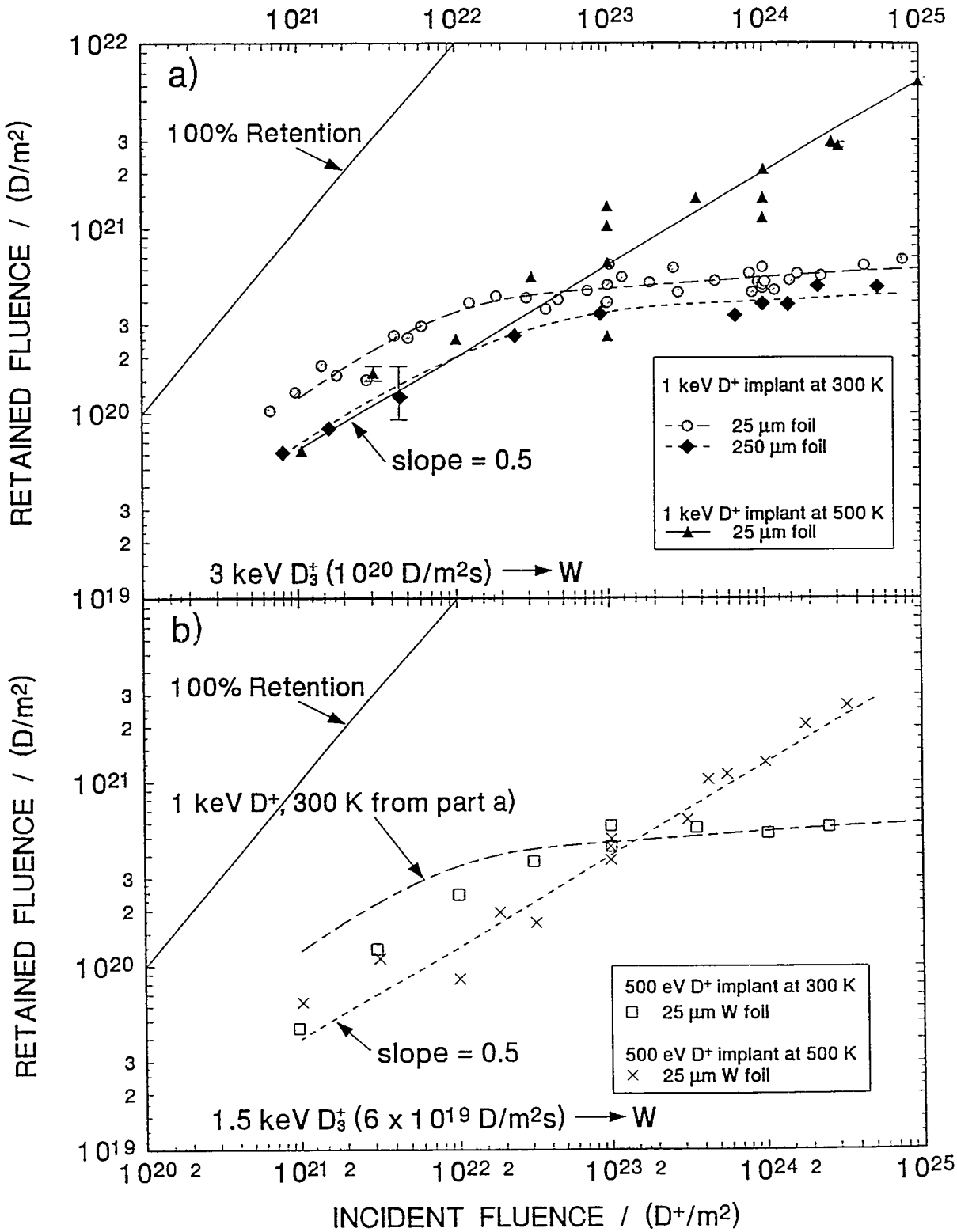

Haasz et al, Fig 5

Haasz et al., J. Nucl. Mater. 258-263 (1998) 889

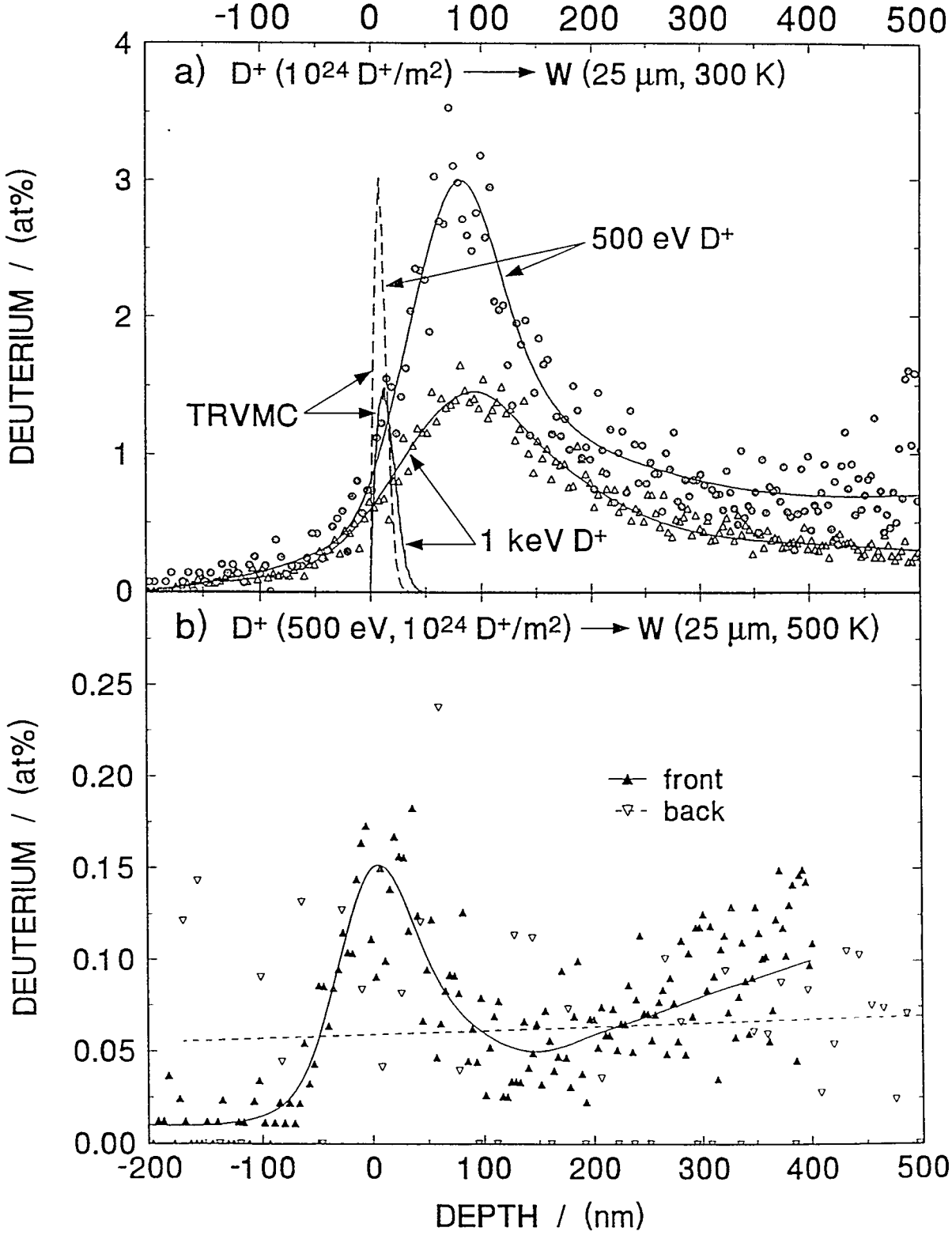

Haasz et al, Fig 6

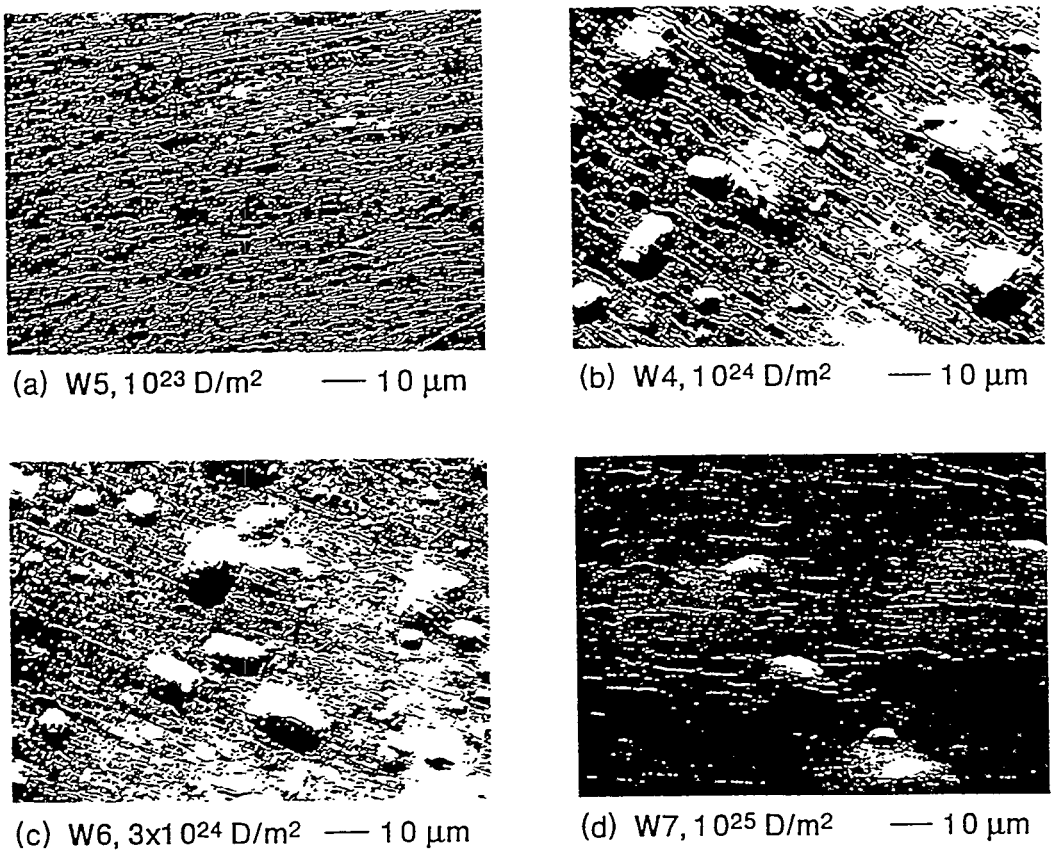

Fig. 3. SEM photographs of 500 eV/D⁺ implanted specimens. (a) specimen W5 (reference, probe fluence ~ 10^{23} D/m²) after a cumulative fluence of 10^{24} D/m²; (b) specimen W4 (damage fluence ~ 9×10^{23} D/m²) after a cumulative fluence of 1.0×10^{25} D/m², (c) specimen W6 (damage fluence ~ 3×10^{24} D/m²) after a cumulative fluence of 9.3×10^{24} D/m², (d) specimen W7 (damage fluence ~ 10^{25} D/m²)

Fig. 4. Cross-sectional SEM photograph of specimen W7 (damage fluence ~ 10^{25} D/m²) showing a large blister

Haasz et al, Fig 7

Low C^+ fluence at 300 K

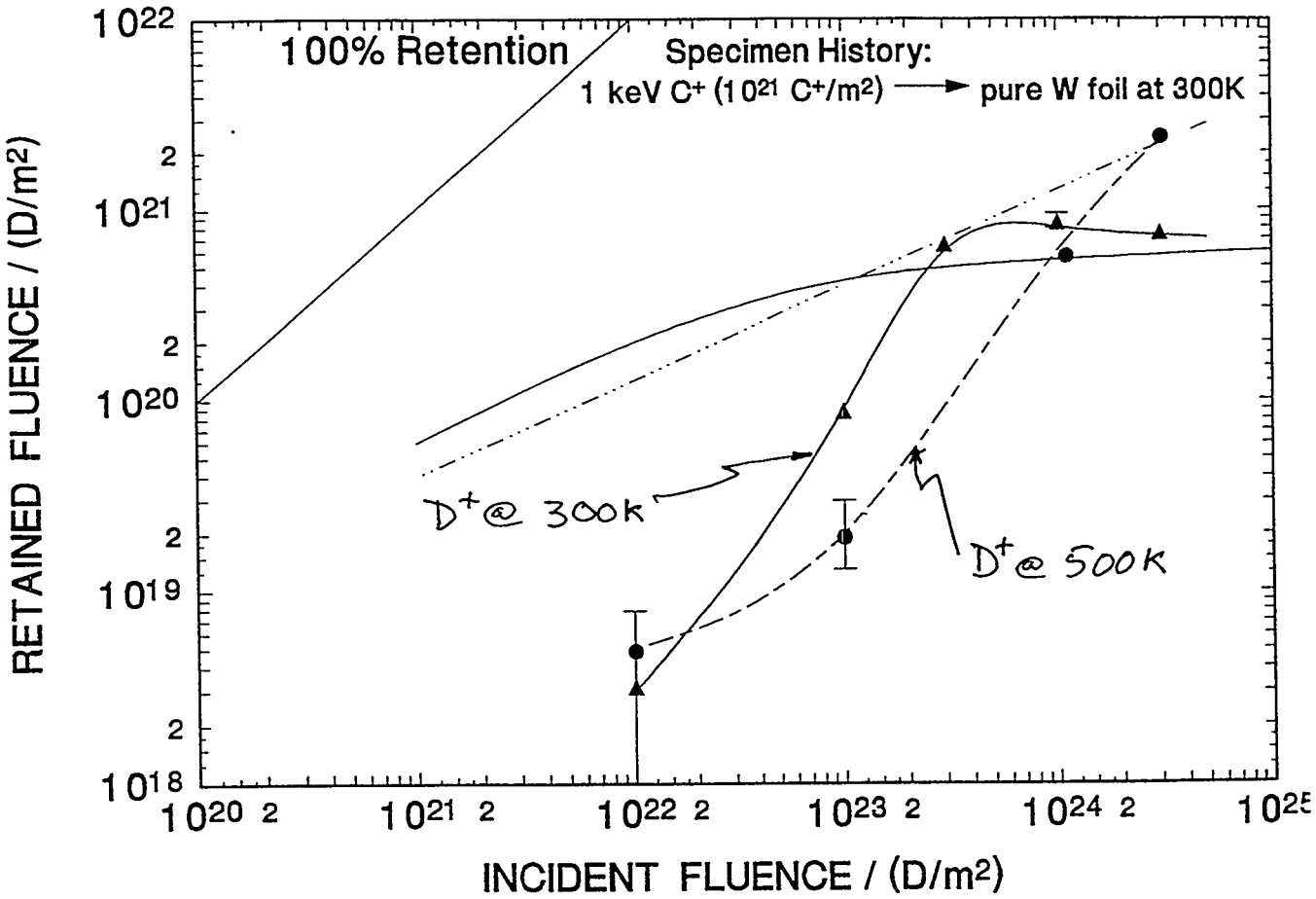

——	500 eV/D+ at 300K [Haasz et al, 1998]
-·····-	500 eV/D+ at 500K [Haasz et al, 1998]
—▲—	1 keV C+ at 300K + 500 eV/D+ at 300K
--●--	1 keV C+ at 300K + 500 eV/D+ at 500K

Haasz et al, Fig. 8

Low C^+ fluence at 500K

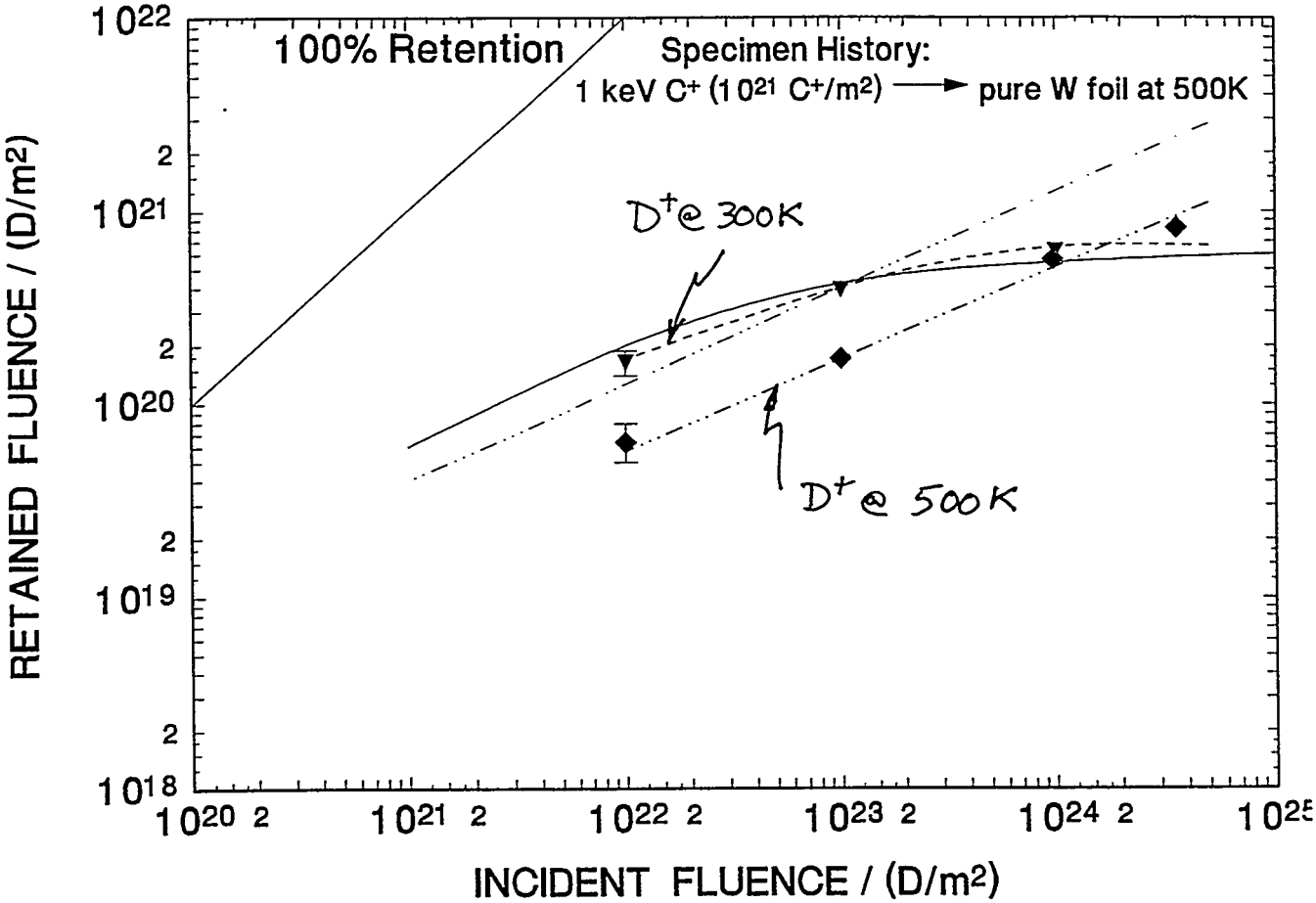

Haasz et al, Fig 9

High C^+ fluence at 300K & 500K

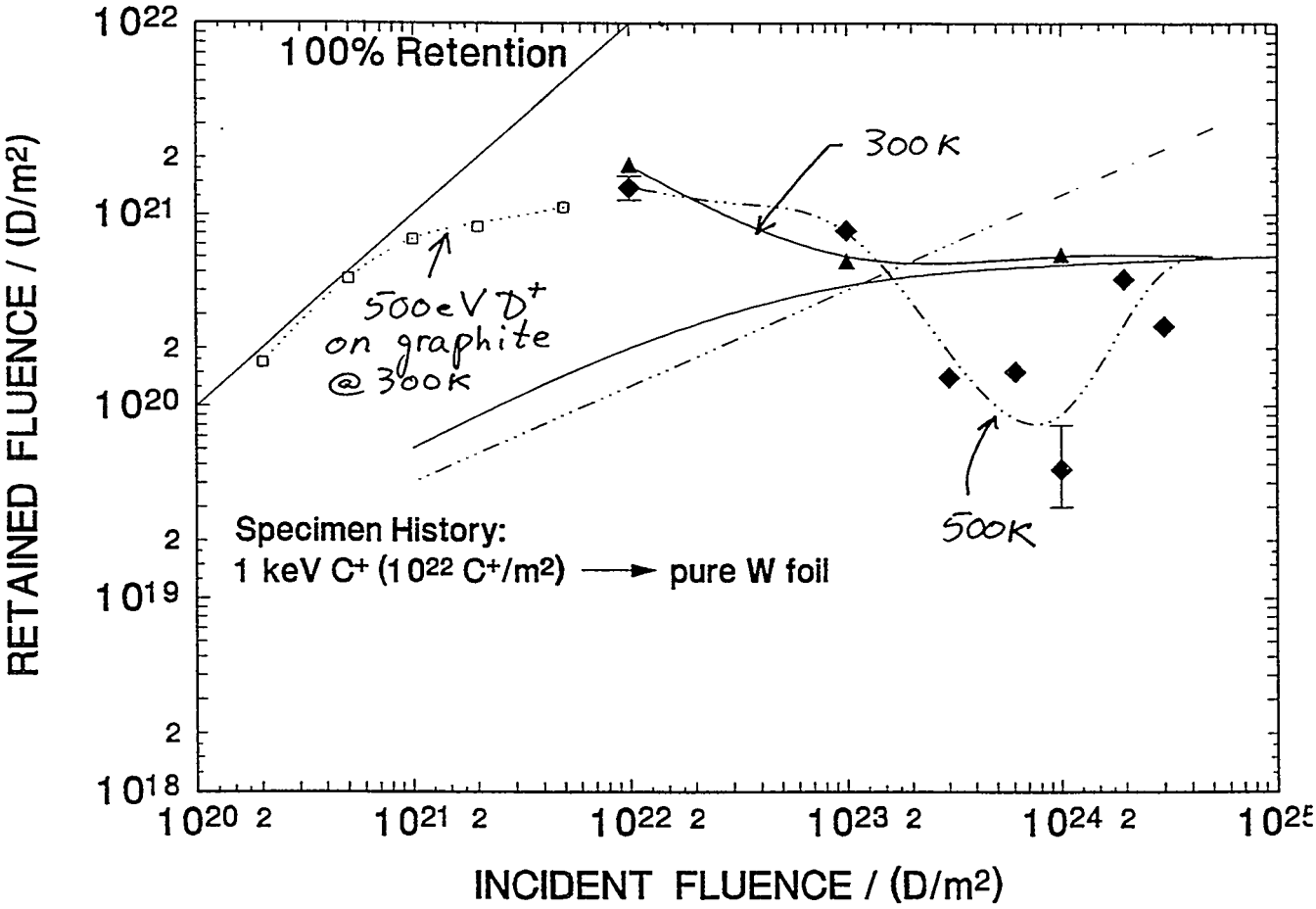

——	500 eV/D+ at 300K [Haasz et al, 1998]
-·-·-	500 eV/D+ at 500K [Haasz et al, 1998]
—▲—	1 keV C+ + 500 eV/D+, both at 300K
-◆-	1 keV C+ + 500 eV/D+, both at 500K
·□	500 eV D+ on graphite at 300K [Wampler et al, 1981]

Haasz et al, Fig 10

Comparison with W specimen pre-exposed to high-fluence D^+ plasma in PISCES

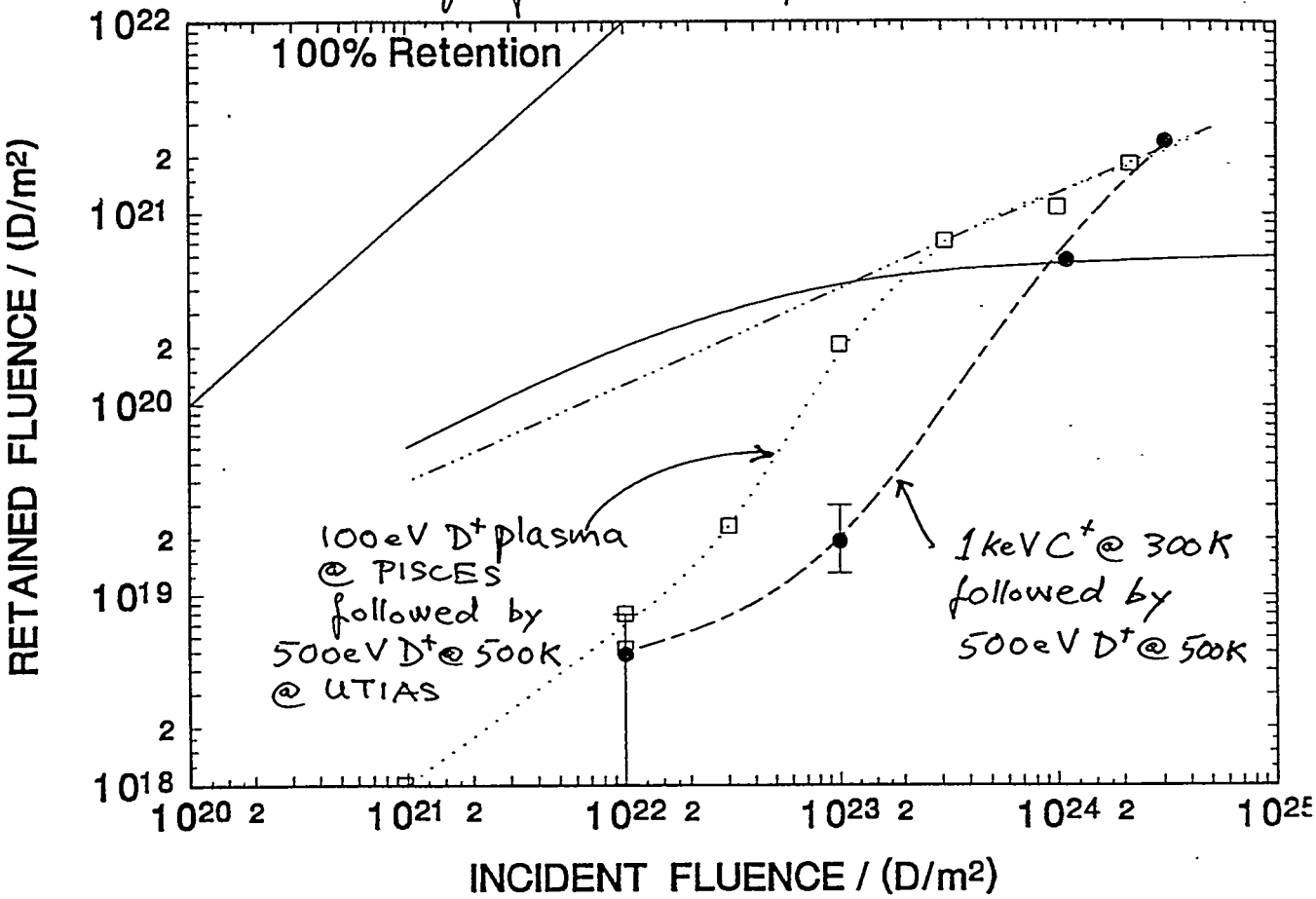

——	500 eV/D+ at 300K [Haasz et al, 1998]
—·—·—	500 eV/D+ at 500K [Haasz et al, 1998]
··□··	500 eV/D+ at 500K on PISCES
–●–	1 keV C+ at 300K + 500 eV/D+ at 500K

Haasz et al, Fig 11

KTH

RETENTION OF HYDROGEN IN TEXTOR LIMITERS

Marek RUBEL

Alfvén Laboratory, Royal Institute of Technology, Stockholm, Sweden

With contributions from:

Tetsuo Tanabe: ***CIRSE, Nagoya University, Japan***

Volker Philipps, Matej Mayer and Peter Wienhold:
FZ-Jülich, Germany

US – Japan Workshop on
Plasma – Surface Interactions
and
High Heat Flux Component for Next Fusion Devices
Santa Fe, New Mexico, USA
November 1 – 4, 1999

OUTLINE

1. INTRODUCTION & MOTIVATION

2. MATERIALS & METHODS

3. RESULTS

   LONG TERM SAMPLES
   [FORMATION OF FLAKES]

   LIMITER TILES

4. SUMMARY & CONCLUSIONS

THE MAJOR AIM OF THE INVESTIGATION:

TO ASSESS THE FUEL ACCUMULATION [CO-DEPOSITION / CO-IMPLANTATION] ON and IN PLASMA FACING COMPONENTS

SOME NUMBERS MOTIVATING THE STUDIES:

- **RADIOACTIVITY**

$$1\ g\ T \rightarrow 1.2 \times 10^{4}\ Ci = 4.44 \times 10^{14}\ Bq$$

- **DEPOSITION OF FUEL (atoms cm^{-2})**

$$2 \times 10^{19}\ cm^{-2} \rightarrow 0.5\ g\ (T)\ m^{-2}$$

METHODS

1. ION BEAM ANALYSIS

- Nuclear reaction analysis (NRA)
- Deuterium $^{3}He(d,p)^{4}He$
- Boron $^{11}B(p,\alpha)^{8}Be$
- Carbon $^{12}C(p,p)^{12}C$
- Rutherford backscattering spectroscopy (RBS)

2. SCANNING ELECTRON MICROSCOPY

3. ENERGY DISPERSIVE X-RAY SPECTR.

DEUTERIUM ANALYSIS

$^3He\ (d,p)\ ^4He$ [Q = 18.3636 MeV]

REACTION CROSS – SECTION

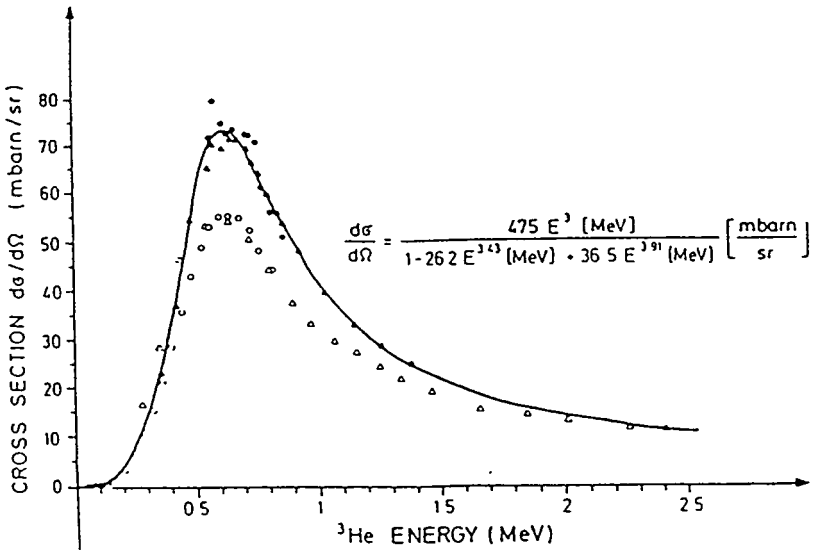

INFORMATION DEPTH IN GRAPHITE MATRIX

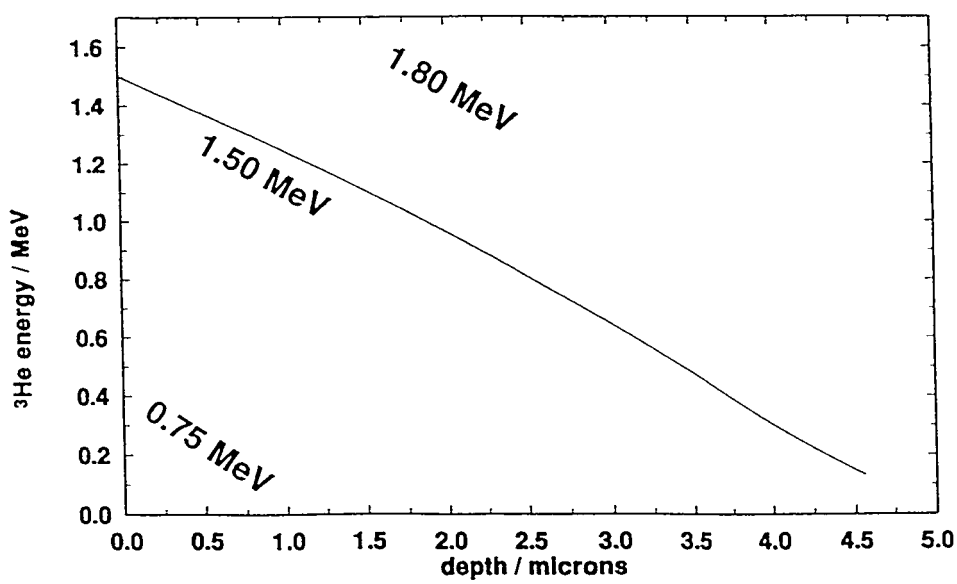

E_0 = 0.75 MeV d = 1.4 μm
E_0 = 1.50 MeV d = 4.5 μm
E_0 = 1.80 MeV d = 6.2 μm

ALT II
DEUTERIUM CONTENT AND DISTRIBUTION AN THE THIN CO-DEPOSIT IN THE AREA WITHOUT FLAKES

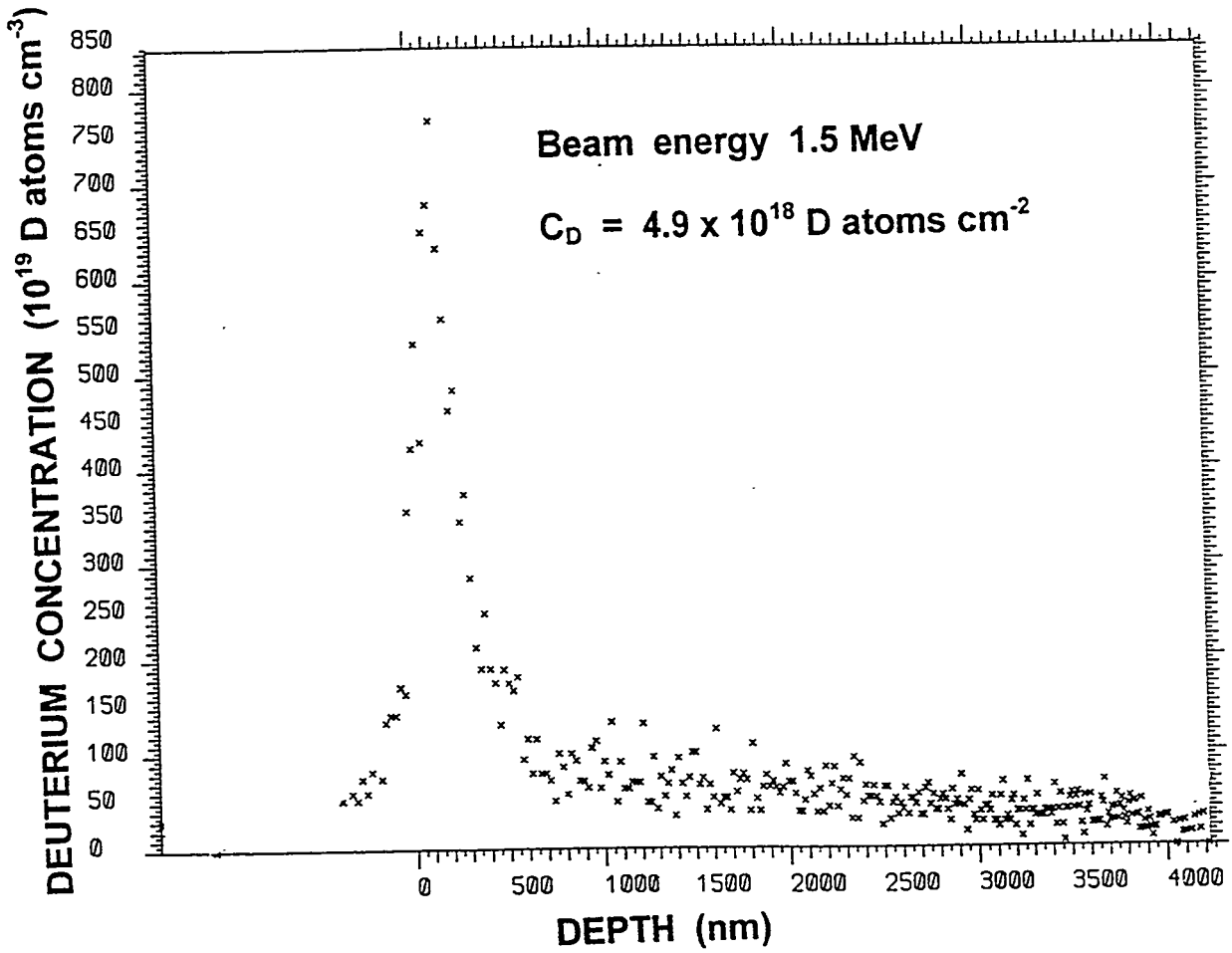

DEUTERIUM IN THE ALT II TILE

AREA WITH A FLAKING CO-DEPOSIT

DEPTH PROFILES RECORDED AT TWO DIFFERENT ^{3}He ENERGIES: 1.5 and 1.8 MeV

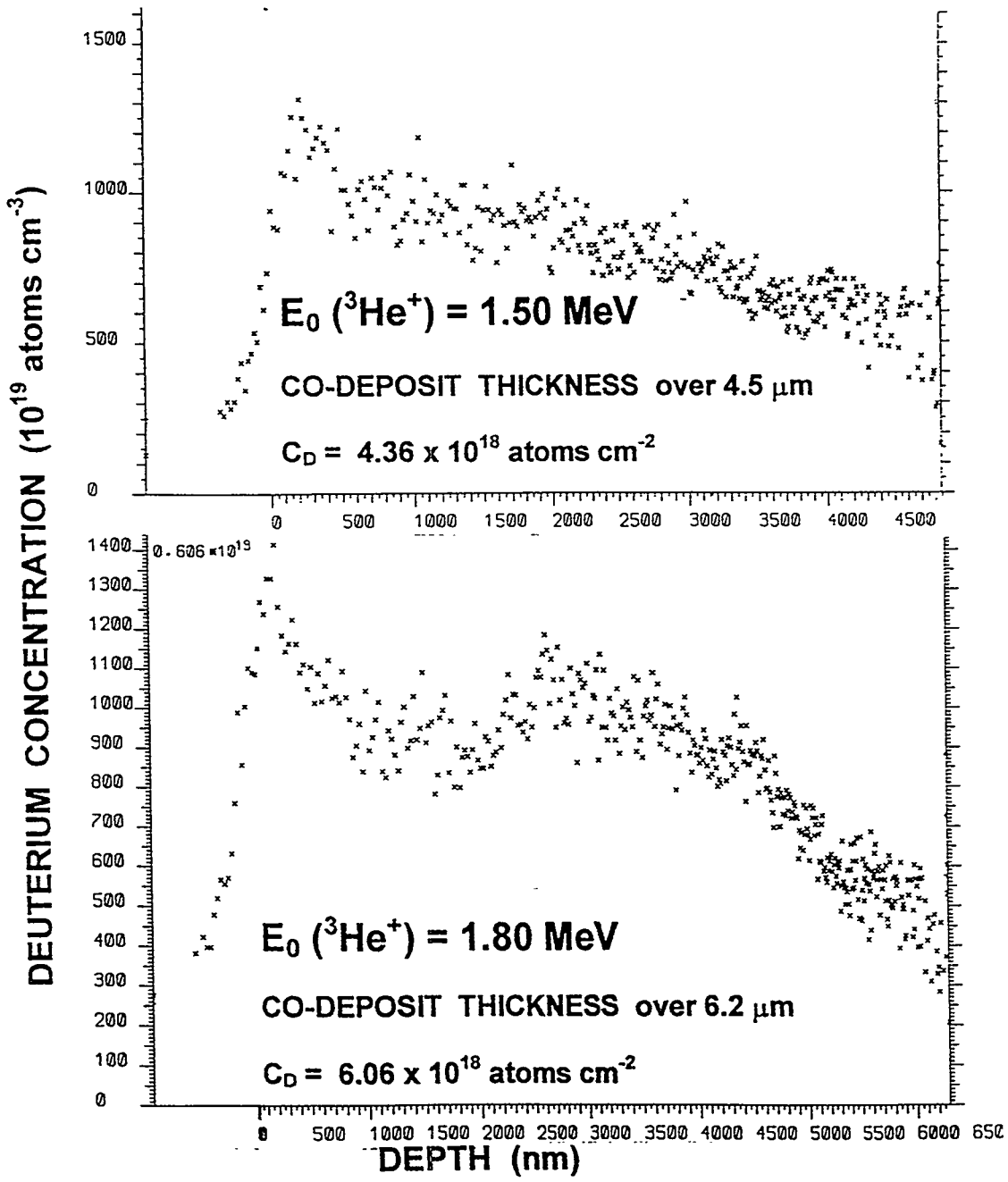

IMPURITY ATOMS ON THE ALT II TILE

ANALYSIS (RBS) OF THE FLAKING CO-DEPOSIT

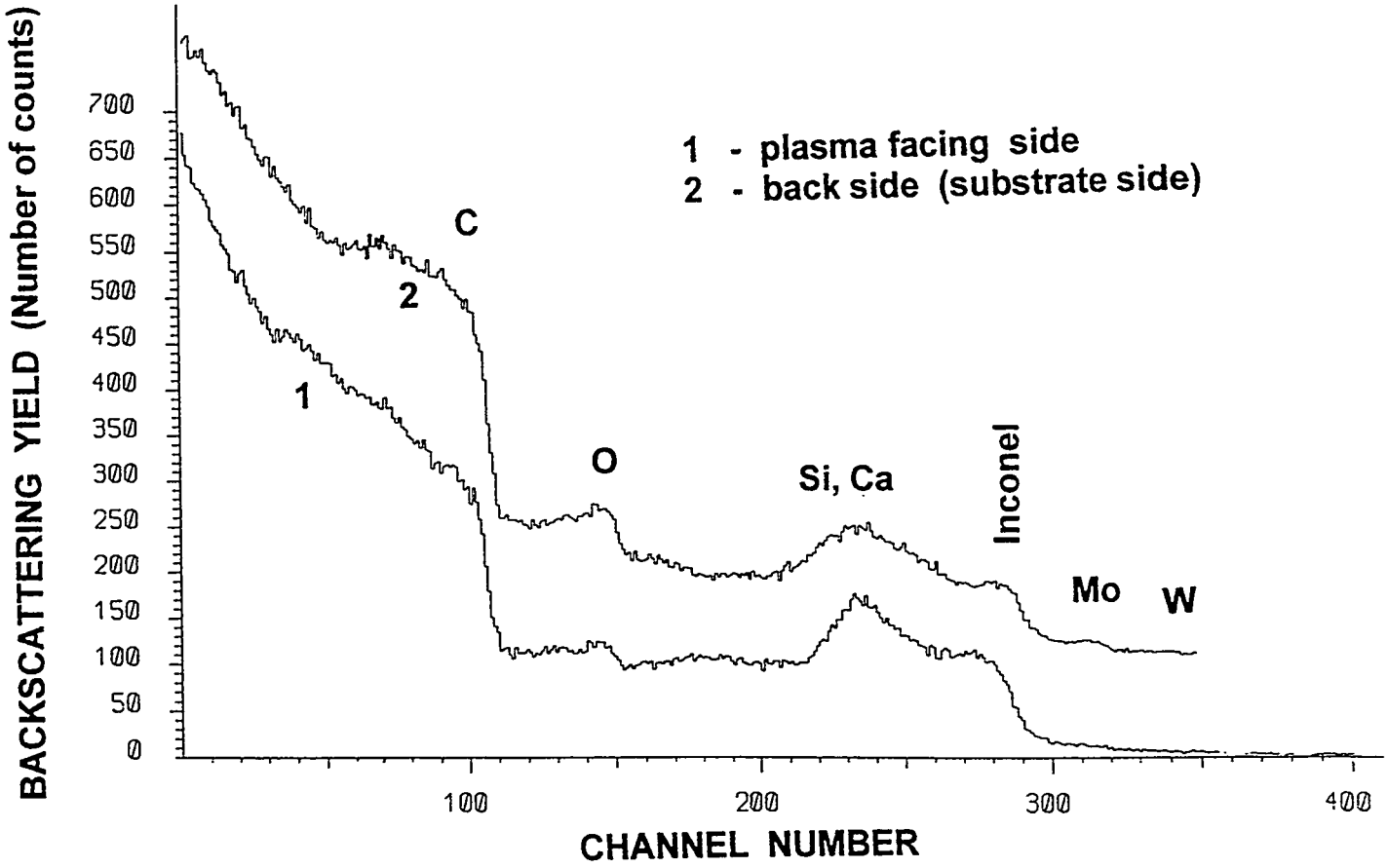

A FLAKE DETACHED FROM THE LIMITER TILE (ALT II, tile 20)

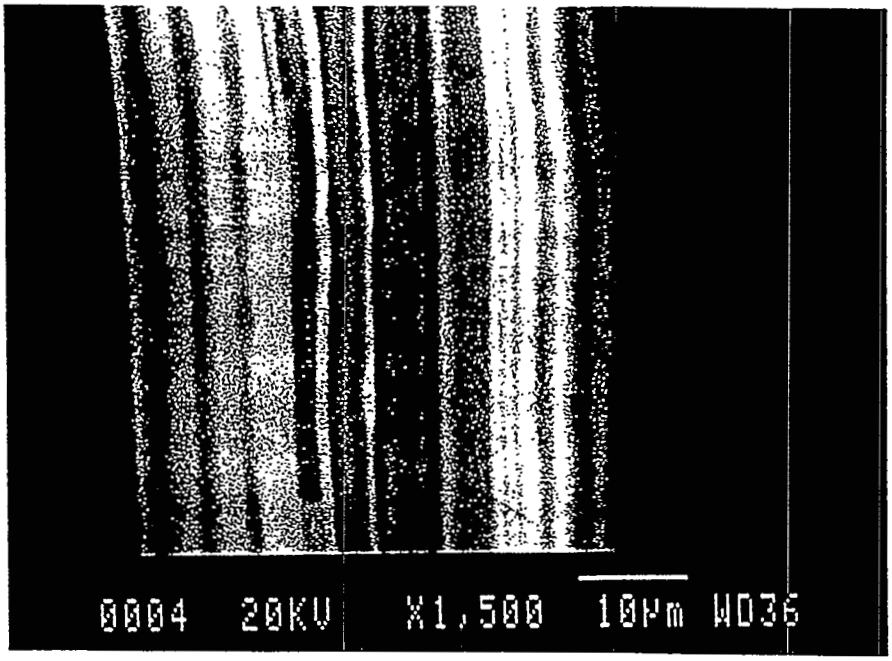

CROSS SECTION: STRATIFIED STRUCTURE

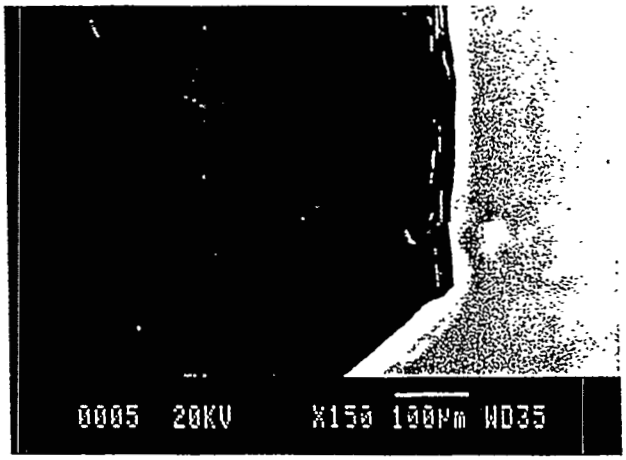

SUBSTRATE SIDE

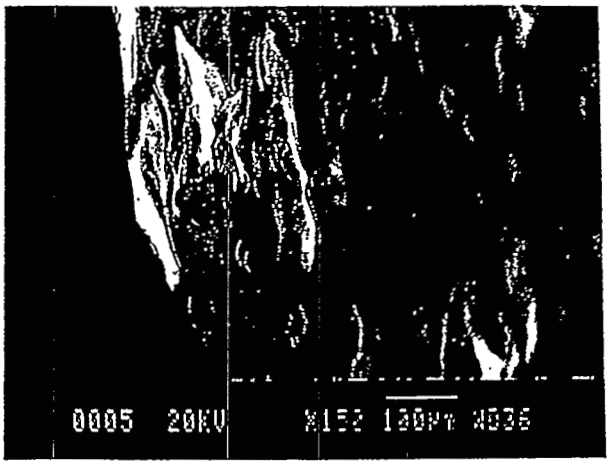

PLASMA FACING SIDE

DEUTERIUM CONTENT AND DISTRIBUTION ON BOTH SIDES OF THE DETACHED FLAKE

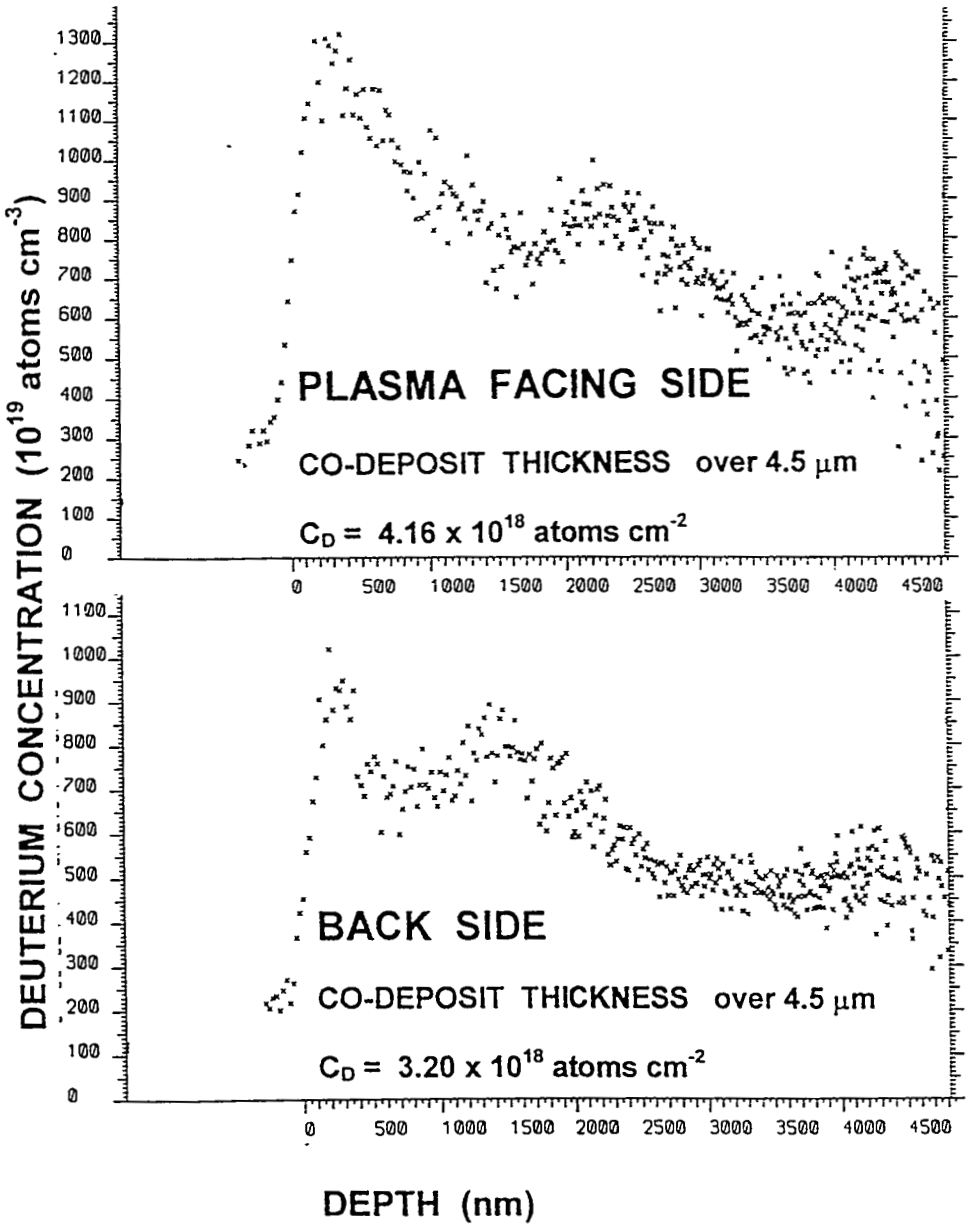

ESTIMATED TOTAL DEUTERIUM CONTENT IN THE FLAKING CO-DEPOSIT ON THE ALT TILE:

3.5×10^{19} D atoms cm^{-2} in 45 μm layer

DEUTERIUM IN THE ALT II TILE

SURFACE AFTER THE REMOVAL OF A FLAKING CO-DEPOSIT

DEPTH PROFILES RECORDED AT TWO DIFFERENT ^3He ENERGIES: 1.5 and 1.8 MeV

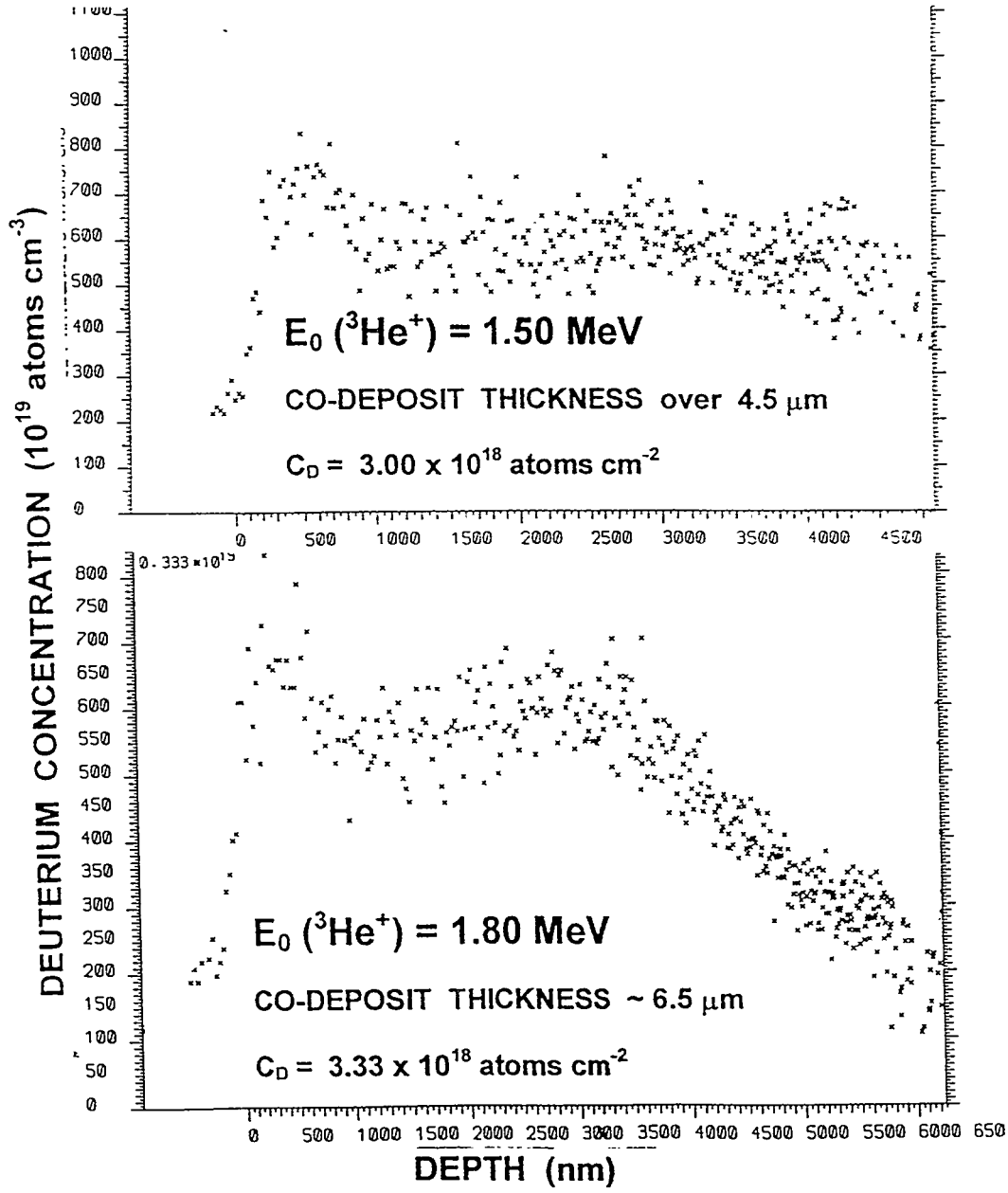

CONCLUSION:

DEUTERIUM DEPOSITED IN THE LAYER ~ 6.5 μm THICK

DEUTERIUM DISTRIBUTION AND CONTENT IN ALT II TILE (20): SUMMARY OF RESULTS

	D CONTENT
AREA 1: **HIGH and UNIFORM in DEPTH** ***THICK FLAKING LAYER***	~ 94×10^{19}
AREA 2: **$3.2 - 7.8 \times 10^{17}$ cm^{-2}** ***LAYER up to 5 μm*** ***NON-UNIFORM DEPTH PROFILE***	~ 2.0×10^{19}
AREA 3: **$2.6 - 3.5 \times 10^{17}$ cm^{-2}** ***THIN LAYER***	~ 1.7×10^{19}
BACK SIDE OF THE TILE: **$0.9 - 1.8 \times 10^{17}$ cm^{-2}** ***THIN LAYER***	~ 0.5×10^{19}
TOTAL	**1×10^{21}**

SUMMARY & CONCLUSIONS

- Hydrogen rich co-deposits and dust particles have been studied to assess the distribution and content fuel and impurity atoms (C, B, W).

- The distribution of erosion and deposition zones shows a complicated pattern caused by the ripple of the magnetic field and the curved shape of the limiter surface.

- Co-deposition of deuterium on graphite tiles of the toroidal belt limiter: 1×10^{21} D atoms per tile.

  - Thickness of the layers in the deposition zones: about 45 μm.
  - An average growth rate of the deposit: 3 μm s^{-1}.
  - The deuterium-to-carbon concentration ratio (C_D/C_C) in the co-deposit: typically 0.1.
  - Deuterium is found even in the hottest areas of PFC: 5×10^{16} D atoms cm^{-2}.

Based on the present results, the total D inventory on the toroidal limiter (224 tiles) is about 2×10^{23} D atoms after 14100 s of the operation (8 month).

SUMMARY & CONCLUSIONS

- Several types of plasma facing components from TEXTOR have been studied to assess the distribution and content of deuterium.

- The distribution of erosion and deposition zones has shown a complicated pattern caused by the ripple of the magnetic field and the curved shape of the limiter surface.

- The greatest co-deposition of deuterium has been found on graphite tiles of the toroidal belt limiter: 1×10^{21} D atoms per tile.

  - Thickness of the layers in the deposition zones: about 45 μm.

  - An average growth rate of the deposit: 3 nm s^{-1}.

  - The deuterium-to-carbon concentration ratio (C_D/C_C) in the co-deposit: typically 0.1.

Based on the present results, the total D inventory on the toroidal limiter (224 tiles) is about 2×10^{23} D atoms after 14100 s of the operation (8 month).

TRITIUM DISTRIBUTION IN ALT II TILES RESULTS & INTERPRETATION (1)

The distribution of D and T in the tiles differs:

T content is higher (!) in the erosion zone than in the deposition zone rich in D.

- **Deuterium: co-deposited low energy species**
- **Tritium: implanted high energy non-confined ions (1.0 MeV) from the D – D reaction**

$$D + D \rightarrow T\ (1\ MeV) + H\ (3\ MeV)$$

- ***Range of 1.0 MeV tritons in graphite: ~ 8 μm***
- ***$\beta^-(T)$ = 18.6 keV***
- ***$\beta^-(T)$ range in graphite: ~ 3.9 μm (ρ = 1.85 g/cm3)***

ALT II TOROIDAL BELT LIMITER
TILE 20

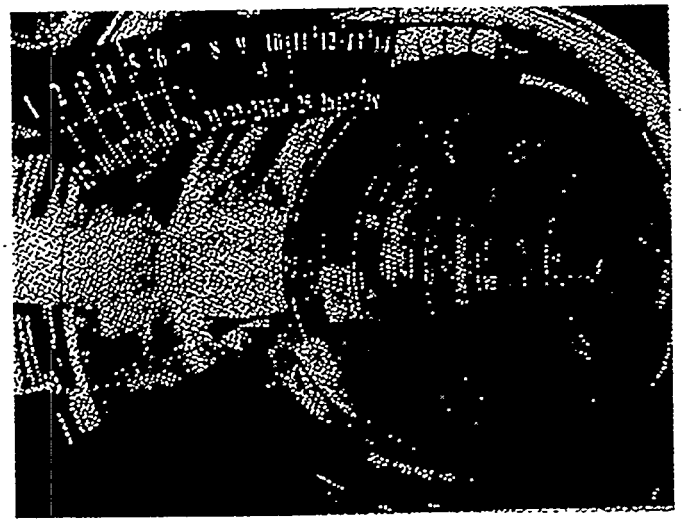

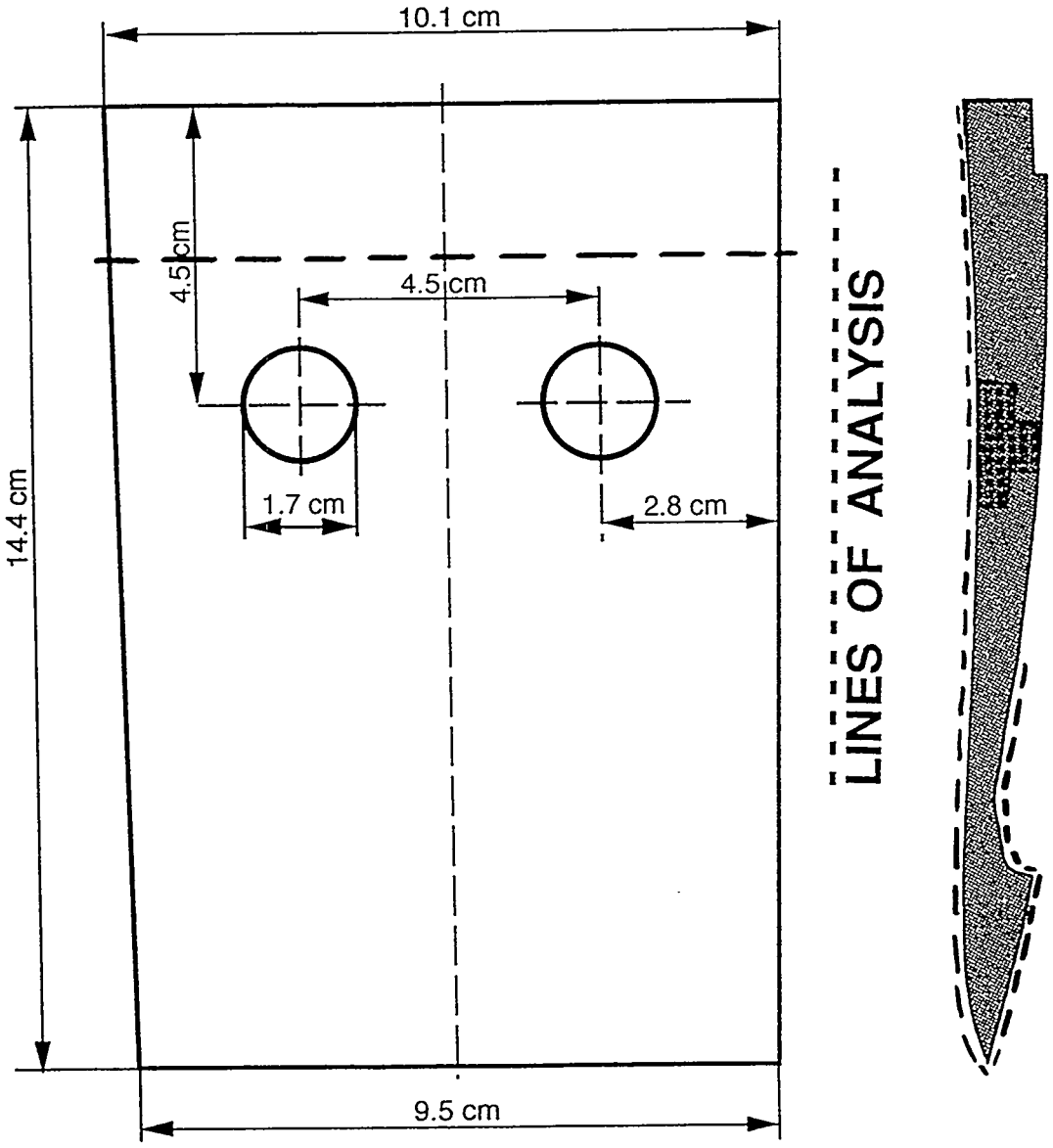

Critical Plasma Wall Interaction Issues for Plasma Facing Materials and Components in ITER-Class Tokamaks

Gianfranco Federici (ITER JCT)

Acknowledgements:

C.H. Skinner (PPPL)
G. Janeschitz, R. Tivey (ITER)
J.N. Brooks, A. Hassanein (ANL)
J.P. Coad (JET)
A.A. Haasz (UTIAS)
N. Noda (NIFS)
V. Philipps (IPP Juelich)
J. Roth (IPP Garching)
W. Wampler (SNLA)
D. Whyte (GA/UCSD)
C.H. Wu (EFDA)

US-Japan Workshop on High Heat Flux Components and Plasma Surface Interactions for Next Fusion Devices
November 1-4 , 1999, Santa Fe, NM - U.S.A.

TRITIUM DISTRIBUTION IN ALT II TILES RESULTS & INTERPRETATION (2)

CONCLUSIONS:

1. **The same amounts of T impinge on the tile in the erosion and deposition zones:**

   - **Deeply implanted T is not instantly removed from the erosion zone.**

   - **T implanted in the deposition zone is "diluted" in the growing layer of the co-deposit.**

2. **Not all β^-(T) radiation reaches the tile surface and the imaging plate *(detection limit in graphite ~4.0 μm).***

3. **The signal recorded maybe (is) influenced by:**

- **Surface roughness (flakes in the deposition zone).**
- **β^- stimulated X-ray emission from impurity atoms.**
- **β^- stimulated secondary electrons.**

DIFFICULT TO QUANTIFY TRITIUM FROM D – D PROCESS.

Outline

- Motivation
- Scale-up to Next Step Devices and Related Issues
- Present Conception of the ITER Device
- Candidate Plasma Facing Materials
- Critical PMI Design Issues and Key R&D Findings
  - First Wall
  - Divertor and baffle
- R&D Needs
- Summary

Motivation

- Plasma surface interactions lead to impurity generation and recycling of hydrogen isotopes, determining plasma fuelling - **both key parameters in fusion plasma performance.**

- Plasma surface interactions lead to wall erosion and an in-vessel tritium inventory - **both key factors in engineering of fusion reactors.**

⇒ Plasma surface interactions must be controlled to prevent damage to the walls and obtain sufficient wall lifetimes to permit acceptable maintenance periods.

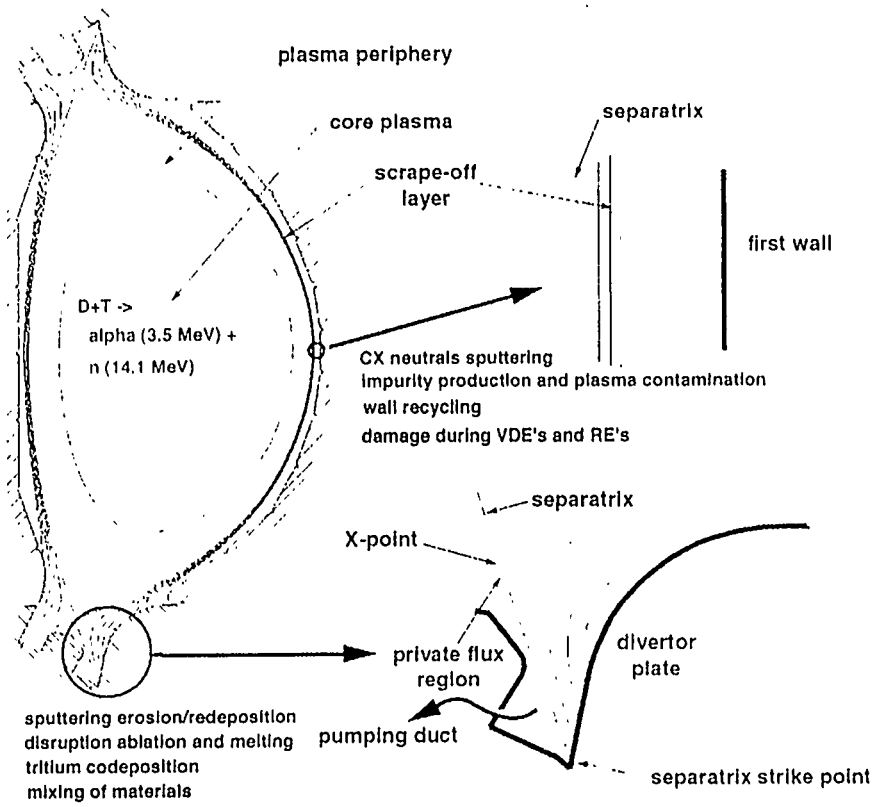

The boundary plasma constitutes a buffer zone that protects the walls from the hot plasma and shields the plasma core from impurities originating at the walls.

Scale-up to Next Step Devices and Related Issues

PARAMETERS (log scale)	Units	Existing	ITER [RTO-RC]	FIRE
Temperature (peak)	KeV	3- >45	30	14
Density (peak)	$10^{20}m^{-3}$	0.5-10	1	7
Confinement time	s	0.2-1	6	0.6
Energy content	MJ	1-15	1000 [500]	33
Pulse duration	s	10-25	1000 [>100]	20
Duty factor		<0.003	<0.1	0.003
Cumulative run time	10^3s/y	7-30	>1000	60
Tritium x pulse	g	0.2	300 [50-100]	0.3
Av. n-wall loading	MW/m^2	~0.002* (JET)	1 [0.5]	3.3
Av. neutron fluence	$MW/m^2 \cdot yr$	~0.001* (JET)	~1 [0.5]	0.01
Power density (aver.)	MW/m^3	~0.28	~0.54	12

Critical PSI Issues of Next Step Devices

The pulse lengths of current tokamaks are too short and the stored thermal and magnetic energies are too small to erode significant thicknesses of first-wall/divertor material. In existing fusion devices:

- erosion of the main chamber and divertor strike plates acts as a source for impurities in the discharge, but has no impact on the erosion lifetime;
- fuel economy and safety have never been an issue in most of today D-fuelled fusion devices (except TFTR and JET where tritium has been used).

However, in a long pulse device such as ITER, modelling shows that:

- *erosion of PFCs will be on a cm scale per year operation and represents a 3-4 orders of magnitude change from present tokamaks;*
- *the material erosion lifetime of PFCs becomes sufficiently short that several replacements will be required during the lifetime of the device.*
- *large scale erosion raises tritium codeposition (fuel economy and safety) and dust (safety) issues and control of radioactivity inventories is required.*

For the first time in fusion research, erosion and its consequences (e.g., codeposition) might affect the operational schedule of a fusion device.

The Challenge of Off-Normal Events

Disruption events, frequent in todays tokamaks, are a key driver for the design and material selection for a Next-step. In ITER, they demand the use of C.

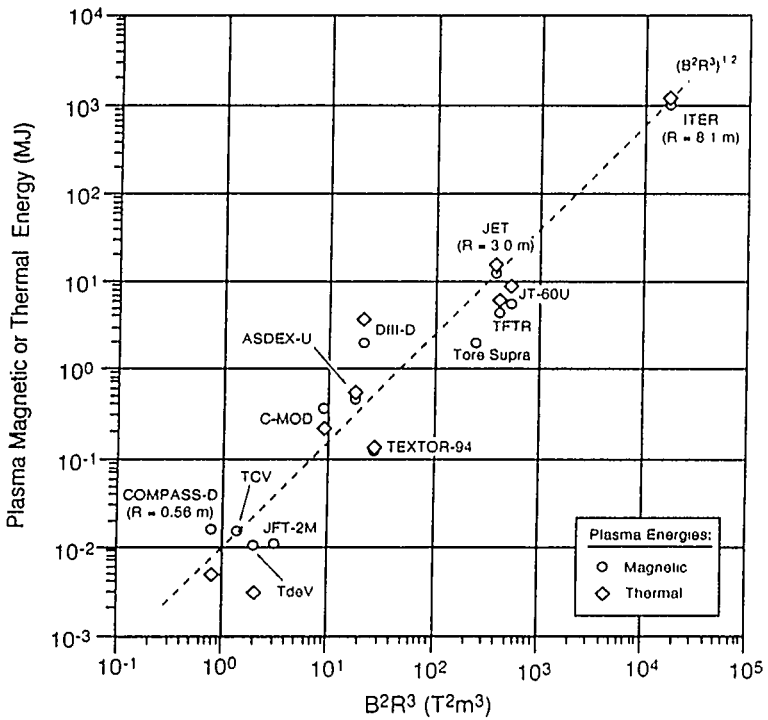

- Thermal quenches accompanying disruptions and ELMs bring very high (GW/m^2) transient heat loads which can vaporise and melt significant amounts of material (eg., divertor).
  - Complexity of the problem and paucity of relevant data on properties of vapour shielding and melt layers during off-normal transients makes predictions uncertain.
- Use of C-based materials is the simplest solution since they do not melt, but, the problem of T retention due to codeposition with redeposited C presents a formidable challenge that must be overcome.

An important goal is to minimise thermal quench frequency (disruption control) and reduce thermal quench energy deposition through dissipative methods.

Design Requirements for PFCs in a Next Step

The successful development of high-performance PFCs is central to the overall development of fusion energy and has posed progressively more difficult challenges as the power and pulse duration of fusion devices have increased.

Active cooling of PFCs is required

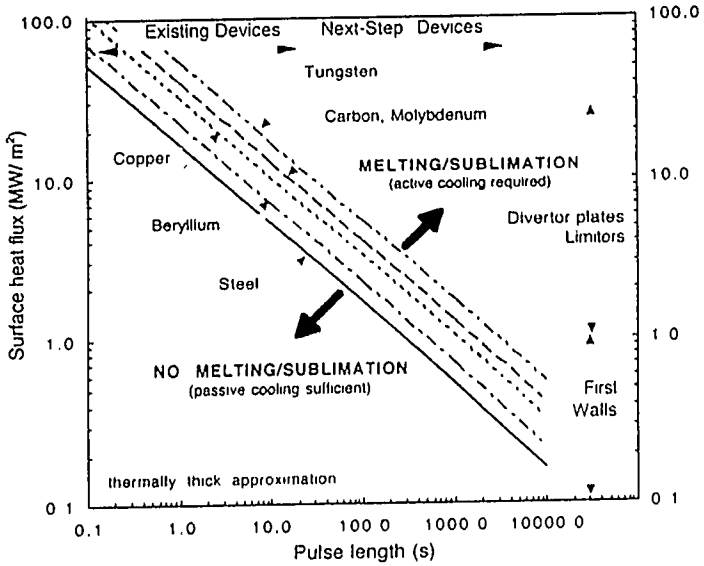

- Handle high cyclic heat loads;
- Acceptable erosion lifetimes;
- Withstand disruptions and ELMs;

Erosion lifetime of PFCs becomes an issue

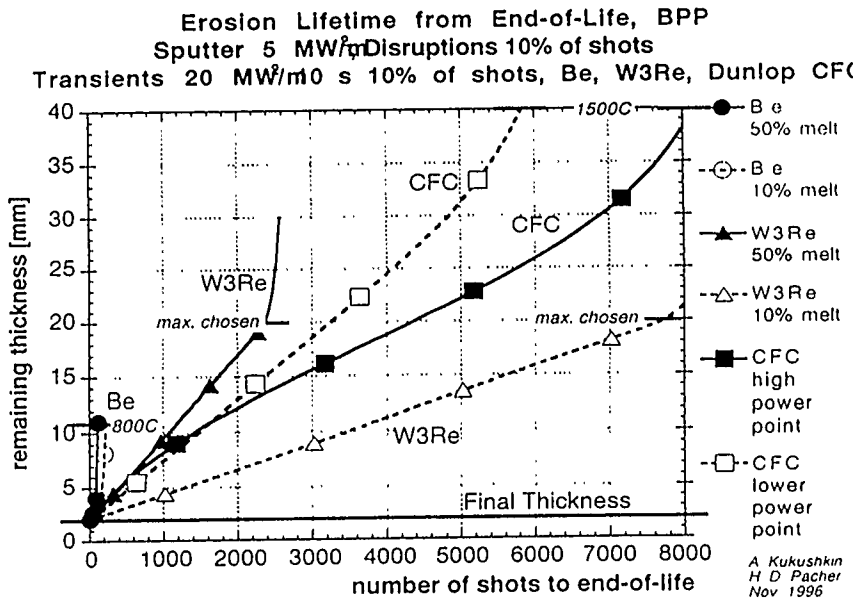

- Avoid tritium accumulation;
- Remotely maintainable;
- Survive neutron radiation.

Present Conception of the ITER Device

During the last year of the ITER EDA, it was decided that a redesign was necessary in order to retain the retain the original goals and objectives as much as possible but with a cost objective of about half that of the original EDA design.

Reduced-technical objectives (RTO) reduced-cost (RC) design variants of ITER are now being considered.

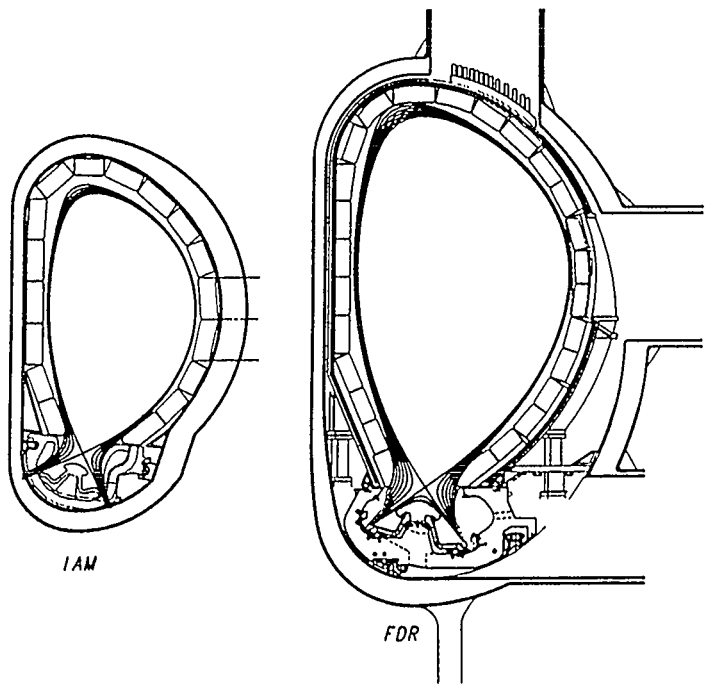

Parameters	ITER FDR	ITER RTO-RC
Major radius (m)	8.14	6.0-6.5
Plasma current (MA)	21	13-17
Q ($=P_{fusion}/P_{heating}$) inductive	Q => ∞	Q ≥10
Q ($=P_{fusion}/P_{heating}$) steady-state	≥ 5	≥5
Neutron wall flux (MW/m^2)	1.0	≥0.5
Neutron fluence ($MW{\cdot}a/m^2$)	1.0	≥0.3
Fusion Power (MW)	1,500	500-700
Inductive flat top(s)	1,000	300-500

Selection of the Plasma Facing Materials

Beryllium: First wall, limiter.

Advantages:

- good O_2 gettering ability; absence of chemical sputtering;
- low Z (low plasma contamination and radiation losses);
- low tritium inventory
- potential for in-situ PS repair.

Shortcomings:

- Its low melting points makes it inadequate for HHF applications

Tungsten: Divertor baffle, side-walls, liner

Advantages:

- low physical sputtering yield and high threshold energy provides the best erosion lifetime in areas where CX sputtering is the dominant erosion mechanisms;
- does not codeposit with H-isotopes.

Shortcomings:

- lack of operation experience;
- melt layer behaviour under disruptions; thermal distortion of surfaces.

Carbon: Divertor plate near strike points

Advantages:

- low radiation in plasma, excellent thermal properties and resistance to disruption impact.

Shortcomings:

- Due to T codeposition, should be restricted to small areas or avoided.

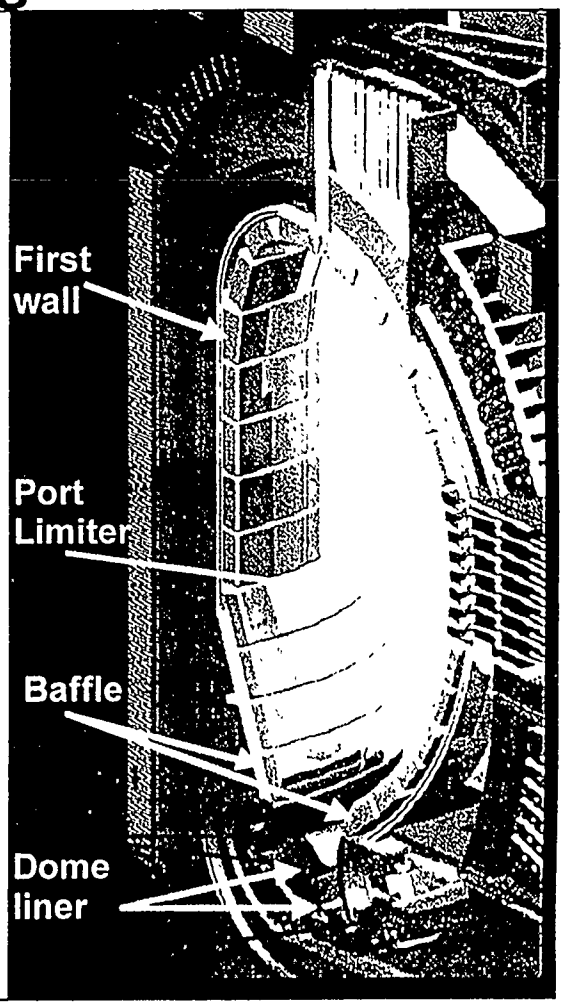

⇒ **Mixed-material effects are expected to play an important role in ITER.**

Rationale in ITER RTO/RC

- In ITER we are aggressively pursuing the development of all tungsten armoured targets capable of intercepting the SOL strike points.

- The reference design remains with CFCs in the region of the vertical target near the strike points. We believe that to assume anything else would be very imprudent, bearing in mind the uncertainties surrounding the effects of surface melting of the W during disruptions.

- If we were to build the machine today, we would opt for a CFC target that is 'forgiving' in terms of frequent major off-normal events, e.g., disruptions, ELMs.

- Perhaps with operating experience in today's tokamaks and in ITER during the H and D phases that show we can limit the number and the severity of disruptions we will decide to replace the CFC targets with those bearing W. This could even be before we switch to D-T operation avoiding problems of codeposition of T with eroded C.

- Maintaining the use of CFC has an impact on:

  1) Wall conditioning;
  2) Tritium control and removal of the codeposited layers.

Anticipated Effects Resulting from Mixing of Materials

Particle-induced erosion of multi-material first wall/divertor surfaces will be inevitable, leading to material mixing and cross-contamination of all surfaces.

First wall:

- oxidation of Be and deposition of some sputtered W and C transported from divertor;
  - **effect on gettering (saturation effects?); plasma contamination?; wall conditioning.**
  - **+ could diminish erosion.**

Divertor:

- Be eroded from the first wall will be deposited in the divertor:
  - **+ possible reduction of C chemical erosion (experimental data from PISCES);**
  - **contribute to T codeposition with redeposited carbon; deleterious effects on removal?**
- C eroded from the divertor surfaces receiving high ion flux will re-deposit and implant on nearby tungsten surfaces:
  - **formation of W carbides etc. will alter H-retention and recycling properties of W.**

Overview RTO/RC ITER PFC Design

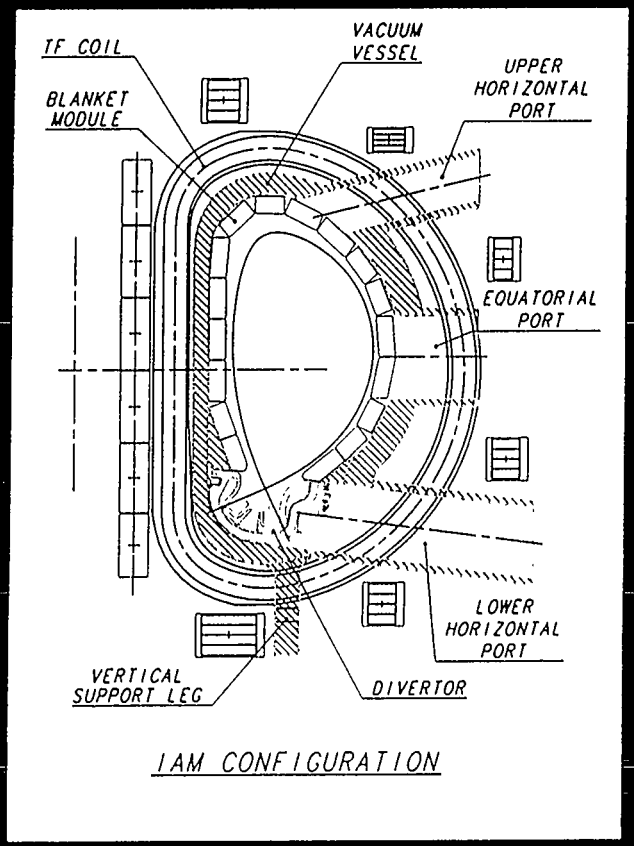

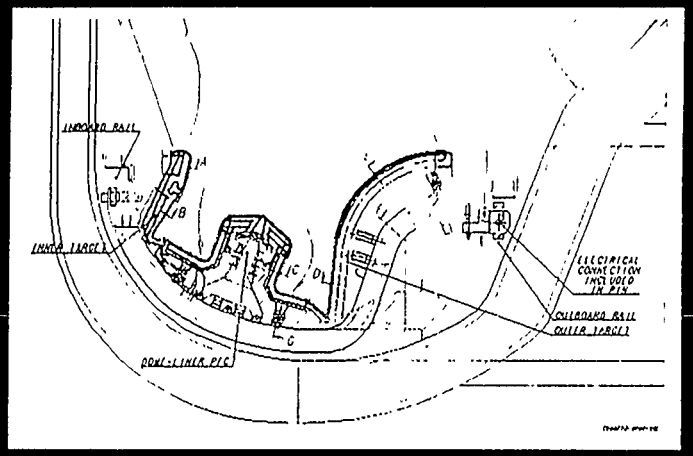

Divertor vertical target

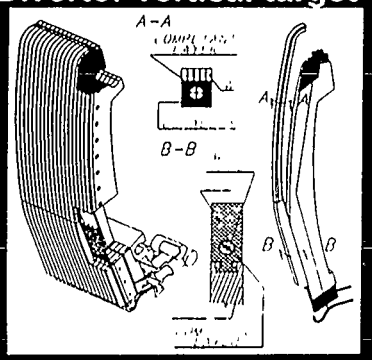

Divertor cassette liner

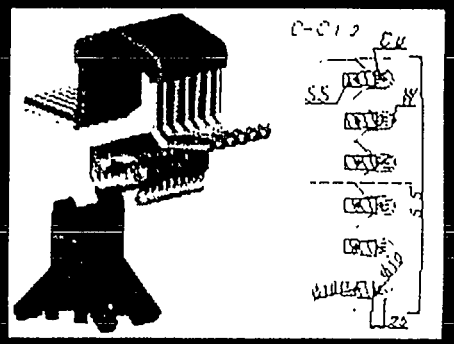

Heated deposition areas to minimise T-rerention

First Wall PFCs: Loads and Issues

Loads

First wall must handle

- radiative power from bremsstrahlung during burn; **Q=<0.5 MW/m^2, f=10^{19}-10^{20} D+T/m^2·s, E=10-1000 eV;**
- transiently radiation power during disruptions;
- transiently plasma contact during VDE's and REs (**);
- EM forces due to halo currents.

Start-up limiter must handle

- high thermal and particle loads during direct plasma contact at start and end of the discharge w. low plasma contamination and acceptable lifetime **Q≈8 MW/m^2, f=10^{21}-10^{22} D+T/m^2·s, E= 100-500 eV.**

Primary PSI Issues

- **Energetic CX neutrals erosion:**
  - ⇒ **plasma contamination;**
  - ⇒ **contribute to codeposition in the divertor.**
- **Implantation T inventory;**
- **Damage during VDEs, Ras.**

- **High heat loads at start and end of discharge due to misalignments.**
- **Ions erosion during start-up:**
  - ⇒ **plasma contamination;**
  - ⇒ **erosion lifetime.**

(**) Protection against VDE's and runaway electrons could also be achieved by introducing a series of poloidal limiters (made of actively cooled Be or CFC blocks).

Critical Issues and Results of R&D

- **Erosion of the wall due to charge exchange (CX) neutral fluxes act as a source of plasma impurities and deposited layers in the divertor.**

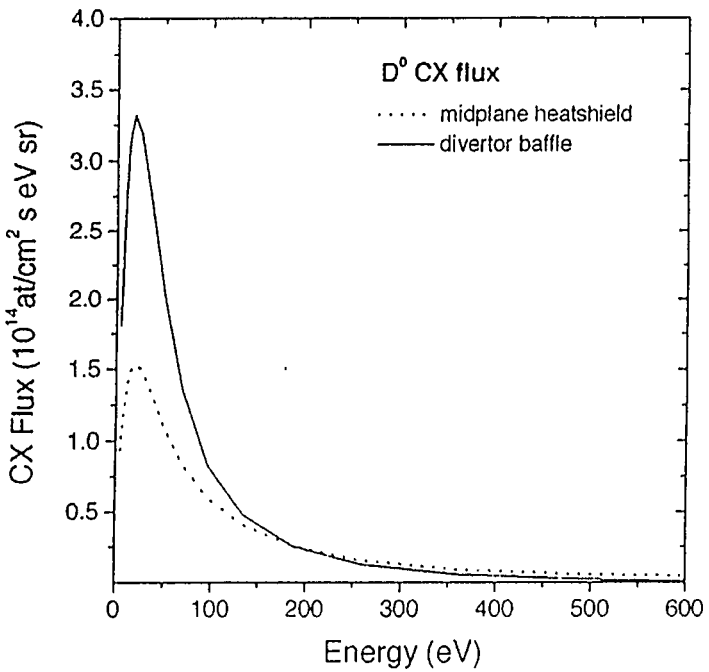

Energy distribution of the CX flux to the inner wall and the divertor baffle of ASDEX-U as calculated using the B2/EIRENE code

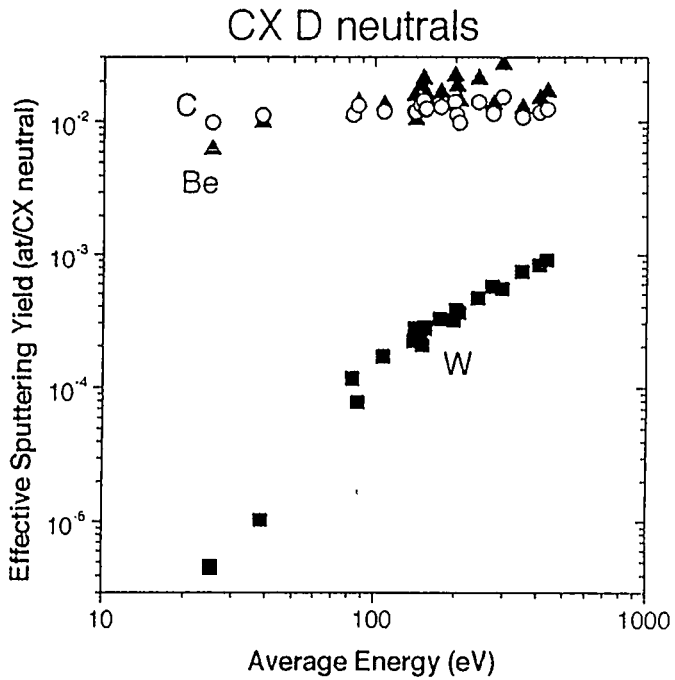

Dependence of the effective sputtering yield of Be, C, and W by D CX neutrals on the average energy of the neutrals.

Plasma Spray Repair of Eroded Beryllium

- **It has been demonstrated in laboratory using Be tiles originally eroded in ISX-B operation. The repaired surfaces adhere well during subsequent HHF testing.**

ISX-B Be limiter tiles used for plasma-spraying investigations.

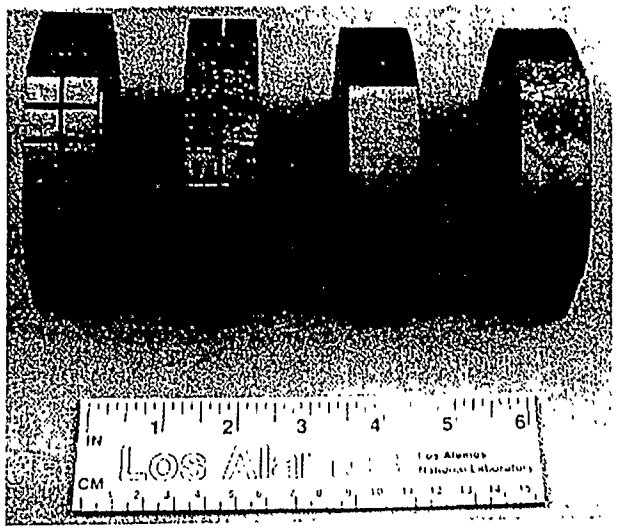

Coatings 1 to 1.5 mm thick with a porosity of 7-12%.

- Tests were performed on Be PS coatings applied to both a damaged and undamaged surface of an ISX-B Be limiter tile.
- The performance of the coating was influenced by the condition of the surface to be coated.
  - coating on an undamaged tile survived only **80 cycles** at **5 MW/m²** for **10 s pulse** lengths and **60 s** cool-downs before cracking was observed in the coating, with formation of hot spots on the surface.
  - coating on a badly melted tile survived **500 cycles** (same conditions) before cracking was observed and ~ **680 cycles** before the formation of hot spots.

The improved performance of the Be coating on the damaged ISX-B tile was attributed to the preferential grain boundary separation that occurred along the columnar grains present in the remelted layer on the surface of the damaged tile.

Tritium Retention in Be is Expected to be Less Serious than Previously Anticipated

- Recent implantation experiments at low E, high fluxes and high particle fluences in Be showed that after ~$10^{22}/m^2$, further implantation results in negligibly increased inventory.

Implantation

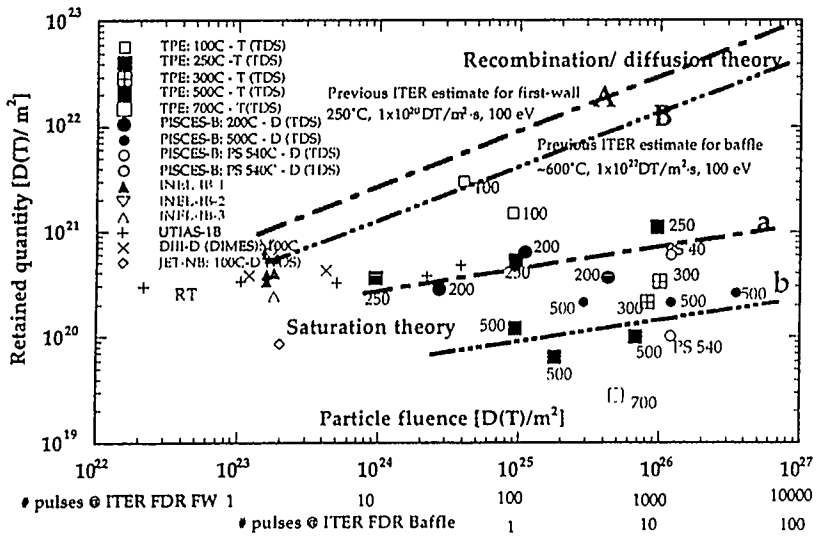

Codeposition

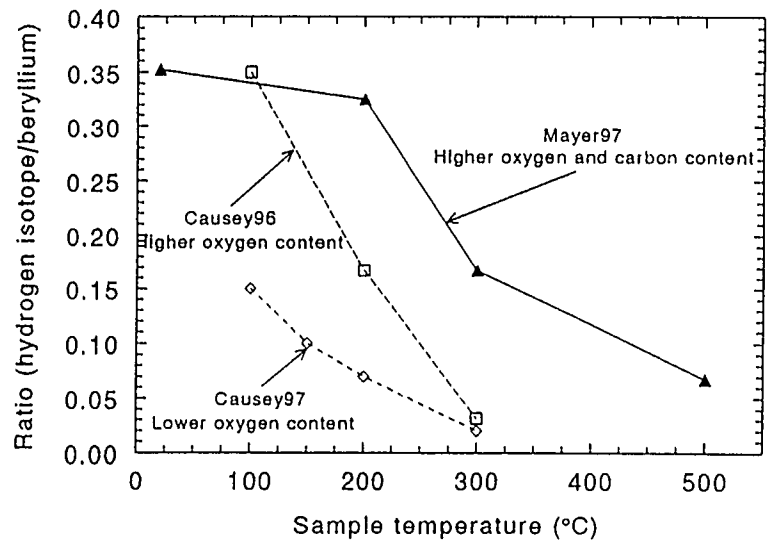

- **Details of mechanisms responsible for this effect are only partially understood, but the rapid onset of a surface-connected porosity that provides a rapid return path back to the plasma seem to be important at a high implantation flux.**

Divertor and Baffle PFCs: Loads and Issues

Loads

Divertor target (near strike-points) must handle:

- high particle and moderate heat fluxes during detached or PD plasma operation: **Q=<10 MW/m^2, f=10^{22}-10^{24}D+T/m^2·s, E≤5 eV;**
- transiently (few sec.) localised large thermal loads during attached operation: **Q>20 MW/m^2;**
- large thermal loads during disruptions, ELMs;
- EM forces due to eddy and halo currents;

Divertor liner (private region) must handle:

- radiative power in the divertor chamber.

Baffle must handle:

- radiative power from X-point; **Q=1-3 MW/m^2**
- interaction with energetic CX neutrals; **f=10^{20}-10^{22} D+T/m^2·s (E_{av}<100eV)** with acceptable lifetime and minimum plasma contamination;
- transiently plasma contact for VDE's,ELMs;
- EM loads due to eddy and halo currents.

Primary PSI Issues

- **Large scale erosion during normal and off-normal conditions:**

  ⇒ tritium codeposition;

  ⇒ erosion lifetime;

  ⇒ dust accumulation;

  ⇒ material mixing.

  ⇒ T codeposition and material mixing.

- **Energetic CX neutrals erosion:**

  ⇒ plasma contamination;

  ⇒ erosion lifetime.

- **Damage during ELMs, and other off-normal transients.**

The Use of High Z Metals as Divertor Materials

- Operation with relatively clean core plasmas has been demonstrated in Alcator C-Mod with an all-Mo wall and in ASDEX with W divertor plates.
- The proper selection and location of the PFCs, combined with modern plasma control capabilities, allow to take advantage of the low sputtering yields of these materials.

W transport in ASDEX-Upgrade

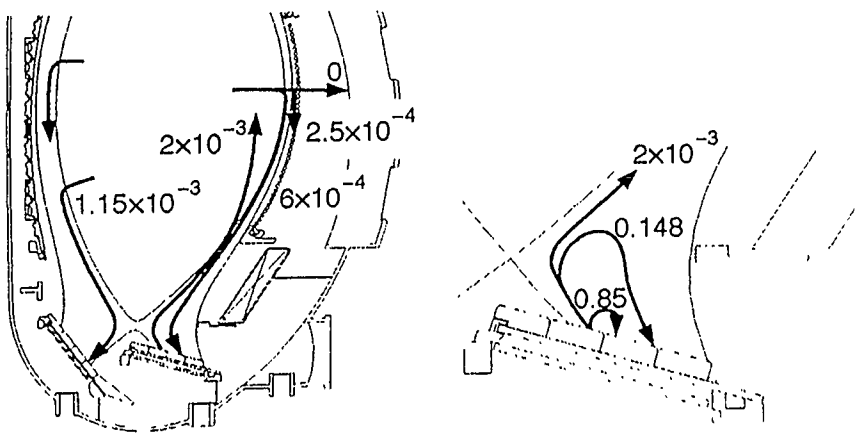

- W sputtered from the outer divertor plate has a high probability to be promptly redeposited **(~85%)**.
- **~12%** is redeposited w/o ever entering confined central plasma.
- In ASDEX-U, W atom concentrations in the central plasma reached levels > $2\text{-}10^{-5}$ only in a few cases.

B2/EIRENE code calculations

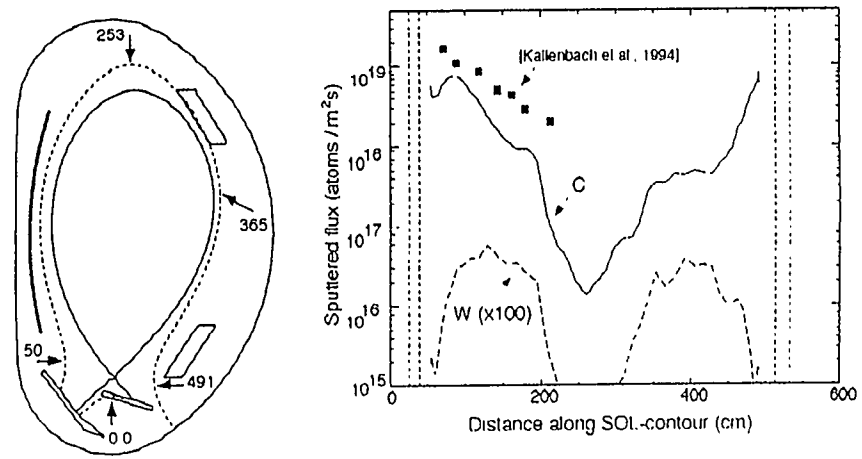

- Distribution of the sputtered atom flux from the ASDEX-U wall for a C and W due to CX sputtering.
- The C values can be compared to spectroscopically measured fluxes from the inner heat shield.

Power Handling of W-Clad Components

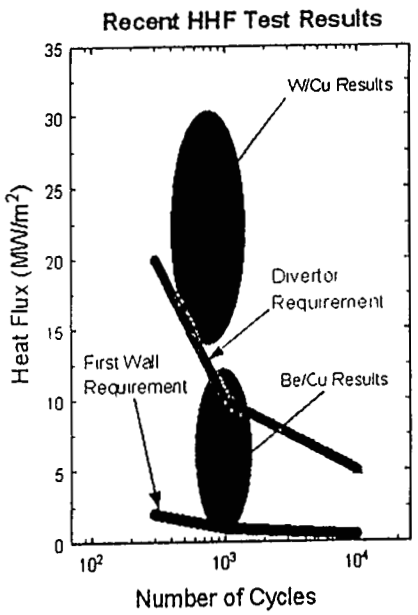

Best results
Beryllium:
4000 cycles at 12 MW/m^2 (5mm);

Tungsten:
>400 cycles at 20 MW/m^2 (10mm);
>1000 cycles at 15 MW/m^2 (10mm).

- Recent encouraging developments of actively cooled copper-backed tungsten components offer the promise of handling steady-state power loads of > 20 MW/m^2 without the tritium retention problem posed by C.

W armour design

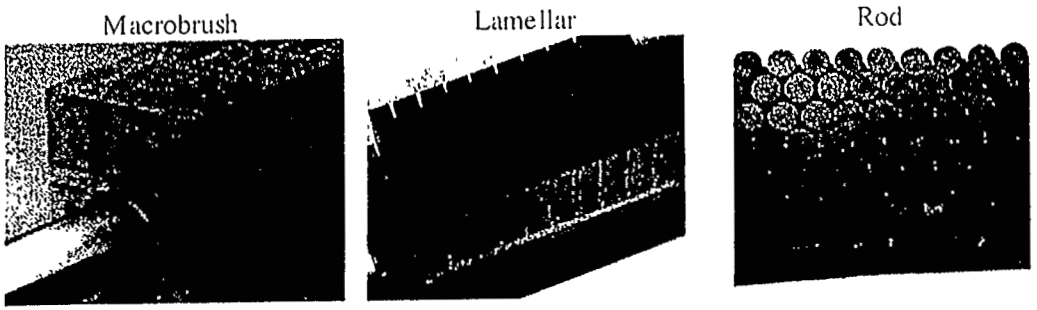

- However, the ability of such W materials to withstand the high heat flux during transients without suffering damaging melting is yet unclear and may require disruption mitigation like killer pellets, liquid jets or large gas puffs.

Carbon Erosion and Tritium Codeposition

They are identified to be a major issue in ITER. New findings are available.

- In C divertor tokamaks, codeposition occurs mainly in the divertor
- This occurs, even when the divertor material is not C, as with the JET Mk-I Be divertor or ASDEX-Upgrade W divertor, as other C PFCs provide a source of C for codeposition
- Detailed dedicated experiments in plasma simulators and in tokamaks have substantiated the prediction that chemical erosion will be reduced at high particle fluxes > $10^{22}/m^2s$.
- Part. detached divertor conditions led to the minimisation of gross erosion in DIII-D.

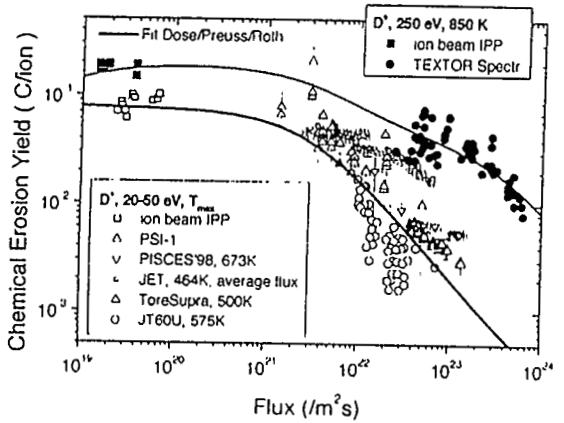

Marked divertor asymmetry

- Inner leg: net-deposition;
- Outer leg: net-erosion

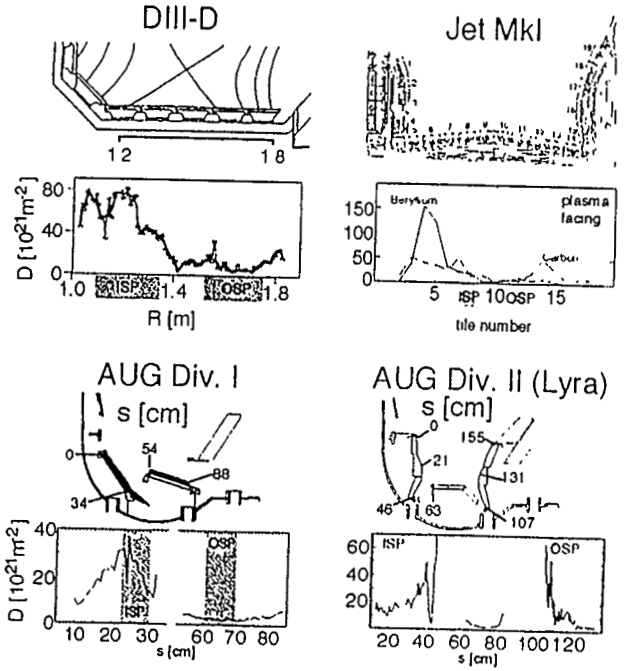

- Extrapolation to ITER is uncertain
- Need to identify root causes.

Tritium Retention due to Codeposition with Redeposited C Presents a Formidable Challenge that must be Overcome.

- **D and T are retained in large quantities with C PFCs mainly due to codeposition with eroded C, e.g. 40-50% in large limiter machines (TFTR, JET pre-1992) and ~15% in JET post-1992.**
  - Intense codeposition in regions which are shaded from ion flux but near C surfaces receiving high ion flux.
  - JET has shown that deposition on cold surfaces shadowed from the plasma can produce deposits which retained much of the T trapped after DTE1.
  - Since ions cannot reach these shaded surfaces, this C deposition must be due to neutral C atoms or molecules from dissociation of hydrocarbons.

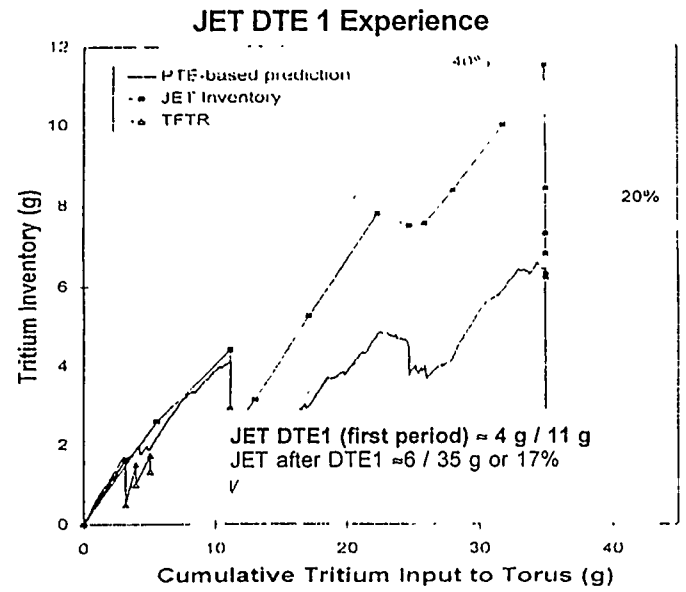

When exposed to air, codeposits completely decompose releasing T at a temperature ≥250°C
- **represent a radiological hazard under accident conditions;**
- **need to minimise the in-vessel inventory (in ITER 1 kg-T);**

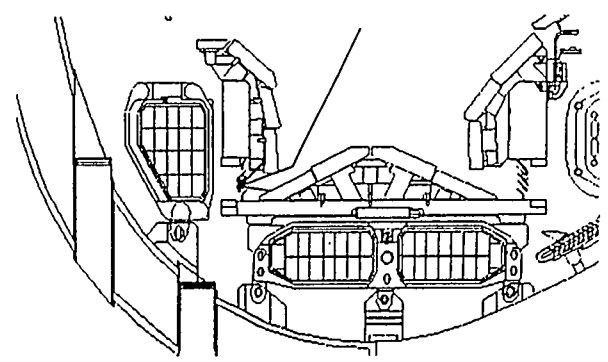

If C is uded in some place there is a need for frequent cleanups methods yet to be established.

Modelling of Erosion/Codeposition Effects

Modelling calculations for ITER by J. Brooks (ANL) show that lifetime of the C-plate could be short and T retention will be dominated by codeposition in C.

Divertor design (year)	Strike-point electron temp.,eV	Divertor surface material	Peak net erosion rate, nm/s	T codep. rate gT/1000s	Comments
1. "High-Recycling" (1989)	60	carbon	7	3	high heat loads of concern for this regime
"	40	tungsten	< 0.03	~0	
2. "Gas-Bag" (1995)	7	beryllium	190	nc	highly speculative regime
"	70	tungsten	0.3	nc	
3. "Radiative" (1997)	8	carbon	6	1	
"	8	beryllium	10	3	recent data implies < T codep.
"	8	tungsten	< 0.003	~0	
4. "Semi-detached" (1998)	< 3	carbon	15	14	Chem. Sputt. highly important

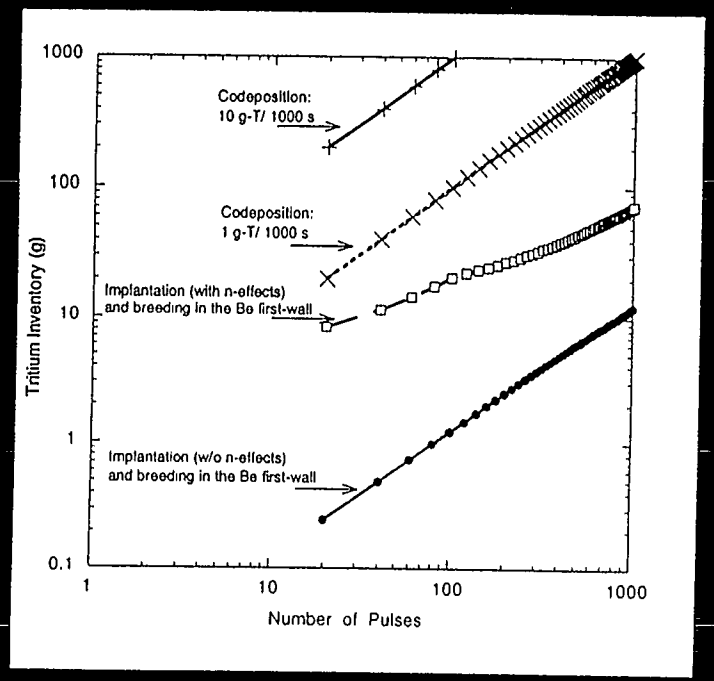

Contribution of the Be first-wall is calculated to be 0.1-0.6 g

DEGAS+ => calculate CX fluxes, energy, used as input in WBC+MC code=>calculate sputt., imp. SOL transport wall-sputtered Be atoms show that Be will flow primarily in the divertor 50% to hot region (temp. ≥ 500°C) does not lead to codeposition; 50% to cold region => it leads to codeposition.

One Concern in ITER is the Formation of T-codeposits on Cooler Surfaces of the Divertor not in Direct Line-of-Sight of the Plasma.

- **The low temperature, high density divertor conditions may lead, in the case of C deposition, to a polymer-like CH film.**
  - At elevated temperatures (≥500K) the deposited layer may decompose, forming heavy hydrocarbons and radicals, which could be transported and deposited onto cooler areas where the deposited layer is stable, such as the inner louvres of the JET divertor or the ASDEX-U divertor bottom.

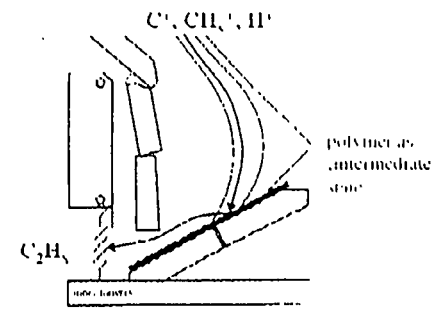

- **IN RTO/RC ITER, we are investigating the use of a W 'hot liner' (temp. range: 500- 1000°C) which promises to reduce the amount of tritium trapped by allowing the C and H-isotopes to be pumped as hydrocarbon gases.**
  - This is achieved by mechanically mounting radiatively cooled W sheets on water cooled Cu-SS structures.
  - The W sheets are formed in such a way that they do not allow a direct view between plasma and the pump duct.
- **Results of R&D are promising but not conclusive. However, CH_3 radicals which have a very low sticking coefficient may be uniformly deposited on cooler areas of the vessel wall and deep into the pump duct.**

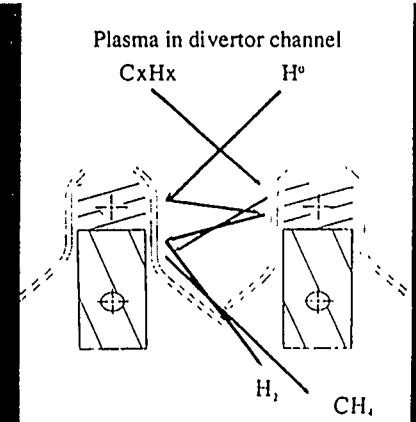

ITER Design of the divertor liner

There is Currently no Good way to Remove Tritium from Thick Codeposited C layers.

Tokamak operation experience with T shows that present conditioning methods are marginal in controlling inventory within allowable limits and would not be adequate for ITER.

- Develop and test in-situ efficient cleaning techniques much more efficient than those applied in today's tokamaks.
- Methods avoiding breaking vacuum to introduce equipment are preferred to minimise shutdown times.
- A constraint in tritium removal techniques in ITER is the presence of the toroidal field.

Techniques involving exposure to O_2 (e.g., thermo-oxidative erosion > 570K, or O plasma discharges) have been found to be most effective in labs to remove the films.

JET codeposited Film

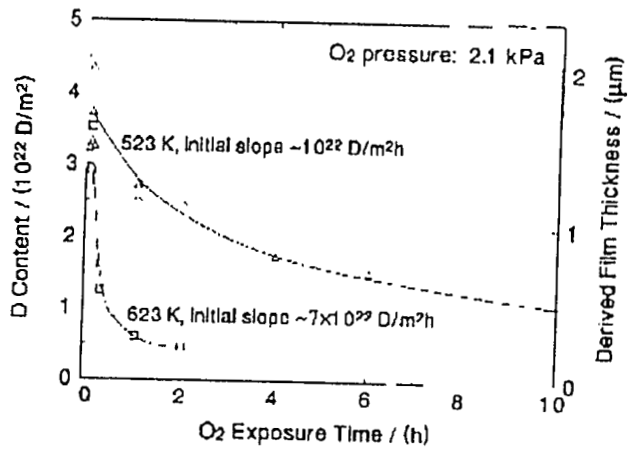

J.W. Davis, and A.A. Haasz, PSI 98

- For C, erosion rates strongly depend on the microstructure of codeposited layers;
- Ventilation (which entails oxidation) was also effective in removing T from TFTR and JET.

Drawbacks of using oxygen, especially at elevated temperatures, are collateral effects on other reactor vessel components, and recovery time for normal plasma operation.

Dust Represents a Potential Safety Hazard for ITER

- It can cause steam-induced H explosions, and it can increase the spread of radioactivity during an accident involving a sudden vent, if mobilised.
- Understanding the amount of dust expected in fusion devices and its physical and chemical characteristics is needed to verify assumptions currently used in safety analyses.
- Studies performed in various tokamaks where dust have been collected after scheduled vents. Large uncertainties on the total amount of dust and sources.

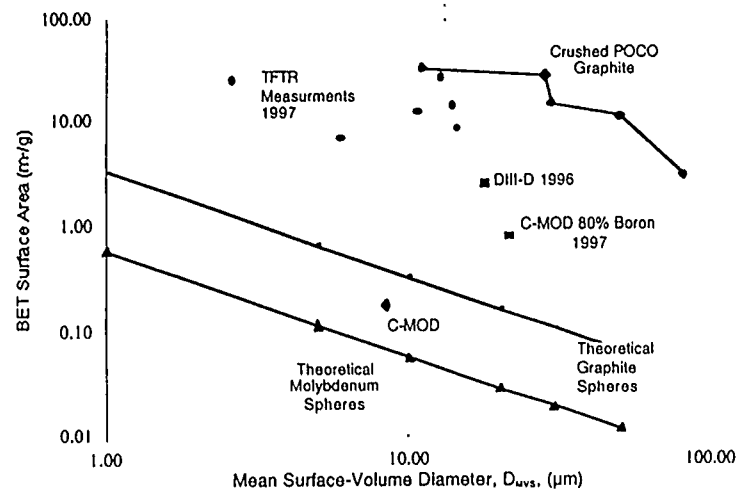

courtesy K. McCarthy et al. (INEEL)

- **Main source of dust in ITER is expected to come from breaking of redeposited films produced during sputtering and disruptions. Effects of other mechanisms (e.g., arcing) are still open to debate and need further R&D.**

Preliminary dust production estimates and limits (kg) in ITER; (G. Federici/ R. Little - SOFE 97)

	Sputtering (kg)	Disruptions (kg)	Possible Reaction	Limits Hot areas (kg)	Limits Cold areas (kg)
First Wall Be	90	10 - 45	$Be + H_2O \rightarrow BeO + H_2$	10	100
Divertor CFC	30-150	≤10	$C + H_2O \rightarrow CO + H_2$	20	200
Divertor W	0	>25	$W + 3H_2O \rightarrow WO_3 + H_2$	10	100

Flakes Have Been Found in Various Tokamaks

JET louvres during the MkIIA campaign

- Deposits 40 μm thick were spalling from the louvres beyond the inner corner of the divertor;
- D/C ratio of the flakes was ~0.7;
- Following DTE1 with the same JET configuration T was also codeposited in these films.

Heavy deposition at sides of a TEXTOR limiter

- Films up to 170 μm thick have been observed;
- Film breaks up into particles of ~5 μm size;
- D/C ratio of films is 10^{-3} as limiters get hot during discharges
- Similar deposits seen on limiters in JET pre-86.

Also in ASDEX-Upgrade

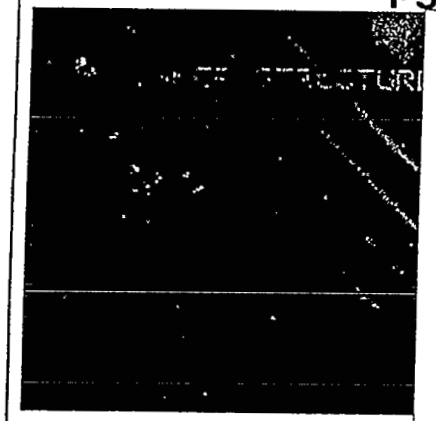

Flaking on TFTR isotropic graphite wall tiles

- Deposits started spalling after exposure to air for ~2 years after last pulse;
- D/C ratio probably in range 0.1-0.2;
- TFTR operates with wall at room temperature, though some plasma -heating of surfaces - situation thus intermediate between TEXTOR and JET limiters (hot wall) and JET louvres (cold and no plasma contact);
- Less flaking from CFC tiles.

Further R&D Needs

- **We know a lot more now than few years ago. Dedicated experiments (in labs and tokamaks) together with theory and simulation have provided useful information for the design of the Next Step.**
- **However, we still need to conduct a vigorous R&D to improve understanding in:**

A) Modelling of tokamak PSI data:

- enhance the modelling of PSIs and develop a quantitative understanding of underlying mechanisms;

B) Wall diagnostics:

- Dedicated in-situ, time-dependent diagnostics necessary for understanding PMIs (e.g., film thickness diagnostics), and a means of measuring erosion/deposition and retention under different operational conditions;
- "*Archaeological*" studies of limited utility to challenge the models;
- Instrumentation/access similar to that for the DiMES probe in DIII-D are very useful.

C) "Composite" wall materials experiments:

- Conduct tests in tokamaks with the proper wall materials to provide a realistic test-bed which would closely mirror whichever situation is proposed for a Next Step.
  - Such experiments would help answer questions such as the magnitude of erosion and tritium codeposition, dust formation in the vessel, the ease of tritium removal from mixed-materials, as well as operational aspects (e.g. of using Be on the first-wall).

D) Development and testing of tritium codeposits removal techniques.

- Develop and test in tokamaks methods for tritium removal from plasma-facing surfaces with minimum impact on machine availability.

E) Development and Optimisation of Critical First-Wall Components:

- Consider design solutions that could **minimise the retention of tritium** (e.g., by ensuring that regions of probable deposition are kept "hot" during operation) or **enhance the formation of films in specific areas** (e.g., by means of "cold catchers" which could be periodically heated to recover the tritium).

- Explore new design solutions without using C. The primary alternative material for high heat flux regions is tungsten. However, efforts to reduce transients and mitigate disruptions in existing tokamaks must continue with high priority.

Disruption Mitigation and Control Methods are needed to Enable Safe High Operation

- Recent tests with high Z pellets (C-MOD, DIII-D) and high pressure He gas (DIII-D) have demonstrated ability to "soften" thermal quench and vessel forces during VDE disruptions.
  - The pellet causes sufficient impurity radiation to dissipate the plasma's thermal energy. This increased dissipation reduce the HF to the divertor (H in the figure).
- Develop low-Z mitigation techniques (i.e. massive gas-puff, liquid jet injector, etc.).
- Integrate detection and mitigation systems into the control system of an existing tokamak to test and demonstrate reliability.

Comparison of VDE discharges mitigated with an Ar pellet (courtesy: Taylor, P.L., et al. GA)

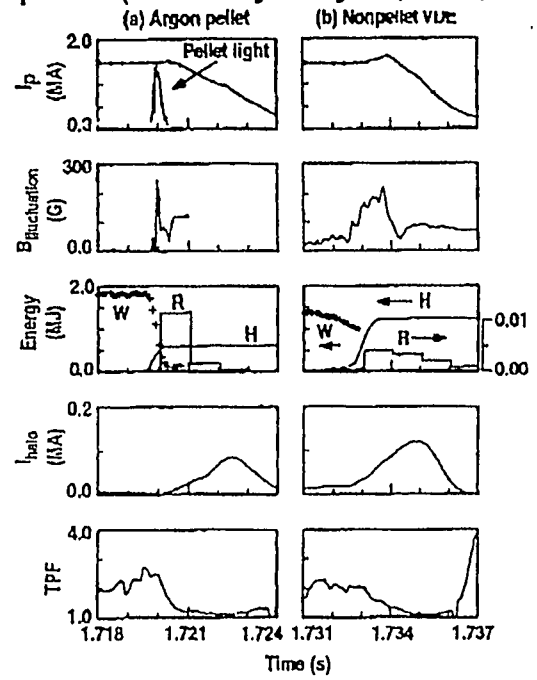

W: stored thermal energy
H: integrated heat to the divertor floor
R: radiated energy

Summary

- **The control of plasma wall interactions is central to the goal of building a Next Step.**
  - The **long pulse duration** and **high plasma energy content** will be the most significant changes from present machines. Erosion of PFCs will be orders of magnitude higher from today's tokamaks.
  - The experience of today's tokamaks, and the developments of sophisticated models, have provided, thanks to the ITER CDA and EDA activities a bridge to designing a Next Step device and predicting and optimising its performance.
- **Erosion products (codeposited tritium, mixed-materials and dust) will constrain the operation of a Next Step: erosion lifetime of components/ tritium economy and supply/ safety.**
  - Technical innovation and R&D are urgently required to mitigate the effects.
  - Avoiding the use of C in the divertor is feasible but solutions are needed for disruptions mitigation).
- **Information provided by future dedicated operation experience in existing tokamaks and laboratories will be useful to control and to mitigate plasma wall interaction processes and to optimise the design.**

We must ensure that there is a productive synergism/communication between PFM and plasma edge communities, tokamak and non-tokamak programs.

Plasma Facing Components – 1

Development of HHF Components for the RTO / RC ITER: Recents results and further R&D Plans

S. Chiocchio, R. Tivey, A. Antipenkov, V. Barabash, G. Federici, C. Ibbott, G. Janeschitz, E. Martin

ITER Joint Central Team, Joint Work Site, D-85748 Garching, Germany

Outline

- Brief overview on RTO/RC ITER:
  Requirements & Design Drivers

- Divertor layout and High Heat Flux Components Design

- Status of HHF testing:
  Thermohydraulic performance and Fatigue lifetime

- The issues for the next step and plans for the R&D

☞ Summary

Requirements & Design Drivers

- The divertor geometry needs to ensure that the majority of the neutral recycling fluxes are beneath the dome
  - Allows to achieve partial detachment at reasonable SOL density which in turn yields acceptable target power loads and sufficient He exhaust
- The divertor targets need to be configured such that, during transients when the full SOL power reaches it, the peak heat flux is comparable to the 1998 ITER design value, i.e. 20 $MW.m^{-2}$
- The gas conductance through the divertor structure (including toroidal support rails) has to be sufficient to allow a throughput of 200 Pa $m^3 \cdot s^{-1}$ at a pressure ~ 4 Pa with a pumping speed of 160 $m^3\ s^{-1}$
- The total nuclear heating of each toroidal field coil must be limited and in particular the total heat into the first turn of the conductor should be < 750 W,
  - 10% of which (75 W) should be the maximum nuclear heating to the first turn caused by radiation leaking through the divertor;
- The goal is to reach 50% of the 1998 ITER Divertor cost
- To reduce the cost of the heat transfer system there is a desire to limit the number of coolant loops and thus to limit the water throughput in the divertor to 1000 kg s^{-1}

Divertor Layout (4)

- ⇨ The new Divertor Cassette assembly consists of less parts than in the ITER 1998 design
  - ⇨ Simplifications and cost savings

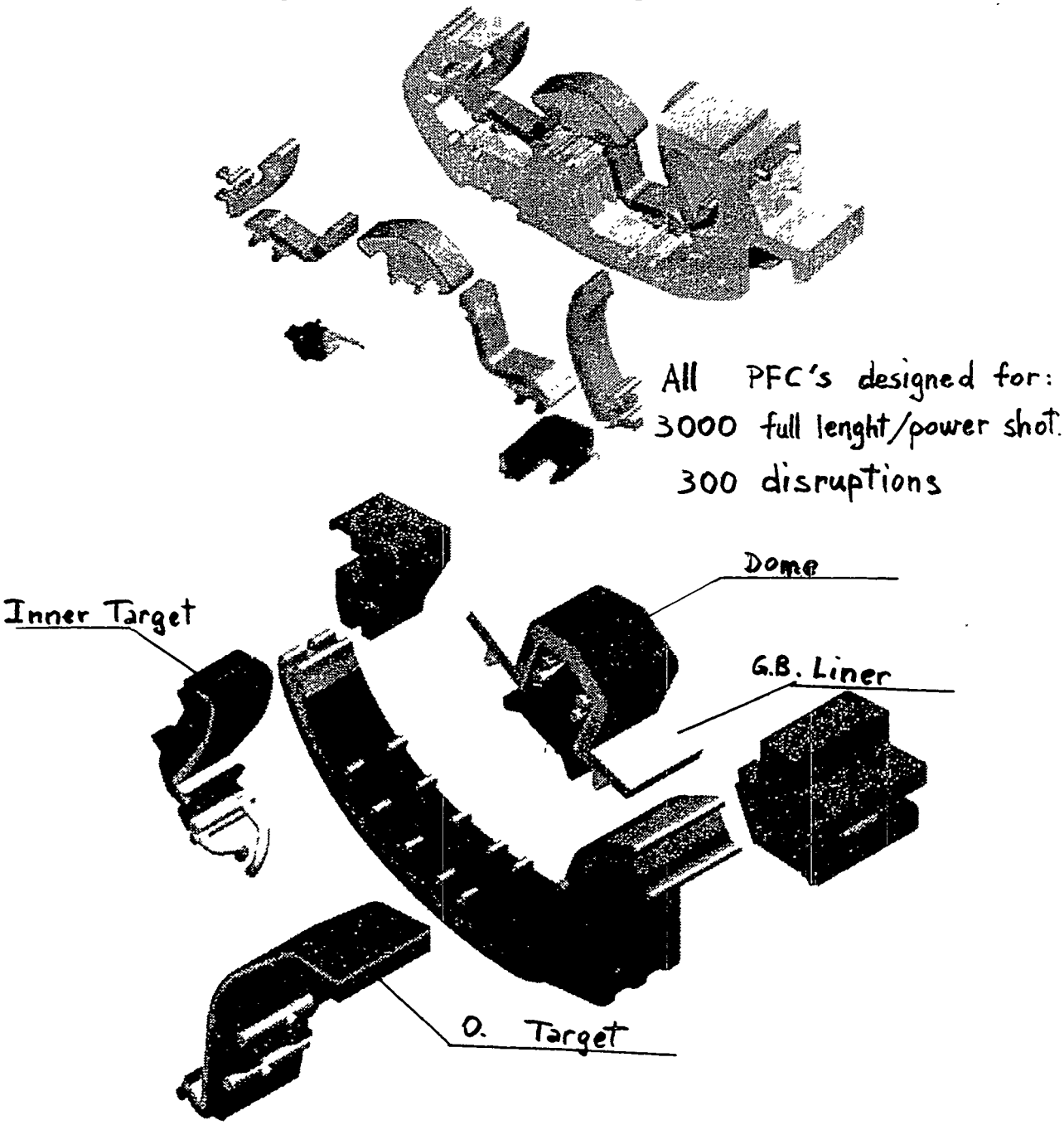

Vertical Target and Dump Target Design . I

⇨ Outer Vertical Target in ITER 1998

- ⇨ Vertical and dump targets were separated and the 10 mm diameter pipes at the bottom end provided the flexibility for thermal expansion of the strike zone area

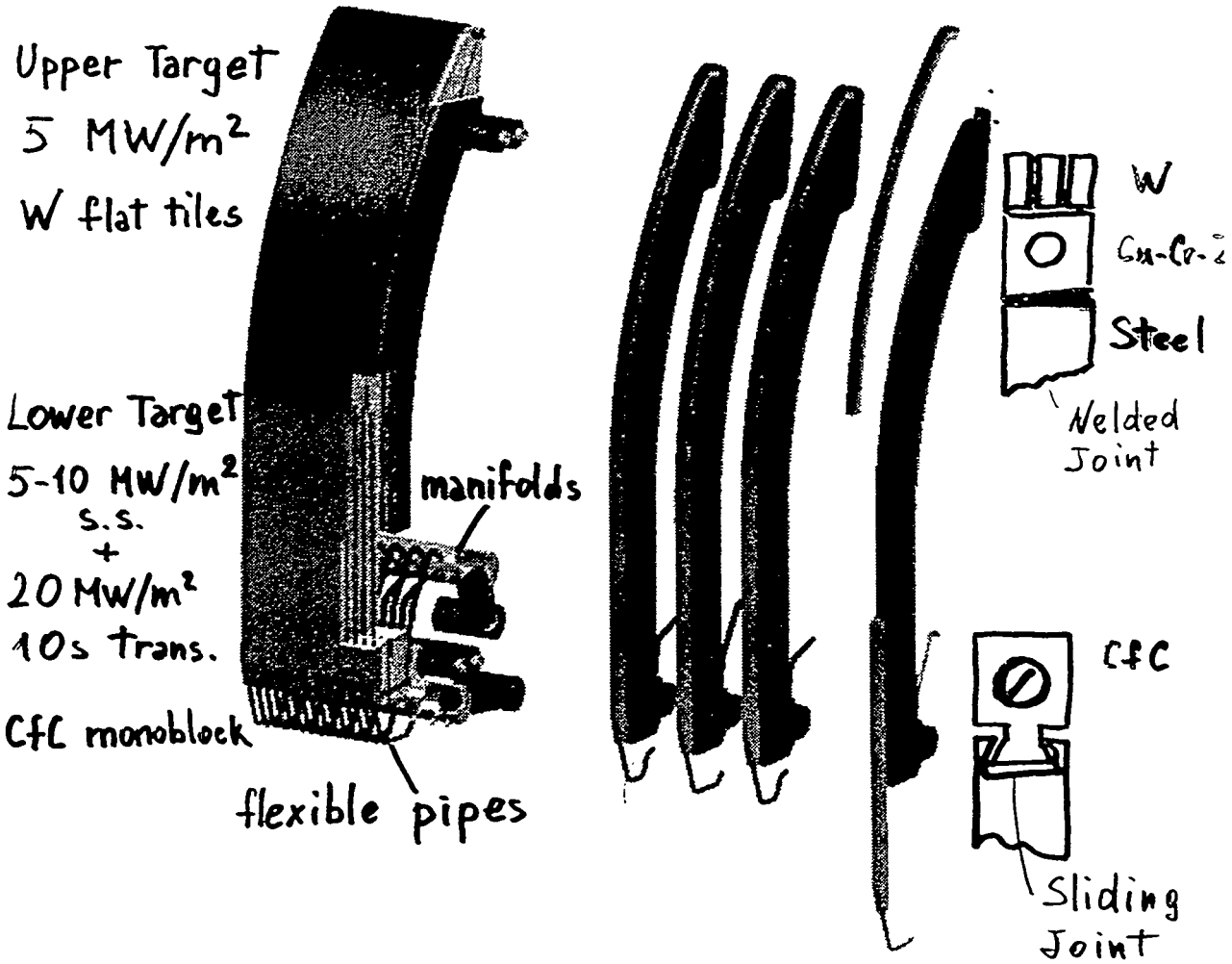

- ⇨ In RC-ITER the magnetic flux expansion is larger at the target ➔ the angle between target and separatrix increases ➔ the angle between VT and dump target increases
  - ⇨ Keeping the above design would mean to interlace the expansion pipes of the VT and the dump target

Vertical Target and Dump Target Design (3)

- ⇨ Second possibility : annular flow, i.e. a hairpin return
  - ➔ expansion at the bottom of the VT
  - ➔ reduction of the number of sub-components
- ⇨ This approach needs confirmation by R&D (mainly performed in JA) before it can become reference

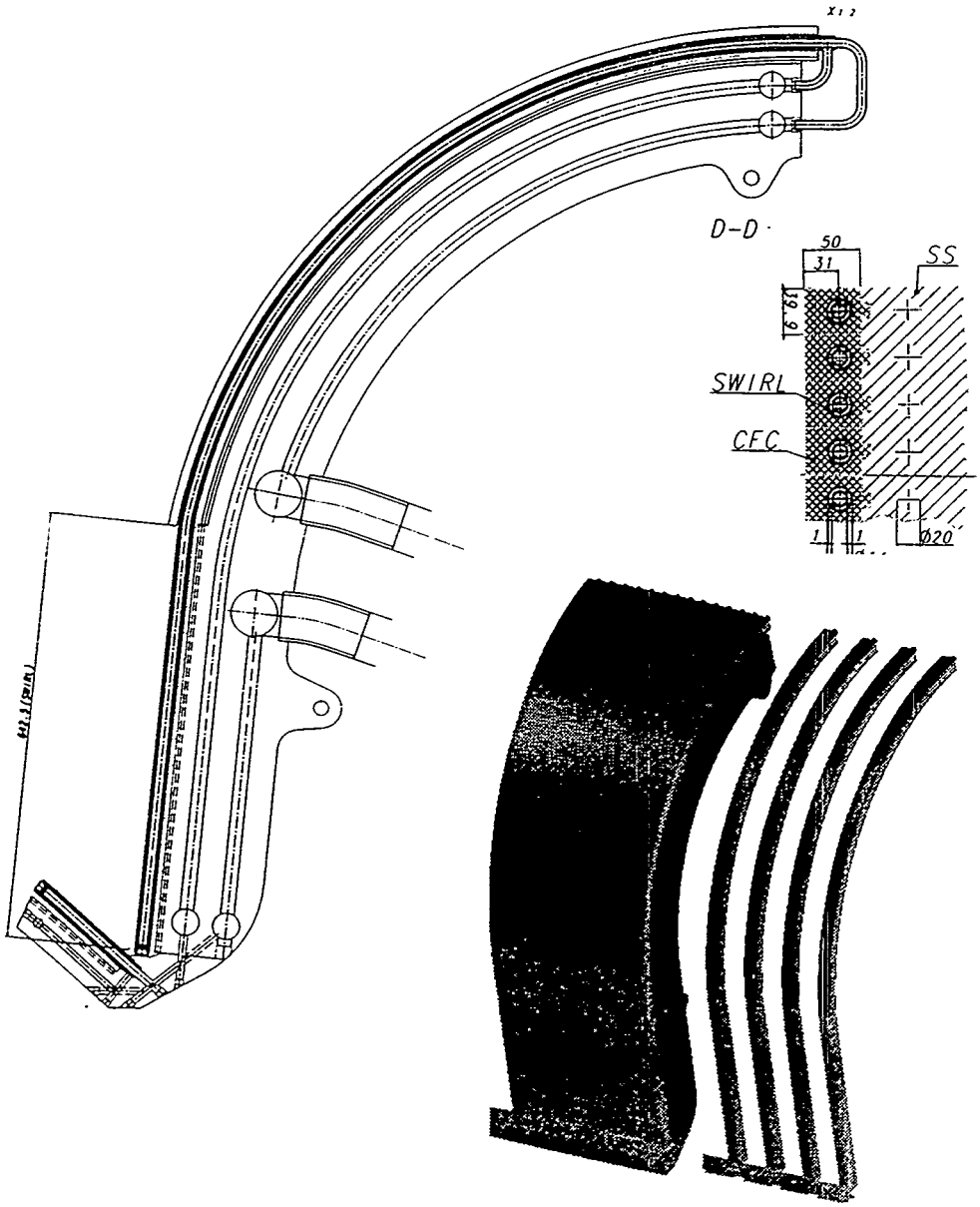

Liner and Dome Design

- Dome and Liner have a heatflux capability of 5 MWm^{-2} and up to 1 MWm^{-2}, respectively

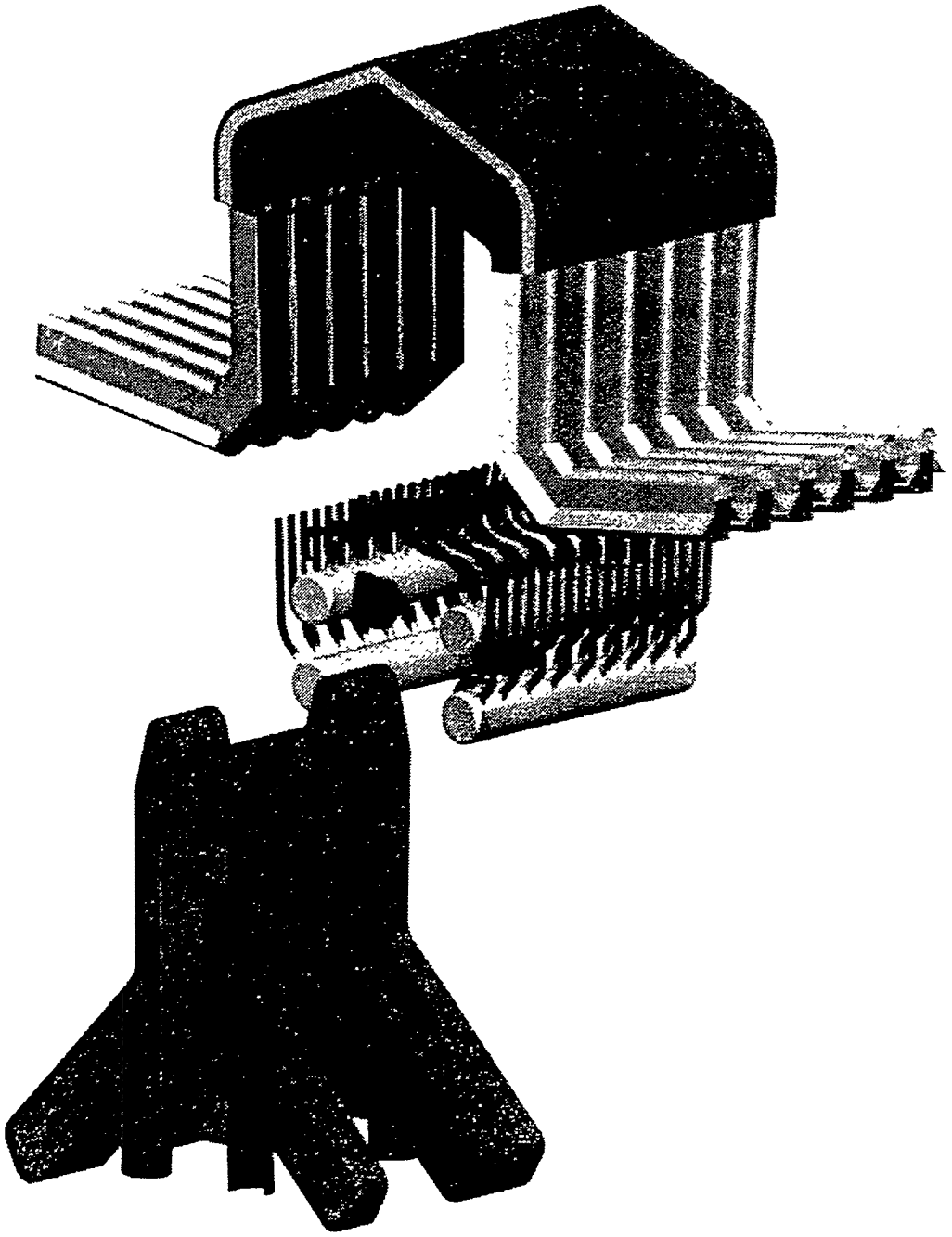

Liner and Dome Design (1)

- ⇨ The W clad liner is designed to reduce the amount of T co-deposition (temperature between 500°C and 1000°C)
- ⇨ This is achieved by mechanically mounting radiatively cooled W sheets on water cooled Cu-SS structures
  - ⇨ The W sheets are formed in such a way that they do not allow a direct view between plasma and the pump duct

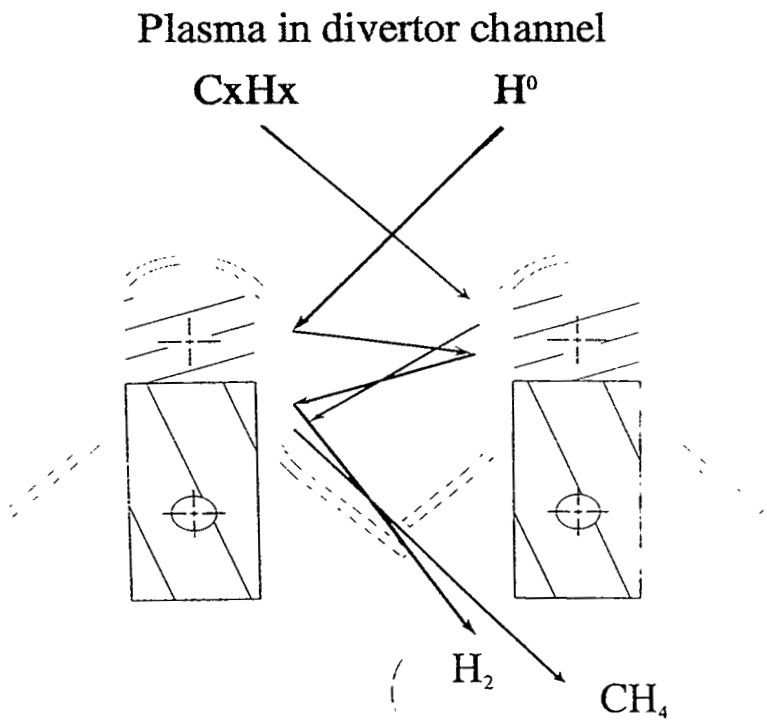

- ⇨ However, the co-deposition may lead to a polymer-like hydrogenated C film, which is unstable at temperatures ≥ 500°K and decomposes to heavy hydrocarbons and radicals.
- ⇨ In particular CH_3 radicals have a very low sticking coefficient and may therefore be uniformly deposited on cool areas of the vessel wall and deep into the pump duct (cleaning ?)
- ⇨ **If this is an important process CFC might have to be eliminated from the ITER machine !!**

Results of HHF testing

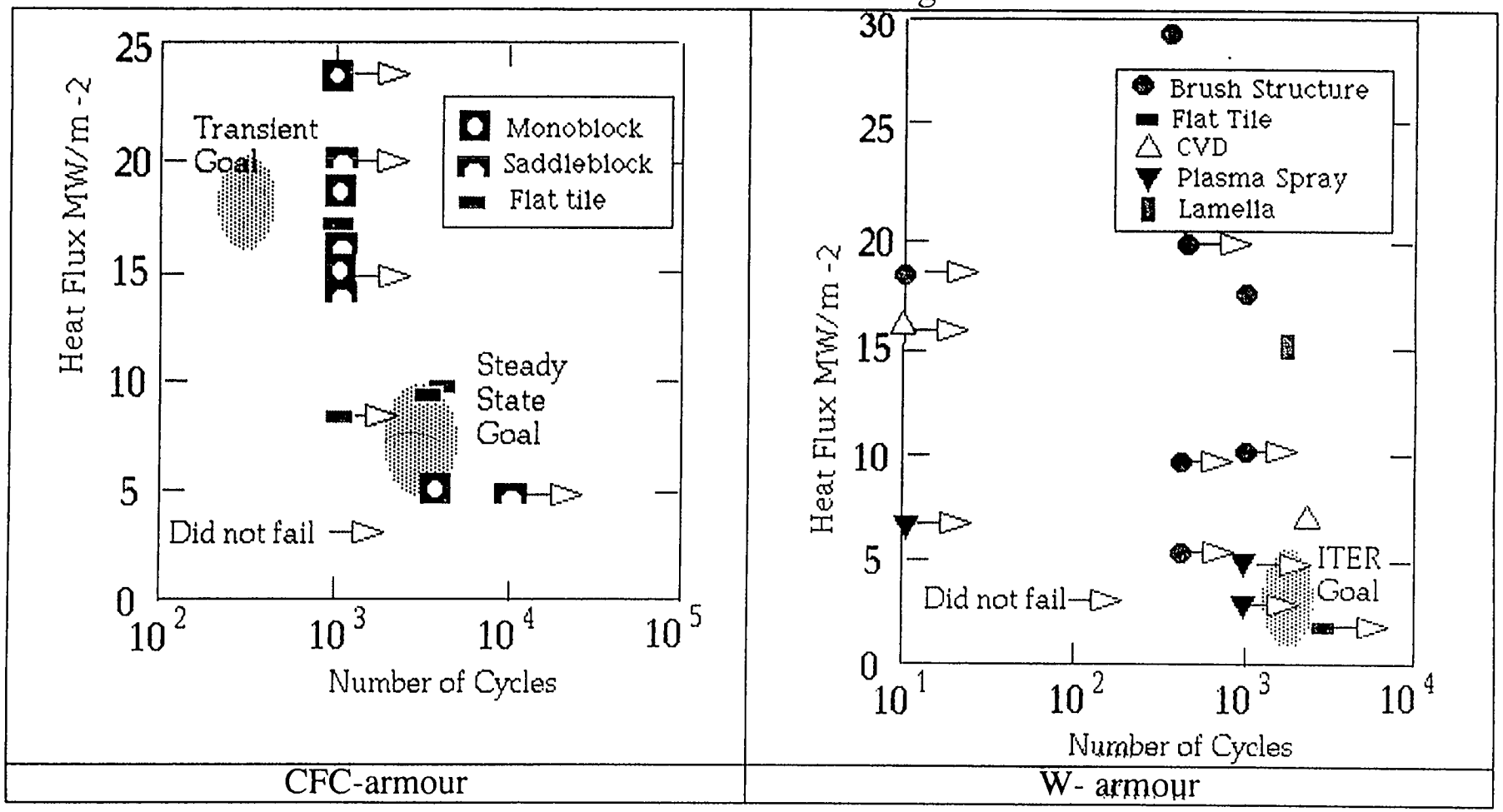

Results of HHF testing of the CFC/Cu mock ups
(Silver-free joining technologies)

Armour/ Geometry, mm	Technology/ parameters	Cu Alloy	Cool. T, °C	Heat Flux, MW/m^2	Cycles	Observation	HT
Dunlop C 1, Monoblock, 40 x 22 mm, Thickn.: 6/12 mm#	AMC +Ti brazing (880 °C, 10 min); (	CuCrZr	20	15 24	1000 1000	No damage No damage	EU
Dunlop C II (3 tiles) SEP NS31 (2 tiles) Flat tile:24 x 30 x10	AMC + EB welding 2 mm Cu interlayer	CuCrZr	40	5 9 18	100 1000 1000	No damage No damage No damage	EU
SEP NS31 monoblock 23x19x18, 27 tiles	AMC (0.5 mm pure Cu) Ti brazing ~880 °C, 10 min	DS Cu	140	20 19	800 200	No fatigue damage	EU
3D-CFC Saddle	Cu-Mn braze on OFHC Cu clad	DS-Cu	RT	20	1000	3 tiles no damage, 1 tile eroded	JA
2D CFC monobock 30x33x60	Cu-Ti braze	DS-Cu	RT	5 20	3000 1000	No damage No damage, CFCs erosion ~ 1 cm	JA

#Thickness of 6 mm used for heat flux test above 15 MW/m^2

Results of HHF testing of the W/Cu mock-ups
(Silver-free joining technologies)

Armour/ Geometry, mm	Technology/ parameters	Cu Alloy	Cool. T, °C	Heat Flux, MW/m^2	Cycles	Observation	HT
W-La2O3 macrobrush 4.5x4.5x10	Casting of OFHC Cu (2 mm) + e-beam welding	DS Cu	40	9 16	1000 1000	No damage 1 tooth fell off after 927 cycles, creep deformation	EU
W-La2O3 macrobrush 4.5x4.5x10	Casting of OFHC Cu (2 mm) + e-beam welding	CuCrZr	40	9 16	1000 1000	No damage 1 tooth fell off after test, some creep deformation	EU
W lamella type ~ 20x[illegible]x8	Casting of OFHC Cu + CuInSnNi fast brazing (800°C, <1 min)	CuCrZr	RT	15	2150	Some creep deformation	RF
W 10x10x10	Casting of OFHC Cu + CuInSnNi fast brazing (800°C, <1 min)	CuCrZr	RT	20	400	No damage	RF
W rod ∅ =1.6 mm 10 mm	Plasma sprayed copper back, HIPed to CuCrZr at 450°C	CuCrZr	RT	5 10 18	500 500 10	No damage No damage No damage	US
W rod ∅ =3.2 mm 10 mm	Vacuum hot pressed into OFHC/CuCrZr at 450°C.	CuCrZr	RT	5 10 18	500 500 10	No damage No damage No damage	US

Issues for HHFC in the next step (1)

Among the achievements of the R&D programme carried-out in the frame of the ITER EDA one has to list:

- the demonstration that actively cooled component can withstand heat flux in the order of 20 MW/m2 with reasonable margin to CHF;
- the selection of armour and heat sink materials able to provide a sufficient lifetime
- the development of a few methods for the armour-heat sink joining which can withstand the largest heat flux in the divertor;
- the development of inspection techniques for the control of the joints

However further improvements are necessary to achieve the objectives of RTO/RC ITER of cost effective and reliable design.

- the fabrication methods must be simplified to become compatible with a quasi-series production of the HHF for the FW and divertor;
- the reliability of the final product must be improved;
- the lifetime of the component must be extended;
- the irradiated properties of the materials shall be considered
- the cost must decrease

Issues for HHFC in the next step (2)

Cost considerations

Based purely on scaling from industrial cost it is estimated that IAM will achieve a ~ 40% cost reduction with respect to the 1998 ITER divertor design.

Additional savings come through simplifications of the design and the manufacturing process.

The PFCs accounted for 70% of the total cost, and the cassette bodies, support shoes, diagnostic blocks and assembly of the cassettes (excluding RH and installation costs) accounted for the remaining 30%.

The PFCs are built by armoured slices and the number of slices is a strong driver for their cost.

- The manufacture of fewer, but larger PFCs due to less toroidal segmentation : ~ 2% saving of the FDR costs.
- ☞ The use of single armour vertical targets : 15 - 20% saving of target cost (2.5 % saving of the divertor cost).
- ☞ Radiative tungsten tiles on the liner: a 10% cost saving in each liner is possbile (5% saving of the cost of divertor)

Issues for HHFC in the next step (3)

Cost considerations

- alternatives of joining tungsten armour to the Cu heat sink:
  coarser pin or tile castellation as proposed (RF HT)
  hot pressing of tiles (US HT)
  Improved W joining methods by the EU and JA HTs.

- CfC monoblock based on a 16 mm bore tube (JA HT). Basing all the PFCs on this pitch would lead to using 25% fewer toroidal slices, which in turn would save 5 - 7% on the cost.

- Manifold simplifications beneath the V and fewer slices using co-axial flow with a hair-pin return tape (annular flow). CHF tests performed by the EU (~ 30% higher pressure drop than swirl tape) .

Issues for HHFC in the next step (4

Target with a single geometry

Ideally, a full CFC or full W target would simplify the construction and reduce the cost, but:

CFC	large erosion in the upper part of the target
W	concerns on melting and plasma contamination

Monoblock geometry :

CFC	large monoblock on straight tube
W	thin monoblock : reduces the thermal stress and can be used on curved tube.

Flat tile geometry :

CFC	large flat tiles
W	brush, lamellae or rods.

Issues for HHFC in the next step - 5 -

Monoblock:

tiles do not detach
"low" temperature a the interface
"low" thermal stress at the interface

However:
Joining step produce larger stress than flat tile;

Inspection is difficult in presence of swirl promoter;

Small gaps between tube and tile required for brazing;

To be developed for curved surface;

Defects in the join can lead to large heat peaking to the coolant ➔ burn-out of the tube before detachment.

Flat tile geometry:

Simple to manufacture (even for curved surface)
has "low" residual stress
is "easy" to inspect

However:
Depending on the channel geometry the temperature at the interface is higher than with thin tube

Joining defects result in tile detachment

R&D objectives

Flat tiles

1) Analysis of cascade effects

2) Development of channel geometry to reduce interface temperature (hypervapotron, circular channels)

3) tile and heat sink design to reduce edge singularities

4) test of lamella and brush geometry

5) manifolding of the pipes

Liner radiative tiles

1) Construction methods

2) Control of surface temperature

R&D objectives

Monoblocks

- low temperature joining to reduce residual stress
- suitable thermal cycles for Cu-Cr-Zr
- evaluation of maximum allowable defect (detachment and tube burn-out)
- inspection methods
- W monoblocks
- larger width of the monoblock (to reduce cost)
- Monoblock with air-pin water return
- twist tape fixing inside the tube and effects of gaps onto CHF

US-Japan Workshop on High Heat Flux Components
and Plasma Surface Interactions for Next Fusion Devices
Santa Fe, NM, US, 1-4 November 1999

Overview of development of high heat flux components in JAERI

M. Akiba, K. Ezato,K. Sato, S. Suzuki, M. Taniguchi

Presented by M. Akiba
JAERI

Our R&D program consists of ITER R&Ds, Demo oriented R&Ds, and application.

- ITER
  - R&Ds to construct "ITER" in Japan.
  - Demo-relevancy becomes much more important.
- Base Program
  - The base program consists of
    - —Demo oriented R&Ds
    - —Application R&Ds
  - Issues of Demo reactors are
    - —decrease cost
    - —increase safety & reliability••••in particular reduction of radioactive waste is important.
  - Application R&Ds: R&Ds on 14 MeV neutron facility (IFMIF)

Issues of Demo Reactor would be•••

- Joining technology have almost been developed for C/Cs and tungsten.
- What material should be used for cooling tubes of high heat flux components?

Material	R-activity	T-conductivity	Strength	Score	Remarks	Pr.#
RAFS*	4	3	4	11	available	1
					new design criteria	
Cu	1**~2	5	3~4***	10~11	available	2
SS	3	2	4	9	available	4
A-RAFS	4	3	5	12	developing	3
SiC/SiC	5	3	4	12	developing	3
					He cooling	
V	5	3	4	12	developing	3
					Lq.metal cooling	
W	4	4	4	12	developing	3

* Reduced Activation Ferritic Steel, such as F82H

** Zr93 has long half-life time, ~ 1 Myears.

*** DSCu

Topics

- Results of the large-scale divertor mock-ups for ITER
- Components for integration tests of ITER divertor cassette
- Results of high heat flux tests on reduced activation ferritic steel (Demo reactor oriented R&Ds)

A small divertor mock-up made of reduced activation ferritic steel

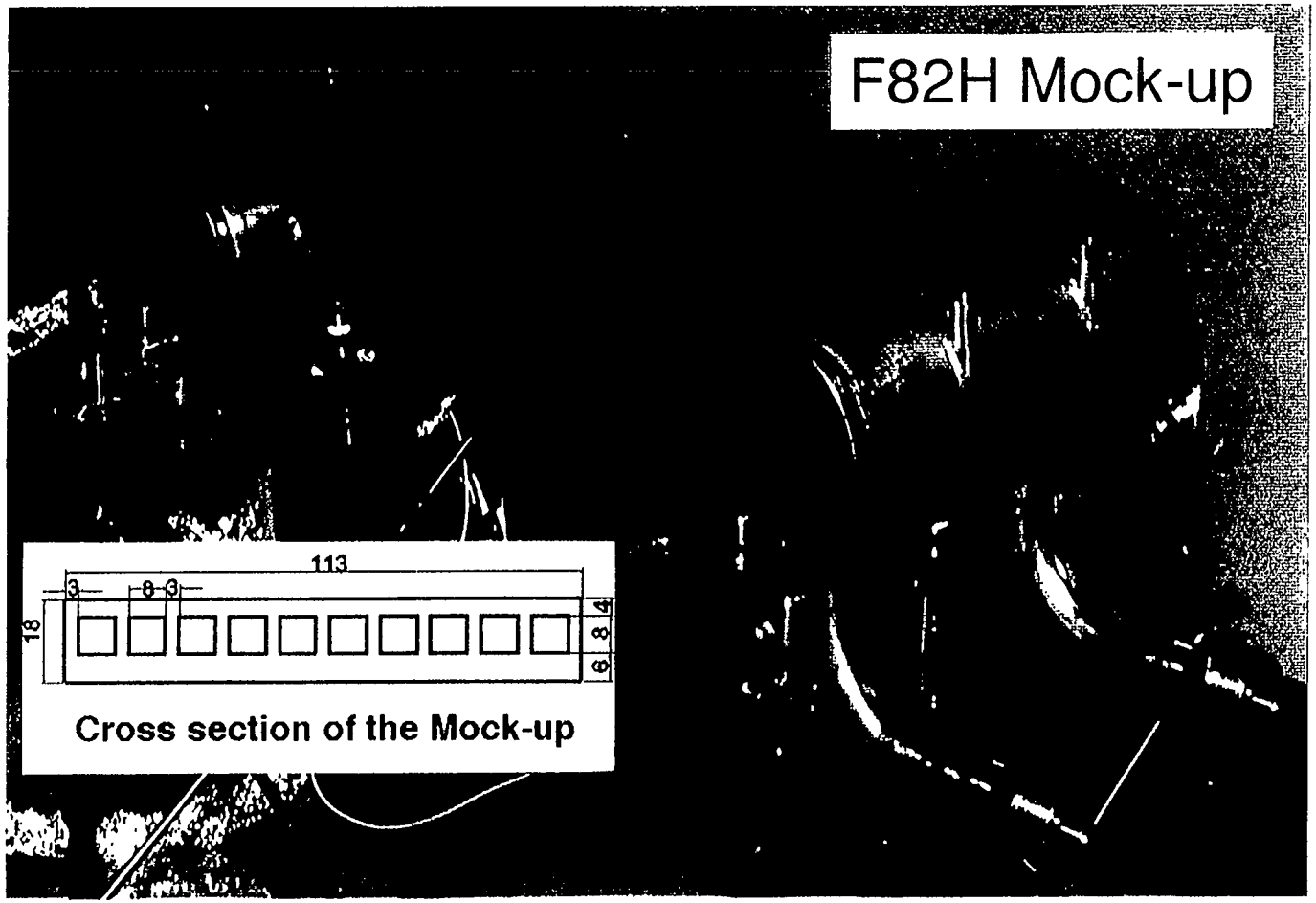

The mock-up has withstood 5 MW/m^2 for 10,000 cycles without failure.

- The mock-up was tested at a heat flux of 5 MW/m^2 with the electron beam test facility (JEBIS).
- Cooling conditions are; 10 m/s, 2 MPa.

Surface temperature evolutoin of the mock-up

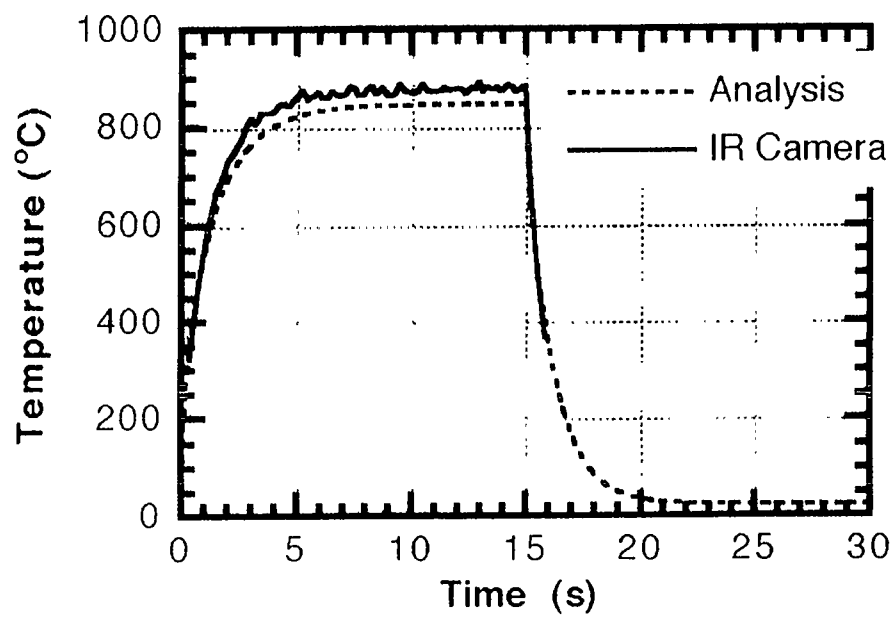

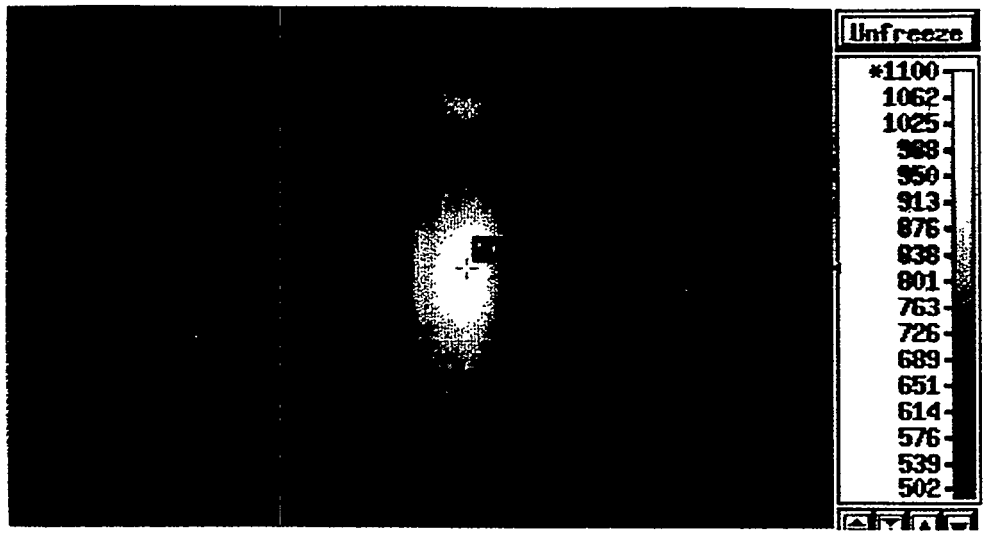

IR image of FW mock-up

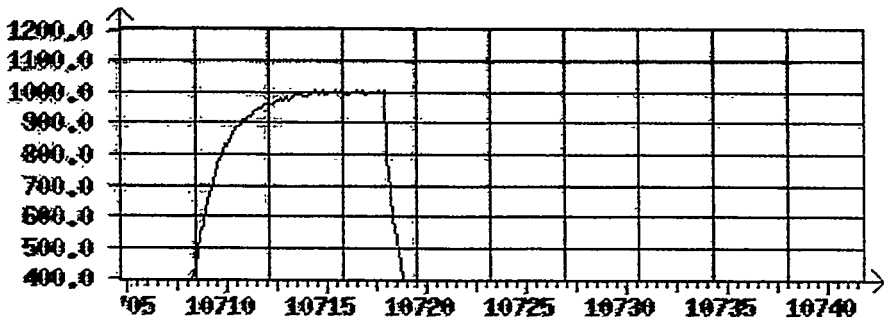

Time evolution of surface temperature at "SP01"

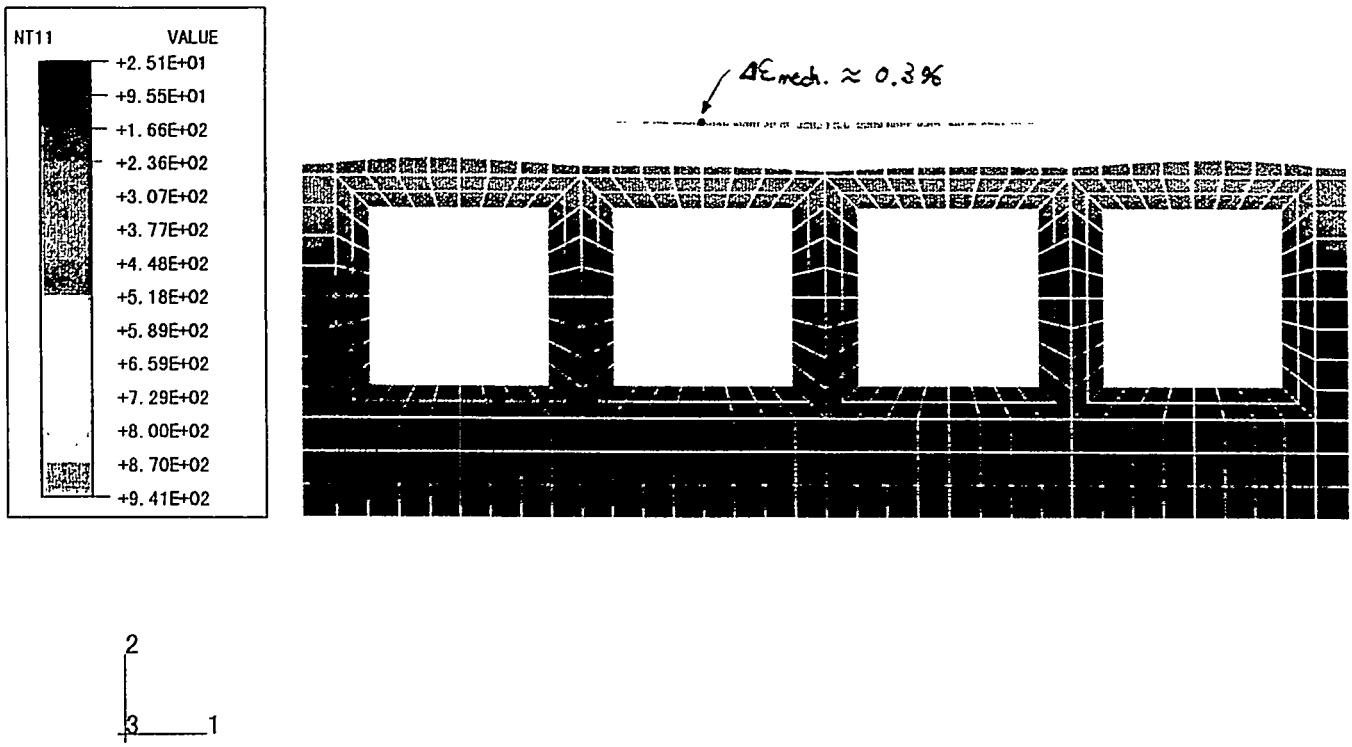

Isothermal contour of the mock-up at 10 s

F82H can be applicable even for divertor components with regular replacement.

- After 10,000 cycles, cracks were observed on the surface. It is caused by high temperature and stresses at the surface.
- For demo reactor application, the divertor components made of F82H will be replaced regularly.

Surface of the mock-up after 10,000 cycles

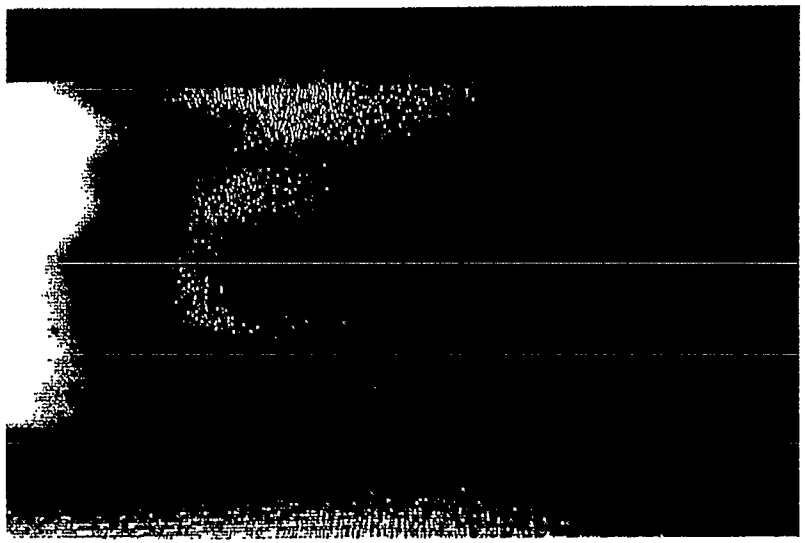

High Heat Flux Tests of W Rod Armored Mockups

R. E. Nygren and D. L. Youchison, Sandia National Laboratories
D. Dreimeyer, G. Wille, Kevin Slattery, Boeing co.
S. O'Dell, Plasma Processes. Inc.

- W-rod armored mockups showed excellent performance in thermal response tests at up to 30 MW/m^2 and in thermal cycling tests of 500 cycles (10s on, 10s off) at ~25MW/m^2.
- Melting of rod tips and a subsequent "self repair" of a degraded thermal bond were seen.
- Issues for further development in both testing and manufacturing of the mockups were identified.
- Evaluation of the surface heat flux was found to be somewhat problematic.

There has been wide spread interest in W armored PFCs and several approaches taken.

- In the US, we developed W-rod armor for ITER and are now developing other applications (e.g., FIRE in the US)
- In Russia, also for ITER, mockups with square W tiles have been manufactured. These were tested at Sandia.
- In Japan, JAERI is exploring W-rod armor. NIFS and universities (e.g., Kyushu U. and Ibaraki U.) are studying W coatings on graphite and CFC tiles.
- W-coated graphite and CFC limiters have been exposed in TEXTOR.

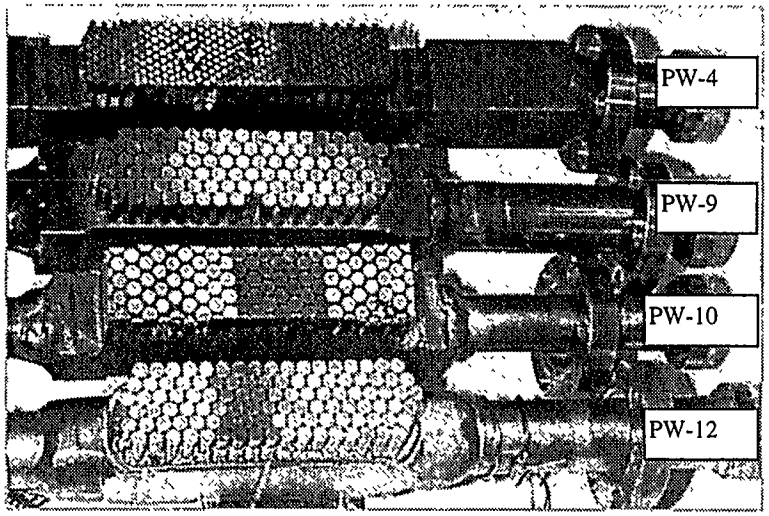

Mockup Name	W rod Mat'l	dia. (mm)	Embedding Method	Heat Sink Mat'l
PW-4	pure W	1.58	HIPping/ h.c.	CuNiBe
PW-9	W-2%La	3.16	HIPping/ h.c.	CuCrZr
PW-8&10	W-2%La	3.16	plasma spray	CuCrZr
PW-11&12	W-2%La	3.16	HIPping/ h.c.	CuCrZr

PW-10 reached ~30MW/m^2 in thermal response tests and successfully withstood 500 cycles at ~25 MW/m^2.

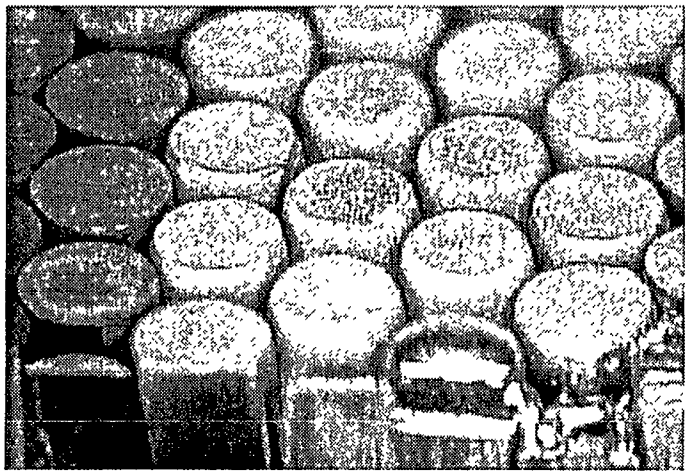

In thermal cycling, regions A and B were alternately heated for 10s.

- In thermal cycling, two regions (A and B) were alternately heated for 10s.
- Rod tips in heated zone A (photo) are lighter in color.
- Severe erosion is evident (rounded edges, slightly cupped surface).
- The temperature may have reached ~3600°C, but generally was 2800-3000°C.
- The surface temperature rods was increasing and rods splayed slightly.
- During the latter part of the test, the rods overheated and melting of some tips occurred, but the heat sink itself survived.

Honeycomb on PW-11 overheated

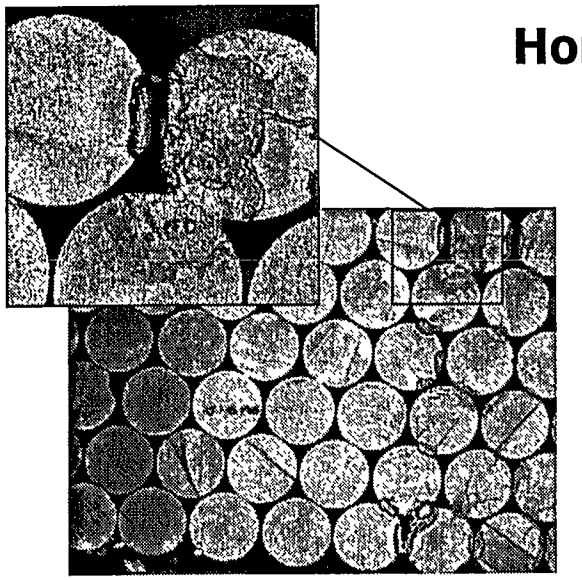

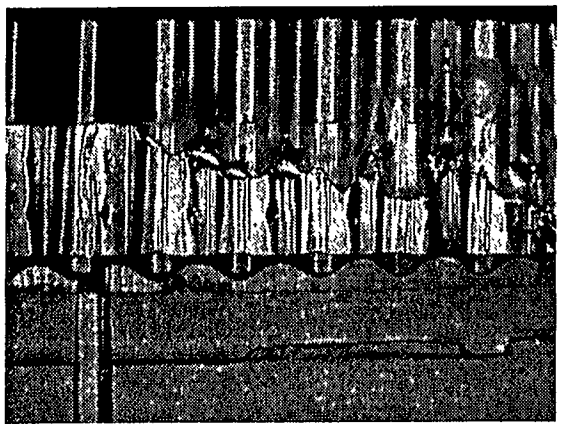

In assembling and HIPping PW-11, rods were held in a honeycomb.

We hoped the good honeycomb-rod contact would keep the honeycomb from overheating.

The SS honeycomb melted. Material contaminated the surface.

Tests were stopped at a "relatively" low heat flux of 11MW/m^2.

Surface Temperature, Heat Flux and Absorbed Power

There is a disagreement over what performance (surface temp. and heat flux) for the US and Russian mockups. Both are good but the values are disputed.

We measure absorbed power well; estimating the heated area is hard.

To "correct" surface temperature:

- **we map the pyrometer spot on an IR image,**
- **set emissivity so $T_{ave}=T_{apyrometer}$,**
- **assume $T_{max} = T_{tip}$ of the rods.**

The "IR" data in are the corrected values for several points.

Vertical arrows near "a" and "b" indicate two such corrections.

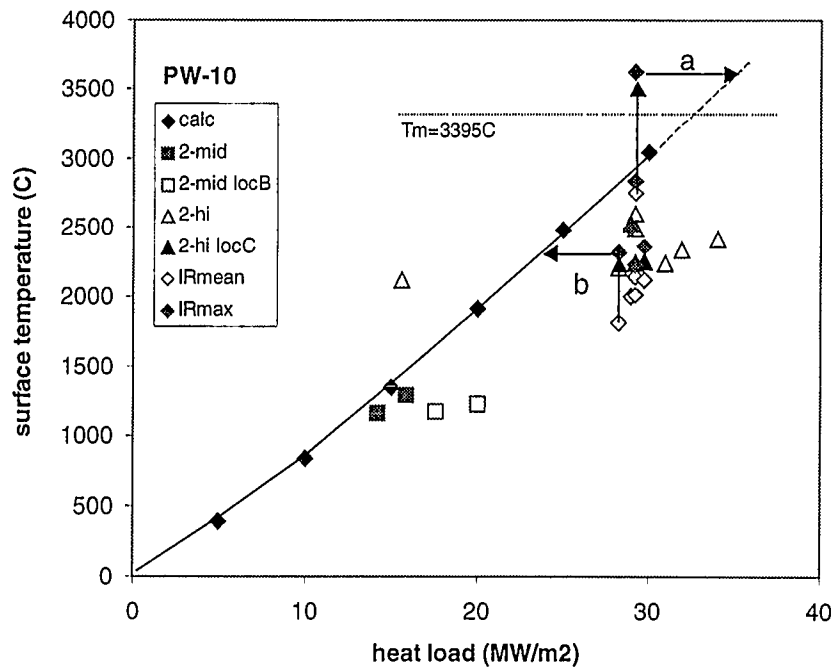

Conclusions: The W rod approach is excellent!

- US and Russian mockups have performed well.
- BUT, our data are not consistent. The heat flux values are suspect because of uncertainty in the heated area.
- At high heat fluxes, we use the maximum power of EBTS (30kW), and we decrease the heated area to increase the heat flux, e.g., at ~25MW/m^2 on PW-10, the pattern has an axial length of ~12mm or about 4 rod diameters. In the test, a group 2-3 rods wide appears to be hotter than the rest. The hotter central cluster is easily seen in the video as the rods cool down.

We can correct this problem by heating a larger area and we plan to retest at an already-tested mockup in EB1200. We also plan to build and test a larger mockup in EB1200.

KTH

MATERIAL MIXING ON TUNGSTEN - COATED PLASMA LIMITERS

Marek RUBEL[1] and Tetsuo TANABE[2]

[1]Alfvén Laboratory, Royal Institute of Technology, Stockholm, Sweden

[2]Center for Integrated Research in Science and Engineering, Nagoya University, Japan

US – Japan Workshop on
Plasma – Surface Interactions
and
High Heat Flux Component for Next Fusion Devices
Santa Fe, New Mexico, USA
November 1 – 4, 1999

POLOIDAL LIMITER BLOCKS FROM TEXTOR VPS TUNGSTEN (0.5 mm) ON GRAPHITE

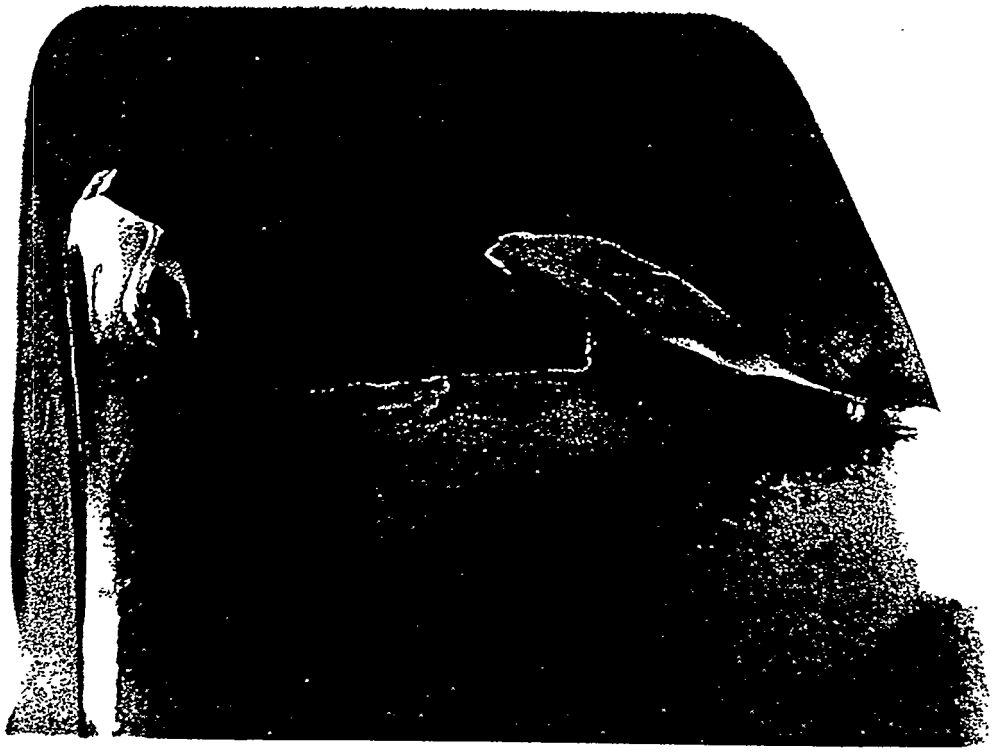

ANALYSES OF THE MAIN POLOIDAL LIMITED COATED WITH A VPS TUNGSTEN LAYER

1. DISTRIBUTION AND CONTENT OF:

- DEUTERIUM IN VARIOUS PARTS OF THE LIMITER,
- CARBON AND BORON ON TUNGSTEN,
- TUNGSTEN (and BORON) on GRAPHITE.

[2. STRUCTURE OF:

- TUNGSTEN LAYER
- MELTED ZONES (re-crystallization)
- TUNGSTEN – RHENIUM – GRAPHITE INTERLAYER].

LINEAR THERMAL EXPANSION OF MATERIALS
[coefficient α]

Material	α (10^{-6} K^{-1})	T (K)
Graphite EK98	3.41	300 – 570
	4.26	1273
Tungsten	4.20	773
	4.58	1273
Rhenium	6.12	773
	6.65	1273
	8.00	2773
W – Re 5%	4.30	773
	4.73	1273

Melting point (K)

W 3683

Re 3453

INITIAL STRUCTURE OF VPS TUNGSTEN

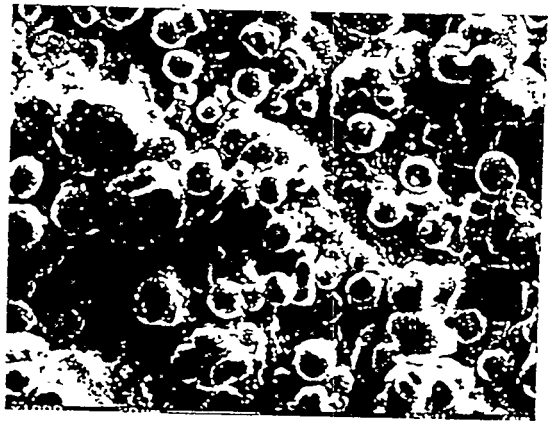

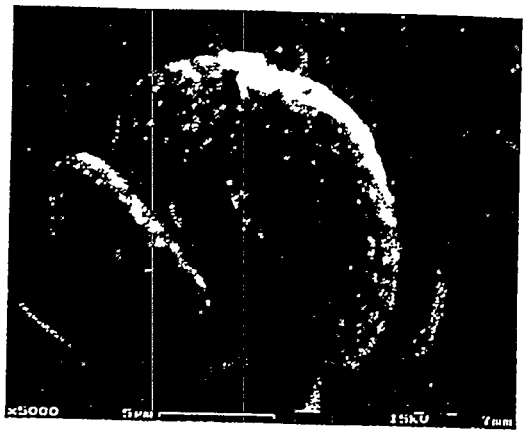

CARBON DEPOSIT
(CLOSE TO THE MELT ZONE OF TUNGSTEN)

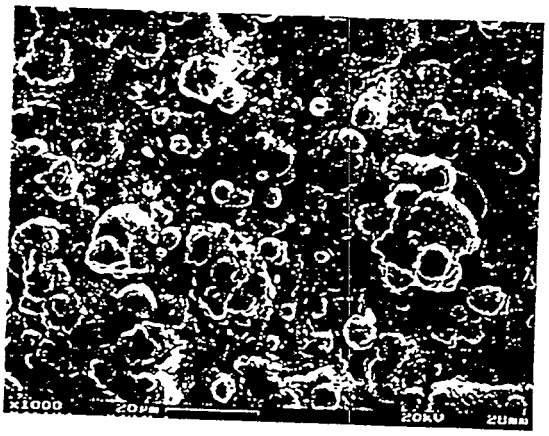

TUNGSTEN IN THE MELT ZONE

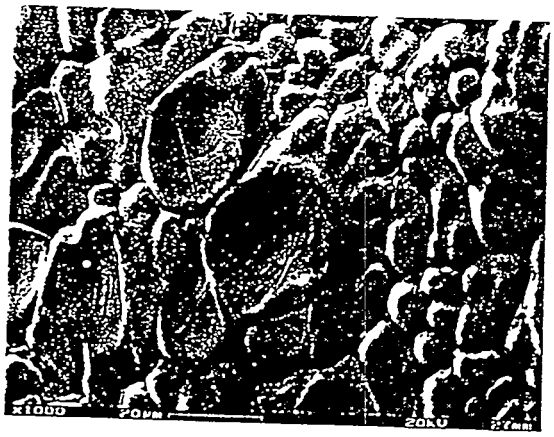

POLOIDAL LIMITER: SUMMARY OF RESULTS FOR D, B and C ON TUNGSTEN COATING

[ANALYSIS PERFORMED EVERY 1 or 2 mm]

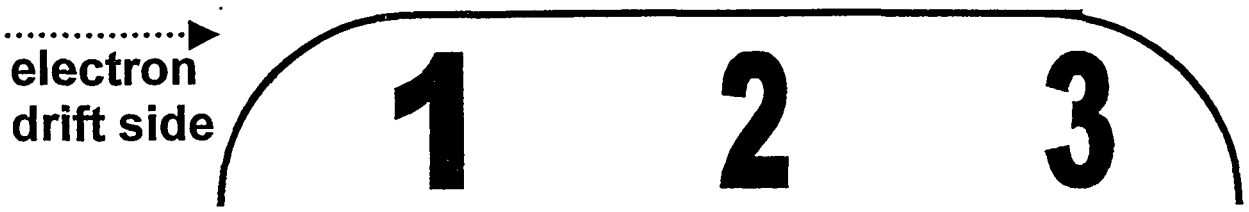

SPECIES	CONCENTRATION		
	Area 1	Area 2	Area 3
DEUTERIUM (10^{16} cm^{-2})	24 – 36	8 – 16	0.4 – 4
CARBON (10^{18} cm^{-2})	5.2- 8.3	0.6 – 1.4	1.4 – 3.4
BORON (10^{18} cm^{-2})	1.4 – 2.8	0.9 – 1.7	0.05 – 2.1

- DEUTERIUM IS DETECTED OVER THE WHOLE LIMITER SURFACE – EVEN IN AREAS WHICH WERE VERY HOT.
- INTERMIXING OF C, B, W IN THE SURFACE REGION (DEEP DIFFUSION or COMPOUND FORMATION)
- VERY SMALL QUANTITIES OF D, B, C ARE OBSERVED ON THE BACK SIDE OF THE DETACHED W COATING.

TUNGSTEN DISTRIBUTION ON THE GRAPHITE SURFACES OF THE POLOIDAL LIMITERS

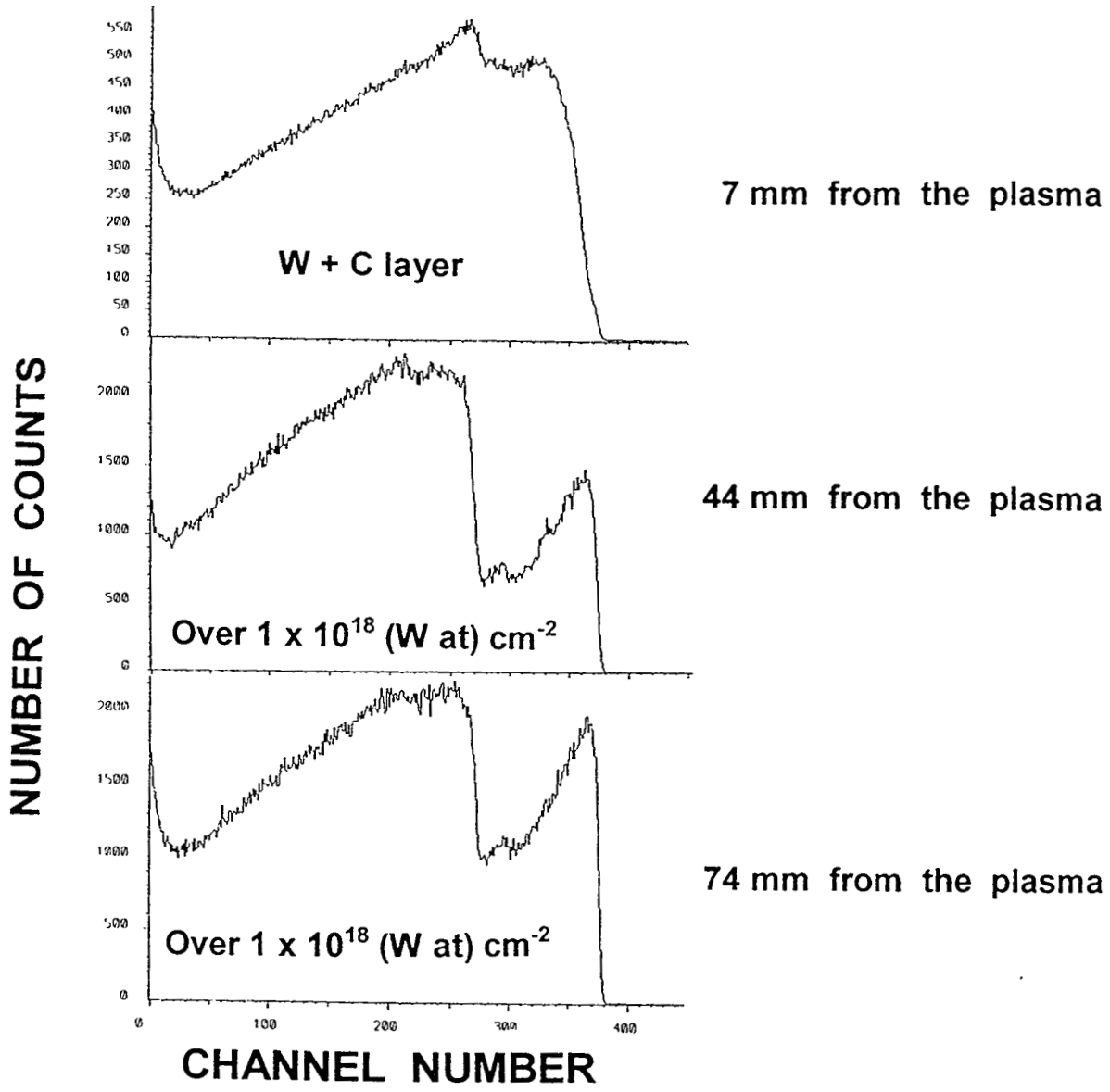

Tungsten eroded from the VPS layer is distributed over the whole limiter surface, i.e. deposited on graphite surfaces in the gaps between the limiter tiles.

RBS spectra prove distinct intermixing of carbon and tungsten (together with boron). The result may suggest the formation of mixed compounds.

SUMMARY & CONCLUSIONS

Graphite limiters coated with a VPS tungsten layer were studied.

- Cracking, melting of the layer occurred during the plasma operation.
- Heat loads caused the detachment of the W layer from the graphite substrate.
- Strong intermixing or compound formation (W – C – Si – B) occurred on the limiter surface.
- Deuterium is found ($1 - 5 \times 10^{16}$ D atoms cm^{-2}) even on the hottest areas of the limiter surface.
- Deuterium presence is associated with the co-deposition of carbon.
- The results do not allow conclude whether and how much of D is retained in tungsten. Previous results showed [redacted] the deuterium content in sole tungsten in the range $5 - 10 \times 10^{14}$ cm^{-2}.

1999 US/JA Workshop on PSI and HHF Components in Next Fusion Devices
November 1-4, 1999
St. Francis Hotel, Santa Fe, NM

Heating Test of Reduced Activation Ferritic Steel F-82H First Wall

JAERI ***T. HATANO, S. SUZUKI***

Background

- F-82H : a primary candidate structural material of DEMO
- HIP bonding method proposed by JAERI in fabrication technology development of the DEMO blanket
- Selection of the optimum condition : 1040 °C, 150 MPa and 2 hours
- Successfully fabrication of HIP-bonded F-82H first wall panel

HIP-bonded F-82H first wall panel with built-in cooling tubes

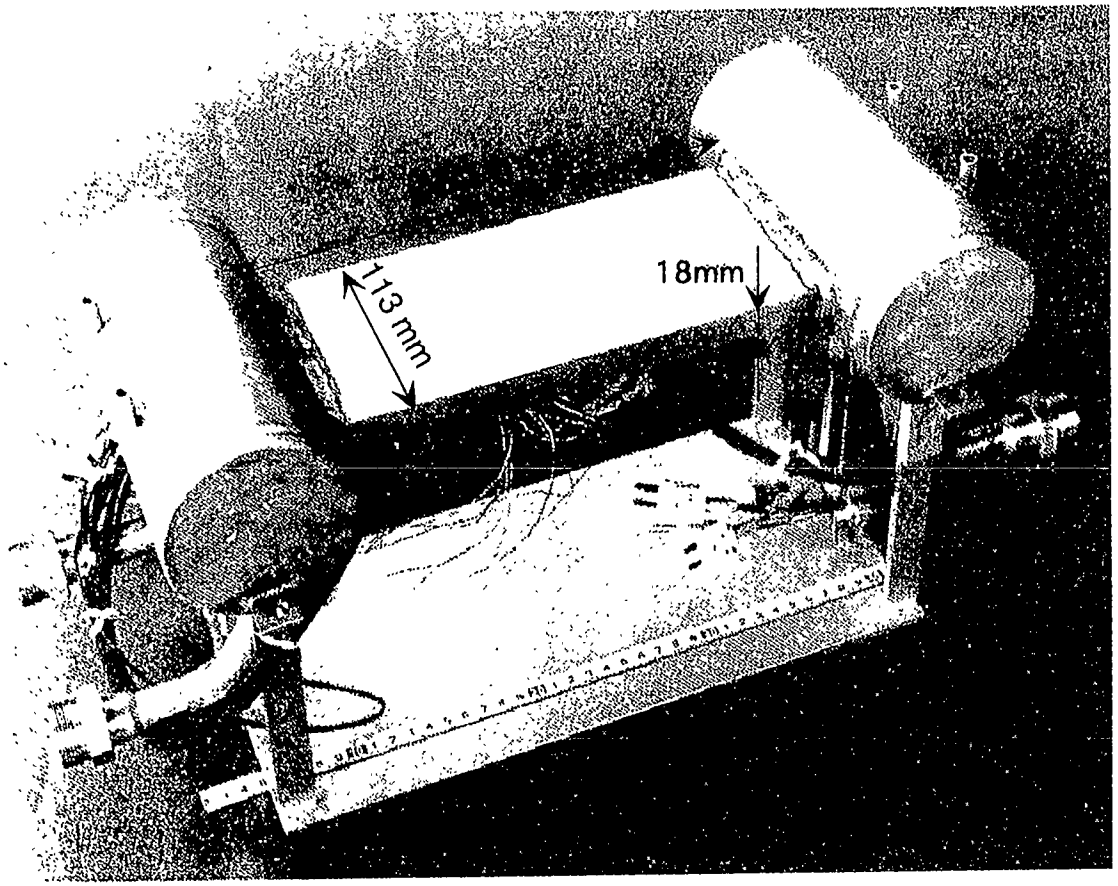

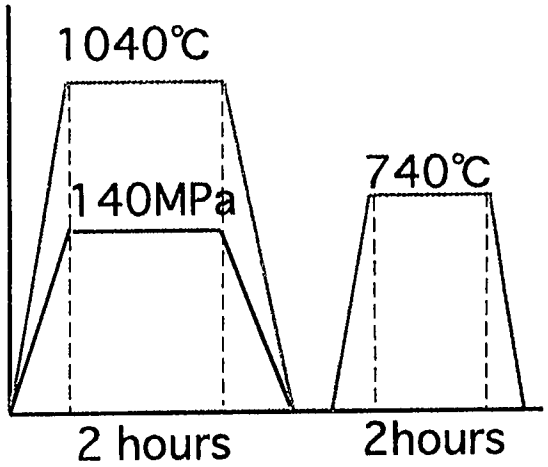

HIP conditions

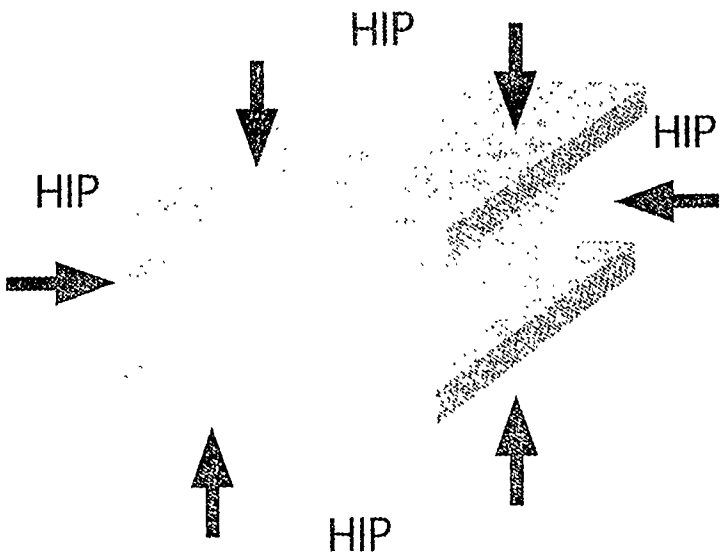

DEMO First Wall／Blanket Concept

Water cooled ceramic breeder blanket concept in SSTR

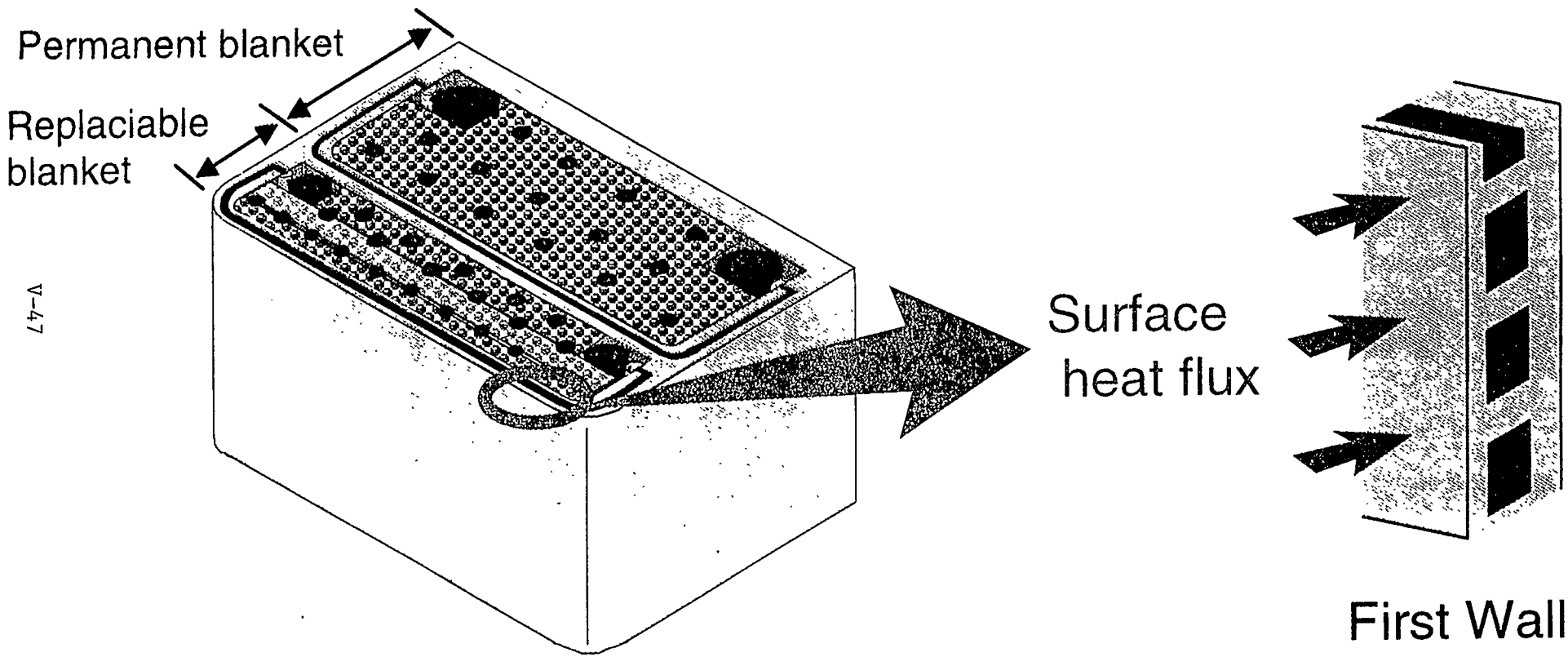

Breeder zone

: Breeder pebble layer

: Neutron Multiplyer pebble layer

Objective

At first in the world, heating tests with the HIP-bonded F-82H first wall panel

- Thermo-mechanical performance against heat flux
- Integrity of HIP-bonded interfaces
- Thermal fatigue lifetime

High Heat Flux Test Conditions

Simulate temperature distribution of the first wall under normal plasma operation of SSTR

Max. Temp. : 460 °C (surface heat flux of 0.5 MW/m^2 and neutron wall load of 3.0 MW/m^2)

Item	JEBIS	ITER (TB)	SSTR
Surface heat flux [MW/m^2]	2.7	0.5	0.9
Neutron wall load [MW/m^2]	—	1.0	3.0
Heating／cooling time [s]	15／15	1000	—
Cycle number	5000	10000	—
Cooling temperature [℃]	20	285～325	285～325
Cooling pressure [MPa]	1.0	15.5	15.5

Heat flux profile at heating test

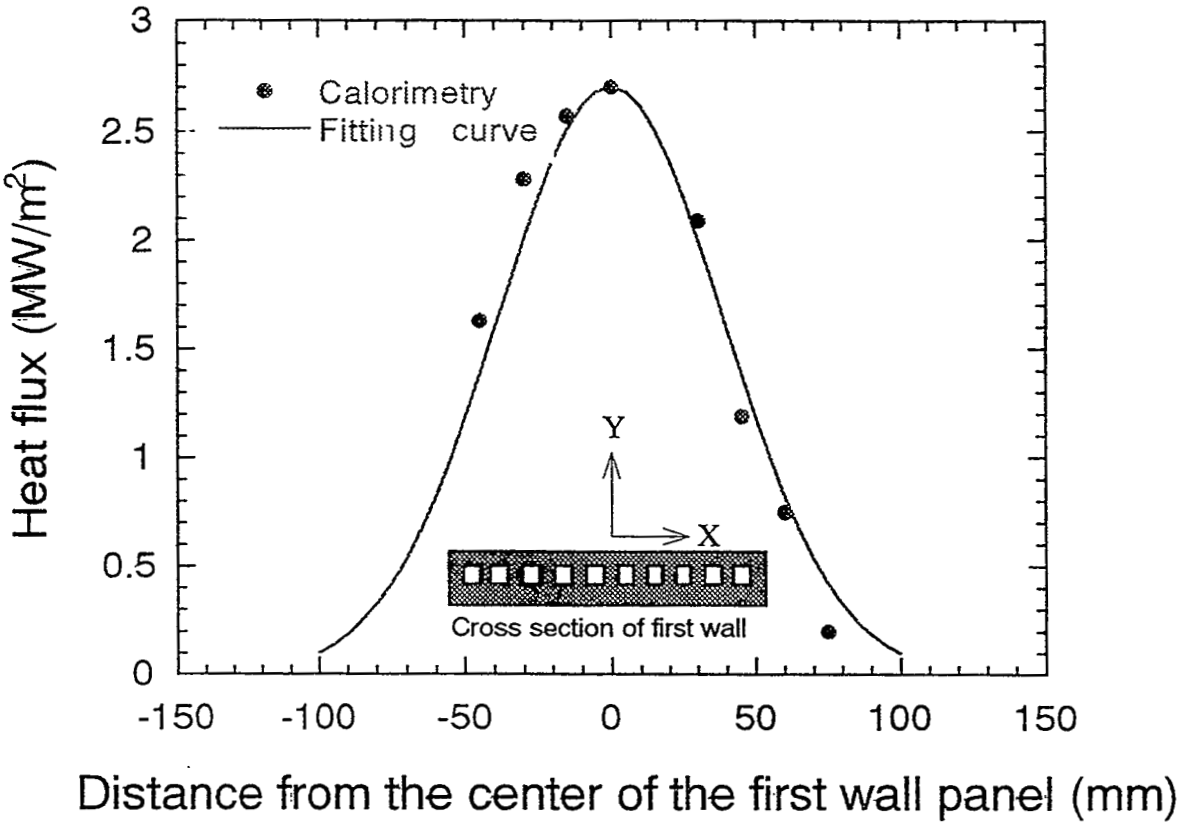

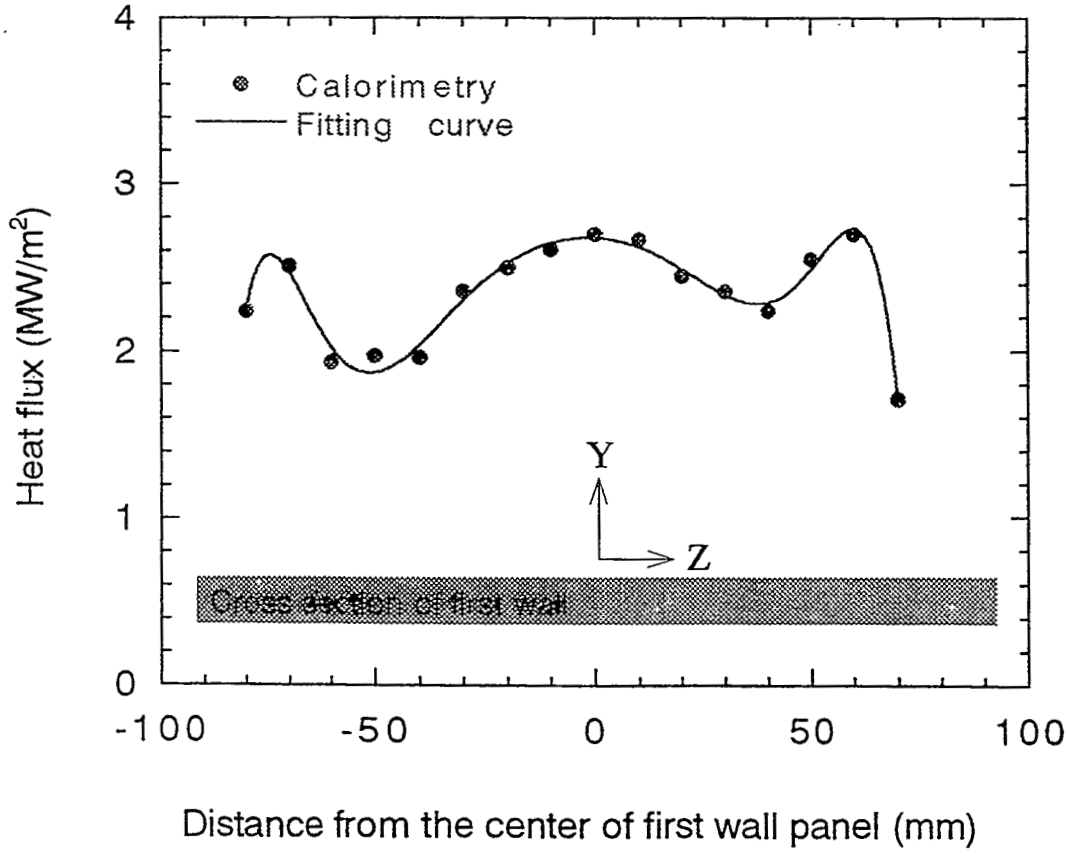

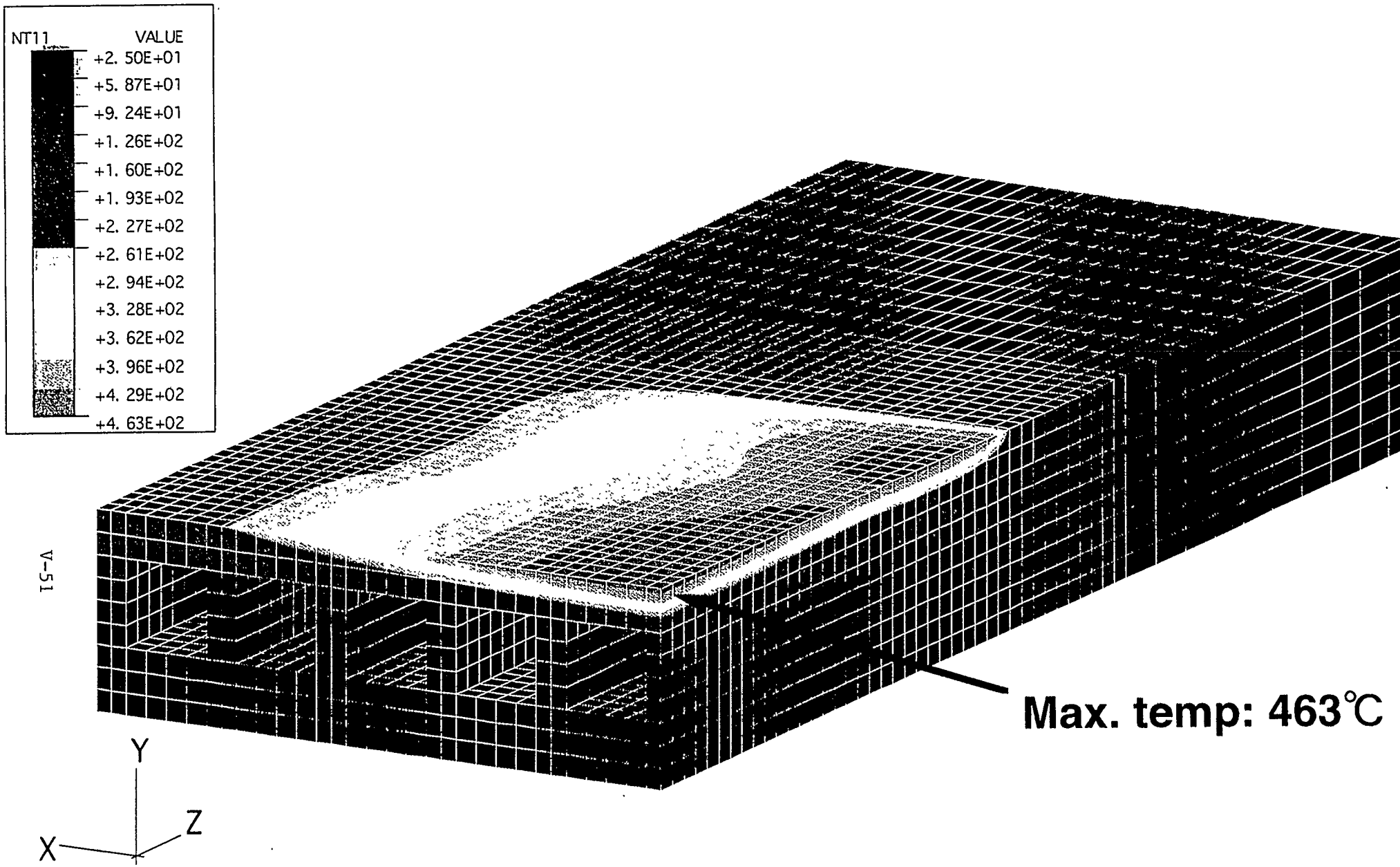

Thermal distribution of the FEM model
(heat load = 2.7 MW/m^2, 15 s)

Temperature responses at heated surface measured with IR camera and calculated by thermal analysis

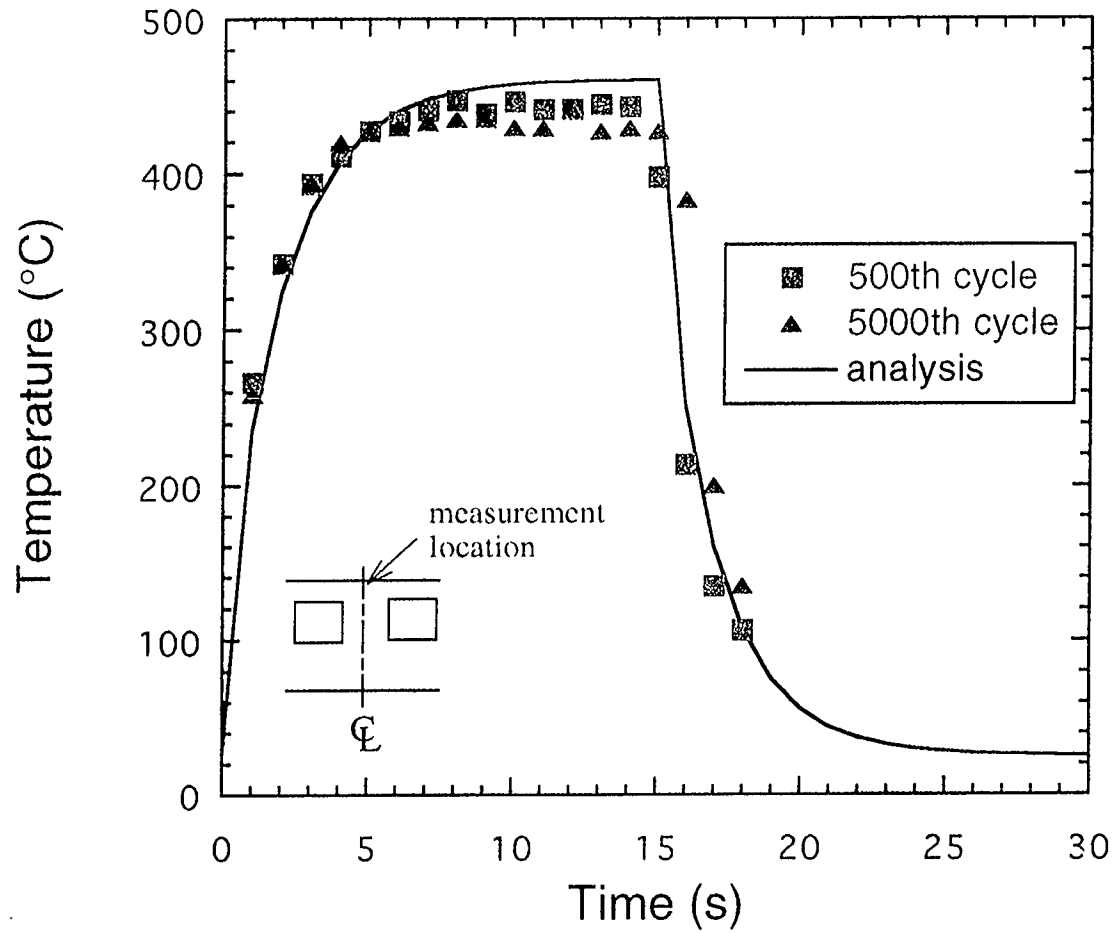

Temperature responses in the 500th and 5,000th cycle agreed well and they also agreed well with the analysis

Post-mortem analysis

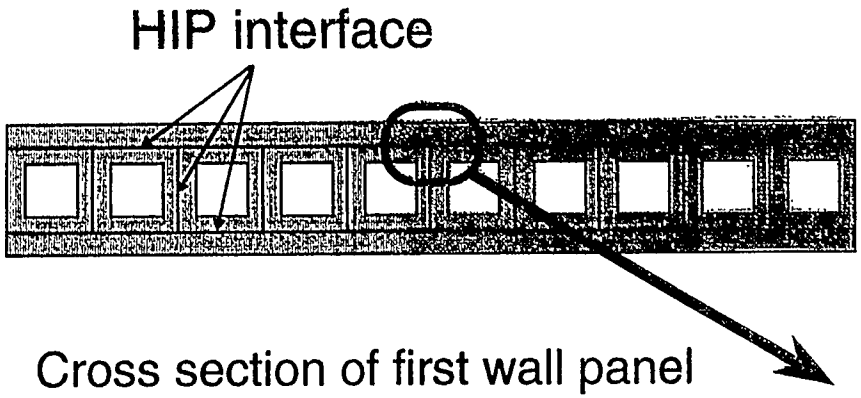

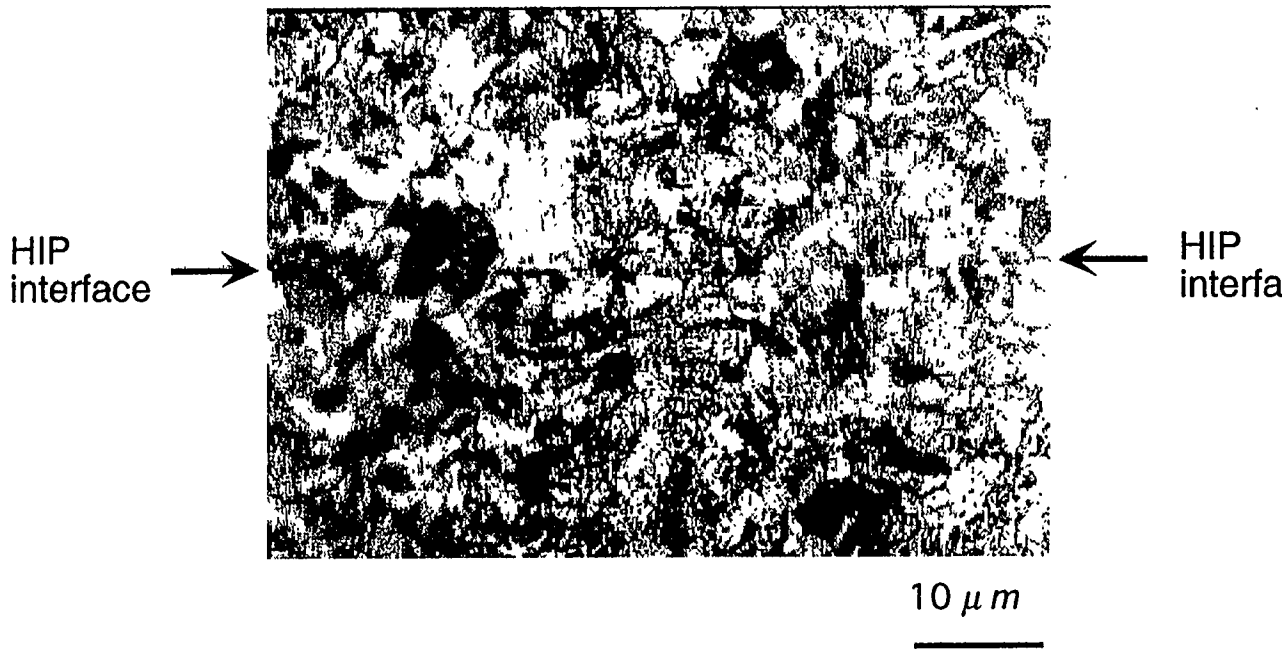

Microphotograph of the F-82H/F-82H HIP bonded interface

(2.5 mm under the heat loaded surface)

Test Results

- No degradation of thermal responses measured with IR camera during the test.
- Good agreement between measurement and analysis
- No exfoliation and cracks in the F82H HIP-bonded interface by SEM and optical microscope

Discussion

Maximum strain amplitude in one cycle was evaluated to be 0.46 % on the heated surface from results of thermo-structural analysis

Strain amplitude in the HIP-bonded interface was evaluated 0.45% from results of thermo-structural analysis

⇩

Fatigue lifetime of the HIPed first wall panel is expected to be almost the same as that of F-82H base metal

Comparision with thermal fatigue of F-82H FW panel and mechanical fatigue of round bar specimen

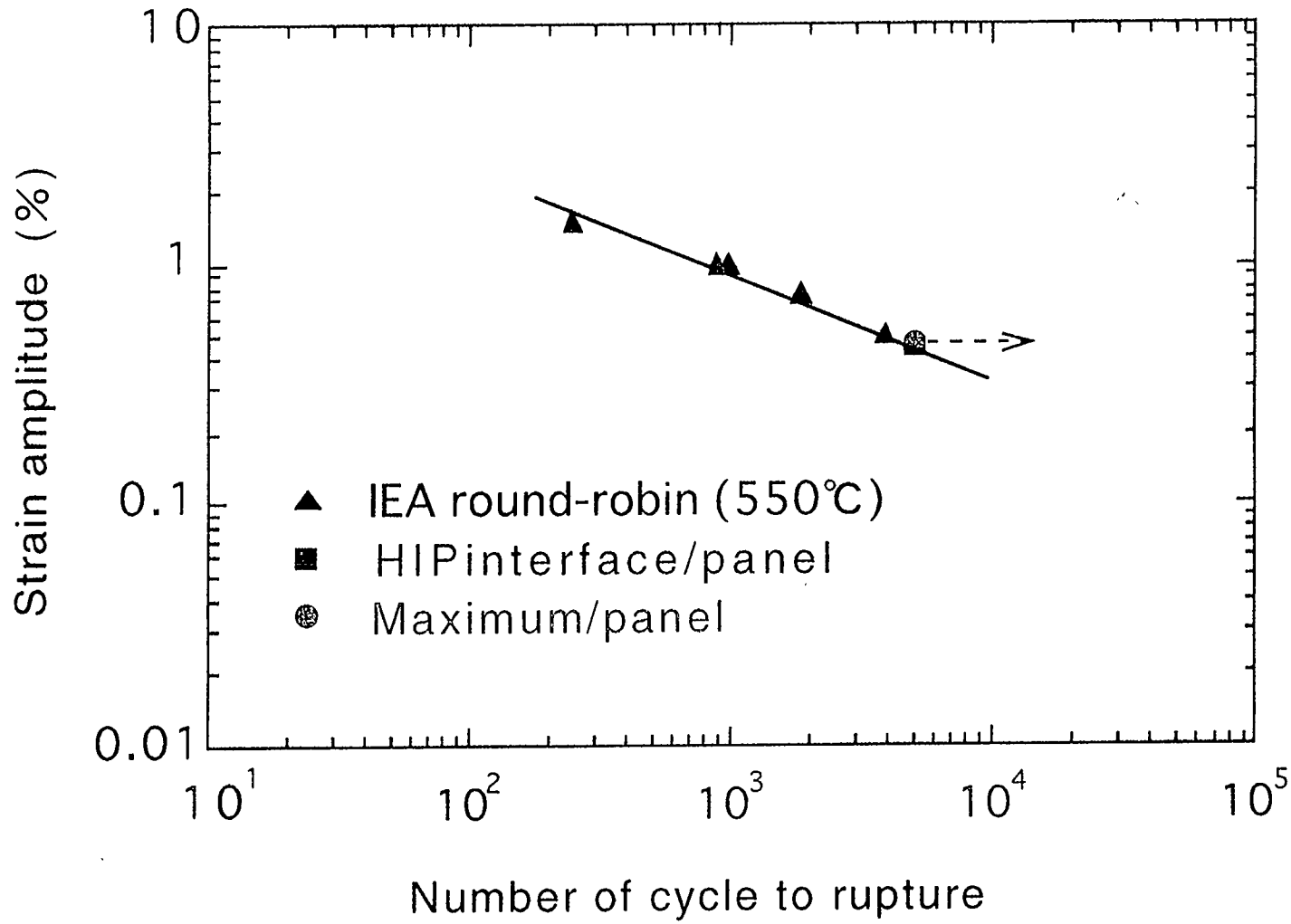

The fatigue lifetime of the F-82H panel reveals to be longer than the raw fatigue data of F-82H

Conclusion

(1) The first wall panel endured heat flux of 2.7 MW/m^2 x 5000 cycles simulating the maximum temperature of the water-cooled DEMO blanket.

(2) Integrity of the HIP-bonded interfaces in the F-82H first wall panel was confirmed by measurement of temperature response during the test and also post-mortem.

(3) Thermal fatigue lifetime of the panel was expected to be almost the same as that of F-82H base metal. The HIP-bonded F-82H first wall panel has sufficient heat removal and thermo-mechanical performance to be applied to the DEMO blanket.

(4) Further investigation on the mechanism and the effect of the hardening at the heated region is necessary.

Plasma Facing Components – 2

Effect of Divertor Plasma on the Pebble Fall for Pebble Divertor Concept

M. Nishikawa, T. Okui, K. Matsuhiro and M. Isobe
Graduate School of Engineering, Osaka University

Contents

- Effect of pebble charged by divertor plasma
  Charge on surface of pebble in divertor plasma
- Effect of plasma pressure and plasma momentum flux on the pebble
- Discharging process of the pebble ejecting from the plasma
- Effect of electric field generated by charged pebble
  In the case that the charge remains still on the pebble,
- Design of pebble collector

Supra-high temprature laboratory,Course of Electromagnetic Energy Engineering,
Graduate School of Engineering, Osaka University

→ ○ Japanese Activities on Liq. and Pebble Divertors

Various forces on pebble

- Gravitational force
- Electrostatic force
- Electromagnetic force
- Plasma pressure
- Momentum flux of plasma

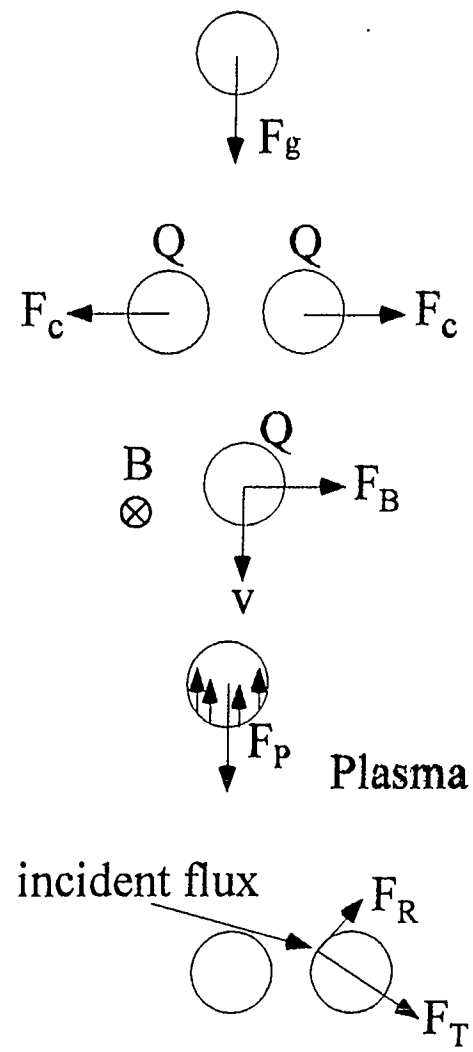

Plasma pressure and momentum flux effect

Plasma parameters and momentum flux at the divertor for different ITER CDA operating points

Configuration	Ion flux($10^{23}m^{-2}s^{-1}$)	kT_i(eV)	Momentum flux (Pa)
Duble null A	4	10	50
Single null A	2	210	105
Single null B	2.5	137	106

~200 eV

50 ~ 100 Pa

A is for ignited operation

B is for quasi-steady-state operation

static pressure ~ 150 Pa

ref : Neil B. Morley et al., Estimates of the effect of a plasma momentum flux on the free surface of a thin film liquid metal, Fusion Engineering and Design 28(1995)176-180

Supra-high temprature laboratory,Course of Electromagnetic Energy Engineering,
Graduate School of Engineering, Osaka University

Charging of pebble in divertor plasma

- **Plasma parameter**

$n_i = n_e = n = 10^{19}\,\mathrm{m}^{-3} \qquad T_i = T_e = 200eV$

Electric field

$$\left(\frac{d\phi}{dx}\right)^2 = \frac{2en}{\varepsilon_0}\left[-2\phi_0\left\{\left(\frac{\phi}{\phi_0}\right)^{1/2}-1\right\}+\frac{kT_e}{e}\left\{\exp\left(\frac{e(\phi-\phi_0)}{kT_e}\right)-1\right\}\right]$$

$$\phi_0 = -0.5T_e$$

$$\phi = \phi_f + \phi_0 = -2.6T_e - 0.5T_e = -3.1T_e$$

Electric field on pebble surface

$$E = 6.4\times10^{6}\,(\mathrm{V/m}) = \sigma/\varepsilon_0$$

- **Charge** $Q = 4\pi\varepsilon_0 r^2 E\,(\mathrm{C})$

r: pebble radius (m)

$\varepsilon_0 = 8.84\times10^{-12}\,(\mathrm{F/m})$

$Q \sim 1.8\times10^{-10}$ [C]

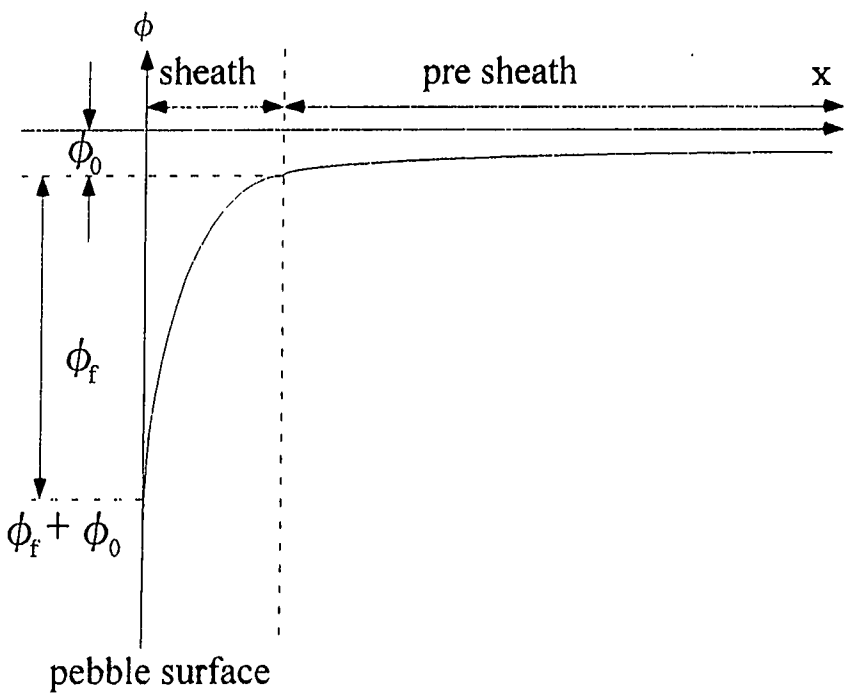

distribution of electric potential

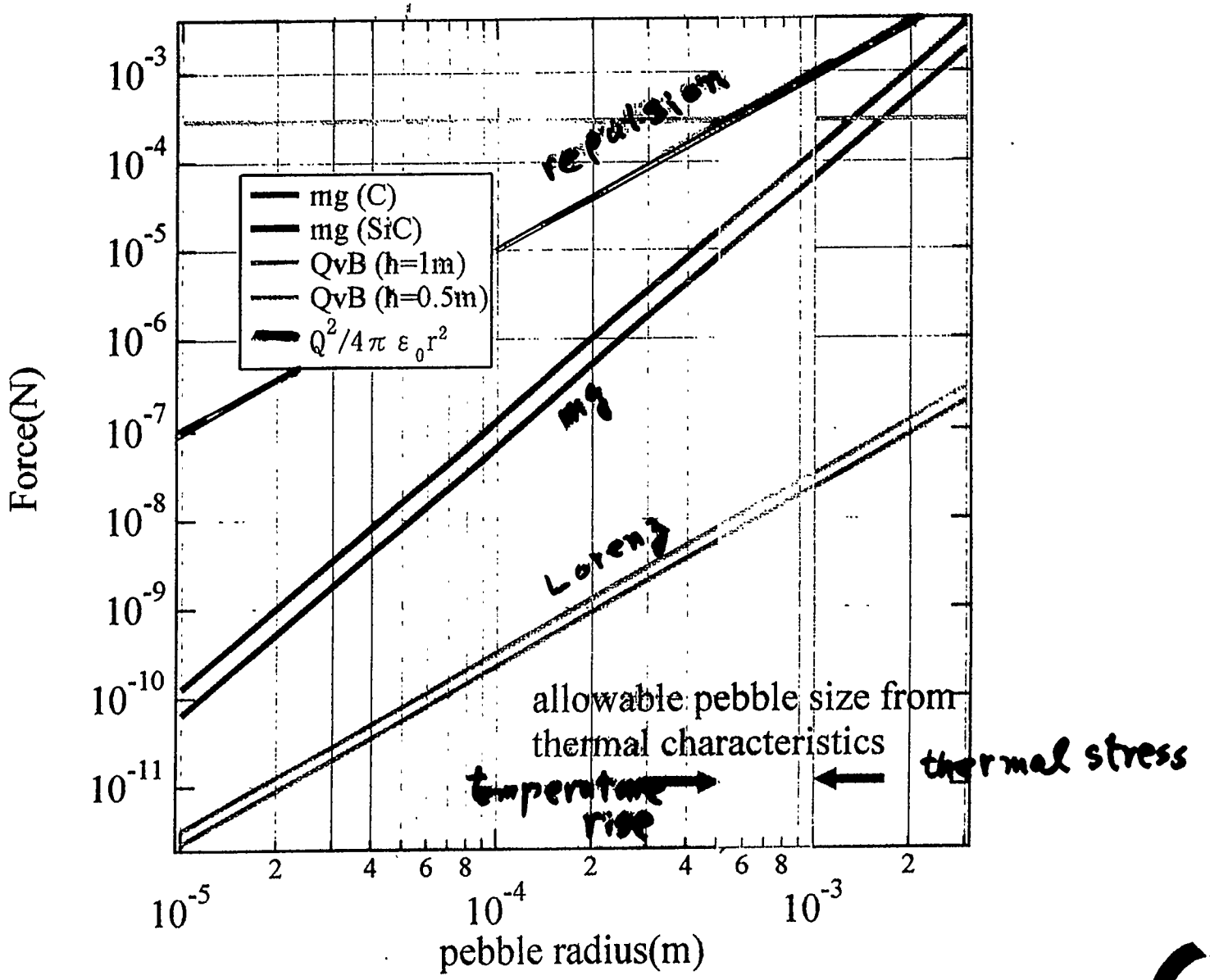
mg (C)
mg (SiC)
QvB (h=1m)
QvB (h=0.5m)
$Q^2/4\pi\varepsilon_0 r^2$
repulsion
mg
Lorentz
allowable pebble size from
thermal characteristics
temperature rise
thermal stress
Force(N)
pebble radius(m)
10^{-3}
10^{-4}
10^{-5}
10^{-6}
10^{-7}
10^{-8}
10^{-9}
10^{-10}
10^{-11}
10^{-5}
10^{-4}
10^{-3}
2 4 6 8 2 4 6 8 2

Deceleration of pebble by plasma pressure

Force along falling direction
(Strike zone width=0.1m)

$$F = mg - P\pi\left(2rz - z^2\right) \qquad \left(0 \le z \le 10^{-3} m\right)$$

$$F = mg \qquad \left(10^{-3} m < z < 10^{-1} m\right)$$

$$F = mg - P\pi\left(2r(1.01\times10^{-1} - z) - (1.01\times10^{-1} - z)^2\right)$$

$$\left(10^{-1} m \le z \le 1.01\times10^{-1} m\right)$$

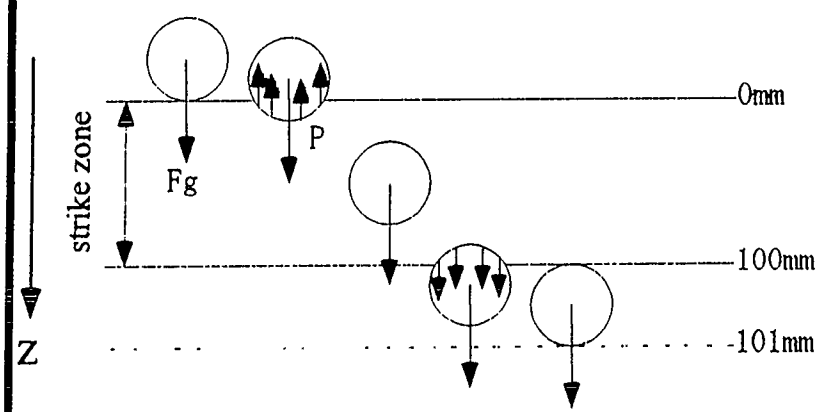

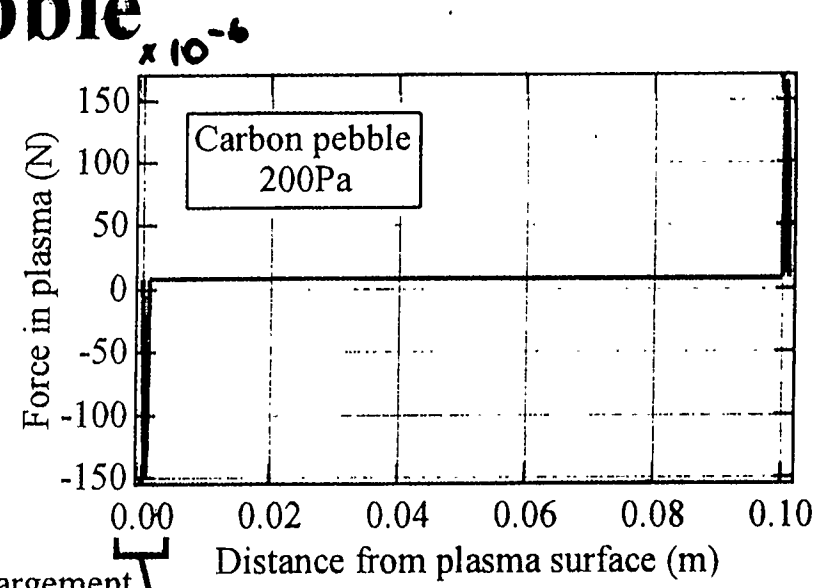

enlargement

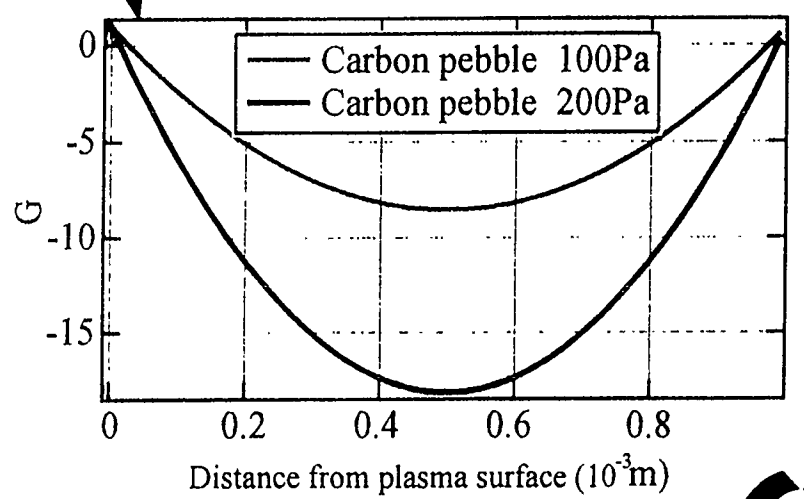

Supra-high temprature laboratory,Course of Electromagnetic Energy Engineering,
Graduate School of Engineering, Osaka University

Change of irradiation time

Irradiation time

$$t = \frac{v_{100mm} - v_{1mm}}{g}$$

v_{1mm} : velocity at 1mm under the plasma surface

v_{100mm} : velocity on 100mm under the plasma surface

Passage time difference

$$\text{Passage time difference} = \frac{t_p - t_g}{t_g}$$

t_p: Passage time in plasma puressure

t_g: Passage time in only gravity

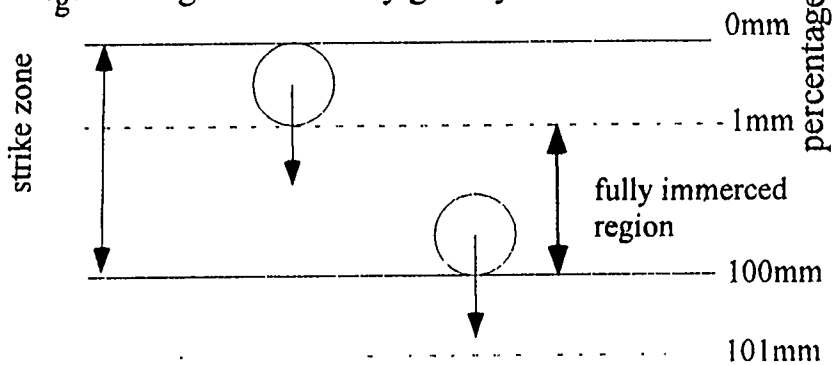

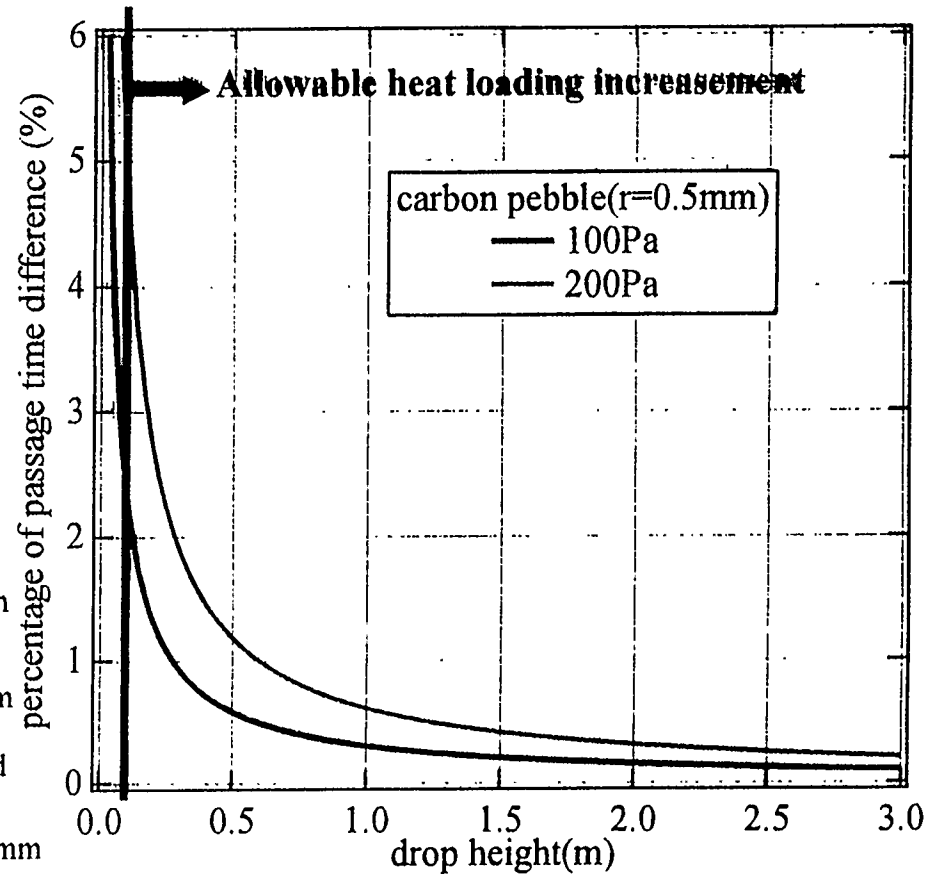

Supra-high temprature laboratory,Course of Electromagnetic Energy Engineering,
Graduate School of Engineering, Osaka University

The force by momentum flux

assumption

force by momentum flux act against point G'

conditions

Distanace of adjoining pebbles: 2×10^{-3} (m)

Pebble radius: 5×10^{-4} (m)

Incident angle: 5degree

S: irradiated cross section=1.74×10^{-7} (m^2)

G: ~~The center of gravity~~ acting point (3.07×10^{-4} m, 0, 0)

θ : The angle between incident flux and thrust direction

$$\theta = \sin^{-1}\frac{\overline{OG}}{a} = \sin^{-1}\frac{3.07\times10^{-4}}{5\times10^{-4}} = 37.9^{\circ}$$

F_T: Thrusting force $F_T = PS\cos\theta$

F_R: Rotational force $F_R = PS\sin\theta$

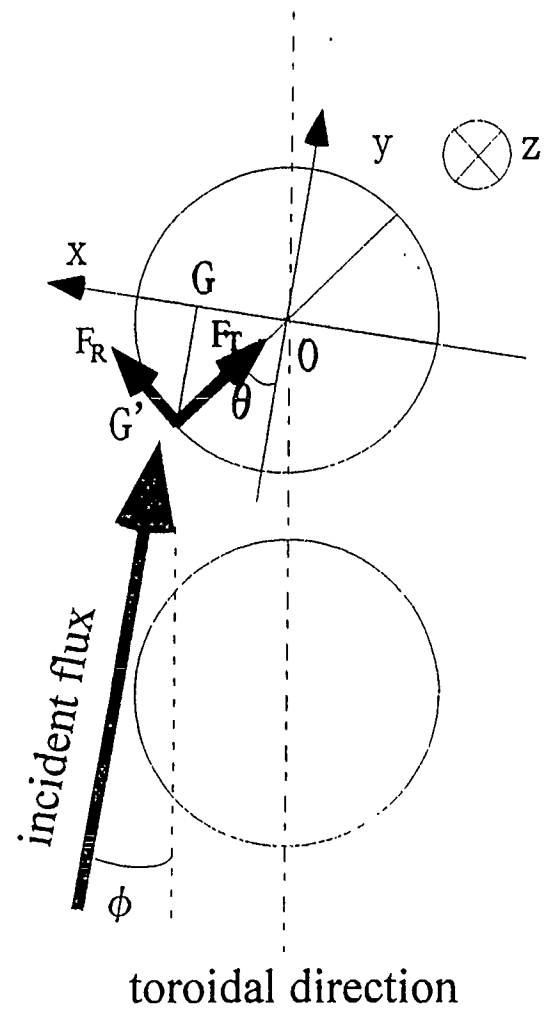

Supra-high temprature laboratory,Course of Electromagnetic Energy Engineering,
Graduate School of Engineering, Osaka University

Thrust and rotation of pebble

d : Thrust lenght $d = \frac{1}{2} \cdot \frac{F_T}{m} t^2$

N : Number of rotation $N = \frac{1}{2\pi} \cdot \frac{F_R \cdot a}{I} \cdot t^2$

t : Passage time from plasma surface

$$t = \left(-v_0 + \sqrt{v_0^2 + 2gz} \right) / g$$

v : velocity of plasma surface

I : Inertial moment $I = \frac{2}{5} m a^2$

m : mass of 0.5mm radius pebble

$m_C = 8.4 \times 10^{-7}$(kg)

$m_{SiC} = 1.6 \times 10^{-6}$(kg)

Condition

P=50Pa and 100Pa

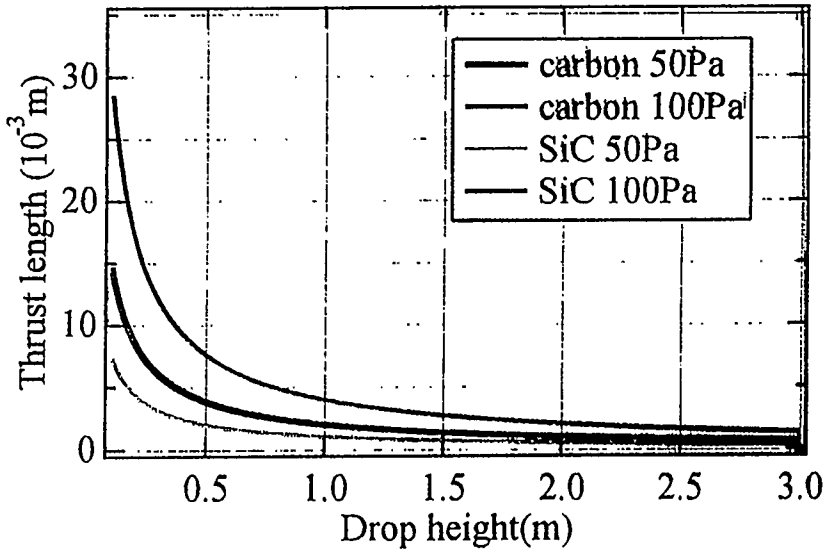

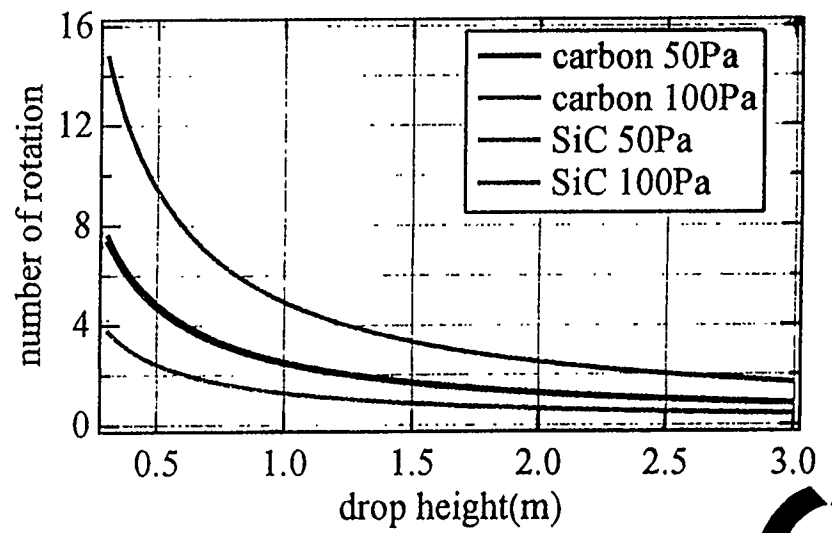

Supra-high temprature laboratory,Course of Electromagnetic Energy Engineering,
Graduate School of Engineering, Osaka University

Discharge process of the pebble ejecting from the plasma

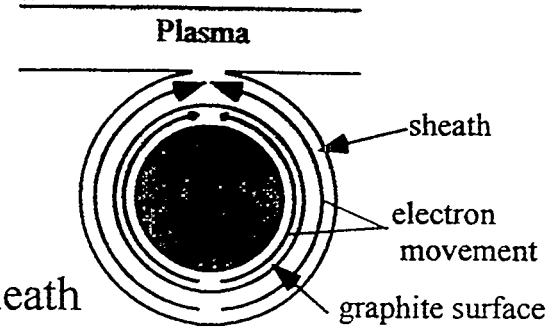

Electric resistivity

$\eta_e = 5\times10^{-7}[\Omega\mathrm{m}]$: in the sheath

$\eta_c = 1\times10^{-5}[\Omega\mathrm{m}]$: in the graphite

$$\frac{\eta_c}{\eta_e} = 20$$

Carrier particle density

$n_p = 1\times10^{19}[/\mathrm{m}^3]$: in the sheath

$n_c = 5\times10^{24}[/\mathrm{m}^3]$ (hole - electron) : in the graphite

Mobility ratio

$$\frac{\mu_e}{\mu_c} = \left(\frac{\eta_c}{\eta_e}\right)\left(\frac{n_c}{n_e}\right) = 10^7$$

Mobility in the sheath

$$\mu_e = \frac{1}{n_e e \eta_e} = 1.25\times10^6[\mathrm{m}^2/\mathrm{V\,s}]$$

Mobility in the graphite

$$\mu_c = \mu_e\times10^{-7} = 1.25\times10^{-1}[\mathrm{m}^2/\mathrm{V\,s}]$$

1) ejection time of the pebble from the plasma τ_0

$$\tau_0 = \frac{d}{v_0} \quad \sim 3\times10^{-4}[\mathrm{sec}]$$

2) electron release time from the sheath τ_e

$$\tau_e = \frac{\pi d}{2v_e} = \frac{\pi d}{2\mu_e E} = \frac{(\pi d)^2}{4\mu_e V} \quad \sim 3\times10^{-15}[\mathrm{sec}]$$

3) electron release time from graphite surface τ_c

$$\tau_c = \frac{\pi d}{v_c} = \frac{\pi d}{2\mu_c E} = \frac{(\pi d)^2}{4\mu_c V} \quad \sim 3\times10^{-8}[\mathrm{sec}]$$

- Residual chrage electrons Q_r

sheath

$$\frac{Q_r}{Q_0} \sim e^{-t/\tau_c}\Big|_{t=\tau_0} \sim 0$$

surface

$$\frac{Q_r}{Q_0} \sim e^{-t/\tau_e}\Big|_{t=\tau_0} \sim 0$$

Conditions for caluculation

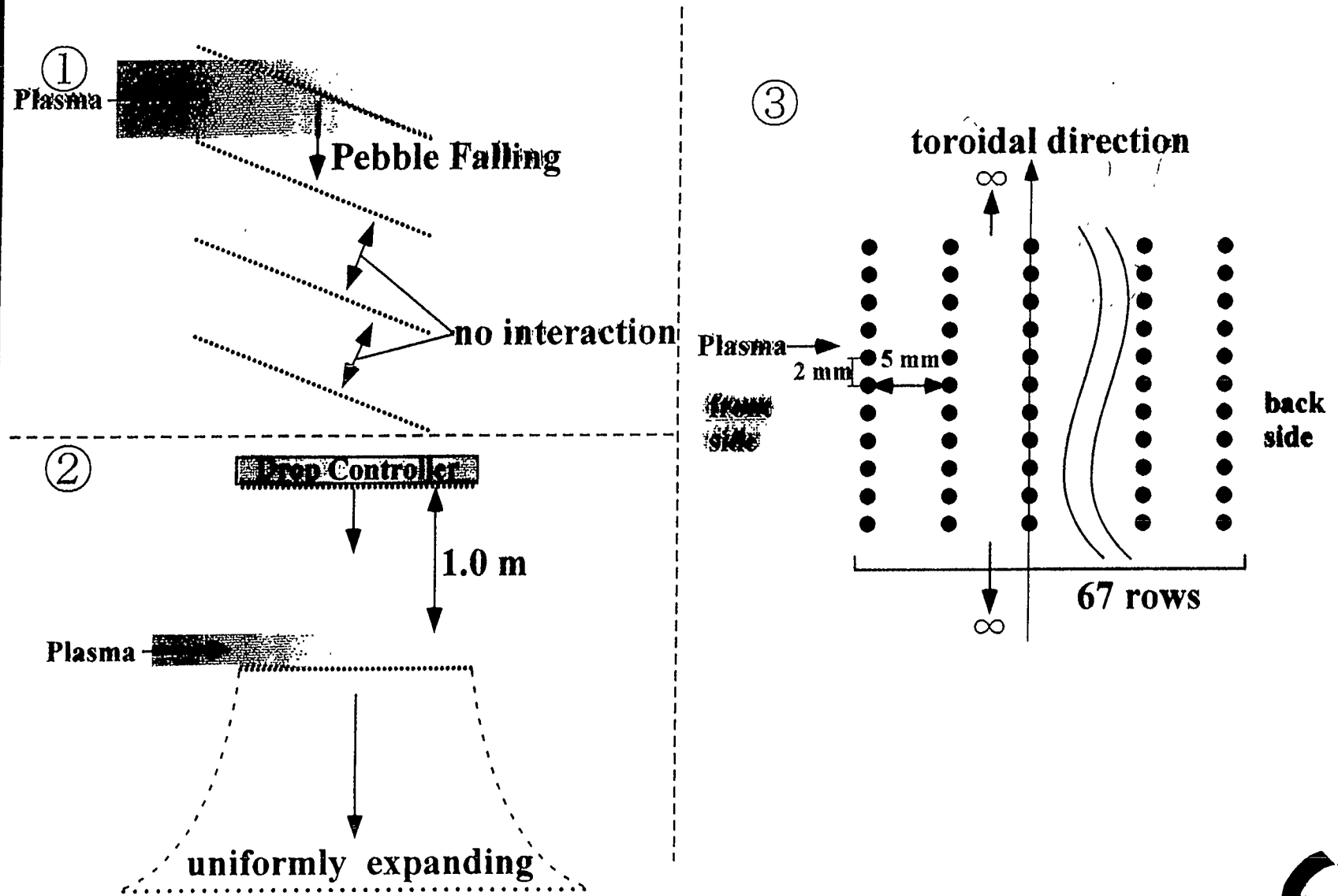

Supra-high temprature laboratory,Course of Electromagnetic Energy Engineering,
Graduate School of Engineering, Osaka University

Expansion by Coulomb Repulsion

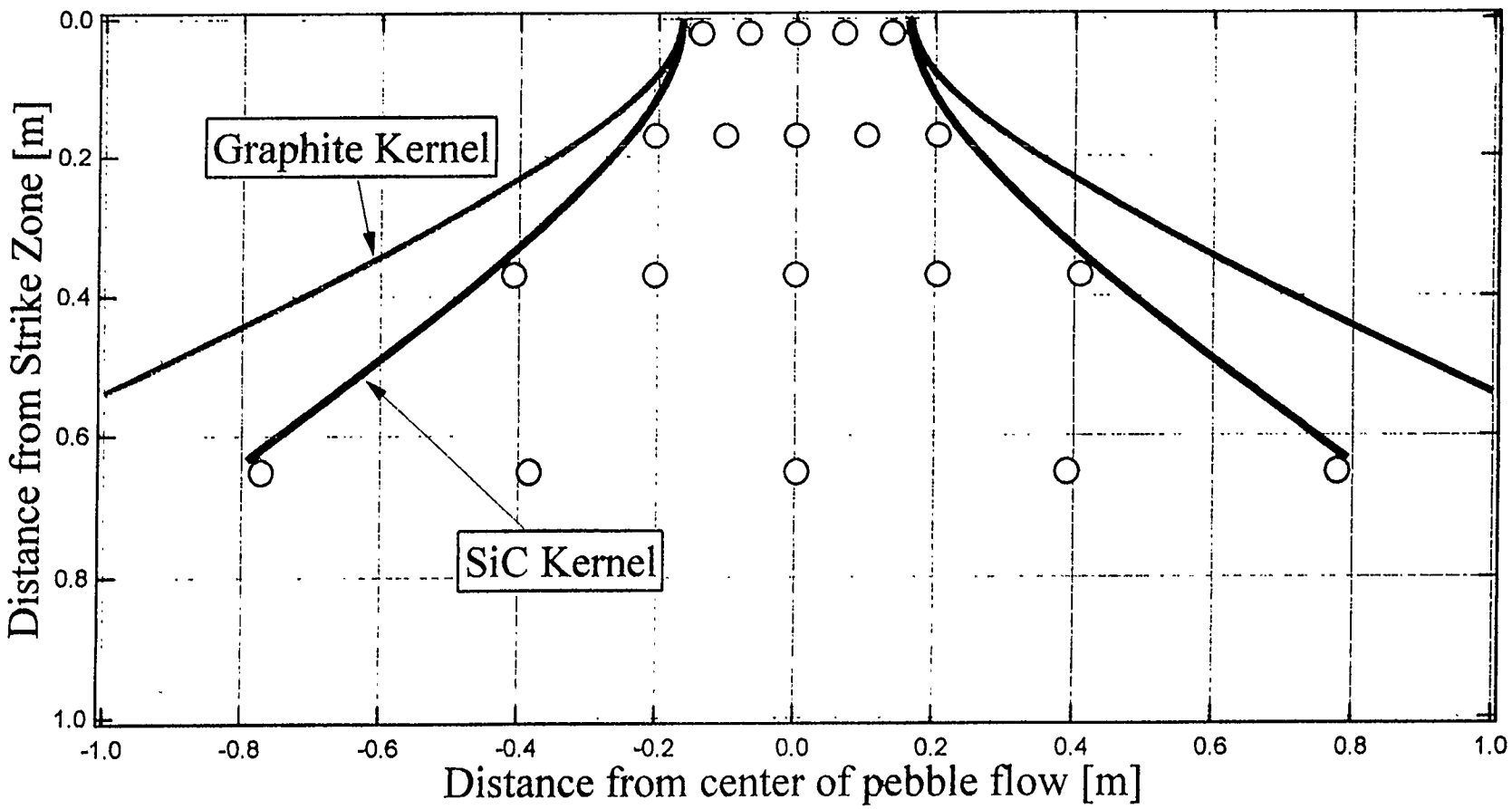

Supra-high temprature laboratory,Course of Electromagnetic Energy Engineering,
Graduate School of Engineering, Osaka University

Design of Pebble Collecter

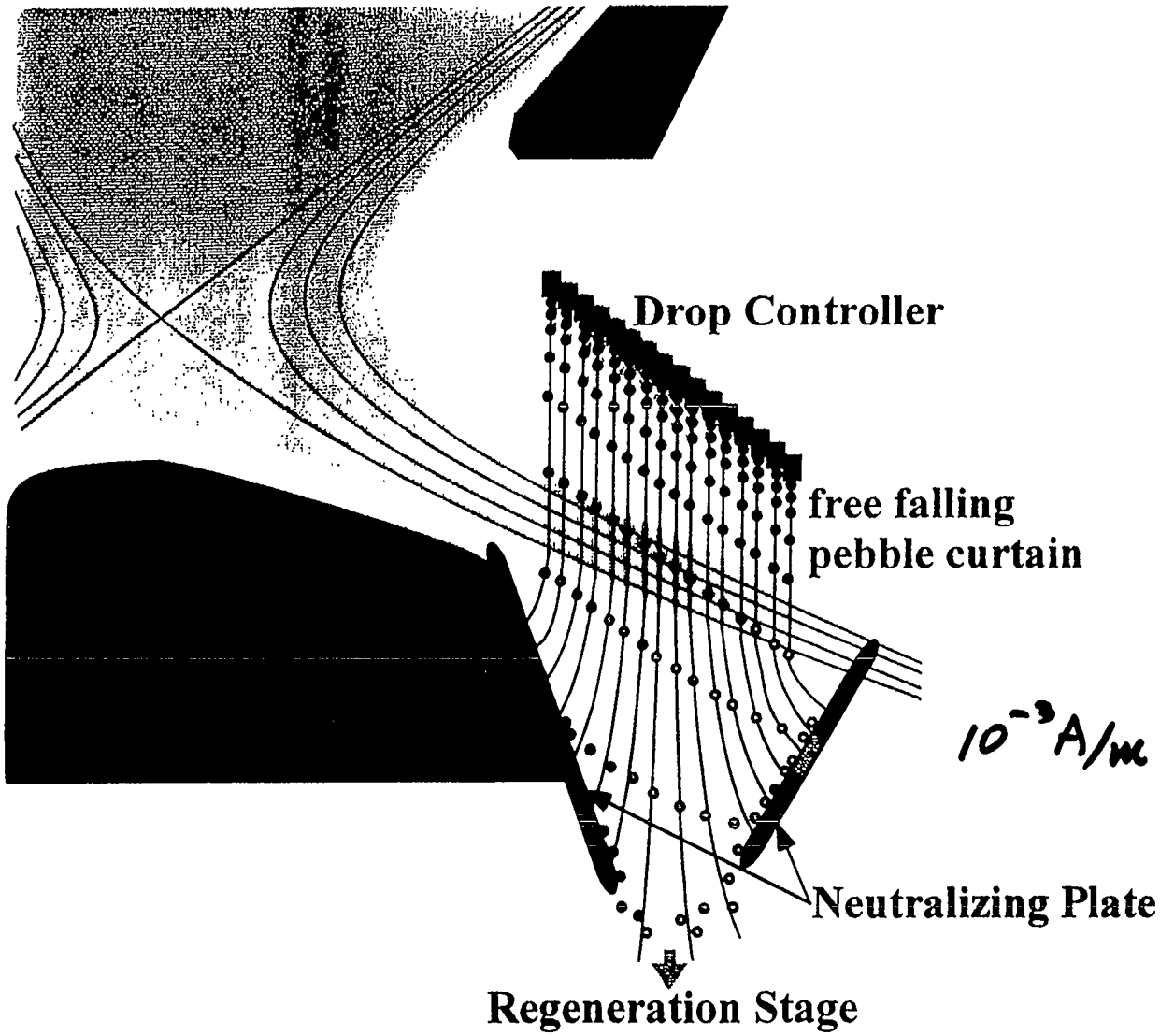

Supra-high temprature laboratory,Course of Electromagnetic Energy Engineering,
Graduate School of Engineering, Osaka University

Summary

1) In previous studies, the proper pebble size is available to be 0.5 to 1 mm for the reason of the limitations of surface temperature rise, thermal stress and mass flow rate of the pebble in the divertor plasma.

2) In the pebble divertor concept with the functions of removal of high heat loading and pumping effect, we selected divertor plasma condition appropriate for ITER-CDA condition that is a simple divertor.

3) Charging of the pebble and sheath around the pebble is considered for the repulsion force estimation.

4) Pebble is reacted by the force due plasma pressure when the pebble goes through into the divertor plasma. This deceleration phenomenon is found not to be effective for the irradiation time.

5) Pebble is moved like as thrust and rotation by plasma momentum flux.

6) Discharging process of the pebble ejecting from plasma is discussed and the charged particle is found to be released to the plasma during ejecting phase.

7) If the plasma is disrupted rapidly in the time shorter than the electron release time, the surface charge of the pebble remains to be acted for repulsive force.

8) Even if the worst case is occurred, the system is designed to be operated safety by of the neutralizing plate equipped in the downward of the diverter.

Japanese Activities on Liquid and Pebble Divertors

Moving Solid State Divertor

- Pebble Divertor
  OSAKA U. (Nishikawa)
- Belt-Moving Divertor
  NIFS (Hirooka)

Liquid Metal Divertor

- NaK Loop, Na Loop,
  Li Loop Experiment (MHD Loss, ...
  OSAKA U. (Miyazaki, Horiike)
- Flow velocity and Temp. Measurement of Liq. Metal by Micro-Ultraacoustic Sensor
  OSAKA U. (Nishikawa)
- Na Loop, Hg Loop Experiment
  (Divertor Cooling with Boiling Liq. Metal)
  TOKYO Inst. Tech. (Takahashi, Yano)
- FLiBe Loop
  TOHOKU U. (Toda)
  NIFS (Sagara)
- ICF Reactor Concept (KOYO)
  (Liq. Wet wall Cooling)
  OSAKA U. (Yamanaka, Nakai)

Moving-surface plasma-facing components for steady-state particle control

- Continuous removal of:
  - (1) fuel particles
  - (2) heat
  - (3) impurities.
- Balanced erosion - getter coating (Li, Be, B) conditions possible.
- Long lifetime with a low-Z surface.
- Reduced MHD and activation effects with a SiC-SiC fabric belt (commercially available).
- Moving speed controllable.
- Modular application possilbe.

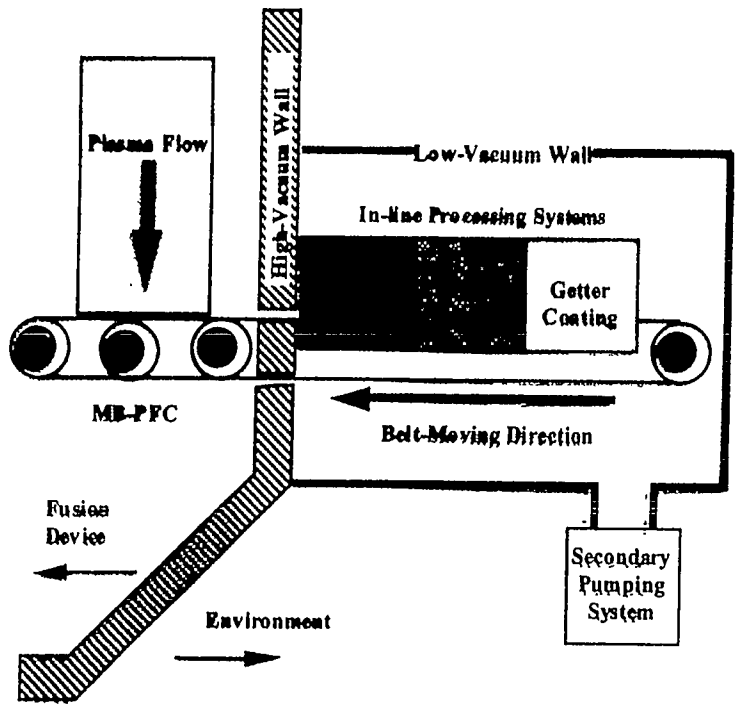

NIFS

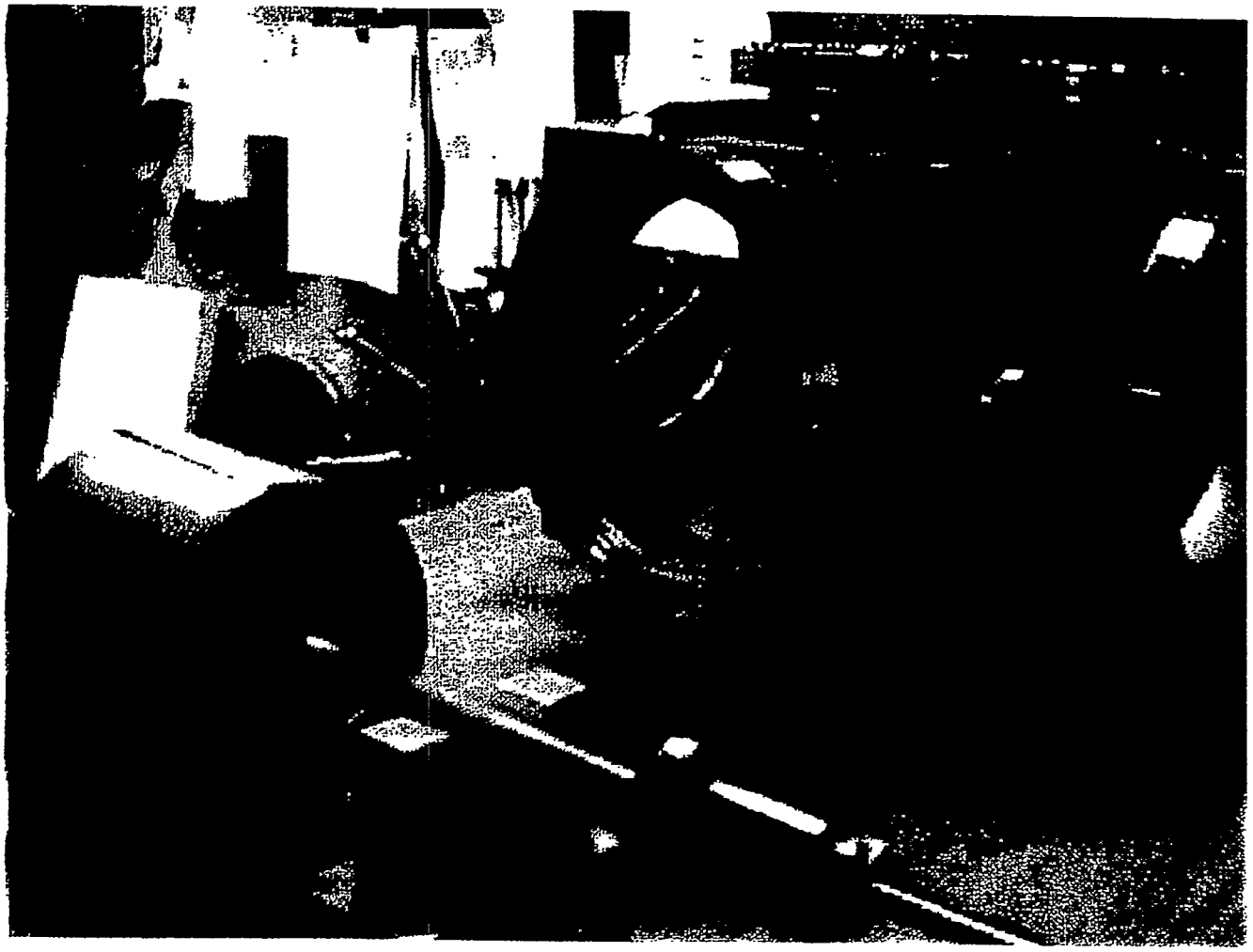

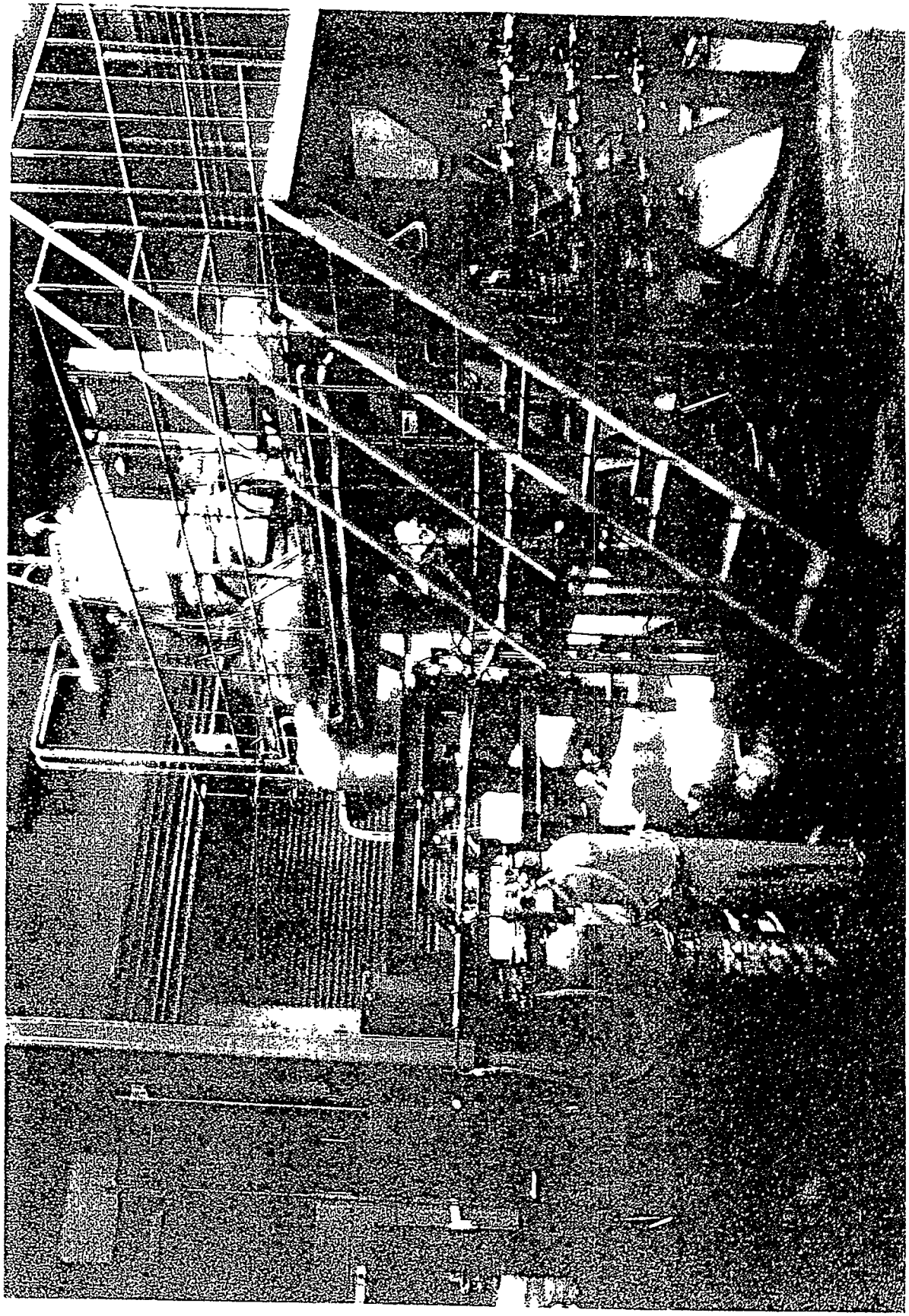

Experimental Device

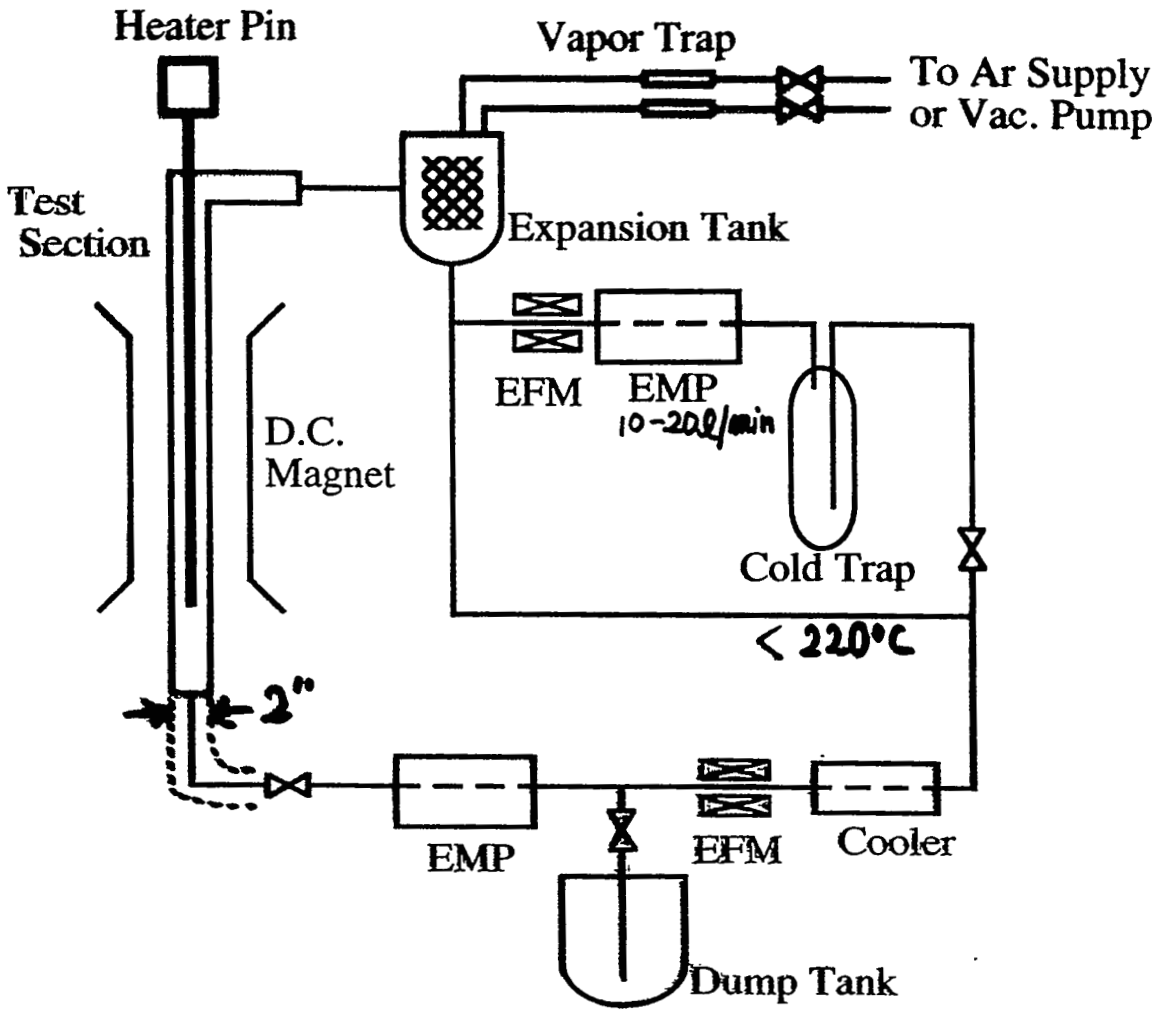

EMP	**500 l/min 5atm (Test Section 6m/sec)**
Loop Piping	**2B(Sch40S) = 52.7mm I.D. 3.9mm Thickness**
Li Inventory	**230 L**
DC Magnet	**Pole Gap 175mm**
	Max. Magnetc Flux Density 0.8 T

Effect of imperfect insulation coating on MHD pressure drop

Peal off the fix ratio of vinyl coating in SS316 test tube
B = 0.4 to 1.5 T, v = 0 o 1.2 m, ~1"tube
NaK loop 40 l/min

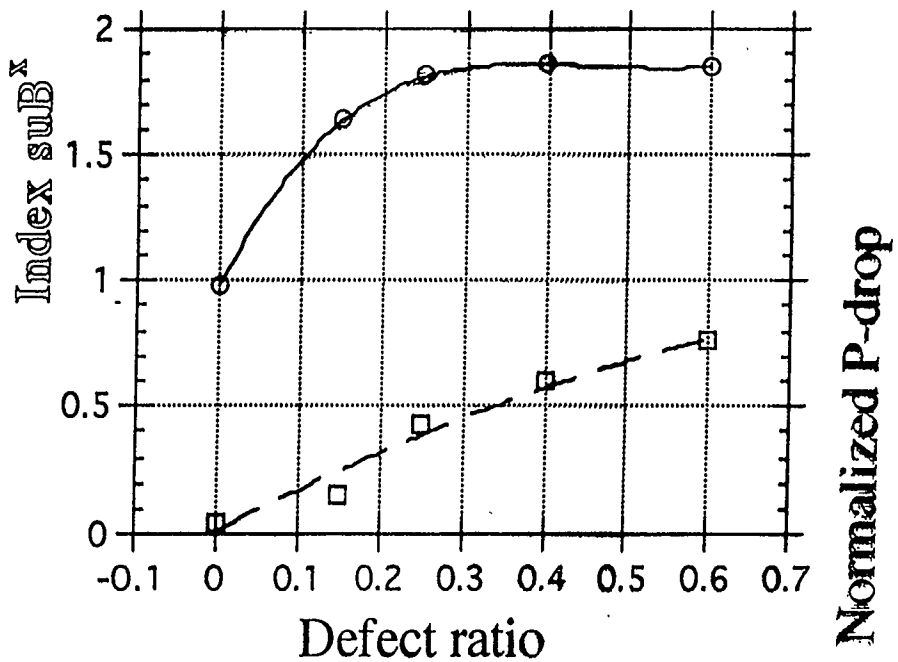

Advantages of Liquid Metal Boiling Flow for Divertor Cooling

- Higher heat transfer coefficient of boiling cooling due to phase change compared with non-boiling cooling
- Lower MHD pressure drop of boiling two-phase flow compared with liquid metal single-phase flow
- Higher heat transfer coefficient specific to liquid metal compared with that of ordinary fluid

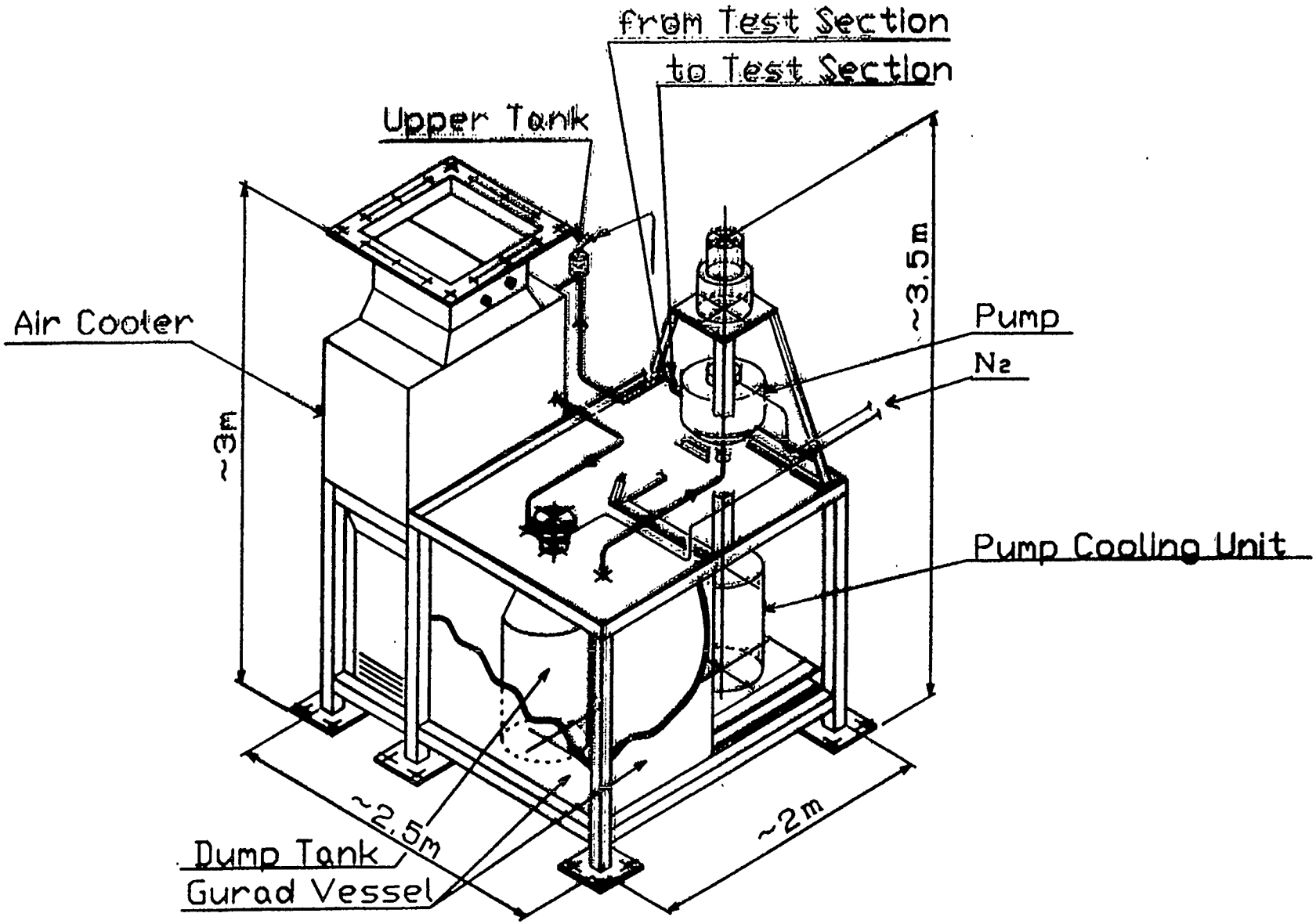

Molten Salt(FLIBE) Circulating Equipment

Experiment of pebble divertor

- Pumping performance and irradiation of multi layer pebble -

M.Isobe, K. Matsuhiro and M.Nishikawa
Osaka University, Japan

Outlines

1. Pebble Drop Divertor Concept
2. High heat/particle flux irradiation on multi-layer pebble
3. Transient hydrogen release measurement after high flux irradiation for the pumping concept
4. Summary

Pebble Drop Divertor Concept

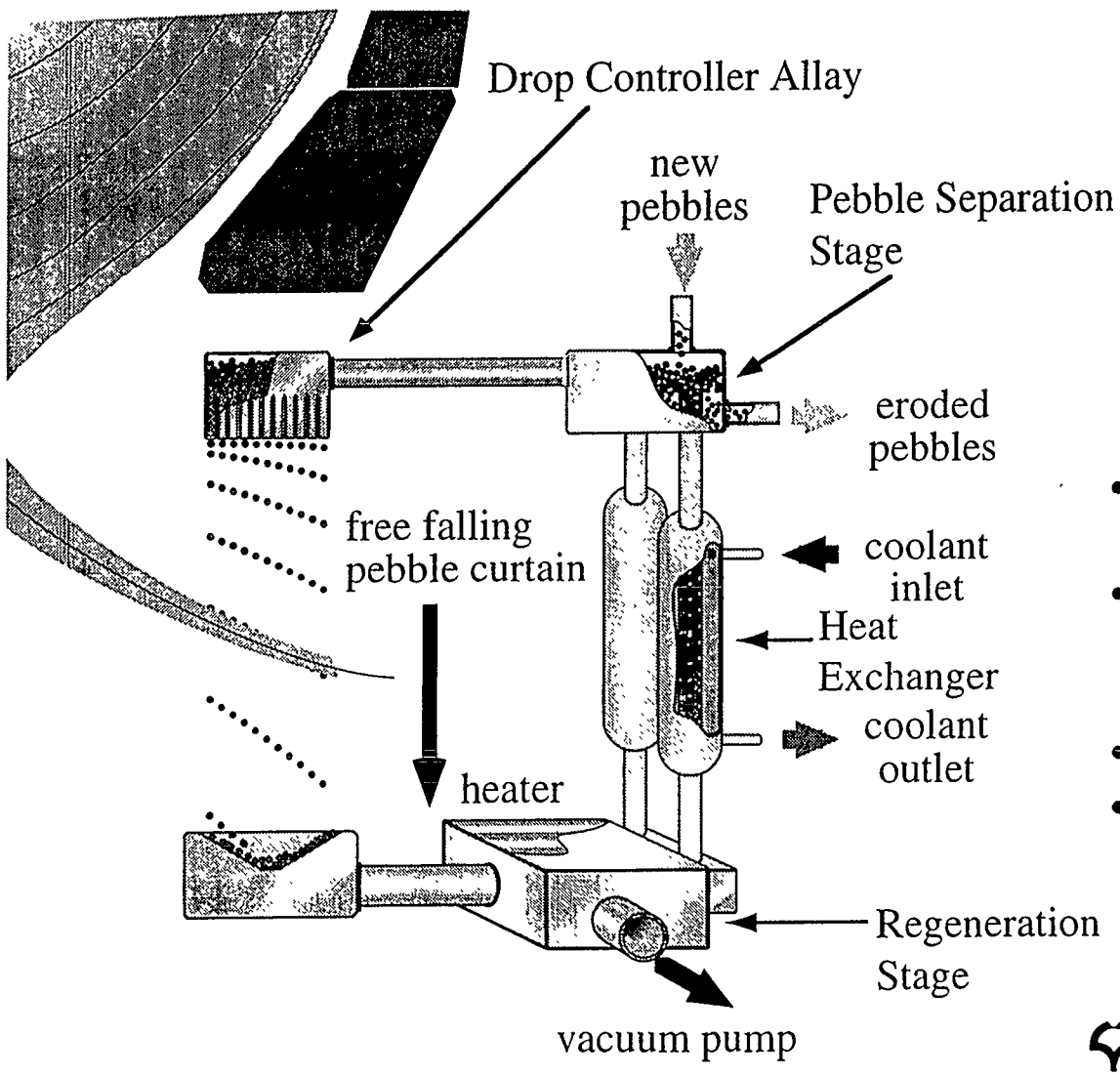

The advantage of pebble drop divertor

- **applicable to high heat load operation**
- **conventional low-Z plasma facing materials can be used without erosion problem**
- **low bulk tritium retention**
- **continuous wall pumping**

Supra-high Temperature Engineering Laboratory
Graduate School of Engineering, Osaka Univ.

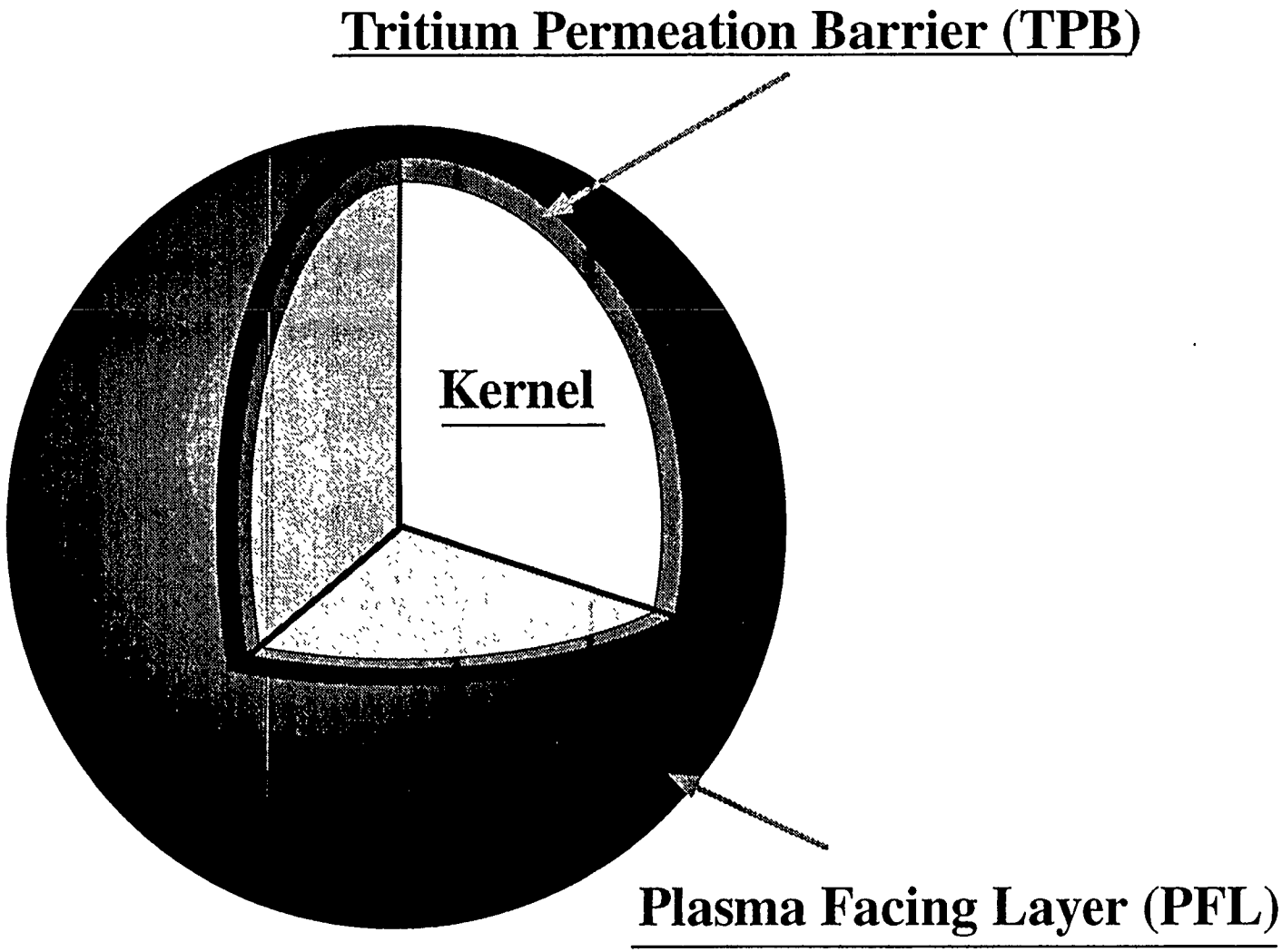

Multi-layer Pebble

Target of Irradiation Experiments

(1) **Integrity of multi-layer pebble under high heat flux irradiation**

- Kernel
- Coating layers
- Interface between layers
- Abnormal erosion of surface layer

(2) **Pumping performance**

- Pumping capacity
- Operational temperature
- Regeneration conditions

Test Pieces of Multi-Layer Pebble

SiC Kernel Pebble

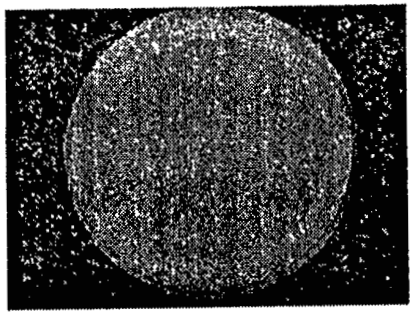

Carbon Kernel Pebble

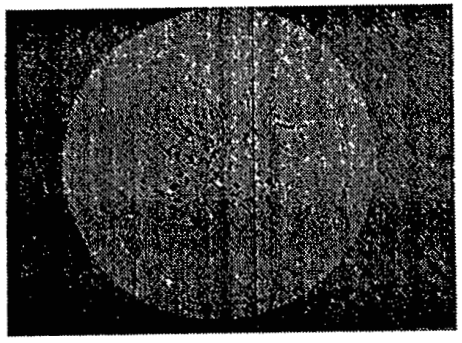

Ref. TRISO fuel particle for HTGCR

Structure	
UO_2 kernle	:600μm (diameter)
Buffer PyC	:60μm
IPyC	:30μm
SiC	:25μm
OPyC	:45μm

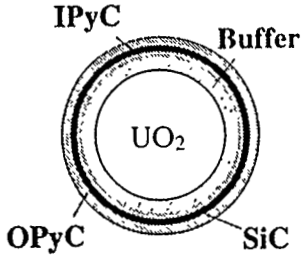

TRISO Coated Fuel Particle

Specification of Test Pieces

No.	Kernel		IPyC		TBL		PFL	
	Material	Diameter [μm]	Material	Thickness [μm]	Material	Thickness [μm]	Material	Thickness [μm]
C-1	C	807±40	CVD-C	7.79±1.20	CVD-SiC	7.19±1.25	CVD-C	87.65±15.4
C-2	C	807±40	CVD-C	7.79±1.20	CVD-SiC	15.66±2.17	CVD-C	58.12±10.7
SiC-1	SiC	1124±63	-	-	CVD-SiC	57.74±6.52	CVD-C	37.55±3.45
SiC-2	SiC	1124±63	-	-	CVD-SiC	109.28±5.36	CVD-C	32.48±5.04

Electron Beam Irradiation for Heat Load Test

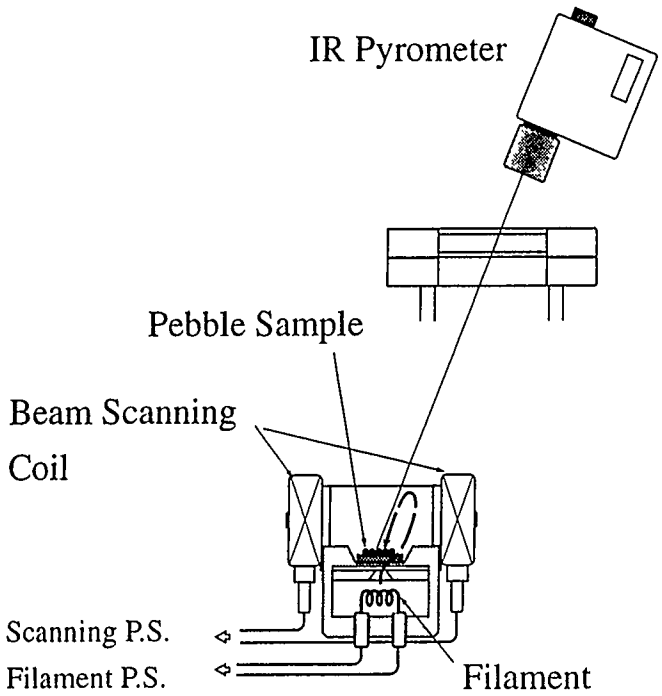

E-type Electron Beam Gun

E-Beam Irradiation System

Irradiation Parameters

Extraction Voltage	: 4 kV
Emission Current	: 30 mA
Beam Spot Size	: 3 × 6 mm
Heat Load	: 6.7MW/m^2
Scanning Period	: 6 sec.

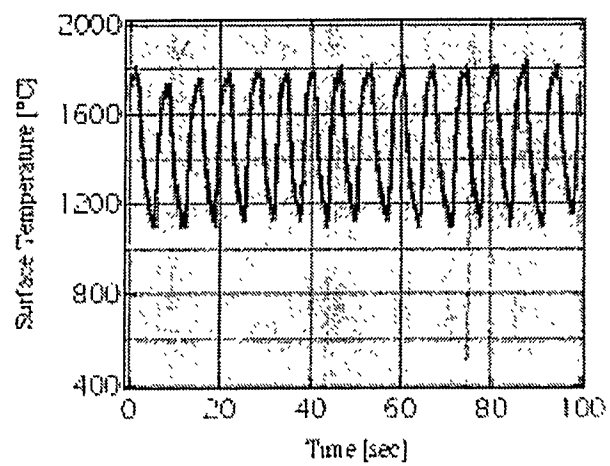

Temperature Evolution during Irradiation
(C-2 pebbles, 100 scans)

Supra-high Temperature Engineering Laboratory
Graduate School of Engineering, Osaka Univ.

Sequence of Integrity Test

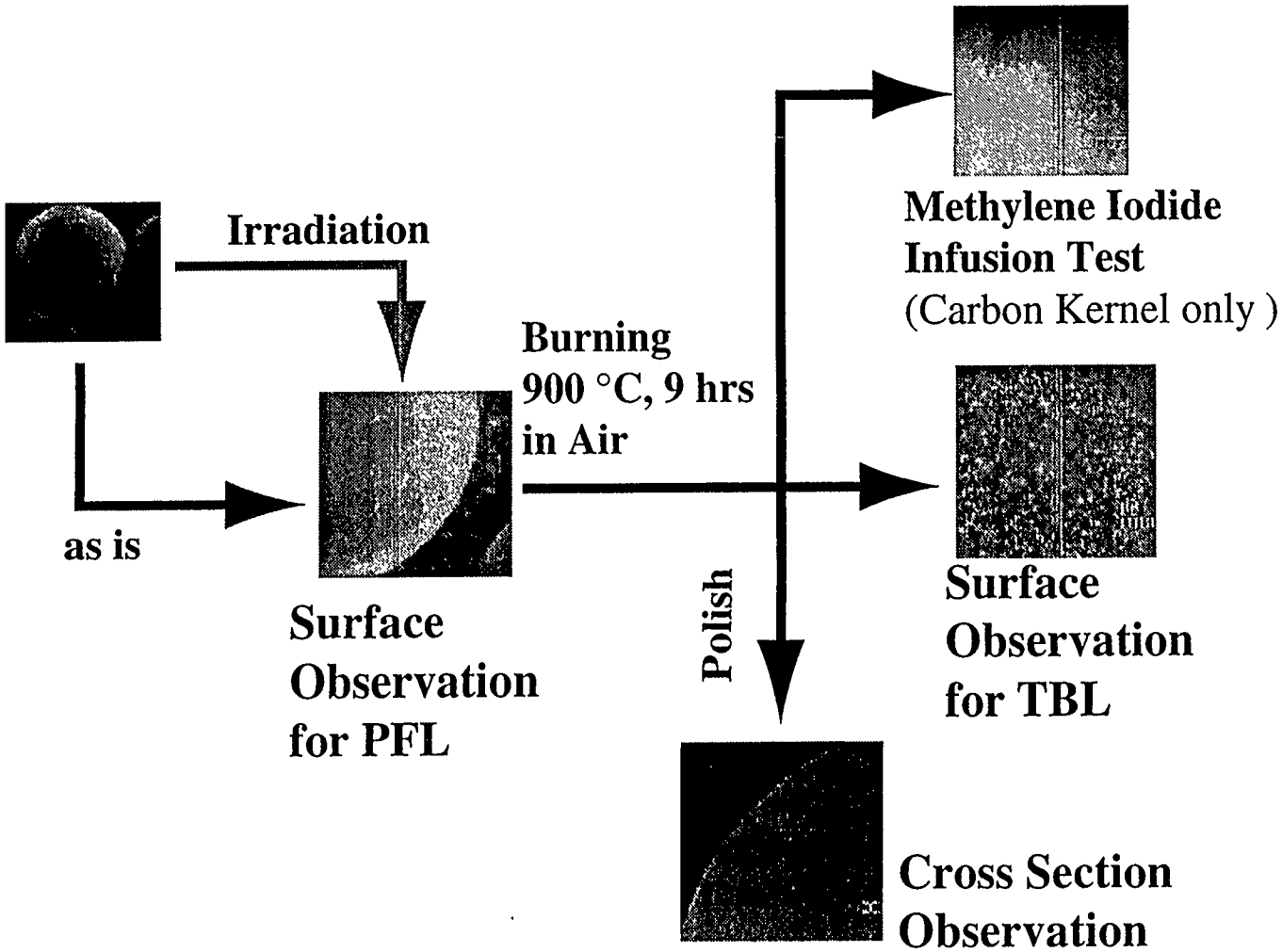

Integrity of Multi-Layer after Electron Beam Irradiation

	C-2		SiC-1	
	30scan	100scan	30scan	100scan
PFL observation	OK	OK	*1	*1
TPB observation	OK	OK	OK	OK
Methylene iodine infusion	OK	OK	*2	*2

*1 Surface layer were flaked off before irradiation
*2 Not applicable to SiC kernel

(a)
Before irradiation

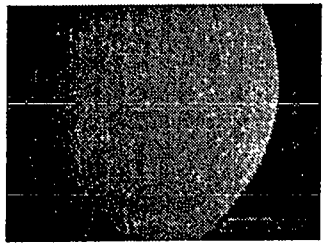

(b)
After 100 scans of irradiation

Surface observation of carbon kernel pebble (C-2) by SEM

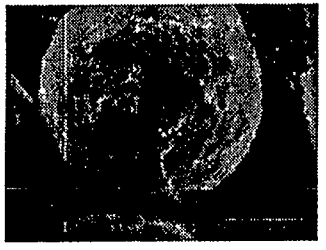

(a)
Before irradiation

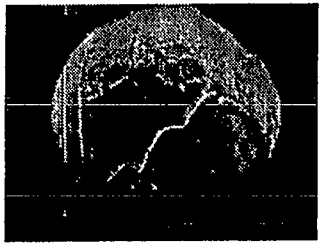

(b)
After 100 scans of irradiation

Surface observation of SiC kernel pebble (SiC-1) by SEM

Deuterium Beam Irradiation for Erosion Test

Irradiation Parameters

Species	:	D_3
Beam Energy	:	5 keV
Particle Flux	:	6.2×10^{21} D/m^2·s
Beam Pulse	:	1.5 - 3.0 s
Incident Angle	:	45, 60 degree
Irradiated Area	:	1×10^{-4} m^2

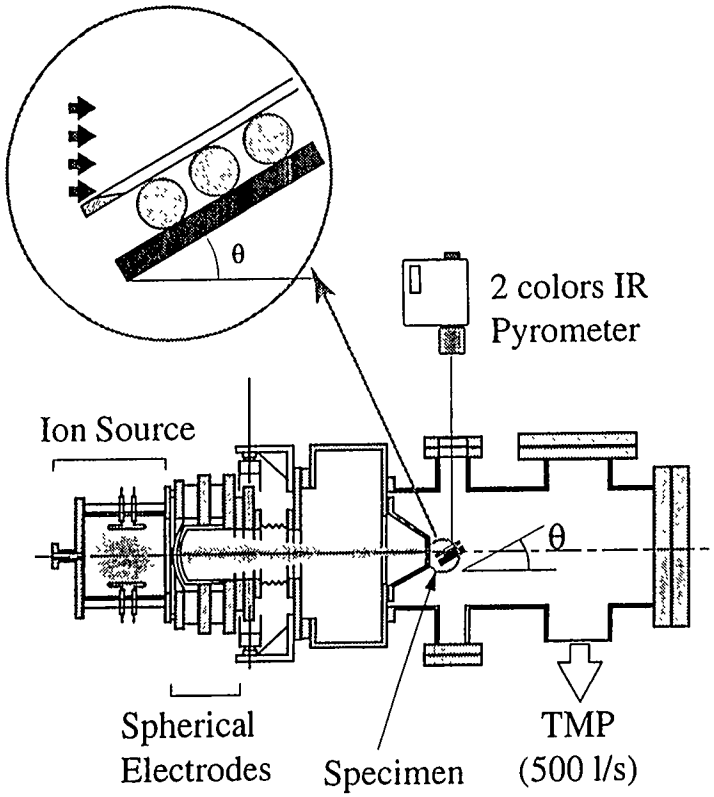

Neutral Beam Irradiation System

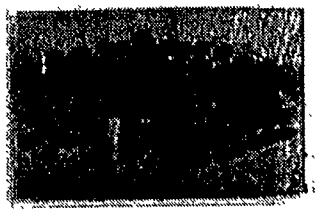

Specimen
(C-1 pebbles)

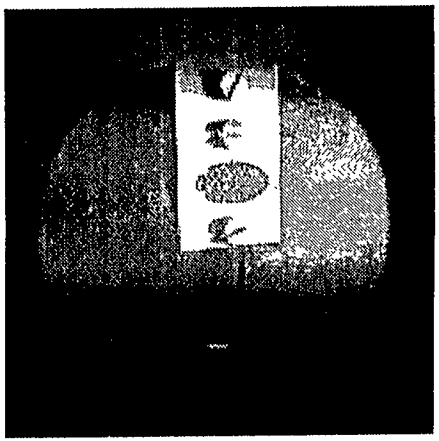

Specimen Irradiated by
Neutral Beam

Supra-high Temperature Engineering Laboratory
Graduate School of Engineering, Osaka Univ.

Erosion of Graphite Plasma Facing Layer

Erosion Yield by Weight loss method

		Fluence [D atoms/m^2]	Loss [μm]	Erosion Yield Y
Carbon Kernel	$\theta = 60°$	1.3×10^{24}	310	0.060
	$\theta = 45°$	2.1×10^{24}	420	0.068
SiC Kernel	$\theta = 60°$	1.2×10^{24}	300	0.060
	$\theta = 45°$	2.3×10^{24}	280	0.041

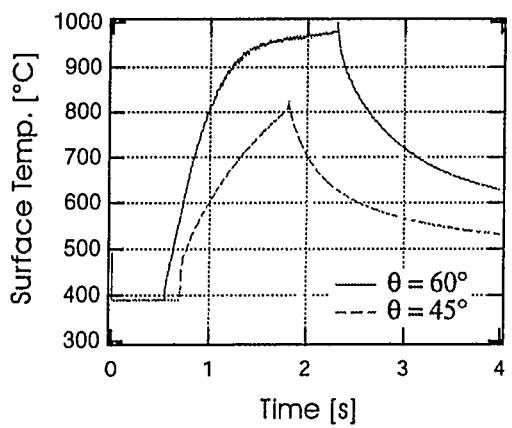

Surface Temperature of Pebble during Neutral Beam Irradiation (C-1 specimen)

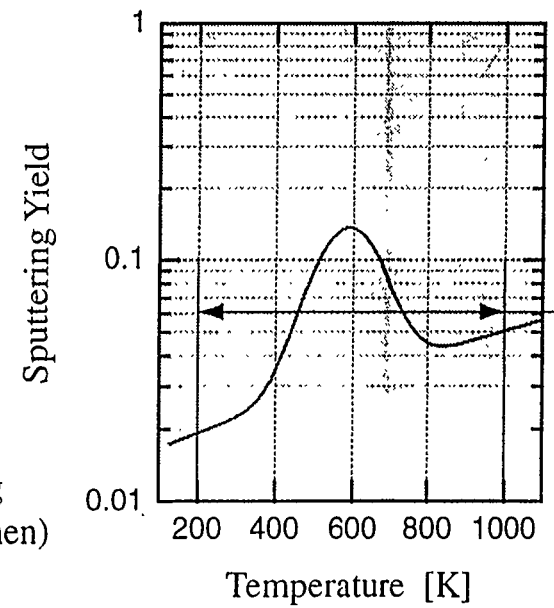

Averaged Yield (200-1000°C) ~ 0.061

Temperature Dependence of Erosion Yield by 1keV D^+ beam

Interface Failure of SiC Kernel Pebbles

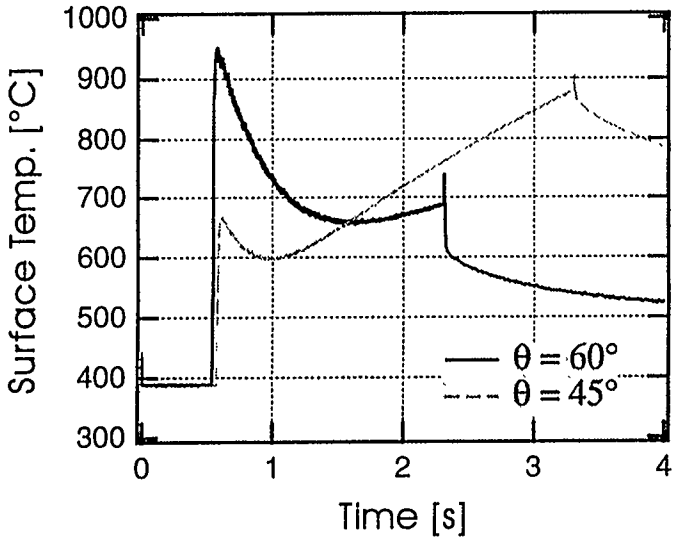

Surface Temperature of SiC Pebble during Neutral Beam Irradiation (SiC-2 specimen)
Sudden temperature rise is observed.

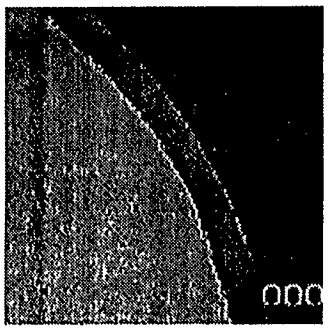

(a) Normal interface

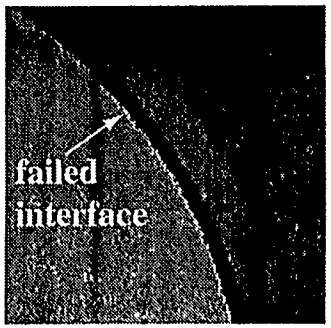

(b) interface failure

Cross section of SiC pebble before irradiation

Pumping Concept using Hydrogen Retention of Graphite

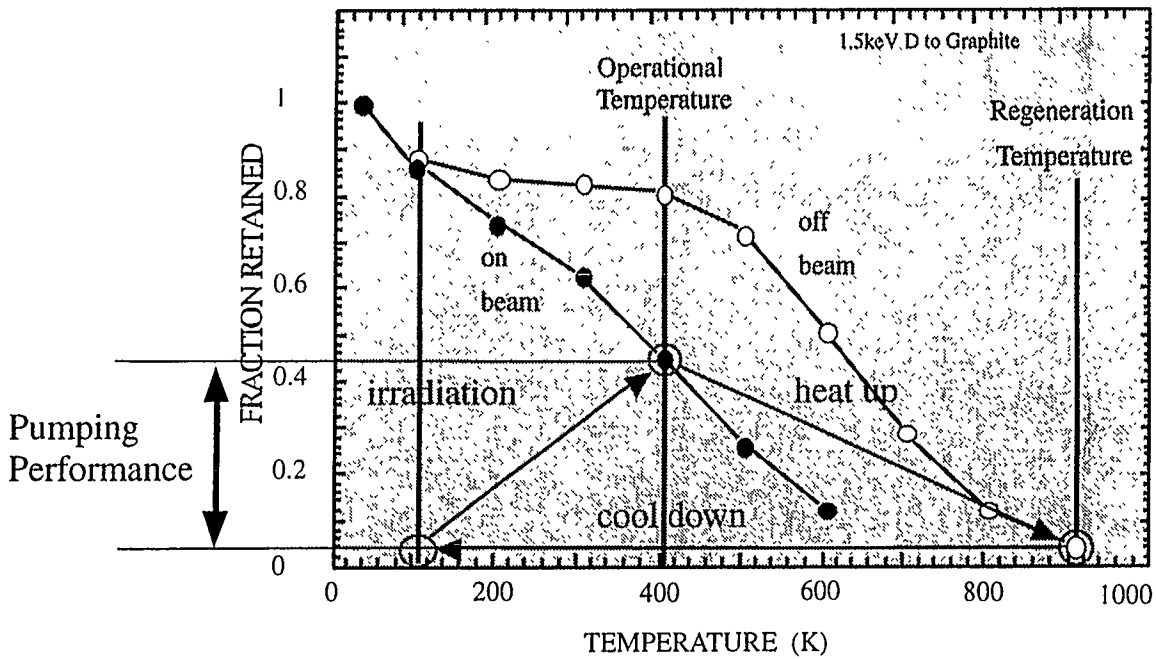

Ref. A. Sagara, et.al
"Design of Carbon Sheet Pump for LHD and Demonstration of Hydrogen Pumping"

Advantage

Large pumping capacity

Problems

Large heating energy to desorb fuel gas
Low operational temperature

Temperature dependence of satureated amount of retained hydrogen in graphite

Pumping Concept by using Transient gas Release

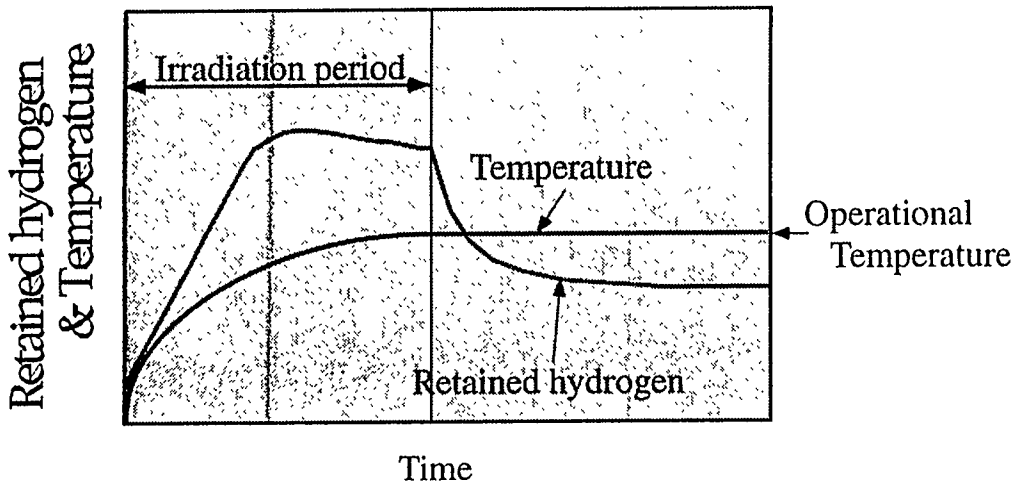

Advantage

Smaller heating energy

Problems

Lower pumping performance than the static case

No experimental data of transient release

Fig. Time evolution of retained hydrogen in graphite and temperature of graphite when the temperature is kept at the operational temperature after high flux irradiation.

In this case, hydrogen transiently releases from graphite just after the irradiation. → Its release can be used for the pumping.

Experimental

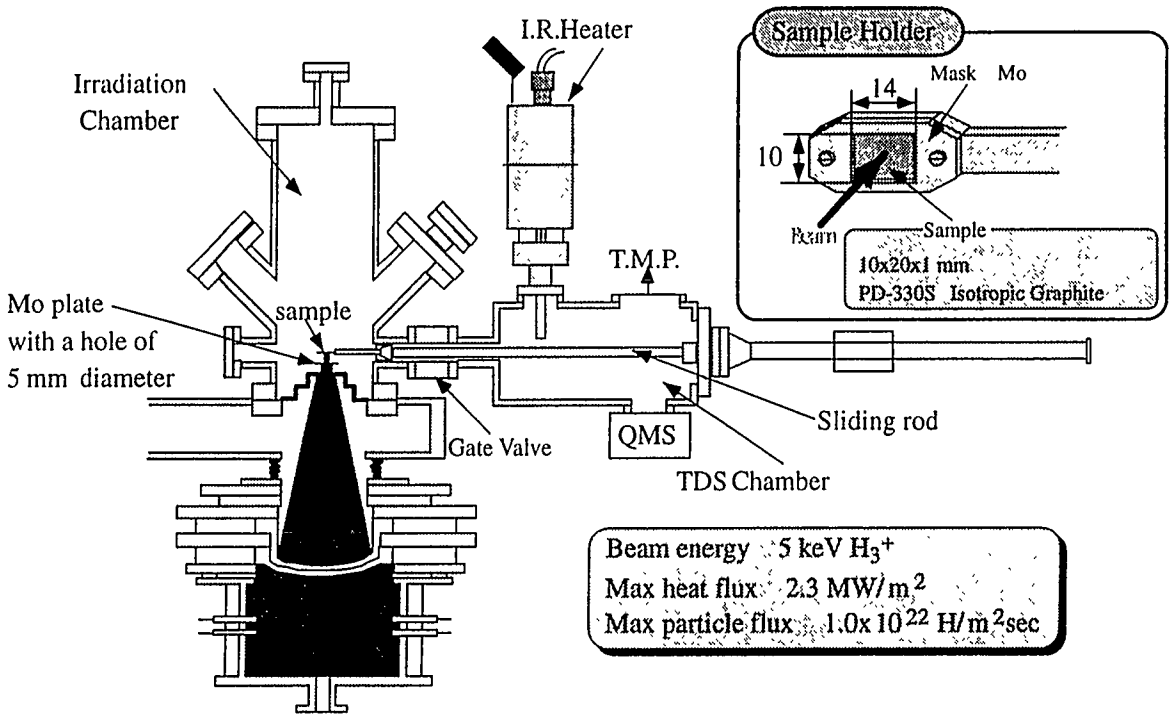

Schematic view of the experimental system for high flux irradiation and hydrogen release measurement.

Experimental Conditions

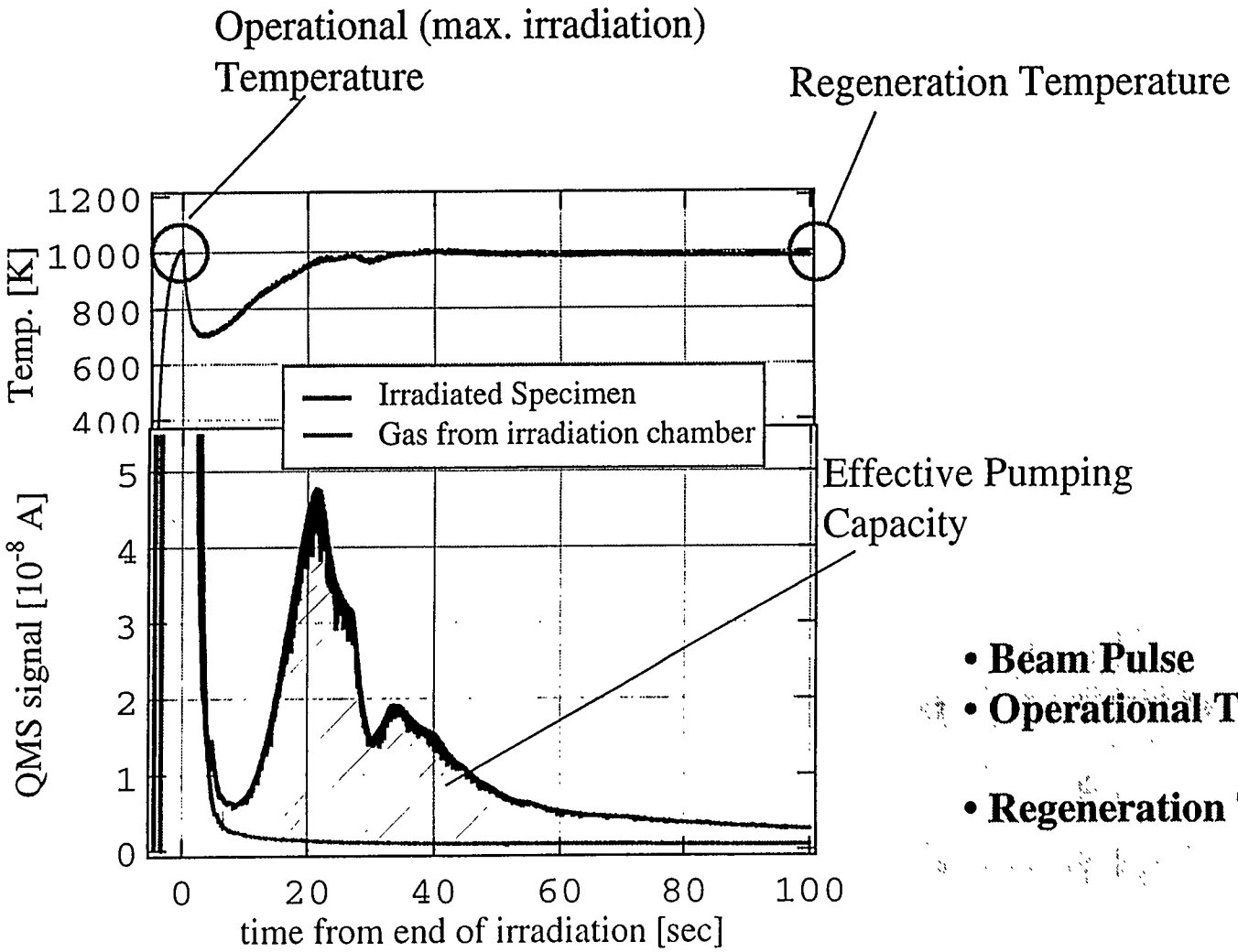

- **Beam Pulse 4sec**
- **Operational Temperature [K] 573,773, 973**
- **Regeneration Temperature [K] 573, 773, 973**

Supra-high Temperature Engineering Laboratory
Graduate School of Engineering, Osaka Univ.

Pumping Capacity (Operational Temp. = Regeneration Temp.)

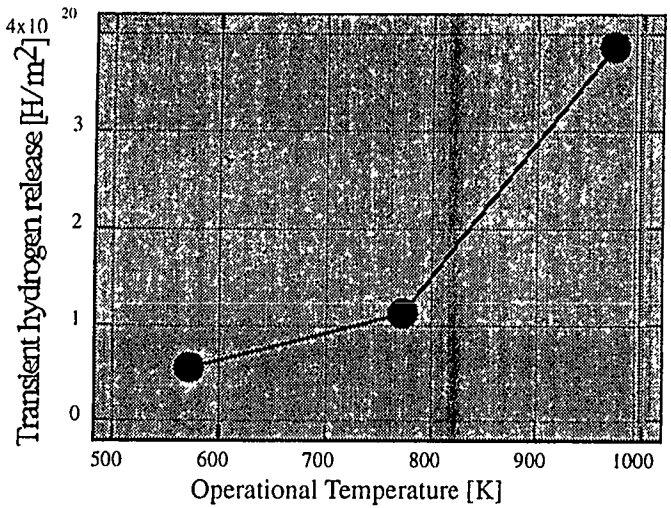

Fig. Operational temperature dependence of the transient hydrogen release from the graphite sample

The amount of transient hydrogen release was increasing with increase of the operational temperature.

→ The pumping performance of the pebble drop divertor by using the transient hydrogen release is increasing with increase of the operational temperature in the region to 1000 K.

Estimation of the Pumping Capacity of Pebble Drop Divertor

Pumping performance calculated by the transient hydrogen release at the operational temperature of 973 K.
(We assume that a pebble curtain is moving flat surface.)

Pumping speed per 1 meter of the toroidal length of divertor at pebble drop divertor	7.5 Pa m^3/s
Total pumping speed of the pebble drop divertor of the Tokakmak associated with ITER (major radius: 8.1 m)	380 Pa m^3/s
The gas feed in steady state operation of ITER	200 Pa m^3/s

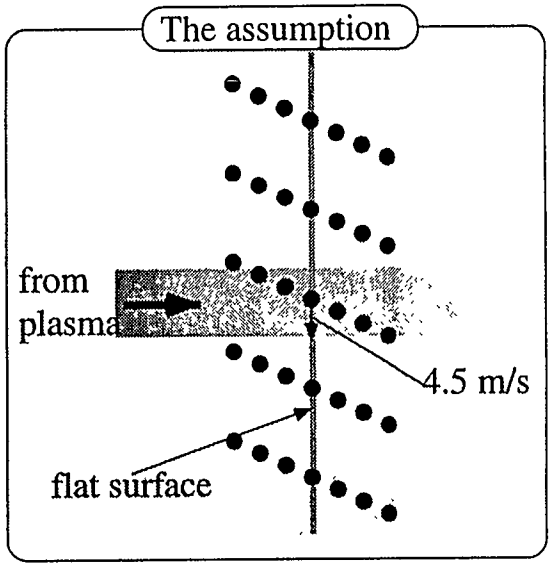

The pumping performance of the pebble drop divertor will satisfy the specification of fuel gas feed in steady state operation of ITER.

Summary

High Heat Flux Test of Multi-Layer Pebble

- Two types of divertor pebbles are fabricated to test the integrity of multi-layer coating in high flux irradiation. The one had a SiC kernel and the other had a carbon kernel. Both pebbles had SiC tritium permeation barrier layer and graphite plasma facing layer.
- Each type of pebbles was irradiated by 6.7MW/m^2 of electron beam gun. The failures caused by irradiation were not observed.
- The pebbles were irradiated by 5keV, D_3 beam with 6.2×10^{21}/m^2·s of particle flux. The erosion yield measured by weight loss was the same as the bulk graphite.
- The SiC kernel pebbles were shown that there were interface failures caused by fabrication process.

Pumping Concept using Transient Gas Release

- The amount of the transient hydrogen release was inceasing with increase of the operational temperature. The amount of maximum transient hydrogen release was 4.4 x 10^{20} H/m^2 at the operational temperature of 973 K.
- The pumping performance of the pebble drop divertor will satisfy the specification of fuel gas feed in steady state operation of ITER.

1999 US/Japan Workshop

Recent Results and New Opportunities in Thermal Hydraulics

D.L. Youchison[1], R.E. Nygren[1],
C.H. Cadden[2], D.E. Driemeyer[3], G.W. Wille[3]
S. Griegoriev[4], M.T. North[5]

[1] Sandia National Laboratories, P.O. Box 5800, Albuquerque, NM 87185-1129
[2] Sandia National Laboratories, P.O. Box 969, Livermore, CA 94551-0969
[3] The Boeing Company, P.O. Box 516, St. Louis, MO 63166-0516
[4] Efremov Institute, St. Petersburg, 189631 Russia
[5] Thermacore, Inc. 780 Eden Rd., Lancaster, PA 17601

November 03, 1999

OUTLINE

I. Flow instabilities in multi-channel, helium-cooled heatsinks

II. CHF testing of hypervapotrons and porous coatings

III. Heat transfer enhancement with helical wire inserts (HWIs)

IV. Opportunities for collaborative study

5931 01.01.03 11/03/99
dly:1999 US/Japan

Dual-channel circumferential flow porous metal helium divertor module exceeded original design specifications.

Helium divertor module design specifications

Parameter	Specification
Cross-section dimensions and shape	4.45 cm x 3.18 cm, rectangular
Outer shell material	GlidCop™ Al-15 bar
Porous medium	OFE copper powder
Particle diameter	0.102 cm, 12HP
Inner tube material	OFE copper D-shaped tubes
Number of channels	2
Panel length	4.45 cm
Heated area	6.45 cm^2
Heat load	12.9 kW
Maximum heat flux	2000 W/cm^2
Maximum surface temperature	400 °C
Test orientation	Horizontal
Helium pressure	4 MPa
Helium flow rate per channel	2.5 g/s
Total helium flow rate	5.0 g/s
Blower power	90 W

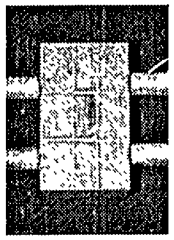

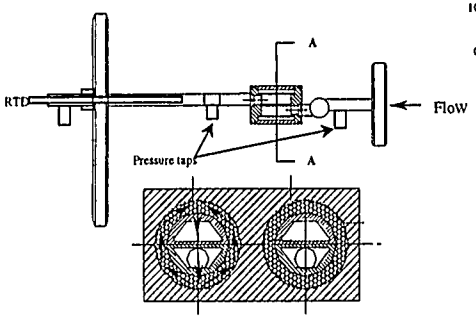

SECTION A-A

Helium divertor module is a dual channel, circumferential flow, porous metal device.

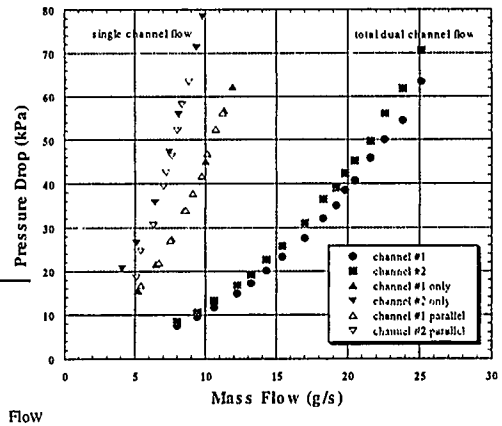

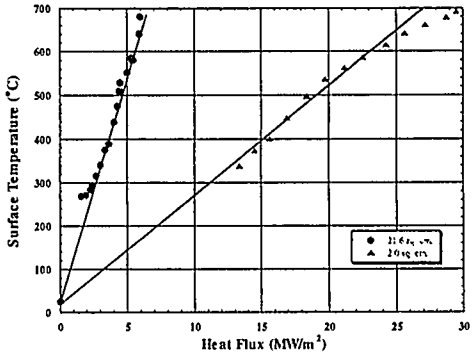

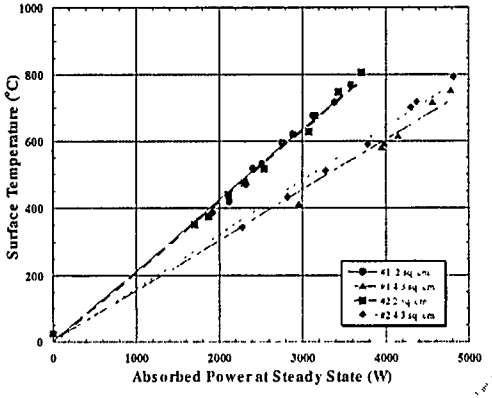

5931 01.01.03 11/03/99
dly:1999 US/Japan

Power sharing indicates little difference in mass flow distributions.

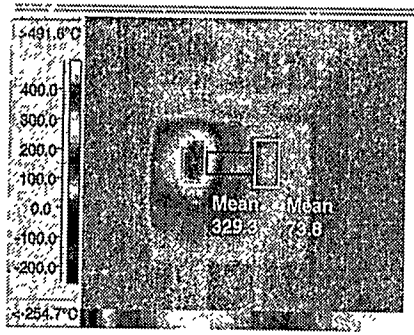

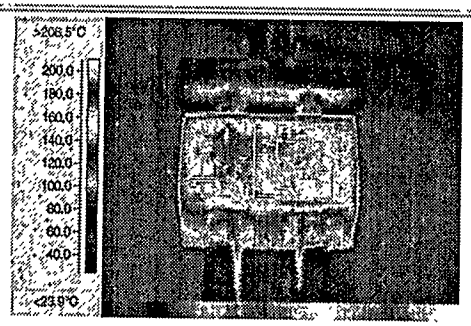

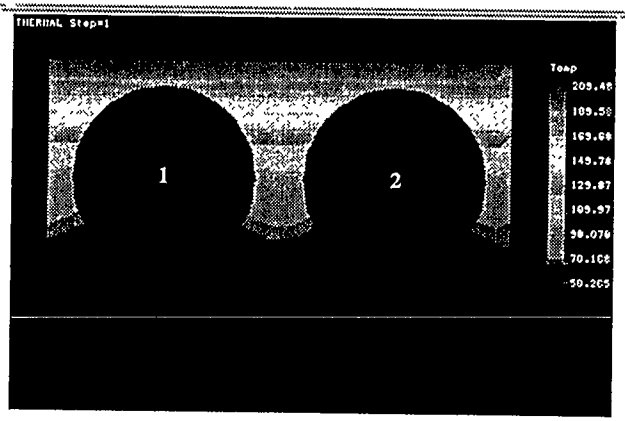

Uniform Heating

Channel	Heated Area (cm^2)	Heat Flux (MW/m^2)	Absorbed Power (W)	Mass Flow (g/s)	Surface Temperature (°C)
Channel #1	21.6	6	6437	7.8	680
Channel #2	21.6	6	6488	11	680
Channel #1	2	29.5	2774	11.05	691
Channel #2	2	29.5	3125	8.05	691

Non-uniform Heating

Channel	Heated Area (cm^2)	Heat Flux (MW/m^2)	Absorbed Power (W)	Mass Flow (g/s)	Surface Temperature (°C)
Channel #1	4.3	14.8	4780	11.05	753
Channel #2	4.3	0	1592	8.05	
Channel #1	2	23.7	3578	10.8	769
Channel #2	2	0	1165	7.6	
Channel #1	4.3	0	1263	10	
Channel #2	4.3	14.1	4814	8.3	793
Channel #1	2	0	1023	10.2	
Channel #2	2	24.9	3949	8.25	806

A steady state temperature profile through the center plane of the divertor module was obtained by numerical modeling. A heat flux of of 227 W/cm^2 applied to the top surface revealed a constant heat transfer coefficient of 20,400 $W/m^2 \cdot K$ on the inside wall of channel #1 and 26,000 $W/m^2 \cdot K$ on the inside wall of channel #2.

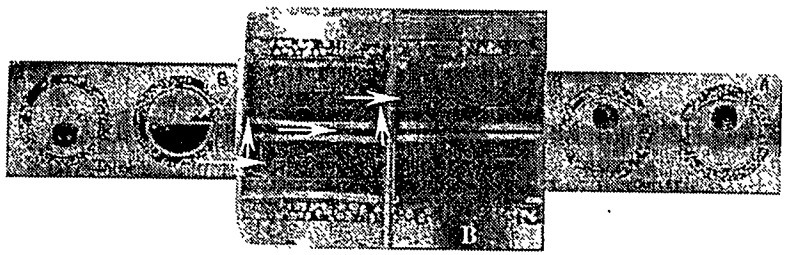

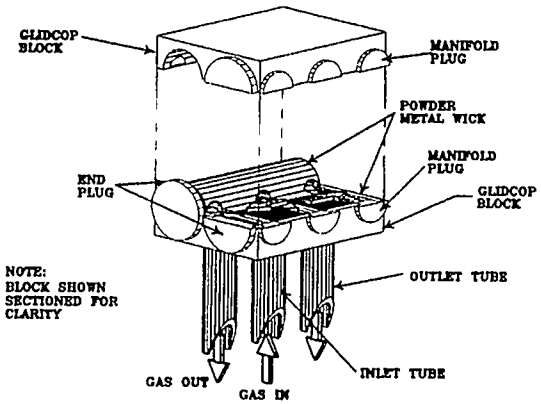

5931 01.01.03 11/03/99
dly:1999 US/Japan

CHF tests were performed on attached-fin hypervapotrons and porous coated mock-ups.

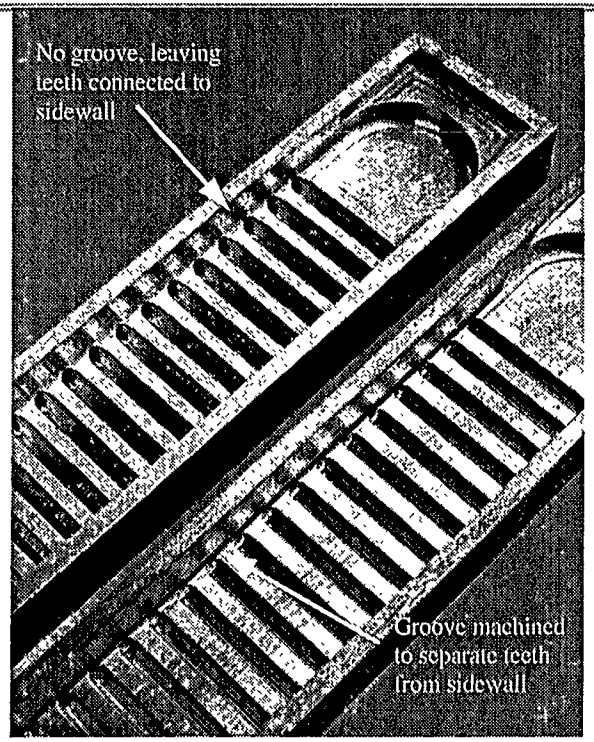

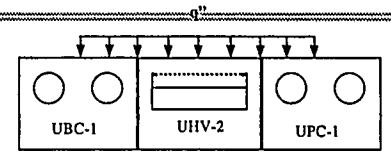

attached-fin hypervapotron channel (UHV-2) with side shields

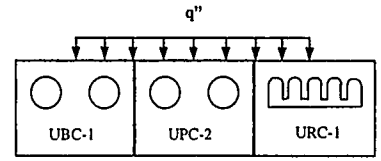

porous-coated CuCrZr channels (UPC-2) with side shields

Fig. 3. Full beamwidth overspray for uniform heat loading required high performance side shields.

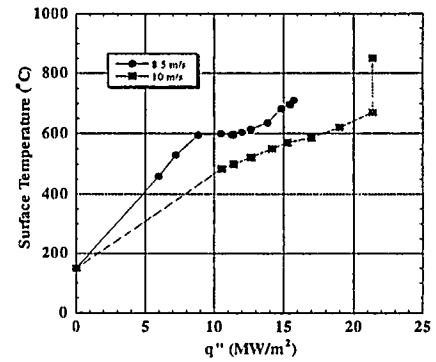

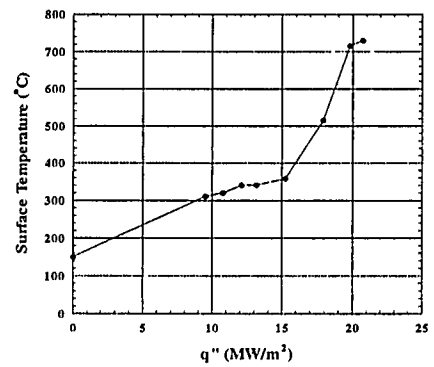

HV: 21.3 MW/m^2
PC: 24.5 MWm^2
ST22: 27.4 MW/m^2

CHF values for HV in agreement with JAERI CHF database, but 30% lower than CEA database. ???

5931 01.01.03 11/03/99
dly:1999 US/Japan

Collaboration with JAERI and CEA on ST22 CHF testing was highly successful.

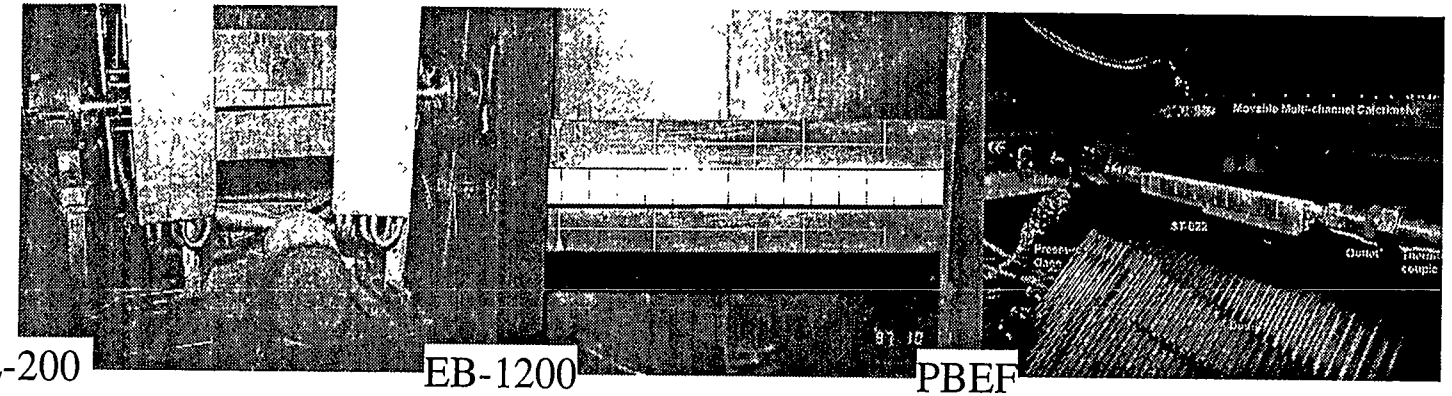

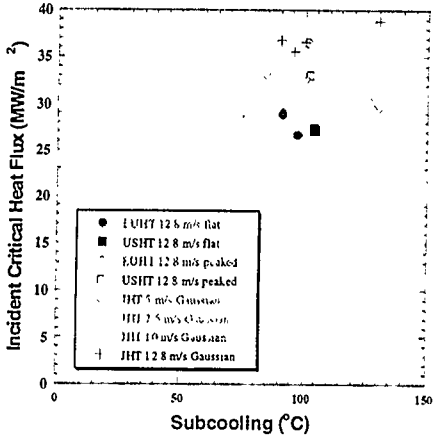

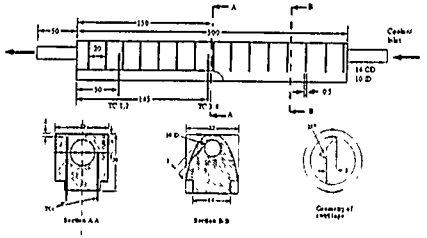

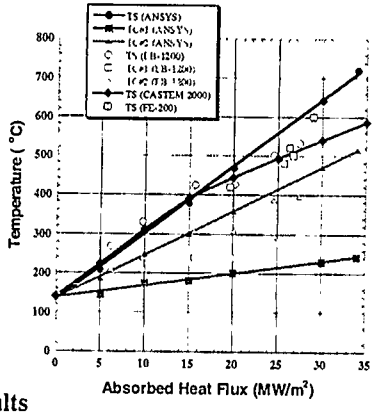

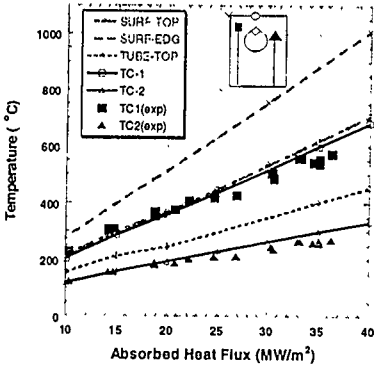

CHF Results

Test Facility	CEA FE-200	Sandia EB-1200	JAERI PBEF
Uniform profile	26.7	27.4	
Peaked profile	36.6	33	38

Bore scope examinations were conducted to verify braze integrity.

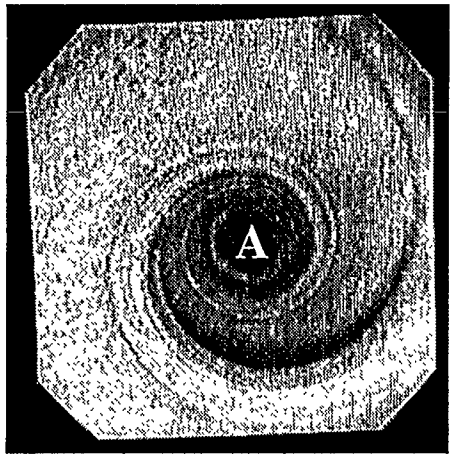

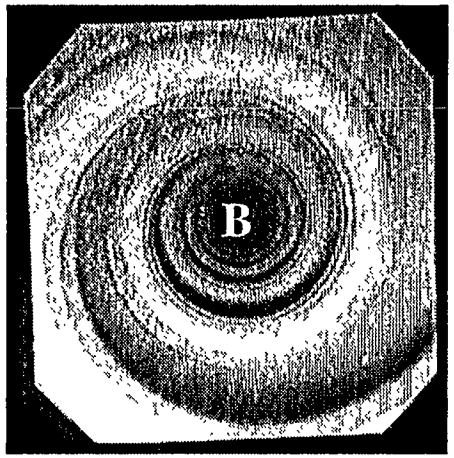

Mock-up C

End A: 20-mm-pitch
End B: 10-mm-pitch

Mock-up A

End A: 10-mm-pitch
End B: 5-mm-pitch

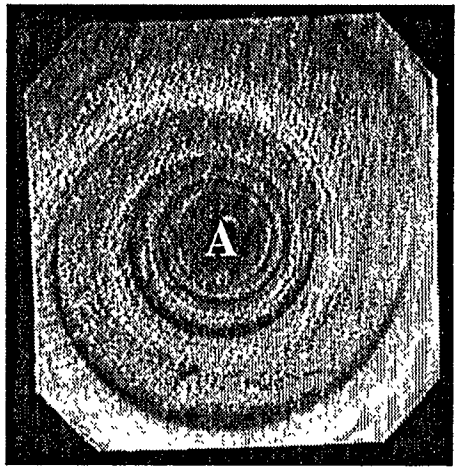

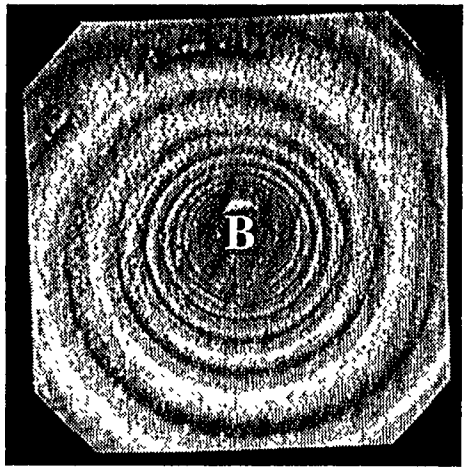

5931 01.01.03 11/03/99
dly:1999 US/Japan

X-rays were taken to locate the wire windings and position TCs.

X-Ray Image of HWI Mockup A

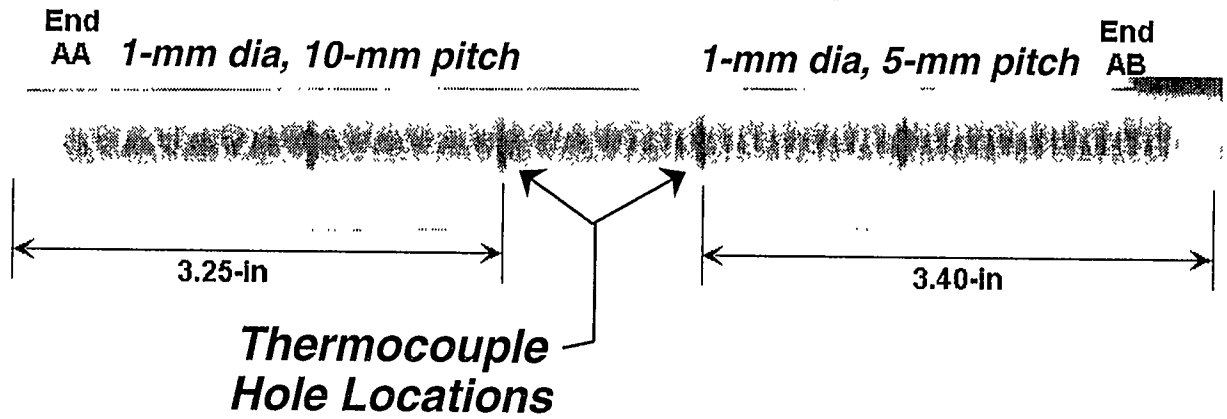

X-Ray Image of HWI Mockup C

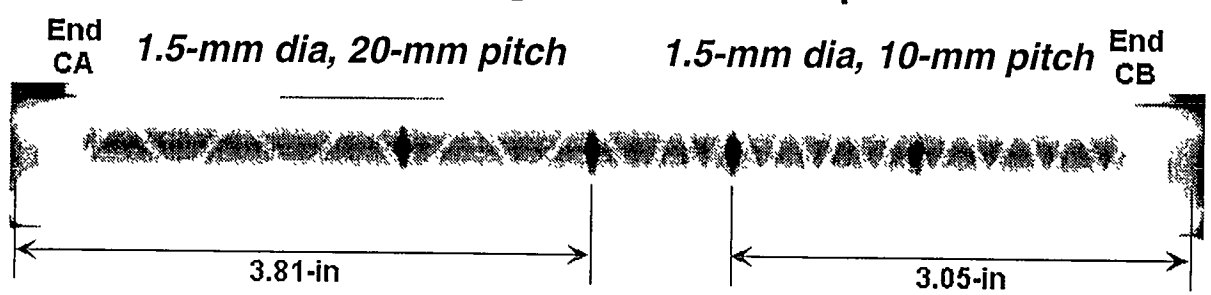

5931 01.01.03 11/03/99
dly:1999 US/Japan

The 20-cm-long HWIs were tested in the Electron Beam Test System (EBTS).

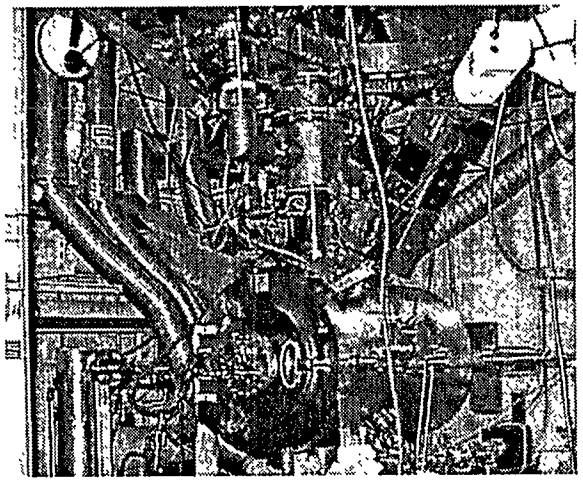

EBTS Operating Parameters

Beam Power	30 kW
Acceleration Voltage	30 kV
Beam Current	0.002 - 1 ampere
Target Area	0.1 to 100 cm^2
Pulse Length	from 2 ms to CW

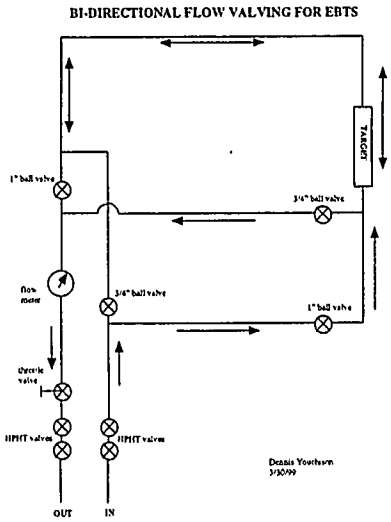

Diagnostics for HWI Exp'ts

instrument	measurement
Pyrometers (2)	Surface temperatures
Infrared camera & Video digitizer	Surface temperature profiles
Thermocouples (10 of 16)	Bulk temperatures
Residual gas analyzer	Partial pressures
Water calorimetry	Heat removal capability
Bore scope	*in situ* observations
TV monitoring system	Visual records

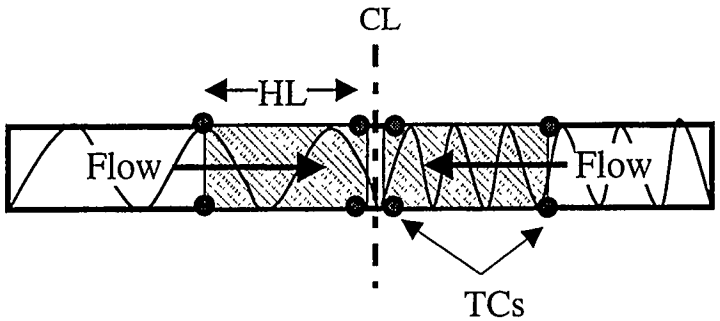

Heated Length, HL=3.6 to 2.2 cm

5931 01.01.03 11/03/99
dly:1999 US/Japan

CHF test plan investigated each pitch under 8 different flow conditions.

Evaluate a full 4-element matrix of wire diameters and pitches

- 1.0-mm diameter at 10-mm and 5-mm pitches
- 1.5-mm diameter at 20-mm and 10-mm pitches

Reverse water flow during testing so wire pitch being evaluated is at entrance end during CHF test

Perform tests over standard ITER matrix of conditions so results can be correlated with prior CHF tests on swirl tape, porous coatings, and hypervapotron mockups

- 100 & 130°C Inlet Subcooling – 4, 5 MPa Inlet Pressure
- 7, 12 m/s flow velocity – Uniform heat flux profile

Thermal response curves to CHF were obtained using a uniform heating profile.

5931 01.01.03 11/03/99
dly:1999 US/Japan

The 1.5-mm-dia wire thermal response curves reveal a few surprises. Response of 1-mm-dia wire was more consistent.

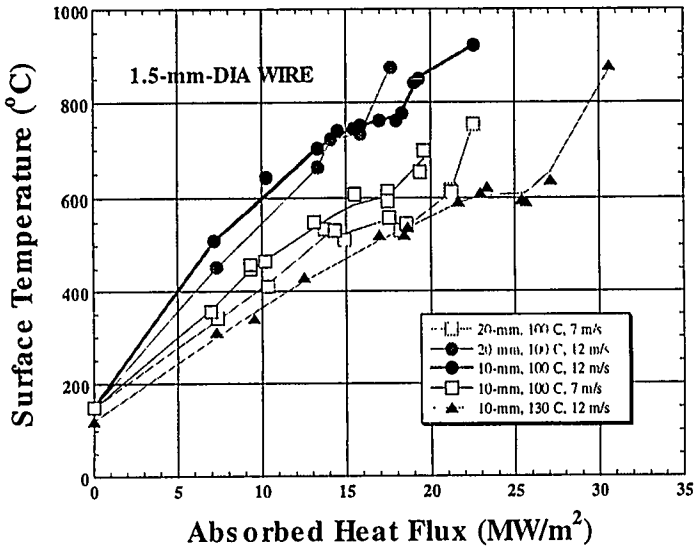

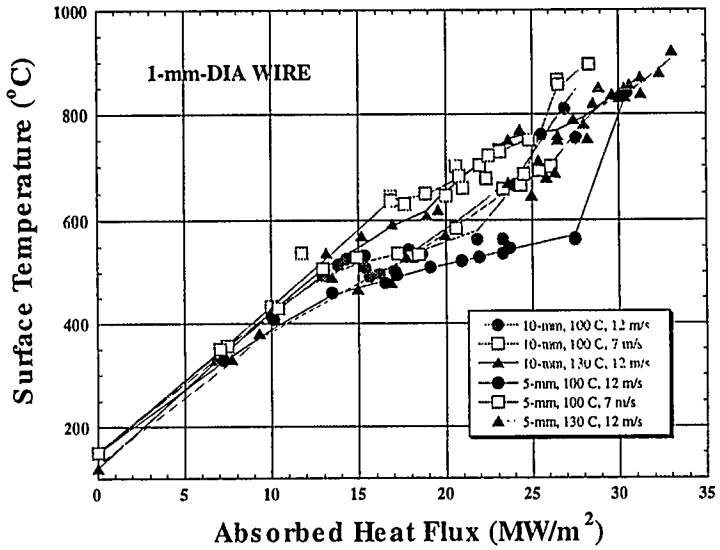

1.5-mm-DIA wire performed better at at 7 m/s compared to 12 m/s.
10-mm pitch better than 20-mm pitch at 12 m/s, not at 7 m/s.

1-mm-DIA wire performed better at 12 m/s compared to 7 m/s.
5-mm pitch better than 10-mm-pitch at all velocities.

k inconel = .077 W/cm °C
k CuCrZr = 3.5 W/cm °C

Inconel/CuCrZr

1.0 DIA	1.5 DIA
.203 (5)	.157 (10)
.105 (10)	.09 (20)

5931 01.01.03 11/03/99
dly:1999 US/Japan

At moderate flow velocities, HWIs show less sensitivity to velocity than swirl tubes.

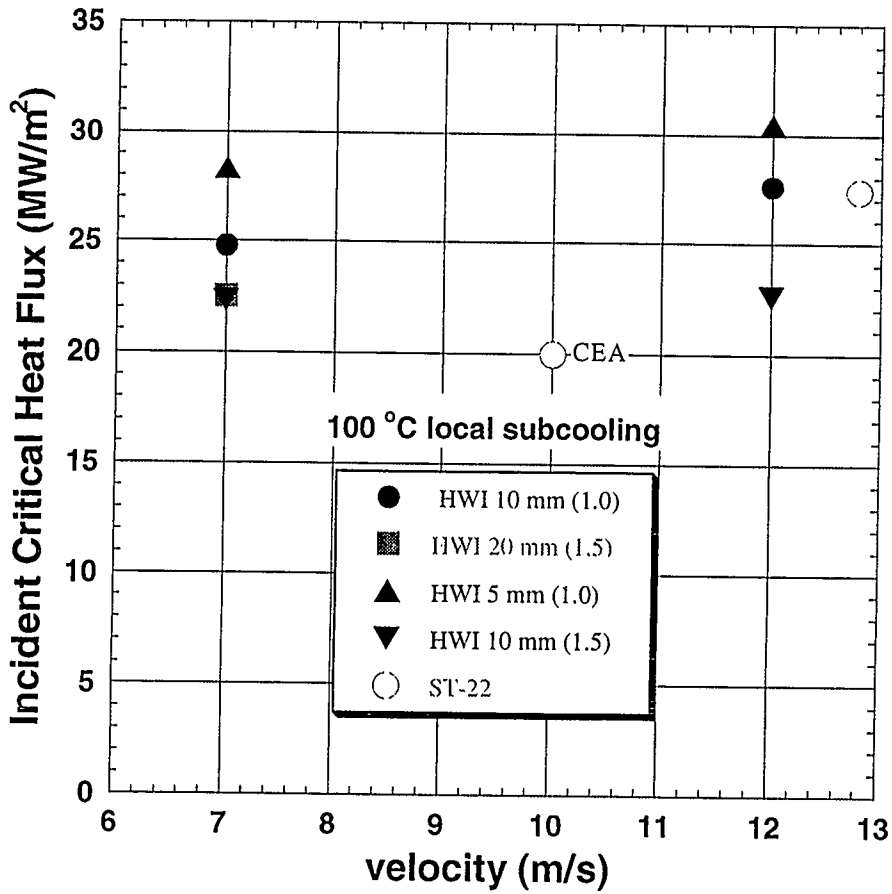

5931 01.01.03 11/03/99
dly:1999 US/Japan

Helical wire inserts exhibit excellent CHF performance compared to other heat transfer enhancement techniques recently tested at Sandia's PMTF.

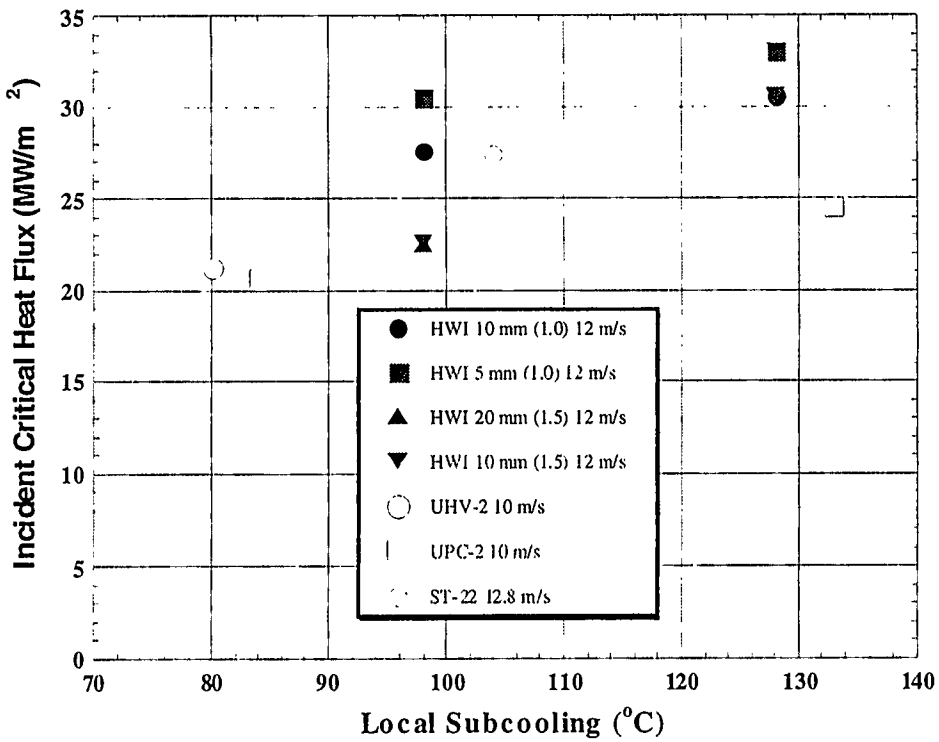

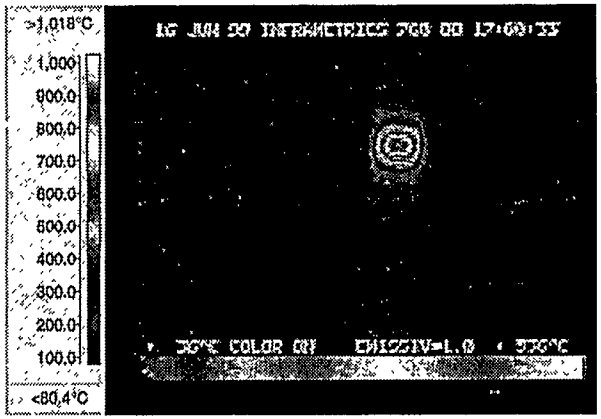

5931 01.01.03 11/03/99
dly:1999 US/Japan

Flow characteristics, obtained for each HWI mock-up, show relatively high pressure drops.

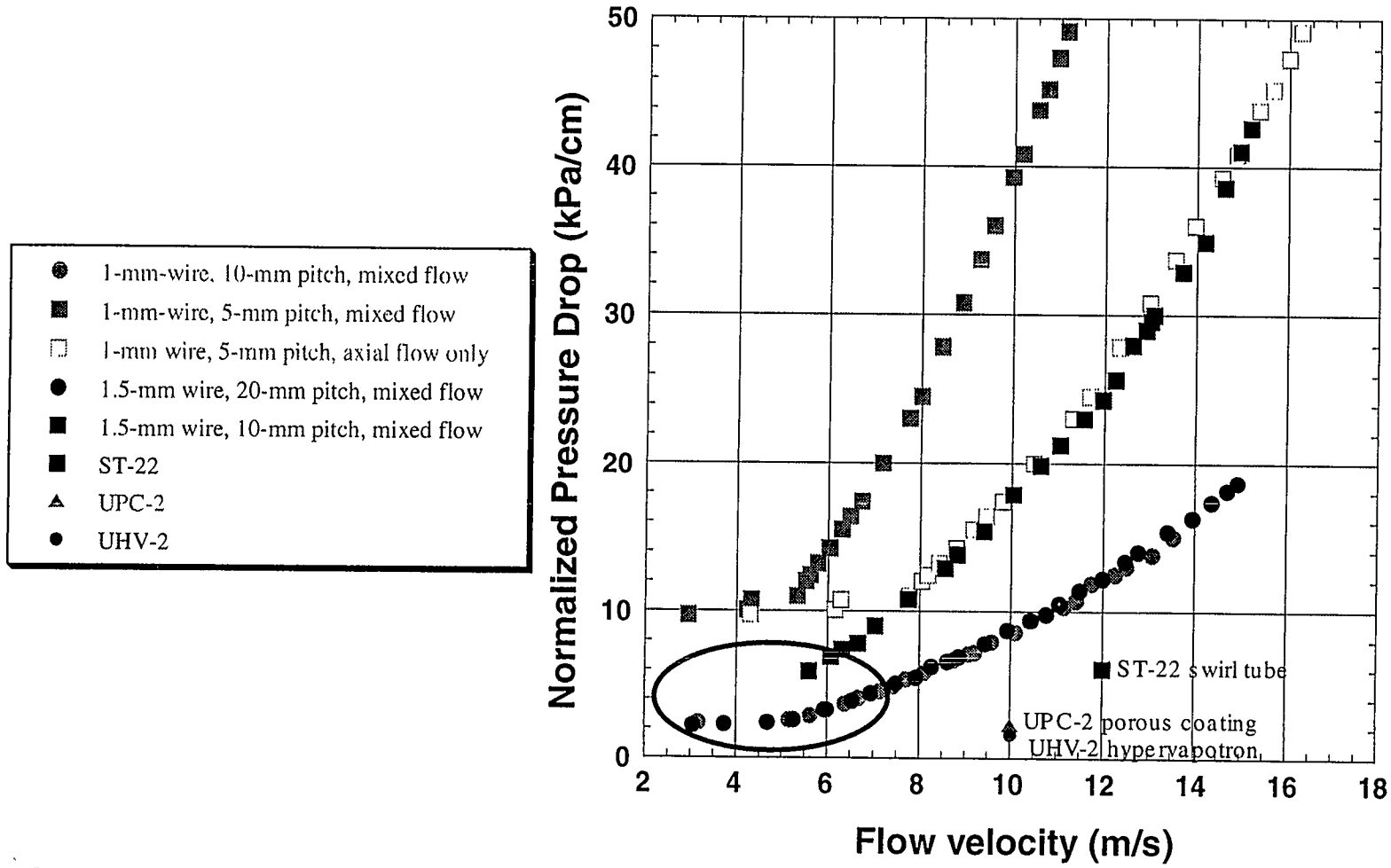

5931 01.01.03 11/03/99
dly:1999 US/Japan

CHF enhancement often entails a pressure drop penalty which entails increased pumping power and more expense.

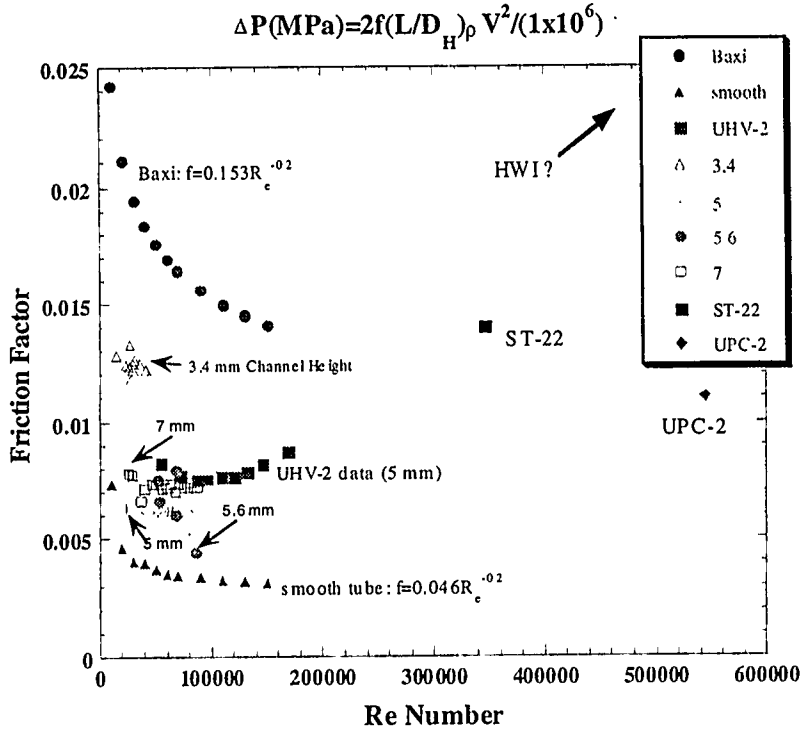

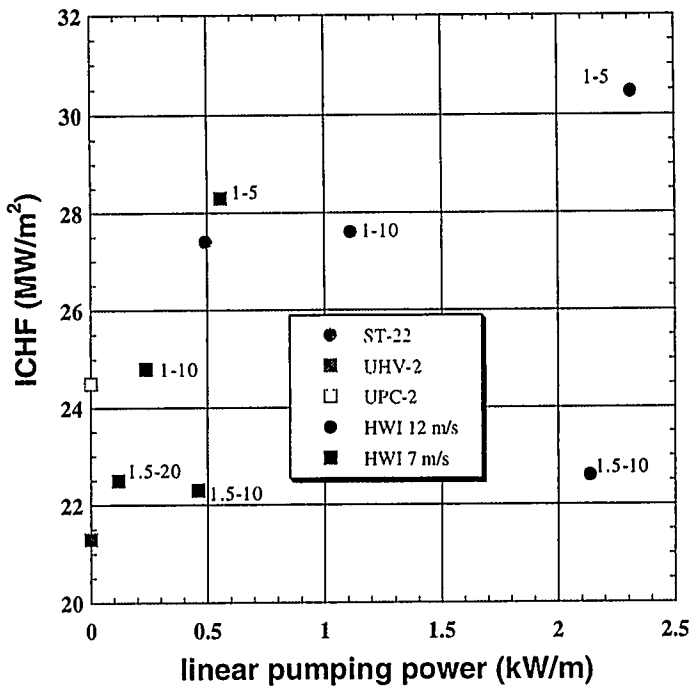

5931 01.01.03 11/03/99
dly:1999 US/Japan

Concluding Remarks

Opportunities for collaboration exist in TH of advanced heatsinks.

- A pressure drop correlation is needed for HWI and screw tube.
- Like the HV, the thermal hydraulics for HWIs is poorly understood. A coupled CFD and heat transfer model is required. (university participation in Japan)
- SNL Film3.0 post-CHF enhancement to ABAQUS for smooth and swirl tubes is available.
- CHF database comparison and cross check of experiments has proven helpful.
- Advanced diagnostics and facility designs for liquid metal experiments are necessary. (thermography and calorimetry)
- Specialist workshops on gas cooling, liquid metals, joining techniques, wall conditioning, etc. help focus the community.

5931 01.01.03 11/03/99
dly:1999 US/Japan

HWI mock-ups were fabricated at Boeing using two wire sizes each with two different wire pitches brazed in by Sandia - California.

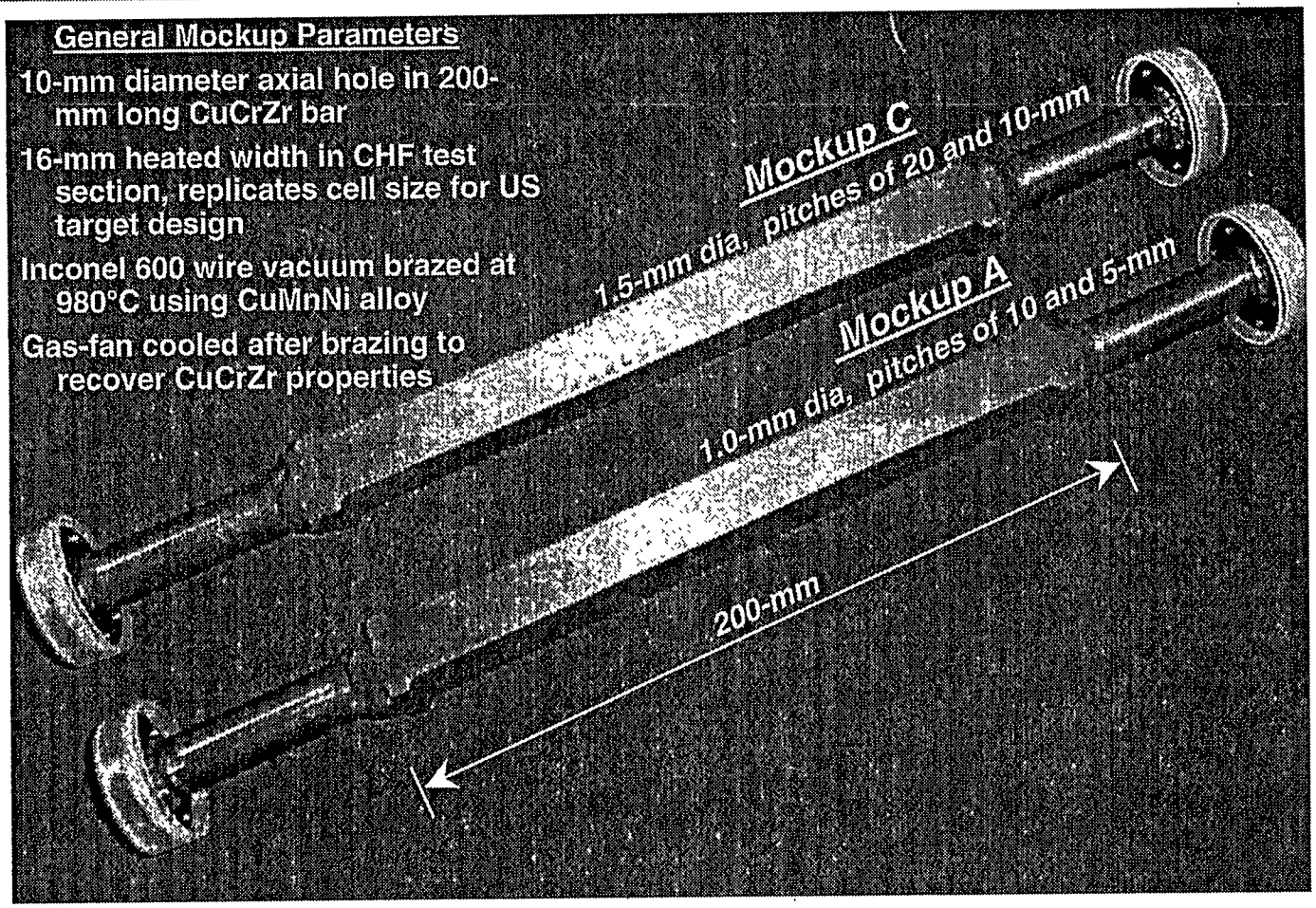

5931 01.01.03 11/03/99
dly:1999 US/Japan

JOINT EUROPEAN TORUS

Design Issues and Fatigue Lifetime of JET Hypervapotron Beam Stopping Elements

Dragoslav Ćirić
Test Bed Group,Neutral Beam Heating Division
JET Joint Undertaking, Abingdon, Oxfordshire OX14 3EA, UK

Acknowledgements:
M. Akiba, K. Sato, K. Yokoyama (JAERI)
H-D. Falter, D. Martin (JET)

1999 US-Japan Workshop on Plasma Surface Interactions and High Heat Flux Components for Next Fusion Devices
November 1-4, 1999, St. Francis Hotel, Santa Fe, New Mexico

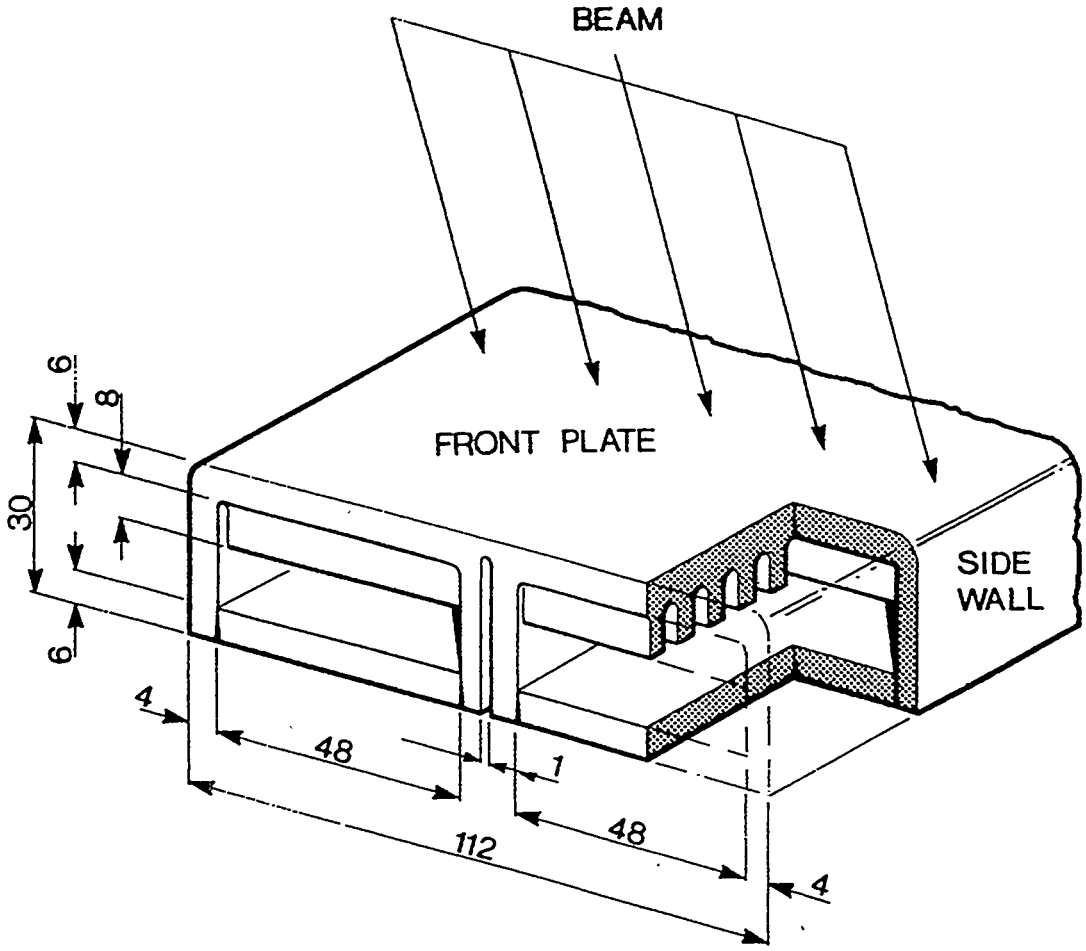

Dimensions of the standard JET flat Hypervapotron

Hypervapotrons at JET

- Beam stopping elements (dumps, scrapers, calorimeters) of two JET Neutral Beam Injector boxes and the Neutral Beam Test Bed - total of ~300 elements dissipating up to 100 MW of power.
- Most of the elements have been in use from the beginning of NB operation at JET in 1986 ⇒ tens of thousands of full stress cycle at peak power density of ~10 MW/m^2 (0.5 MW per element).
- None of beam stopping elements have failed so far.

Reasons for Testing

- Recent JET program (introduction of large quantities of Tritium) and prolonged operation of JET facility required validation of the safety and adequacy of the design ⇒ fatigue tests.
- The most loaded component (NIB 4 Box Scraper) limits the neutral beam power injected into JET plasma ⇒ modifications and replacement of the Box Scraper.
- Hypervapotrons considered as heat sinks and beamline elements of ITER.

Tested Components

a) Standard JET hypervapotron geometry (reduced length, one cooling channel);

b) Modified geometry (thinner front wall, lower fin height) - new Box Scraper element;

c) Full size Box Scraper prototype.

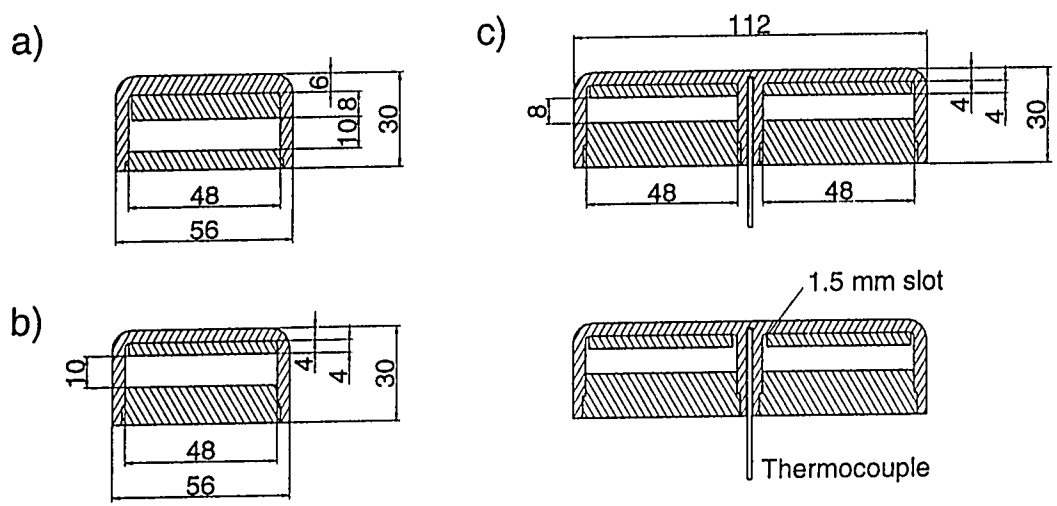

Figure 1: Cross-sections of hypervapotrons used in the tests.

Elements (a) and (b) fabricated from the existing calorimeter elements, which have experienced >15000 cycles at full power (~10 MW/m²).

Elements (a) and (b) tested using electron beams at JAERI Electron Beam Irradiation System (JEBIS).

Element (c) characterised using Hydrogen beams at JET NB Test Bed.

Table 1: Hypervapotron geometry and experimental conditions

Test element	a) Standard JET hypervapotron	b) New Box Scraper hypervapotron	c) New Box Scraper prototype
Material	CuCrZr	CuCrZr	CuCrZr
Front wall thickness (mm)	6	4	4
Fin height (mm)	8	4	4
Length of the element (m)	0.45	0.45	0.975
Number of cooling channels	1	1	2
Water channel W×H (mm^2)	48×10	48×10	48×8
Water flow (l/s)	1.8	2.8	2.3 – 6.6
Water velocity (m/s)	3.7	5.8	3.0 – 8.6
Heat flux source	Electron beam	Electron beam	Hydrogen beam
Pulse on period (s)	2	1	5
Pulse off period (s)	3	3	-
Exposed length (mm)	110	140	975
Angle of incidence (degrees)	90	90	29
Peak power density (MW/m^2)	13	16	3.5 – 19.0
Average power density (MW/m^2)	10	13	1.5 – 8
Maximum total power (MW)	.06	.1	0.8
Pre-pulse temperature (°C)	< 50	< 50	< 50
Maximum surface temperature (°C)	430	370	450
Total number of cycles	10061	7009	250
Diagnostics used in experiment	IR & video imaging	IR & video imaging	IR & video imaging, water & inertial calorimetry
Experimental facility	JAERI – JEBIS	JAERI – JEBIS	JET - NB Test Bed

Fatigue Tests at JEBIS

Objective

a) To check survivability of the existing aged components (standard design) at present full power load.
b) To check the adequacy of the new hypervapotron design for higher power.

Experimental conditions

- Fixed electron beam power: average power equal to the design value for a specific element (peak power density ~30% above nominal value).
- Pulse on and off periods adjusted to allow heat-up to ~90% of the equilibrium surface temperature and cool-down to <50°C.
- Only central regions of the elements exposed to the heat flux - adequate for simulating stress cycle conditions.

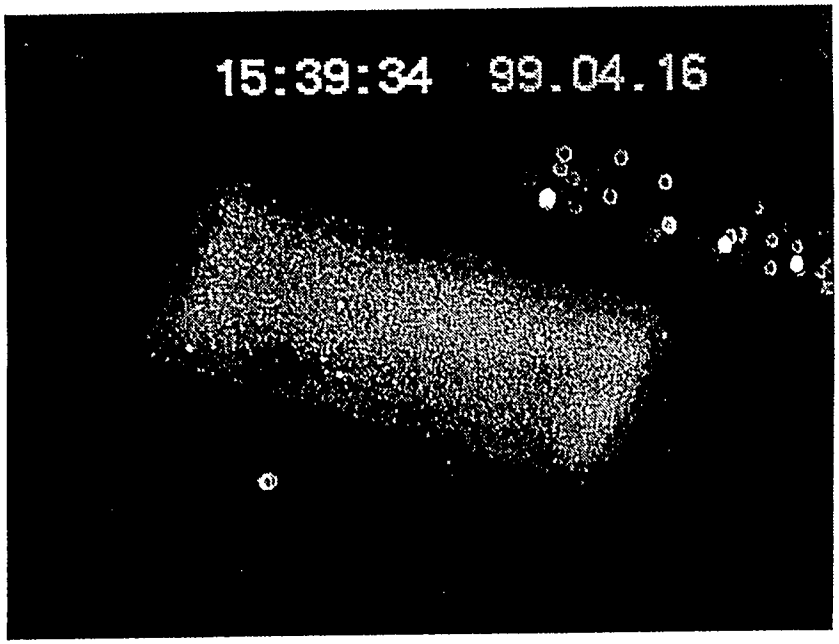

Figure 2: New Box Scraper element exposed to electron beam at the end of the fatigue test.

Fatigue Tests at JEBIS (continued)

Surface temperature

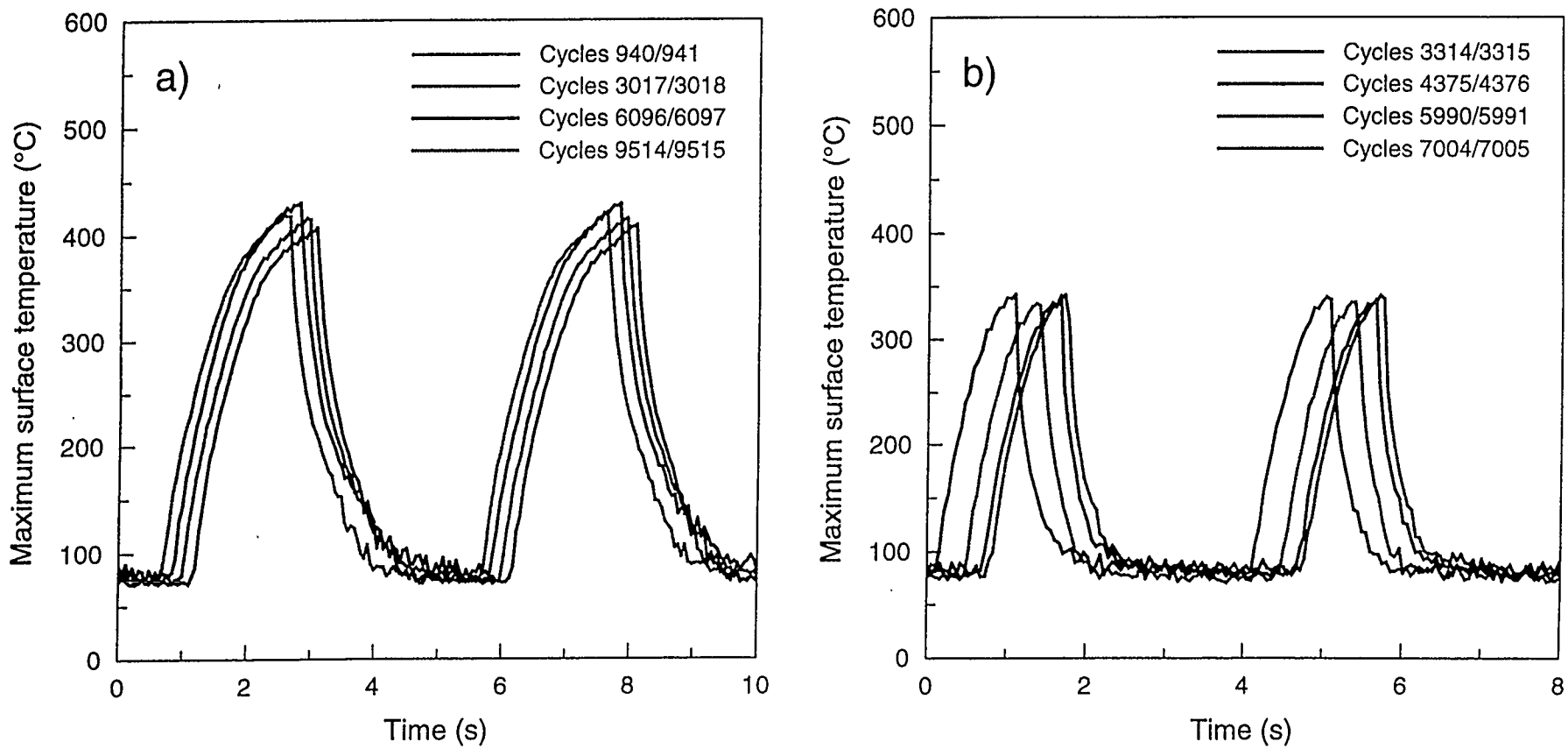

Figure 3: Variation of surface temperatures (centres of exposed regions) for a) standard JET element (13 MW/m², 3.7 m/s) and b) new Box scraper element (16 MW/m², 5.8 m/s)

Fatigue Tests at JEBIS (continued)

Outcome

- High reproducibility and uniformity of the surface temperature ⇒ mechanical and thermal properties unchanged during entire test.
- Above 10000 cycles for standard element and above 7000 cycles for new element.
- Both elements perfectly flat. No signs of plastic deformation or surface cracks.
- Only notable change: slight discoloration of the region exposed to electron beam.

Conclusion

- The results of the test give us confidence that hypervapotrons presently used at JET have enough lifetime for several more years of operation at even higher power.

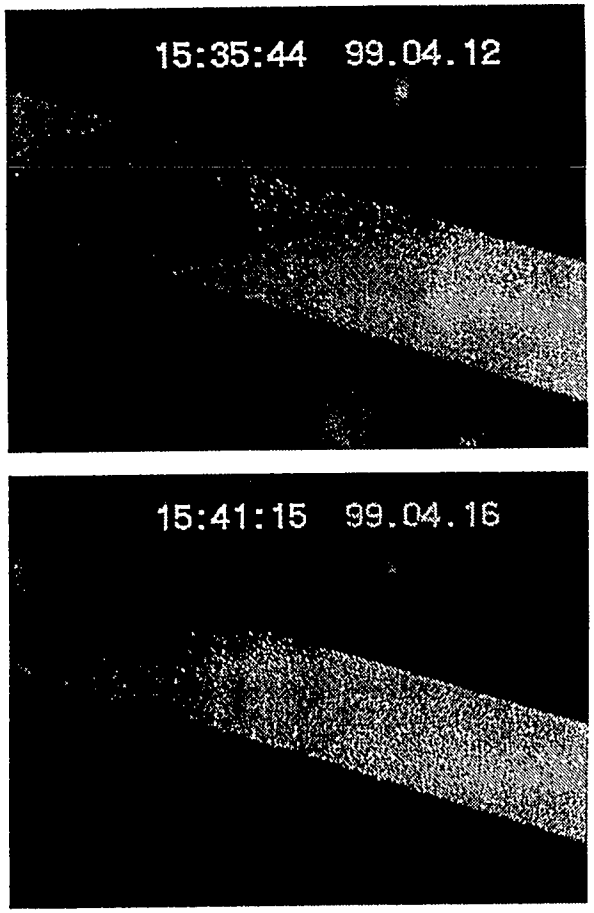

Figure 4: Video images of hypervapotrons after the fatigue test: a) standard JET hypervapotron and b) new Box Scraper hypervapotron.

Box Scraper Prototype

Goal

- To improve power handling capabilities of the JET Octant 4 NIB and to allow possible neutral beam upgrade.
- Design parameters:

Water velocity:	≥ 4 m/s	(3 m/s)
Peak power density:	13 MW/m²	(10 MW/m²)
Total power:	0.7 MW	(0.5 MW)
Surface temperature	< 450°C	(< 450°C)

VI-70

Modifications to standard hypervapotron geometry

- Front face thickness reduced from 6 to 4 millimetres. This will reduce the temperature difference across the front wall and allow higher power density while maintaining surface temperature below 450°C (strength limitation of CuCrZr material).
- Fin height reduced from 8 to 4 millimetres. This should improve heat transfer properties of the element - in the present design the bottom of the fin is at low temperature and does not contribute significantly to the heat removal.
- Water channel reduced to from 48×10 mm² to 48×8 mm² to increase slightly water velocity at same water flow - limitation in water flow available at JET.

Box Scraper Prototype (continued)

Experimental conditions

- The whole element is exposed to Hydrogen beam - simulation of operational conditions.
- Six thermocouples installed inside the central web (2 mm below the front surface) to measure element temperature during the heat pulse and to allow IR camera calibration.
- Water calorimetry used to measure total power on the element and water temperature rise.
- Two different sections (with and without cooling slot) tested by steering the Hydrogen beam above and below the beam centre line.
- Power density scans on both sections performed at several flow velocities (3, 4 and 6 m/s) within the range of water flows presently available at JET, and at higher velocity of 8.5 m/s, which is the intended nominal velocity for the new beam dump elements on the Mega Amp Spherical Tokamak (MAST) at Culham.

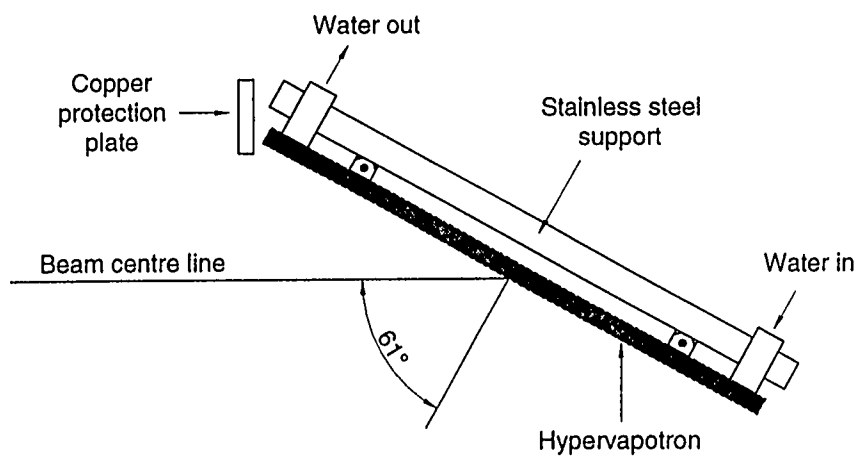

Figure 5: Layout of the Box Scraper prototype test at JET NB Test Bed.

Box Scraper Prototype (continued)

Power density distribution

- Beams operated at perveance match to eliminate power density excursions.
- Power density profiles measured using inertial calorimeter (0.8 metres upstream).
- Element bending (radius R [m] = $60/P_{max}$ [MW/m²]) taken into account in the evaluation of actual power density on hypervapotron.

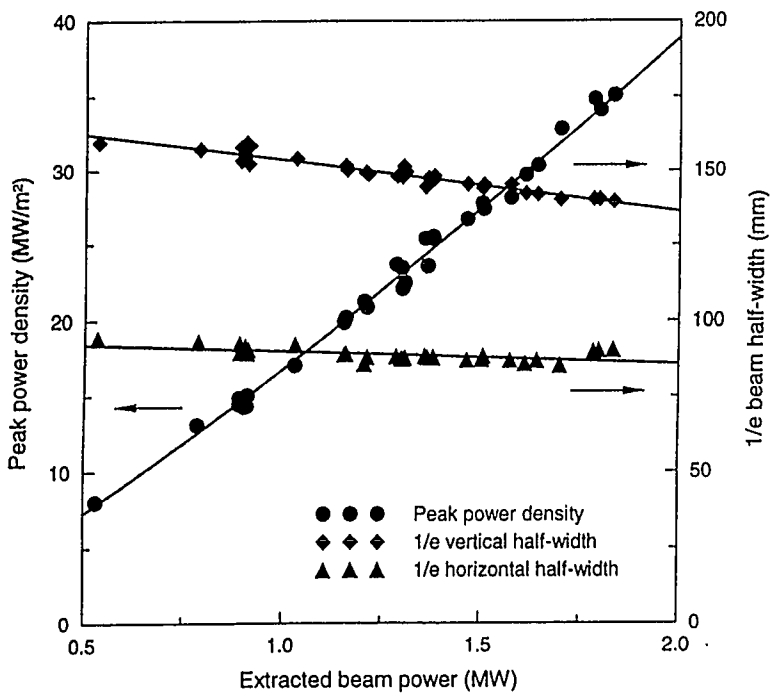

Figure 6: Hydrogen beam gaussian parameters (beam coordinate system).

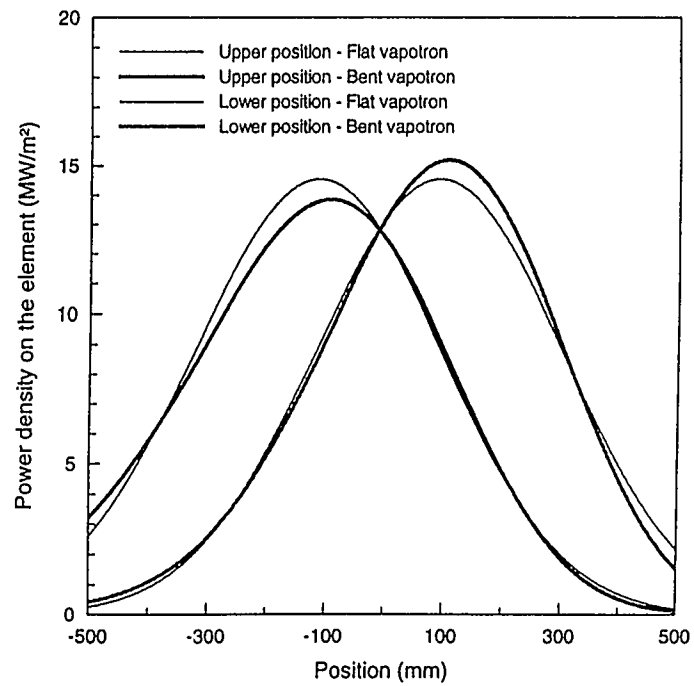

Figure 7: Power density distribution on hypervapotron at two nominal beam positions used during the test.

Box Scraper Prototype (continued)

Overheating of the central web

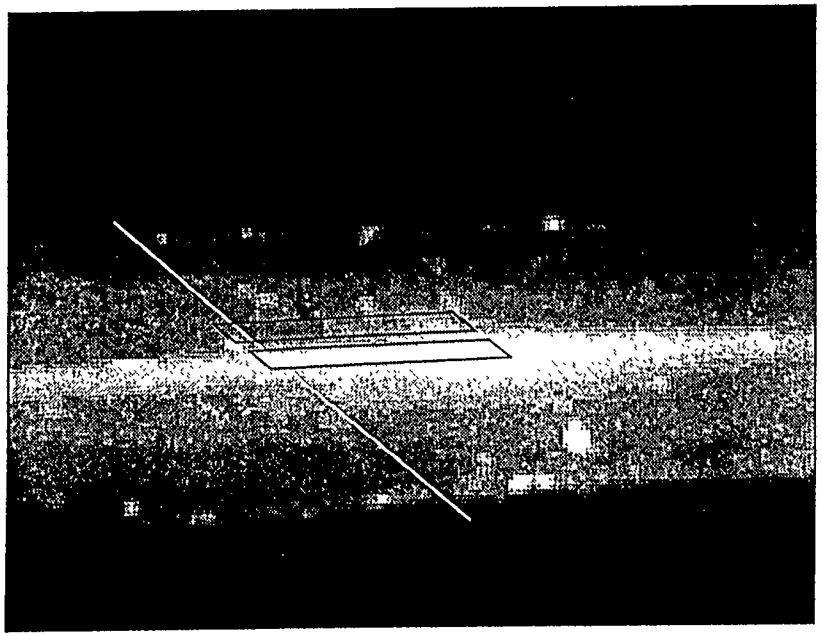

Figure 8: IR Image of the central region of the hypervapotron at the end of 5 seconds long beam pulse at 10.6 MW/m² (water velocity 5.6 m/s).

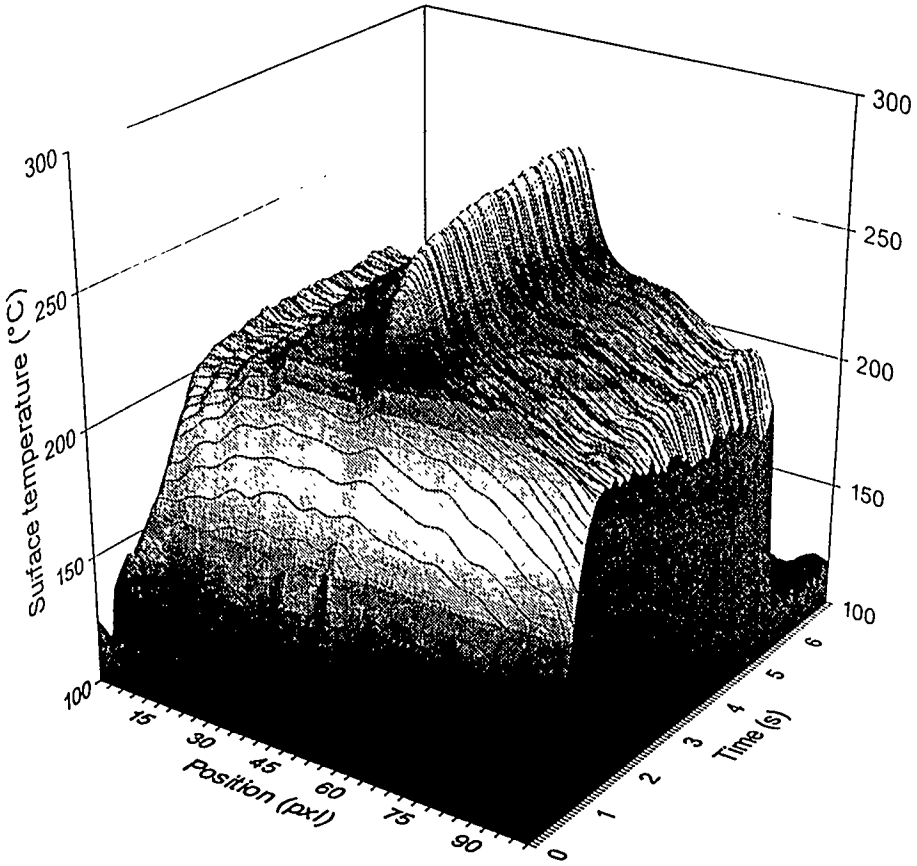

Figure 9:Time evolution of surface temperature profile along the line indicated in Figure 8.

Box Scraper Prototype (continued)

Overheating of the central web

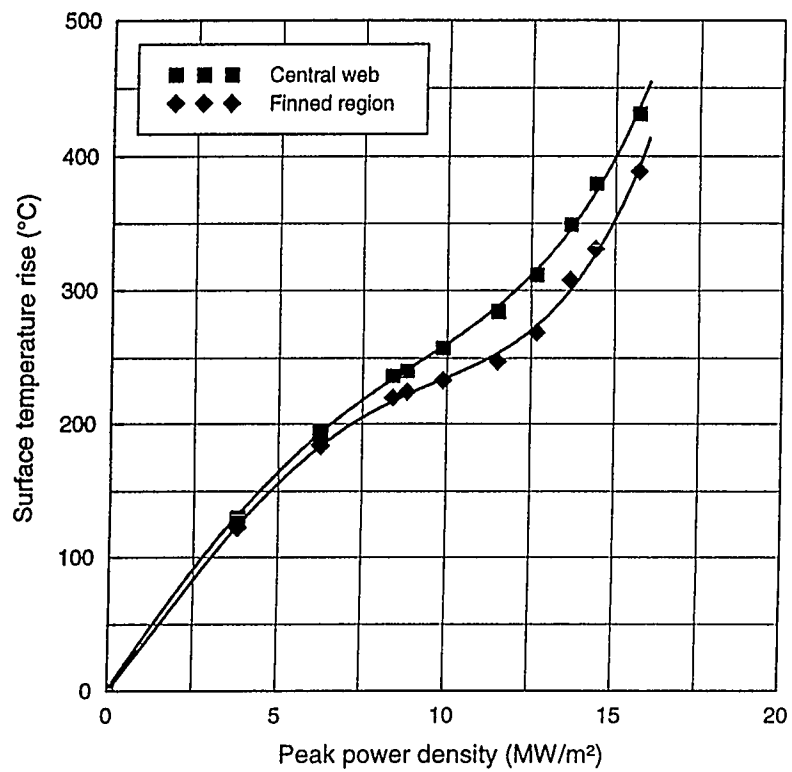

Figure 10: Variation of the surface temperature with peak power density at water flow velocity of 6.15 m/s. Central web is always at higher temperature: ~40°C at power densities above 10 MW/m².

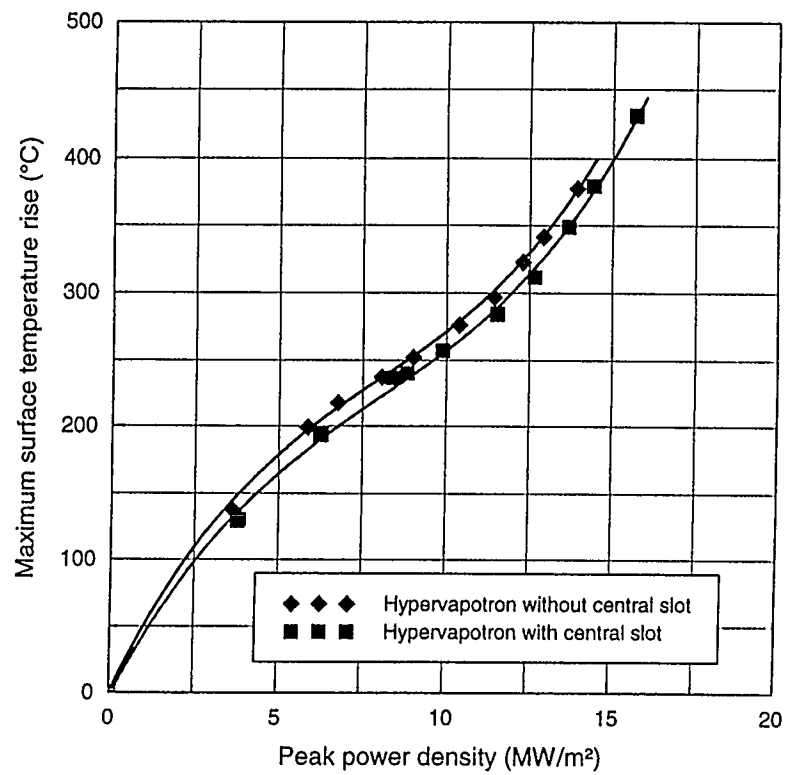

Figure 11: Maximum surface temperature rise (central web) as a function of peak power density for two sections of the prototype element at water flow velocity of 6.15 m/s (maximum difference ~15°C).

Box Scraper Prototype (continued)

Thermocouple temperature waveforms

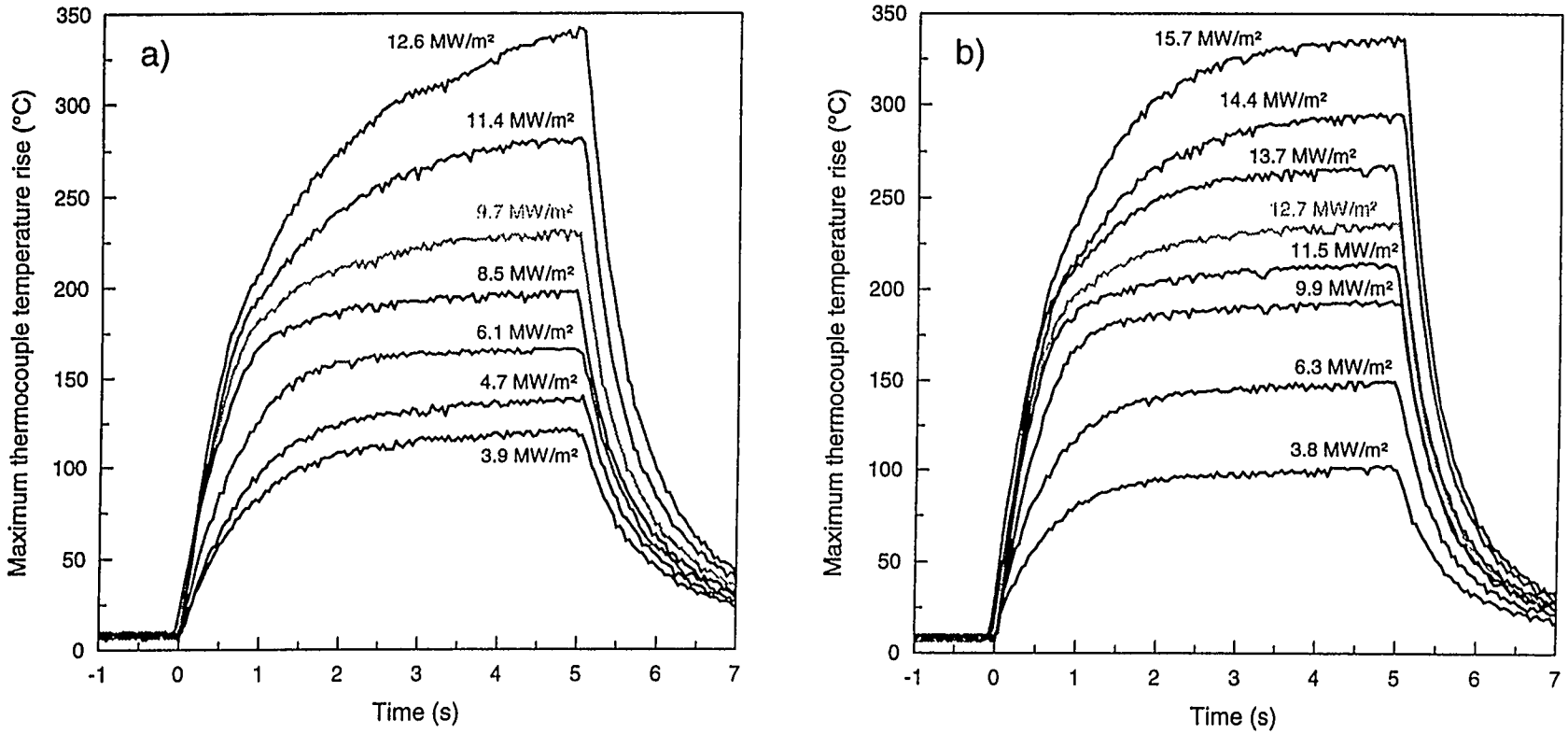

Figure 12: Thermocouple temperature rise for different peak power densities and water flow velocity of a) 4.00 m/s and b) 6.15 m/s. Note that equilibrium conditions are reached even at highest power density at higher water velocity of 6.15 m/s.

Box Scraper Prototype (continued)

Power density scans at various water velocities

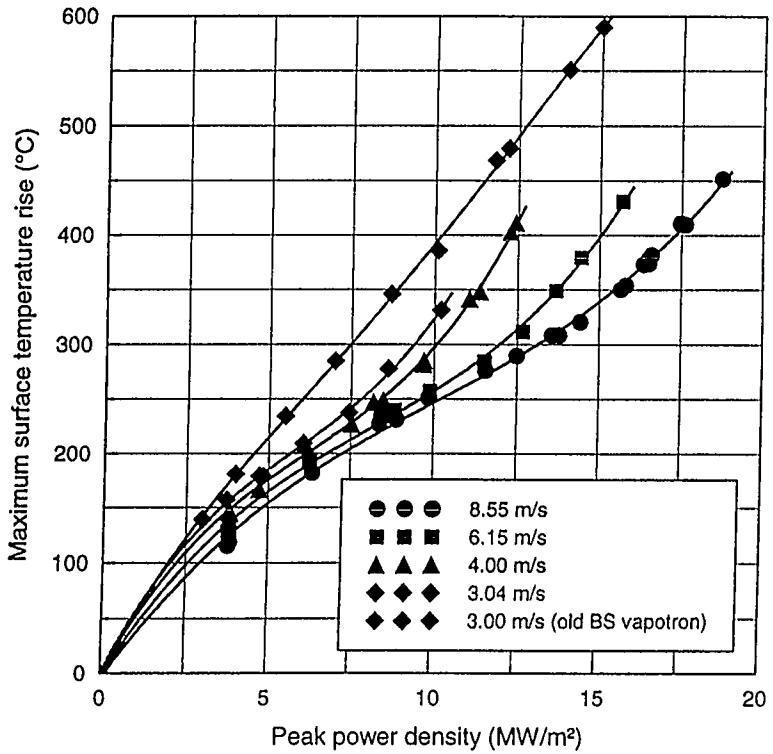

Figure 13: Maximum surface temperature (central web) as a function of peak power density for various water velocities. Central web surface temperatures are derived from thermocouple values at the end of 5 seconds long beam pulses. Graph also includes data for old Box Scraper hypervapotron at water flow velocity of 3 m/s.

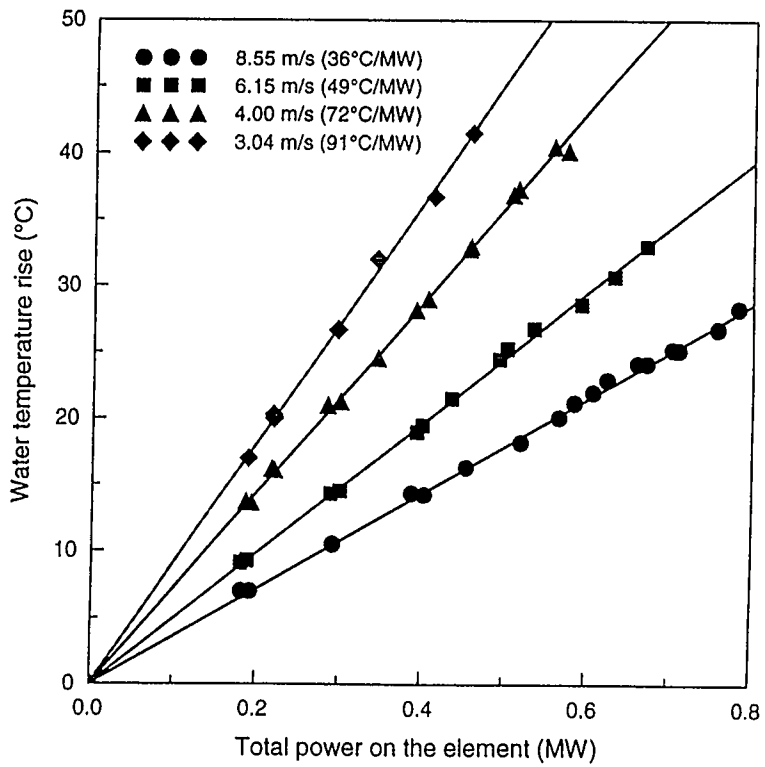

Figure 14: Cooling water temperature rise as a function of total power on the element for various water velocities. Total power is derived from water calorimetry data.

Box Scraper Prototype (continued)

Summary of results

- Overheating of the central web present on both sections of the element (temperature ~40°C higher than in the finned region at power densities above 10 MW/m^2).
- Additional cooling slot has little effect the temperature of the central web region.
- Equilibrium conditions reached at power densities above 10 MW/m^2 when hypervapotron operates in the "noisy" boiling regime.
- Maximum surface temperature below 450°C can be maintained at power densities of ~13 MW/m^2 for water velocities > 4 m/s.
- Maximum water temperature rise is below 50°C for total power of 0.7 MW and water velocity above 4 m/s.
- All design parameters were confirmed in the test.
- Hypervapotron can be used safely for power densities above 15 MW/m^2 at water velocities above 6 m/s.

Operation of JET Facility beyond Year 1999

Framework

- When the JET Joint Undertaking terminates on 31 December 1999 the JET Device, buildings and other assets will pass to the UKAEA.
- Future operation of the JET facility will be organised under the umbrella of European Fusion Development Agreement (EFDA) through two contractual agreements:

  JET Implementing Agreement (JIA)

  JET Operation Contract (JOC)

- JET Implementing Agreement was signed by European Commission and was send to other parties (EUROATOM Associations) for signature.
- When JIA becomes effective the JET Operation Contract (between EURATOM and UKAEA) will be signed.
- Both JIA and JOC define the JET operation until 31 December 2002.
- Jérôme Pamela has been designated as the JET Associate Leader (JAL).

Operation of JET Facility beyond Year 1999 (continued)

JET Workprogramme

- JET Associate Leader will prepare a JET Workprogramme each year in consultation with the UKAEA Senior Manager and the the Associations.
- The Workprogramme will specify, for each year, the scientific and technical tasks (S/T tasks) to be undertaken and the operation of the JET facilities required to implement them.
- JET Workprogramme will be prepared within the framework of EFDA Workplan which will be produced by EFDA Leader
- The EFDA Steering Committee has established a JET Sub-Committee (JET SC) to organise and supervise activities at the JET Facilities and JET Associate Leader will be responsible to them for the execution of the JET Workprogramme.
- The Workprogramme will be realised through several Task Forces - Most of the Task Force Leaders have been designated.

Plasma Facing Components – 3

US-Japan Workshop on High Heat Flux Components
and Plasma Surface Interactions for Next Fusion Devices
Santa Fe, NM, US, 1-4 November 1999

Thermal hydraulics of sawtooth-finned cooling tubes

K. Ezato, K. Sato, S. Suzuki
Presented by M. Akiba
JAERI

CHF experiment on screw tubes with different pitch

◇Effect of screw pitch on heat transfer enhancement

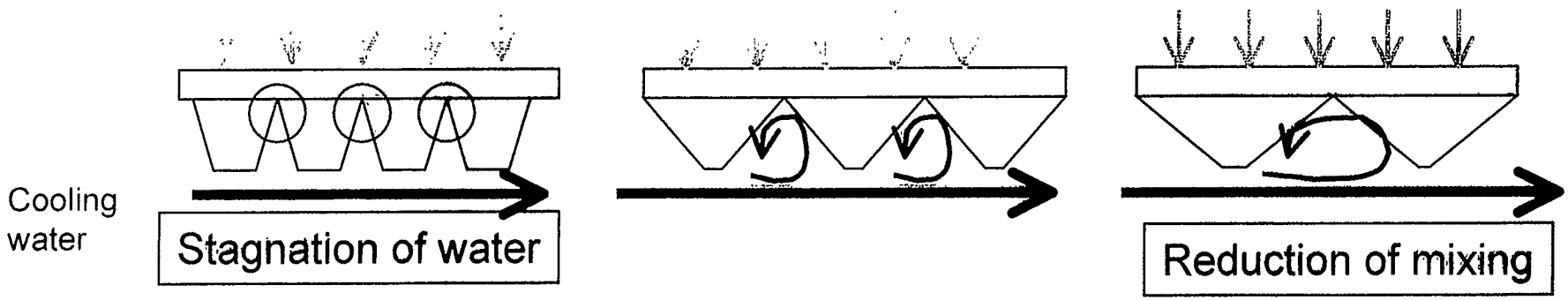

Measurement of CHF using several screw pitch size

Test piece : Cu pipe with OD=14mm
Thread geometry : ISO standard

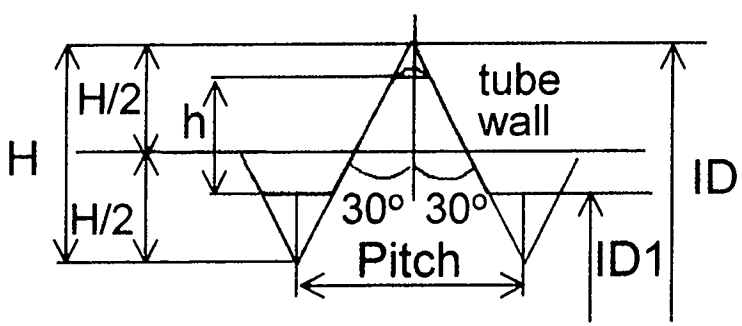

Geometry of Screw tube

Name	Pitch	ID1	h
M10 x P1.75	1.75	8.1	0.95
M10 x P1.5	1.5	8.3	0.81
M10 x P1.25	1.25	8.7	0.68
M10 x P1.0	1.0	8.9	0.54
M10 x P0.75	0.75	9.2	0.41

Detection of burnout

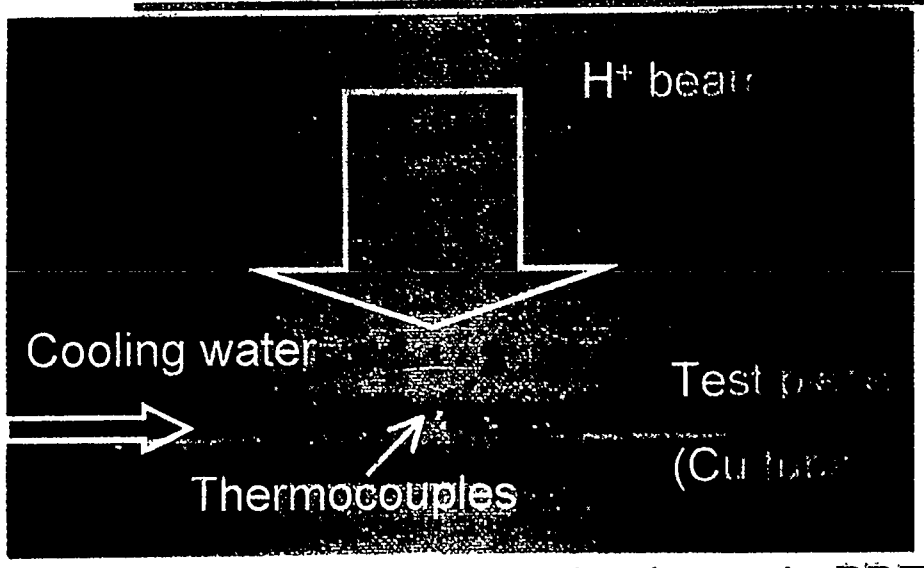

HHF experiment using H+ ion beam in PBEF

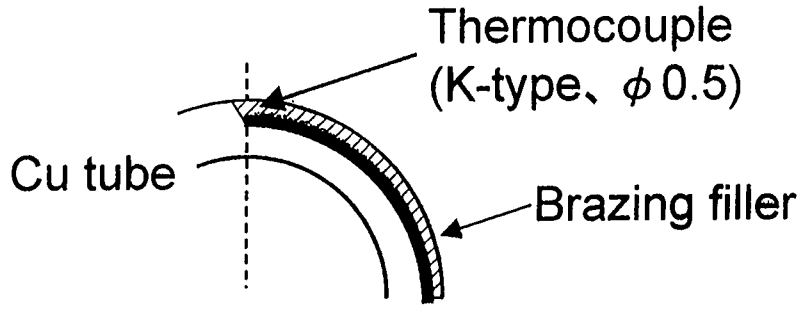

TC position: 0.2mm depth below the surface

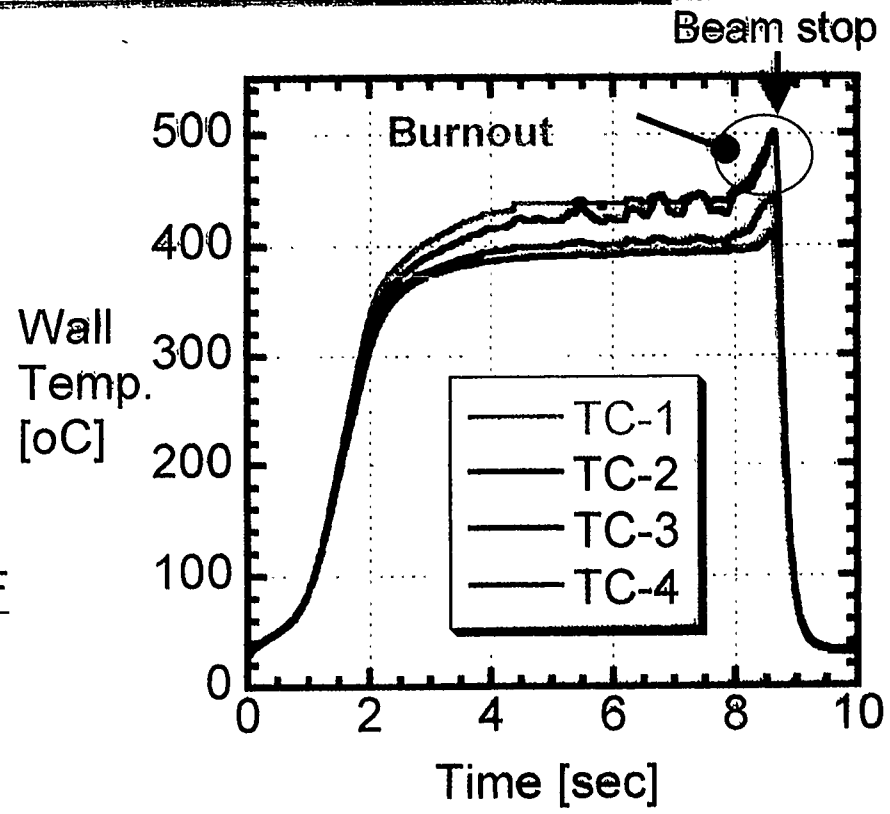

Thermal response in burnout

Exp. condition: M10 x P0.75
10m/sec、34MW/m^2

To prevent the cooling tube from melting by the detection of the temperature excursion

CHF using screw tube is larger than that of swirl tube in low velocity region.

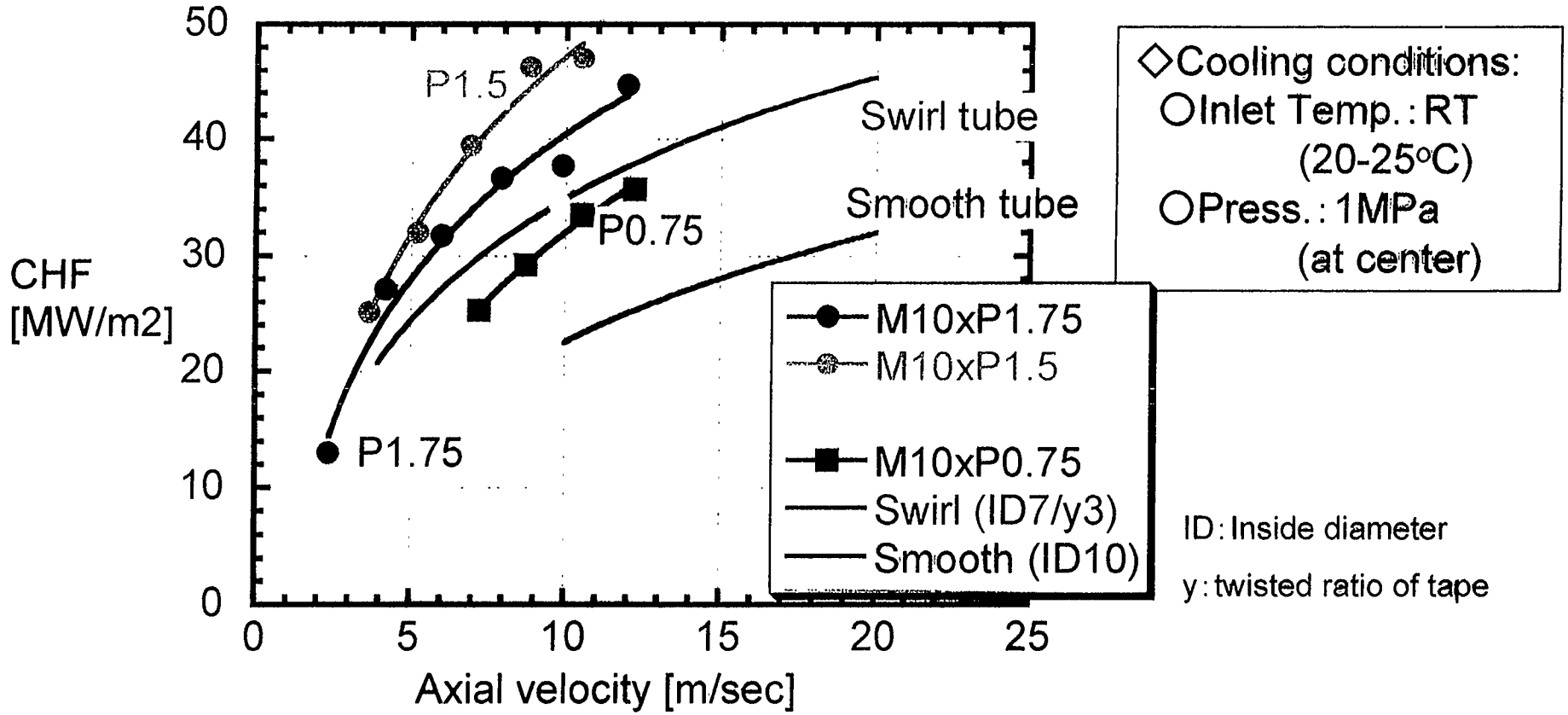

Max. CHF is obtained using screw tube with P1.5.
This is optimum geometry in this experiment.

CHF: defined as heat flux at outside of the cooling tube
axial velocity: defined using min. Inside diameter

Pumping power for the screw tube is reduced to about 40% from that of the swirl tube if same CHF is obtained.

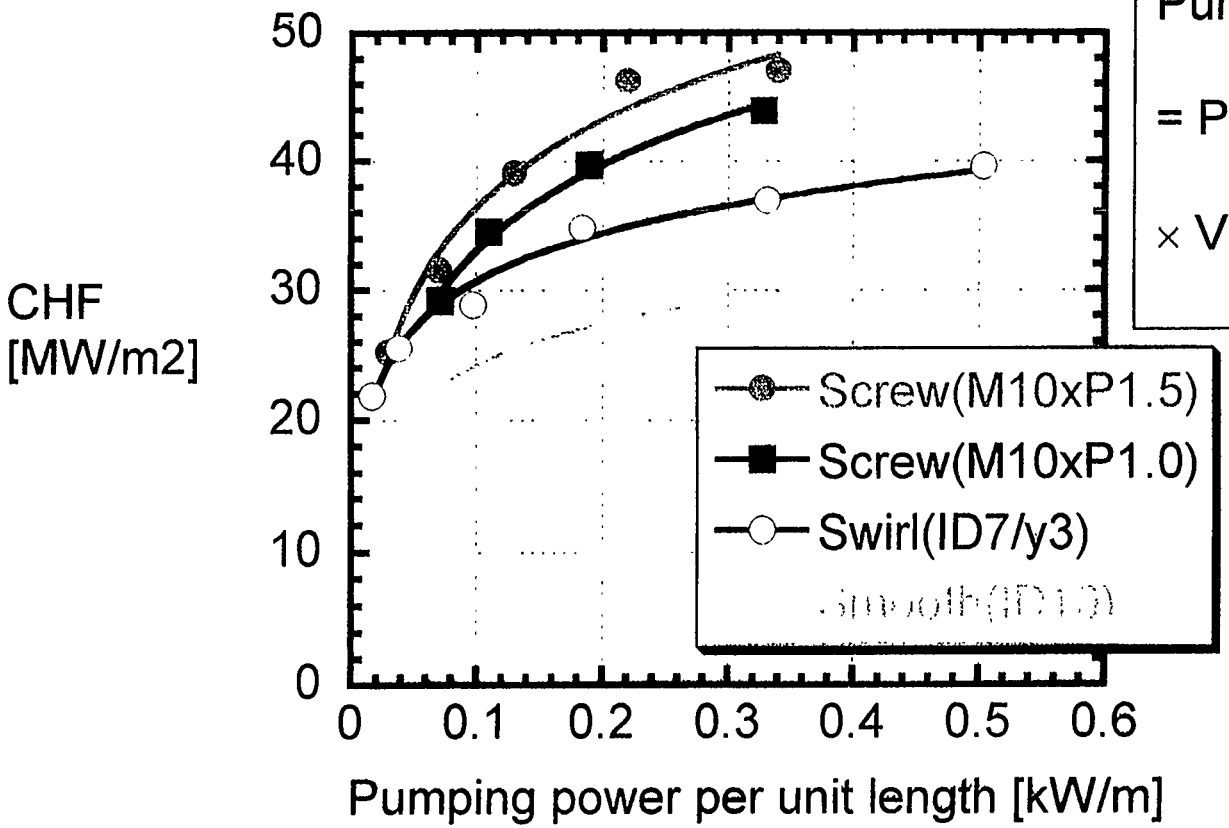

Pumping power per unit length [W/m]
= Press. drop per unit length [Pa/m]
× Volumetric flow rate [m3/sec]

Inlet Temp. : RT

Pressure: 1MPa

◇The screw geometry is very effective to enhance CHF.
◇The screw tube has very high cooling performance.

CHF : defined as heat flux at outside of the cooling tube.

Saw-toothed fin duct for CHF experiment

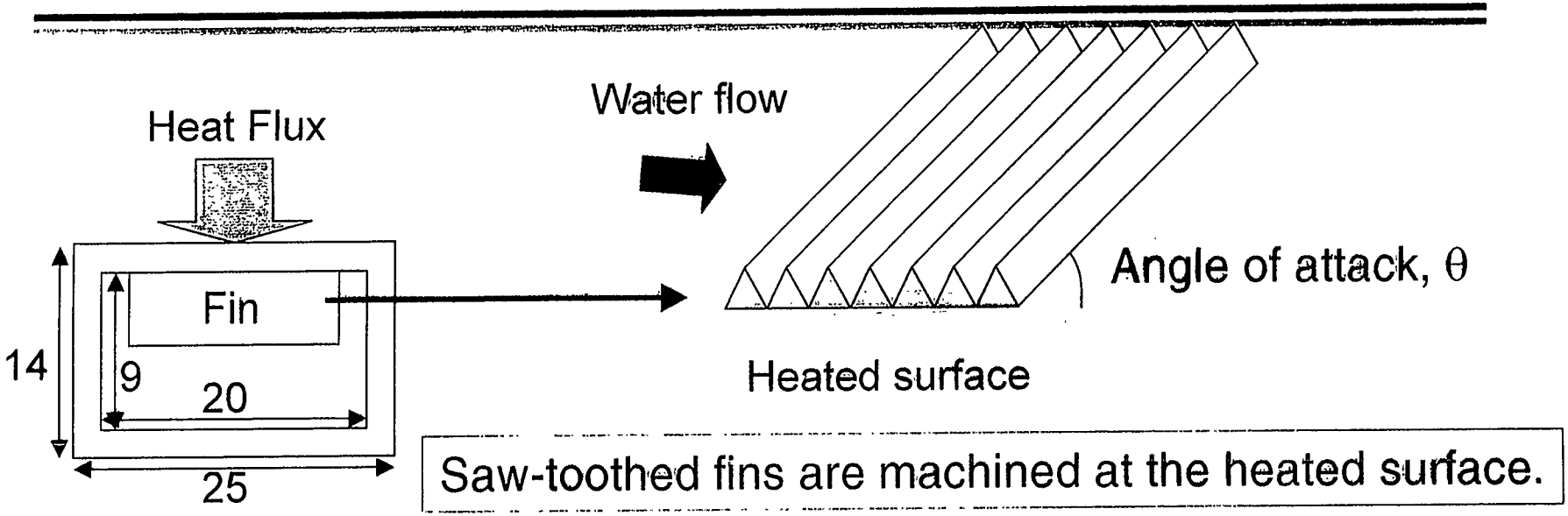

Saw-toothed fins are machined at the heated surface.

Fin geometry : regular triangle
Fin height : 3.5 mm, Fin base: 4.0 mm
Angle of attack : 90° and 70°

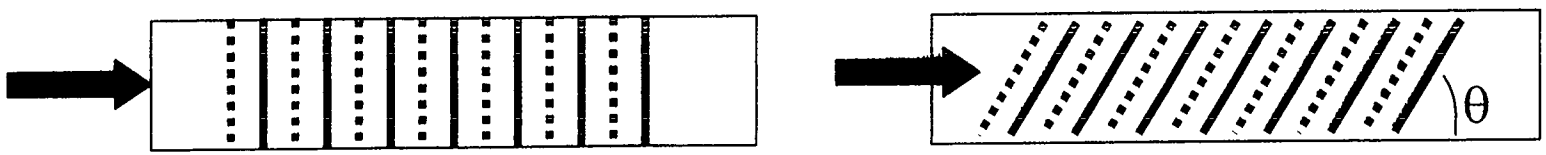

Angle of attack : θ = 90° θ =70°

Saw-toothed fin duct has improvement in CHF.

Test facility : PBEF(H^+ ion beam)

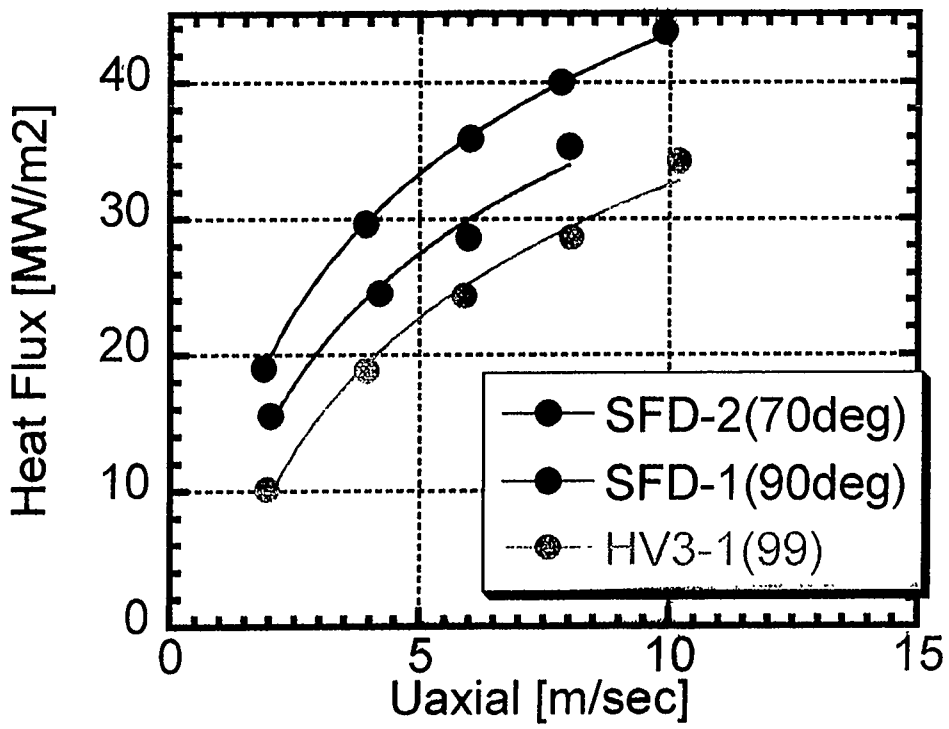

SFD: Saw-toothed fin duct
fin height : 3.5mm,
fin base:4 mm

HV3-1:Hypervapotron
fin height: 4 mm,
fin gap : 3 mm
fin thickness: 3 mm

Cooling conditions:
Inlet Temp. = RT(20-25°C).
Press. = 1MPa at center.

◇Inclination of Fin is effective to enhance CHF.
◇Using SFD, CHF is increased to 30% from those of Hypervapotron.

Pumping power for saw-toothed fin duct is remarkably reduced compared with that of Hypervapotron if same CHF is obtained.

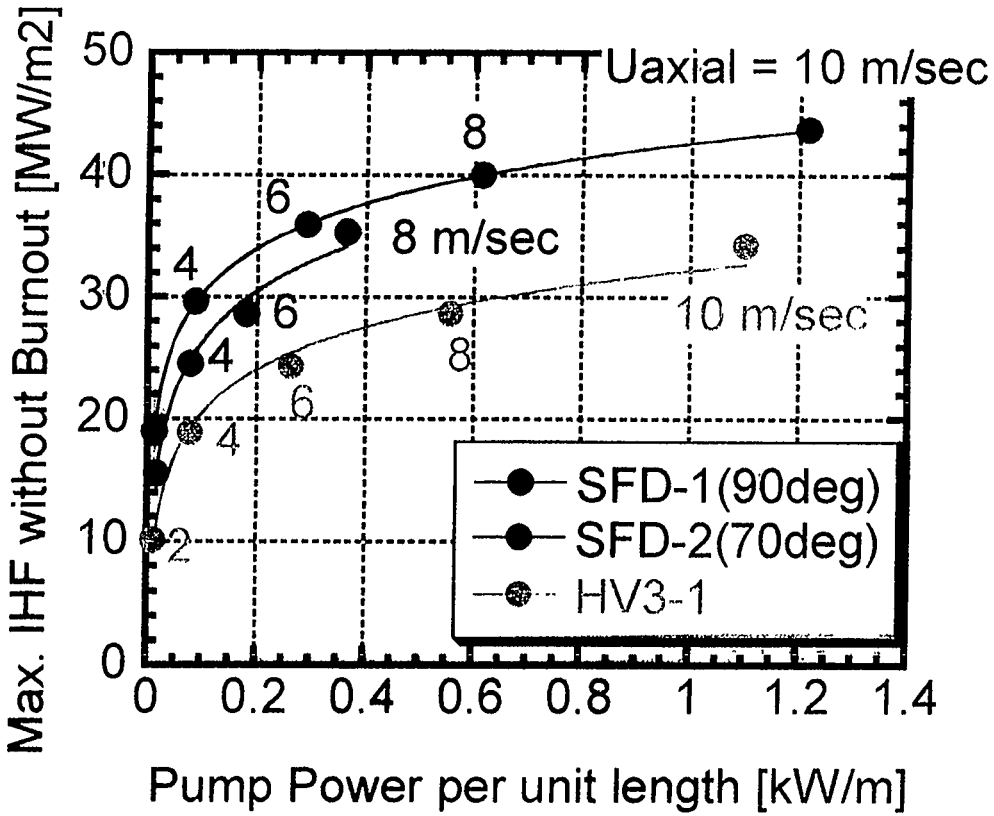

SFD: Saw-toothed fin duct
fin height : 3.5mm,
fin base:4 mm

HV3-1:Hypervapotron
fin height: 4 mm,
fin gap : 3 mm
fin thickness: 3 mm

Saw-toothed fin duct has good cooling performance compared with Hypervapotron.

Summary

New type of high performance cooling structures are examined through CHF experiment.

— Screw tube, whose inside is machined like a nut (ISO standard).

- ❒Effect of fin pitch on CHF enhancement is studied. In this test campaign, M10 x P1.5 has best performance.
- ❒Pumping power for the screw tube is reduced to about 40 % from that of the swirl tube if same CHF is obtained.

— Saw-toothed fin duct, hypervapotron with the slotted teeth replaced by a saw tooth geometry.

- ❒Effect of attack of angle is studied. Tested angles are 90° and 70° to the flow direction. SFD with fins of 70° to the flow has better performance. This might comes from secondary flow between fins.
- ❒SFD has improvement in CHF versus pumping power compared with hypervapotron with almost same fin size.

— Detailed mechanism of CHF enhancement using these cooling structures will be investigated.

THERMAL HYDRUALIC ANALYSIS OF FIRE DIVERTOR

CHANDU BAXI

GENERAL ATOMICS

PRESENTED BY

DR. CLEMENT WONG

GENERAL ATOMICS

WHAT IS FIRE ?

- FUSION IGNITION RESEARCH EXPERIMENT
- HIGH POWER DENSITY, ADVANCED PHYSICS & IGNITION
- ONLY OUTER DIVERTOR COOLED BY WATER DURING INITIAL PHASE

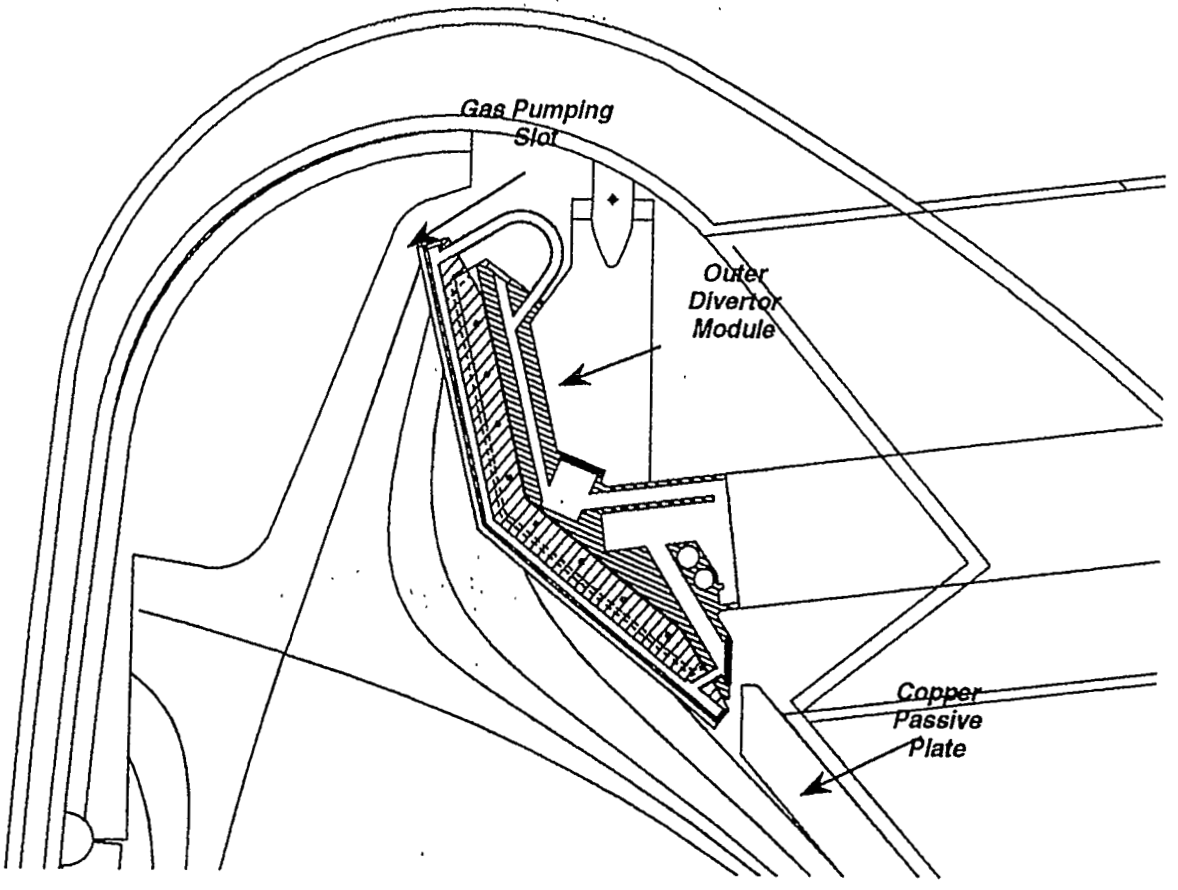

Cross Section through Actively-Cooled Outer Divertor Module

Trimetric View of Outer Module
2 Parallel Channels in Each Plate
Flow Enters at Top End
Flows Through 2 Plates in Series

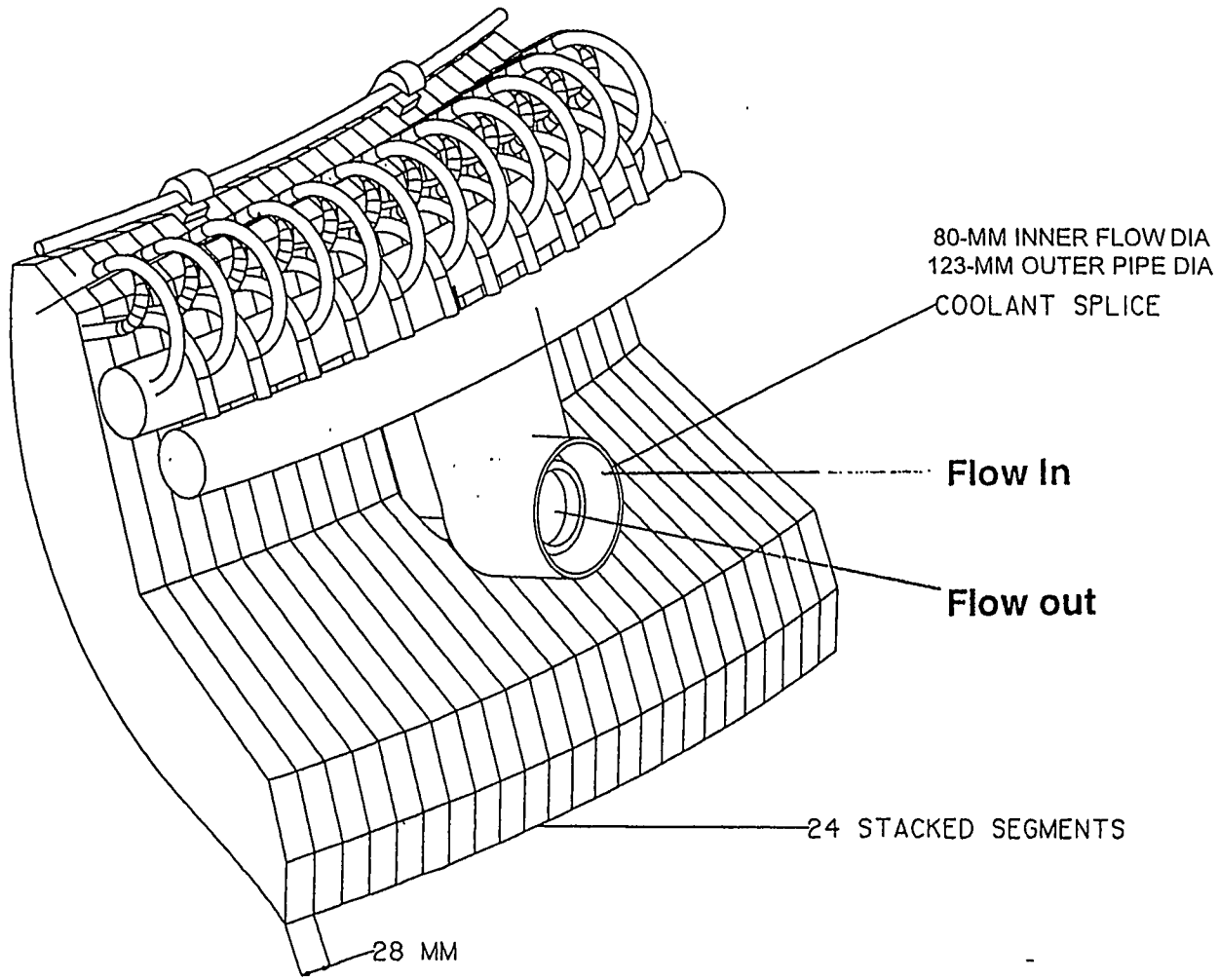

Divertor Module Power Flow Summary

	Baseline(67MW,10s)			Long Pulse(21MW,200s)			Long Burn(52MW,50s)		
Parameter	Inner	Baffle	Outer	Inner	Baffle	Outer	Inner	Baffle	Outer
Total Power(MW)	8.6	10.7	34.3	2.7	3.4	10.9	6.7	8.3	26.6
Peak Power Per Module(MW)	0.46	0.58	2.32	0.15	0.18	0.73	0.36	0.45	1.80
Peak Heat Flux(MW/m2)			20			<10			<10

Divertor Heat Sink Terminology

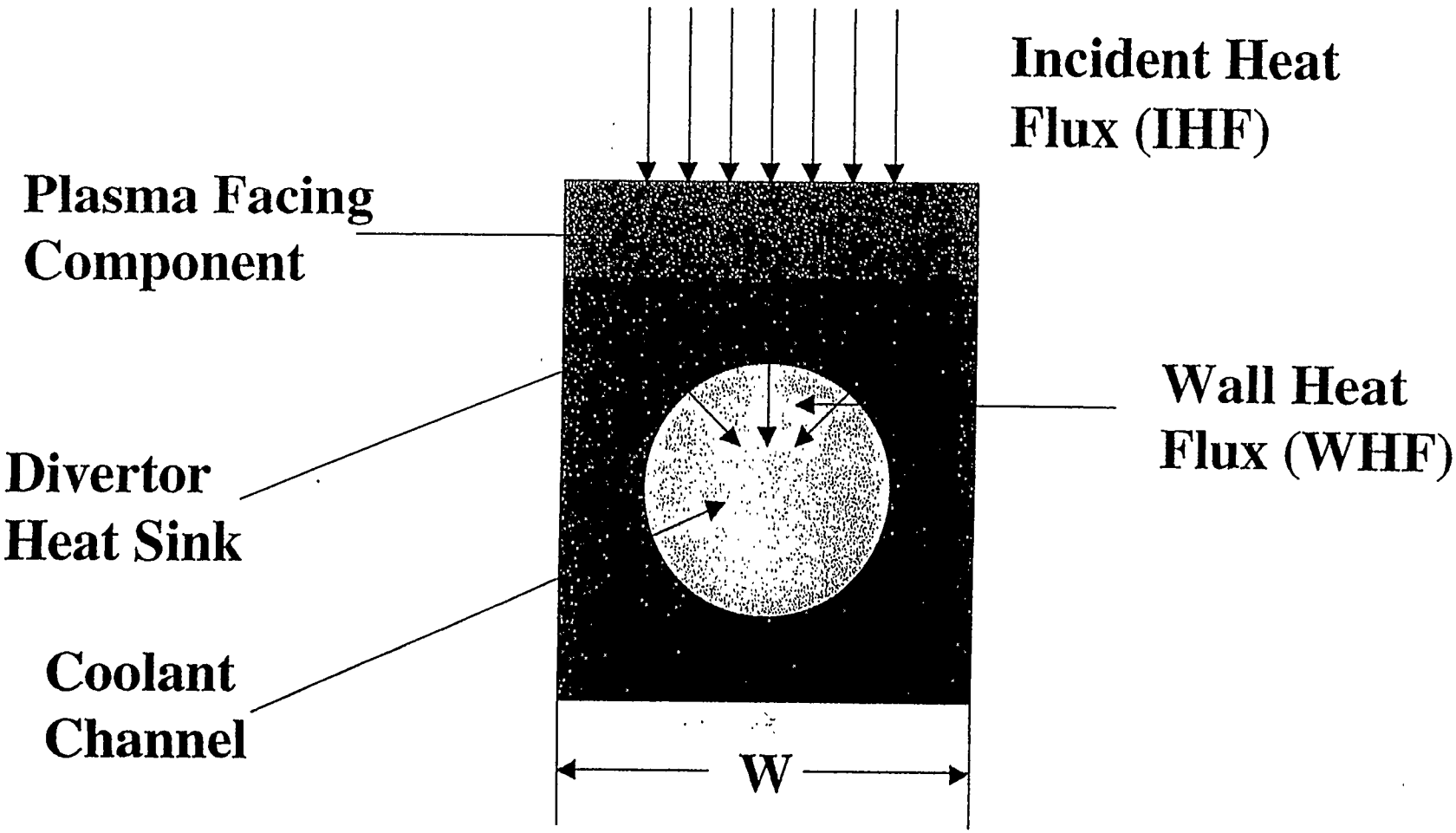

PFC
TUNGSTEN RODS IMBEDDED IN Cu HEAT SINK (FOR FIRE: D = 3 mm & HEIGHT = 5 mm)

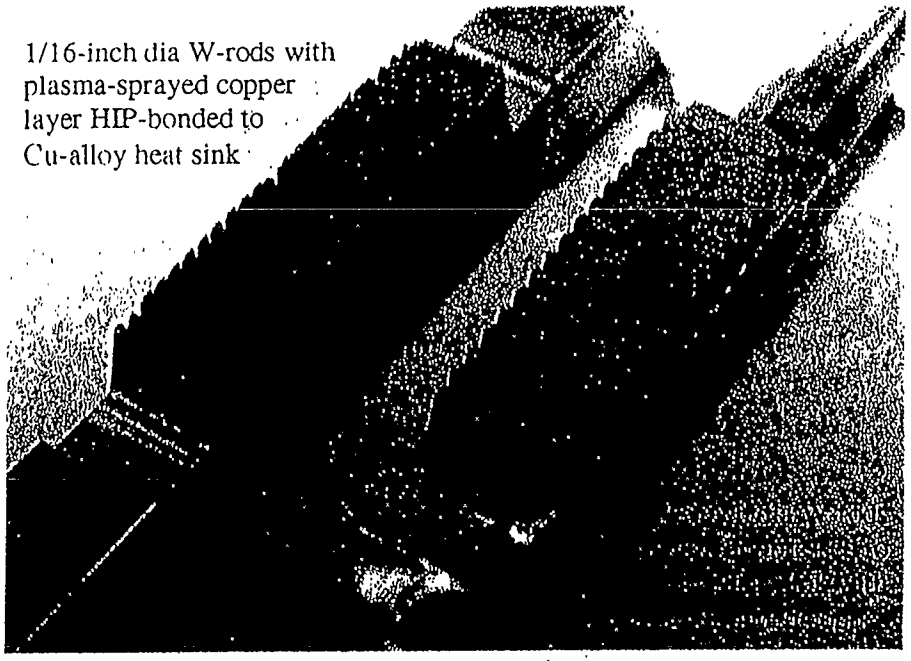

. Two of the Tungsten Brush Armor Configurations Tested at 25 MW/m².

THERMAL CONDUCTIVITY OF W-Cu INTERPHASE (CALCULATED BY 3D FE ANALYSIS)

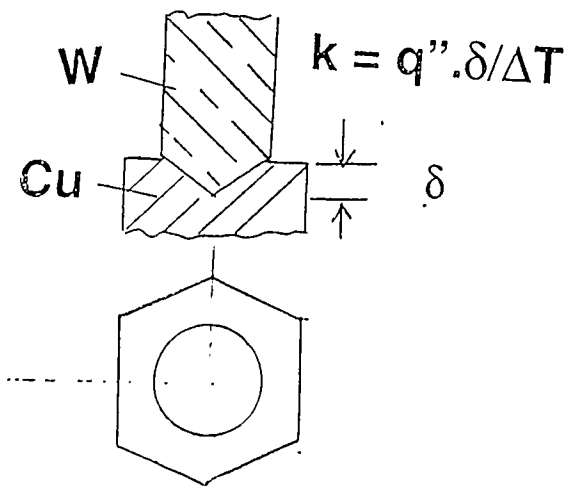

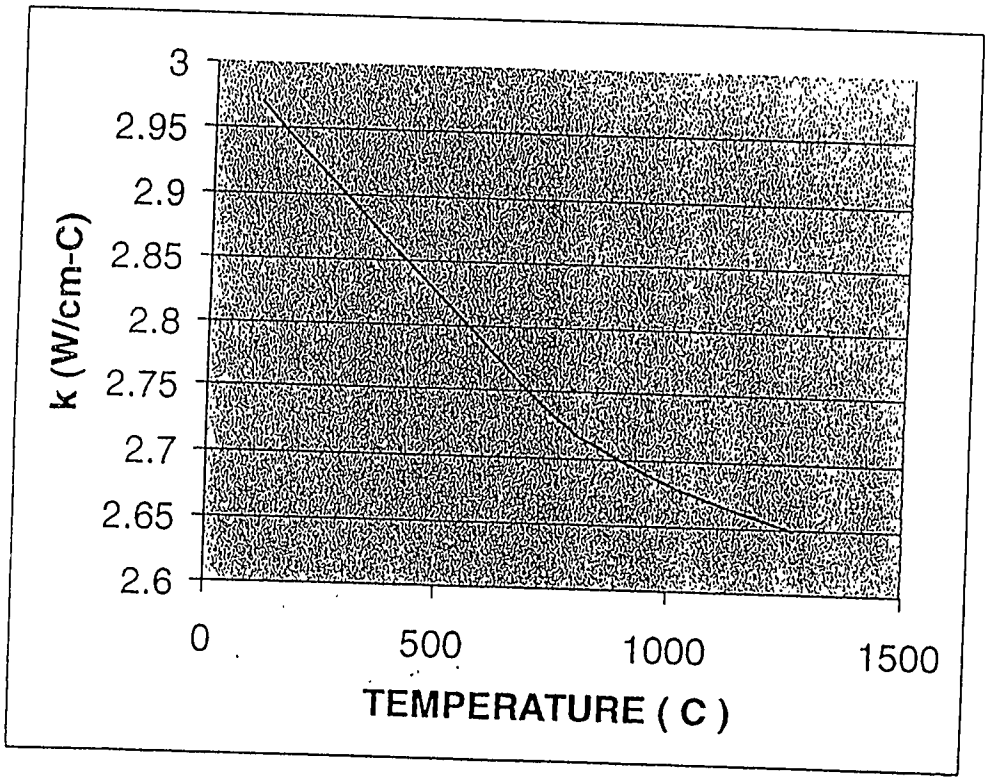

HEAT TRANSFER ENHANCEMENT REDUCES THE FLOW VELOCITY REQUIRED

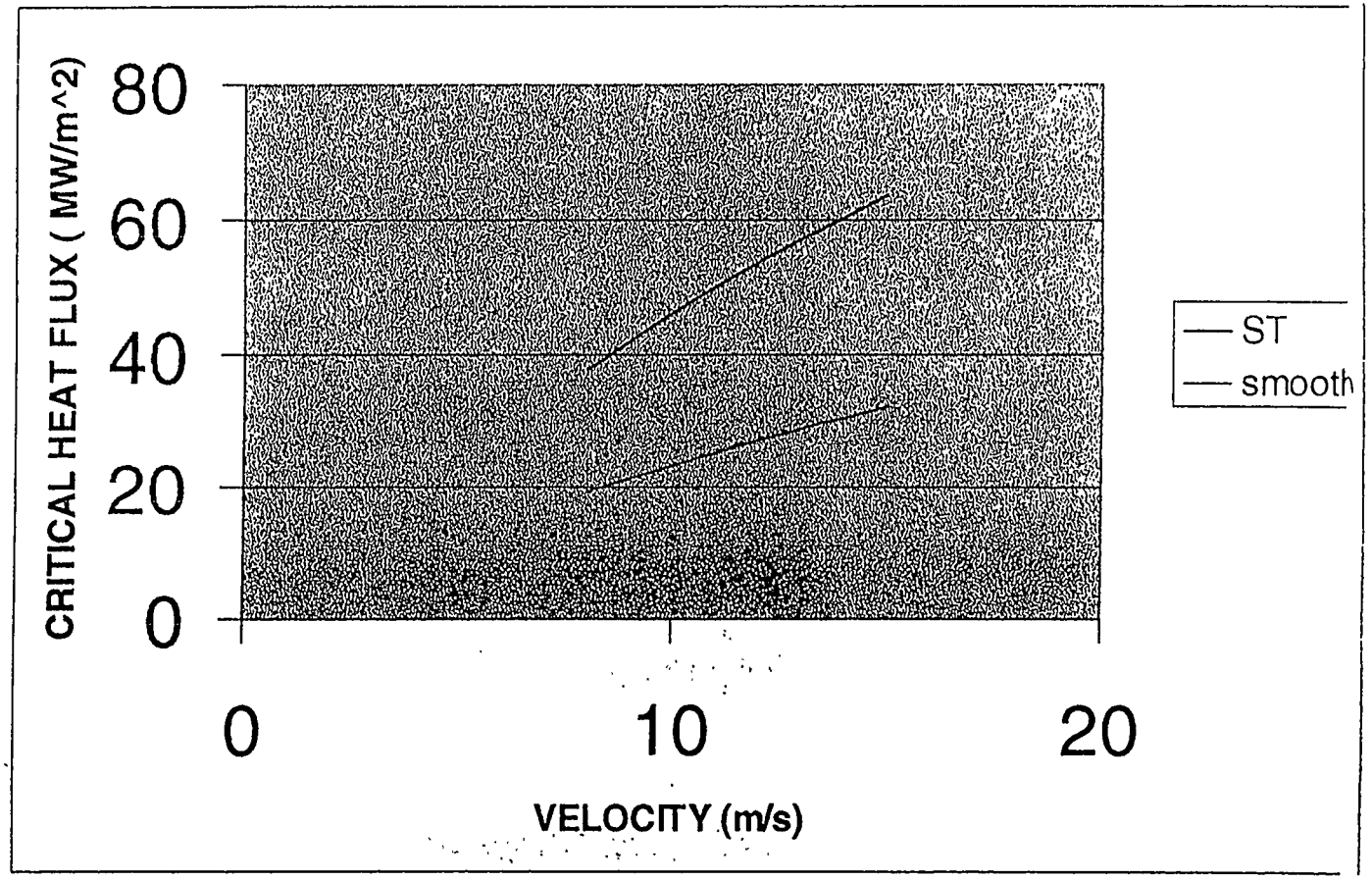

SS TEMPERATURE DISTRIBUTION FOR 20 MW/m^2

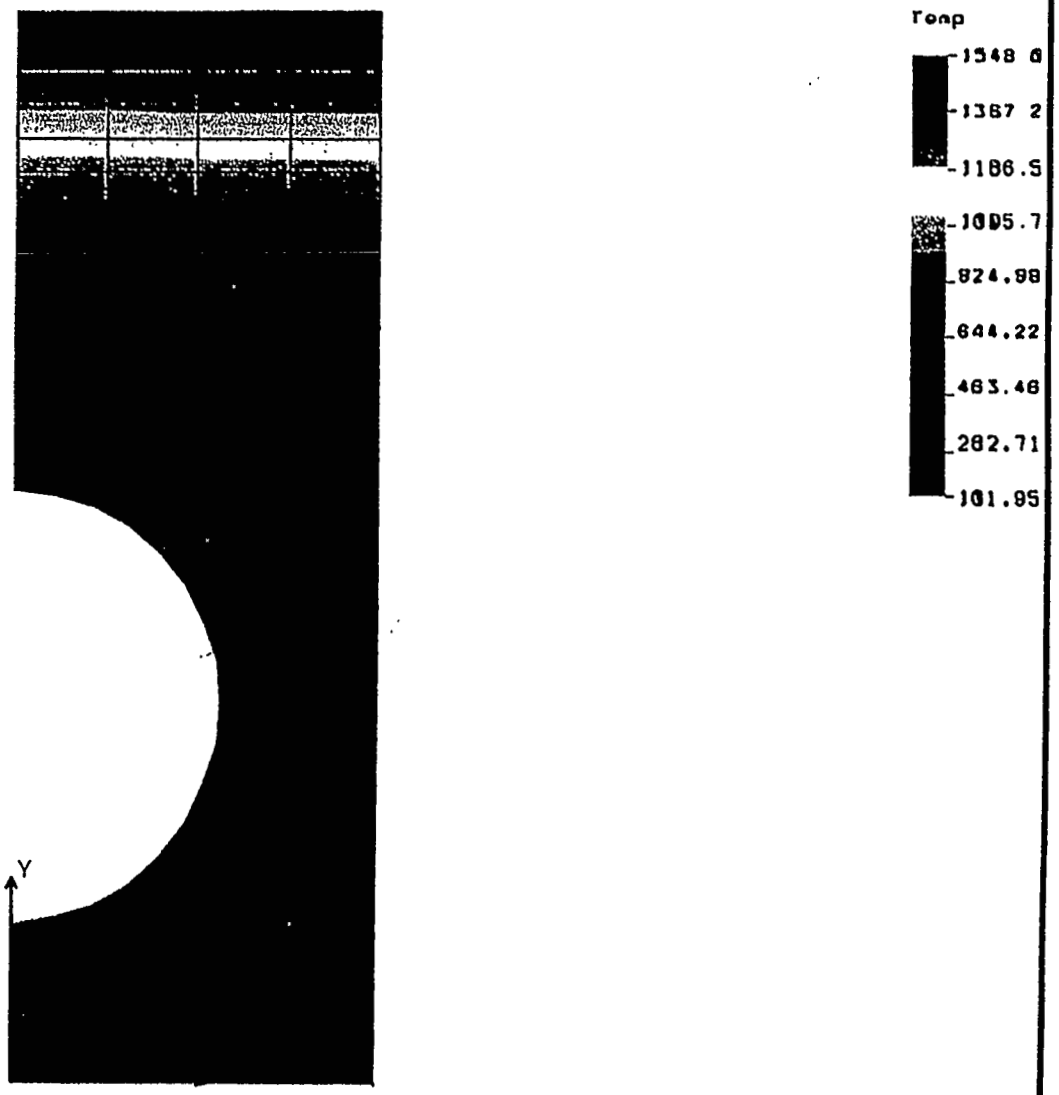

AN INLET PRESSURE OF 1.5 MPa, AND 10 m/s, CHF 45 MW/m^2

(INCIDENT q_i = 20 MW/m^2, q_w/q_i = 1.5, q_w = 30 MW/m^2)

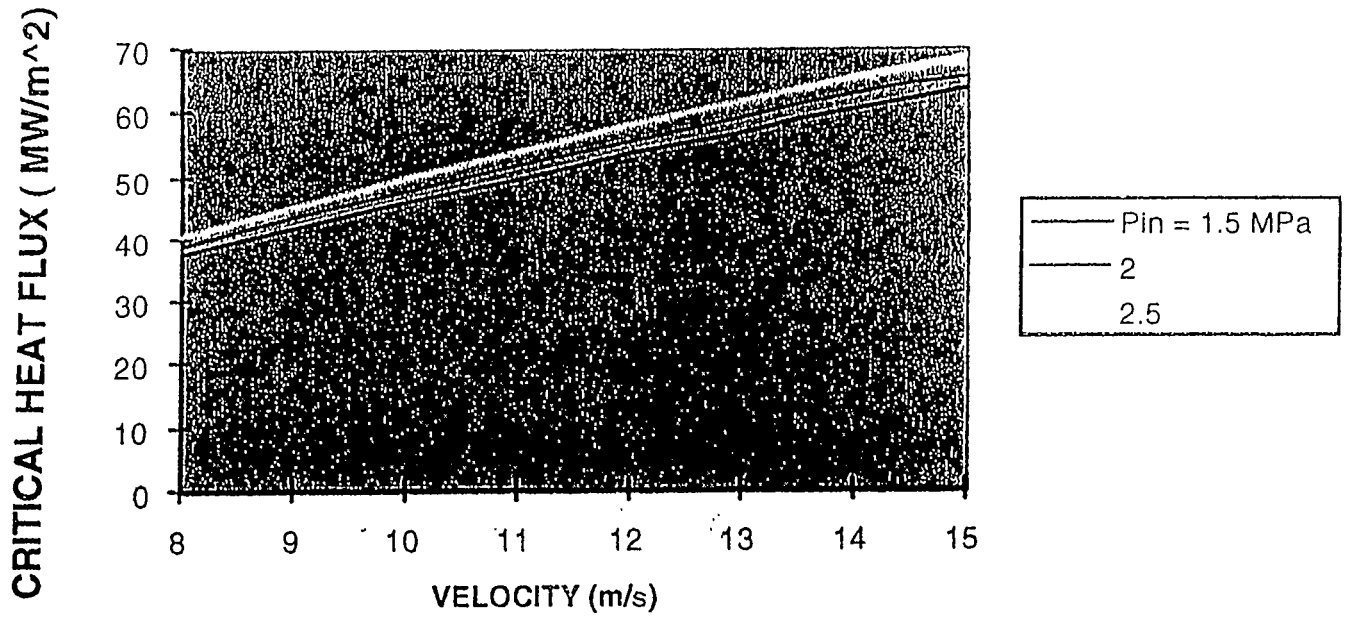

RATIO OF WALL TO INCIDENT HEAT FLUX (CALCULATED BY FE ANALYSIS)

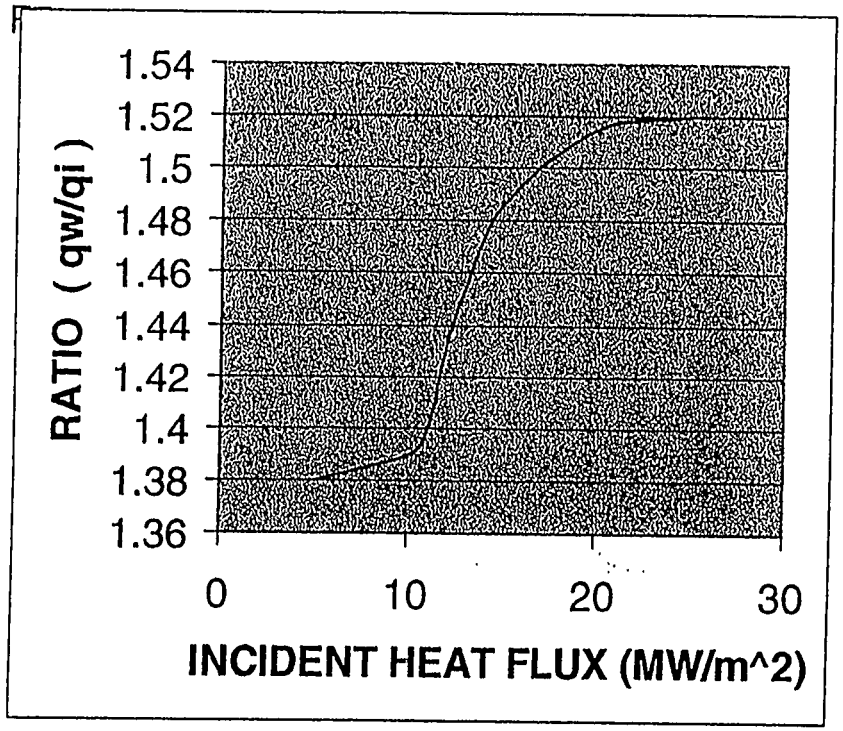

MAXIMUM PFC TEMPERATURE (C) DURING A TRANSIENT

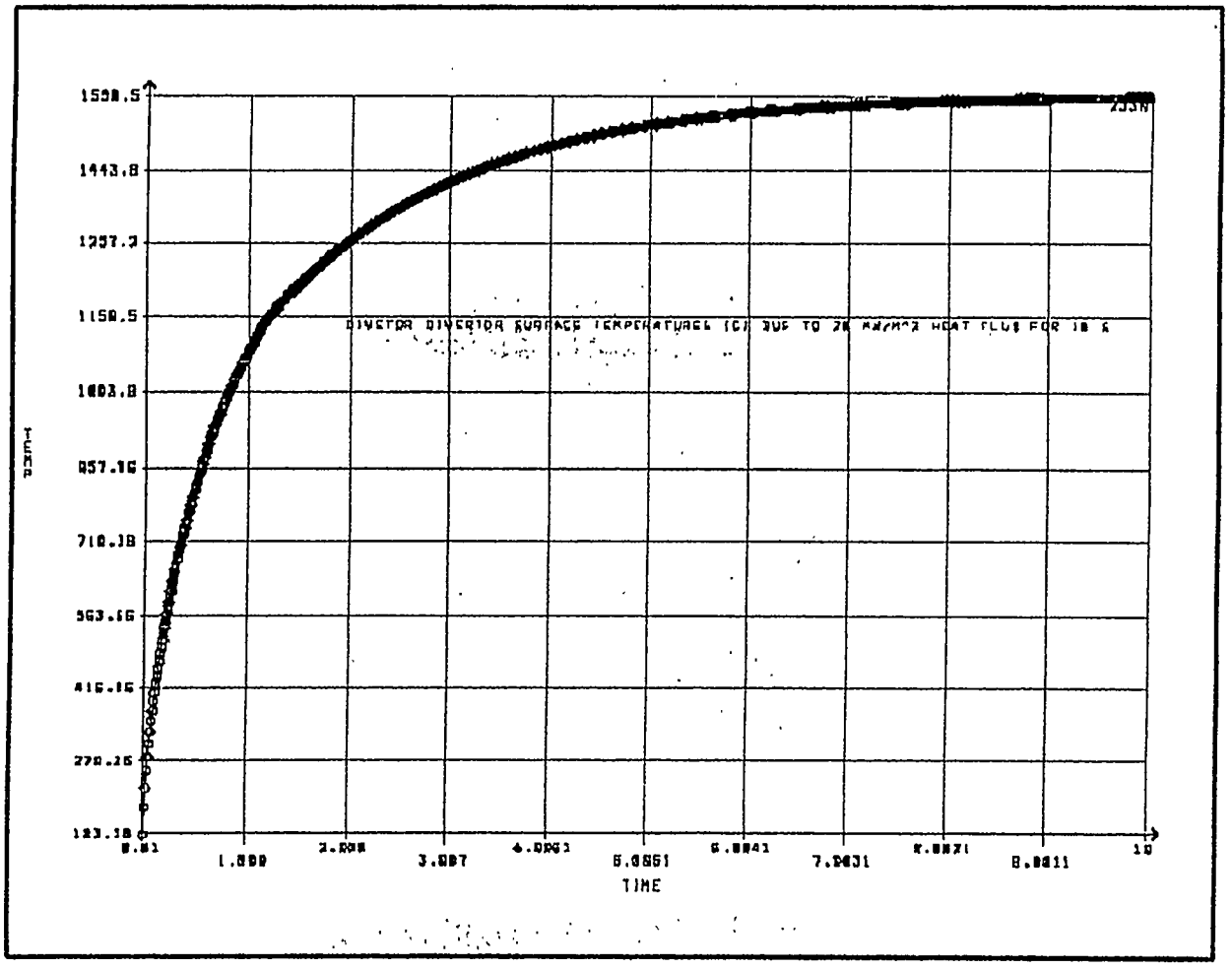

PFC MAXIMUM SURFACE TEMPERATURES

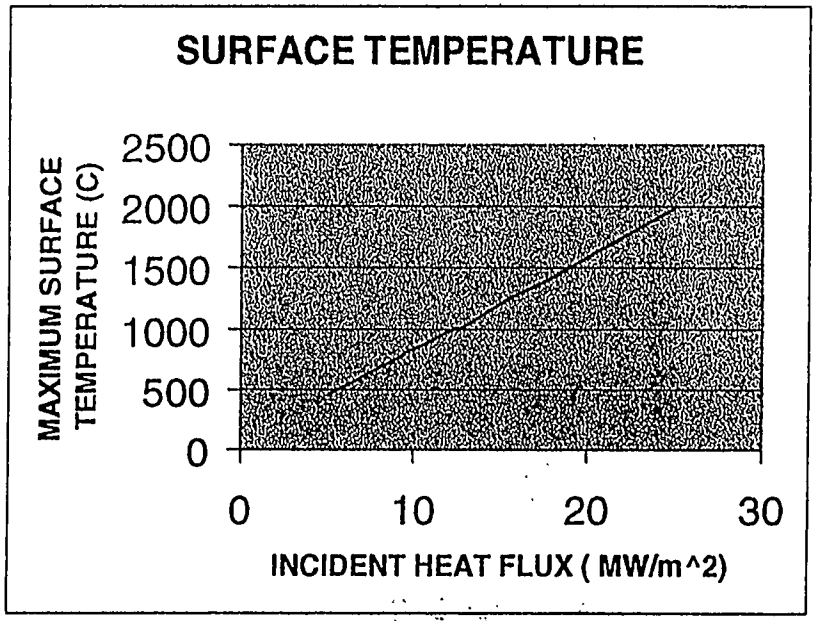

Summary of Thermal Hydraulic Parameters
For Outer Divertor

Parameter	Value
Inlet Temperature (C)	30
Inlet Pressure (Mpa)	1.5
Module Size (mmXmm)	672X550
Maximum Power(MW)	2.32
Peak Heat Flux (MW/m2)	20
Coolant Channel Size (mm)	8
Number of Coolant Channels per Module	48
Number of Channels in Series	2
Flow Velocity(m/s)	10
Volume Flow Per Module(l/s)	9.0
Pressure Drop(Mpa)	0.445
Maximum Exit Temperature (C)	88.8
Minimum Subcooling (C)	92

CONCLUSIONS

- INLET AT 1.5 MPa, 30 C & OUTLET AT 1 MPa, 90 C
- MARGIN ON CHF ~ 1.5
- PEAK PFC TEMPERATURE 1550 C, FOR 20 MW/m^2 FOR 10 s
- A SATISFACTORY DIVERTOR THERMAL HYDRAULIC DESIGN CAN BE ACHIEVED FOR THE FIRE DIVERTOR

PFC Armor and Materials

Research and Development of Tungsten-Coated Divertor Plate

K. Tokunaga, N. Yoshida
Research Institute for Applied Mechanics, Kyushu University

Y. Kubota, N. Noda
National Institute for Fusion Science

Y. Imamura, A. Kurumada, T. Oku
Faculty of engineering, Ibaraki University

T. Sogabe
Toyo Tanso Co.,LTD.

T. Suzuki
Kawasaki Heavy Industries,Ltd.

T. Kato
Nippon Plansee K.K.

L. Ploechl
Plansee Aktiengesellschaft

Presented at
US-Japan Workshop on High Heat Flux Components and Plasma Surface Interactions for Next Fusion Devices
Nov. 1-4, 1999, Hotel St. Francis, Santa Fe, New Mexico

Introduction

- Tungsten seems a promising candidate material for plasma facing components in next experimental fusion devices because of its low sputtering yield and good thermal properties.

- The disadvantages of tungsten as a plasma facing material are its heavy weight and poor workability.

- One way to circumvent these disadvantages is to coat tungsten on light carbon materials that have shown good heat load resistance in the present plasma confinement devices.

- From the viewpoints of thermal conductivity and mechanical strength, it seems that carbon/carbon fiber composites (CFC) are preferable as a substrate material for high heat flux loading.

- Thick tungsten coatings on CFC and isotropic fine grained graphite were successfully produced by vacuum plasma spray (VPS) technique and their good thermal and adhesion properties has been confirmed by high heat flux tests.

Objectives

- To develop W-coated CFC and Graphite divertor plate mock-up.
- To develop silver-free braze material and brazing method between carbon and Cu based alloy.

  CFC tile and isotropic fine grained graphite tiles coated with VPS-W were jointed on a OFHC block by using silver-free titanium brazing technique as well as silver brazing.

- To evaluate thermal response and thermal fatigue lifetime of W-coated CFC and graphite divertor plate mock-ups.

  Heat flux tests using an electron beam facility were carried out.

Outline

(1) *Tungsten coated carbon*

(2) Tungsten coated carbon brazed on OFHC block with a cooling tube

(3) High heat flux tests on the mock-ups

(4) Summary

W-coated CFC/graphite

VPS(Vacuum Plasma Spray)-W on carbon material substrate

substrate	C/C composite CX-2002U isotropic fine graphite IG-430U
intermediate layer (diffusion barrier for C)	PVD multilayer of W and Re
heat treatment	1300°C
thickness of W	0.5mm, 1.0mm
porosity of W	7.5%
size	20mm x 20mm x 10mm^t

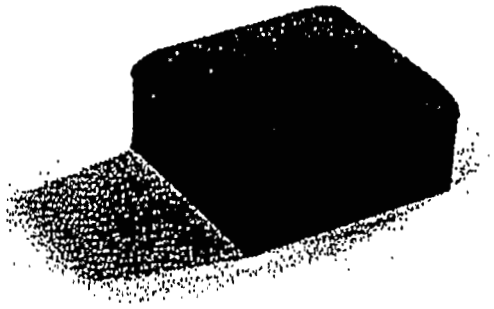

VPS-W/IG-430U (#6)
Thickness of W : 1.0 mm

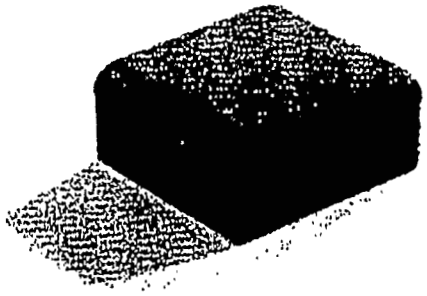

VPS-W/CX-2002U (#12)
Thickness of W : 1.0 mm

Surface morphology of VPS-W

VPS-W(0.5mm)/CX-2002(#10)

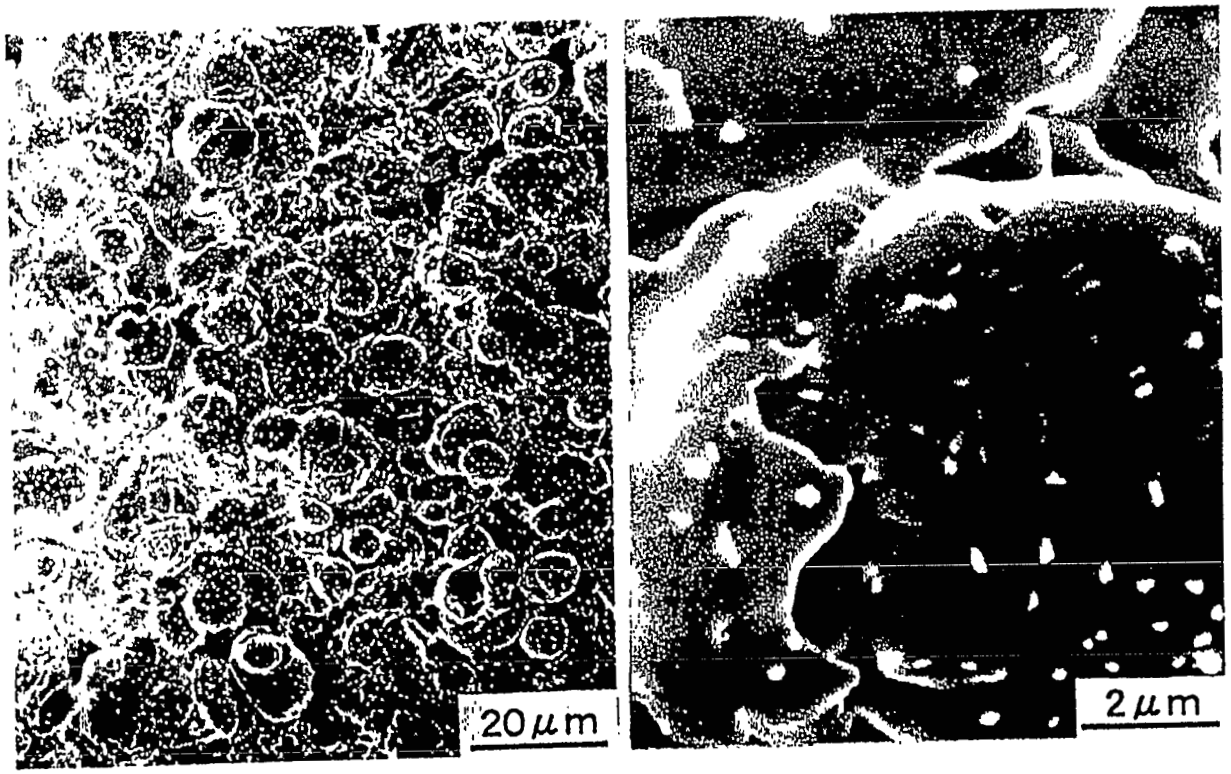

Multilayer structure of W/C interface

VPS-W(1.0mm)/CX-2002U(#6)

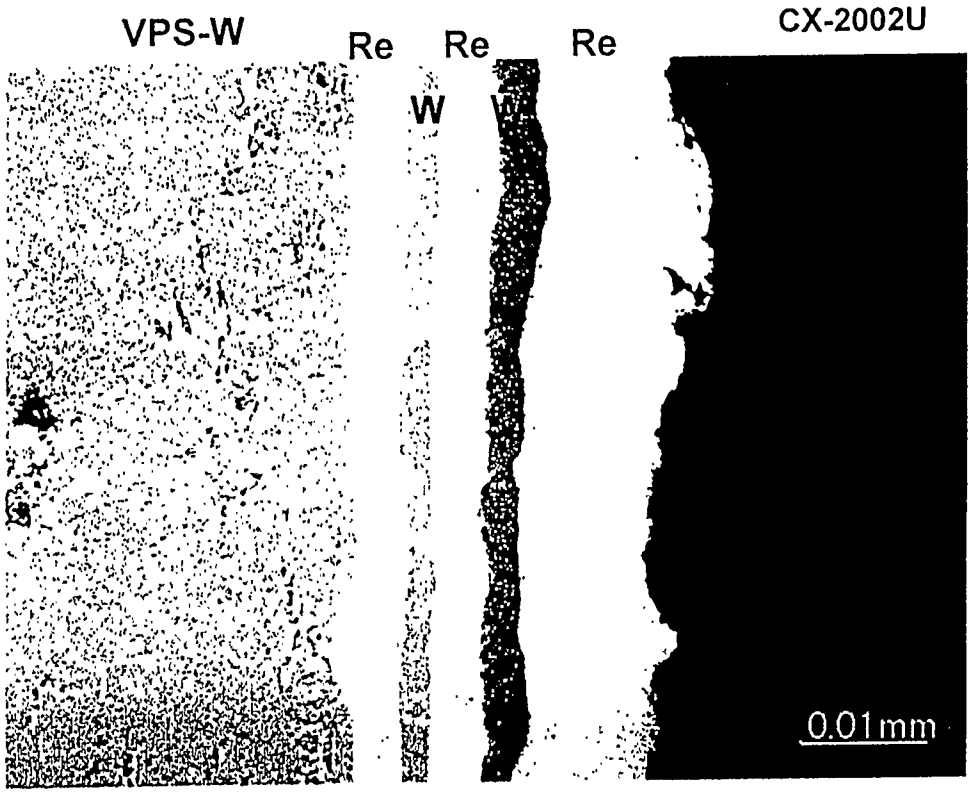

The PVD W-Re multilayer diffusion barrier coating is patented by Plansee.

Brazing of tile and OFHC block

VPS-W coated CX-2002U and IG-430U tiles were brazed on OFHC block with a cooling tube.

(1)silver-free titanium brazing (Ibaraki University)

insert material : Ti foil

braze temperature : 860 °C ～ 1000°C

VPS-W/IG-430U/OFHC: micro cracks were formed at corners of the IG-430U part during the brazing process

IG-430U/OFHC, W/CX-2002U/OFHC, CX-2002U/OFHC mock-ups : no damage

(2) silver-base brazing (Kawasaki Heavy Industries,Ltd.)

insert material : Ag-Ti-In

braze temperature : 750 °C, 850 °C

no damage during the brazing process

W-coated CFC/OFHC

VPS-W(1.0mm)/CX-2002U(#7)/OFHC

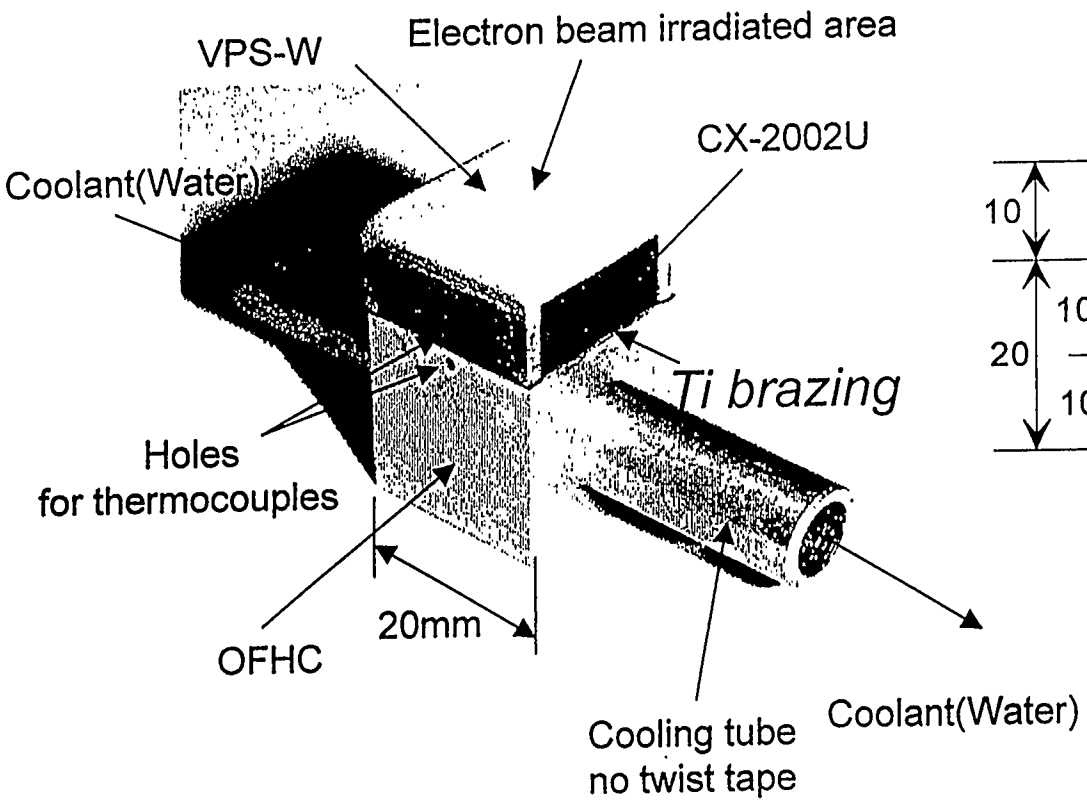

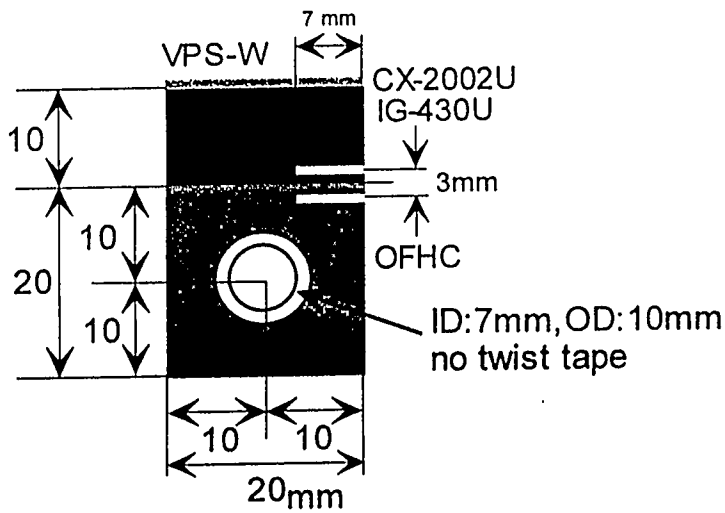

Crack formation at corners of IG-430U

VPS-W(0.5mm)/IG-430U(#19)/OFHC
Ti brazing

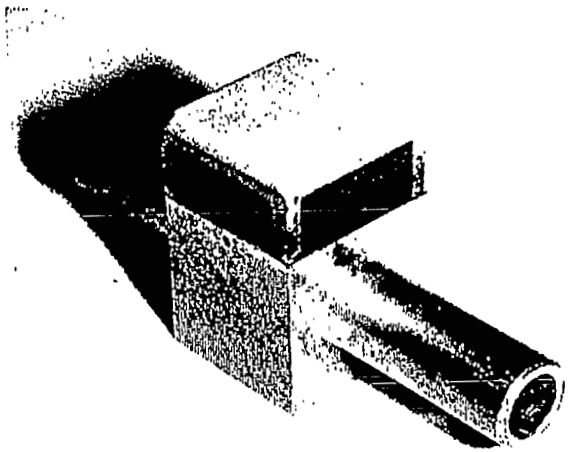

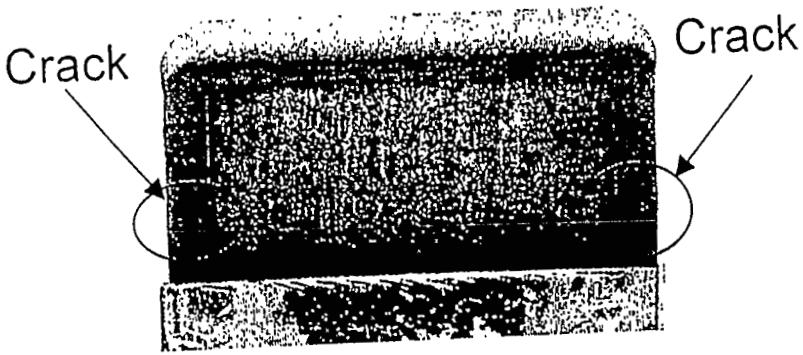

Electron beam facility

Active Cooling Teststand (ACT) in NIFS

E-beam energy: 30 keV
Loading time: 20 s
Beam size: 30 mm x30 mm
Heat flux: ~~0.5~~ 2.0 ~ ~~5.5~~ 10.0 MW/m^2
In situ measurements:
•surface temperature
•vacuum pressure
•emitted particles (QMS)

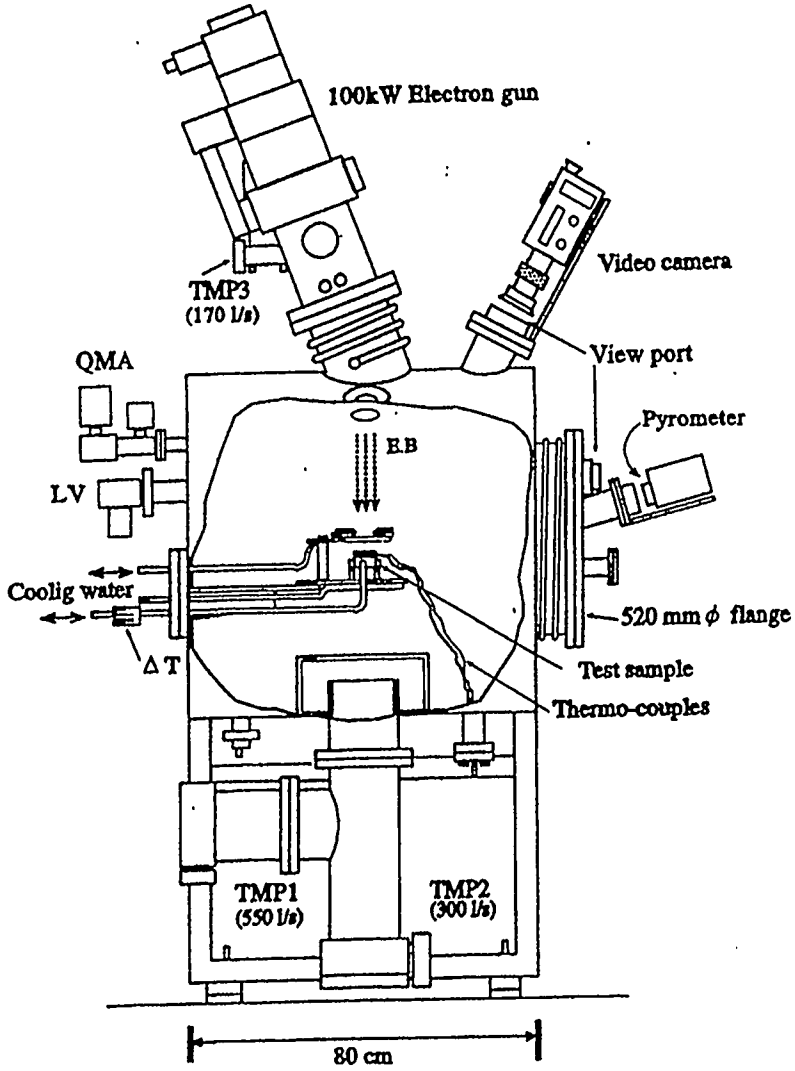

High heat flux test in ACT

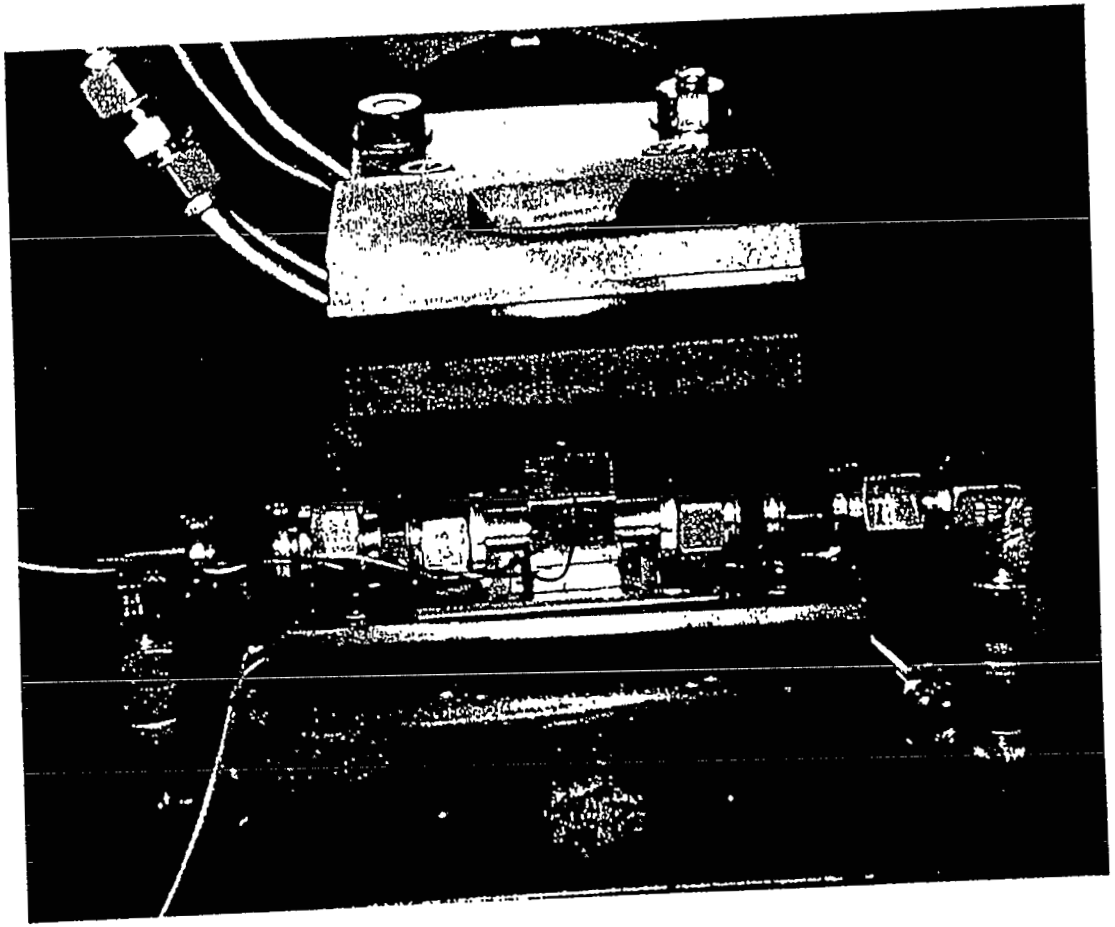

High heat flux test

- The electron beam with a energy : 30 keV
- Shape of beam irradiated : uniform beam profile
- Beam duration :
  ramp-up : 20 s, steady state : 20 s, ramp down : 1s (20/20/1)
- Heat flux : from 2 to 10 MW/m^2.
- Thermal fatigue tests : up to 160 cycles, 10 MW/m^2, 20/20/1s ON /65s OFF
- The surface temperature : a optical pyrometer(300～3000℃) calibrated
- Temperatures of upper side(T1) and lower side(T2) of the brazed area : thermocouples
- Water flow velocity : 14.4 m/s
- Pressure : 0.5 MPa
- Inlet temperature : 25° C
- Surface modification : SEM

Time evolution during electron beam

VPS-W(0.5mm)/CX-2002U(#20)/OFHC

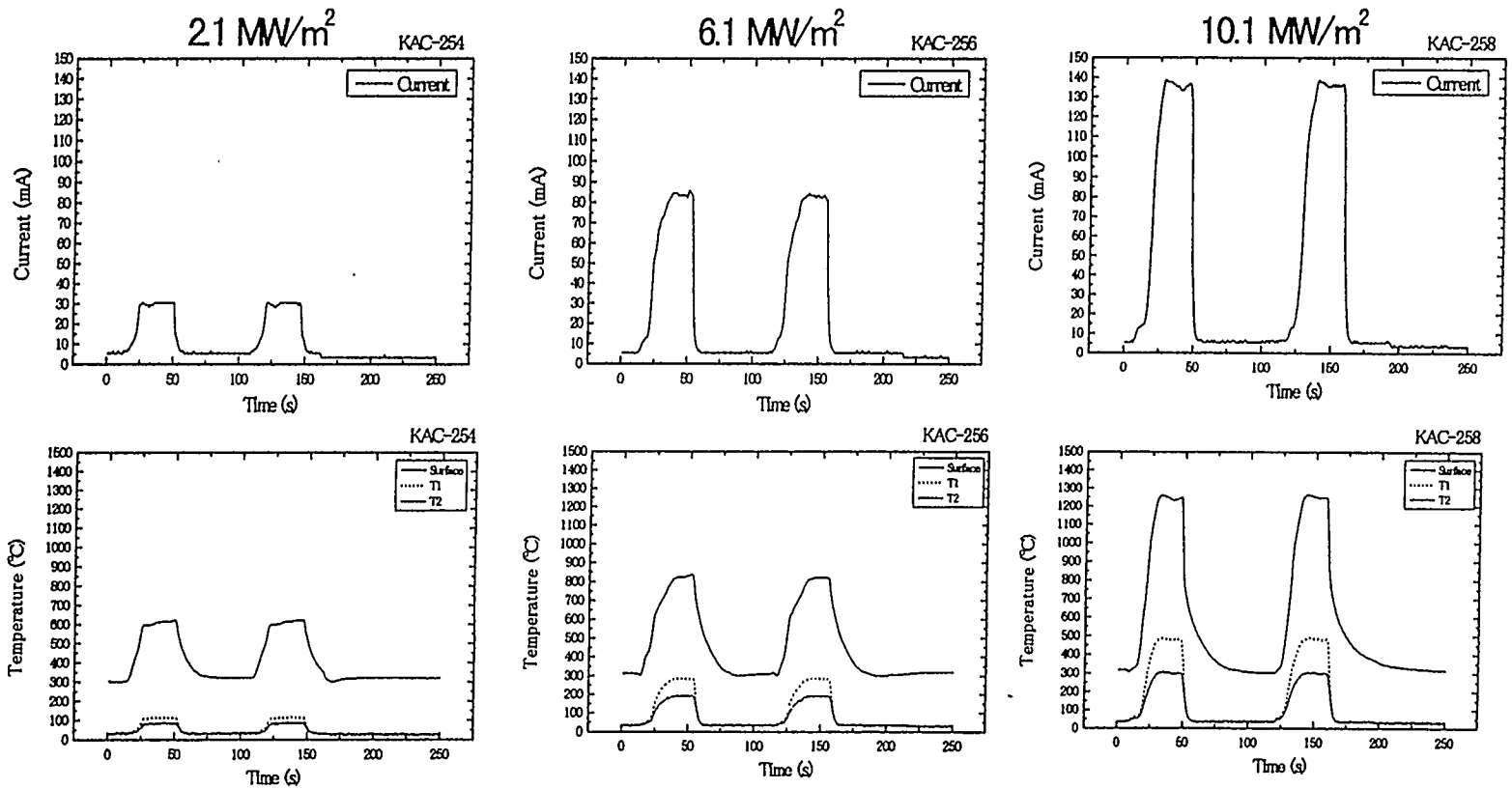

Steady state temperatures during irradiation

VPS-W(1.0mm)/IG-430U(#2)/OFHC & IG-430U/OFHC

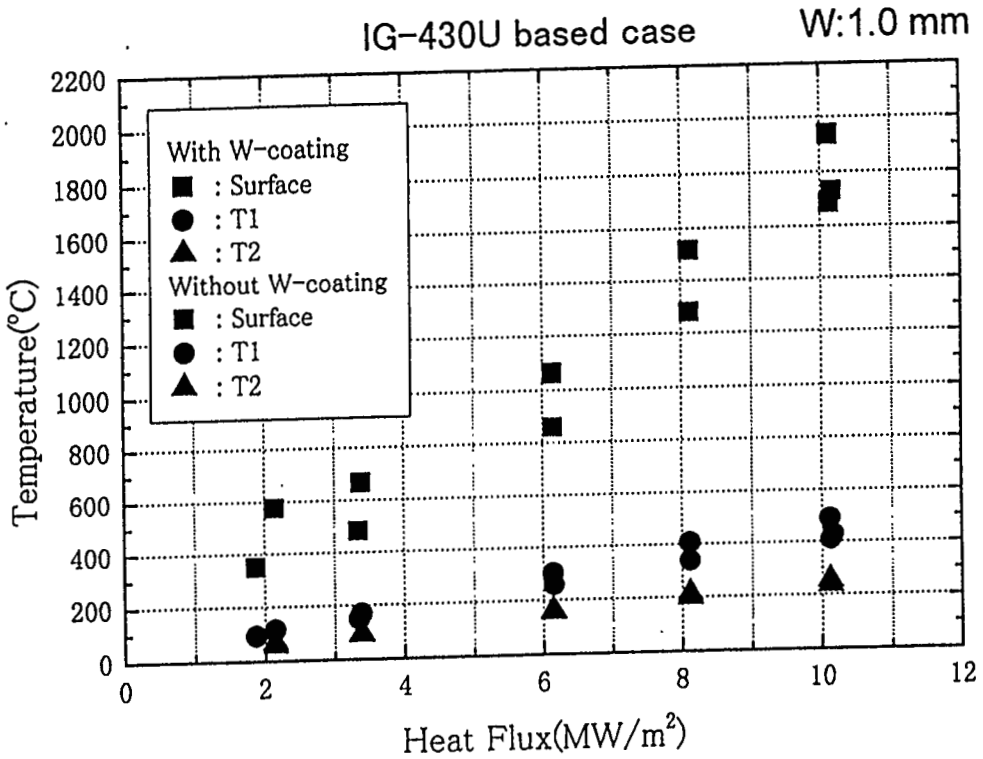

Steady state temperatures during irradiation

VPS-W(0.5mm)/CX-2002U(#20)/OFHC & CX-2002U/OFHC

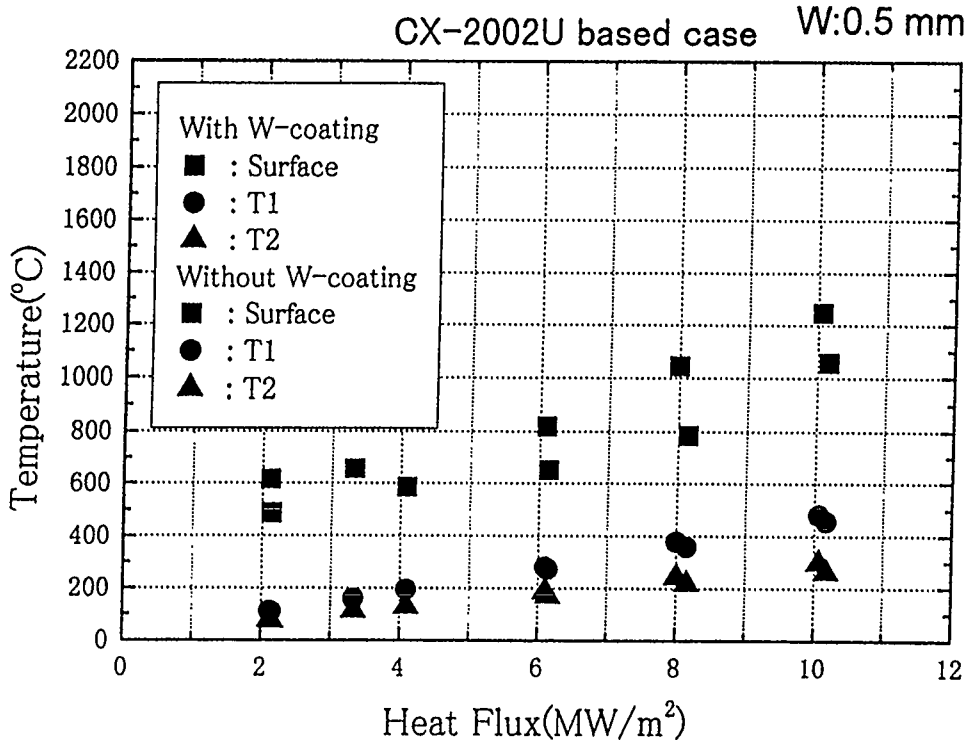

Temperature change by thermal fatigue

VPS-W(0.5mm)/CX-2002U(#20)/OFHC

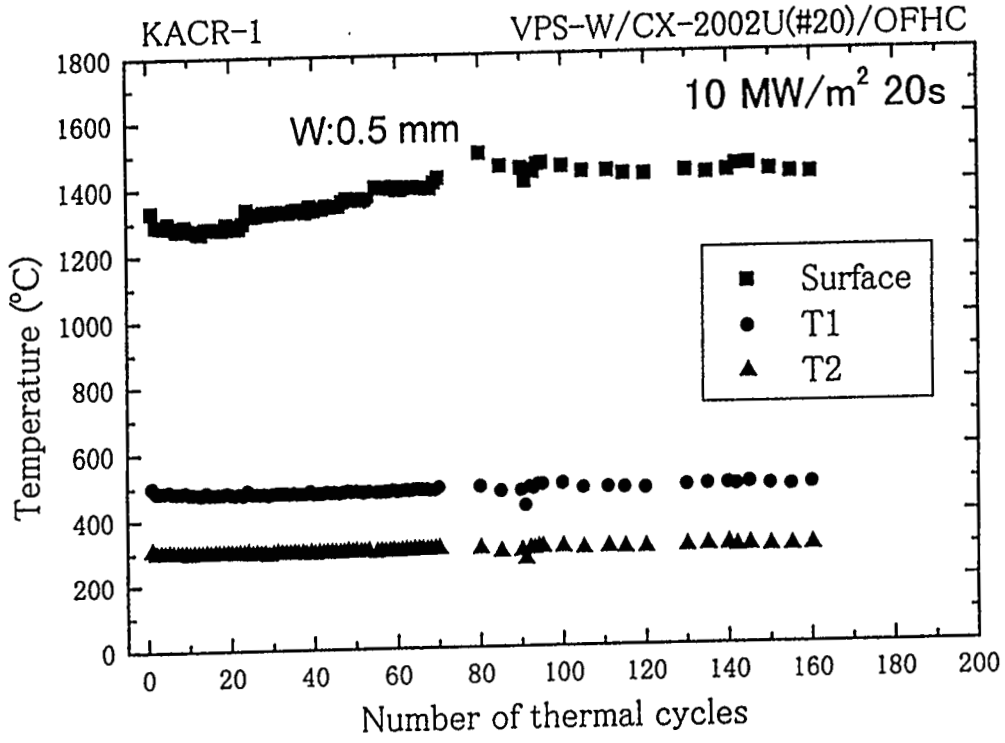

Summary

- For development of light high-Z plasma facing components, VPS-W coated CX-2002U and IG-430U were brazed on the OFHC with a cooling tube by using Ti foil as a brazing material.
- Thermal response and thermal fatigue tests on the mock-ups were carried out under an actively cooling condition using electron beam.
- In the case of W/IG-430U/OFHC, micro-cracks were formed at the corners of the IG-430U part during brazing process, but not for W/CX2002U/OFHC.
- (Ti brazing)
- No cracks and no exfoliation were formed in W-coating and at brazing interface by heat loads up to 10 MW/m^2.
- Surface temperature increases about 250-300 °C by coating VPS-W of 1 mm thick.

(continued)

Summary

- For development of light high-Z plasma facing components, VPS-W coated CX-2002U and IG-430U were brazed on the OFHC with a cooling tube by using Ti foil as a brazing material.

- Thermal response and thermal fatigue tests on the mock-ups were carried out under an actively cooling condition using electron beam.

- In the case of W/IG-430U/OFHC, micro-cracks were formed at the corners of the IG-430U part during brazing process, but not for W/CX2002U/OFHC.
  (Ti brazing)

- No cracks and no exfoliation were formed in W-coating and at brazing interface by heat loads up to 10 MW/m^2.

- Surface temperature increases about 250-300 °C by coating VPS-W of 1 mm thick.
  (Ti brazing)

(continued)

Future plan

- Detail of thermal response and fatigue lifetime
- Irradiation effects of hydrogen and helium on VPS-W carbon tile
- Interaction with plasma particles (hydrogen isotope, helium) on VPS-W carbon tile

US-Japan Workshop on HHFC and PSI in Next Fusion Devices (Santa Fe, Nov.1-4, 1999)

Evaluation of Integrity for Carbon Divertor Model Joined with Copper by using Ti Foil

Y. IMAMURA*, T. OKU*, A. KURUMADA*, Y. TOMOTA*, K. KAWAMATA*, Y. KUBOTA**, N. NODA** and O. MOTOJIMA**

* Faculty of Engineering, Ibaraki University: 4-12-1, Nakanarusawa, Hitachi, Ibaraki, 316-8511, Japan

** National Institute for Fusion Science: 322-6, Oroshi, Toki, Gifu, 509-5292, Japan

Outlines:

1. Background and Purpose
2. Carbon divertor model
3. Electron beam heating test
4. Mechanical properties after heat load test
5. Conclusions

Background:

- Plasma facing components : divertor plate
  - thermal radiation, high heat load, bombardments of charged particles, plasma disruption, electromagnetic force, etc.
  - erosion, sputtering, injection into plasma, tritium inventory, etc.
- Structure of plasma facing components :
  - brazing armor tile with heat sink block to be cooled actively.

- Carbon materials (C/C composite, graphite) : armor tile
  - low atomic number, high thermal conductivity, excellent heat resistance, excellent thermal shock resistance
- Oxygen-free high conductivity copper : heat sink material
  - high thermal conductivity, high heat transfer coefficient

- Silver wax brazing :
  - heavy radioactivity due to nuclear transmutation.

Purpose:

- Development of plasma facing components having high performance.
- Manufacturing a carbon divertor model joined a C/C composite with oxygen-free copper by inserting only titanium foil.
- Evaluation of the integrity of the joined part by measuring mechanical properties and microstructures before and after heat load tests.

Conclusions:

- Bending strengths were nearly equal to the mother material (CX-2002U) and the enough joining strength was confirmed.
- Temperatures of the carbon divertor model were constant during the cyclic heat load tests and the integrity of the joined part was confirmed at the heat flux less than 12.5MW/.
- Bending strength of the specimen cut out from the carbon divertor model varied widely, however SEM did not observe thermal cracks like a delamination after the cyclic heat load test of 12.5MW/m^2. Therefore, the integrity of the joined part was confirmed at the heat flux less than 12.5MW/m^2.

High Heat Flux Tests of Carbon Composites for KSTAR and NSTX

R. E. Nygren and D. L. Youchison, Sandia National Laboratories
K. H. Im and J. Kim, Korea Basic Science Institute, Taejon, Korea,
H. C. Park and K. S. Kim, Daewoo Heavy Industries Ltd., Changwon, Korea

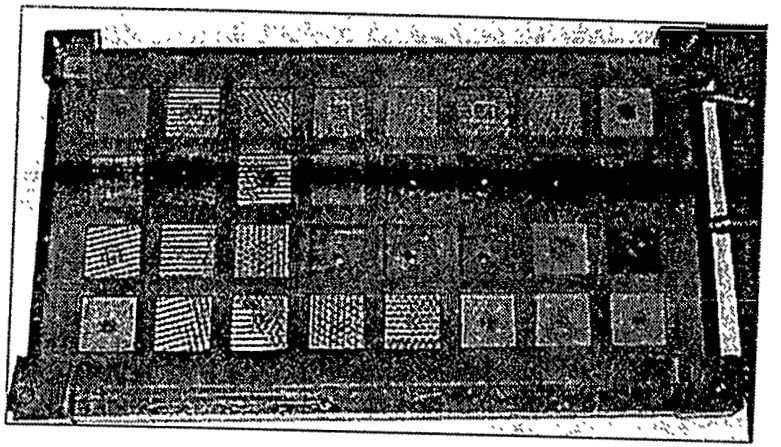

sample holder with KSTAR samples

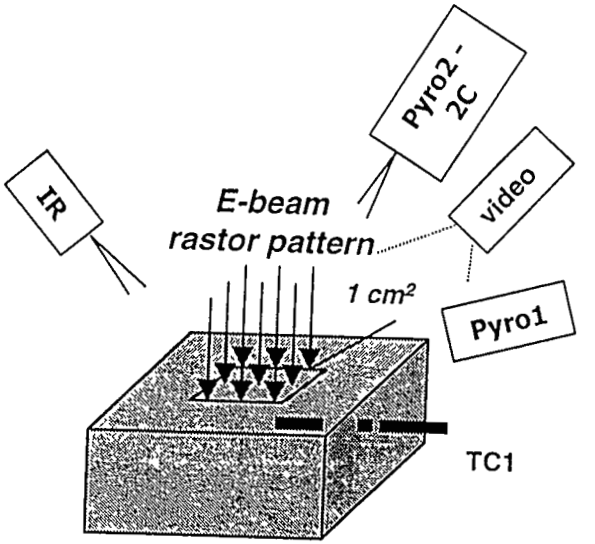

Sandia National Laboratories

Conclusions on KSTAR Testing

- The Daewoo CFCs performed well. Sample K20 had the longest time to reach 2600°C (at 92MW/m^2) in this test or TPX test of many CFCs.
- K20 is 2-D type. 3-D samples with higher k-parallel and k-perp but lower densities, did not perform as well. Heat flows downward and also radially outward from the central heated area. Radially outward flow may be more important in how fast the surface temperature at the center rises.
- Of samples with long times to reach 2600°C, the time for K20 was slightly longer than samples K8, K9, K10 and K11. All these samples all had a similar architecture, but K20 had a higher processing temperature a somewhat higher thermal conductivity.
- Weight loss measurements were also taken, and K20 had the least weight loss* within the group of Daewoo samples tested.

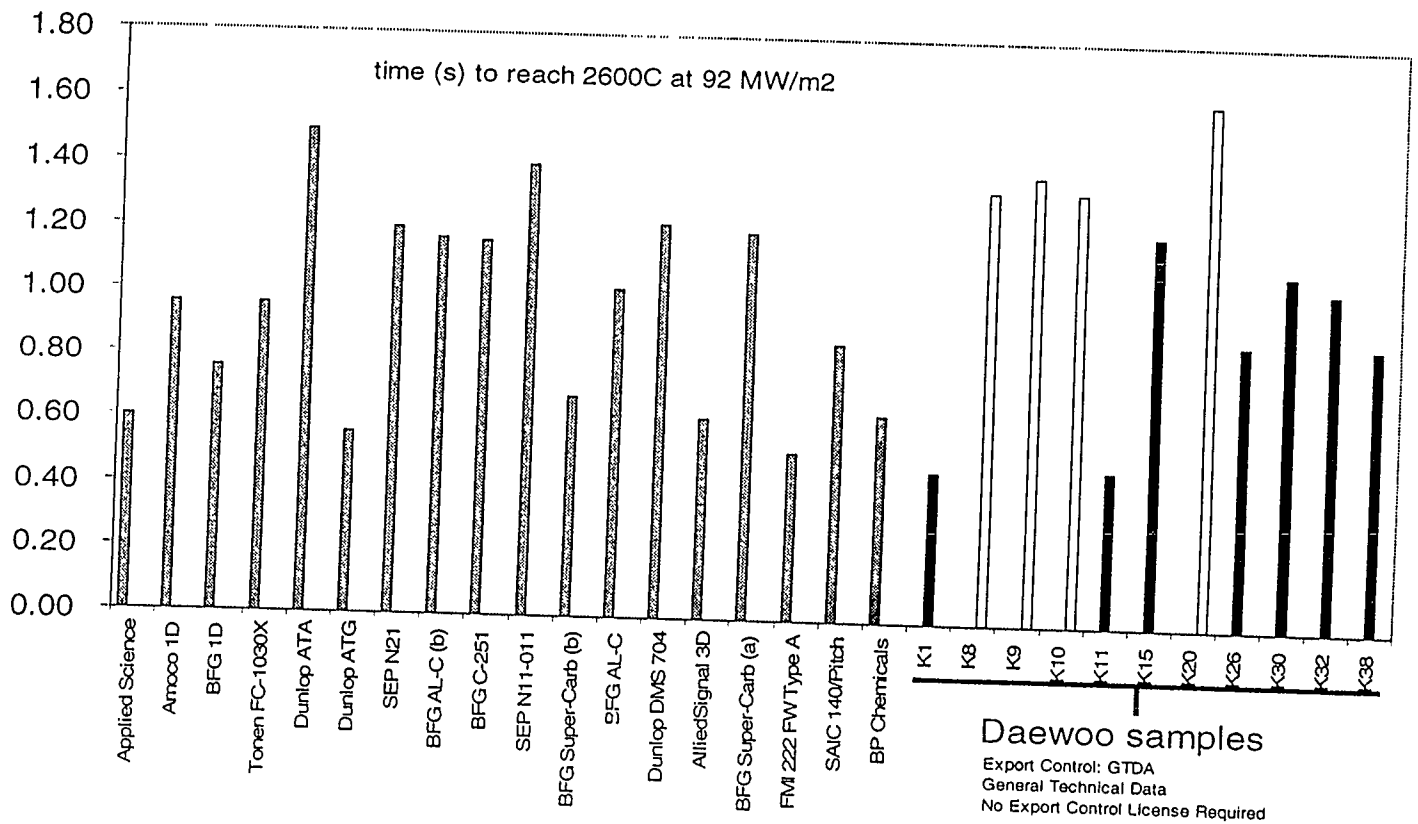

Export Control: GTDA General Technical Data No Export Control License Required

Sandia National Laboratories

Surface Features

The samples were observed with a low magnification optical microscope and a scanning electron microscope (SEM) before and after testing. The the most prominent feature is the blackening of the surface where substantial vaporization of carbon has occurred. Other features observed include some cracking in the fiber tows and in the matrix. Also, in the first round of tests, separation of some fibers from the surface was observed. The photos below show typical features.

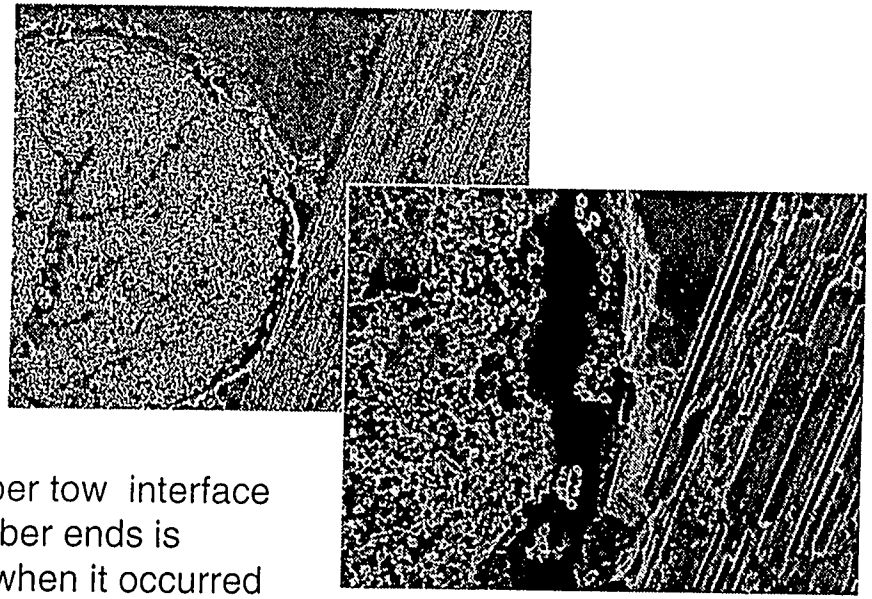

K1 - Cracking at fiber tow interface and loss of some fiber ends is typical of damage when it occurred

summary of shots December 1998

35	1.5	177308	177316	
35	1.5	177334	177335	all ----------
35	1.5	177344	177361	
50	1.5	177364	177391	K17,K25,K31,K35,K11,K12,K27 trip
55	1.5	177399	177425	K29 trip, skip [K17,K25,K31,K35,K11,K12,K27]
75	1.5	177432	177451	K1,K2,K3,K4,K5,K33,K39,K38,K14,K48,K47 trip, skip [K17,..]
100	1.5	177488	177503	test [K3,K4,K5,K6,K15,K45,K51,K42,K7,K8,K9,K10,K33]; K3,K15 trip
60	3	177504	177517	test [K3,..+K38]; K3,K6,K38,K7,K8,K9,K10 trip >2s
60	3.5	177519	177535	test [K3,..+K38]; K3,K4,K5,K6,K38,K7,K8,K9,K10 trip >2s;K6,K51 trip >3s; K15,K45 full 3.5s
60	5	177532	177535	test K6,K15,K45,K51; K6,K15,K51 trip>2s; K45 trip >3s

For KSTAR, a total of 28 samples were tested.

6 were duplicates - samples with TCs next to samples without TCs.

The TCs were used to measure the absorbed heat and to calculate the fraction of the beam power absorbed.

The samples were tested to 100MW/m^2 with 1.5s shots. Then selected samples were tested at 60MW/m^2 for shots up to 3.5s.

Sandia National Lab. : KSTAR High Heat Flux Test December 1998

No.	Type I.D	weave	Thermal Conductivity z-dir.	Normal	Parallell	Density (g./cc)	wt. loss (g.)
13	4D-Thr	4-D	**121.7**	121.7	141.5	1.82	0.0017
15	4D-TG-C	4-D	**185.1**	185.1	242.6	1.87	0.0137
17	4D-TG-D-R	4-D	**97.8**	97.8	96.5	1.70	0.0009
25	Fi-BD-P	Quasi 3-D	**27.6**	20.3	27.6	1.57	0.0000
27	Fi-BD-N	Quasi 3-D	**20.3**	20.3	27.6	1.57	0.0010
29	Chop-TG-P	Chopped	**35.0**	35.0	17.5	1.82	0.0004
31	Chop-TG-N	Chopped	**17.5**	17.5	35.0	1.82	0.0001
33	Chop-Pitch-P	Chopped	**159.9**	159.9	41.0	1.73	0.0006
35	Chop-Pitch-N	Chopped	**41.0**	159.9	41.0	1.73	0.0001
38	2D-Pitch-BD-P	2-D	**157.4**	54.4	157.4	1.73	0.0013
39	2D-Pitch-BD-N	2-D	**54.4**	157.4	54.4	1.73	0.0007
42	2D-Phenol-1.78	2-D	**162.1**	24.5	162.1	1.78	0.0012
45	To-Yo 10x10						0.0007
47	4D-TG -HIP	4-D	**78.8**	78.8	120.7	1.72	0.0009
48	2D-Phenol-1.52	2-D	**101.6**	12.7	101.6	1.52	0.0017
51	3D-TG	3-D	**241.9**	241.9	167.5	1.67	0.0083

Sandia National Lab. : KSTAR High Heat Flux Test August 1998

No.	Type I.D	weave	Thermal Conductivity z-dir.	Normal	Parallell	Density (g./cc)	wt. loss (g.)
1	4D-nae	4-D	**125.0**	125.0	117.0	1.95	0.0006
2	4D-nae	4-D	**125.0**	125.0	117.0	1.95	0.0006
3	4D-24	4-D	**61.0**	61.0	54.0	1.82	0.0002
4	4D-24	4-D	**61.0**	61.0	54.0	1.82	-0.0002
5	4D-24	4-D	**61.0**	61.0	54.0	1.82	0.0001
6	4D-24	4-D	**61.0**	61.0	54.0	1.82	0.0000
7	2D-L-24-P	2-D	**104.0**	30.0	104.0	1.98	-0.0049
8	2D-L-24-P	2-D	**104.0**	30.0	104.0	1.98	-0.0025
9	2D-L-24-P	2-D	**104.0**	30.0	104.0	1.98	0.0003
10	2D-L-24-P	2-D	**104.0**	30.0	104.0	1.98	0.0004
11	4D-KO	4-D	**100.5**	100.5	117.5	1.88	0.0000
13	4D-nae	4-D	**125.3**	125.3	117.0	1.96	0.0015
20	2D-L-2700-P	2-D	**144.6**	37.8	144.6	1.97	0.0002
26	4D-2(n)	4-D	**104.0**	104.0	103.6	1.79	0.0004
30	4D-3	4-D	**206.7**	206.7	191.0	1.71	0.0003
31	4D-3	4-D	**206.7**	206.7	191.0	1.71	0.0003
32	4D-4	4-D	**187.7**	143.6	187.7	1.94	0.0007
38	4D-7	4-D	**144.1**	144.1	162.6	1.86	0.0009
15	4D-TG-C	4-D	**185.1**	185.1	242.6	1.87	0.0005
51	3D-TG	3-D	**241.9**	241.9	167.5	1.67	0.0000
	Quasi 3-D	3-D					0.0000

Export Control: GTDA General Technical Data No Export Control License Required

Sandia National Laboratories

HHF Tests of 2nd Batch of KSTAR Samples

K7
upper frame
is ~2cm
lower frame
is~5X

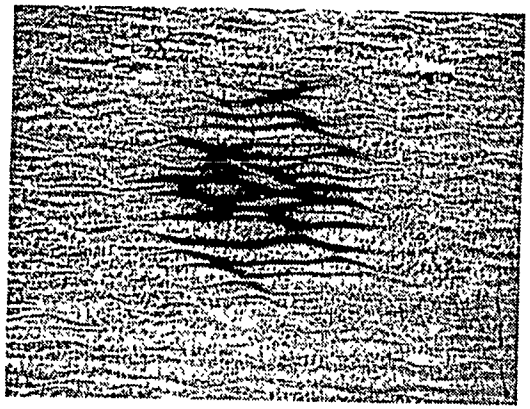

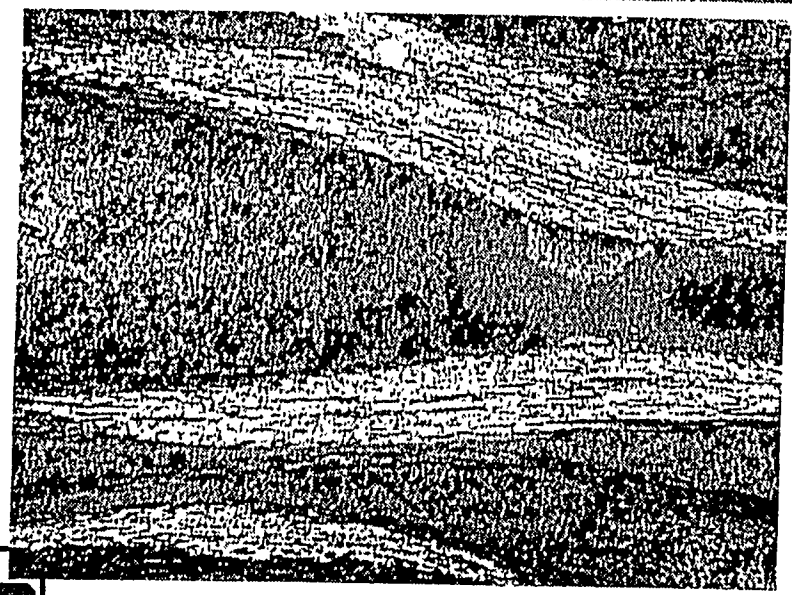

K20
upper frame
is ~2cm
lower frame
is~5X

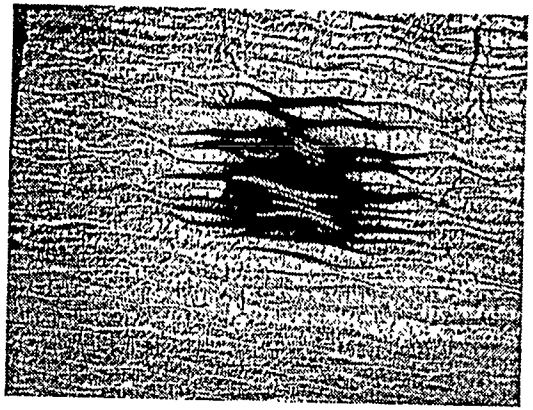

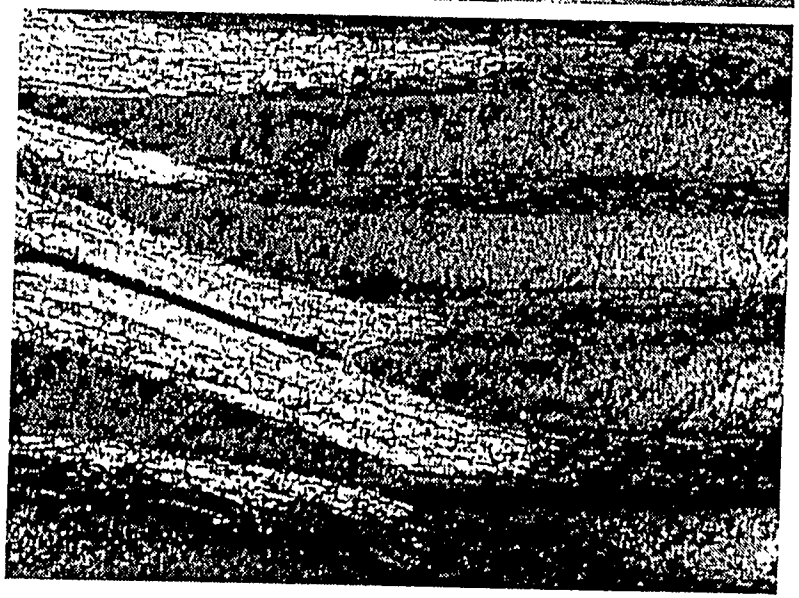

Export Control: GTDA General Technical Data No Export Control License Required

Sandia National Laboratories

NSTX Armor High Heat Flux (HHF) Tests

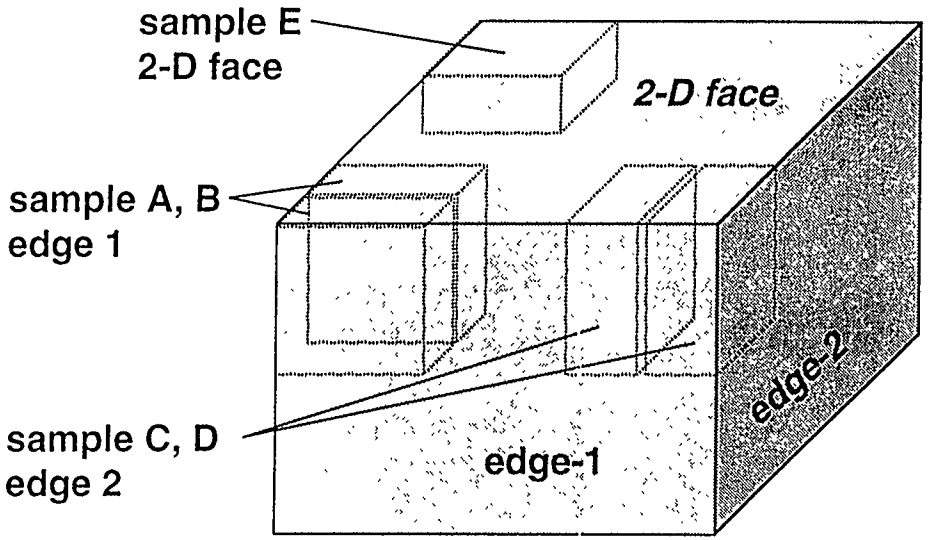

2-D carbon fiber composite
Allied Signal (Type 865-19-4)

Result: no apparent damage for exposures to 120 MW/m^2 for 1.5 s.
We know that CFCs are tough materials.

NSTX armor HHF Tests

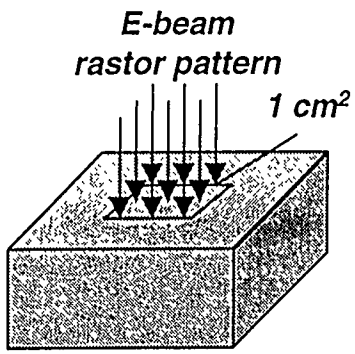

ID	Energy	Wt. loss
A	377 kJ	0.0018 g. (*Low value ??*)
B	494	0.0063
C	356	0.0066
D	285	0.0095
E	271	0.0027 (*face, no tow ends*)

case	heat flux	comment
1-6	5-35 MW/m^2	All samples OK, all shots 1.5 s
7-9	50-140	Short shots (P,T trips), calorimetry & focus issues
9 rerun	100	All OK, New TC, refocus beam
10	120	All OK
11	60	Longer shots, >2 s until T trip ends shot

Development of a Tungsten Alloy Database for APEX

S.J. Zinkle

Metals & Ceramics Division, Oak Ridge National Lab

US-Japan Workshop on High Heat Flux Components
Santa Fe, November 1-4, 1999

Possible Structural Materials for High Wall Loading Concepts

- **Low-activation materials**
  - Vanadium alloys
  - Ferritic/martensitic (8-9%Cr) steels, ODS steels
  - SiC/SiC composites

- **Refractory alloys**
  - Nb-1Zr
  - Nb-18W-8Hf
  - T-111 (Ta-8W-2Hf)
  - TZM (Mo-0.5Ti-0.1Zr-0.02C)
  - Mo-Re
  - W-(5-25%)Re
  - W-TiC

- **Ni-based superalloys**

- **Porous-matrix metals and ceramics**

- **Intermetallics**
  - TiAl
  - Fe_3Al

- **Composites**
  - C/C
  - metal matrix composites
  - Cu-graphite
  - Ti_3SiC_2 composites

- **Conventional structural alloys**
  - Austenitic stainless steel

Recrystallized mechanical properties are used for the refractory alloys (rather than stress-relieved properties) in order to provide conservative design margins

Factors Affecting Selection of Structural Materials

- Unirradiated mechanical and thermophysical properties
- Chemical compatibility/corrosion effects
- Materials availability / fabricability / joining technology / cost
- Radiation effects
- Safety aspects (decay heat, induced radioactivity, etc.)

Resources for Structural Materials Database

- Fusion Materials Properties Handbook / ITER Materials Properties Handbook, ed. J.W. Davis (Boeing/St Louis)

  - V alloy chapter has not been updated in latest version of IMPH (pub. 5)
  - limited or no information for F/M steels, SiC/SiC

- Aerospace Structural Metals Handbook (1963-1988), ed. W.F. Brown, Jr.
  - mechanical and thermophysical properties of refractory alloys vs. temperature

- Proc. Conf. on Refractory Alloys for Space Nuclear Power Applications, eds. R.H. Cooper, Jr. and E.E. Hoffman, CONF-8308130 (1984)

- ITER Materials Assessment Report G A1 DDD 01 97-08-13 W01.1 (Chapter 2.2, W alloys)

- Original research publications

Ultimate Strength of Group VI Refractory Alloys

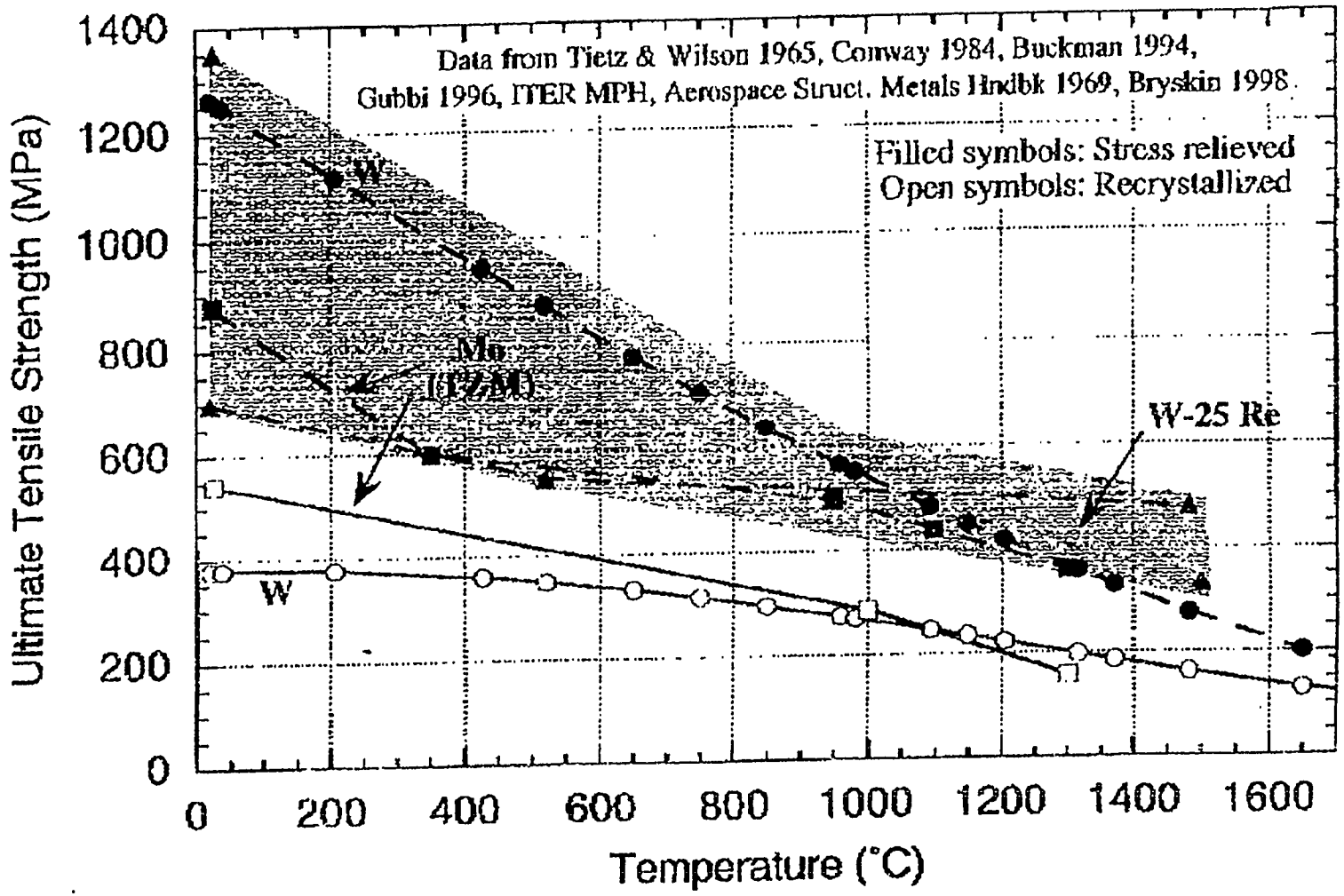

Fracture Toughness of Pure Tungsten

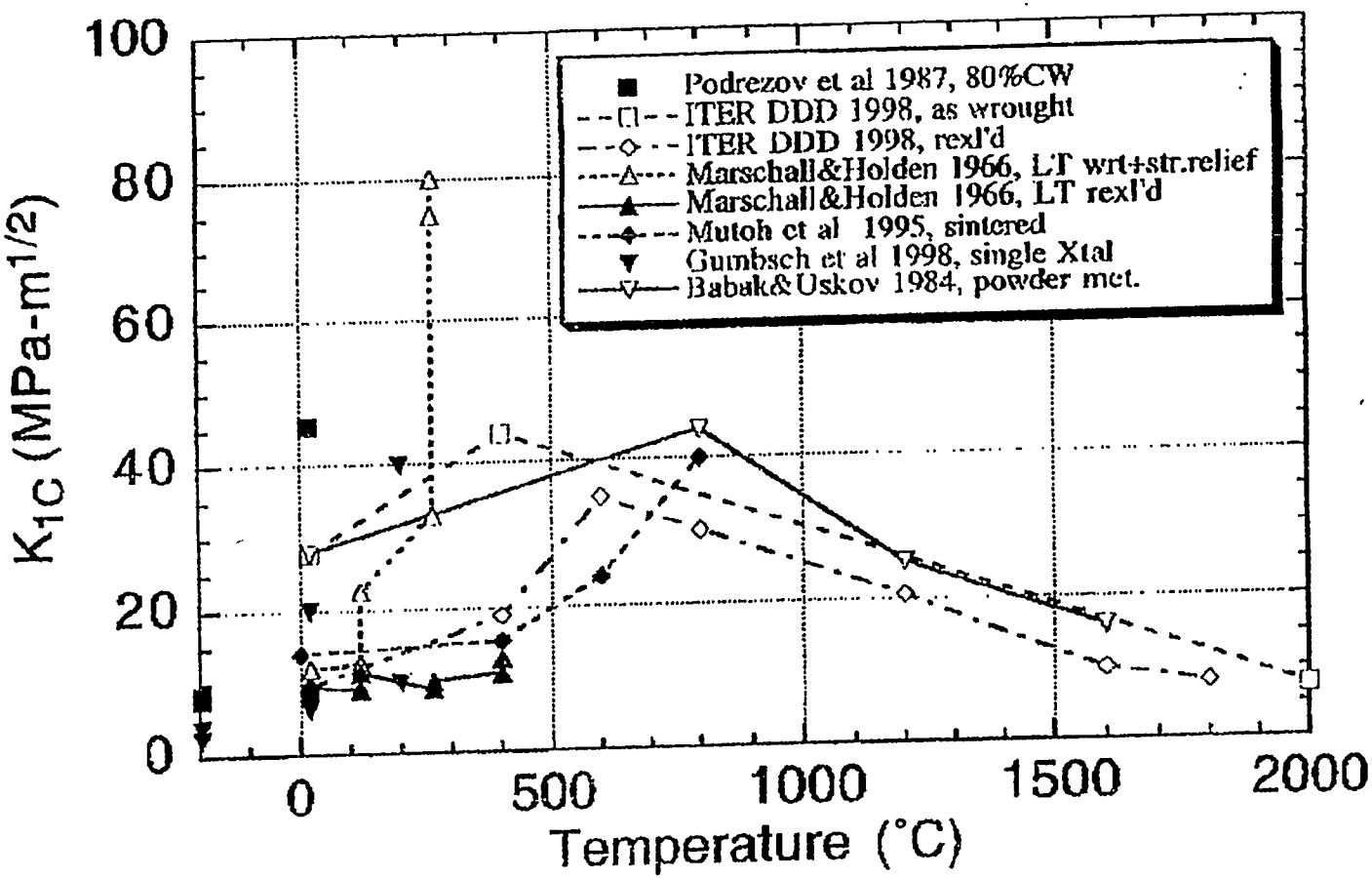

•Pure W has very low fracture toughness (similar to rad.-embrittled FM steel or V alloys)

Effect of Thermomechanical Processing and Alloying Additions on the Fracture Toughness of W

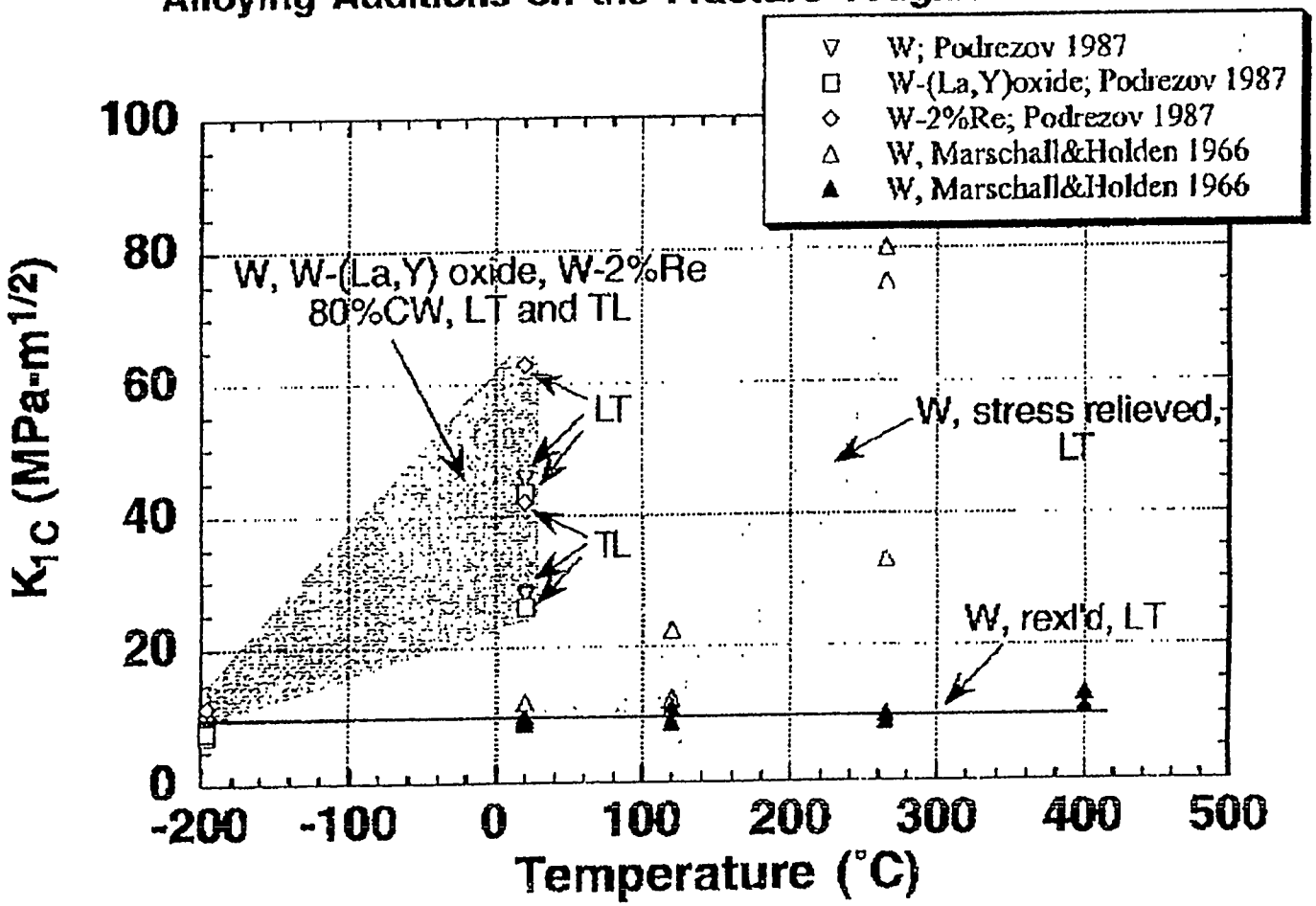

• Alloying additions and thermomechanical working give improved toughness

Effect of Strain Rate on the Tensile DBTT of Tungsten

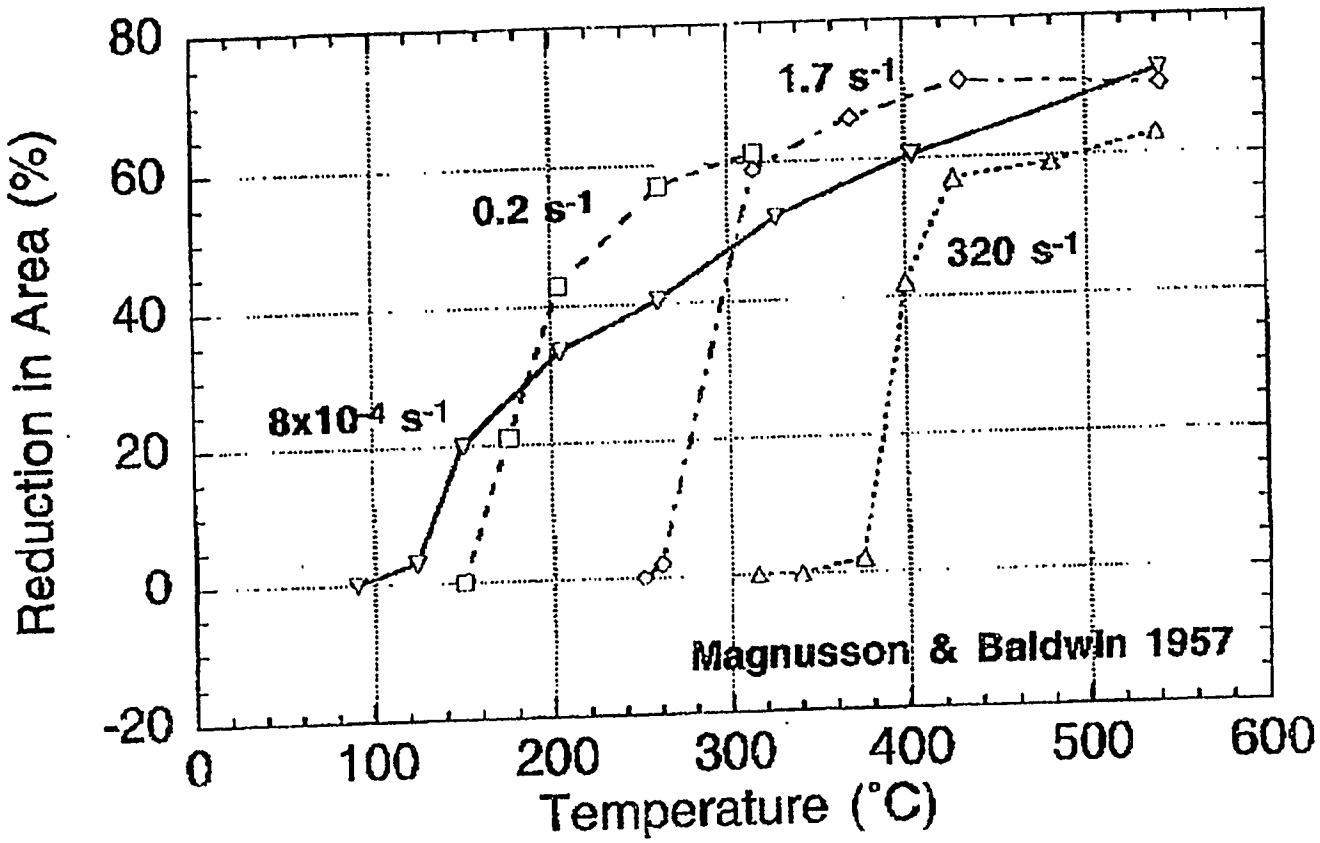

- The DBTT is dependent on numerous factors, including strain rate and notch acuity ("tensile DBTT" is not a meaningful design parameter)

Overview of Radiation Effects in Refractory Metals

- Void swelling is not anticipated to be a lifetime-limiting issue due to the BCC structure of the high-temperature refractory alloys
  - existing fission reactor data base indicate moderate swelling (<2%) for doses up to 10 dpa or higher
  - effects of fusion-relevant He generation on swelling is uncertain
  - swelling regimes are ~600 to 1000•C for all 4 classes of refractory alloys

- The Group Vb alloys (Nb, Ta) exhibit better ductility before and after irradiation
  - very limited mechanical properties data base on irradiated Nb, Ta alloys
  - extensive mechanical properties data base on irradiated Mo alloys (but at relatively low irradiation temperatures)

- Very limited or no fracture toughness/Charpy impact data on irradiated high temperature refractory alloys
  - "tensile DBTT" of Mo, W alloys increases to very high values even for low doses at moderate temperatures (e.g., 600•C test after ~1 dpa at 300•C for W, W-10Re)

- Refractory alloys are generally designed for use in stress-relieved condition (rather than recrystallized) in order to achieve of higher strength
  - radiation-enhanced recrystallization and/or radiation creep effects need to be investigated (designs should use recrystallized strengths to be conservative)

Radiation Effects on Mechanical Properties of High-Temperature Refractory Alloys

W and W Alloys: P/M or CVD W, W-1% La_2O_3, W-Mo-Y (alloy W-13I)

- Tensile elongation ~0 for T_{irr}= 400, 500•C, 0.5-1.5x10^{26} n/m^2, ≤2 dpa (Steichen 1976, Wiffen 1984, Gorynin et al 1992); irradiations at 700•C are in progress

- Un-notched bend bar DBTT>900•C for W, W-10%Re irradiated at 300•C, 0.5x10^{26} n/m^2, (~1 dpa); most rapid embrittlement observed for W-10%Re (Krautwasser et al 1990)

- Irradiation data at doses >0.1 dpa is not yet available for "radiation embrittlement-resistant" W-TiC alloys (Kurishita et al.);

- Mechanical property specimens need a stress concentrator (notch) in order to make a quantitative assessment of the relative radiation resistance

=> estimated minimum operating temperature ~900•C, based on DBTT considerations (scaling from Mo alloy data base)

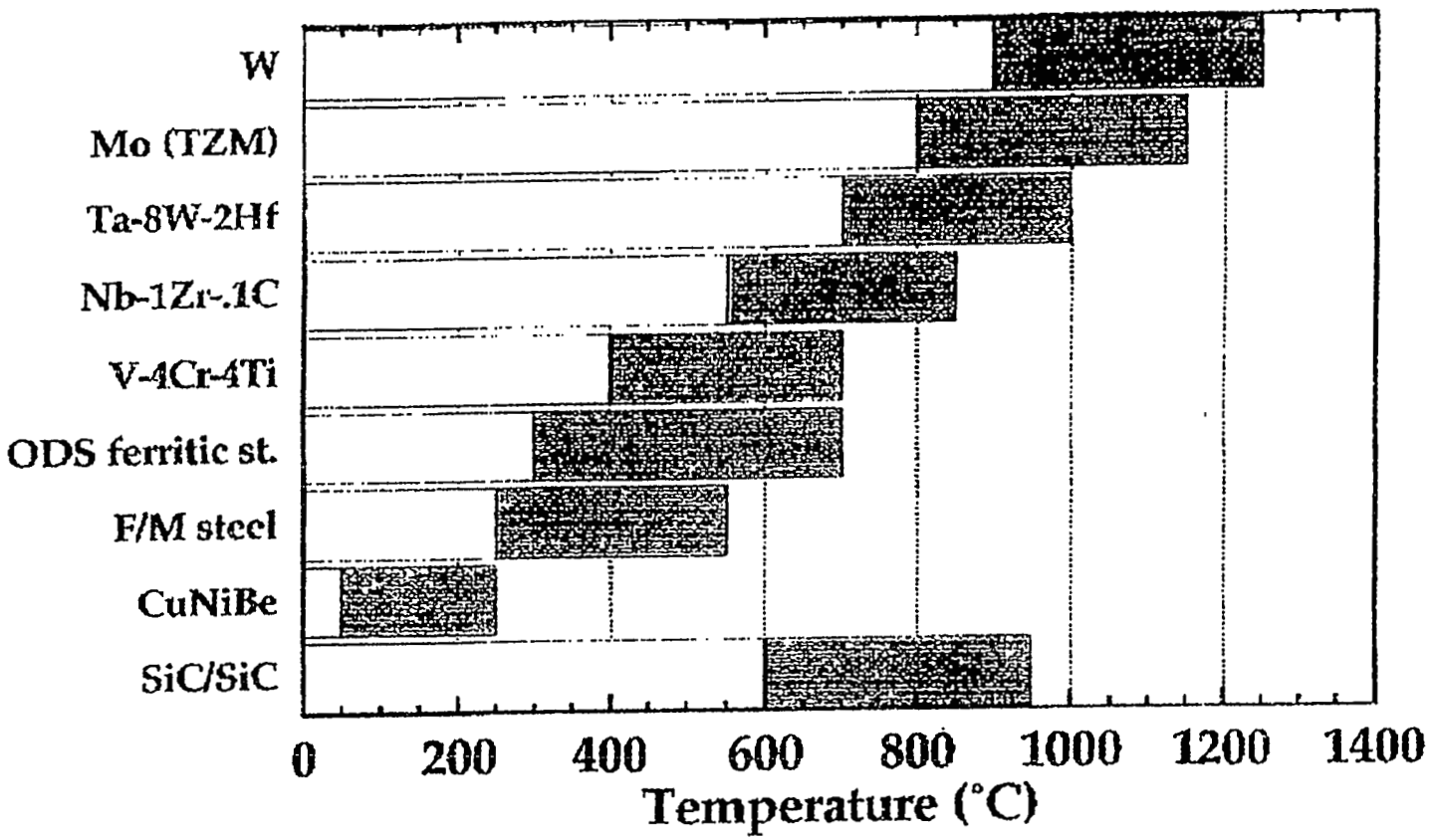

- Lower temperature limit based on radiation hardening/ fracture toughness embrittlement (K_{IC}< ~30 MPa-m$^{1/2}$)—large uncertainty for W due to lack of data
- Upper temperature limit based on 150 MPa creep strength (1% in 1000 h); chemical compatibility considerations may cause further decreases in the max operating temp.

Appendix A

Workshop Agenda

AGENDA:1999 US-JAPAN WORKSHOP ON PLASMA SURFACE INTERACTIONS AND HIGH HEAT FLUX COMPONENTS FOR NEXT FUSION DEVICES

November 1-4, 1999 St. Francis Hotel, Santa Fe, New Mexico

MON	**11/1**			
9:00	I1	10	NYGREN	Welcome & Review of Agenda
9:10	I2	10	ULRICKSON	Introductory Remarks
9:20	I3	10	NODA	Introductory Remarks
			ULRICKSON	**Plasma Edge Studies - 1**
9:30	E1	25	NODA	Helical-Divertor Installation and Its Performance in LHD
9:55	E2	25	NODA	Long Pulse Discharges in LHD
10:20	E3	20	CASTRO	Negative Transferred-Arc Cleaning: A Method for Roughening and Removing Surface Contamination from Plasma Facing Materials
10:40		*break*		
10:50	E4	25	SUZUKI	Structure of Helical Divertor Plasmas in LHD
11:15	E5	25	HIROOKA	Particle Balance Modeling for Steady-state Reactors and Its Application to Recent Observations in LHD
11:40	E6	20	NYGREN	Summary of NSTX PFC Activities and Proposal for Liquid Metal Experiment in CDXU
12:00	E7	25	MASAKI	In-vessel Observation of JT-60U and Its Divertor Modification
12:25		*lunch*		
			NYGREN	**Plasma Edge Studies - 2**
2:00	E8	20	WONG	Recent Results from DiMES
2:20	E9	20	WHYTE	Long Term Evolution of Graphite Tiles in DIII-D
2:40	E10	25	TANABE	W Poloidal Limiter Experiments in TEXTOR-94
3:05	E11	20	*BROOKS*	*Erosion/Redeposition Modeling: Recent Results for Li and C Divertor Surfaces (not presented)*
3:25		break		
			NODA	**Meeting Summaries**
3:35	M1	15	LIVSHITS	Hydrogen Workshop
3:50	M2	15	NYGREN	ISFNT
4:05	M3	15	ZINKLE (NYGREN)	ICFRM
4:20	M4	15	ULRICKSON	SOFE
4:35	D1	15	NYGREN	Discussion: schedule/plans for future meetings
4:50			*adjourn*	
7:00			**reception**	**St. Francis Hotel lobby**

Revised 4nov1999

TUE	**11/2**		***WAMPLER***	***Plasma Surface Interactions - 1***
8:30	S1	25	LIVSHITZ	Implantation Pump in LHD
8:55	S2	25	SUZUKI	Wall pumping in LHD
9:20	S3	20	DOERNER	Plasma-lithium Interaction Measurements in PISCES
9:40	S4	25	YOSHIDA	Impact of Mixed-Material Deposition on Plasma-Surface Interaction
10:05	S5	20	BASTASZ	Deployment of Active Probes & H Sensor in DIII-D
10:25		*break*		
			DOERNER	***Plasma Surface Interactions - 2***
10:35	S6	25	TANABE	Plasma Wall Interactions Observed by Balmer Lines Emission in TPE
11:00	S7	20	*YE*	*Space-Charge Limited Emission Current from Material Surface in a Plasma (not presented)*
11:20	S8	25	ISOBE	Chemical Sputtering with High Flux Ion Beam
11:45	S9	25	ECKSTEIN	Ion Beam Sputtering of Be onto C
12:10	S10	20	WAMPLER	Long Term Retention of Deuterium and Tritium in Alcator C-Mod
12:30		*lunch*		
			DOYLE	***Plasma Surface Interactions - 2 continued***
2:00	S11	20	HAAS	Retention of H in W coated with C
2:20	S12	20	RUBEL	Retention of Hydrogen in TEXTOR Limiters
2:40	S13	20	*HASSANEIN (BROOKS)*	*Recent Progress in Disruption Effects Modeling (not presented)*
3:00	S14	20	FEDERICI	Critical PWI Issues for Plasma Facing Materials and Components in ITER-Class Devices
3:20		*break*		
3:30	D2	120	NYGREN	**Discussion: What PSI issues are most important for future development of fusion?**
5:30		*adjourn*		

1999 US-Japan Workshop on PSI and HHF Components in Next Fusion Devices

WED	**11/3**		***YOUCHISON***	***Plasma Facing Components - 1***
8:30	P1	30	CHIOCCHIO	Development of HHF Components for the RTO/RC-ITER Divertor: Recent Results and Further R&D Plans
9:00	P2	30	AKIBA	Overview of Development of High Heat Flux Components in JAERI
9:30	P3	20	NYGREN	HHF Testing of W Brush Armor Mockups
9:50	P4	20	RUBEL	Damage of W and Mo Limiters
10:10	P5	25	HATANO	Heating Test of Reduced Activation Ferritic Steel F-82H First Wall
10:35		*break*		
			WONG	***Plasma Facing Components - 2***
11:00	P6	25	NISHIKAWA	Effects of divertor plasma on the pebble fall for pebble divertor concept
11:25	P7	25	ISOBE	Experiment of pebble divertor
11:50	P8	20	YOUCHISON	CHF Testing Results from PMTF
12:10	P10	20	CIRIC	JET NB Dump Performance
12:30		*lunch*		
			NYGREN	***Plasma Facing Components - 3***
2:30	P11	25	AKIBA/ ESATO	Thermal-hydraulics of Sawtooth-finned Cooling Tubes
2:55	P12	20	BAXI (WONG)	Thermal-hydraulic Analysis of FIRE Divertor
3:15	*D3*	60	NYGREN	**Discussion: What is direction of PFC development for fusion?**
4:15		*break*		
4:30	*D4*	60	NYGREN	**Discussion: What are productive directions to develop this workshop?**
5:30			adjourn	

Revised 4nov1999

THUR	**11/4**		***NYGREN***	***PFC Armor and Materials***
9:00	C1	25	TOKUNAGA	Research and Development of Tungsten-Coated Divertor Plate
9:25	C2	25	KURAMADA	Evaluation of Integrity for Carbon Divertor Model Joined with Copper by using Ti Foil
9:50	C3	20	NYGREN	HHF Testing of NSTX and KSTAR CFCs
10:10		*break*		
10:20	C4	20	ZINKLE (NYGREN)	Development of a Tungsten Alloy Data Base for APEX
			NYGREN	***Collaborations***
10:40	F1	15	NYGREN	Future collaborations in US program
10:55	F2	15	NODA	Future collaborations in Japanese program
11:10	F3	5	NODA	closing remarks
11:15	F4	5	NYGREN	closing remarks
11:20			*adjourn*	

Appendix B

List of Participants And Addresses

List of Participants

Masato AKIBA
Phone: +81-294-38-5038
Fax: +81-294-38-5047

Japan Atomic Energy Research Institute
2-2-2 Uchisaiwai-cho
Chiyoda-ku, 100-0011, Tokyo, JAPAN
e-mail: akiba@naka.jaeri.go.jp

Bob BASTASZ
Phone: 510-294-2013
Fax: 510-294-3231

Sandia National Laboratories, MS9162
P.O. Box 969
Livermore, CA 94551, USA
e-mail: bastasz@ca.sandia.gov

Sam BERK
Phone: 301-903-4171
Fax: 301-903-1233

US Department of Energy
Office of Energy Research
ER-52, Germantown
Washington, DC 20585, USA
e-mail: sam.berk@mailgw.er.doe.gov

Rich CASTRO
Phone: 505-667-5191
Fax:

Los Alamos National Laboratory
MST-6, Materials Technlogy – Metallurgy
P.O. Box 1663
Los Alamos, NM, 87545, USA
e-mail: rcastro@lanl.gov

Stefan CHICCHIO
Phone: +49-89-3299-4107
Fax: +49-89-3299-4110

International Thermonuclear Experimental Reactor GWS
Boltzmannstr. 2
Garching, D-85748, GERMANY
Chiccs@itereu.de

Dragoslav CIRIC
Phone: +44-1235-464570
Fax: +44-1235-464838

JET Joint Undertaking
Oxon, OX14 3 EA
Abingdon, UNITED KINGDOM
e-mail: dcir@jet.uk

Russ DOERNER
Phone: 619-534-7830
Fax: 619-534-7716

University of California at San Diego
9500 Gilman Drive, Building 302
La Jolla, CA 92093-0035, USA
e-mail: rdoerner@fusion.ucsd.edu

Barney DOYLE
Phone: 505-844-7568
Fax: 505-844-7775

Sandia National Laboratories
Mail Stop 1056
Albuquerque, NM 87185, USA
e-mail: bldoyle@sandia.gov

Gianfranco FEDERICI
Phone: +49-89-329-94228
Fax: +49-89-329-04110

International Thermonuclear Experimental Reactor (ITER)
Boltzmannstr. 2
Garching, 85748, GERMANY
e-mail: federig@ipp.mpg.de

Toshihisa HATANO
Phone: +81-29-270-7570
Fax: +81-29-270-7539

Japan Atomic Energy Research Institute
Department of Fusion Engineering Research
Naka Fusion Research Establishment
801-1 Mukoyama
Naka-machi, Naka-gun
Ibaraki-ken, 311-0193, JAPAN

Yoshi HIROOKA
Phone: 619-534-9720
Fax: 619-534-7716

University of California at San Diego
9500 Gilman Drive, Building 302
La Jolla, CA 92093-0035, USA
e-mail: yhirooka@fusion.ucsd.edu

Michiro ISOBE
Phone: 81-6-687-7511
Ext. 3699
Fax: 81-6-6879-7867

Osaka University
Graduate School of Engineering
2-1 Yamahda-oka, Suita-shi
Osaka, 565-0871, JAPAN
e-mail: mi@ppl.eng.osaka-uac.jp

Akira KURUMADA
Phone: 81-294-38-5038
Fax: 81-294-38-5047

Ibaraki University
Faculty of Engineering
4-12-1, Nakanarusawa-town,
Hitachi-city, Ibaraki-prefecture, 316-8511, JAPAN
e-mail: kurumada@mech.ibaraki-ac.jp

Dr. Kei MASAKI
Phone: +81-29-270-7432
Fax: +81-29-270-7449

Japan Atomic Energy Research Institute
801-1 Mukouyama
Naka-machi, Naka gun
Ibaraki-ken, JAPAN 311-01
e-mail: masakik@fusion.naka.jaeri.go.jp

Masahiro NISHIKAWA
Phone: +81-6-6879-7234
Fax: +81-6-6879-7235

Osaka University
Graduate School of Engineering
Osaka, 591-8011, JAPAN
e-mail: nisikawa@ppi.eng.osaka-u.ac.jp

Richard NYGREN
Phone: 505-845-3135
Fax: 505-845-3130

Sandia National Laboratories, MS1129
Fusion Technology Department, 6428
Albuquerque, NM, 87185-1129, USA
e-mail: renygre@sandia.gov

Marek RUBEL
Phone: +46-8-16-10061
Fax: +46-8-15-8674

Alfven Laboratory
Royal Institute of Technology
Teknikringen, Stockholm, S-100 44 SWEDEN
e-mail: rubel@msi.se

Hajime SUZUKI
Phone: 81-572-58-2148
Fax: 81-572-58-2618

National Institute for Fusion Science
322-6 Oroshi-cho
Toki-shi, 509-5292, JAPAN
e-mail: hsuzuki@LHD.nifs.ac.jp

Prof. Tetsuo TANABE
Phone: 81-52-789-5157
Fax: 81-52-789-5177

Nagoya University
Department of Energy Engineering and Science
Nagoya, 464-8603, JAPAN
tanabe@cirse.magoya-u.ac.jp

Kazutoshi TOKUNAGA
Phone: 81-92-583-7986
Fax: 81-92-583-7690

Kyushu University
Kasuga-koen, kasuga-shi
Fukuoka, 816-0942, JAPAN
e-mail: tokunaga@riam.kyushu-u.ac.jp

Michael ULRICKSON
Phone: 505-845-3020
Fax: 505-845-3130

Sandia National Laboratories
Mail Stop 1129
Albuquerque, NM, 87185, USA
e-mail: maulric@sandia.gov

Bill WAMPLER
Phone: 505-844-7775
Fax: 505-844-8985

Sandia National Laboratories
Mail Stop 1056
Albuquerque, NM, 87185 USA
e-mail: wrwampl@sandia.gov

Dennis WHYTE
Phone: 858-436-6576
Fax: 858-534-7716

University of California, San Diego
Fusion Energy Research Program
Mail Code 0417
9500 Gilman Drive
La Jolla, CA 920-930417 USA

Clement WONG
Phone: 619-454-4258
Fax: 619-454-2266

General Atomics
P.O. Box 85608
San Diego, CA 92186-5608 USA
e-mail: won@gav.gat.com

Prof. Naoaki YOSHIDA
Phone: 81-92-583-7716
Fax: 81-92-583-7690

Research Institute for Applied Mechanics
Kyushu University
6-1 Kasugakoen, Kasuga, Fukuoka 816-8580
JAPAN
e-mail: yoshida@riam.kyushu-u.ac.jp

Dennis YOUCHISON
Phone: 505-845-3138
Fax: 505-845-3130

Sandia National Laboratories
Mail Stop 1129
Albuquerque, NM 87185, USA
e-mail: dlyouch@sandia.gov

DISTRIBUTION

DISTRIBUTION

1 Mohamed ABDOU
University of California, Los Angeles
Mechanical & Aerospace Engineering
Department
44-114 Engineering IV
Box 951597
Los Angeles, CA 90095-1597, USA

1 Dr. Masato AKIBA
Japan Atomic Energy Research Institute
2-2-2 Uchisaiwai-cho
Chiyoda-ku, 100-0011, Tokyo, JAPAN

1 Charles BAKER
University of California, San Diego
9500 Gilman Drive
La Jolla, CA 92093, USA

1 Chandu BAXI
General Atomics
P.O. Box 85608
San Diego, CA 92186-5608, USA

1 Rainer BEHRISCH
Max Planck Instit fuer Plasmaphysik
D-85748, Garching, GERMANY

2 Samuel E. BERK
Facilities and Enabling Technologies Division
Office of Fusion Energy Sciences
Office of Science (SC-52)
US Department of Energy
Washington, DC 20585, USA

1 Jeffrey BROOKS
Argonne National Laboratory
Fusion Power Program
9700 S. Cass Avenue
Argonne, IL 60439, USA

1 Rich CASTRO
Los Alamos National Laboratory
MST-6, Materials Technology – Metallurgy
P.O. Box 1663
Los Alamos, NM, 87545, USA

1 Stefan CHICCHIO
International Thermonuclear Experimental
Reactor GWS
Boltzmannstr. 2
Garching, D-85748, GERMANY

1 Dragoslav CIRIC
JET Joint Undertaking
Oxon, OX14 3 EA
Abingdon, UNITED KINGDOM

1 Robert CONN
University of California at San Diego
9500 Gilman Drive, Building 302
La Jolla, CA 92093-0035, USA

1 James DAVIS
University of Toronto
21 King's College Circle
Toronto, Ontario M5S 3J3, CANADA

1 Russ DOERNER
University of California at San Diego
9500 Gilman Drive, Building 302
La Jolla, CA 92093-0035, USA

1 Daniel DRIEMEYER
The Boeing Company
MS S106 7211
P.O. Box 516
St. Louis, MO 63166, USA

1 Wolfgang ECKSTEIN
Institute of Plasma Physics
Max-Planck-Institut fur Plasmaphysik
Boltzmannstrasse 2
D-85748 Garching b. Munchen, GERMANY

1 Gianfranco FEDERICI
ITER Garching Joint Work Site
Max-Planck-Institut fur Plasmaphysik
Boltzmannstrasse 2
D-85748 Garching bei Munchen, GERMANY

1 Anthony HAASZ
University of Toronto
21 King's College Circle
Toronto, Ontario M5S 3J3, CANADA

2 Ahmed HASSANEIN
Argonne National Laboratory
Fusion Power Program
9700 S. Cass Avenue
Argonne, IL 60439, USA

1 Toshihisa HATANO
Japan Atomic Energy Research Institute
Department of Fusion Engineering Research
Naka Fusion Research Establishment
801-1 Mukoyama
Naka-machi, Naka-gun
Ibaraki-ken, 311-0193, JAPAN

1 Yoshi HIROOKA
National Institute for Fusion Science
322-6 Oroshi-cho, Toki 509-52, JAPAN

1 Michiro ISOBE
Osaka University
Graduate School of Engineering
2-1 Yamahda-oka, Suita-shi
Osaka, 565-0871, JAPAN

1 Prof. Satoshi ITOH
Advanced Fusion Research Center
Research Institute for Applied Mechanics
Kyushu University
87, Kasuga 816, JAPAN

1 Dr. Y. KUBOTA
National Institute for Fusion Science
322-6 Oroshi-cho, Toki-shi 509-5292, JAPAN

1 Henry KUGEL
Princeton Plasma Physics Laboratory
P.O. Box 451
Princeton, NJ 08543-0451

1 Akira KURUMADA
Ibaraki University
Faculty of Engineering
4-12-1, Nakanarusawa-town,
Hitachi-city, Ibaraki-prefecture, 316-8511, JAPAN

1 Bruce LIPSCHULTZ
Massachusetts Institute of Technology
Plasma Science and Fusion Center
Room No. 17-103
77 Massachusetts Avenue
Cambridge, MA 02139, USA

1 Alexander LIVSHITS
Bonch-Bruyevich University
61 Moika, Street
Petersburg, 191186, Russia

1 Stan LUCKHARDT
University of California, San Diego
9500 Gilman Drive
La Jolla, CA 92093, USA

1 Richard MAJESKI
Princeton Plasma Physics Laboratory
P.O. Box 451
Princeton, NJ 08543-0451

1 Dr. Kei MASAKI
Japan Atomic Energy Research Institute
801-1 Mukouyama
Naka-machi, Naka gun
Ibaraki-ken, 311-01 JAPAN

1 Dr. S. MASUZAKI
National Institute for Fusion Science
322-6 Oroshi-cho, Toki-shi 509-5292, JAPAN

1 Richard MATTAS
Argonne National Laboratory
Fusion Power Program
9700 S. Cass Avenue
Argonne, IL 60439, USA

1 Kathy McCARTHY
Idaho National Engineering Laboratory (INEL)
Fusion Safety Program
P.O. Box 1625 (MS 3880)
Idaho Falls, ID 83415-3880

1 Dale MEADE
Princeton Plasma Physics Laboratory
P.O. Box 451
Princeton, NJ 08543-0451, USA

1 Peter K. MIODUSZEWSKI
Fusion Energy Division
Oak Ridge National Laboratory
P. O. Box 2009
Oak Ridge, TN 37831-8070, USA

1 Ralph MOIR
Lawrence Livermore National Laboratory
Magnetic Fusion Energy Division
P.O. Box 808 (L-637)
Livermore, CA 94551-9900

1 Dr. T. MORISAKI
National Institute for Fusion Science
322-6 Oroshi-cho, Toki-shi 509-5292, JAPAN

1 Neil MORLEY
University of California, Los Angeles
43-133 Engineering IV
405 Hilgard Avenue
Los Angeles, CA 90024-1597, USA

1 Prof. Osamu MOTOJIMA
National Institute for Fusion Science
322-6 Oroshi-cho, Toki 509-52, JAPAN

1 Farouk NAJMABADI
University of California at San Diego
9500 Gilman Drive, Building 302
La Jolla, CA 92093-0035, USA

1 Hiroo NAKAMURA
Japan Atomic Energy Research Institute/ITER
801-1 Mukouyama
Naka-machi, Naka gun
Ibaraki-ken, 311-01, JAPAN

1 Prof. M. NISHIKAWA
Osaka University
Department of Electronic, Information Systems, and
Energy Engineering
Graduate School of Engineering
2-1 Yamada-Oka, Suita, Osaka 565-0871, JAPAN

1 Prof. Nokuaki NODA
National Institute for Fusion Science
322-6 Oroshi-cho, Toki-shi 509-5292, JAPAN

1 Dr. Noriyasu OHNO
Nagoya University
Department of Energy Engineering and Science
Graduate School of Engineering
Nagoya, 464-8603, JAPAN

1 Shigeki OHTSU
University of Tokyo
Dept. of Quantum Eng. & Systems Science
7-3-1 Hongo Bunkyo-ku Tokyo, 113, JAPAN

1 Dr. N. OHYABU
National Institute for Fusion Science
322-6 Oroshi-cho, Toki-shi 509-5292, JAPAN

1 Erol OKTAY
U.S. Department of Energy
Office of Fusion Energy Sciences, G256/66
19901 Germantown Road
Germantown, Maryland 20874-1290

1 Martin PENG
Princeton Plasma Physics Laboratory
P.O. Box 451
Princeton, NJ 08543-0451, USA

1 Marek RUBEL
Alfven Laboratory
Royal Institute of Technology
Teknikringen, Stockholm, S-100 44 SWEDEN

1 Dave RUZIC
University of Illinois
Fusion Studies Laboratory
100 Nuclear Engineering Laboratory
103 South Goodwin Avenue
Urbana, IL 61801-2984, USA

1 Dr. Akio SAGARA
National Institute for Fusion Science
Research Operations Division, LHD Project
Shimoishi-cho-322-6, Toki-shi, 509-52, JAPAN

1 Lance SNEAD
Oak Ridge National Laboratory
P.O. Box 2008
Oak Ridge, TN 37831

1 Ron STAMBAUGH
General Atomics
Fusion Group
P.O. Box 85608
San Diego, CA 92186-5608, USA

1 Hajime SUZUKI
National Institute for Fusion Science
322-6 Oroshi-cho
Toki-shi, 509-5292, JAPAN

1 Dai Kai SZE
Argonne National Laboratory
9700 South Cass Avenue, Bldg. 207
Argonne, IL 60439, USA

1 Prof. S. TAKAMURA
Nagoya University
Department of Energy Engineering and Science
Graduate School of Engineering
Nagoya, 464-8603, JAPAN

1 Prof. Tetsuo TANABE
Nagoya University
Department of Energy Engineering and Science
Nagoya, 464-8603, JAPAN

1 Mark TILLACK
University of California at San Diego
9500 Gilman Drive
La Jolla, CA 92093, USA

1 Prof. K. TOKUNAGA
Research Institute for Applied Mechanics
Kyushu University
6-1 Kasugakoen, Kasuga, Fukuoka 816-8580, JAPAN

1 Yoshio UEDA
Osaka University
Department of Electronic, Information Systems, and
Energy Engineering
Graduate School of Engineering
Osaka, 591-8011, JAPAN

1 Jon WATKINS
Sandia National Laboratories
C/O General Atomics (GA) 13-350
P.O. Box 85608
San Diego, CA 92186-5608

1 Dennis WHYTE
University of California, San Diego
Fusion Energy Research Program
Mail Code 0417
9500 Gilman Drive
La Jolla, CA 920-930417 USA

1 R. Scott WILLMS
Los Alamos National Laboratory
Fusion Energy Program Office
MS P-24/E526
Los Alamos, NM 87545

1 Clement WONG
General Atomics
P.O. Box 85608
San Diego, CA 92186-5608, USA

1 Minyou YE
Nagoya University
Graduate School of Engineering
Foro-cho, Chikusa-ku
Nagoya, 464-8603, JAPAN

1 Prof. Naoaki YOSHIDA
Research Institute for Applied Mechanics
Kyushu University
6-1 Kasugakoen, Kasuga, Fukuoka 816-8580, JAPAN

1 Steve ZINKLE
Oak Ridge National Laboratory
P.O. Box 2008
Oak Ridge, TN 37831

1	MS0736	T. E. Blejwas, 6400
3	MS1056	B. L. Doyle, 1111 W. R. Wampler, 1111 D. Walsh, 1111
8	MS1129	M. A. Ulrickson, 6428 (1) R. E. Nygren, 6428 (2) D. L. Youchison, 6428 (1) T. J. Tanaka, 6428 (1) 6428 File (3)
4	MS9161	Ken Wilson, 8716 Rion Causey, 8716 Don Cowgill. 8716 Dean Buchenauer, 8716
1	MS9402	Bob Bastasz, 8724
1	MS9402	Ben Odegard, Jr., 8724

1	MS9403	Chuck Cadden, 8240
1	MS9018	Central Technical Files, 8940-2
2	MS0899	Technical Library, 9616
1	MS0612	Review & Approval Desk, 9612 For DOE/OSTI